

NGAL-105-002-105

77097

406P

(NASA-CR-180382) OPTICAL RADIATION FROM
SHOCK-COMPRESSED MATERIALS Ph.D. Thesis
(California Inst. of Tech.) 406 p Avail:
NTIS HC A18/MF A01 CSCL 200

N87-30144

Unclas

G3/70 0099097

Optical Radiation from Shock-Compressed Materials

Thesis by
Robert Frederik Svendsen, Jr.

In Partial Fulfillment of the Requirements
for the Degree of
Doctor of Philosophy

California Institute of Technology
Pasadena, California

1987

(Submitted July 17, 1987)

To Norman, Nancy, Carol and Bob, who have never failed to love me in their own special ways, and to Wendy, who taught me to love and desire that in life which I have, and can have, and not that which I cannot.

Acknowledgements

The words that follow represent the most pleasurable and effortless, yet in many ways the most difficult, part of this thesis. I am deeply grateful to my thesis advisor and friend, Tom Ahrens (alias TJA), for giving me the freedom to explore and the opportunity of personal learning. I sincerely thank Hiroo Kanamori, my academic advisor, for guiding me through class requirements with a minimum of pain and suffering, and a maximum of useful learning. When I first came to Caltech, Barclay Kamb took me on a journey to the worlds of glacialogy, Alaska, and Pear Lake. In the process of finishing my degree, I have lost touch with these worlds, but never the ideas and inspirations. I am sincerely indebted to you, Barclay, for making an investment I have yet to fully repay. In this same vein, Dave Stevenson introduced me to the worlds of condensed matter and "good science." I make no claims for having learned the latter, but his teaching of the former, plus some time and space to wander, lead to much of the work represented in Chapter V. I am deeply grateful to you, Dave, for letting me "borrow" from your work, and giving me the chance to learn it at a snail's pace.

The majority of my thesis consists of experimental work, and none of it would have been possible without the efforts of Papo Gelle, Mike Long, Chuck Manning and Leon Young. Their insight, hard work and willingness to befriend a mere graduate student definitely made the experimental work in this thesis a reality. Thanks also to Bill Barber, Gunther Hahn, Wayne Miller, and the various unsung machinists who helped design and build most of the essential experimental "apparati." I am deeply grateful to my fellow shock-wave connoisseurs, Bill Anderson, Greg Miller, Sally Rigden, Jim Tyburczy, and especially Mark Boslough, Doug Schmitt and Jay Bass, for teaching me what they would, and putting up with what they couldn't. To have your friends as co-workers just can't be beat, but of course, anything wrong with the the experiments in this

thesis is entirely their fault.

To "cornerstones" of the lab, Dee, Nancy, Sue, Virginia, Barbara, Betty, Ann H., Ann F. and Janet, thanks for giving generously, and keeping the larger, more important picture squarely in front of my mind. Also I thank Dorothy Coy for treating me and the other geological and planetary science (GPS) graduate students, and our special needs, with the utmost care, efficiency and compassion.

To the infamous SeismoVAX and its owner, Rob Clayton, I certainly owe many millions of dollars in computer money, and most sincere thanks for regarding shock waves as honorary seismic waves over the last six years. I am indebted to Don Anderson for directing a unique research environment known as the Seismolab, and creating enough niches in this environment to allow even this thesis to be christened "geophysics." And to Bob Sharp, thanks is hardly enough for sharing your vast wisdom, teaching Ge 136, running project Pahoehoe, and for your tireless, selfless efforts on behalf of the GPS graduate students, and their personal and professional education.

I acknowledge and sincerely thank the National Science Foundation, and the National Aeronautics and Space Administration, for financial support of the work represented by this dissertation. Tally ho and away we go!

Abstract

Recent observations of shock-induced radiation from oxides, silicates and metals of geophysical interest constrain the shock-compressed temperature of these materials. In these experiments, a projectile impacts a target consisting of a metal driver plate, metal film or foil layer, and transparent window. We investigate the relationships between the temperature inferred from the observed radiation and the temperature of the shock-compressed film or foil and/or window. Changes of the temperature field in each target component away from that of their respective shock-compressed states occur because of: 1) shock-impedance mismatch between target components, 2) thermal mismatch between target components, 3) surface roughness at target interfaces, and 4) conduction within and between target components. In particular, conduction may affect the temperature of the film/foil-window interface on the time scale of the experiments, and so control the intensity and history of the dominant thermal radiation sources in the target. We use this type of model to interpret the radiation emitted by a variety of shock-compressed materials and interfaces.

In a series of experiments on films ($\sim 1 \mu\text{m}$ thick) and foils ($\sim 10\text{--}100 \mu\text{m}$ thick) of Fe in contact with Al_2O_3 and LiF windows, Fe at Fe- Al_2O_3 interfaces releases from experimental shock-compressed states between 245 and 300 GPa to interface states at pressures between 190 and 230 GPa, respectively, and temperatures between 4000 and 8000 K, respectively. These temperatures are $\approx 200\text{--}1500$ K above model calculations for Fe experiencing no reshock at ideal (smooth) Fe- Al_2O_3 interfaces. We attribute this discrepancy to localized dissipation at the Fe- Al_2O_3 interface, producing higher interface temperatures than uniform compression and energy transfer. This behavior is observed for both Fe foils and films. Both 190 GPa, localized heating due to gaps or interface-surface roughness does not apparently affect the temperature of Fe- Al_2O_3 interfaces. In

contrast, from the same range of shock states, Fe at Fe-LiF interfaces releases to states between 130 and 160 GPa (because it has a lower shock impedance than Al_2O_3); both the data and model imply that Fe-LiF interfaces respond ideally to shock-compression up to 140 GPa (where the data end). Both the Fe- Al_2O_3 data and the model suggest that the degree of reshock and localized heating is strongly pressure-dependent above the solid Fe-liquid Fe phase boundary. LiF appears to be a more ideal window than Al_2O_3 also because it is a poorer thermal inertia (*i.e.*, $k\rho c_p$, where k is the thermal conductivities, ρ is the mass density, and c_p is the specific heat at constant pressure) match to Fe than is Al_2O_3 .

In the absence of energy sources and significant energy flux from other parts of the target, the rate of change of the film/window or foil/window, interface temperature, $dT_{\text{INT}}(t)/dt$, is proportional to $-\mu \exp(-\mu^2)$, where $\mu \equiv \delta_{\text{FW}} / 2\sqrt{\kappa_{\text{F}} t}$, δ_{FW} is the thickness of the high-temperature (reshocked) zone in the film/foil layer at the film/foil-window interface, κ_{F} is the thermal diffusivity of the film/foil material, and $0 \leq t \leq t_{\text{exp}}$ (t_{exp} is the time scale of the experiment, 200-400 ns). On this basis, the temperature of a thin ($\delta_{\text{FW}} \ll 2\sqrt{\kappa_{\text{F}} t_{\text{exp}}}$) reshocked layer relaxes much faster than that of a thick ($\delta_{\text{FW}} \gg 2\sqrt{\kappa_{\text{F}} t_{\text{exp}}}$) layer. We estimate $\sqrt{\kappa_{\text{F}} t_{\text{exp}}} \sim 10 \mu\text{m}$ for Fe under the conditions of Fe- Al_2O_3 and Fe-LiF interfaces at high pressure. In this case, a 100- μm -thick reshocked Fe layer would relax very little, remaining near $T_{\text{INT}}(0)$ on the time scale of the experiment, while a 1- μm -thick reshocked Fe layer would relax on a time scale of $\lesssim 10$ nsec, which is much less than t_{exp} , to a temperature just above $T_{\text{INT}}(\infty)$, *i.e.*, the temperature of the ideal (smooth) interface.

Greybody model fits to radiation from an Fe film- Al_2O_3 interface resolve a gradually increasing effective greybody emissivity, $\hat{\epsilon}_{\text{gb}}(t)$, and a gradually decreasing greybody temperature, $T_{\text{gb}}(t)$. This behavior is characteristic of most

Fe-Al₂O₃ interface experiments. The decrease of $T_{gb}(t)$ can be explained in terms of the reshock model for the film/foil-window interface temperature, $T_{INT}(t)$. For this experiment, the model implies that the thickness of the reshocked film layer, δ_{FW} , is approximately equal to the conduction length scale in the film, $\sqrt{\kappa_F t_{exp}}$ ($\sim 10 \mu\text{m}$ for Fe). Further, assuming 1) $T_{gb}(t) = T_{INT}(t)$, 2) the thermal inertia of the film is an order of magnitude less than the window, and $\delta_{FW} \lesssim 2\sqrt{\kappa_F t_{exp}}$, the greybody constrains the temperature rise due to localized heating through reshock, ΔT_{FW} , to $\lesssim 2000\text{K}$. A slight decrease of the Al₂O₃ absorption coefficient upon shock compression can explain the slight increase of $\hat{\epsilon}_{gb}(t)$ with time; this may be consistent with the low-pressure observation that the refractive index of Al₂O₃ seems to decrease with pressure.

In contrast to the Fe-Al₂O₃ results, greybody fits to radiation from an Fe foil-LiF interface show a relatively constant greybody temperature, and a decreasing greybody emissivity. The constant greybody temperature implies a constant interface temperature, as expected for an interface experiencing minimal reshock, while the decaying $\hat{\epsilon}_{gb}(t)$ is consistent with a shock-induced increase in the absorption coefficient of LiF. Setting $T_{INT}(0) = T_{gb}(0)$, we fit a simplified version of the full radiation model to these data and obtain an estimate of the absorption coefficient ($\sim 100 \text{ m}^{-1}$) of LiF shock-compressed to 122 GPa.

Shock-compressed MgO radiates thermally at temperatures between 2900 and 3700 K in the 170-200 GPa pressure range. A simple energy-transport model of the shocked-MgO-targets allows us to distinguish between different shock-induced radiation sources in these targets and to estimate spectral absorption-coefficients, $a_{\lambda\text{MgO}}$, for shocked MgO (*e.g.*, at 203 GPa, $a_{\lambda\text{MgO}} \sim 6300, 7500, 4200$ and 3800 m^{-1} , at 450, 600, 750 and 900 nm, respectively). The experimentally inferred temperatures of the shock-compressed states of MgO are

consistent with temperatures calculated for MgO, assuming that 1) it deforms as an elastic fluid, 2) it has a Dulong-Petit value for specific heat at constant volume in its shocked-state, 3) it undergoes no phase transformation below 200 GPa, and 4) the product of the equilibrium thermodynamic Grüneisen's parameter, γ , and the mass density, ρ , is a constant and equal to 4729.6 kg/m^3 .

Optical radiation from shock-compressed crystal $\text{CaMgSi}_2\text{O}_6$ (diopside) constrains crystal $\text{CaMgSi}_2\text{O}_6$ Hugoniot temperatures of 3500-4800 K in the 150-170 GPa pressure range, while glass $\text{CaMgSi}_2\text{O}_6$, with a density 87% of that of crystal $\text{CaMgSi}_2\text{O}_6$, achieves Hugoniot temperatures of 3600-3800 K in the 105-107 GPa pressure range. The radiation history of each of these materials implies that the shock-compressed states of each are highly absorptive, with effective absorption coefficients of $\gtrsim 500\text{--}1000 \text{ m}^{-1}$. Calculated Hugoniot states for these materials, when compared to the experimental results, imply that crystal $\text{CaMgSi}_2\text{O}_6$ Hugoniot states in the 150-170 GPa range represent a high-pressure phase (HPP) solid (or possibly liquid) phase with an STP density of $\approx 4100 \pm 200 \text{ kg/m}^3$, STP Grüneisen's parameter of $\approx 1.5 \pm 0.5$ and STP HPP-LPP specific internal energy difference, $\Delta e_i^{\alpha-\beta}$, of $0.9 \pm 0.5 \text{ MJ/kg}$. These results are consistent with a $\text{CaSiO}_3\text{-MgSiO}_3$ perovskite high-pressure phase assemblage. For glass $\text{CaMgSi}_2\text{O}_6$, we have the same range of HPP properties, except that $\Delta e_i^{\alpha-\beta}$ is $2.3 \pm 0.5 \text{ MJ/kg}$, a strong indication that the glass $\text{CaMgSi}_2\text{O}_6$ Hugoniot states occupy the liquid phase in the system $\text{CaMgSi}_2\text{O}_3$. Comparison of the pressure-temperature Hugoniot of crystal $\text{CaMgSi}_2\text{O}_6$ with the Hugoniots of its constituent oxides (*i.e.*, SiO_2 , CaO and MgO) demonstrates the primary influence of the HPP STP density of these materials on the magnitude of the temperature in their shock-compressed states. The crystal Di pressure-temperature Hugoniot constrained by the experimental results lies at 2500-3000 K between 110 and 135 GPa, within the plausible range of temperature profiles in the mantle near the core-mantle boundary.

In the context of the above model considerations, we constrain the Hugoniot temperature of Fe shock-compressed to 300 GPa via thermal radiation from the Fe film/foil-window interfaces discussed above. The temperature of the film/foil-window interface is obtained from measurements of the spectral radiance of the interface, for the duration of the shock transit through the window, using a 4-wavelength optical radiometer. The model indicates that the experimental observations constrain the interface temperature, rather than the temperature of the Al_2O_3 or LiF windows. Our results further imply that Al_2O_3 remains at least partially transparent to at least 230 GPa and $\sim 9,000$ K. Without correcting the Hugoniot temperatures inferred from the interface temperatures for the effects of reshock, we infer a melting temperature of Fe along its Hugoniot of 6700 ± 400 K at 243 GPa. Combining these estimates with the lower-pressure (≤ 100 GPa) static Fe melting data of Williams and Jeanloz (1986), we infer a melting temperature for Fe of approximately 7800 ± 500 K at the pressure of the Earth's outer-inner boundary. Assuming that Fe or an Fe-light element alloy is forming the inner core from an Fe-light element mixture in the liquid outer core, this temperature also represents an upper bound to the temperature at the outer-inner core boundary.

Liquid-state and solid-state model fits to melting data for Fe, FeS and FeO provide constraints for calculating ideal phase relations in Fe-FeS and Fe-FeO systems in the pressure range corresponding to the earth's outer core. The liquid-state model fit to the Fe melting data of Williams and Jeanloz (1986) places constraints on the temperature and other properties along the liquidus above the range of their data. The temperature along the best-fit Fe liquidus is 5000 K at 136 GPa and 7250 K at 330 GPa, which is somewhat lower than that implied by the Hugoniot results (~ 7800 K). This discrepancy may be due to the reshock effect discussed above, or some inaccuracy in the extrapolation, presuming the Hugoniot results represent the equilibrium melting behavior of

Fe. Constraints on the solidi of FeS and FeO from the comparison of data and solid-state model calculations imply that FeS and FeO melt at approximately 4610 K and 5900 K, respectively, at 136 GPa, and approximately 6150 K and 8950 K, respectively, at 330 GPa. Calculations for the equilibrium thermodynamic properties of solid and liquid Fe along the coincident solidus and liquidus imply that the entropy of melting for Fe is approximately independent of pressure at a value of approximately R (where R is Ryberg's constant), while the change in the molar heat capacity across the transition increases with pressure from approximately $0.5 R$ to $4R$ between standard pressure and 330 GPa. We use these constraints to construct ideal-mixing phase diagrams for Fe-FeS and Fe-FeO systems at outer core pressures, assuming that Fe and FeS, or Fe and FeO, respectively, are the solid phases in equilibrium with the liquid Fe-FeS or Fe-FeO mixtures, respectively. The composition of the Fe-X ($X=O$ or S) liquid mixture relative to the eutectic composition of the Fe-FeX system determines whether Fe or FeX will solidify at the liquidus. For these ideal mixing calculations, the eutectic composition is controlled by the ratio of the end-member (*i.e.*, Fe and FeX) melting temperatures at a given pressure. If Fe and FeX have the same melting temperature, for example, the eutectic composition is 25 mole % X; if the melting temperature of FeX is greater or less than Fe, the eutectic composition will be displaced to more Fe or FeX rich compositions, respectively. Since, as quoted above, the melting temperature of FeO is about 1500 K greater than that of Fe at 330 GPa, which is in turn about 1000 K greater than that of FeS at this pressure, we note that calculated Fe-FeO eutectic compositions at 330 GPa (15-20 mole % O) are less than 25 mole % O, while calculated Fe-FeS eutectic compositions at 330 GPa (23-30 mole % S) are generally greater than 25 mole % S. The mass density of the Earth's outer core just above the inner core boundary is approximately 12160 kg/m^3 , and we note that this is also the density of an ideal mixture of 93 mole % Fe and 7 mole %

S (*i.e.*, 14 mole % FeS), and a similar mixture of approximately 72 mole % Fe and 28 mole % O (56 mole % FeO). Consequently, these calculations and considerations imply that an O-rich outer core is more likely to lie on the FeO-rich side of the Fe-FeX eutectic, while an S-rich outer core is more likely to lie on the Fe-rich side of the Fe-FeX eutectic.

The temperature of the Fe-FeS eutectic are lower than the Fe-FeO eutectic, being approximately 5000 K at 330 GPa. Note that the eutectic temperature represents a lower bound to temperatures at the outer-inner core boundary under the hypothesis that this boundary represents the liquidus in an Fe-X mixture. Eutectic and end-member melting temperatures in both the Fe-FeS and Fe-FeO systems imply, in the context of the outer-inner core boundary-phase boundary hypothesis, that previous widely-accepted temperature profiles for the outer core, ranging from $\lesssim 3000$ K at the 136 GPa, the core-mantle boundary, to $\lesssim 4200$ K at 330 GPa, the outer-inner core boundary, are about 1000-1500 K too low. This possibility implies that at least one boundary layer of 1000-1500 K exists in the mantle, possibly at its base in the D'' region.

Table of Contents

Acknowledgements	iii
Abstract	v
Table of Contents	xii
List of Figures	xiii
List of Tables	xvi
Introduction: Shock Compression and Continuum Mechanics	1
Chapters:	
I. Optical Radiation from Shock-Compressed Materials and Interfaces ...	18
1. Introduction	21
2. Model Considerations	22
3. Model Assumptions	29
4. Initial Conditions	32
4.1 Shock-Compressed State	32
4.2 Release-Reshock States	53
4.3 Application to Fe Targets	64
5. Conductive Transport in the Target	71
6. Radiative Transport in the Target	89
7. Models and Data	93
8. Summary	111
9. Appendix A. Equilibrium Thermodynamics and Shock Compression	116
A.1 Solid-State Model	117
A.2 Connection of Hugoniot and Isentrope	120
A.3 Relations between Isentropic and Hugoniot Properties	122
10. Appendix B. Isentropic Release and Reshock	128
B.1 Phase Transition during Release	1129
B.2 Complete Release and Reshock	134
11. Appendix C. Energy Transport in the Target	140
12. Appendix D. Conductive Transport Model	152
13. Appendix E. Radiative Transport Model	164

14. References	175
II. Shock-Induced Temperatures of MgO	182
1. Introduction	183
2. Experimental	185
3. Model Calculations and Data Analysis	189
4. Discussion	221
5. Summary	229
6. References	231
III. Shock-Induced Temperatures of CaMgSi₂O₆	238
1. Introduction	240
2. Experimental	240
3. Data Analysis	242
4. Hugoniot Calculations and Comparison with Data	256
5. Discussion	267
6. Summary	271
7. References	271
IV. The Temperatures of Shock Compressed Iron	277
1. Introduction	278
2. Experimental Method	282
3. Results	287
4. Discussion	296
5. References	303
V. Ideal Fe-FeS, Fe-FeO Phase Relations and The Earth's Core	307
1. Introduction	309
2. High Pressure Liquid-State Model for Fe	311
3. Solid-State Model and Hugoniot Calculations	323
4. Fe-FeO, Fe-FeS Phase Diagrams and Implications for the Core	343
5. Summary	360

6. Appendix A. Liquid-State Equilibrium Thermodynamic Model	364
7. Appendix B. High-Temperature Solid-State Model	379
8. References	383

List of Figures

Chapter I:

2.1 Target assembly	23
2.2 Schematic target radiation history	27
4.1 Equations of state: isentropic specific internal energy	40
4.2 Equations of state: isentropic pressure	51
4.3 Specific heat models and Hugoniot temperature	56
4.4 Effect of compression on Lindemann phase boundary	62
4.5a Release and reshock temperatures for Fe-Al ₂ O ₃ targets	65
4.5b Release and reshock temperatures for Fe-LiF targets	67
5.1 Initial conditions for conductive transport in target	73
5.2a Temperature profiles for constant reshock layer thickness	80
5.2b	80
5.3a Temperature profiles for constant Peclet number	82
5.3b	82
5.4a Temperature profiles with varying Peclet number.....	84
5.4b	84
5.5a Temperature profiles with Peclet of 10.....	86
5.5b	86
7.1a Spectral radiance history of an Fe-Al ₂ O ₃ target	97
7.1b Chi-square of greybody fit to spectral radiance history	97
7.1c Greybody effective normal emissivity of Fe-Al ₂ O ₃ target	97
7.1d Greybody temperature of Fe-Al ₂ O ₃ target	97
7.2a Spectral radiance history of an Fe-Al ₂ O ₃ target	100
7.2b Chi-square of greybody fit to spectral radiance history	100
7.2c Greybody effective normal emissivity of Fe-Al ₂ O ₃ target	100
7.2d Greybody temperature of Fe-Al ₂ O ₃ target	100
7.3 Confidence limits on greybody fit to data of Figure 7.1a	104
7.4 Confidence limits on greybody fit to data of Figure 7.2a	106

7.5	Fit for effective normal absorption coefficient of shocked LiF	109
7.6	Reshock temperature versus reshock layer thickness	112

Chapter II:

2.1	Geometry of light-gas gun shock-induced radiation experiment	186
3.1	Radiation history at 750 nm for shot 146	189
3.2	Spectral radiance data for shot 146	190
3.3	Thermal-inertia mismatch at Ta-Ag and Ag-MgO interfaces	202
3.4	Model Ag-MgO interface temperature histories	206
3.5a	Radiation model fits to data at 600 nm	209
3.5b	Radiation model fits to data at 750 nm	209
3.6a	Greybody model fits to shot 145 data	218
3.6b	Greybody model fits to shot 146 data	218
3.7a	Greybody effective emissivity of shot 146 data	222
3.7b	Greybody temperature of shot 146 data	222
4.1	Hugoniot temperature of MgO and related materials	227

Chapter III:

2.1	Geometry of light-gas gun shock-induced radiation experiment	241
3.1a	Radiation history at 750 nm for shot 197, Di glass	245
3.1b	Radiation history at 750 nm for shot 146, Di crystal	246
3.2a	Greybody model fits to shot 140 data	252
3.2b	Greybody model fits to shot 169 data	252
3.2c	Greybody model fits to shot 197 data	252
4.1a	Comparison of model shock temperatures and data	262
4.1b	262
4.1c	262
5.1	Hugoniot Temperature of $\text{CaMgSi}_2\text{O}_6$ and Related Materials	269

Chapter IV:

1.1	Effect of a phase boundary on Hugoniot	279
2.1	Shock-induced radiation detection system	284
2.2	Target geometry	285

3.1 Typical radiation histories at 450, 600, 750 and 900 nm	289
3.2 Typical greybody model fits to spectral radiance data	292
4.1 Fe shock temperature results	298

Chapter V:

2.1a Liquid-state model fits to Fe melting data	318
2.1b	318
2.2a Effect of variable packing fraction on liquid-state fits	324
2.2b	324
3.1 Solid-state model fits to Fe, FeS and FeO melting data	336
3.2 Fe Hugoniot-melting curve intersection	339
4.1 End-member melting temperatures and eutectic composition	348
4.2 End-member melting temperatures and eutectic temperature	350
4.3a Ideal Fe-FeO phase relations at 136 GPa	353
4.3b Ideal Fe-FeS phase relations at 136 GPa	353
4.4a Ideal Fe-FeO phase relations at 330 GPa	357
4.4b Ideal Fe-FeS phase relations at 330 GPa	357
4.5 Melting temperatures and the earth's core	361

List of Tables**Chapter I:**

4.1 Standard Temperature-Pressure (STP) Parameters	44
5.1 STP and High-Pressure Thermal-Inertia Mismatch Estimates	77
7.1 Simplified Radiation Model Parameters	110
C.1 Order-of-Magnitude Shock Compression/Release Parameters	146

Chapter II:

3.1 Standard Temperature-Pressure (STP) Parameters	196
3.2 Model Parameter Estimates for MgO Experiments	201
3.3 Thermal-Inertia Mismatch Estimates at STP and High-Pressure ...	204
3.4 Radiation Model Parameters for Shot 146	212
3.5 Greybody Fits to Radiation Data at t_r	217

4.1 Experimental Results and Model Estimates	229
--	-----

Chapter III:

2.1 Microprobe Analyses of Starting Materials	243
3.1 Radiation Data and Fits	247
4.1 Standard Temperature-Pressure (STP) Parameters	257
4.2 CaMgSi ₂ O ₈ STP Parameters	266
5.1 Experimental Results and Model Estimates	268

Chapter IV:

4.1 Experimental Results	297
--------------------------------	-----

Chapter V:

2.1 Standard-Pressure (0.1 MPa) Liquid Fe Properties	322
3.1 High-Pressure Phase STP Properties of Fe, FeS and FeO	333
3.2 High-Pressure Solid and Liquid Fe Model Properties	342

Introduction: Shock Compression and Continuum Mechanics

In this thesis I explore certain aspects of the thermomechanical response of selected silicates, oxides and metals of geophysical interest to shock compression, via observations of shock-induced optical radiation from these materials. Although microscopic processes lie at the heart of each phenomenon, the experimental foundation of our work requires an interpretive, conceptual framework much more abstract and general than any particular microscopic physical theory can provide. This framework is provided by continuum mechanics, which enfolds and abstracts the "physics" of countless microscopic models and viewpoints, via their appropriate macroscopic (*e.g.*, thermodynamic) limit. With this framework, we have a representation of the phenomena partial to no particular "microphysics," and so accessible to all. The purpose of this introduction is to outline and detail the continuum framework we use to represent and interpret experimental results on shock-compressed materials.

In our experiments, a projectile impacts a target at velocities between 4.5 and 6.5 km/s, generating a shock wave in the target. This target is usually composed of two or three different materials sandwiched together in a plane-layer-style geometry (see Figure 2.1, Chapter I). From the physical viewpoint, the shock wave is a three-dimensional region with some thickness δ (typically $\lesssim 10^{-8}$ m in the materials of interest here: Kormer, 1968), and propagates through the material with a velocity of propagation \mathbf{u} (typically $|\mathbf{u}| \sim 10^{3-4}$ m/s). Shock compression produces large (factor of 2 to orders of magnitude) changes in any given local thermomechanical (TM) field, *i.e.*, TM field density, ψ (*e.g.*, mass density, ρ ; note that ψ may be a scalar, vector or higher-order tensor in what follows), over δ and on a very short time scale (*i.e.*, $\tau \equiv \delta/|\mathbf{u}| \sim 10^{-11-12}$ seconds), resulting in large gradients ($\sim |\psi|/\delta$) in these TM fields across the shock-front region. We assume that these length and time scales are sufficiently short so that, from the macroscopic viewpoint, they may

be idealized as infinitesimal and instantaneous, respectively. In this case, we may idealize the shock front macroscopically as a moving surface, which we designate as $\Sigma = \Sigma(t)$. This surface divides the material, which we idealize as a body $B = B(t)$, with material boundary $\partial B = \partial B(t)$, occupying the spatial volume $V = V(t)$ in Euclidean three-space, with spatial boundary $\partial V = \partial V(t)$, into spatial regions "ahead" (+ region, Figure I.1a) and "behind" (- region, Figure I.1a) the shock front. This surface representation for the shock front is defined by the limit $\delta \rightarrow 0$, and we note that, in this limit, the gradients of ψ across the shock front (mathematically) become infinite. Consequently, ψ loses a continuous representation in V , being (mathematically) discontinuous across Σ in this representation. In this case, the surface Σ is referred to as singular (Truesdell and Toupin, 1960, Sect. 173) with respect to ψ , such that

$$[[\psi]] \equiv \psi^- - \psi^+ \neq 0 \quad [I.1]$$

where $[[\psi]]$ is the "jump" of ψ across Σ , and ψ^+ and ψ^- are the limiting values of ψ "just" ahead and behind Σ , respectively. Note that Σ is oriented such that $\mathbf{u} \cdot \hat{\nu} > 0$, where $\hat{\nu}$ is the unit normal vector to Σ (Figure I.1a), and (\cdot) represents the inner vector product operator. This concept of a singular surface forms the basis for the continuum mechanical description of shock compression. We assume that Σ possesses no fields or properties other than a motion (*i.e.*, \mathbf{u} ; it can be much more complicated). As is commonly done, we write all and higher-order tensors in boldface or component form in what follows, and the summation convention applies for all diagonally-repeated roman or greek indices.

Since ψ usually changes with time during the experiment, we need to formulate relations for how ψ changes with time in V , and across ∂V and Σ , *i.e.*, we need to formulate a balance relation for ψ . We are particularly interested in a balance relation for ψ across Σ when Σ is a shock front, but for now Σ

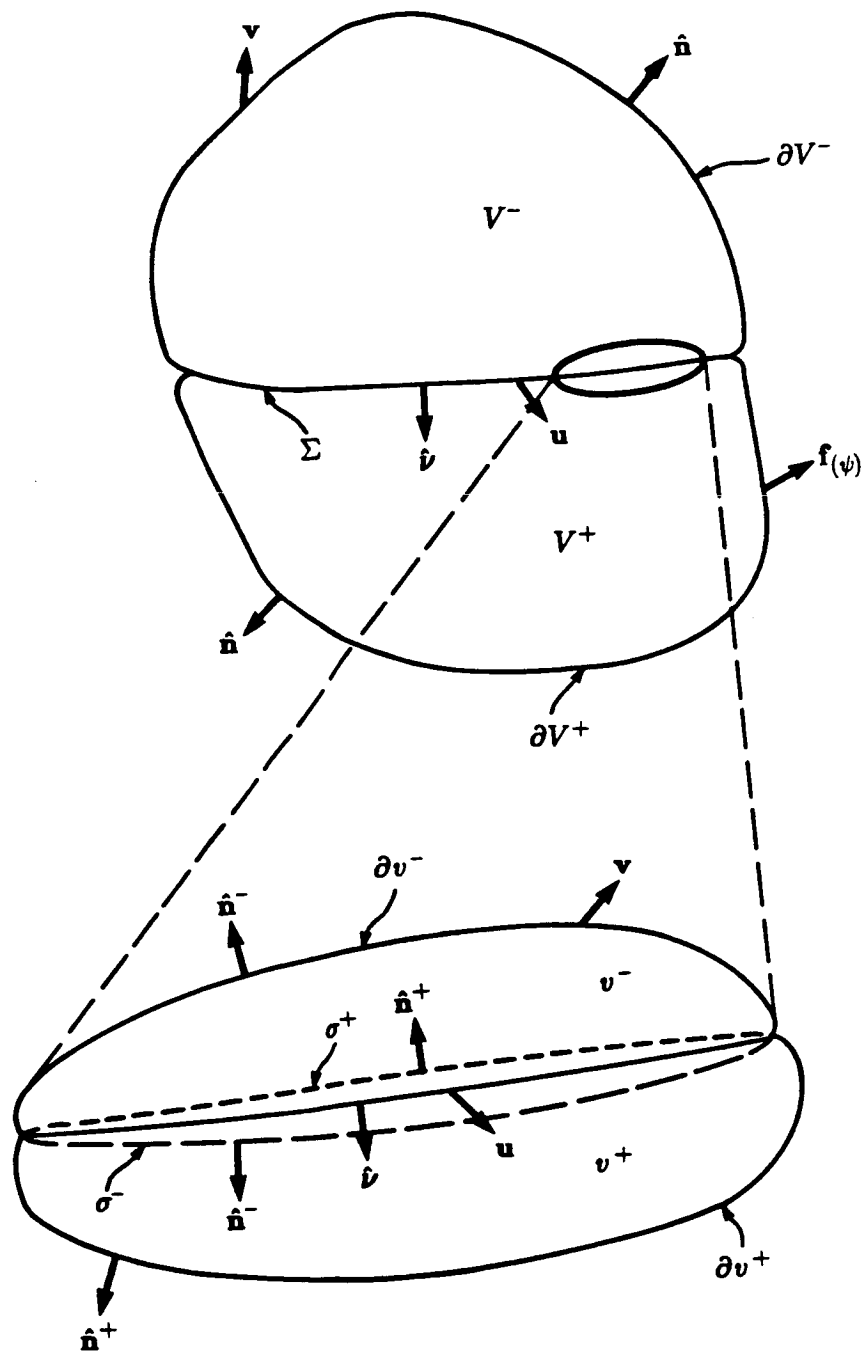


Figure I.1

represents any singular surface for ψ . Now, from the macroscopic-experimental viewpoint, we can really only formulate a balance relation for the total "amount" of ψ in V , *i.e.*,

$$\Psi = \Psi(t) \equiv \int_V \psi dv \quad [I.2].$$

Following the classic approach, we let $B \rightarrow V$ deform and keep track of the instantaneous value of Ψ . In particular, we assume Ψ may change with time via 1) production of ψ in V , *i.e.*,

$$P_{(\psi)} = P_{(\psi)}(t) \equiv \int_V p_{(\psi)} dv \quad [I.3]$$

and 2) the net total transport of ψ out of V through ∂V , *i.e.*,

$$F_{(\psi)} = F_{(\psi)}(t) \equiv \int_{\partial V} \mathbf{f}_{(\psi)} \cdot \hat{\mathbf{n}} da \quad [I.4]$$

In [I.3], $P_{(\psi)}$ is the total production and/or supply, $p_{(\psi)}$ is the production-supply density of ψ in V , which is assumed continuous in V . Also, in [I.4], $F_{(\psi)}$ is the net amount of ψ transported out of V , $\mathbf{f}_{(\psi)}$ is the net efflux of ψ , or flux of ψ out of, V , $\hat{\mathbf{n}}$ is the unit outward normal vector to ∂V , da is an infinitesimal area element on ∂V , and $\mathbf{f}_{(\psi)}$ is assumed continuous on ∂V . With these, the instantaneous rate of change of Ψ in B is represented by the global balance, *i.e.*,

$$\frac{d}{dt} \Psi = P_{(\psi)} - F_{(\psi)} \quad [I.5]$$

or

$$\frac{d}{dt} \int_V \psi dv = \int_V p_{(\psi)} dv - \int_{\partial V} \mathbf{f}_{(\psi)} \cdot \hat{\mathbf{n}} da \quad [I.6]$$

Assuming that ψ and its first partial derivatives are continuous in V , the Reynolds' transport theorem (*e.g.*, Truesdell and Toupin, 1960, Sect. 81) implies

that the change in the total amount of ψ with time is also given by

$$\frac{d}{dt} \int_V \psi dv = \int_V [\partial_t \psi + \nabla \cdot (\psi \mathbf{v})] dv \quad [I.7]$$

In [I.7], ∇ is the spatial gradient operator, and \mathbf{v} is the displacement velocity of the material since V and ∂V instantaneously coincide with B and ∂B , by definition. In this sense (*i.e.*, instantaneous), V is a fixed material volume, and ∂V a fixed material boundary. If we further assume that ψ and \mathbf{v} are continuous on ∂V , and that ∂V encloses V , Gauss' divergence theorem (*e.g.*, Truesdell and Toupin, 1960, Sect. 130) implies that

$$\int_V \nabla \cdot (\psi \mathbf{v}) = \int_{\partial V} \psi \mathbf{v} \cdot \hat{\mathbf{n}} da \quad [I.8].$$

Using [I.6]-[I.8], then, we may write

$$\int_V \partial_t \psi dv = \int_V p(\psi) dv - \int_{\partial V} (\psi \mathbf{v} + \mathbf{f}_{(\psi)}) \cdot \hat{\mathbf{n}} da \quad [I.9]$$

or

$$\int_V \partial_t \psi dv = \int_V p(\psi) dv - \int_V \nabla \cdot (\psi \mathbf{v} + \mathbf{f}_{(\psi)}) dv \quad [I.10]$$

assuming that $\mathbf{f}_{(\psi)}$ and its first partial derivatives with respect to space are continuous in V . We note that [I.9] and [I.10] are valid only when B does not contain Σ , since if B does contain Σ , ψ , \mathbf{v} and $p(\psi)$ are then in general not continuous in V . Also, in this case, $\mathbf{f}_{(\psi)}$ and \mathbf{v} are generally not continuous on ∂V , and since Σ splits ∂V , it no longer encloses V , and Gauss' divergence theorem is no longer valid. Consequently, when B contains Σ , we cannot use the transport and divergence theorems as done in [I.6]-[I.8] to instantaneously balance ψ in V as a whole. However, since the discontinuities in ψ , *etc.*, are restricted (*i.e.*, localized and isolated) to the shock front, we are free to assume that ψ , *etc.*, are

continuous in part or all of V^+ and V^- . In this context, consider an arbitrary subregion of V , designated $v = v(t)$ (Figure I.1b), that encompasses part of Σ , designated σ , such that v is naturally divided into regions v^+ and v^- ahead and behind σ , respectively. We assume ψ , *etc.*, are continuous in each of these regions, and suffer at most a jump discontinuity of the form [I.1] across σ . The extent of this subregion relative to V is controlled only by the continuity assumptions imposed on ψ , *etc.*, and their first partial derivatives.

Noting that the shock front forms part of the boundary of each of these regions, let σ^+ represent this boundary for v^+ , and σ^- that for v^- (Figure I.1b). Then we may draw an entire (*i.e.*, closed) boundary around v^+ , *i.e.*, $\partial v^+ \cup \sigma^+$, and around v^- , *i.e.*, $\partial v^- \cup \sigma^-$, where \cup represents the operation of union in the set theoretic sense. Since ∂v^+ and ∂v^- are, by assumption, instantaneously material boundaries, they move with the material displacement velocity, \mathbf{v} ; however, σ^+ and σ^- move with the displacement velocity, \mathbf{u} , of the surface, σ . Defining a general displacement velocity \mathbf{w} such that

$$\mathbf{w} \equiv \begin{cases} \mathbf{v} & \text{on } \partial v^\pm \\ \mathbf{u} & \text{on } \sigma^\pm \end{cases} \quad \text{[I.10]}$$

and letting $\hat{\mathbf{n}}^+$ and $\hat{\mathbf{n}}^-$ be the outward-facing unit normal vectors to $\partial v^+ \cup \sigma^+$ and $\partial v^- \cup \sigma^-$, respectively, we may write a transport relation for ψ in each of these subregions, *i.e.*,

$$\begin{aligned} d_t \Psi^+ &= \frac{d}{dt} \int_{v^+} \psi dv = \int_{v^+} [\partial_t \psi + \nabla \cdot (\psi \mathbf{w})] dv \\ &= \int_{v^+} \partial_t \psi dv + \int_{\partial v^+} \psi \mathbf{v} \cdot \hat{\mathbf{n}}^+ da + \int_{\sigma^+} \psi^+ \mathbf{u} \cdot \hat{\mathbf{n}}^+ da \end{aligned} \quad \text{[I.11]}$$

and

$$d_t \Psi^- = \frac{d}{dt} \int_{v^-} \psi dv = \int_{v^-} [\partial_t \psi + \nabla \cdot (\psi \mathbf{w})] dv$$

$$= \int_{v^-} \partial_t \psi dv + \int_{\partial v^-} \psi \mathbf{v} \cdot \hat{\mathbf{n}}^- da + \int_{\sigma^+} \psi^- \mathbf{u} \cdot \hat{\mathbf{n}}^- da \quad [\text{I.12}].$$

Note that we have $\psi \rightarrow \psi^+$ on σ^+ and $\psi \rightarrow \psi^-$ on σ^- , by their definition above, in the integrals over the singular surface. Now in Figure I.1b, we see that $\hat{\mathbf{n}}$ and $\hat{\nu}$ are oriented in opposite directions on σ^+ but in the same directions on σ^- . In this case, $\hat{\mathbf{n}}^+ = -\hat{\nu}$ on σ^+ , but $\hat{\mathbf{n}}^- = \hat{\nu}$ on σ^- . Putting these into [I.11] and [I.12], we have

$$d_t \Psi^+ = \int_{v^+} \partial_t \psi dv + \int_{\partial v^+} \psi \mathbf{v} \cdot \hat{\mathbf{n}}^+ da - \int_{\sigma^+} \psi^+ \mathbf{u} \cdot \hat{\nu} da \quad [\text{I.13}]$$

$$= \int_{v^+} p(\psi) dv - \int_{\partial v^+} \mathbf{f}(\psi) \cdot \hat{\mathbf{n}}^+ da \quad [\text{I.14}],$$

and

$$d_t \Psi^- = \int_{v^-} \partial_t \psi dv + \int_{\partial v^-} \psi \mathbf{v} \cdot \hat{\mathbf{n}}^- da + \int_{\sigma^+} \psi^- \mathbf{u} \cdot \hat{\nu} da \quad [\text{I.15}]$$

$$= \int_{v^-} p(\psi) dv - \int_{\partial v^-} \mathbf{f}(\psi) \cdot \hat{\mathbf{n}}^- da \quad [\text{I.16}],$$

where [I.14] and [I.16] come from the general balance, [I.5], applied to the regions $v^+ \cup \partial v^+ \cup \sigma^+$ and $v^- \cup \partial v^- \cup \sigma^-$, respectively. If we add [I.13] and [I.15] together, we obtain

$$\begin{aligned} d_t \{\Psi^+ + \Psi^-\} &= \int_{v^+} \partial_t \psi dv + \int_{v^-} \partial_t \psi dv \\ &\quad + \int_{\partial v^+} \psi \mathbf{v} \cdot \hat{\mathbf{n}}^+ da + \int_{\partial v^-} \psi \mathbf{v} \cdot \hat{\mathbf{n}}^- da + \int_{\sigma} [|\psi|] \mathbf{u} \cdot \hat{\nu} da \end{aligned} \quad [\text{I.15}].$$

From [I.14] and [I.16], we also have

$$d_t \{\Psi^+ + \Psi^-\} = \int_{v^+} p(\psi) dv + \int_{v^-} p(\psi) dv - \int_{\partial v^+} \mathbf{f}(\psi) \cdot \hat{\mathbf{n}}^+ da - \int_{\partial v^-} \mathbf{f}(\psi) \cdot \hat{\mathbf{n}}^- da \quad [\text{I.16}]$$

Since, by assumption, Ψ is additive in v , we have

$$\Psi = \Psi^+ + \Psi^- \quad [I.17].$$

Further, we note that

$$v = v^+ \cup v^- \rightarrow \int_v = \int_{v^+ \cup v^-} = \int_{v^+} + \int_{v^-} \quad [I.18],$$

$$\partial v = \partial v^+ \cup \partial v^- \rightarrow \int_{\partial v} = \int_{\partial v^+ \cup \partial v^-} = \int_{\partial v^+} + \int_{\partial v^-} \quad [I.19],$$

and

$$\sigma = \sigma^+ \cup \sigma^- \rightarrow \int_{\sigma} = \int_{\sigma^+ \cup \sigma^-} = \int_{\sigma^+} + \int_{\sigma^-} \quad [I.20].$$

Also, note that $\hat{\mathbf{n}}^+ = \hat{\mathbf{n}}^-$ on ∂v . With these, we may write [I.15] as

$$d_t \Psi = \int_v \partial_t \psi dv + \int_{\partial v} \psi \mathbf{v} \cdot \hat{\mathbf{n}} da + \int_{\sigma} [|\psi|] \mathbf{u} \cdot \hat{\nu} da \quad [I.21],$$

which is the form of Reynolds' transport relation appropriate for balancing ψ in an arbitrary region of V where ψ possesses at most a surface (*i.e.*, isolated) discontinuity. Combining [I.16] and [I.21], then, we obtain the instantaneous balance relation for ψ in $v(t)$ containing a part of the singular surface $\sigma(t)$, *i.e.*,

$$\begin{aligned} \int_v \partial_t \psi dv + \int_{\partial v^+} \psi \mathbf{v} \cdot \hat{\mathbf{n}}^+ da + \int_{\partial v^-} \psi \mathbf{v} \cdot \hat{\mathbf{n}}^- da + \int_{\sigma} [|\psi|] \mathbf{u} \cdot \hat{\nu} da \\ = \int_v p(\psi) dv - \int_{\partial v^+} \mathbf{f}(\psi) \cdot \hat{\mathbf{n}}^+ da - \int_{\partial v^-} \mathbf{f}(\psi) \cdot \hat{\mathbf{n}}^- da \end{aligned}$$

or

$$\int_v \partial_t \psi dv + \int_{\partial v} (\psi \mathbf{v} + \mathbf{f}(\psi)) \cdot \hat{\mathbf{n}} da + \int_{\sigma} [|\psi|] \mathbf{u} \cdot \hat{\nu} da = \int_v p(\psi) dv \quad [I.22].$$

Note that, if there is no singular surface in v , $[|\psi|] = 0$ and [I.22] reduces to the

classic instantaneous balance relation for Ψ , *i.e.*,

$$\int_v \partial_t \psi dv + \int_{\partial v} \psi \mathbf{v} \cdot \hat{\mathbf{n}} da = \int_v p(\psi) dv - \int_{\partial v} \mathbf{f}(\psi) \cdot \hat{\mathbf{n}} da \quad [\text{I.23}].$$

To obtain an instantaneous balance relation for Ψ on σ , we assume that the functions $\partial_t \psi$ and $p(\psi)$ are bounded in v , and that \mathbf{v} and $\mathbf{f}(\psi)$ are defined and continuous on both $v^+ \cup \partial v^+ \cup \sigma^+$ and $v^- \cup \partial v^- \cup \sigma^-$ such that \mathbf{v}^+ and $\mathbf{f}_{(\psi)}^+$ are the limiting values of \mathbf{v} and $\mathbf{f}(\psi)$, respectively, as $\partial v^+ \rightarrow \sigma^+$, while \mathbf{v}^- and $\mathbf{f}_{(\psi)}^-$ are similar limits for \mathbf{v} and $\mathbf{f}(\psi)$, respectively, as $\partial v^- \rightarrow \sigma^-$. With these assumptions, the volume integrals in [I.22] vanish in the limit $\partial v \rightarrow \sigma$. In this case, [I.22] becomes

$$\int_{\sigma^+} [\psi^+ \mathbf{v}^+ + \mathbf{f}_{(\psi)}^+] \cdot \hat{\mathbf{n}}^+ da + \int_{\sigma^-} [\psi^- \mathbf{v}^- + \mathbf{f}_{(\psi)}^-] \cdot \hat{\mathbf{n}}^- da + \int_{\sigma} [|\psi|] \mathbf{u} \cdot \hat{\nu} da = 0 \quad [\text{I.24}]$$

As noted above to obtain [I.14], $\hat{\mathbf{n}}^+ = -\hat{\nu}$ and $\hat{\mathbf{n}}^- = \hat{\nu}$ on σ . Putting these into [I.24], we have

$$\int_{\sigma} [|\psi(\mathbf{u}-\mathbf{v}) - \mathbf{f}_{(\psi)}|] \cdot \hat{\nu} da = 0 \quad [\text{I.25}]$$

which is the balance relation for Ψ on σ .

In an appropriate coordinate system, the component form of [I.22] may be written,

$$\int_v \partial_t \psi dv + \int_{\partial v} (\psi v^k + f_{(\psi)}^k) \hat{n}_k da + \int_{\sigma} [|\psi|] u^k \hat{\nu}_k da = \int_v p(\psi) dv \quad [\text{I.26}]$$

and

$$\int_{\sigma} [|\psi(u^k - v^k) - f_{(\psi)}^k|] \hat{\nu}_k da = 0 \quad [\text{I.27}]$$

($k=1,2,3$) respectively. If the fields ψ , $u^k \hat{\nu}_k$, $v^k \hat{\nu}_k$, and $f_{(\psi)}^k \hat{\nu}_k$ are

homogeneous on $\Sigma(t)$, then $\sigma(t)$ and da are arbitrary, and [I.27] takes the local form

$$[[\psi(u^k - v^k) - f_{(\psi)}^k]] \dot{\nu}_k = 0 \quad \text{[I.28]}$$

and this is similar to the results of Truesdell and Toupin (1960, Sect. 193). Alternatively, if there is no singular surface propagating through V , and all relevant fields are homogeneous in $V \cup \partial V$, v and dv are arbitrary, and [I.27] reduces to its local form:

$$\partial_t \psi + [\psi v^k + f_{(\psi)}^k]_{,k} = P(\psi) \quad \text{[I.29].}$$

Since [I.25]-[I.29] are based solely on so-called "kinematic" considerations, they have no concrete physical meaning at this point. To give them such meaning, we identify ψ with the TM fields that are balanced, or conserved, during the deformation of $B(t)$. These are summarized in the following table:

Table I.1

	ψ	$f_{(\psi)}$	$P(\psi)$
Mass	ρ	0	0
Momentum	ρv_k	$-t^{km}$	ρb^k
Energy	$\rho(e + \frac{1}{2} v_k v^k)$	$q^k - v_m t^{km}$	$\rho v_k b^k + \rho r$
Entropy	ρs	$T^{-1} q^k$	$P(s)$

In this table, t^{km} are the components of Cauchy stress tensor, b^k represents the components of the body force, e is the specific internal energy, q^k are the components of the heat flux vector, r is the specific internal energy supply, s is the

specific entropy and T is the absolute temperature.

The relations [I.27] and [I.28] are valid for any singular surface in the context of the assumptions used to obtain them. Since we are interested in a particular kind of singular surface, *i.e.*, the shock front, we may further reduce [I.28], using Table I.1, to the relations used for interpretation of experimental results, as follows. Defining $U^k \equiv u^k - v^k$ as the velocity of propagation of σ , we may substitute the different manifestations of ψ from Table I.1 into [I.28] to obtain

$$[[\rho U_{(\hat{\nu})}]] = 0 \quad \text{[I.30]}$$

the balance of mass,

$$[[\rho U_{(\hat{\nu})} v^k]] + [[t^k]] = 0 \quad \text{[I.31]}$$

the balance of momentum,

$$[[\rho U_{(\hat{\nu})} (e + \frac{1}{2} v_k v^k) + (v_m t^m - q_{(\hat{\nu})})]] = 0 \quad \text{[I.32]}$$

the balance of energy, and

$$[[\rho U_{(\hat{\nu})} s - T^{-1} q_{(\hat{\nu})}]] \geq 0 \quad \text{[I.33]}$$

the balance of entropy, where the last is an inequality via the requirement of a nonnegative entropy production across the shock front. In these relations, $U_{(\hat{\nu})} \equiv U^k \hat{\nu}_k$ is the component of the propagation velocity normal to σ , $t^k \equiv t^{km} \hat{\nu}_m$ are the components of the Cauchy stress vector, and $q_{(\hat{\nu})} \equiv q^k \hat{\nu}_k$ is the component of the heat flux normal to σ . The mass balance, [I.30], is the first of the relations we use to interpret experimental results. Using [I.30], we may simplify [I.31], [I.32] and [I.33] to

$$\rho^\pm U_{(\hat{\nu})}^\pm [[v^k]] + [[t^k]] = 0 \quad \text{[I.34],}$$

$$\rho^\pm U_{(\hat{\nu})}^\pm [[(e + \frac{1}{2} v_k v^k)]] + [[v_m t^m - q_{(\hat{\nu})}]] = 0 \quad \text{[I.35],}$$

and

$$\rho^\pm U_{(\hat{\nu})}^\pm ||s|| - ||T^{-1}q_{(\hat{\nu})}|| \geq 0 \quad [I.36],$$

respectively. Note that [I.34]-[I.36] represent 5 equations in 24 unknowns: ρ^\pm , $U_{(\hat{\nu})}^\pm$, v^k , t^k , e^\pm , $q_{(\hat{\nu})}^\pm$, s^\pm and T^\pm .

From the physical viewpoint, shock compression produces a "sudden" change in the velocity of the material in a direction normal to the the shock front. In the context of the singular surface representation of the shock front, we idealize this change as a discontinuity in the component of the material velocity normal to σ , *i.e.*,

$$||v_{(\hat{\nu})}|| \neq 0 \quad [I.37]$$

where $v_{(\hat{\nu})} \equiv v^k \hat{\nu}_k$. Also, note that $||u^k|| = 0$. To substitute [I.37] into [I.34]-[I.36], we must cast these relations into normal and tangential forms. To do this, we define τ_α^k ($\alpha=1,2$) as vectors tangent to σ such that

$$\hat{\nu}^k = \frac{(\tau_1 \times \tau_2)^k}{|\tau_1 \times \tau_2|} \quad [I.38],$$

i.e., $\hat{\nu}$, τ_1 and τ_2 form a right-handed system. In [I.38], \times represents the outer vector product operator. With these, we may resolve any vector into components normal and tangent to Σ . In this case, we may write

$$v^k = v_{(\hat{\nu})} \hat{\nu}^k + v_{(\tau)}^\alpha \tau_\alpha^k \quad [I.39]$$

and

$$t^k = t_{(\hat{\nu})} \hat{\nu}^k + t_{(\tau)}^\alpha \tau_\alpha^k \quad [I.40].$$

Noting that

$$\hat{\nu}_k \hat{\nu}^k = 1 \quad , \quad \hat{\nu}_k \tau_\alpha^k = 0 \quad [I.41],$$

and, assuming σ is planar, that

$$\tau_{\alpha}^k \tau_{k\beta} = \delta_{\alpha\beta} = \begin{cases} 0 & \alpha \neq \beta \\ 1 & \alpha = \beta \end{cases} \quad [I.42]$$

we may put [I.39] and [I.40] into [I.34]-[I.36] and obtain

$$\rho^{\pm} U_{(\hat{\nu})}^{\pm} [|v_{(\hat{\nu})}|] + [|t_{(\hat{\nu})}|] = 0 \quad [I.43]$$

$$\rho^{\pm} U_{(\hat{\nu})}^{\pm} [|v_{(\hat{\tau})}^{\alpha}|] + [|t_{(\hat{\tau})}^{\alpha}|] = 0 \quad [I.44]$$

$$\rho^{\pm} U_{(\hat{\nu})}^{\pm} [|e + \frac{1}{2}(v_{(\hat{\nu})}^2 + v_{(\hat{\tau})\alpha} v_{(\hat{\tau})}^{\alpha})|] + [|v_{(\hat{\nu})} t_{(\hat{\nu})} + v_{(\hat{\tau})\alpha} t_{(\hat{\tau})}^{\alpha} - q_{(\hat{\nu})}|] = 0 \quad [I.45]$$

and

$$\rho^{\pm} U_{(\hat{\nu})}^{\pm} [|s|] - [|T^{-1} q_{(\hat{\nu})}|] \geq 0 \quad [I.46].$$

At this point, we make the mechanical constitutive assumption that the material on either side of the shock front is an elastic, or barotropic, fluid, *i.e.*,

$$t^{km\pm} = -P^{\pm} \delta^{km} \quad [I.47]$$

With this, we have

$$t_{(\hat{\nu})}^{\pm} = t^k \pm \hat{\nu}_k = \hat{\nu}_k t^{km\pm} \pm \hat{\nu}_m = -P^{\pm} \hat{\nu}_k \hat{\nu}^k = -P^{\pm} \quad [I.48]$$

via [I.34], and

$$t_{(\hat{\tau})}^{\alpha\pm} = t^{m\pm} \tau_{m\alpha} = \hat{\nu}_k t^{km\pm} \tau_{m\alpha} = -P^{\pm} \hat{\nu}_k \tau_{\alpha}^k = 0 \quad [I.49]$$

from [I.41]₂. Putting [I.48] and [I.49] into [I.43]-[I.46], we obtain

$$[|P|] = \rho^{\pm} U_{(\hat{\nu})}^{\pm} [|v_{(\hat{\nu})}|] \quad [I.50],$$

$$\rho^{\pm} U_{(\hat{\nu})}^{\pm} [|v_{(\hat{\tau})}^{\alpha}|] = 0 \quad [I.51],$$

$$\rho^{\pm} U_{(\hat{\nu})}^{\pm} [|e + \frac{1}{2} v_{(\hat{\nu})}^2|] + [|v_{(\hat{\nu})} t_{(\hat{\nu})} - q_{(\hat{\nu})}|] = 0 \quad [I.52],$$

and

$$\rho^{\pm} U_{(\hat{\nu})}^{\pm} [|s|] - [|T^{-1} q_{(\hat{\nu})}|] \geq 0 \quad [I.53],$$

where we have used [I.51] in [I.45] to obtain [I.52]. Relation [I.50] is the second

of the relations used to interpret experimental results. Using the momentum balance, [I.43], we may write

$$\rho^{\pm} U_{(\dot{\nu})}^{\pm} \left[\frac{1}{2} v_{(\dot{\nu})}^2 \right] + [v_{(\dot{\nu})} t_{(\dot{\nu})}] = \frac{1}{2} (v_{(\dot{\nu})}^+ t_{(\dot{\nu})}^- - v_{(\dot{\nu})}^- t_{(\dot{\nu})}^+) + \frac{1}{2} [v_{(\dot{\nu})} t_{(\dot{\nu})}] \quad [I.54]$$

Putting this into the energy relation, [I.52], we obtain

$$\begin{aligned} \rho^{\pm} U_{(\dot{\nu})}^{\pm} [e] &= \frac{1}{2} (v_{(\dot{\nu})}^- t_{(\dot{\nu})}^+ - v_{(\dot{\nu})}^+ t_{(\dot{\nu})}^-) - \frac{1}{2} [v_{(\dot{\nu})} t_{(\dot{\nu})}] + [q_{(\dot{\nu})}] \\ &= -\frac{1}{2} [v_{(\dot{\nu})}] (t_{(\dot{\nu})}^+ + t_{(\dot{\nu})}^-) + [q_{(\dot{\nu})}] \end{aligned} \quad [I.55].$$

From the mass balance, we have

$$[v_{(\dot{\nu})}] = \frac{1}{\rho^+} [|\rho|] U_{(\dot{\nu})}^- \quad [I.56].$$

Putting this into [I.55], we obtain

$$\begin{aligned} [e] &= -\frac{1}{2} \frac{1}{\rho^- \rho^+} [|\rho|] (t_{(\dot{\nu})}^+ + t_{(\dot{\nu})}^-) + \frac{1}{\rho^{\pm} U_{(\dot{\nu})}^{\pm}} [q_{(\dot{\nu})}] \\ &= -\frac{1}{2} \left[\frac{1}{\rho} \right] (P^+ + P^-) + \frac{1}{\rho^{\pm} U_{(\dot{\nu})}^{\pm}} [q_{(\dot{\nu})}] \end{aligned} \quad [I.57].$$

where we have used the elastic fluid constitutive assumption represented by [I.47]. Finally, if we make the nonmechanical constitutive assumption that the shock front is adiabatic, *i.e.*, $[q_{(\dot{\nu})}] = 0$, [I.57] reduces to

$$[e] = \frac{1}{2} \left\{ \frac{1}{\rho^+} - \frac{1}{\rho^-} \right\} (P^+ + P^-) \quad [I.58]$$

which is the third relation used to interpret experimental shock-compression data. Relation [I.58] is known as the Rankine-Hugoniot relation (*e.g.*, Rice *et al.*, 1958). With the assumption of adiabaticity, [I.53] reduces to

$$\rho^{\pm} U_{(\dot{\nu})}^{\pm} [s] \geq \left[\frac{1}{T} \right] q_{(\dot{\nu})}^{\pm} \quad [I.59]$$

If we further assume there is no heat flow throughout $V \cup \partial V$ such that $q_{(\dot{\nu})}^{\pm} = 0$,

[I.59] reduces to

$$[s] \geq 0 \quad [I.60],$$

implying that the specific entropy must increase across an adiabatic shock front separating two non-heat-conducting, elastic fluids, which is usually assumed the case (*e.g.*, Bethe, 1942) for shock-compression experiments. Relations [I.30], [I.50] and [I.58] represent the balances of mass, momentum and energy, respectively, used in the following chapters to interpret experimental shock-compression results, and for various related calculations of Hugoniot, or shock-compressed, states. Along with [I.60], they constitute a thermodynamic description for the "experimental" shock front.

The shock front represents a kind of boundary in the target, across which we may use, given the necessary experimental or other information, [I.30], [I.50] and [I.58] to calculate the change in density, material velocity, pressure, specific internal energy, *etc.*, during shock compression. As stated above, however, different materials make up the target, introducing a further "discontinuity" into the field description of the target as a whole. Consequently, we must also find the balance of mass, momentum, energy and entropy across the boundaries between target layers. Since we assume that, as each target layer is compressed and the shock front passes on into the next target layer during the experiment, the layers do not separate or blow apart at their interface, this boundary may be regarded as a material surface, such that $u_{(\hat{\nu})} = v_{(\hat{\nu})}^{\pm}$, or $U_{(\hat{\nu})}^{\pm} = 0$. This states that, at a material surface or interface, the surface moves with the displacement velocity of the material on either side of it. Consequently, at such an interface, the balance of momentum and energy take on the forms

$$[t_{(\hat{\nu})}] = 0 \quad , \quad [t_{(\hat{\tau})}^{\alpha}] = 0 \quad [I.61]$$

and

$$[[v_{(\dot{\nu})}t_{(\dot{\nu})} + v_{(\tau)\alpha}t_{(\tau)}^{\alpha} - q_{(\dot{\nu})}]] = 0 \quad [I.62]$$

respectively, from [I.43]-[I.44] and [I.45], respectively. Further, the entropy inequality, [I.46], simplifies to

$$-[[T^{-1}q_{(\dot{\nu})}]] \geq 0 \quad [I.63]$$

Substituting the mechanical constitutive assumption, [I.47], into [I.61], the balance of momentum at a material interface in the target takes the form

$$[[P]] = 0 \quad [I.64].$$

Likewise, the balance of energy becomes

$$[[v_{(\dot{\nu})}P]] + [[q_{(\dot{\nu})}]] = 0 \quad [I.65].$$

Note that [I.63] is unaffected by this assumption. If we further assume that heat flux and temperature are continuous across the boundary between each layer, as we do in all energy-transport models presented in this thesis (see Chapter I, Appendix C), [I.65] and [I.63] reduce to

$$[[v_{(\dot{\nu})}P]] = 0 \quad [I.66],$$

and

$$-q_{(\dot{\nu})}^{\pm} [[\frac{1}{T}]] = 0 \quad [I.67],$$

respectively. Note that [I.67] implies no entropy production on the boundaries between the target components. Relations [I.64], [I.66] and [I.67] then represent boundary conditions appropriate for the assumed constitutive nature of each target component, and consequently are consistent with the analogous shock-front relations given above. We note that the balance of momentum across the shock front, [I.50], combined with [I.65] for the balance of momentum at the boundary between adjacent target components, forms the basis for the impedance match technique (*e.g.*, Rice *et al.*, 1958), which is used to calculate

the density, pressure, *etc.*, of the high-pressure, shock-compressed states of each target component throughout this thesis.

References

Kormer, S. B., Optical study of the characteristics of shock-compressed condensed dielectrics, *Sov. Phys. Uspekhi*, **11**, 229-254, 1968.

Rice, M. H., R. G. McQueen, and J. M. Walsh, Compressibility of solids by strong shock waves, *Solid State Phys.*, **6**, 1-63, 1958.

Truesdell, C. and R. Toupin, The classic field theories, in *Handbuch der Physik*, **III/1**, 226-902, edited by S. Flügge, Springer-Verlag, Berlin, 1960.

Chapter I

Optical Radiation from Shock-Compressed Materials and Interfaces§

Bob Svendsen†, Jay D. Bass‡ and Thomas J. Ahrens†

†Seismological Laboratory,
California Institute of Technology, Pasadena, California 91125, USA.

‡Department of Geology,
University of Illinois, Urbana, Illinois 61801, USA.

§submitted to *Physics Reports*

Abstract

Recent observations of shock-induced radiation from oxides, silicates and metals of geophysical interest constrain the shock-compressed temperature of these materials. In these experiments, a projectile impacts a target consisting of a metal driver plate, a metal film or foil layer, and a transparent window. We investigate the relationships between the temperature inferred from the observed radiation and the temperature of the shock-compressed film or foil and/or window. Changes of the temperature field in each target component away from that of their respective shock-compressed states occur because of: 1) shock-impedance mismatch between target components, 2) thermal mismatch between target components, 3) surface roughness at target interfaces, and 4) conduction within and between target components. In particular, conduction may affect the temperature of the film/foil-window interface on the time scale of the experiments, and so control the intensity and history of the dominant thermal radiation sources in the target. Comparing this model to experimental data from Fe-Fe-Al₂O₃ and Fe-Fe-LiF targets, we note that:

1. Fe at Fe-Al₂O₃ interfaces releases from experimental shock-compressed states between 245 and 300 GPa to interface states between 190 and 230 GPa, respectively, with temperatures \approx 200-1500 K above model calculations for Fe experiencing no reshock at smooth Fe-Al₂O₃ interfaces. This is so for both Fe foils and films. Below 190 GPa, reshock heating does not apparently affect the temperature of Fe-Al₂O₃ interfaces. In contrast, from the same range of shock states, Fe at Fe-LiF interfaces releases to states between 130 and 160 GPa (because it has a lower shock impedance than Al₂O₃). The data and model imply that Fe experiences little or no reshock at Fe-LiF up to 140 GPa (where the data end), suggesting 1) that LiF forms a more ideal interface with Fe than does Al₂O₃, or 2) that the Fe-LiF

interfaces experience less shock heating than Fe-Al₂O₃ interfaces because Fe-LiF interfaces reshock to lower pressures. Both the Fe-Al₂O₃ data and the model suggest that the degree of reshock is strongly pressure-dependent above the solid Fe-liquid Fe phase boundary. LiF appears to be a more ideal window than Al₂O₃ also because it is a poorer thermal inertia match to Fe than is Al₂O₃.

2. In the absence of energy sources and significant energy flux from other parts of the target, the rate of change of the film ($\sim 1 \mu\text{m}$ thick)/window (3-4 mm thick), or foil ($\sim 10\text{-}100 \mu\text{m}$ thick)/window, interface temperature, $T_{\text{INT}}(t)$, is proportional to $-\mu \exp(-\mu^2)$, where $\mu \equiv \delta_{\text{FW}} / 2\sqrt{\kappa_{\text{F}}t}$, δ_{FW} is the thickness of the reshocked zone in the film/foil layer at the film/foil-window interface, κ_{F} is the thermal diffusivity of the film/foil material, and $0 \leq t \leq t_{\text{exp}}$ (t_{exp} is the time scale of the experiment, 200-400 ns). On this basis, the temperature of a thin ($\delta_{\text{FW}} \ll 2\sqrt{\kappa_{\text{F}}t_{\text{exp}}}$) reshocked layer relaxes much faster than that of a thick ($\delta_{\text{FW}} \gg 2\sqrt{\kappa_{\text{F}}t_{\text{exp}}}$) layer. We estimate $\sqrt{\kappa_{\text{F}}t_{\text{exp}}} \sim 10 \mu\text{m}$ for Fe under the conditions of Fe-Al₂O₃ and Fe-LiF interfaces at high pressure. In this case, a 100- μm -thick reshocked Fe layer would relax very little, remaining near $T_{\text{INT}}(0)$ on the time scale of the experiment, while a 1- μm -thick reshocked Fe layer would relax almost instantaneously (i.e., on a time scale much less than t_{exp}) to a temperature just above $T_{\text{INT}}(\infty)$.
3. Greybody fits to an Fe-Fe film-Al₂O₃ experiment produce a gradually increasing effective greybody emissivity, $\hat{\epsilon}_{\text{gb}}(t)$, and a gradually decreasing greybody temperature, $T_{\text{gb}}(t)$. This behavior is characteristic of most Fe-Fe-Al₂O₃ experiments. The decrease of $T_{\text{gb}}(t)$ can be explained in terms of the model for the film/foil-window interface temperature, $T_{\text{INT}}(t)$. For this

experiment, the model implies that the thickness of the reshocked film layer, δ_{FW} , is approximately equal to the conduction length scale in the film, $\sqrt{\kappa_{\text{F}} t_{\text{exp}}}$ ($\sim 10 \mu\text{m}$ for Fe). Further, assuming $T_{\text{gb}}(t) = T_{\text{INT}}(t)$, the greybody fit constrains the amount of reshock, ΔT_{FW} , to $\lesssim 2500\text{K}$ with $\sigma_{\text{WF}} \sim 0.1$ and $\delta_{\text{FW}} \lesssim 2\sqrt{\kappa_{\text{F}} t_{\text{exp}}}$. A slight decrease of the Al_2O_3 absorption coefficient upon shock compression can explain the slight increase of $\hat{\epsilon}_{\text{gb}}(t)$ with time; this may be consistent with the observation that the refractive index of Al_2O_3 seems to decrease with pressure.

4. In contrast to the Fe-Fe- Al_2O_3 results, greybody fits to data from an Fe-Fe foil-LiF target show a relatively constant greybody temperature, and a decreasing greybody emissivity. The constant greybody temperature implies a constant interface temperature, as expected for an interface experiencing minimal reshock, while the decaying $\hat{\epsilon}_{\text{gb}}(t)$ is consistent with a shock-induced increase in the absorption coefficient of LiF. Setting $T_{\text{INT}}(0) = T_{\text{gb}}(0)$, we fit a simplified version of the full radiation model to these data and obtain an estimate of the absorption coefficient ($\sim 100 \text{m}^{-1}$) of LiF shock-compressed to 122 GPa.

§1. Introduction

Traditional studies of the behavior of shock-compressed materials assess the mechanical response of these materials to shock compression (*e.g.*, the change of density with pressure). Since this approach cannot directly constrain the temperature of the high-pressure state, other means are needed to provide a complete equilibrium thermodynamic description (*i.e.*, pressure-density-temperature) for these materials. To this end, recent studies record shock-induced radiation from initially transparent materials (*e.g.*, alkali halides, summarized by Kormer, 1968; Al_2O_3 , Urtiew, 1974; SiO_2 and Mg_2SiO_4 , Lyzenga and

Ahrens, 1980) and from opaque materials at interfaces viewed through transparent or semitransparent windows (*e.g.*, Mg, Urtiew and Grover, 1977; Ag, Lyzenga, 1980; Fe, Bass *et al.*, 1987). These recent observations constrain some temperature in the target. In this paper we explore relationships between the experimentally constrained temperature and the temperatures of different high-pressure states achieved in the target components and at their interfaces during the experiment. We attempt this in the context of a simple model of energy transfer and transport in the targets. To give the model considerations some weight, we compare model details and results to the recent observations of Bass *et al.* (1987) on shock-induced radiation from Fe films and foils.

§2. Model Considerations

Consider the target depicted in Figure 2.1, representative of that used in the experiments of Lyzenga (1980) and Bass *et al.* (1987). This generic target consists of 1), a 1.5-mm-thick, metallic "driver" plate (DP), 2), a metallic film (1 to 10- μm -thick) or foil (10 to 100- μm thick) layer (FL) and 3), a dielectric, transparent window (TW, 3 to 4-mm-thick). The target is constructed so that the shock impedance (*i.e.*, the product of the initial density and shock wave velocity) of the DP is greater than or equal to that of the FL, which in turn has a shock impedance greater than or equal to that of the TW. An edge mask (Figure 2.1) prevents the detectors from recording radiation from the edge of the target assembly. Radiation emitted from the center of the assembly, where uniaxial compression takes place, reflects from the mirror into the detectors.

The experiment begins when a projectile impacts the DP (Figure 2.1), generating a shock wave that propagates through the DP to the DP-FL interface. Since this interface is formed by mechanical juxtaposition of the metallic DP and FL surfaces, it is "rough" on a ~ 1 μm -scale (Urtiew and Grover, 1974). The shock front thickness is $\lesssim 0.01$ μm in the materials and at the pressures of

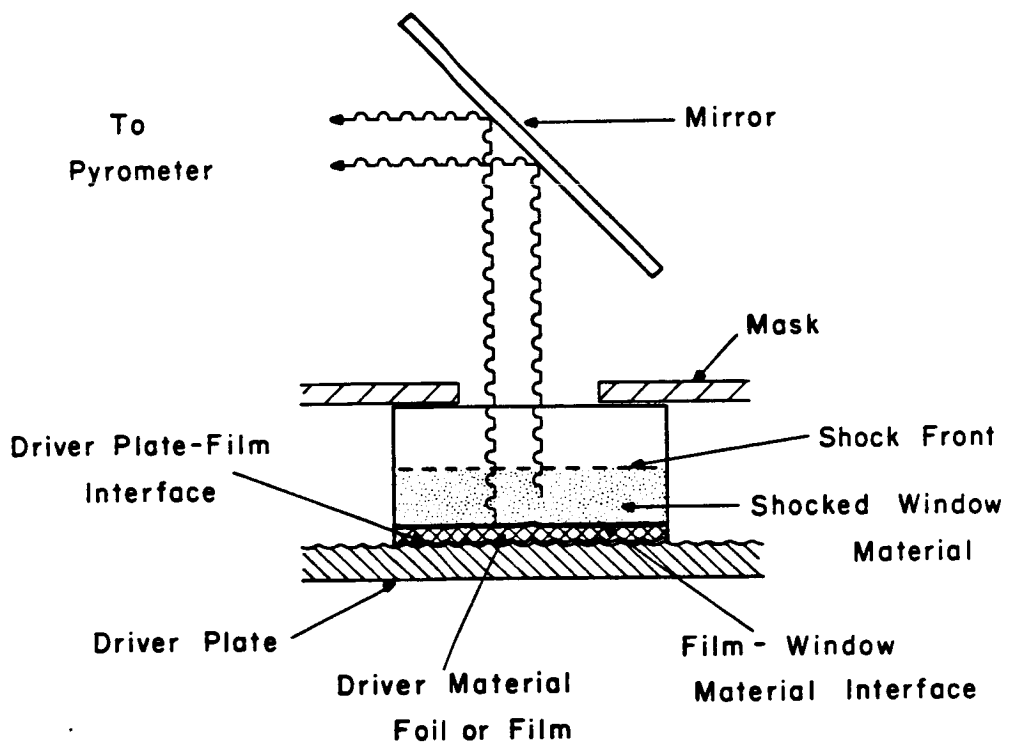


Figure 2.1. Target assembly.

interest (*e.g.*, Kormer, 1968). With respect to the shock wave, then, the DP and FL surfaces are, prior to compression, partially free. Consequently, the shock wave accelerates the DP material at the DP-FL interface across the gap, and simultaneously reflects from the DP surface at the DP-FL interface as a release wave propagating back into the DP and releasing the DP to near-zero pressure. This moving DP surface then impacts the FL surface, generating shock waves of approximately equal magnitude that propagate backward into the just released DP, and forward into the unshocked FL. The former shock wave compresses the just released DP material from its low-pressure, high-temperature release state to one with approximately the same pressure as its previous shock-compressed state; wave reverberations quickly bring this DP state to a state with a pressure equal to that of the shock-compressed FL and a temperature well above that of the previous (*i.e.*, first) DP shock-compressed state. If the backward-propagating shock wave overtakes the release wave at some distance behind the DP-FL interface, this distance defines the thickness of a reshocked DP material layer at the DP-FL interface. However, if the release wave is faster than the reshock wave, the entire DP may experience low pressure release and reshock. In either case, subsequent wave reverberations quickly bring the DP to a state with the same normal (to the interface) material velocity and stress fields as the shocked FL.

Since the DP material accelerating across the DP-FL interface impacts a rough FL surface, a thin (on the scale of the surface roughness) layer of film or foil material compresses, much like a porous material (Urtiew and Grover, 1974), to a much higher temperature than achieved by the shock-compressed FL material beyond this zone. As with the DP material at the DP-FL interface, the shock front traversing the FL reflects from a partially free surface at the FL-TW interface as a low pressure release wave and accelerates the FL material across the interface to impact with the TW material. Since the TW surface at

this interface is smooth relative to the shock front thickness, and is much more incompressible than either the DP or FL, the impacting FL material should not heat a thin layer of TW material, but rather only shock the TW up to high pressure and its Hugoniot temperature. Closure of the FL-TW interface generates backward and forward traveling shock waves, and the former wave compresses the low pressure, high temperature, released FL material to a state with approximately the same pressure as the first FL shock-compressed state; wave reverberations quickly bring this FL state to a state with a pressure equal to that of the shock-compressed transparent window (shocked window: SW) and a temperature much-higher than the first FL shock-compressed state. If the backward-propagating shock wave overtakes the release wave, it cuts off the zone of release/reshock in the FL material. In this case, the combined wave releases the remaining FL material, and then the DP, to a state with approximately the same normal velocity and stress as the SW. Alternatively, if the shock wave does not overtake the low pressure release wave, the entire FL and/or DP is release and reshocked. In either case, subsequent wave reverberations should quickly bring both the DP and FL to states possessing normal stress and material velocity fields equal to those of the SW.

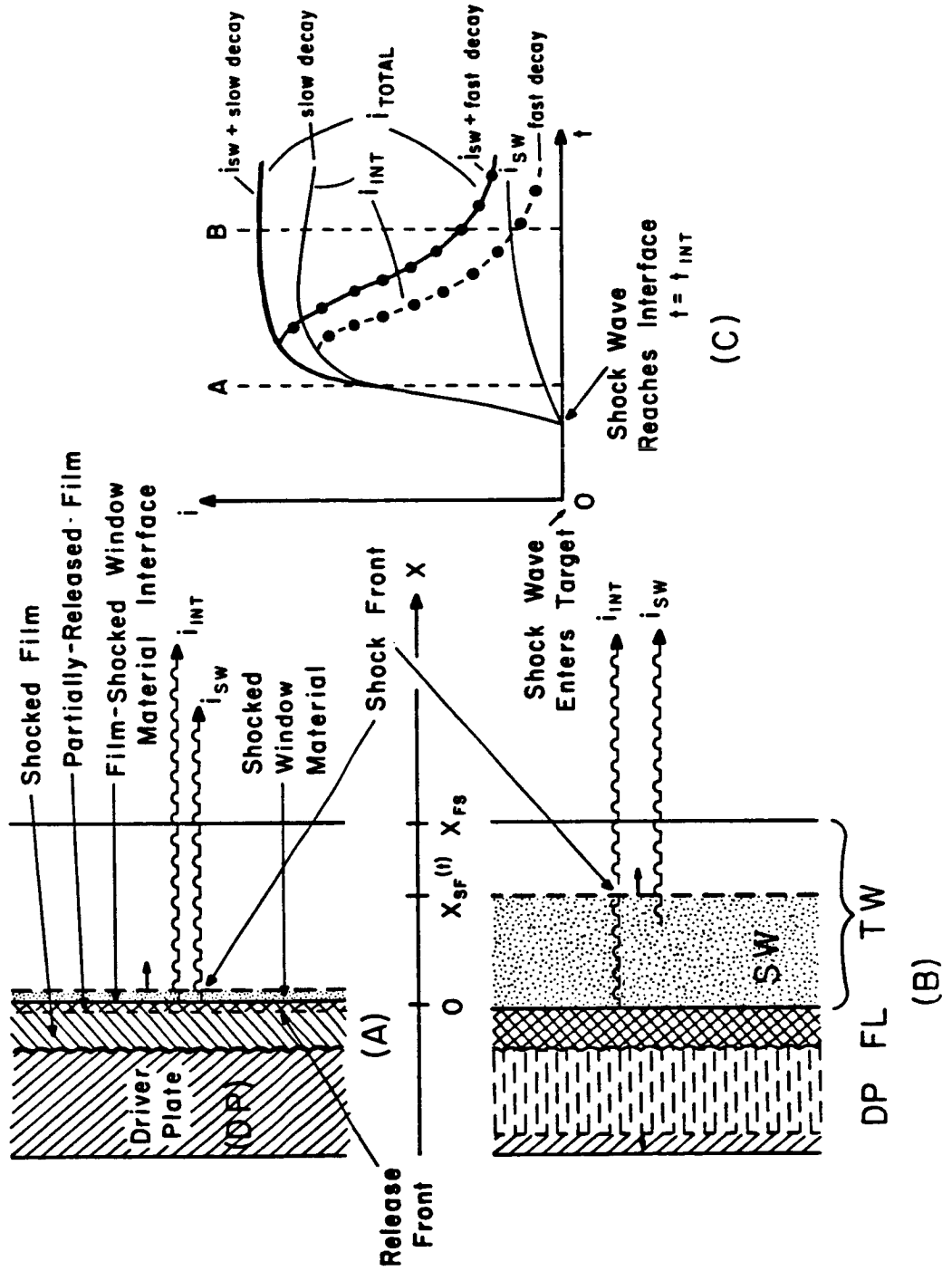
Since the reshocked layers at each interface are significantly hotter than the surrounding material (see Urtiew and Grover, 1974, and discussion below), the temperature and radiation histories of targets with smooth versus rough interfaces should be quite different. This difference should be sufficiently distinct to be experimentally resolvable, as we show below. We investigate the dependence of the radiation history on the nature of the interface by use of both mechanically formed foil-TW interfaces and vacuum-coated film-TW interfaces. In particular, we expect the vacuum-coated film-TW interface to be much smoother than the mechanically formed foil-TW interface. However, this assumption turns out to be somewhat naive, as shown below. Since the TW

surface at the FL-TW interface is smooth (defined above), we presume that any roughness of this interface is due to roughness of the FL surface there.

As the FL material at the FL-TW interface is compressed, released, and possibly reshocked, it heats up and begins to radiate. Consequently, the observed radiation intensity rises sharply (Figure 2.2, part A). As the shock wave travels forward into the TW, the thickness of the SW increases (Figure 2.2, part B); consequently, so does its contribution to the total observed radiation (note increase with time in Figure 2.2, part C). If the TW is highly absorbing and/or scattering, or shock-compressed to such a state (as is apparent in many experiments: Boslough, 1985), the radiation intensity from the interface will decay with time (Figure 2.2, part C, dash-dot curve labeled fast decay); if not, the interface source will dominate the observed radiation history (Figure 2.2, part C, continuous curve labeled slow decay) when the FL at the FL-SW interface is at a higher temperature than the SW. The recorded radiation is the sum of either the interface slow-decay or fast-decay contribution, and the SW contribution. Given these possibilities, we must account for the the degree of geometric (interface roughness) and material (shock-impedance) mismatch at each interface, especially at the FL-SW interface, in attempting to constrain the conditions of the FL Hugoniot state from observed radiation.

Even if each interface has little or no roughness, the DP, FL, and TW may shock-compress to such different temperatures that the resulting temperature gradients between the layers drive significant relaxation of the FL-SW interface temperature on the time scale of the experiment. Dynamic phase changes or other energy sources and/or sinks present in the FL, FL at the interface, and/or SW on the time scale of the experiment may also introduce time dependence into the temperature and effective emissivity inferred from the radiation observations (Grover and Urtiew, 1974). Consequently, we must examine whether or not the temperature profile of the compressed/released/reshocked target system

Figure 2.2 Dynamic model geometry. Shock front reaches film/foil layer (FL)-transparent window (TW) interface ($x=0$) at time t_{INT} , when radiation is first detected. Interface radiation (i_{INT}) dominates the early radiation history (A). If 1) the interface temperature decays slowly, and 2) the FL-TW interface, shocked window and shock front remain relatively transparent, i_{INT} will dominate the observed radiation history during the experiment (" i_{SW} +slow decay" curve). However, if the FL-TW interface and/or shock front develop significant reflectivity, and/or the SW develops significant opacity, i_{INT} will decay quickly (dash-dot curve), and may fall below the radiation intensity of the SW, i_{SW} , on the time scale of the experiment. The total intensity is then represented by the " i_{SW} +fast decay" curve.



relaxes via conductive and/or radiative transport on the time scale of the experiments, leading to time-dependent (thermal) radiation sources. We must also account for the effects through the SW, shock-front, unshocked window (USW), and the TW free surface on the FL-SW interface and SW source radiation of propagation (Boslough, 1984). We focus on processes at the FL-TW interface as represented in the observed radiation.

§3. Model Assumptions

We assume all sources contributing to the observed radiation intensity are thermal and in local thermodynamic equilibrium. We can then relate the source intensity to the wavelength, λ , and absolute temperature, T , through the Planck function, $I_{\text{P}}(\lambda, T)$, given by

$$I_{\text{P}}(\lambda, T) \equiv \frac{2C_1}{\lambda^5(e^{C_2/\lambda T} - 1)} \quad [3.1],$$

where $C_1 \equiv 5.9544 \times 10^{-17} \text{ W}\cdot\text{m}^2/\text{sr}$ and $C_2 \equiv 1.4388 \times 10^{-2} \text{ m}\cdot\text{K}$ are constants. Comparison of the observed radiation wavelength dependence with that of a blackbody source, as represented by $I_{\text{P}}(\lambda, T)$, implies that materials shock compressed to high pressures are dominantly thermal radiators ($\gtrsim 70 \text{ GPa}$: Lyzenga *et al.*, 1983; Boslough, 1984). At lower pressures, however, most materials apparently radiate both thermally and nonthermally (SiO_2 : Kondo and Ahrens, 1983; Brannon *et al.*, 1984; Schmitt *et al.*, 1986). Several of these materials are initially dielectrics (*e.g.*, SiO_2 : Lyzenga *et al.*, 1983). The processes responsible for this radiation (defect electronic transitions?) are presently unidentified, but are suggested by spectrometric observations (Kondo and Ahrens, 1983).

In principle, energy transport in the target occurs by both radiation and conduction; our task is much more difficult if both radiation and conduction

contribute equally to this process. In simple terms, we can understand the likely relative contribution of radiation and conduction to energy transport within layers and across interfaces via dimensional analysis. The relevant non-dimensional number is known as the Stark number (Siegel and Howell, 1981), Sk_R , referenced to some state R, and given by (Equation [C.18])

$$Sk_R \equiv \frac{k_R \Delta T_R}{a_R x_R^2 n_R^2 \sigma_{SB} T_R^4} .$$

This number represents the ratio of conductive to radiative flux, whether across a layer or within an "infinite" medium. It is composed of the material properties k_R , a_R and n_R , *i.e.*, the thermal conductivity, radiation absorption coefficient, and refractive index, respectively. The remaining parameters, which may be material, include x_R , t_R , T_R and ΔT_R , the governing length scale, time scale, a reference temperature and temperature range, respectively. Also, $\sigma_{SB} \equiv 5.6696 \times 10^{-8} \text{W/m}^2 \cdot \text{K}^4$ is the Stefan-Boltzmann constant. For the layered geometry of the target, we may associate x_R with the layer thickness, t_R with the time scale of the experiment, T_R with the shock-compressed or released temperature of the layer, and ΔT_R with the change in temperature across a given layer in the target such that $\Delta T_R/x_R$ reflects the magnitude of the average temperature gradient across the layer. From this parameter we see that radiative transport dominates conductive transport in 1) an optically-thick ($a_R \rightarrow \infty$), 2) poorly conducting ($k_R \rightarrow 0$) and/or 3) high-temperature medium, all other parameters being finite. Applying this parameter to the balance of energy in a target consisting of a metallic DP and FL (*e.g.*, Fe), and dielectric TW (*e.g.*, Al_2O_3), we find (Appendix C) that $Sk_R \sim 10$ and $\sim 10^3$ for the TW and DP or FL, respectively. In addition, viewing each layer as an infinite medium implies that conduction affects the balance of energy in both the FL and TW over a length scale of $\lesssim \sqrt{\kappa_R t_{\text{exp}}} \sim 10^{-6}$ m, where κ_R is a characteristic thermal diffusivity and $t_{\text{exp}} \sim 10^{-7}$ sec (the experimental time scale). This confines the influence of this

process on energy transport in the target to the immediate vicinity of the interface. In addition, the radiative component of the energy flux is negligible to the balance of energy, compared to the conductive flux, in the FL, across the interface, and in the shocked TW, if $a_r \lesssim 10^7 \text{ m}^{-1}$ (Appendix C). This condition is almost certainly satisfied for the SW (LiF: Wise and Chhabildas, 1986; Al_2O_3 : Bass *et al.*, 1987, but see Urtiew, 1974), and probably satisfied for the FL and across the FL-TW interface (Appendix C). Note that this condition is analogous to that for the validity of the "diffusion approximation" to the classic radiative transport relation (Siegel and Howell, 1981), where this approximation becomes reasonable above the bound of a_r stated. With these estimates in mind, we may decouple radiative transport from the energy balance in the target components and across their interfaces, and treat radiation separately. We emphasize that this analysis is limited by our ability to estimate the values of many key properties (e.g., thermal conductivity) of the appropriate high-pressure states of the DP and TW.

We assume that a given shock-compressed or -released state of any component of the target contributing to the observed radiation is one of constant and uniform density, stress, and material velocity. Consequently, our model is not directly applicable to the low-pressure regime ($\lesssim 70 \text{ GPa}$), where many shock-compressed materials deform heterogeneously (Grady, 1980; Kondo and Ahrens, 1983; Schmitt *et al.*, 1986; Svendsen and Ahrens, 1986). Such behavior would require us to consider source distributions, spatially averaged effective emissivities and time-dependent thermomechanical processes, all beyond the scope of the simple equilibrium thermodynamic framework used here.

§4.1 Initial conditions: Shock-Compressed State

The model is referenced to the first shock-compressed (Hugoniot) state of each material in the target. Although this state is reached via a nonequilibrium, irreversible process (shock compression), we assume that thermodynamic equilibrium is achieved in the Hugoniot state itself. This requires the shock-compressed state to be one of constant, uniform density, material velocity, stress and energy. In this context, we may connect the initial and shock-compressed states (*i.e.*, two different equilibrium states) via a classical thermodynamic path (*i.e.*, a path connecting a series of states in equilibrium) representing a change in specific internal energy equal to that judged by the general balance of energy across a shock-front.

We assume that the material 1) initially occupies a state with temperature T_i , and pressure P_i , 2) shock compresses adiabatically and 3) as a fluid. Under these assumptions, the general balance of energy across the shock front is represented by the Rankine-Hugoniot relation (*e.g.*, Rice *et al.*, 1958)

$$e(s_H, \rho_H) = e(s_i, \rho_i) + \frac{1}{2\rho_i} \eta_H [P_H + P_i] \quad [4.1],$$

with

$$\eta_H \equiv 1 - \frac{\rho_i^\alpha}{\rho_H} \quad [4.2].$$

In this relation, $e(s_i, \rho_i)$ is the specific internal energy of the initial state with mass density $\rho_i = \rho(T_i, P_i)$ and specific entropy $s_i = s(T_i, P_i)$, while $e(s_H, \rho_H)$ is the specific internal energy of the shock-compressed state with mass density $\rho_H = \rho(T_H, P_H)$ and specific entropy $s_H = s(T_H, P_H)$. The subscripts "i" and "H" stand for the initial and shock-compressed (Hugoniot) states, respectively. The initial state is usually standard temperature and pressure (STP), of course, but the following considerations apply to any initial state. Since [4.1] is valid

whether or not shock compression induces a phase transformation in the material, we may also write it in the form

$$e(s_H^\beta, \rho_H^\beta) = e(s_i^\alpha, \rho_i^\alpha) + \frac{1}{2\rho_i^\alpha} \eta_H [P_H + P_i],$$

appropriate for the change in specific internal energy resulting from a shock-induced transformation of some phase α , stable at T_i and P_i , to some other phase β , stable at the pressure and temperature of the shock-compressed state. The equilibrium thermodynamic path energetically equivalent to [4.1] may be constructed as follows (McQueen *et al.*, 1967; Ahrens, *et al.*, 1969). The difference in specific internal energy between α and β at T_i and P_i may be written

$$\Delta e_i^{\beta-\alpha} \equiv \Delta e^{\beta-\alpha}(T_i, P_i) \equiv e(s_i^\beta, \rho_i^\beta) - e(s_i^\alpha, \rho_i^\alpha) \quad [4.3].$$

Unless otherwise designated, all the following relations in this section apply to a single phase (β), so we drop the phase superscripts except when necessary for clarity. Having connected α and β energetically at T_i and P_i via [4.1], we compress β isentropically from its density at T_i and P_i , ρ_i , to its shock-compressed density, ρ_H , resulting in a change in its specific internal energy given by

$$\Delta e_{s_i}(\rho_H) \equiv e(s_i, \rho_H) - e(s_i, \rho_i) = \int_{\rho_i}^{\rho_H} \rho^{-1} P_{s_i}(\rho) d \ln \rho \quad [4.4],$$

where $P_{s_i}(\rho) = P(s_i, \rho)$ is the pressure as a function of density along the β -isentropes centered at s_i . Note that the the subscript "s" denotes constant specific entropy. Since this last state and the Hugoniot state are at the same density, ρ_H we may connect them by an equilibrium thermodynamic path at constant density. With $s = s(T, \rho)$ and so $T ds = c_v dT$ at constant density, where $c_v = c_v(T, \rho)$ is the specific heat at constant volume (density), we have

$$e(s_H, \rho_H) = e(s_i, \rho_H) + \int_{T_{S_i}}^{T_H} c_v(T, \rho_H) dT \quad [4.5].$$

In [4.5], $T_{S_i}(\rho_H) = T(s_i, \rho_H)$, the temperature of the β -state at a density ρ_H along the β -isentrope centered at s_i , is given by the solution of

$$\left\{ \frac{\partial \ln T}{\partial \ln \rho} \right\}_s = \gamma \quad [4.6],$$

where γ is the equilibrium thermodynamic Grüneisen's parameter. Also in [4.5], T_H is the temperature of the β state with specific internal energy equal to [4.1]. If, as is commonly done (*e.g.*, Boehler and Ramakrishnan, 1980; Anderson, 1986), we assume γ is a function of density alone, then the relation

$$\rho \gamma \left\{ \frac{\partial e}{\partial P} \right\}_\rho = 1 \quad [4.7]$$

yields

$$e(s_H, \rho_H) = e(s_i, \rho_H) + \frac{1}{\rho_H \gamma_H} \left\{ P_H - P_{S_i}(\rho_H) \right\} \quad [4.8],$$

and from [4.6], we have

$$T_{S_i} \equiv T(s_i, \rho_H) = T_i \exp \left\{ \int_{\rho_i}^{\rho_H} \gamma(\rho) d \ln \rho \right\} \quad [4.9].$$

Combining [4.1], [4.4], and [4.5], we obtain

$$\int_{T_{S_i}}^{T_H} c_v(T, \rho_H) dT = -[\Delta e_i^{\beta-\alpha} + \Delta e_{S_i}(\rho_H)] + \frac{1}{2\rho_i^\alpha} \eta_H [P_H + P_i] \quad [4.10],$$

a relation for the equilibrium thermodynamic temperature of a state of β with specific internal energy equal to that of its Hugoniot state. We may also

combine [4.1], [4.4] and [4.8] to obtain

$$\frac{\rho_H}{\rho_i^\alpha} \left\{ 1 - \left(1 + \frac{1}{2} \gamma_H \right) \eta_H \right\} [P_H + P_i] = [P_{s_1}(\rho_H) + P_i] - \rho_H \gamma_H [\Delta e_i^{\beta-\alpha} + \Delta e_{s_1}(\rho_H)] \quad [4.11]$$

(*e.g.*, Jeanloz and Ahrens, 1980). Both [4.10] and [4.11] represent the balance of energy across the shock front, assuming that the shock-compression process connects states in thermodynamic equilibrium. However, since [4.11] further depends upon the assumption that $\gamma = \gamma(\rho)$, while [4.10] does not, these two relations are not completely equivalent. We use [4.10] to find T_H as a function of P_H or ρ_H , once we have relations for η_H , $\Delta e_i^{\beta-\alpha}$, Δe_{s_1} , c_v and T_{s_1} .

We calculate η_H as a function of either v_H , the material velocity of shock-compressed material, phase β , or P_H , from the balance relations for mass and momentum across the shock front (*e.g.*, Rice *et al.*, 1958; Appendix A),

$$\rho_H U_H = \rho_i^\alpha U_i \quad [4.12]$$

and

$$P_H - P_i = \rho_i^\alpha U_i (v_H - v_i) \quad [4.13],$$

by making the constitutive assumption that $U_i \equiv u - v_i$, the speed of propagation of the shock front with respect to the material velocity of the initial state, v_i , is a function of the change or "jump" in material material velocity across the shock front, $v_H - v_i$. Note that $U_H \equiv u - v_H$ is the speed of propagation with respect to the shocked material, and u is the speed of displacement (*i.e.*, the "intrinsic" velocity) of the shock front. For experimental U-v data, of course, $U_i = u$ and $[v] = v_H$, *i.e.*, $v_i = 0$; also, $P_i = 0.1$ MPa and $T_i = 298$ K. Such data for Fe (Brown and McQueen, 1986) and many other materials (*e.g.*, Marsh, 1980) are reasonably well-fit by a linear relation between U_i and $(v_H - v_i)$, *i.e.*,

$$U_i \equiv a_i + b_i (v_H - v_i) \quad [4.14].$$

In [4.14], a_i and b_i are, respectively, the intercept and slope of the U-v relation

centered at ρ_i^α . Eliminating U_i and $v_H - v_i$ from [4.12]-[4.14], we obtain

$$P_H - P_i = \frac{\rho_i^\alpha a_i^2 \eta_H}{(1 - b_i \eta_H)^2} \quad [4.15]$$

(McQueen *et al.*, 1967), the so-called shock wave equation-of-state. We may rearrange this to obtain $\eta_H = \eta_H(P_H)$, *i.e.*,

$$\eta_H = \frac{1}{b_i} [\mu - (\mu^2 - 1)^{1/2}] \quad [4.16]$$

with

$$\mu \equiv 1 + \frac{\rho_i^\alpha a_i^2}{2b_i(P_H - P_i)} \quad [4.17].$$

The value of either [4.15] or [4.16] is limited by the validity of the linear U-v relation, [4.14], and the fact that $(P_H - P_i) \rightarrow \infty$ as $b_i \eta_H \rightarrow 1$ (Prieto and Renero, 1970; Appendix A). As stated, the U-v relation, [4.14], is referenced to ρ_i^α , the initial density of the low-pressure phase, α .

The change in specific internal energy along the isentrope of β referenced to (T_i, P_i) upon shock-compression, $\Delta e_s(\rho_H)$, is generally calculated from some "equation-of-state" (*e.g.*, spatial finite strain: Stacey *et al.*, 1981), $P(s_i, \rho)$, for β referenced to (T_i, P_i) . However, for shock-compressed materials, the energy balance, [4.11], already contains such an equation-of-state, as we now show. Recall that, to obtain [4.11], we shock-compressed the material from a density ρ_i^α to ρ_H , incurring a phase transformation in the process. Imagine now that we can shock-compress the β -phase of the material from its "initial" density, $\rho_i = \rho^\beta(T_i, P_i)$, to ρ_H . The energy balance for this "metastable" shock-compression locus is given by [4.11] if we replace ρ_i^α with ρ_i and set $\Delta e^{\beta-\alpha} = 0$, *i.e.*,

$$\frac{\rho_H}{\rho_i} \left\{ 1 - \left(1 + \frac{1}{2} \gamma_H \eta_H^* \right) [P_H + P_i] \right\} = [P_s(\rho_H) + P_i] - \rho_H \gamma_H \Delta e_s(\rho_H) \quad [4.18],$$

with $\eta_H^* \equiv 1 - \rho_i / \rho_H$. Noting that

$$P_{s_1}(\rho) \equiv P(s_1, \rho) \equiv \rho^2 \left(\frac{\partial e}{\partial \rho} \right)_{s_1} = \rho^2 \left(\frac{d\Delta e_{s_1}}{d\rho} \right) \quad [4.19],$$

[4.18] may be written

$$\rho_H \left(\frac{d\Delta e_{s_1}}{d\rho_H} \right) - \gamma_H \Delta e_{s_1}(\rho_H) = \frac{1}{\rho_i} \left\{ 1 - \left(1 + \frac{1}{2} \gamma_H \eta_H^* \right) [P_H + P_i] \right\} - \frac{P_i}{\rho_H} \quad [4.20],$$

which is an ordinary differential equation for $\Delta e_{s_1}(\rho_H)$. We solve this numerically, subject to the initial ($\rho_H = \rho_i$) conditions 1) $\Delta e_{s_1}(\rho_i) = 0$, and 2)

$$\left\{ \rho_H^2 \left(\frac{d\Delta e_{s_1}}{d\rho_H} \right) \right\}_{\rho_H = \rho_i} = P_{s_1}(\rho_i) = P_i \quad [4.21].$$

If we put these initial conditions into [4.20], we find that $P_H(\rho_i)$ should be equal to P_i ; however, for $P_H(\rho_H)$ as given by [4.15], we have, with $\eta_H \equiv 1 - \rho_i^\alpha / \rho_H$,

$$P_H(\rho_i) = P_i + \frac{\rho_i^\alpha a_i^2 \eta_i}{(1 - b_i \eta_i)^2} \quad [4.22],$$

which is not equal to P_i unless $\rho_i = \rho_i^\alpha$; usually, however, $\rho_i > \rho_i^\alpha$. As stated above, [4.14]-[4.16] do represent the P_H - ρ_H states of the high-pressure phase, β , but in terms of the density of the low-pressure (initial) phase, ρ_i^α , and a_i and b_i , which are referenced to ρ_i^α and the initial state, (T_i, P_i) . So, instead of [4.15], what we need is a relation for P_H referenced to ρ_i , rather than ρ_i^α , such that $P_H(\rho_i) = P_i$. To obtain this relation, which is equivalent to the "metastable" Hugoniot of McQueen *et al.* (1967), we first define a metastable U-v relation for β Hugoniot states, *i.e.*,

$$U_i^* = a_i^* + b_i^*(v_H^* - v_i^*) \quad [4.23],$$

which is referenced to ρ_i . Then we use [4.14]-[4.16], which provide P_H as a function of ρ_H (or vice-versa), ρ_i^α , a_i and b_i , for β , to write a_i^* and b_i^* as functions of ρ_i^α , a_i , b_i and ρ_i . Doing this in Appendix A, we obtain

$$a_i^* = a_i^*(\rho_i) = (1-\eta_i) \left\{ \frac{\rho_i^\alpha (1+b_i\eta_i)}{(1-b_i\eta_i)^3} \right\}^{1/2} a_i \quad [4.24]$$

and

$$b_i^* = b_i^*(\rho_i) = \frac{1}{4} \left\{ 1 + \frac{[4(1-\eta_i)b_i + (2-\eta_i)b_i^2\eta_i - 1]}{(1-b_i\eta_i)(1+b_i\eta_i)} \right\} \quad [4.25]$$

([A.55] and [A.56], respectively). Note that, from these relations, $a_i^* \rightarrow a_i$ and $b_i^* \rightarrow b_i$ as $\rho_H \rightarrow \rho_i^\alpha$, i.e., as $\eta_H \rightarrow 0$. With a_i^* and b_i^* so constrained, we have, analogous to [4.15], the relation

$$P_H = P_i^* + \frac{\rho_i (a_i^*)^2 \eta_H^*}{(1 - b_i^* \eta_H^*)^2} \quad [4.26],$$

where we have set $P_i^* = P_H(\rho_i)$, as given by [4.23]. Relation [4.26] is the form of P_H needed to solve [4.20] for $\Delta e_{s_1}(\rho_H)$. Once we have $\Delta e_{s_1}(\rho_H)$ via solution of [4.20], [4.18] provides the equation-of-state, i.e.,

$$P_{s_1}(\rho_H) = \rho_H \gamma_H \Delta e_{s_1}(\rho_H) + \frac{\rho_H}{\rho_i} \left\{ 1 - \left(1 + \frac{1}{2} \gamma_H \right) \eta_H^* \right\} [P_H + P_i] - P_i \quad [4.27].$$

With ρ_i^α known *a priori*, and a_i and b_i constrained from experimental U-v data, then, we need only ρ_i^β to obtain a_i^* and b_i^* from this method. As discussed in Appendix A, if we know this density sufficiently well, then we also gain estimates of K_{s_1} and K'_{s_1} , the isentropic bulk modulus and its first pressure derivative, referenced to the initial state (T_i, P_i) , since

$$K_{s_1} = \rho_i (a_i^*)^2 \quad [4.28]$$

when we assume that a_i^* is equal to the bulk elastic wave velocity, and

$$K'_{s_1} = 4b_i^* - 1 \quad [4.29]$$

(Ruoff, 1967), assuming only that β shock-compresses as an elastic (or barotropic) fluid (see the Introduction to this thesis).

In Figure 4.1a, we compare $\Delta e_s[\rho_H(P_H)]$ for ϵ -Fe as given by [4.20], based on [4.26], with Δe_s for ϵ -Fe as given by 1) third-order spatial finite strain (Stacey *et al.*, 1981), 2) the third-order Ullman-Pan'kov equation-of-state (Ullman and Pan'kov, 1976), and 3) Murnaghan's equation-of-state (*e.g.*, Stacey *et al.*, 1981), all three of which have the form $\Delta e_s = \Delta e_s(\rho_i, K_s, K'_s, \rho_H)$. The parameters used for this calculation are given in Table 4.1. For compatibility and a fair comparison, of course, we constrain K_s and K'_s by [4.28] and [4.29], respectively. As noted by Somerville and Ahrens (1980), the third-order Ullman-Pan'kov relation is compatible with the linear U-v relation, [4.14], since both make similar predictions for higher-order derivatives of K_s (see Appendix A). The calculations presented in Figure 4.1a demonstrate that the value of $\Delta e_s(\rho_H)$ predicted by each of these methods is essentially the same. Note that the Murnaghan isentrope is off-scale in Figure 4.1a. For the derivatives of $\Delta e_s(\rho_H)$, of course, the minor differences between the difference expressions for $\Delta e_s(\rho_H)$ are magnified, as shown in Figure 4.1b, where we plot $P_s[\rho_H(P_H)]$ as given by [4.27], and compare it with the values for $P_s[\rho_H(P_H)]$ given by the equivalent finite strain and Murnaghan relations. In particular, note that the energy balance equation-of-state, [4.27], is a bit "stiffer" than either of the finite strain equations-of-state.

Energetically speaking, the difference between [4.11] and [4.18] is $\Delta e_1^{\beta-\alpha}$. So, if we subtract [4.18] from [4.11] and let $\rho_H \rightarrow \rho_i$, we obtain an estimate of $\Delta e_1^{\beta-\alpha}$, *i.e.*,

$$\Delta e_1^{\beta-\alpha} = \frac{1}{2} \left\{ \frac{1}{\rho_i^\alpha} - \frac{1}{\rho_i} \right\} [P_i^* + P_i] \quad [4.30].$$

From a purely equilibrium thermodynamic viewpoint, $\Delta e_1^{\beta-\alpha}$ is given by

$$\Delta e_1^{\beta-\alpha} = \Delta g^{\beta-\alpha}(T_i, P_i) + T_i \Delta s^{\beta-\alpha}(T_i, P_i) + P_i \frac{\Delta \rho^{\beta-\alpha}(T_i, P_i)}{\rho_i^\alpha \rho_i^\beta} \quad [4.31],$$

where $\Delta g^{\beta-\alpha}$, $\Delta s^{\beta-\alpha}$ and $\Delta \rho^{\beta-\alpha}$ are the difference in specific free enthalpy, specific

Figure 4.1a. Comparison of different estimates for the change in specific internal energy (SIE) along the isentrope anchored to (T_i, P_i) , Δe_{s_i} , of ϵ -Fe as a function of pressure and based on the parameters for ϵ -Fe given in Table 4.1.

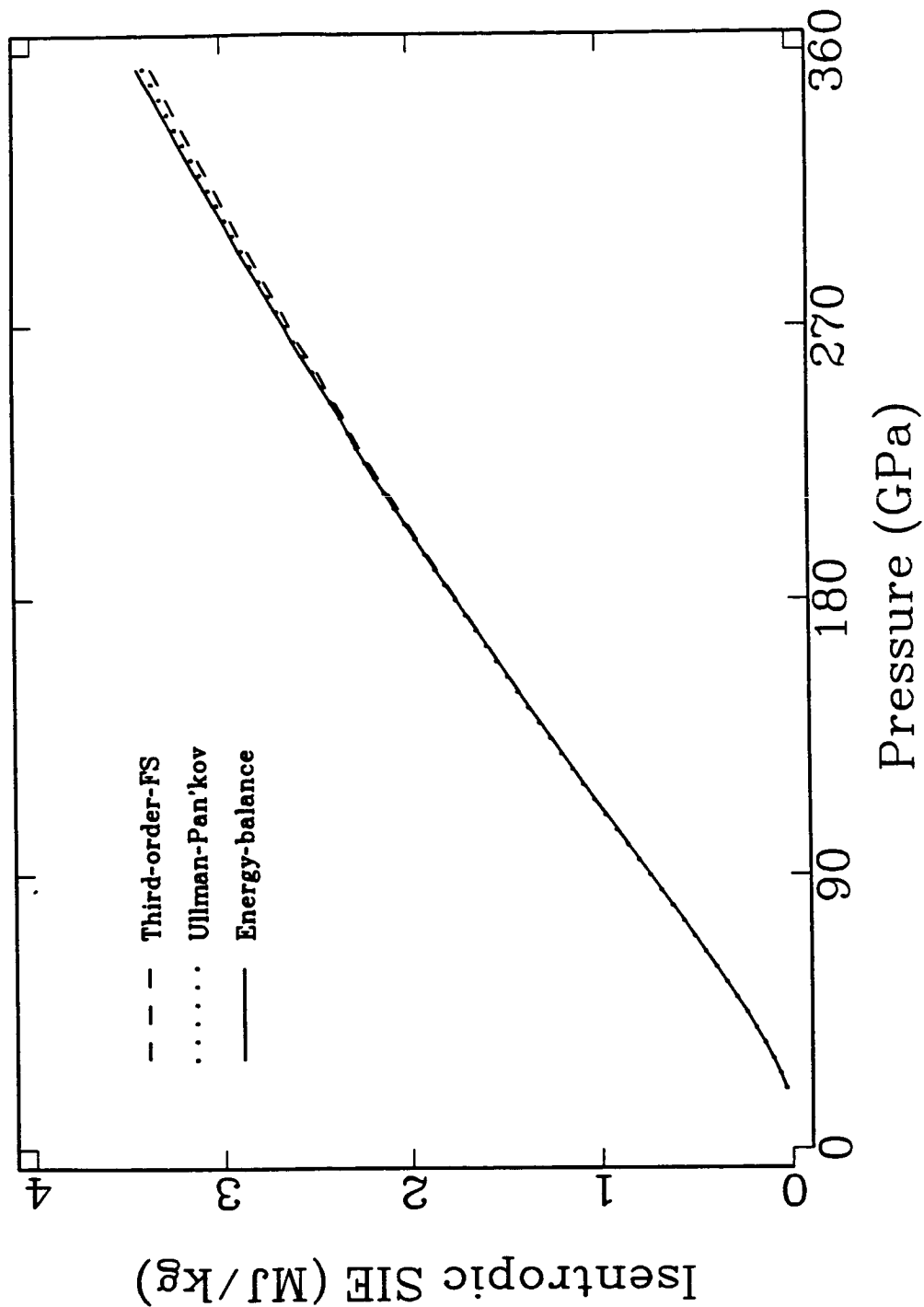


Figure 4.1b. Comparison of different estimates for pressure along the isentrope, P_s , of ϵ -Fe referenced to T_i and P_i , based on the parameters for ϵ -Fe given in Table 4.1.

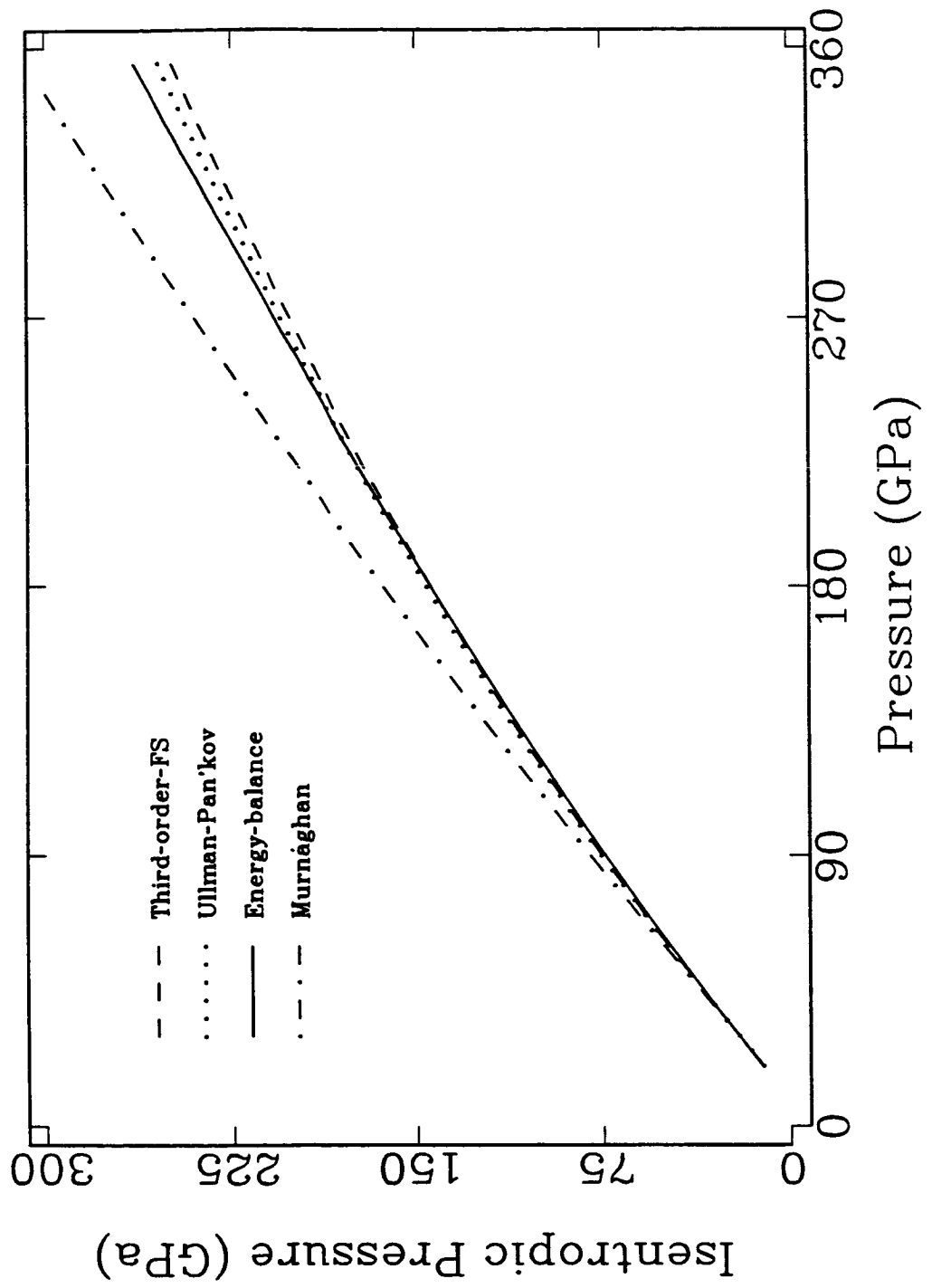


Table 4.1. Standard Temperature-Pressure (STP) Parameters.

Symbol	ϵ -Fe	liquid-Fe	Al ₂ O ₃	LiF	Units
ρ	8352 ^a	7952 ^b	3986 ^c	2650 ^d	kg/m ³
a	4487 ^e	4038 ^e	8908 ^f	5050 ^d	m/sec
b	1.57 ^e	1.58 ^e	0.91 ^f	1.32 ^d	
K_s	168 ^g	130 ^g	254 ^h	68 ^g	GPa
K'_s	5.28 ⁱ	5.31 ⁱ	4.32 ^h	4.28 ⁱ	
c_p	445 ^j		775 ^c	1615 ^d	J/kg·K
α	4.3 ^k		1.6 ^l	10.3 ^l	$\times 10^{-5}K^{-1}$
γ	1.95 ^m		1.32 ^m	1.78 ^m	
q	1.0 ⁿ		1.0 ⁿ	1.0 ⁿ	
Θ_D	385 ^j		1250 ^h	580 ^d	K
T_M	1809 ^c		2345 ^c	845 ^o	K
k	80 ^p		46 ^p	3 ^p	W/m·K
ρ_e	50 ^q		0	0	n Ω ·m

^a Jephcoat *et al.* (1986).

^b Calculated from $\rho(T) = 8136.(1 - 7.608 \times 10^{-5}T)$: Drotning (1981).

^c Robie *et al.* (1978).

^d Van Thiel (1977).

^e Estimated from $U=3955+1.58v$ (Brown and McQueen, 1986).

^f Fit to data in Marsh (1980).

^g Calculated assuming $K_s = \rho a^2$.

^h Anderson *et al.* (1968).

ⁱ Calculated with $K'_s = 4b-1$ (Ruoff, 1967).

^j Andrews (1973).

^k Assumed the same as α -Fe (Touloukian *et al.*, 1975).

^l Touloukian *et al.* (1975).

^m Calculated from $\gamma = \alpha K_s / \rho c_p$.

ⁿ $\gamma(\rho) = \gamma(\rho_i)[\rho_i/\rho]^q$ assumed in all calculations.

^o Weast (1979), p. D-187.

^p assumed the same as α -Fe in Touloukian *et al.* (1970).

^q Inferred from Keeler (1971).

entropy and mass density, respectively, between α and β at T_i and P_i . For the particular case of melting, we assume

$$\Delta e_i^{\beta-\alpha} \approx \Delta h_M - \Delta c_p(T_M - T_i) + P_i \frac{\Delta \rho^{\beta-\alpha}(T_i, P_i)}{\rho_i^\alpha \rho_i^\beta} \quad [4.32],$$

where Δh_M is the enthalpy of melting, and Δc_p is the effective jump of the specific heat at constant pressure across the liquid-solid transition at the melting temperature, T_M , and standard pressure, P_i .

Since both dielectric and metallic solids initially compose our target, we must consider thermodynamic properties that reflect the influence of both ionic and electronic processes. To estimate the harmonic lattice contribution to these properties, we use the Debye model (*e.g.*, Alt'shuler *et al.* 1962; Andrews, 1973). In particular, Andrews (1973) used this model as part of a parameterization of the equilibrium thermodynamic properties of α - and ϵ -Fe. Jamieson *et al.* (1978), Brown and McQueen (1982, 1986), and Boness *et al.* (1986), have all assessed the influence of electronic processes on the material properties of metals at high pressure and temperature. They assume the conduction electrons contribute to the equilibrium thermodynamic properties of a metal as a Sommerfeld free-electron gas (*e.g.*, Wallace, 1972, Sect. 24). This is reasonable for $T \ll T_F$, where T_F is the Fermi temperature. Since the value of T_F for Fe is $\sim 10^5$ K, assuming $T_H \ll T_F$ is quite reasonable for the calculations presented below. So, assuming that lattice-electron and band-structure contributions are negligible, the molar Helmholtz free energy (HFE), $F(T, \rho)$, of a cubic or isotropic Debye solid material, subject to an isotropic state of stress, is given by (Wallace, 1972, Sect. 5)

$$F(T, \rho) = \Phi(\rho) + 3\nu R \left\{ \frac{3}{8} \xi_D + \ln[1 - e^{-\xi_D}] - \frac{1}{3} E_D(\xi_D) \right\} T - \frac{1}{2} \Omega(\rho) T^2 \quad [4.33].$$

In [4.33], $\Phi(\rho)$ represents the zero-temperature lattice contribution to the molar

HFE,

$$\xi_D = \xi_D(T, \rho) = \frac{\Theta_D(\rho)}{T} \quad [4.34],$$

is the Debye similarity parameter,

$$\Omega(\rho) \equiv \Gamma(\rho) - 2A_2(\rho) \quad [4.35],$$

$-\frac{1}{2}\Gamma(\rho)T^2$ is the low-temperature ($T \ll T_F$) electronic contribution to F, $A_2(\rho)T^2$ is the high-temperature anharmonic contribution to F, ν is the number of atoms in the chemical formula, and $E_D(\xi)$ is the Debye internal-energy function (*e.g.*, Gopal, 1966), *i.e.*,

$$E_D(\xi) \equiv \frac{3}{\xi^3} \int_0^\xi \frac{x^3}{[e^x - 1]} dx \quad [4.36].$$

In this approximation, the Debye temperature Θ_D is related to a lattice Grüneisen's parameter, γ_D , by (Wallace, 1972)

$$\gamma_D = \left\{ \frac{d \ln \Theta_D}{d \ln \rho} \right\} \quad [4.37].$$

If we assume

$$\gamma_D(\rho) = \gamma_D(\rho_i) \left\{ \frac{\rho_i}{\rho} \right\}^{\alpha_D} \quad [4.38],$$

then Θ_D is given by

$$\Theta_D(\rho) = \Theta_D(\rho_i) \exp \left\{ \frac{\gamma_D(\rho_i)}{\alpha_D} \left\{ 1 - \left\{ \frac{\rho_i}{\rho} \right\}^{\alpha_D} \right\} \right\} \quad [4.39].$$

For simplicity, we do not separate γ_D into longitudinal and transverse components; in this case, γ_D represents a weighted average of these components. The quantity $\Gamma(\rho)$ is related to the electronic Grüneisen's parameter, γ_e , through (*e.g.*, Wallace, 1972)

$$\gamma_e \equiv - \left\{ \frac{d \ln \Gamma}{d \ln \rho} \right\} \quad [4.40].$$

Assuming γ_e is constant, we have

$$\Gamma(\rho) \equiv \Gamma(\rho_i) \left\{ \frac{\rho_i}{\rho} \right\}^{\gamma_e} \quad [4.41].$$

Noting that the high-temperature ($T > \Theta_D$) anharmonic contribution to the free energy, $A_2(\rho)T^2$, has the same temperature dependence as the electronic contribution to F , we observe that these will have equivalent effects on F . By analogy with [4.41], we assume, for simplicity, that

$$\Omega(\rho) \equiv \Omega(\rho_i) \left\{ \frac{\rho_i}{\rho} \right\}^{\omega} \quad [4.42].$$

For the example calculations involving Fe-targets presented below, we constrain the values of $\Omega(\rho_i)$ and ω empirically. Boness *et al.* (1986) calculated $\Gamma(\rho)$ for the ϵ and γ -phases of iron using the Sommerfeld free-electron-gas theory. In addition, these authors suggest that the electronic density-of-states in liquid iron at high pressure may be approximated by that of the closed-packed ϵ and γ -phases at high pressure, where the liquid should be "close-packed." We make the same assumption.

Relation [4.33] allows us to write expressions for the approximate density- and temperature-dependence of a number of solid-state properties (Appendix A). In particular, the equilibrium thermodynamic Grüneisen's parameter, γ , based on [4.33], is given by

$$\gamma = \gamma_b + (\omega - \gamma_b) \frac{\Omega}{Mc_v} T \quad [4.43]$$

(Equation [A.11]). From this, we note that γ is only weakly temperature-dependent, since $\omega \approx \gamma_b$ in the pressure range of interest. Hence, the thermodynamic model based on [4.33] is approximately consistent with the assumption

above that γ is a function of density alone, upon which [4.8] above is based. Consequently, we assume $\gamma \approx \gamma_D(\rho)$, where $\gamma_D(\rho)$ is given by [4.38], the power-law form (Bassett *et al.*, 1966). In this case, from [4.6] and [4.38], we also have

$$T(s_i, \rho_2) = T(s_i, \rho_1) \exp \left\{ \frac{\gamma_D(\rho_i)}{q} \left\{ \left\{ \frac{\rho_i}{\rho_1} \right\}^{q_D} - \left\{ \frac{\rho_i}{\rho_2} \right\}^{q_D} \right\} \right\} \quad [4.44]$$

for the change in temperature in the material due to isentropic compression or expansion from a starting density ρ_1 to a second density ρ_2 along the isentrope of the material centered at s_i .

With respect to T_H , we are particularly interested in the specific heat at constant volume, $c_v(T, \rho)$, given by

$$c_v(T, \rho) \equiv -T \left\{ \frac{\partial^2 f}{\partial T^2} \right\}_\rho = \frac{3\nu R}{M} \left\{ 4E_D(\xi_D) - \frac{3\xi_D}{[e^{\xi_D} - 1]} \right\} + \frac{\Omega(\rho)}{M} T, \quad [4.45]$$

where M is the molecular weight. Substituting this into [4.10], we obtain

$$\frac{3\nu R}{M} \left\{ E_D(\xi_{DH})T_H - E_D(\xi_{Ds})T_s \right\} + \frac{1}{2M}\Omega_H(T_H^2 - T_s^2) = \Delta e_v(\rho_H) \quad [4.46]$$

with $\Omega_H \equiv \Omega(\rho_H)$ and

$$\Delta e_v(\rho_H) = -[\Delta e_i^{\beta-\alpha} + \Delta e_{s_i}(\rho_H)] + \frac{1}{2\rho_i^\alpha} \eta_{hl}[P_H + P_i] \quad [4.47],$$

being the difference in specific internal energy between the Hugoniot and principal isentrope of β at density ρ_H . Note that $\Delta e_v = 0$ when $T_H = T_s$, $T_H < T_s$ when $\Delta e_v < 0$, and $T_H > T_s$ when $\Delta e_v > 0$. In [4.46]-[4.47], we use $\xi_{Ds} \equiv \Theta_{DH}/T_s$, $\xi_{DH} \equiv \Theta_{DH}/T_H$ and $\Theta_{DH} \equiv \Theta_D(\rho_H)$. Equation [4.46] is an implicit relation for T_H which we evaluate numerically. Since the majority of our calculations are at high temperature ($T > \Theta_D$), and the Hugoniot temperature changes much more drastically with pressure than Θ_D , we may expand $E_D(\xi_{DH})$ into its high-temperature ($\xi_{DH} \rightarrow 0$) form:

$$E_D(\xi_{DH} \rightarrow 0) \sim \frac{3}{(\xi_{DH})^3} \int_0^{\xi_{DH}} x^2 \left\{ 1 - \frac{1}{2}x + \frac{1}{12}x^2 + \dots \right\} dx$$

$$= 1 - \frac{3}{8}\xi_{DH} + \frac{1}{20}\xi_{DH}^2 + O[\xi_{DH}^3].$$

Substituting this into [4.46], we obtain

$$\frac{1}{2}\Omega_H T_H^3 + \frac{3\nu R}{M} T_H^2 - \Lambda_H T_H + \frac{3\nu R}{20M} \Theta_{DH}^2 = 0 \quad [4.48]$$

with $\Lambda_H \equiv \Lambda(\rho_H)$ and

$$\Lambda(\rho_H) \equiv \Delta e_\nu(\rho_H) + \frac{3\nu R}{M} E_D(\xi_{DH}) T_{\xi_1} + \frac{9\nu R}{8M} \Theta_{DH} + \frac{1}{2M} \Omega(\rho_H) T_{\xi_1}^2 \quad [4.49].$$

Relation [4.48] has the solution

$$T_H = 2\sqrt{p} \cos \left\{ \frac{1}{3} \cos^{-1} \left\{ \frac{q}{p\sqrt{p}} \right\} \right\} - \frac{2\nu R}{\Omega_H} \quad [4.50]$$

with

$$p \equiv 4 \left\{ \frac{\nu R}{\Omega_H} \right\}^2 + \frac{2M}{3\Omega_H} \Lambda_H$$

and

$$q \equiv - \frac{\nu R}{\Omega_H} \left\{ \frac{2M}{\Omega_H} \Lambda_H + \frac{3}{20} \Theta_{DH}^2 + 8 \left\{ \frac{\nu R}{\Omega_H} \right\}^2 \right\}.$$

If we set Ω equal to zero in [4.46], we have

$$E_D(\xi_{DH}) T_H(\Omega=0) = E_D(\xi_{DH}) T_{\xi_1} + \frac{M}{3\nu R} \Delta e_\nu(\rho_H) \quad [4.51].$$

which is appropriate for a dielectric material with negligible anharmonic contributions to F . Doing this in in [4.50], we obtain

$$T_H(\Omega=0) = \frac{M}{6\nu R} \Lambda_H' \left\{ 1 + \left\{ 1 - \frac{1}{5} \left\{ \frac{3\nu R \Theta_{DH}}{M \Lambda_H'} \right\}^2 \right\}^{1/2} \right\} \quad [4.52]$$

with

$$\Lambda_H' \equiv \Delta e_v(\rho_H) + \frac{3\nu R}{M} E_D(\xi_{DH}) T_{s_1} + \frac{9\nu R}{8M} \Theta_{DH},$$

for a dielectric material at high ($T > \Theta_D$) temperature with $A_2 T_{s_1}^2 < A_2 T_H^2 \ll 1$. Alternatively, if we assume the classic limit for the harmonic contribution to c_v at high temperature, *i.e.* $3\nu R/M$, [4.46] reduces to

$$T_H(\xi_{DH}=0) = \frac{3\nu R}{\Omega_H} \left\{ \left\{ 1 + \frac{2}{9} \frac{M\Omega_H}{(\nu R)^2} \Lambda_H^* \right\}^{1/2} - 1 \right\} \quad [4.53]$$

with

$$\Lambda_H^* \equiv \Delta e_v(\rho_H) + \frac{3\nu R}{M} E_D(\xi_{DH}) T_{s_1} + \frac{1}{2M} \Omega_H T_{s_1}^2.$$

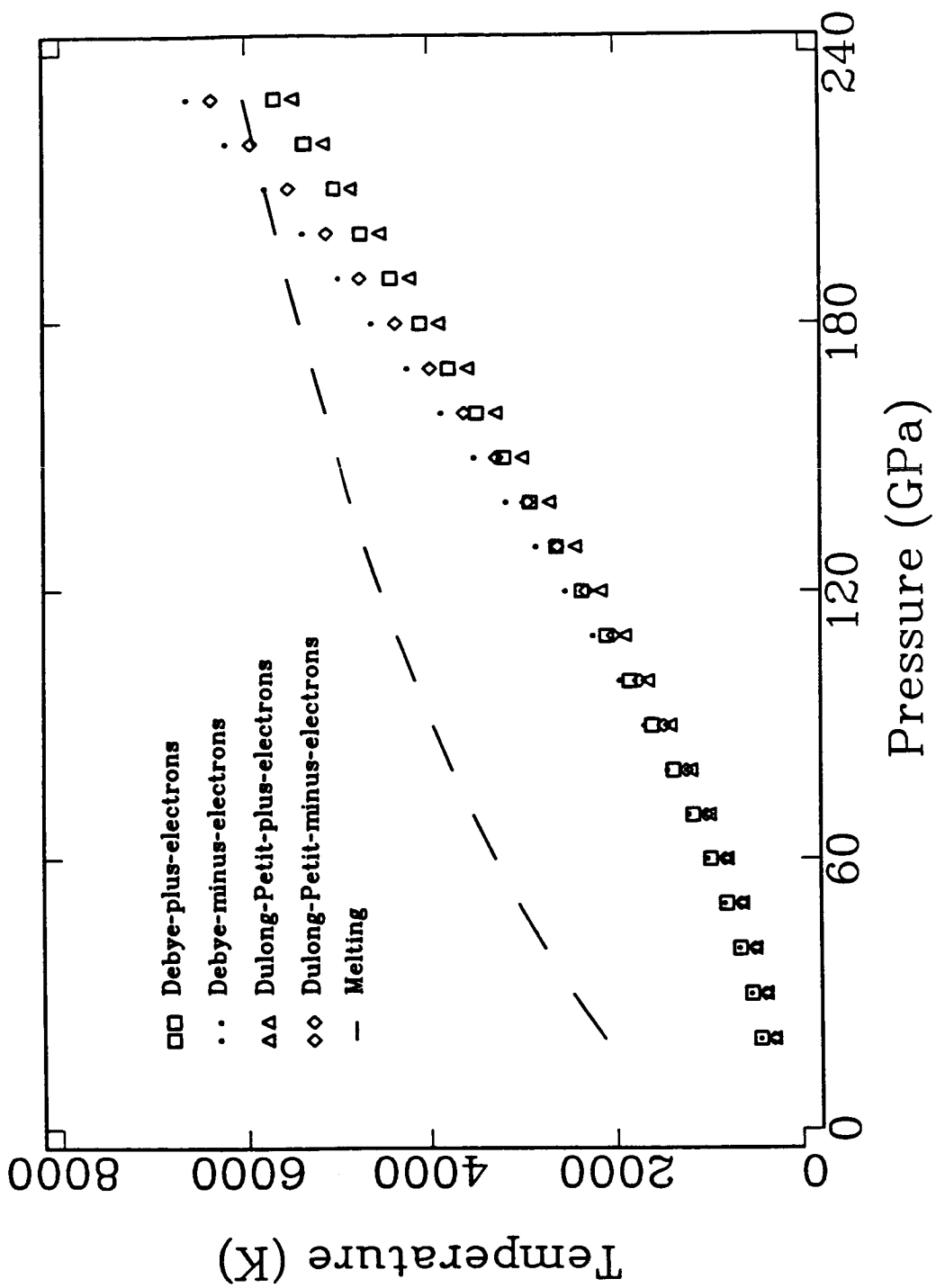
Finally, if we set both Ω and ξ_{DH} equal to zero in [4.46], we have

$$T_H(\Omega=0, \xi_{DH}=0) = E_D(\xi_{DH}) T_{s_1} + \frac{M}{3\nu R} \Delta e_v(\rho_H) \quad [4.54].$$

If we further assume $E_D(\xi_{DH}) \approx 1$ in [4.54], we obtain the relation most commonly used (*e.g.*, Jeanloz and Ahrens, 1980) to calculate T_H .

To demonstrate the effect of these different approximations to c_v on T_H , we plot T_H as a function of pressure for Fe shock-compressed from α -Fe to ϵ -Fe in Figure 4.2, using the parameter set for Fe given in Table 4.1. Below, we constrain Ω from the intersection of Fe-Hugoniot and melting curve, but for this comparison we assume $A_2 = 0$ and use the results of Boness *et al.* (1986) for $\Gamma(\rho)$ (Table 4.1). On the basis of these results, we may conclude that the electronic contribution to c_v of ϵ -Fe dominates its temperature along the Hugoniot of Fe at high pressure. Also for ϵ -Fe, and perhaps not surprisingly, the difference between T_H calculated with the full Debye relation for c_v ([4.46]) and that calculated by assuming the harmonic part of $c_v = 3\nu R/M$ ([4.52]) is very small (about 200 K at 240 GPa). In fact, even for Al_2O_3 , which possesses a

Figure 4.2. Comparison of the effect of different models for the specific heat at constant volume, $c_v(T, \rho)$, on the temperature of the ϵ -Fe Hugoniot states.



a much higher Debye temperature than ϵ -Fe (Table 4.1), Hugoniot temperatures calculated with [4.52] are only about 300 K above those calculated with [4.54] at 200 GPa. Note that the curves in Figure 4.2 converge at low pressure because T_H approaches T_S "faster" than the various approximations to c_v can affect T_H as $P \rightarrow 0$.

From the impedance match and U-v relations of each material, we may obtain the pressure and density of the first shocked-state of each target component. Using this along with an estimate of c_v and the assumed form for γ above allows us to estimate, using [4.20] and [4.44], the changes in specific internal energy and temperature along the appropriate isentrope of the high-pressure phase of each target component. These estimates, along with the model for $c_v(T, \rho)$, allow us to calculate T_H for any phase as a function of P_H . The next step is to estimate the effect of release on the shock-compressed state (T_H , P_H and ρ_H).

§4.2. Initial Conditions: Release and Reshock States

As discussed above, the targets are constructed so that the DP has a higher shock impedance, $\rho_1^0 U$, than the FL, which in turn has a higher impedance than the TW. In this case, both the DP and FL are shock-compressed, released and possibly reshocked. Assuming that a given release state of the DP or FL is in thermodynamic equilibrium, we may again employ the concept of an equivalent equilibrium thermodynamic path to connect respective compressed and released states of each target component. However, since we have no expression for the change in specific internal energy of the material during release that is independent of the details of phase transition (note that [4.1] is such a relation for shock compression), we cannot utilize the same kind of equilibrium thermodynamic path as that constructed above for shock compression. Instead, we must assume something about the release process, and any potential phase

change during release, to construct an equilibrium thermodynamic path between the compressed and released states. The only constraint we have *a priori* is that the release process takes the shock-compressed material at an interface, via the release path, to a state with approximately the same normal components of material velocity and stress as the shock-compressed state of the lower shock-impedance material on the other side of the interface. Subsequent wave-reverberations establish the continuity of normal stress and material velocity, as required for the existence of a material interface.

To proceed further, we assume that heat transport in or out of the target is insignificant on the time scale of the release process; *i.e.*, this process is adiabatic ($\delta q=0$). Considering each compressed target component as an equilibrium thermodynamic system, we further assume that any mechanical work by the system during release is entirely reversible. In the case of a single-phase system, the release path is then both isentropic and adiabatic. The change in temperature with density along this path is related to γ , as given by [4.6] above. Since the impedance match provides us with the pressure of the release state, P_R , we may calculate the temperature, T_R , and density, ρ_R , along an isentropic path that has not crossed a phase boundary through simultaneous solution of [4.6] and

$$\rho(T_R, P_R) = \rho(T_{HR}, P_R) \exp \left\{ - \int_{T_{HR}}^{T_R} \alpha[T, \rho(T, P_R)] dT \right\} \quad [4.55],$$

where $T_R \equiv T(s_H, \rho_R)$ is the temperature, $\rho_R \equiv \rho(T_R, P_R)$ the density of the release state, and $\rho(T_{HR}, P_R)$ is the density along the Hugoniot of the same phase at a temperature T_{HR} and the pressure of the release state, P_R . The coefficient of thermal expansion, $\alpha(T, \rho)$, in [4.56] comes from an equilibrium thermodynamic model for the appropriate phase (Appendix A for solid-state; Svendsen *et al.*,

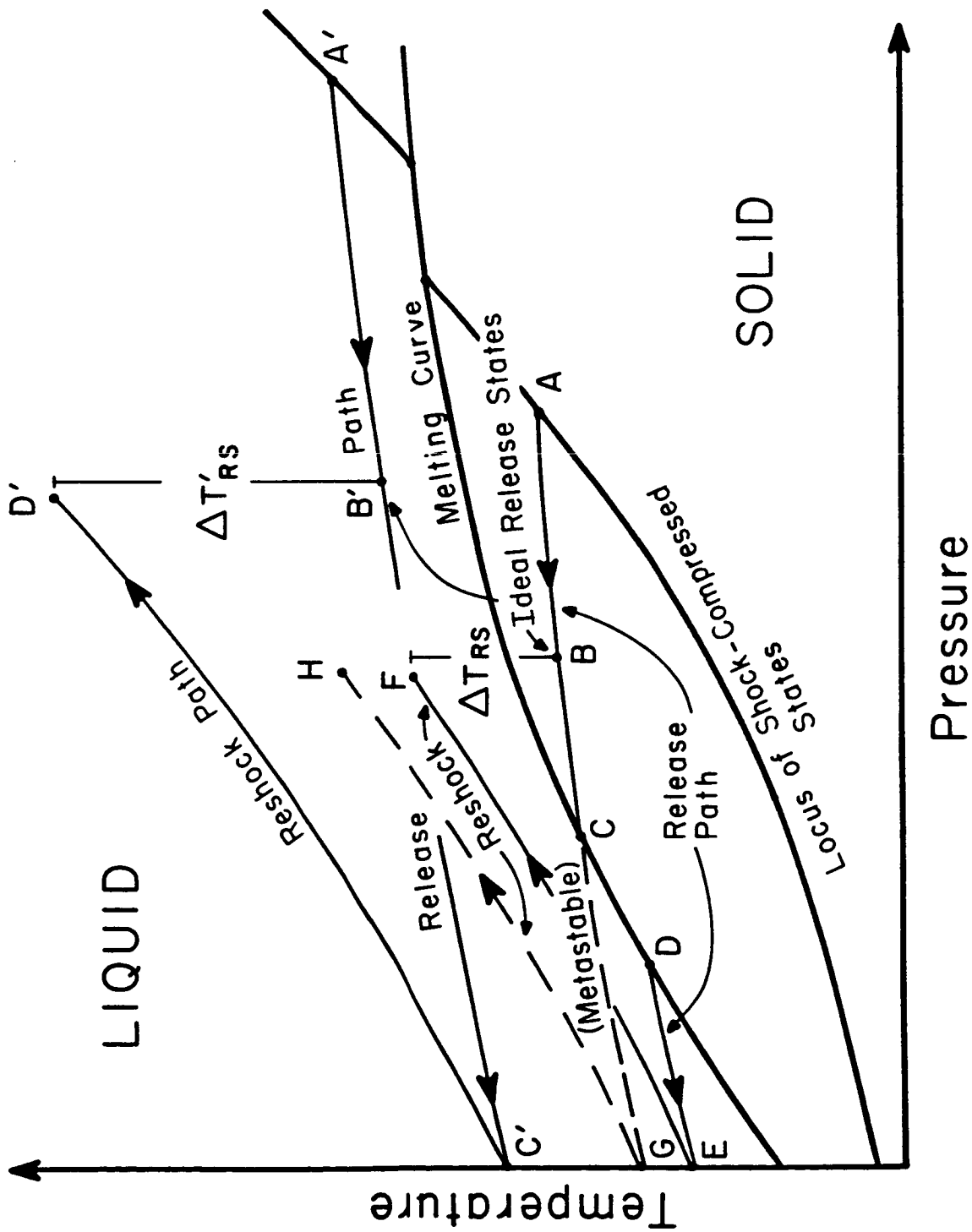
1987, Chapter V, for liquid-state). For example, in the case of solid-state release, α follows from the equilibrium thermodynamic model for $F(T, \rho)$, *i.e.*,

$$\alpha \equiv \frac{\rho \left\{ \frac{\partial^2 F}{\partial T \partial \rho} \right\}_{\rho, T}}{2\rho \left\{ \frac{\partial F}{\partial \rho} \right\}_T + \rho^2 \left\{ \frac{\partial^2 F}{\partial \rho^2} \right\}_T} \equiv \frac{\rho \gamma c_v}{K_T} \quad [4.56]$$

(Appendix A), where $K_T = K_T(T, \rho)$ is the isothermal bulk modulus, and it is referenced to the isentrope or Hugoniot as discussed in Appendix A.

To bound the nature of the release process as initiated at an interface, we focus on the extremes: 1) complete contact (\lesssim shock-front thickness) at the interface, or 2) no contact, in which case each material has a free surface at the interface. We refer to the former interface as the “smooth” interface, and to the latter as the “rough” interface. To illustrate the different paths these “end-member” interfaces should take, consider the two examples discussed below and depicted in Figure 4.3. If we shock-compress the DP(FL) to some point A along its Hugoniot below the Hugoniot-melting curve intersection, it will release to a state having, after one or two wave reverberations, the normal stress and material velocity of the shock-compressed FL(TW). If these reverberations are isentropic, the resulting temperature will equal that calculated by direct release to the pressure of the shock-compressed FL(TW). The DP(FL) material at the smooth interface then releases directly to this state, represented by point B in the Figure 4.3. However, the surface of the DP(FL) at the rough interface is partially free; hence, the DP(FL) material at this interface releases to near-zero pressure. If we assume the release path is isentropic, its slope will be less steep than that of the melting curve. In this case, the melting curve and release path will intersect (see point C, Figure 4.3). If the phase transition is slow relative to the rate of decompression, the DP(FL) material will follow the ABCG (metastable) path to low pressure (even though this path is not

Figure 4.3. Possible range of T-P paths taken by DP and FL materials near the DP-FL and FL-TW interfaces, respectively, during an experiment.



necessarily isentropic, as discussed below). However, if the transition is uninhibited, the release path will turn along the phase boundary at the intersection point (point C, Figure 4.3), and the mixed-phase material will decompress along the boundary until the transition is complete, or the mixture reaches low pressure. Assuming the transition completes above zero pressure at point D in Figure 4.3, the now liquid DP(FL) leaves the phase boundary and continues to decompress along DE to zero pressure. As the DP(FL) material closes the interface, it impacts the FL(TW) material and is reshocked and reverberated along a series of paths, collectively symbolized in Figure 4.3 as the paths lying between EF and GH, up to the smooth-interface, release-state pressure, which is that of the shocked FL(TW). Note that the temperature achieved by this set of shock paths is bounded above by the temperature estimated from a single shock compression back up to the Hugoniot pressure of the DP(FL); we use this bound below, along with isentropic release, since it follows directly from the results of the last section. Because the initial state of the reshocked material is at a higher temperature than the unshocked material, the reshocked material attains a higher temperature (ΔT_{rs} higher in Figure 4.3) than the release state of the DP(FL) material at a smooth interface. If the unshocked DP(FL) material is shocked to a higher pressure state than A that is still below the melting curve, a smooth interface may release to a state pinned to the melting curve, or be above the melting curve, as for release from A' in Figure 4.3, in the liquid state. The rough interface released from A' would follow A' B' C' and be reshocked along C' D' to D'. Note that the effect of reshock is much more pronounced as the initial shocked-state pressure increases, regardless of the phase transition.

When the release path encounters a phase boundary, such as the melting boundary shown in Figure 4.4, [4.6] is no longer valid. If we believe the release path remains isentropic through this region, then we must require that, in

addition to releasing adiabatically and doing or experiencing only reversible work, the material also change phase in thermodynamic equilibrium (Appendix B). Under these conditions, the isentropic two-phase path for a congruent phase-transition from phase β to phase π is described by the relation

$$\left\{ (c_p^\beta + \chi \Delta c_p) \Delta v - (\alpha^\beta v^\beta + \chi \Delta(\alpha v)) T_{\text{PB}}(P) \Delta s \right\} dP + \Delta s T_{\text{PB}}(P) \Delta s d\chi = 0 \quad [4.57],$$

where P is the pressure along the phase boundary, $T_{\text{PB}}(P)$, χ is the mass fraction of π , c_p is the specific heat at constant pressure, α is the coefficient of thermal expansion, v is the specific volume, and

$$\Delta \psi \equiv \psi^\pi - \psi^\beta$$

is the jump of any quantity ψ across the phase transition. Since 1) all end-member quantities in [4.57] may be viewed as functions of pressure and temperature, and 2) temperature and pressure are not independent along the equilibrium phase boundary, these quantities are actually function only of pressure or temperature along the boundary. In this case, choosing P as independent, we may solve [4.57] for $\chi = \chi(P)$ (Appendix B) to obtain

$$\chi(P) = \frac{1}{\Delta s \mu(P) \Delta v} \int_{P_{\text{PB}}^\beta}^P \mu(P^*) [T_{\text{PB}}(P) \alpha^\beta v^\beta \Delta s - c_p^\beta \Delta v] dP^* \quad [4.58]$$

with

$$\mu(P) \equiv \exp \left\{ \int^P \frac{1}{\Delta s} \left\{ \Delta(\alpha v) - \frac{\Delta v}{T_{\text{PB}}(P)} \left\{ 1 + \frac{\Delta c_p}{\Delta s} \right\} \right\} dP \right\} \quad [4.59].$$

In [4.58], P_{PB}^β is the pressure at which the release path of β intersects the π - β phase boundary, *i.e.*, where $\chi = 0$. We may evaluate [4.58] numerically along

the phase boundary, $T_{\text{PB}}(P)$, with $\chi(P)$ increasing above zero, until 1) $\chi = 1$ (complete transformation) or 2) $T_{\text{PB}} = T_{\text{PB}}(P_R)$ (partial transformation). In the former case, the new phase then releases to P_R along a path beginning at the pressure and temperature on the phase boundary where $\chi = 1$.

Relation [4.58] is valid along any isentropic path through a first-order mixed-phase region of a single-component system, (*i.e.*, solid-solid, liquid-solid), but now we focus on the solid-liquid phase boundary as discussed above. To utilize [4.58], we need to estimate solid- and liquid-state properties along the solid-liquid boundary $T_M(P)$. We do this by way of semi-empirical models for the solid-state (*e.g.*, Andrews, 1973; Appendix A), and the liquid-state (*e.g.*, Stevenson, 1980; Svendsen *et al.*, 1987, Chapter V), respectively. For the solid state, we use a parameterization of the solidus, $T_M^s(\rho_M^s)$, based on Lindemann's law:

$$\left\{ \frac{dT_M^s}{d\rho_M^s} \right\}_{\text{Lindemann}} \equiv \frac{T_M^s \lambda_M^s}{\rho_M^s} \quad [4.60],$$

where

$$\lambda_M^s \equiv 2\left(\gamma_{\text{pM}}^s - \frac{1}{3}\right) \quad [4.61]$$

for the solid-two phase boundary (solidus). The quantity γ_{pM}^s is the solid phonon Grüneisen's parameter at the melting point, equal to $\gamma_{\text{D}}(\rho_M^s)$ in the Debye approximation we use here. Using [4.61] in [4.60], we may calculate $T_M^s(\rho_M^s)$ once we know the density of the solid along the phase boundary, and the dependence of λ_M^s on the solidus density. For the solid phase, we have already assumed $\gamma_{\text{p}} \equiv \gamma_{\text{D}}(\rho)$, with γ_{D} given by the power-law [4.38] above. Putting [4.38] into [4.61] and the resulting combination into [4.60], we obtain an expression for the solidus, *i.e.*,

$$T_M^s(\rho_M^s) \equiv T_M^s(\rho_{M_1}^s) \left\{ \frac{\rho_{M_1}^s}{\rho_M^s} \right\}^{2/3} \exp \left\{ \frac{2\gamma_{\text{pr}}}{q_r} \left[\left\{ \frac{\rho_r}{\rho_M^s} \right\}^{q_r} - \left\{ \frac{\rho_r}{\rho_{M_1}^s} \right\}^{q_r} \right] \right\} \quad [4.62],$$

where $\rho_M^s \equiv \rho(T_M, P_i)$ is the density of the solid at the melting temperature at standard pressure. To use [4.62] to find $T_M^s(\rho_M^s)$, we need to calculate the change in density along the solidus with pressure. Noting that, in general, the equilibrium thermodynamic properties as developed from [4.33] are functions of temperature and density, we may calculate the variation of any of these properties, $\psi(T, \rho)$, with temperature at constant pressure from the relation

$$\psi(T, P_r) = \psi(T_r, P_r) + \int_{T_r}^T \left(\frac{\partial \psi}{\partial T} \right)_P dT \quad [4.63],$$

where

$$\left(\frac{\partial \psi}{\partial T} \right)_P = \left(\frac{\partial \psi}{\partial T} \right)_\rho - \alpha \rho \left(\frac{\partial \psi}{\partial \rho} \right)_T \quad [4.64]$$

where P_r and T_r are some pressure and temperature at which we know ψ . In particular, putting $\psi = \rho$ into [4.62], as we did to obtain [4.55] above, we may anchor the solidus T_M^s to the solid Hugoniot of the relevant solid phase by solving [4.63] (numerically) simultaneously with

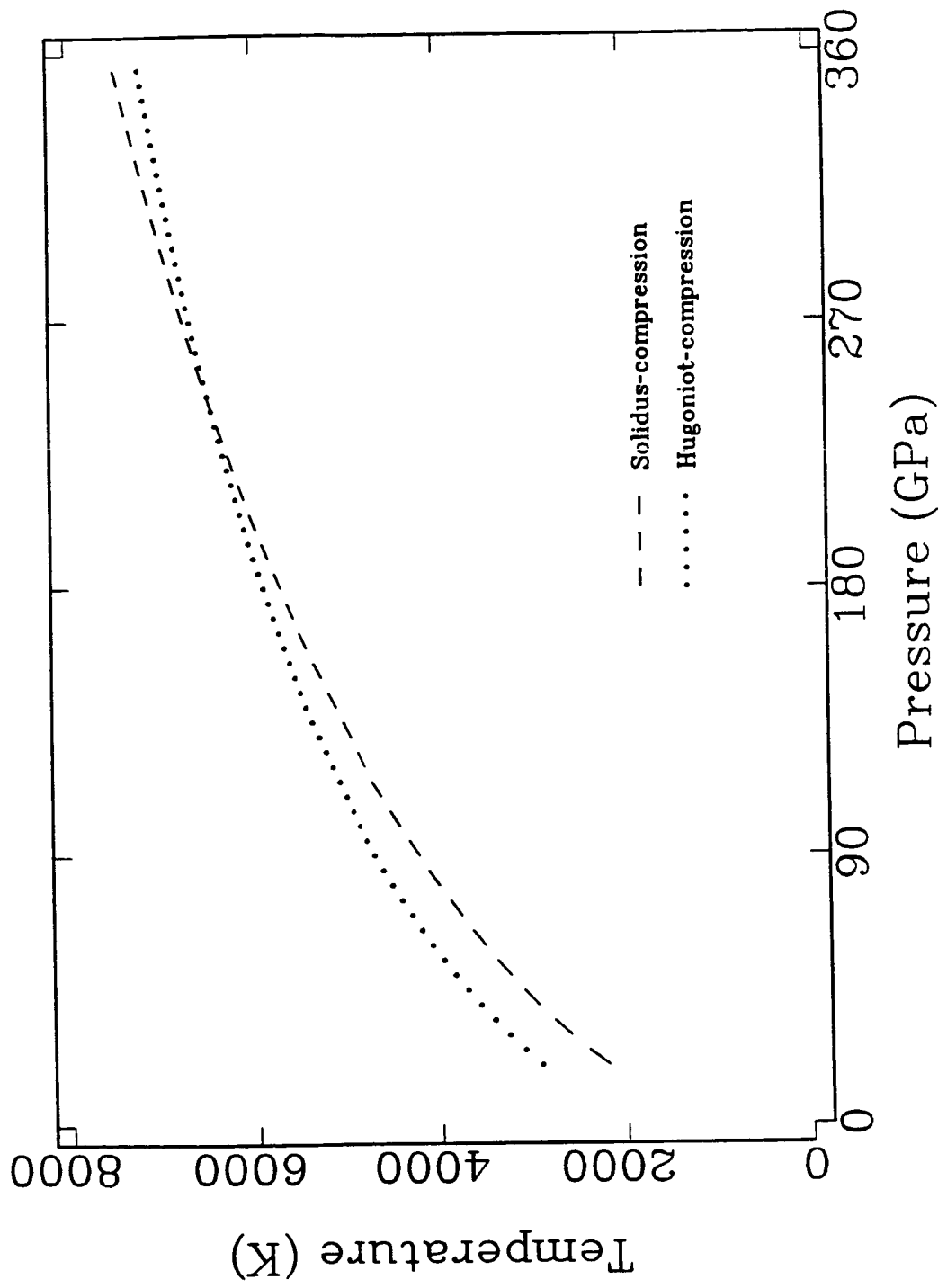
$$\rho(T_M^s, P) = \rho(T_H, P) \exp \left\{ - \int_{T_H}^{T_M^s} \alpha [T, \rho(T, P)] dT \right\} \quad [4.65],$$

where $\rho_M^s = \rho(T_M^s, P)$ and $\rho(T_H, P)$ is the Hugoniot density of the solid phase at the same pressure, with α as given above. In Figure 4.4, we compare this calculation with one in which we assume $\rho(T_M^s, P) = \rho(T_H, P)$. The greatest effect is at low pressure; this is also where the correction is most uncertain.

For the DP-FL and FL-TW interfaces with no contact, the DP and FL release to near-zero pressure, and consequently we cannot use the Hugoniot as a reference state. So instead of [4.55], we solve [4.6] simultaneously with

$$\rho(T_R, 0) = \rho(T_r, 0) [1 - \alpha(T_r, 0)(T_R - T_r)] \quad [4.66],$$

Figure 4.4. Comparison of ϵ -Fe Lindemann solidi calculated from the compression along Hugoniot (dotted curve) with that estimated from the compression along the Hugoniot adjusted to the solidus temperature (dashed curve), as discussed in the text.



where T_r is some reference temperature (*e.g.*, 298 K or T_M), depending on the relevant phase. With the density of the release state, ρ_R , we may estimate the free surface velocity of the DP and FL surfaces at the DP-FL and FL-TW interfaces, respectively, due to isentropic release, via the Riemann integral method (*e.g.*, Fowler and Williams, 1970). We assume, as required by the constraint of isentropic release, that the material velocity is continuous across the phase boundary (*i.e.*, the same for both phases) when calculating the free surface velocity. We then take this free surface velocity as the "projectile" velocity of the DP or FL surface impacting the FL or TW surface, respectively, and use an impedance match to calculate the pressure and density of the reshocked state. To calculate the temperature of the reshock state, we use the appropriate form of [4.46], but referenced to the temperature and density of the complete release state rather than to T_i and ρ_i^α (Appendix B).

§4.3. Initial Conditions: Application to Fe Targets

To exemplify these considerations, we calculate release and reshock states for Fe-Fe- Al_2O_3 and Fe-Fe-LiF targets, as shown in Figures 4.5a-b. The solid and liquid Hugoniot states result from [4.46] and [4.52] (with $A_2=0$ and $\xi_{Dr}=0$), respectively, as based on the parameter set given in Table 4.1. Solid-state properties along the release path and melting curve are referenced to the ϵ -Hugoniot via [4.6], [4.46] and [4.52], while the analogous liquid-state properties are referenced to the experimentally constrained Fe melting curve of Williams and Jeanloz (1986) via a liquid-state model for Fe (Svendsen *et al.*, 1987, Chapter V). The Fe melting-curve data of Williams and Jeanloz (1986), which extend to 100 GPa, are fit to a Lindemann parameterization, referenced to the ϵ -Fe Hugoniot (metastably above 245 GPa) using [4.62] and [4.65] (Svendsen *et al.*, 1987, Chapter V), and then extrapolated to 330 GPa. In calculating these release paths, we ignore all other solid phases of Fe, save ϵ -Fe, which is the

Figure 4.5a. Release/reshock calculations for Fe film/foil- Al_2O_3 interfaces and initial greybody temperatures inferred from Fe-Fe film/foil- Al_2O_3 radiation data of Bass *et al.* (1987). "Release conduction" and "reshock-conduction" symbols represent initial effect of thermal inertia mismatch across the Fe film/foil- Al_2O_3 interface on the indicated states.

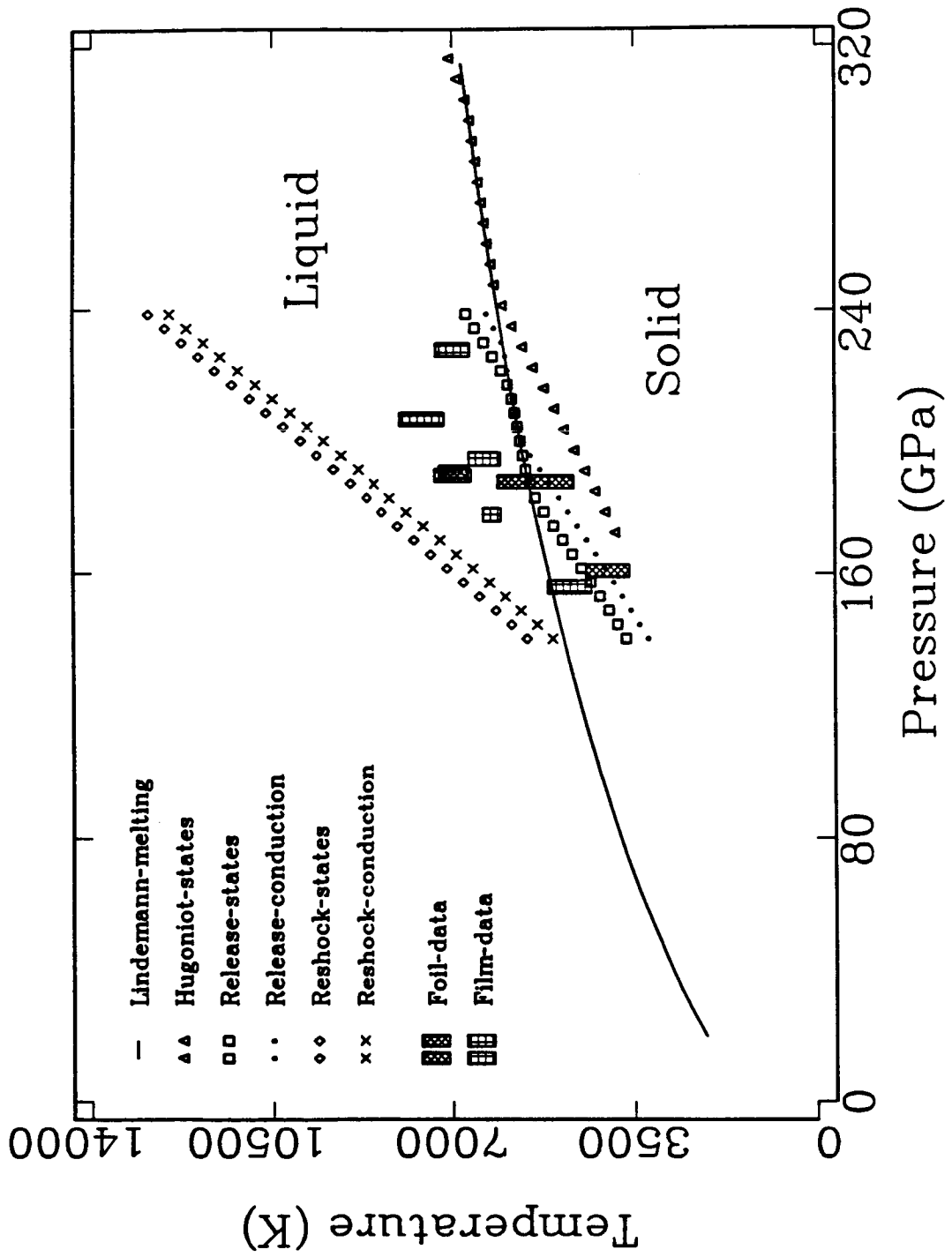
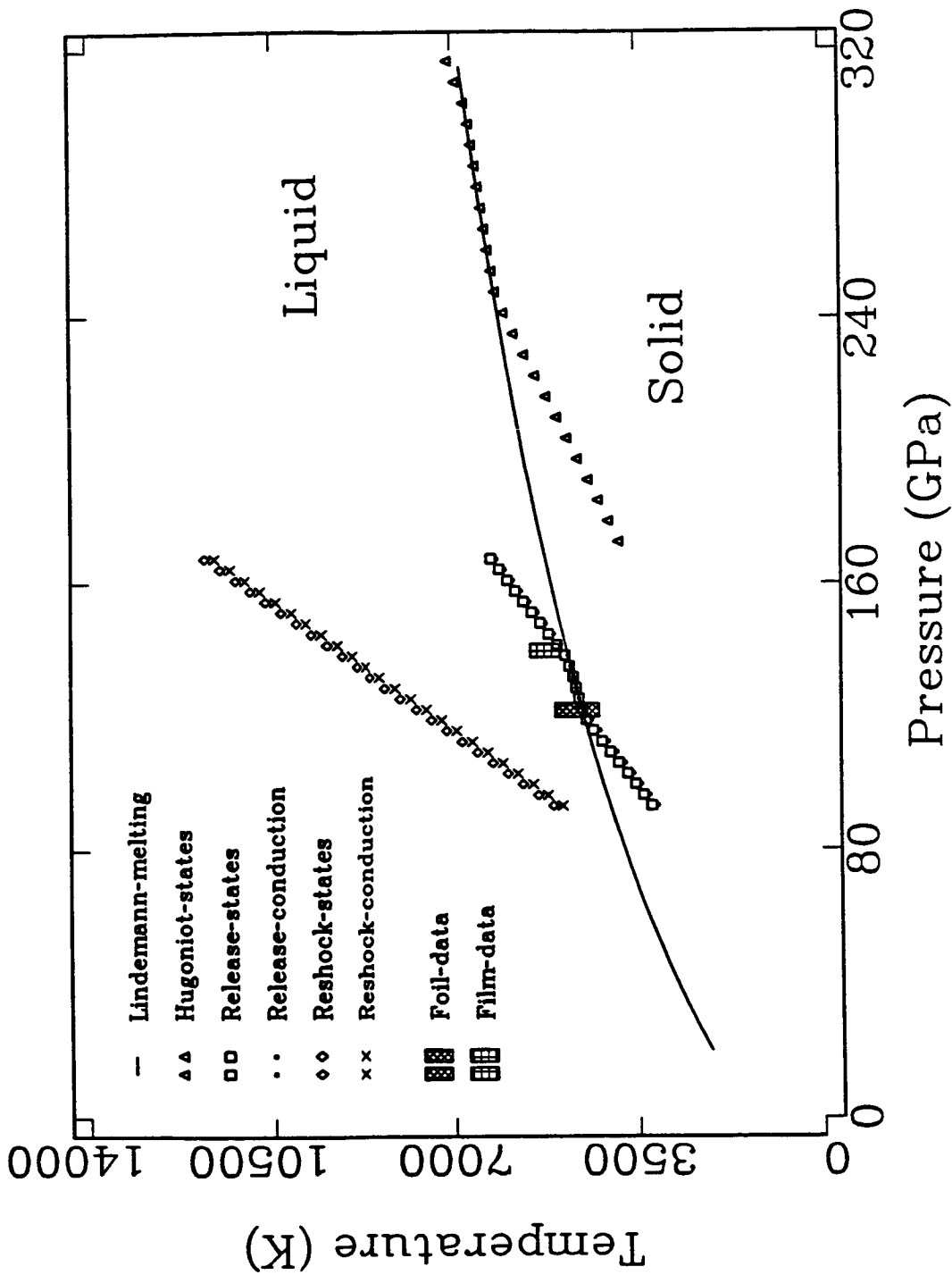


Figure 4.5b. Release/reshock calculations for Fe film/foil-LiF interfaces and initial greybody temperatures from Fe-Fe film/foil-LiF radiation data. The larger shock-impedance mismatch between Fe and LiF results in a lower release-state pressure at Fe-LiF interfaces than at Fe-Al₂O₃ interfaces, when both release from the same Hugoniot pressure.



stable solid phase of Fe along its Hugoniot between 13 (Barker and Hollenback, 1974) and ~ 200 GPa, where the sound-speed measurements of Brown and McQueen (1982, 1986) along the Fe Hugoniot suggest that ϵ -Fe transforms to γ -Fe (?) or possibly a new solid phase (θ : Boehler, 1986). Consequently, γ -Fe and/or another solid-phase is in equilibrium with liquid-Fe above about 5 GPa to perhaps 280 GPa (*e.g.*, Anderson, 1986). In this case, we neglect any effects of an $\epsilon \rightarrow \gamma$ or $\epsilon \rightarrow \theta$ transition in referencing compression along the Fe-melting curve to the ϵ -Fe Hugoniot. As stated above, in calculating the ϵ -Fe Hugoniot states shown in Figures 4.5a-b, we have constrained $\Omega(\rho_i)$, with $\omega = 1.34$, which is the value of γ_e for ϵ -Fe given by Boness *et al.* (1986), by requiring the parameterized Fe-melting curve and ϵ -Hugoniot to intersect at 245 GPa. On the basis of the parameter set given in Table 4.1, this fit constrains $\Omega(\rho_i)$ to be $0.046 \text{ J/kg}\cdot\text{K}^2$. Boness *et al.* (1986) calculated a value of $0.090 \text{ J/kg}\cdot\text{K}^2$ for $\Gamma(\rho_i)$ (adjusted to STP density for ϵ -Fe given in Table 4.1). If we set $\Omega(\rho_i) = 0.090$, the ϵ -Hugoniot based on the parameter set in Table 4.1 intersects the melting curve at ≈ 280 GPa. We note that Boness *et al.* (1986) constrained $\Gamma(\rho_i) = 0.09 \text{ J/kg}\cdot\text{K}^2$ and $\gamma_e = 1.27$ for γ -Fe, while Bukowinski (1977) constrained $\Gamma(\rho_i) = 0.08 \text{ J/kg}\cdot\text{K}^2$ and $\gamma_e = 1.5$ for this phase. With these values for $\Gamma(\rho_i)$, the value of $\Omega(\rho_i)$ constrained above for ϵ -Fe implies some competition between anharmonic and electronic contributions to the specific heat of ϵ -Fe at high pressure.

Brown and McQueen (1986) fit a linear U-v relation to the available Fe-Hugoniot data between 13 and 400 GPa. Since their sound-speed measurements also suggest that Fe melts along the Hugoniot above about 245 GPa, their U-v relation should describe the liquid-solid mixture and pure liquid phase, as well as the solid. On this basis, we use their U-v relation to calculate both the ϵ -Fe Hugoniot and a metastable liquid-Fe Hugoniot referenced to the extrapolated density of liquid-Fe at STP (Table 4.1). With this U-v relation, [4.53] above for T_H ($A_2 = 0$ and $\xi_{D_s} = 0$) and Γ as constrained by Boness *et al.* (1986), we

calculate the metastable Hugoniot of liquid Fe. Using $\Delta e_1^{\beta-\alpha} = 0.14$ MJ/kg for Fe (as compared to the enthalpy of melting at standard pressure, 0.25 MJ/kg, from Desai, 1986), the metastable liquid Fe Hugoniot intersects the melting curve at about 305 GPa. This agrees reasonably well with the results of Young and Grover (1984), who also ignored all other phases of Fe, save ϵ and liquid, in their parameterization of the Fe melting curve. We combine this metastable Hugoniot along with the ϵ -Fe Hugoniot in an ideal mix (*e.g.*, Watt and Ahrens, 1984) to construct the shock-compressed, mixed-phase region shown in Figures 4.5a-b.

For comparison with the calculations, we have plotted the initial interface temperature results from the Fe film/foil experiments of Bass *et al.* (1987) in Figures 4.5a-b. Note that the Fe-Al₂O₃ interface data shown in Figure 4.5a run almost parallel to the reshock locus, thereby exemplifying the strong pressure dependence of the reshock process (Urtiew and Grover, 1974). Comparing the data with the smooth-interface release states, shown as squares in Figure 4.5a, implies that Fe at both film-Al₂O₃ and foil-Al₂O₃ interfaces experiences up to \sim 2500 K of reshock heating between 190 and 230 GPa. As stated above, we naively expected that the film-TW interface would experience consistently less reshocking than the foil-TW interface. The present results contradict this expectation. There appears to be no guarantee that film interfaces will consistently experience any less reshock than the foil interfaces, especially at high pressure. In this case, a well-polished foil surface may actually experience less reshock than a slightly porous film interface.

Figure 4.5b displays the results of the calculation for Fe-LiF interfaces. Because of the larger impedance mismatch between Fe and LiF, the Fe-LiF interface reaches a lower release-state pressure than the Fe-Al₂O₃ interface when both release from the same Hugoniot pressure. The data and calculation imply that lower release-state pressure results in less extreme reshocking. Note that

the Fe-LiF and low-pressure Fe-Al₂O₃ data fall right on the corresponding smooth-release locus. The points labeled "release conduction" and "reshock conduction" refer to the effect of the contrast or mismatch in "thermal inertia" across the Fe-TW interface on the release and reshock temperatures, and as discussed in the following section.

§5. Conductive Transport in the Target

We assume that the temperature profile created by shock compression, release and/or reshock is established on a time scale short enough to represent the initial conditions for energy transport in the target. Urtiew and Grover (1974) considered the problem of energy transfer at material interfaces and demonstrated that a rough ($\gtrsim 1 \mu\text{m}$) interface experiences a higher degree of shock heating than a smooth ($\lesssim 1 \mu\text{m}$) interface, much like a porous material experiences relative to its crystalline counterpart. Since the TW surface at the interface is much less rough ($\lesssim 10^{-8} \text{ m}$) than the DP surface at the interface, it should experience little, if any, direct reshock heating. However, the DP and FL surfaces at the DP-FL interface, as well as the FL surface at the FL-TW interface, may experience significant reshock heating, as discussed above.

Following Grover and Urtiew (1974), we assume that 1) energy transport is parallel to the direction of shock propagation (*i.e.*, one-dimensional), 2) both temperature and heat flux are continuous across each interface in the target, and 3) there are no sources or sinks of energy in any layer or at the interfaces between them. Under these conditions, we may solve the one-dimensional conduction relation:

$$\rho c_p \frac{\partial T}{\partial t} = k \frac{\partial^2 T}{\partial x^2} \quad [5.1]$$

(*e.g.*, Carslaw and Jaeger, 1959) for the temperature profile, $T=T(x,t)$, in each

target component as a function of position along the direction of shock propagation, x , and time, t . The time $t=0$ corresponds to coincidence of the shock front and FL-TW interface. In [5.1], ρ is the density, c_p is the specific heat at constant pressure, and k is the thermal conductivity. Since the temperature profile in the FL, and particularly the temporal variations of temperature at the FL-TW interface, control the intensity of thermal radiation sources at the FL-TW interface, we emphasize these in what follows.

We expect a layer of the DP material at the DP-FL interface and a layer of the FL material at the FL-TW interface to experience some degree of reshocking. Also, the rough FL surface at the DP-FL interface should compress into a thin layer with a much higher temperature than the shock-compressed solid FL material. With this structure, the initial ($t=0$) temperature profile of the DP-FL-TW system is of the form

$$T(x,0) \equiv \begin{cases} T_D & -\infty < x < -(d+\delta_D) \\ T_D+\Delta T_D & -(d+\delta_D) < x < -d \\ T_F+\Delta T_{FD} & -d < x < -(d-\delta_{FD}) \\ T_F & -(d-\delta_{FD}) < x < -\delta_{FW} \\ T_F+\Delta T_{FW} & -\delta_{FW} < x < 0 \\ T_w & 0 < x < \infty \end{cases} \quad [5.2]$$

(Figure 5.1). Here, d is the FL thickness, and T_D and T_F are the temperatures achieved in DP and FL, respectively, by direct release to the pressure of the shock-compressed TW, which has a temperature T_w . Also, $T_D+\Delta T_D$ is the temperature of the reshocked layer with thickness δ_D in the DP at the DP-FL interface, while $T_F+\Delta T_{FW}$ is the temperature of the reshocked layer with thickness δ_{FW} in the FL at the FL-TW interface. If the surface of the FL at the DP-FL interface is also rough on some scale, it will compress like a porous material. Consequently, we assume that a layer with a thickness δ_{FD} and temperature $T_F+\Delta T_{FD}$ forms in the FL at the DP-FL interface. Since the surface of the TW

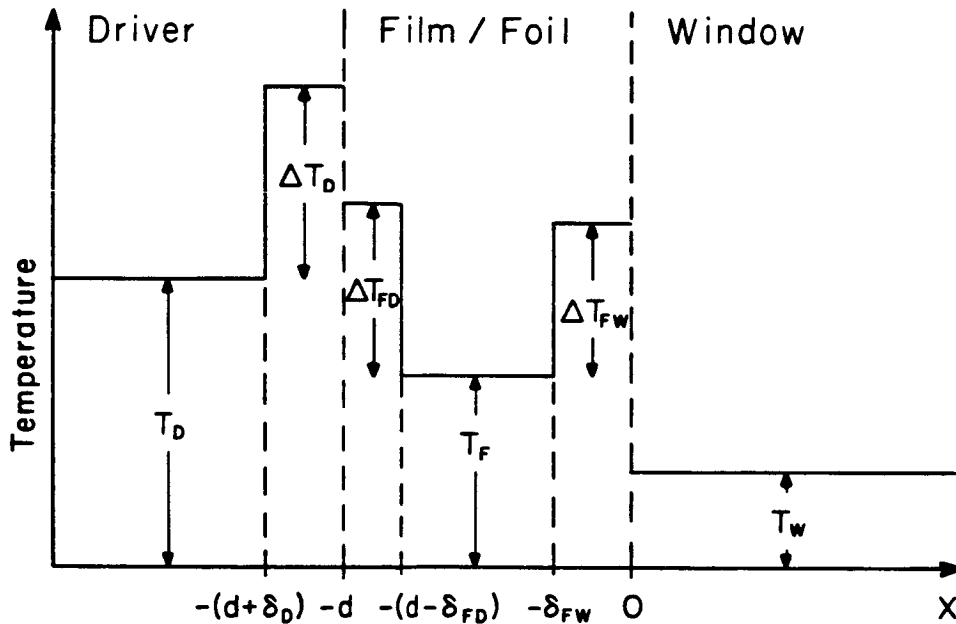


Figure 5.1. Initial conditions for thermal conduction in target. T_D and T_F represent temperatures achieved in the DP and FL, respectively, upon direct release to a state with the pressure of the shock-compressed TW, having a temperature T_W . Variable degrees of reshocking are shown for DP (ΔT_D) and FL (ΔT_{FD}) at the DP-FL interface, and for FL (ΔT_{FW}) at the FL-TW interface; these involve some thickness (δ_D , δ_{FD} , and δ_{FW}) of each target component adjacent to the interface.

is much smoother than the DP or FL surfaces, we assume that there is no reshock heating of the TW material at the FL-TW interface. Note that the DP and TW are idealized as thermal half-spaces, a consequence of our assumption about the rates of shock compression and release relative to conduction. Again, we emphasize that all material properties of each target component are assumed homogeneous, time-independent, and are referenced to their respective states at the pressure of the FL-TW interface.

The governing relation [5.1] for each layer, combined with the boundary conditions of continuity of heat flux and temperature, and the initial conditions [5.2], specify an initial-boundary value problem for $T(\xi, \tau)$ in the target, where $\xi = x/d$ and $\tau = t/t_{\text{exp}}$. We are particularly interested in this profile for the FL layer, and the temporal variation of $T(0, \tau)$, for the FL, which represents the FL-TW interface temperature. Solving this initial-boundary value problem in Appendix D, we obtain expressions for $T_D(\xi, \tau)$, $T_F(\xi, \tau)$, and $T_w(\xi, \tau)$. In particular, we have, for $T_F(\xi, \tau)$, $-1 \leq \xi \leq 0$, $\tau > 0$, the expression

$$T_F(\xi, \tau) = T_F + A(\xi, \tau)\Delta T_D + B(\xi, \tau) [T_D - T_F] \\ + C(\xi, \tau)\Delta T_{FD} + D(\xi, \tau)\Delta T_{FW} + E(\xi, \tau)[T_w - T_F] \quad [5.3]$$

with

$$A(\xi, \tau) \equiv \frac{1}{(1+\sigma_{DF})} \sum_{m=0}^{\infty} (\nu_{DF}\nu_{WF})^m \\ \cdot \left\{ \text{erfc}\{[(2m+1)+\xi]\omega_F\} - \text{erfc}\{[(2m+1)+\xi+\kappa_{FD}\delta_D^*]\omega_F\} \right. \\ \left. - \nu_{WF} \left\{ \text{erfc}\{[(2m+1)-\xi]\omega_F\} - \text{erfc}\{[(2m+1)-\xi+\kappa_{FD}\delta_D^*]\omega_F\} \right\} \right\}$$

$$B(\xi, \tau) \equiv \frac{\sigma_{DF}}{(1+\sigma_{DF})} \sum_{m=0}^{\infty} (\nu_{DF}\nu_{WF})^m \left\{ \text{erfc}\{[(2m+1)+\xi]\omega_F\} - \nu_{WF} \text{erfc}\{[(2m+1)-\xi]\omega_F\} \right\}$$

$$C(\xi, \tau) \equiv \begin{cases} g_F^-(\xi, \tau; -1, \xi) + g_F^+(\xi, \tau; \xi, -1 + \delta_{FD}^*) & \xi \leq -1 + \delta_{FD}^* \\ g_F^-(\xi, \tau; -1, -1 + \delta_{FD}^*) & \xi \geq -1 + \delta_{FD}^* \end{cases}$$

$$D(\xi, \tau) \equiv \begin{cases} g_F^+(\xi, \tau; -\delta_{FW}^*, 0) & \xi \leq -\delta_{FW}^* \\ g_F^-(\xi, \tau; -\delta_{FW}^*, \xi) + g_F^+(\xi, \tau; \xi, 0) & \xi \geq -\delta_{FW}^* \end{cases}$$

and

$$E(\xi, \tau) \equiv \frac{\sigma_{WF}}{(1 + \sigma_{WF})} \sum_{m=0}^{\infty} (\nu_{DF} \nu_{WF})^m \left\{ \operatorname{erfc}\{[2m - \xi]\omega_F\} - \nu_{DF} \operatorname{erfc}\{[2(m+1) + \xi]\omega_F\} \right\}.$$

The functions $g_F^\pm(\xi, \tau; a, b)$ are defined in Appendix D (Equation [D.40]). In these expressions, $\kappa_{FD} \equiv \sqrt{\kappa_F/\kappa_D}$ is the square root of the ratio of the FL thermal diffusivity to the DP thermal diffusivity, with $\kappa \equiv k/\rho c_p$, $\xi \equiv x/d$ is the nondimensional distance, d is the thickness of the FL, $\omega_F \equiv \sqrt{Pe_F/4\tau}$, $\tau \equiv t/t_{exp}$ is the nondimensional time scale, $Pe_F \equiv d^2/\kappa_F t_{exp}$ is the Peclet number, t_{exp} is the time scale of experiment, and $\delta_i^* \equiv \delta_i/d$, where $i=DP, FL$ or TW . Also, we have

$$\sigma_{DF} \equiv \left\{ \frac{k_D \rho_D c_{p,D}}{k_F \rho_F c_{p,F}} \right\}^{1/2} \quad [5.4]$$

and

$$\sigma_{WF} \equiv \left\{ \frac{k_W \rho_W c_{p,W}}{k_F \rho_F c_{p,F}} \right\}^{1/2} \quad [5.5],$$

which are the thermal inertia "mismatches" (Carslaw and Jaeger, 1959, p. 321) between DP and FL, and TW and FL, at the pressure of the FL-TW interface. Also, we have

$$\nu_{WF} \equiv \frac{(\sigma_{WF} - 1)}{(\sigma_{WF} + 1)} \quad [5.6]$$

and

$$\nu_{DF} \equiv \frac{(\sigma_{DF} - 1)}{(\sigma_{DF} + 1)} \quad [5.7].$$

In [5.4] and [5.5], k , ρ and c_p are the thermal conductivity, density and specific heat at constant pressure, respectively, of the designated material for the state of each material at the pressure of shock-compressed TW. To estimate the values of σ_{DF} and σ_{WF} at high pressure, we need the appropriate values of k , ρ and c_p . Density follows from the impedance match and release calculations, while the specific heat at constant pressure results from the classical thermodynamic models discussed above. Assuming that the thermal conductivity, k , may be written in terms of lattice, k_p , and electronic, k_e , components, *i.e.* $k = k_p + k_e$, we assume that $k \approx k_e$ for metallic target components. In this case, we calculate k_D and k_F as a function of temperature from the Wiedemann-Franz-Lorenz (WFL) relation

$$\frac{\rho_e k_e}{T} = 2.45 \times 10^{-8} \text{ W}\cdot\Omega/\text{K}^2 \quad [5.8]$$

(*e.g.*, Berman, 1976), where ρ_e is the electrical resistivity, to estimate k_e from electrical resistance data on shocked metals, respectively. Assuming the thermal conductivity of the TW material is controlled by lattice processes, we may use the thermal conductivity model of Roufosse and Klemens (1974) to estimate k_W . As compared to k_D or k_F , k_W predicted from this model increases much more slowly with pressure, partially accounting for the development of a significant thermal inertia mismatch across the FL-TW target interface. Based on the release/reshock calculations presented above, we calculate σ_{WF} for the Fe- Al_2O_3 and Fe-LiF interfaces using the value of electrical conductivity for ϵ -Fe given in Table 4.1. This value comes from Keeler (1971), who summarized electrical conductivity data on ϵ -Fe between 20 and 140 GPa, and it represents an extrapolation of the trend in the ϵ -Fe data down to standard pressure. We list results of this calculation in Table 5.1. As evident, Fe is more closely matched to Al_2O_3 than LiF; since $T_{DT}(\tau)$ is proportional to $\sigma_{WF}/(1+\sigma_{WF})$ (see [5.9]), there is a greater adjustment of $T_{DT}(\tau)$ at the Fe- Al_2O_3 interface, as is shown below.

Table 5.1. STP and High-Pressure Thermal-Inertia Mismatch Estimates.

	STP	100 GPa	200 GPa
		Ideal interface	
Fe-Al ₂ O ₃	0.56	0.25	0.15
Fe-LiF	0.20	0.11	0.05
		Reshocked interface	
Fe-Al ₂ O ₃	0.56	0.15	0.07
Fe-LiF	0.20	0.08	0.01

We now focus on the FL-TW interface temperature, $T_{\text{INT}}(\tau) \equiv T_{\text{F}}(0,\tau) = T_{\text{W}}(0,\tau)$, since it is responsible for controlling the interface source radiation intensity. Specializing the relation for $T_{\text{INT}}(\tau)$ to the case where the DP and FL are the same material (*e.g.*, Fe), we have $T_{\text{D}} = T_{\text{F}}$; we also assume $\Delta T_{\text{D}} = \Delta T_{\text{FD}}$ for simplicity. In this context, the same equilibrium thermodynamic state exists on either side of the DP-FL interface, and $T_{\text{INT}}(\tau)$ is given by

$$T_{\text{INT}}(\tau) = T_{\text{F}} + G(\tau)\Delta T_{\text{D}} + D(\tau)\Delta T_{\text{FW}} + \frac{\sigma_{\text{WF}}}{(1+\sigma_{\text{WF}})}(T_{\text{W}} - T_{\text{F}}) \quad [5.9]$$

with

$$G(\tau) = \frac{1}{(1+\sigma_{\text{WF}})} \left[\operatorname{erfc}\{(1-\delta_{\text{FD}}^*)\omega_{\text{F}}\} - \operatorname{erfc}\{(1+\delta_{\text{D}}^*)\omega_{\text{F}}\} \right]$$

and

$$D(\tau) = \frac{1}{(1+\sigma_{\text{WF}})} \operatorname{erf}\{\delta_{\text{FW}}^*\omega_{\text{F}}\} .$$

Noting that the complementary error function, $\operatorname{erfc}(x)$, decreases with increasing x , and $\operatorname{erf}(x)$ increases with increasing x , we see that $D(\tau)$ will decay with time, while $G(\tau)$ can either grow or decay. Most radiation observations constrain a decreasing temperature with time (see discussion below); however, there may be some suggestion of the influence of ΔT_{D} on $T_{\text{INT}}(\tau)$ in the data on the Fe-LiF interfaces discussed below.

If we assume $\Delta T_{\text{D}} = 0 = \Delta T_{\text{FD}}$ and/or $\delta_{\text{D}}^* = 0 = \delta_{\text{FD}}^*$, [5.9] reduces to

$$T_{\text{INT}}(\tau) = T_{\text{F}} + D(\tau)\Delta T_{\text{FW}} + \frac{\sigma_{\text{WF}}}{(1+\sigma_{\text{WF}})}(T_{\text{W}} - T_{\text{F}}) \quad [5.10],$$

which is the reshock model considered by Grover and Urtiew (1974). Further, if we let $\delta_{\text{FW}}^* \rightarrow 0$, we have, from [5.10],

$$T_{\text{INT}}(\tau) = T_{\text{id}} \equiv T_{\text{F}} + \frac{\sigma_{\text{WF}}}{(1+\sigma_{\text{WF}})}(T_{\text{W}} - T_{\text{F}}) \quad [5.11]$$

relating the temperature of the smooth FL-TW interface, T_{id} , to the temperature of the direct-release state, T_F . Note that T_{id} approaches T_F as $\sigma_{WF} \rightarrow 0$, and T_w as $\sigma_{WF} \rightarrow \infty$. Also, note that that $T_{INT}(\tau)$, as given by [5.11], will be time-dependent only if the FL-TW interface is reshocked. We use [5.10] with the reshock-state temperature in the FL at the FL-TW interface ($T_F + \Delta T_{FW}$), the shock-compressed temperature of the TW (T_w), σ_{DF} and σ_{WF} , to calculate $T_{INT}(0)$, which is labeled "reshock conduction" in Figures 4.4a-b. Similarly, we use [5.12] to calculate the "release conduction" temperatures from T_F , T_w , and σ_{WF} . As stated above, the Fe-LiF thermal mismatch is greater (*i.e.*, σ_{WF} is much smaller: see Table 5.1) than that of the Fe-Al₂O₃ interface, mainly because LiF is more compressible and less conductive (thermally: see Table 4.1) than Al₂O₃. In this case, the Fe-LiF interface temperature remains closer to the temperature of Fe at the interface than does the Fe-Al₂O₃ interface temperature. Further, the greater compressibility of LiF gives it a much higher shock-compressed temperature than Al₂O₃. For example, T_H for LiF (from [4.52]) at 160 GPa is ≈ 4200 K (ignoring the possibility of melting), while T_H for Al₂O₃ (also from [4.52]) at 230 GPa is ≈ 2750 K. The temperature mismatch is much less across the Fe-LiF interface, and the effect of thermal inertia mismatch on T_{INT} is less extreme.

In Figures 5.2, 5.3, 5.4 and 5.5, we present calculations for $T_F(\xi, \tau)$ and $T_w(\xi, \tau)$ from [5.3] and [D.25], respectively, and the associated $T_{INT}(\tau) = T_F(0, \tau)$, with $\Delta T_D = \Delta T_{FD}$, *etc.*, as assumed to write [5.9], for Fe-Fe-TW targets. To construct these figures, we calculate the compressed/released and reshocked/released states achieved in an Fe-Fe-Al₂O₃ target impacted by a Ta projectile at a velocity of 5.67 km/s; we assume the calculated reshock temperatures at the DP-FL and FL-TW interfaces are the initial values. This impact velocity is that of one of the experiments (Fe-Fe film-Al₂O₃) discussed below. The basic result here is the dependence of the rate of change of $T_{INT}(\tau)$ on Pe_F

Figure 5.2. Variation of the temperature near a reshocked Fe film/foil- Al_2O_3 interface. Part (a) displays the variation of temperature in the FL, $T_F(\xi, \tau)$, and SW, $T_W(\xi, \tau)$, as a function of nondimensional (ND) position, ξ , with respect to the FL-TW interface ($\xi=x/d=0$) at four different times during a 300 ns experiment. The nondimensional range of -1 to 1 corresponds to -d to d, where d is the thickness of the FL layer. "Reshocked layer" refers to the nondimensional thickness of the reshocked layer, δ_{FW}^* . Part (b) depicts the corresponding variation of the interface temperature, $T_{INT}(t)$.

C. Q.

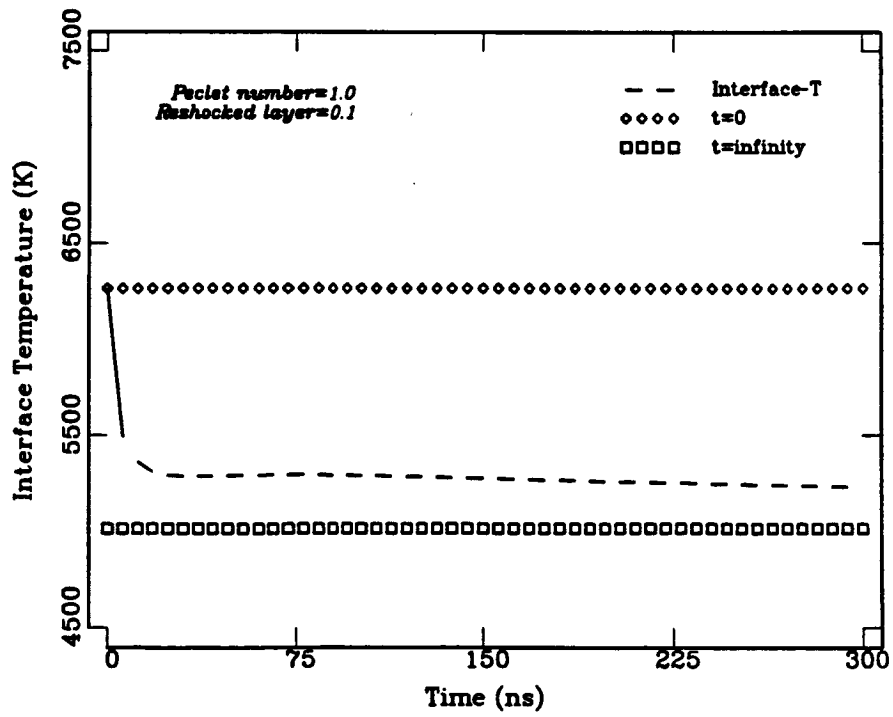
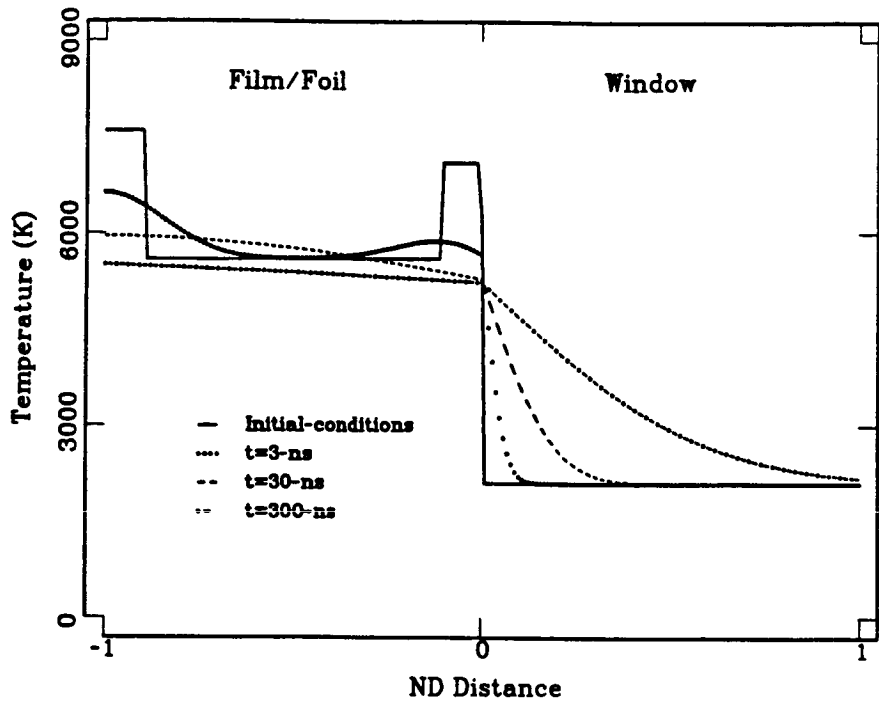


Figure 5.3. Variation of temperature near a reshocked Fe film/foil- Al_2O_3 interface. The reshocked layer depicted in part (a) is thicker than that of Figure 5.2a, and relative to the conduction length scale (as represented by the Peclet number), causing the temperature of the reshocked layer, and so that of the FL-SW interface, to decay more slowly. In part (b), the "t=0" curve corresponds to $T_{\text{INT}}(0)$, while that labeled "t=infinity" corresponds to $T_{\text{INT}}(\infty)$. The magnitude of these asymptotic values of $T_{\text{INT}}(t)$ is governed by that of the FL-SW thermal-inertia mismatch, σ_{WF} .

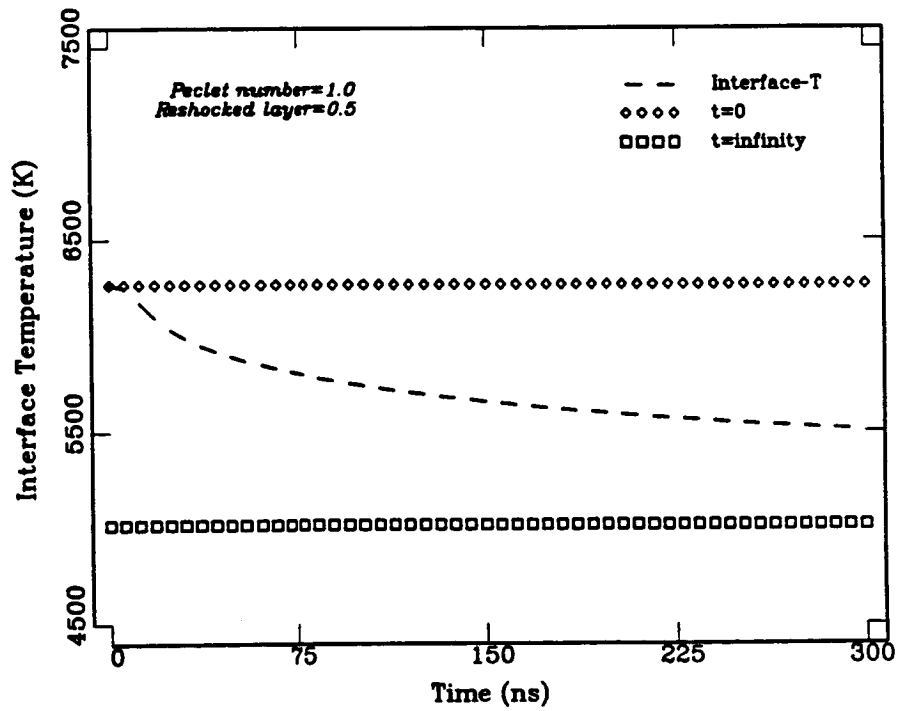
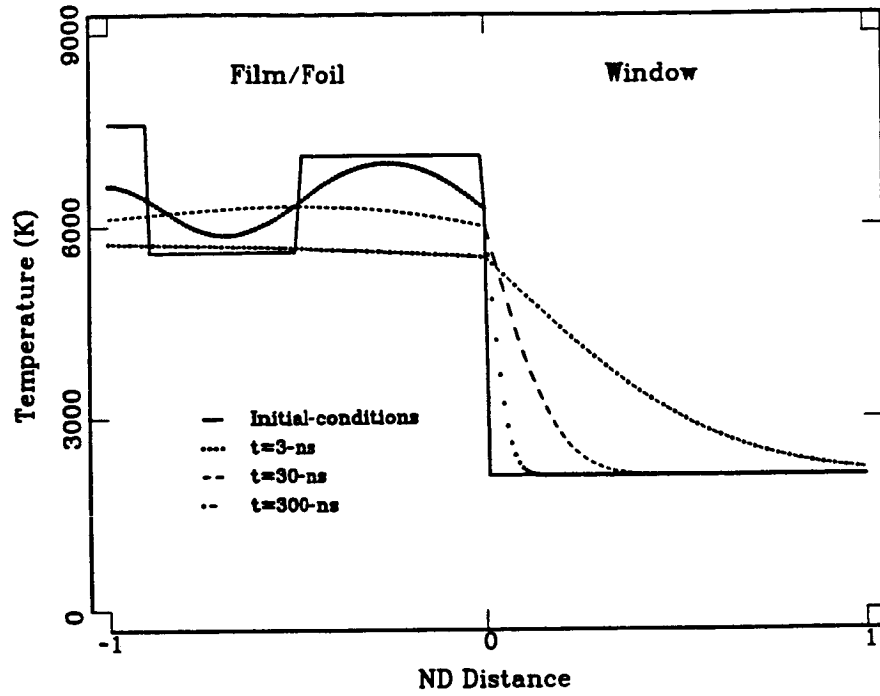


Figure 5.4. Variation of temperature near a reshocked Fe film/foil- Al_2O_3 interface. In this figure and Figure 5.5, we hold the reshocked layer thickness constant and vary the Peclet number, or conduction length scale, $\sqrt{\kappa_F t_{\text{exp}}}$, of the FL. Since the Peclet number is inversely proportional to the conduction length scale, a relatively small Peclet number (0.1) results in a fast decay of $T_{\text{INT}}(t)$, as shown in part (b).

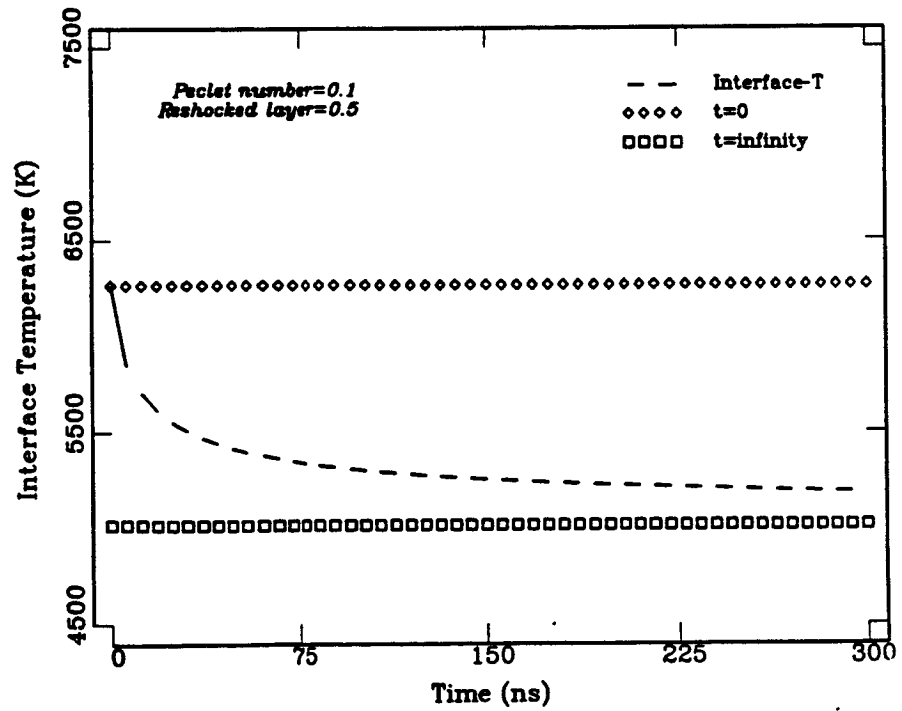
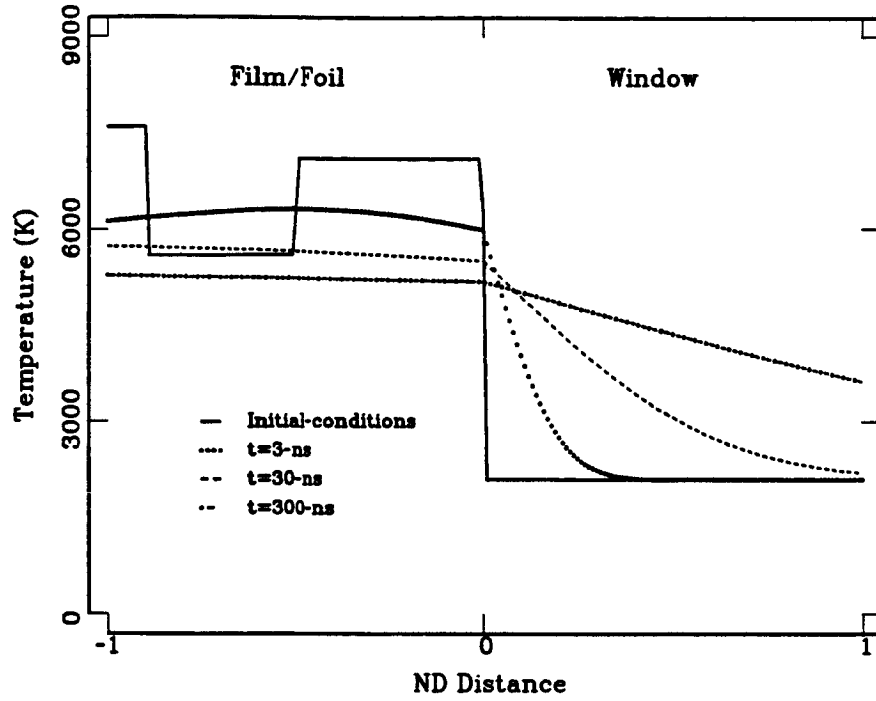
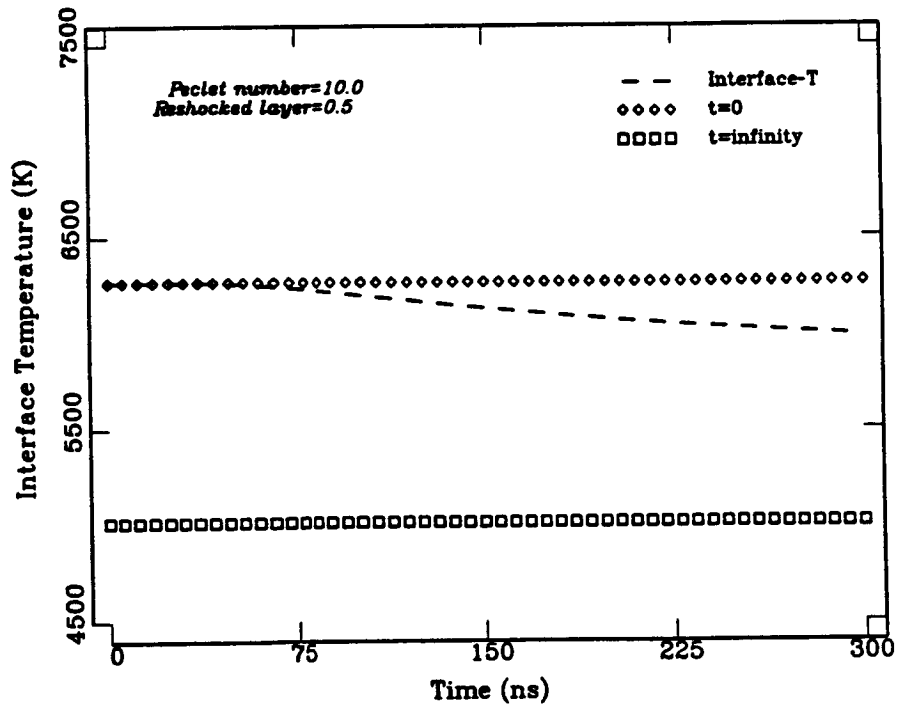
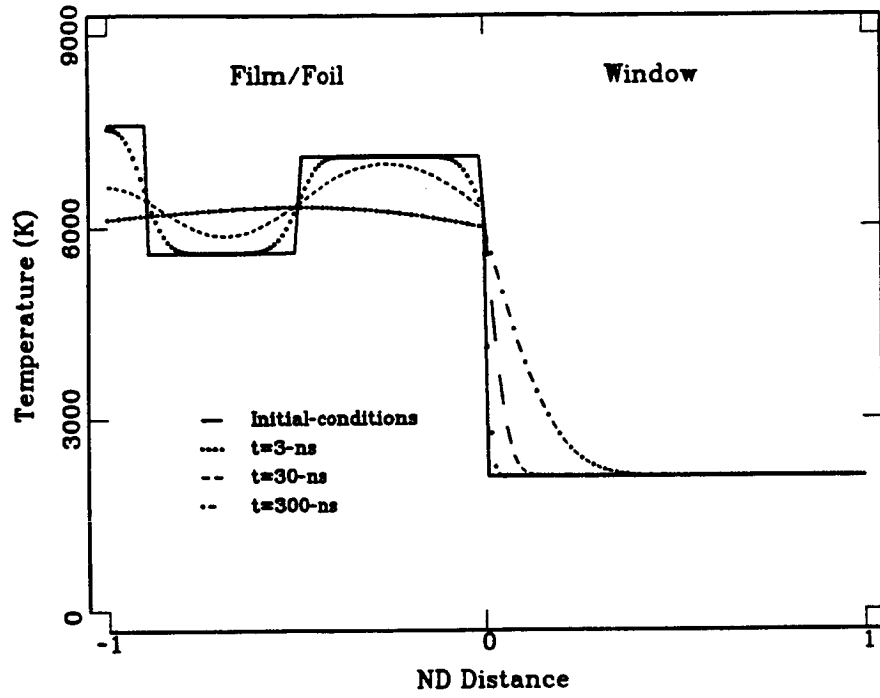


Figure 5.5. Variation of temperature near a reshocked Fe film/foil- Al_2O_3 interface. With a Peclet number of 10, the conduction length scale of the FL is small relative to the thickness of the FL, and the interface temperature decays very little over the time scale of the experiment.



and δ_{FW}^* . From [5.9], the change in $T_{INT}(\tau)$ with time is given by

$$\left\{ \frac{dT_{INT}(\tau)}{d\tau} \right\} = G'(\tau)\Delta T_D + D'(\tau)\Delta T_{FW} \quad [5.12]$$

with

$$G'(\tau) = \frac{2}{(1+\sigma_{WF})} \left\{ \frac{Pe_F}{4\pi\tau^3} \right\}^{1/2} \left\{ (1-\delta_{FD}^*)e^{-[(1-\delta_{FD}^*)\omega_F]^2} - (1+\delta_D^*)e^{-[(1+\delta_D^*)\omega_F]^2} \right\}$$

and

$$D'(\tau) = \frac{-2}{(1+\sigma_{WF})} \left\{ \frac{Pe_F}{4\pi\tau^3} \right\}^{1/2} \delta_{FW}^* e^{-[\delta_{FW}^*\omega_F]^2}.$$

For the particular case we have plotted, and as noted above, unless $\delta_{FW}^* \approx 1$, $\delta_D^* \gtrsim 1$, and/or $\Delta T_D \gg \Delta T_{FW}$, the ΔT_{FW} term dominates $T_{INT}(\tau)$. Since $D'(\tau)$, the coefficient of the dominating term, is always negative, the rate of change of $T_{INT}(\tau)$ will be negative, and $T_{INT}(\tau)$ will consequently decrease with time. Further, when the $D'(\tau)$ term in [5.12] is dominant, $dT_{INT}/d\tau$ is proportional to $-\mu \exp(-\mu^2)$, with $\mu \equiv \delta_{FW}^* \sqrt{Pe_F/4\tau} = \delta_{FW}^* / 2\sqrt{\kappa_F t}$. In other words, over the time scale of the experiment, $t = t_{exp}$, μ represents the ratio of the layer thickness to the conductive length scale, $\sqrt{\kappa_F t_{exp}}$. Note that $\mu \exp(-\mu^2)$ achieves a maximum value near $\mu \sim 1$ and is much smaller (~ 0) for μ much greater or less than unity. In Figures 5.2 and 5.3, we hold Pe_F constant (*i.e.*, the conductive length scale, $\sqrt{\kappa_F t_{exp}}$) and vary the layer thickness, δ_{FW}^* . As shown in Figure 5.2, with $Pe_F = 1$, $T_{INT}(\tau)$ for a thin reshocked layer ($\delta_{FW}^* = 0.1$) relaxes very quickly (*i.e.*, faster than can be resolved experimentally) to near $T_{INT}(\infty)$, while in Figure 5.3, we see that a thicker reshocked layer ($\delta_{FW}^* = 0.5$) will relax much more slowly, and on a resolvable time scale. A similar set of events holds if we fix the layer thickness and vary the conductive length scale of the FL, as we show in Figures 5.3a-b. For a conductive length scale large compared to the reshocked-layer thickness (Figure 5.4, $Pe_F = 0.1$ and $\delta_{FW}^* = 0.5$), $T_{INT}(\tau)$ relaxes relatively

quickly, whereas if the conductive length scale is small relative to the layer thickness (Figure 5.5, $Pe_F=10$ and $\delta_{FW}^*=0.5$), there is little or no resolvable relaxation of $T_{INT}(\tau)$ away from $T_{INT}(0)$. Obviously, δ_{FW} and $\sqrt{\kappa_F t_{exp}}$ trade off in their effects on $T_{INT}(\tau)$, introducing some ambiguity; only their ratio has a distinct effect on $T_{INT}(\tau)$. In any event, for $Pe_F \sim 1$ and intermediate ($\delta_{FW}^* \sim 0.3-0.7$) reshock-layer thicknesses, $T_{INT}(t)$ is time-dependent on an experimentally resolvable time scale, and its variation with time produces a corresponding radiation source time dependence, as we show in the next section.

§6. Radiative Transport in the Target

With a model of the initial temperature profile of the target components and interfaces, we now establish a connection between the radiation intensity of sources at these temperatures and the radiation intensity emerging from the free surface of the TW during the experiment. The target is represented as a series of plane-parallel layers (Figure 2.2) with Fresnel boundaries (Boslough, 1985; Appendix E). We assume that: 1) source radiation is collimated by the target geometry; 2) all radiation sources are thermal, and so their intensity is given by the Planck function; 3) sources are located only at the FL-SW and/or uniformly throughout the SW, particularly along the direction of shock propagation; and 4) all optical properties are independent of wavelength. The model spectral intensity of radiation emerging from the free surface of the USW (unshocked window), $I_{\lambda mod} = I_{\lambda mod}(\lambda, t)$, as a function of wavelength, λ , and time after the shock-front has passed the FL-SW interface, t , is given by

$$I_{\lambda mod}(\lambda, t) \equiv \hat{\epsilon}_{\lambda SW}(t) I_{PI}(\lambda, T_w) + \hat{\epsilon}_{\lambda INT}(t) I_{PI}[\lambda, T_{INT}(t)] \quad . \quad [6.1].$$

The Hugoniot temperature of the SW, T_w , is homogeneous, uniform, and constant since we assume a uniform distribution of SW sources. The interface temperature, T_{INT} , is a function of time, or constant, in the context of the

conduction model discussed above. The "λ" subscript denotes a spectral quantity. In [6.1], we identify

$$\hat{\epsilon}_{\lambda SW}(t) \equiv \Psi_{\lambda}(t) [1 - \tau_{\lambda SW}(t)] [1 + r_{\lambda INT} \tau_{\lambda SW}(t)] \quad [6.2]$$

and

$$\hat{\epsilon}_{\lambda INT}(t) \equiv \Psi_{\lambda}(t) \tau_{\lambda SW}(t) [1 - r_{\lambda INT}] \quad [6.3]$$

as the effective normal spectral emissivities of the SW and FL-SW interface, respectively. As evident from [6.1], $\hat{\epsilon}_{\lambda SW}$ and $\hat{\epsilon}_{\lambda INT}$ are the properties connecting the intensities of the sources within the target and the intensity emerging from the target. The function $\Psi_{\lambda}(t)$ is defined by

$$\Psi_{\lambda}(t) \equiv [1 - r_{\lambda FS}] \tau_{\lambda USW}(t) [1 - r_{\lambda SF}] \quad [6.4]$$

and represents the effect on source radiation of propagation through the FS, USW, and SF. In Equations [6.2]-[6.4], $r_{\lambda FS}$, $r_{\lambda SF}$ and $r_{\lambda INT}$ are the effective normal spectral reflectivities of the FS, SF, and FL-SW interface, respectively. Further,

$$\tau_{\lambda USW}(t) \equiv e^{-a_{\lambda USW}^* (1 - t/t_{exp})} \quad [6.5]$$

and

$$\tau_{\lambda SW}(t) \equiv e^{-a_{\lambda SW}^* t/t_{exp}} \quad [6.6]$$

are the effective normal spectral transmissivities of SW and USW layers, respectively. The quantities $a_{\lambda USW}^*$ and $a_{\lambda SW}^*$ are nondimensional forms of the effective normal spectral absorption coefficients in the USW and SW, respectively, and they are given by

$$a_{\lambda SW}^* \equiv a_{\lambda SW}(x_{FS} - vt_{exp}) \quad [6.7]$$

and

$$a_{\lambda USW}^* \equiv a_{\lambda USW} x_{FS} \quad [6.8],$$

respectively, where $a_{\lambda SW}$ and $a_{\lambda USW}$ are the dimensional counterparts of $a_{\lambda SW}^*$ and

$a_{\lambda_{USW}}^*$, respectively. Also, x_{FS} is the thickness of the TW, and so the position of the FS with respect to the FL-TW interface (Figure 2.2). Note that $a_{\lambda_{SW}}^*$ and $a_{\lambda_{USW}}^*$ mediate the explicit time dependence of $\hat{\epsilon}_{\lambda_{SW}}$ and $\hat{\epsilon}_{\lambda_{INT}}$. In writing [6.7] and [6.8], we have also assumed steady shock propagation such that the position of the shock front in the TW (Figure 2.2) may be written $x_{SF}(t) \equiv (U-v)t$.

From Equations [6.7] and [6.8], $a_{\lambda_{SW}}^*$ and $a_{\lambda_{USW}}^*$ will be of order unity when

$$a_{\lambda_{SW}} \sim (x_{FS} - vt_{exp})^{-1}, \quad a_{\lambda_{USW}} \sim x_{FS}^{-1} \quad [6.9],$$

which are both $\sim 10^3 m^{-1}$, since the thickness of the TW is generally $\sim 10^{-3} m$. So for values of $a_{\lambda_{SW}}$ and/or $a_{\lambda_{USW}}$ much larger or smaller than these "geometric" values, source radiation intensity is resolvable or not affected by propagation through the SW and USW, respectively. The USW is usually transparent, so $a_{\lambda_{USW}} \sim 0$; if the SW is transparent as well, then $a_{\lambda_{SW}} \sim 0$ and, from [6.2] and [6.3], we have

$$\hat{\epsilon}_{\lambda_{INT}}(t) \lesssim \hat{\epsilon}_{\lambda_{INT}}(0) = (1 - r_{\lambda_{FS}})(1 - r_{\lambda_{SF}})(1 - r_{\lambda_{INT}}) \quad [6.10]$$

and $\hat{\epsilon}_{\lambda_{SW}} = 0$. In this case, $I_{\lambda_{mod}}$ is governed entirely by sources at the FL-SW interface, and any time dependence of the observed radiation history is due solely to T_{INT} . Note that the bound on $\hat{\epsilon}_{\lambda_{INT}}$ in [6.10] is also the initial value of $\hat{\epsilon}_{\lambda_{INT}}$ (i.e., it can only decrease with time). However, if the TW becomes opaque upon shock compression, we have $a_{\lambda_{SW}} \rightarrow \infty$. Again, with $a_{\lambda_{USW}} \sim 0$, we have $\hat{\epsilon}_{\lambda_{INT}} \rightarrow 0$ and

$$\hat{\epsilon}_{\lambda_{SW}}(t) \lesssim (1 - r_{\lambda_{FS}})(1 - r_{\lambda_{SF}}) \quad [6.11].$$

In this case, observable sources are confined to the shock front (this is the "ideal case" of Boslough, 1985). The impact of these and other model parameters on $I_{\lambda_{mod}}(\lambda, t)$ is more explicitly depicted by writing the partial derivatives of $I_{\lambda_{mod}}(\lambda, t)$ with respect to λ and t . From Equations [6.1], [6.2], and [6.3], these are

$$\lambda \left\{ \frac{\partial I_{\lambda \text{mod}}}{\partial \lambda} \right\}_t = P(\mu_{\text{SW}}) \hat{\epsilon}_{\lambda \text{SW}}(t) I_{\text{PI}}(\lambda, T_w) + P(\mu_{\text{INT}}) \hat{\epsilon}_{\lambda \text{INT}}(t) I_{\text{PI}}[\lambda, T_{\text{INT}}(t)] - 5 I_{\lambda \text{mod}}(\lambda, t) \quad [6.12]$$

and

$$\begin{aligned} t_{\text{exp}} \left\{ \frac{\partial I_{\lambda \text{mod}}}{\partial t} \right\}_\lambda &= I_{\lambda \text{mod}} a_{\lambda \text{USW}}^* \\ &+ \left\{ [(1-\Gamma_{\lambda \text{INT}}) + 2\Gamma_{\lambda \text{INT}} \tau_{\lambda \text{SW}}(t)] I_{\text{PI}}(\lambda, T_w) - \hat{\epsilon}_{\lambda \text{INT}}(t) I_{\text{PI}}[\lambda, T_{\text{INT}}(t)] \right\} a_{\lambda \text{SW}}^* \\ &+ P(\mu_{\text{INT}}) \hat{\epsilon}_{\lambda \text{INT}}(t) I_{\text{PI}}[\lambda, T_{\text{INT}}(t)] \left\{ \frac{d \ln T_{\text{INT}}}{dt} \right\} \end{aligned} \quad [6.13]$$

with

$$P(\xi) \equiv \frac{\xi}{1 - e^{-\xi}}$$

and

$$\mu_{\text{SW}} \equiv \frac{C_2}{\lambda T_w}, \quad \mu_{\text{INT}} \equiv \frac{C_2}{\lambda T_{\text{INT}}}$$

Relation [6.12] exemplifies the fact that the wavelength dependence of $I_{\lambda \text{mod}}$ is due solely to that of the Planck function, since we have assumed that the optical properties are independent of wavelength. We make this assumption because its not clear at this point that existing data can resolve wavelength-dependent optical properties (*e.g.*, Svendsen and Ahrens, 1987, Chapter II).

Again, for most TW's, we have $a_{\lambda \text{USW}} \sim 0$. If, in addition, $T_{\text{INT}}(t)$ is approximately constant with time, which may occur in a thick ($\text{Pe}_f \gg 1$) or thin ($\text{Pe}_f \ll 1$) FL with a thick ($\delta_{\text{FW}}^* \sim d$) or thin ($\delta_{\text{FW}}^* \ll d$) reshocked layer of FL material, or at the smooth interface, as discussed above, [6.13] reduces to

$$t_{\text{exp}} \left\{ \frac{\partial I_{\lambda \text{mod}}}{\partial t} \right\}_\lambda = \left\{ [(1-\Gamma_{\lambda \text{INT}}) + 2\Gamma_{\lambda \text{INT}} \tau_{\lambda \text{SW}}] I_{\text{PI}}(\lambda, T_w) - \hat{\epsilon}_{\lambda \text{INT}} I_{\text{PI}}[\lambda, T_{\text{INT}}(t)] \right\} a_{\lambda \text{SW}}^* \quad [6.14].$$

This will be positive if

$$[(1-r_{\lambda_{\text{INT}}})+2r_{\lambda_{\text{INT}}}\tau_{\lambda_{\text{SW}}}]I_{\text{PI}}(\lambda, T_w) > \hat{\epsilon}_{\lambda_{\text{INT}}}I_{\text{PI}}[\lambda, T_{\text{INT}}(t)] \quad [6.15],$$

but otherwise negative, since $a_{\lambda_{\text{SW}}}^*$ is always positive. Consequently, with a finite value of $a_{\lambda_{\text{SW}}}^*$ and a time-independent interface temperature, $I_{\lambda_{\text{mod}}}$ will grow or decay with time on the basis of the sign of [6.15]. If the TW is initially transparent and remains relatively transparent upon shock-compression, we have $a_{\lambda_{\text{USW}}}^* \sim 0$ and $a_{\lambda_{\text{SW}}}^* \sim 0$. Putting these into [6.13], we have

$$\left\{ \frac{\partial I_{\lambda_{\text{mod}}}}{\partial t} \right\}_{\lambda} = P(\mu_{\text{INT}})\hat{\epsilon}_{\lambda_{\text{INT}}}I_{\text{PI}}[\lambda, T_{\text{INT}}(t)] \left\{ \frac{d \ln T_{\text{INT}}}{dt} \right\} \quad [6.16]$$

and any variation of $I_{\lambda_{\text{mod}}}$ with time should reflect that of T_{INT} through the Planck function. In particular, $I_{\lambda_{\text{mod}}}$ will increase or decrease as T_{INT} increases or decreases at a given wavelength.

§7. Models and Data

We compare models and data in the context of the standard χ^2 statistic (*e.g.*, Bevington, 1969; Press *et al.*, 1986). In our case, it given by

$$\chi^2(\mathbf{a}) \equiv \sum_{i=1}^{N_{\lambda}} \sum_{j=1}^{N_t} \frac{1}{\sigma_{ij}^2} \left\{ I_{\lambda_{\text{exp}}}(\lambda_i, t_j) - I_{\lambda_{\text{mod}}}(\lambda_i, t_j; \mathbf{a}) \right\}^2 \quad [7.1].$$

In this relation, $I_{\lambda_{\text{exp}}}(\lambda_i, t_j)$, $I_{\lambda_{\text{mod}}}(\lambda_i, t_j; \mathbf{a})$, $\sigma_{ij} \equiv \sigma(\lambda_i, t_j)$ are the experimental and model spectral radiances and the experimental uncertainties, all at a particular wavelength, λ_i , and time, t_j . Also, N_{λ} and N_t are the number of wavelengths and times sampled, respectively, in the experiment. The five-component "vector" \mathbf{a} is the model parameter vector, with components a_k , in our case given by

$$a_k \equiv \{ r_{\lambda_{\text{SF}}}, a_{\lambda_{\text{SW}}}^*, T_{\text{SW}}, r_{\lambda_{\text{INT}}}, T_{\text{INT}}(t) \} \quad [7.2].$$

Since the radiation model is nonlinear with respect to $a_{\lambda_{\text{USW}}}^*$, $a_{\lambda_{\text{SW}}}^*$, T_{SW} and $T_{\text{INT}}(t)$, [7.1] is not strictly a maximum likelihood measure, even if the data

errors are normally distributed. However, if the best-fit values of the a_k (*i.e.*, $a_{k(\min)}$) have uncertainties sufficiently small such that the value of $I_{\lambda\text{mod}}$ can be well approximated by the first two terms of its Taylor series representation about $I_{\lambda\text{mod}}(\lambda, t; a_{k(\min)})$, $\chi^2(\mathbf{a})$ will be very close to the maximum likelihood estimate (Press *et al.*, 1986).

We note that $r_{\lambda\text{FS}}$ and $a_{\lambda\text{USW}}^*$ are not included in [7.1], since they may be calculated or determined from index-of-refraction and absorption data for the TW. From the conduction model, we have explicit expressions (*e.g.*, [5.9]) for the time dependence of T_{INT} , which allow us, in principle, to constrain σ_{WF} , *etc.*, given fitted values of T_{INT} . Similarly, the fitted reflectivities allow us to constrain changes in the indices of refraction across boundaries (*e.g.*, the shock front). Note that, in general, the optical properties constrained from [7.1] cannot be λ -dependent unless we give them, *a priori*, an explicit λ -dependence, with constants whose values are chosen by the fit (*i.e.*, by the data). Since we have no reasonable expectation for this λ -dependence, we cannot truly constrain it. It is for this reason, plus the limited resolving power of the data itself (Boslough, 1984; Svendsen and Ahrens, 1987, Chapter II), that we assume $a_{\lambda\text{SW}}$, $a_{\lambda\text{USW}}$ *etc.*, are independent of λ in the previous section. However, we may determine an apparent λ -dependence of the optical properties if we specialize [7.1] and fit at each wavelength over time, *i.e.*,

$$\chi^2(\lambda_i; \mathbf{a}) \equiv \sum_{j=1}^{N_i} \frac{1}{\sigma_{ij}^2} \left\{ I_{\lambda\text{exp}}(\lambda_i, t_j) - I_{\lambda\text{mod}}(\lambda_i, t_j; \mathbf{a}) \right\}^2 \quad [7.3].$$

Svendsen and Ahrens (1987, Chapter II) constrained $a_{k(\min)}$ in this manner for radiation data from Ta-Ag-MgO targets. We use a very simple version of this approach below with the data of Bass *et al.* (1987) to constrain $a_{\lambda\text{SW}}$. First, however, it is instructive to consider fits to data using simpler models than that represented by [7.1] and [7.3]. Most earlier workers (*e.g.*, Kormer, 1968; Urtiew,

1974; Lyzenga, 1980; Lyzenga *et al.*, 1983) constrained model parameters via the greybody relation

$$I_{\text{gb}}(\lambda, \hat{\epsilon}_{\text{gb}}, T_{\text{gb}}) \equiv \hat{\epsilon}_{\text{gb}} I_{\text{Pl}}(\lambda, T_{\text{gb}}) \quad [7.4]$$

The associated χ^2 statistic is given by

$$\chi_{\text{gb}}^2(t_j; \hat{\epsilon}_{\text{gb}}, T_{\text{gb}}) = \sum_{i=1}^{N_\lambda} \frac{1}{\sigma_{ij}^2} \left\{ I_{\lambda \text{exp}}(\lambda_i, t) - I_{\text{gb}}(\lambda_i, t_j; \hat{\epsilon}_{\text{gb}}, T_{\text{gb}}) \right\}^2 \quad [7.5]$$

Since the summation in [7.5] averages $\hat{\epsilon}_{\text{gb}}$ over all observed wavelengths, it represents a wavelength-averaged (*i.e.*, total) effective emissivity. Given that the only λ -dependence in the greybody model is contained in the Planck function, $I_{\text{Pl}}(\lambda, T)$, the more closely the data follow the blackbody wavelength distribution at a given temperature, the better the fit (*i.e.*, the lower the value of $\chi_{\text{gb}}^2(t_j)$). Since both the data and model depend explicitly on λ , the fit proceeds over all observed wavelengths at a given time during the radiation history. As a result, $\hat{\epsilon}_{\text{gb}}$ and T_{gb} are functions of time.

Since I_{gb} depends nonlinearly on T_{gb} , we must find the best fit values of $\hat{\epsilon}_{\text{gb}}$ and I_{gb} iteratively with the minimization constraints on χ_{gb}^2 . To obtain starting values of $\hat{\epsilon}_{\text{gb}}$ and T_{gb} for the nonlinear fit, and for comparison, we may use Wien's approximation to $I_{\text{Pl}}(\lambda, T)$ in $\chi_{\text{gb}}^2(t_j)$, which follows from $I_{\text{Pl}}(\lambda, T)$ in the limit $\exp(C_2/\lambda T) \gg 1$, *i.e.*,

$$I_{\text{wgb}}(\lambda, \hat{\epsilon}_{\text{wgb}}, T_{\text{wgb}}) \equiv \hat{\epsilon}_{\text{wgb}} I_{\text{w}}(\lambda, T_{\text{wgb}}) = \hat{\epsilon}_{\text{wgb}} \frac{2C_1}{\lambda^5} e^{-C_2/\lambda T_{\text{wgb}}} \quad [7.6]$$

The relative error incurred in approximating I_{Pl} by I_{w} is equal to $\exp(-C_2/\lambda T)$; this approximation is accurate to within 1% for $\lambda T < 3 \times 10^{-3}$ m·K (Siegel and Howell, 1981). Since we can fit Wien's relation to the data in a linear least-squares sense, we can solve for $\hat{\epsilon}_{\text{wgb}}$ and T_{wgb} directly (*i.e.*, without iteration). With these values, we may safely apply an iterative technique to [7.5] to constrain $\hat{\epsilon}_{\text{gb}}$ and T_{gb} and to be assured of a nondivergent fit. We use the Golden

Search (GS) and Levenberg-Marquardt (LM) iterative techniques (Press *et al.*, 1986) to obtain three different fits: 1) GS with $\hat{\epsilon}_{gb}$ variable, 2) GS with $\hat{\epsilon}_{gb}=1$, and 3) LM with $\hat{\epsilon}_{gb}$ variable.

We present a greybody fit to the radiation observations from two experiments of Bass *et al.* (1987) in Figures 7.1 and 7.2. Figure 7.1 displays a fit to data from an experiment on an Fe-Fe film- Al_2O_3 target impacted by a Ta projectile traveling at 5.67 km/s. The trend in $\chi_{gb}^2(t)$ suggests that the fit gets better with time. Strictly speaking, $\chi^2 \sim \nu \pm 2\sqrt{\nu}$ as $\nu \rightarrow \infty$, where ν is the number of degrees of freedom in the fit (*i.e.*, the number of data minus the number of parameters; 2 in this case); we might hope that $\chi_{gb}^2 \sim 2$ represents a reasonable fit for the greybody model. All of the fits show $T_{gb}(t)$ decreasing with time, and for the variable emissivity fits, $\hat{\epsilon}_{gb}(t)$ increases slightly with time. This behavior is characteristic of most Fe-Fe- Al_2O_3 experiments of Bass *et al.* (1987). For all the Fe experiments, we note that $T_{sw} \ll T_{INT}(t)$, and that $\hat{\epsilon}_{gb}(t)$ is inconsistent with $a_{\lambda sw} \rightarrow \infty$ (Boslough, 1985). In this case, from [6.1] have

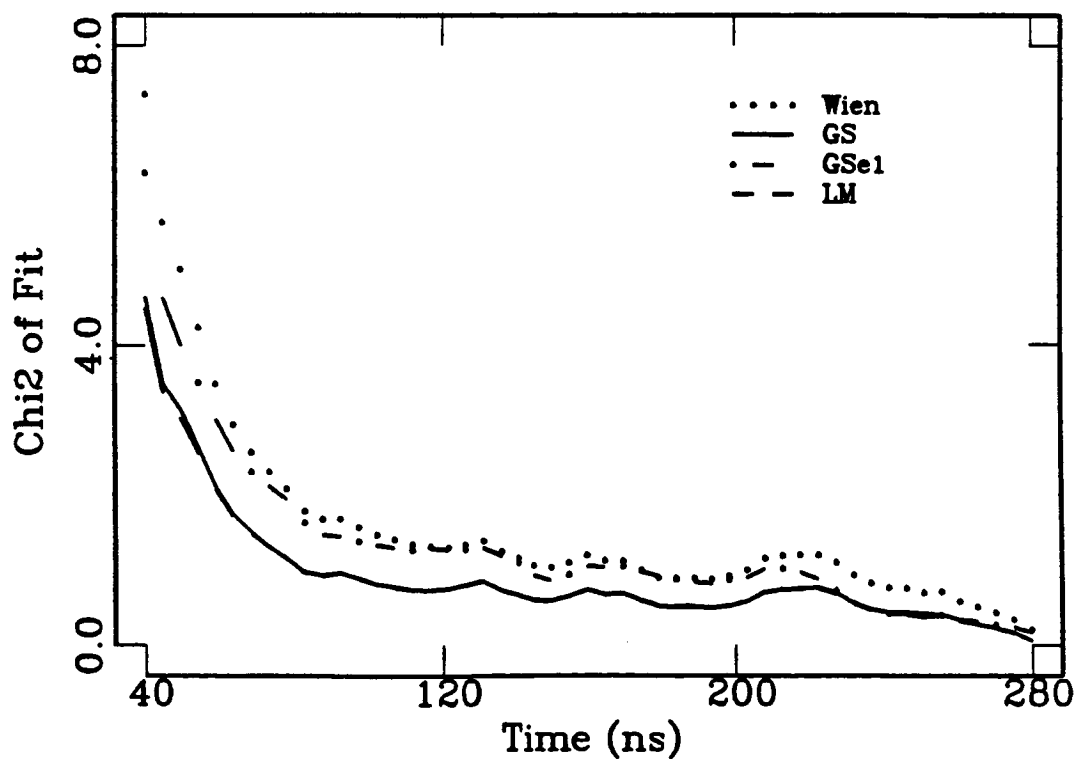
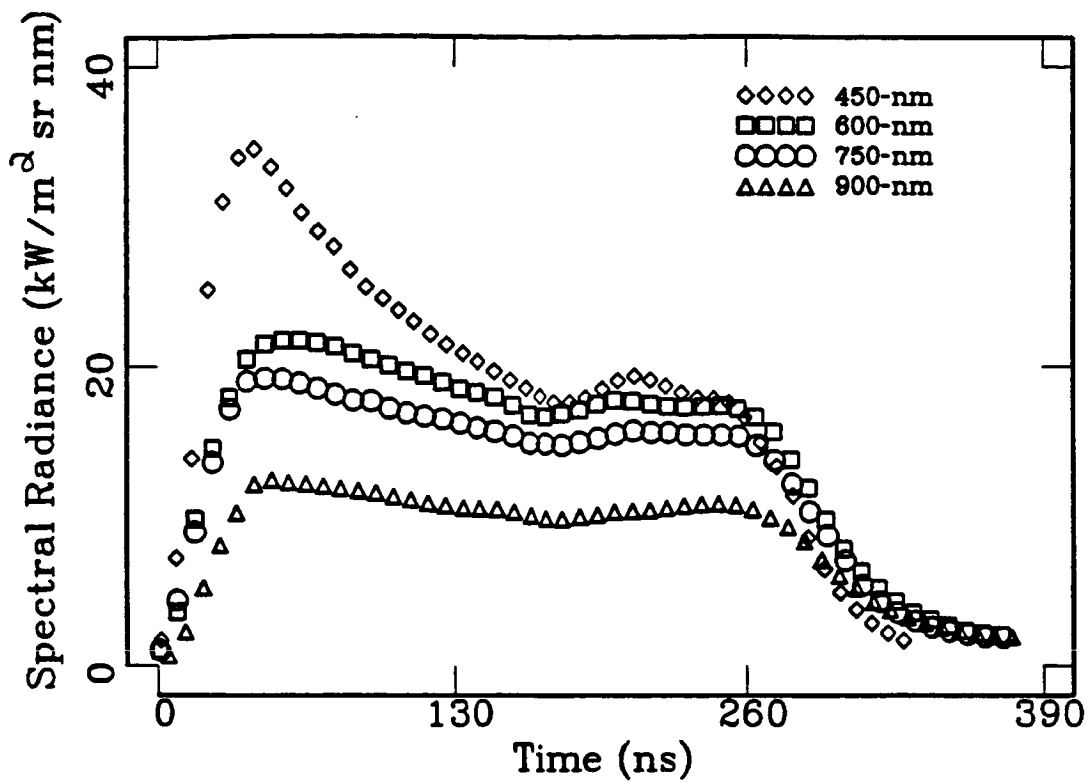
$$I_{\lambda mod}(\lambda, t) \approx \hat{\epsilon}_{\lambda INT}(t) I_{PI}[\lambda, T_{INT}(t)] \quad [7.7]$$

and the decrease of $T_{gb}(t)$ with time (Figure 7.1d) can be explained in terms of $T_{INT}(t)$, as detailed above. Also, the slight increase of $\hat{\epsilon}_{gb}(t)$ with time (Figure 7.1c) can be explained most simply by a slight decrease of the Al_2O_3 absorption coefficient upon shock compression. This may be consistent with the observation that the refractive index of Al_2O_3 seems to decrease with pressure ($\sim -0.001/\text{GPa}$ between 0.1 and 1 GPa: Davis and Vedam, 1967). Since $a_{\lambda sw} \sim 0$ for Al_2O_3 , this observation implies that $a_{\lambda sw} \sim 0$ as well. In this case, [7.7] implies that

$$I_{\lambda mod}(\lambda, t) \approx \hat{\epsilon}_{\lambda INT}(0) I_{PI}[\lambda, T_{INT}(t)] = (1-r_{\lambda FS})(1-r_{\lambda SP})(1-r_{\lambda INT}) I_{PI}[\lambda, T_{INT}(t)] \quad [7.8]$$

for the Fe-Fe- Al_2O_3 experiments.

Figure 7.1. Observed radiation history and χ^2 statistic of greybody model ($\hat{\epsilon}_{gb}, T_{gb}$) to radiation data from Fe-Fe film- Al_2O_3 target impacted by a tantalum projectile at 5.67 km/s, resulting in an Fe Hugoniot pressure of 244 GPa and an Al_2O_3 Hugoniot pressure of 190 GPa, which is also the Fe- Al_2O_3 interface pressure (Bass *et al.*, 1987). Part a) of this figure displays the radiation intensity (spectral radiance) data, collected at four wavelengths: 450, 600, 750 and 900 nm. Part b) displays the "goodness" of the greybody fit, as indicated by $Chi2=\chi^2$, part c) displays the best fit normal greybody effective emissivity, $\hat{\epsilon}_{gb}(t)$, and part d) shows the corresponding greybody temperature, $T_{gb}(t)$. Fits using Wien's law, Golden Search (GS), GS with the effective emissivity set to 1 (GSel), and the Levenburg-Marquardt algorithm (LM) are indicated.



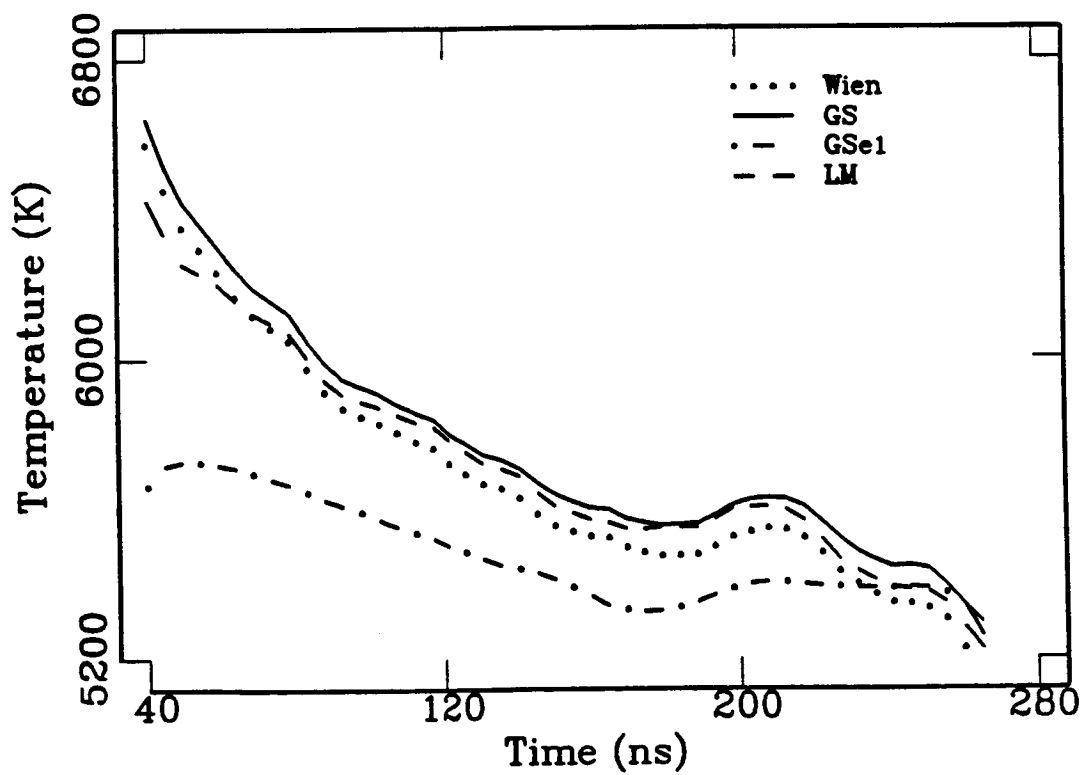
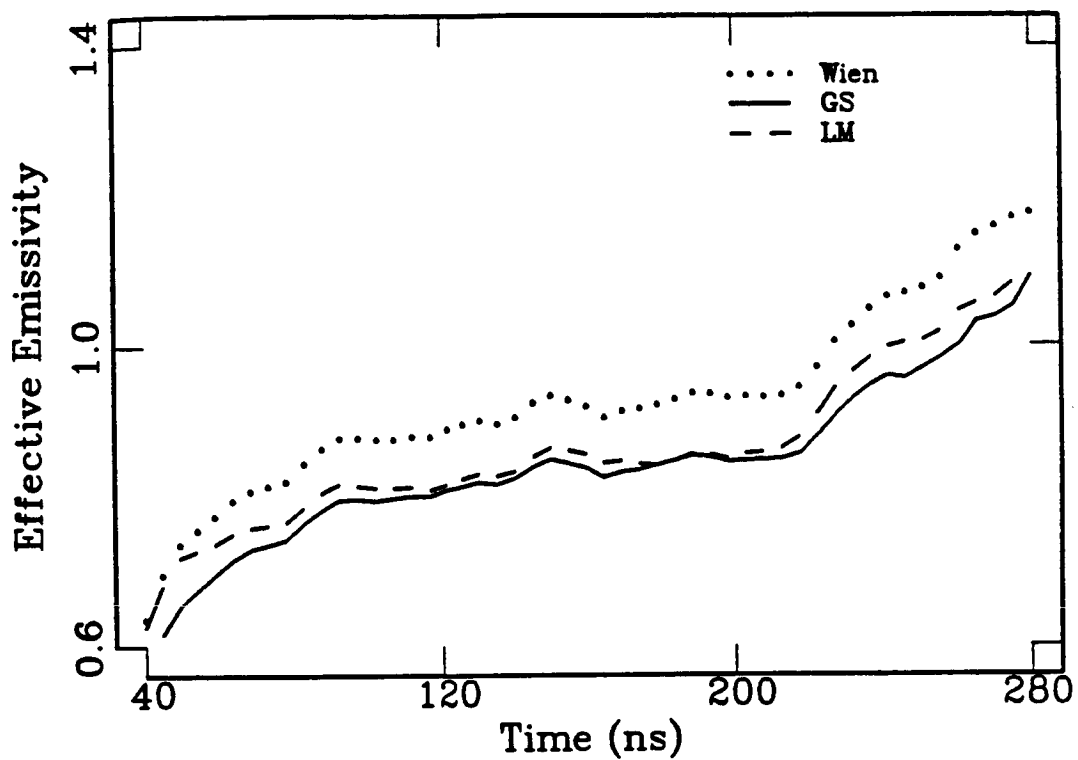
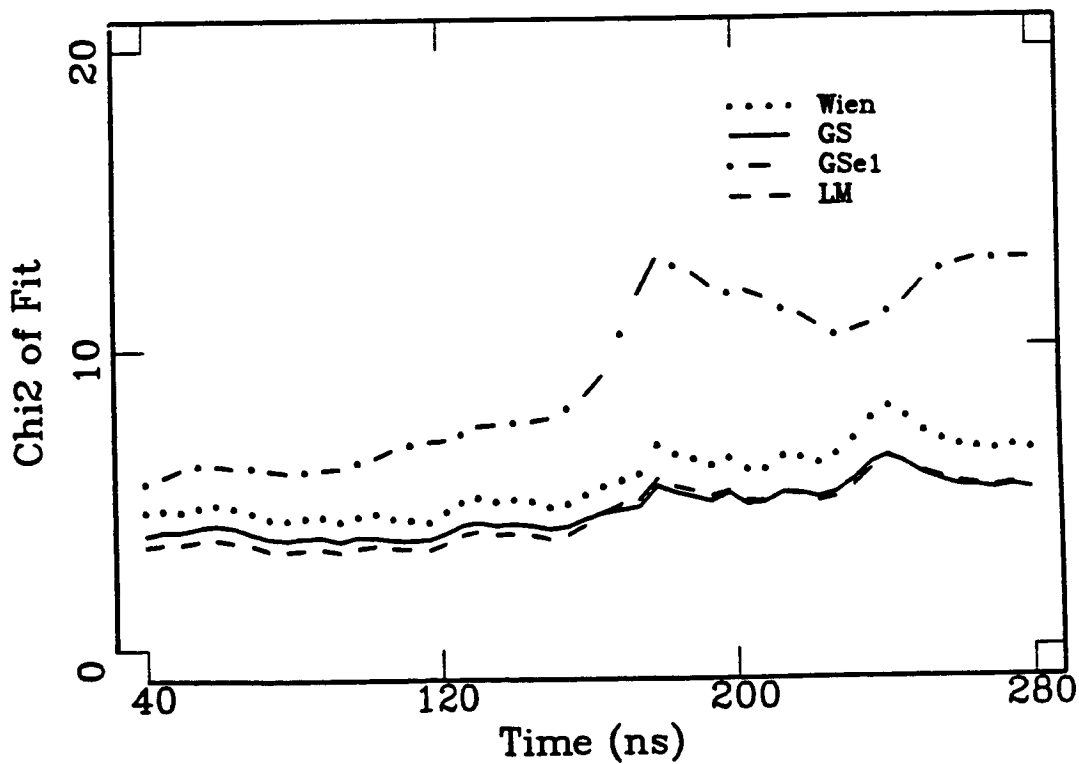
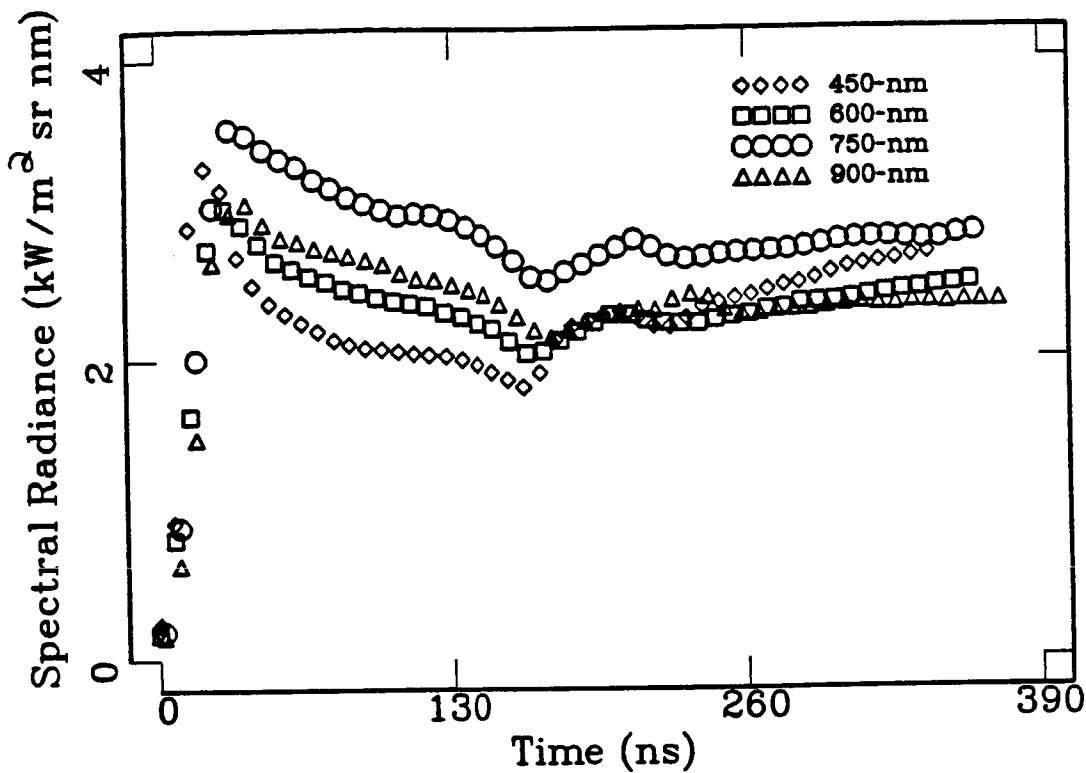
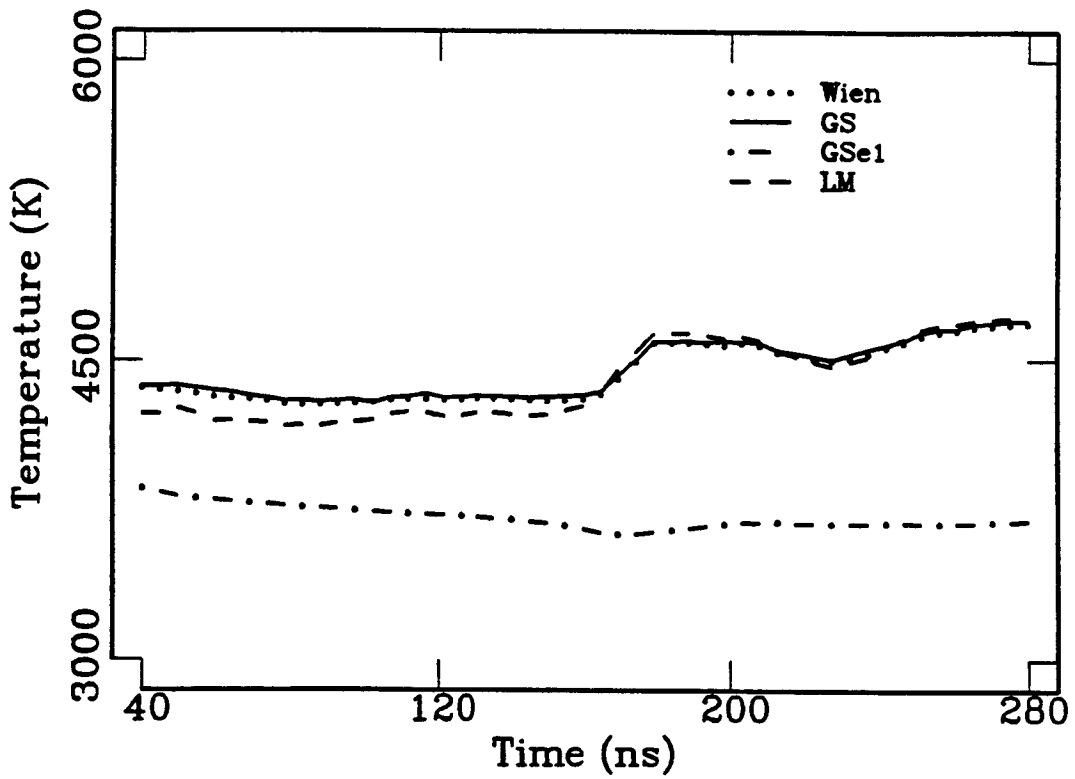
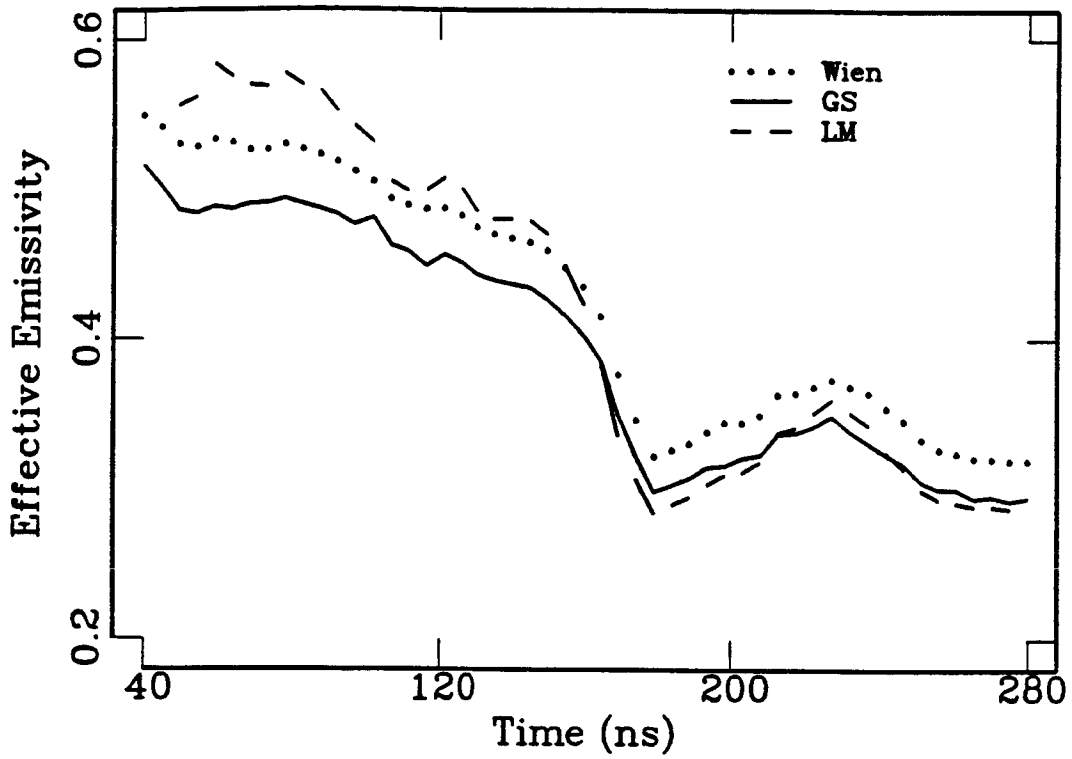


Figure 7.2. Observed radiation history (a), χ^2 statistic (b), greybody effective emissivity (c), and greybody temperature (d) for Fe-Fe foil-LiF target impacted by a tantalum projectile traveling at 5.41 km/s, resulting in an Fe foil Hugoniot pressure of 227 GPa and an LiF Hugoniot pressure of 122 GPa.





In contrast with this last fit, the experimental and greybody fit results displayed in Figures 7.2a-d, for an Fe-Fe-LiF target impacted by a Ta projectile traveling at 5.41 km/s, exhibit a relatively constant greybody temperature (Figure 7.2d) with time and a systematically decaying greybody effective emissivity with time (Figure 7.2c). In this case, $T_{gb}(t)$ implies a relatively constant $T_{\text{INT}}(t)$, as we expect for a smooth interface (Grover and Urtiew, 1974; [5.11] above) or a reshocked interface with $\delta_{\text{FW}} \gg 2\sqrt{\kappa_{\text{F}} t_{\text{exp}}}$ (Figure 5.3d) or $\delta_{\text{FW}} \ll 2\sqrt{\kappa_{\text{F}} t_{\text{exp}}}$ (Figure 5.2b). The reshocked interface with $\delta_{\text{FW}} \gg 2\sqrt{\kappa_{\text{F}} t_{\text{exp}}}$ is less likely than the latter possibility, as implied by the the data-model comparison in Figure 4.5b. The behavior of $\hat{\epsilon}_{gb}(t) \approx \hat{\epsilon}_{\text{INT}}(t)$ reflects a shock-induced increase in the absorption coefficient (*i.e.*, $a_{\lambda\text{SW}} > a_{\lambda\text{USW}}$) of LiF via [6.6], [6.7] and [6.14]. Wise and Chhabildas (1986) found, via laser interferometry, that LiF remains essentially transparent up to 160 GPa. The fluctuations in the fit after about 160 ns may be due to wave reverberations or other dynamic effects, which are beyond the scope of our model, and/or possibly to the influence of reshock at the Fe-Fe foil interface, as mentioned above.

In judging the value of any fit, the resolving power of the data is an issue. In particular, the ability of the data to constrain model parameters may be judged through confidence limits (*e.g.*, Press *et al.*, 1986). We display these for Fe-Fe- Al_2O_3 and Fe-Fe-LiF experiments in Figures 7.3 and 7.4, respectively. Parts a) and b) represent confidence limits for $\chi_{gb}^2(50 \text{ ns})$ and $\chi_{gb}^2(250 \text{ ns})$, respectively. The darkest shaded (*i.e.*, central) region in each diagram represents that part of model-parameter space which explains 68.3% of the data. Similarly, the 95.4% and 99.99% regions explain corresponding percentages of the four-wavelength data. Note that these limits are consistent with the trends in $\chi_{gb}^2(t)$ (Figures 7.1b and 7.2b). The basic information conveyed by these diagrams is a measure of the uncertainty of the fits; for example, from Figure 7.3, the fitted value of $T_{gb}(50 \text{ ns})$ has an uncertainty of about $\pm 400 \text{ K}$ at

Figure 7.3. Confidence limits for the LM fit displayed in Figure 7.1c-d near the beginning (50 ns) and end (250 ns) of that part of the radiation histories fit by the model. The designations 68.3%, 95.4% and 99.99% refer to that fraction of the data (which total 4) satisfied by the range of model values ($\hat{\epsilon}_{gb}, T_{gb}$) encompassed within the appropriate regions and contours, subject to the assumption that the experimental errors are normally distributed.

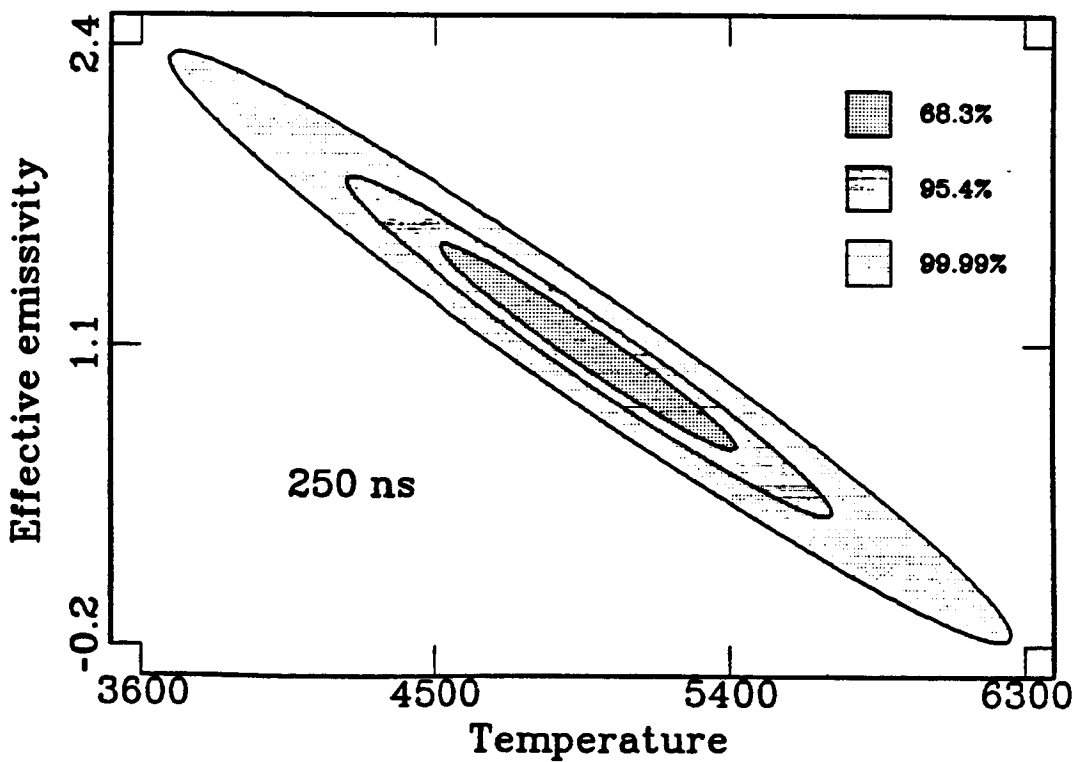
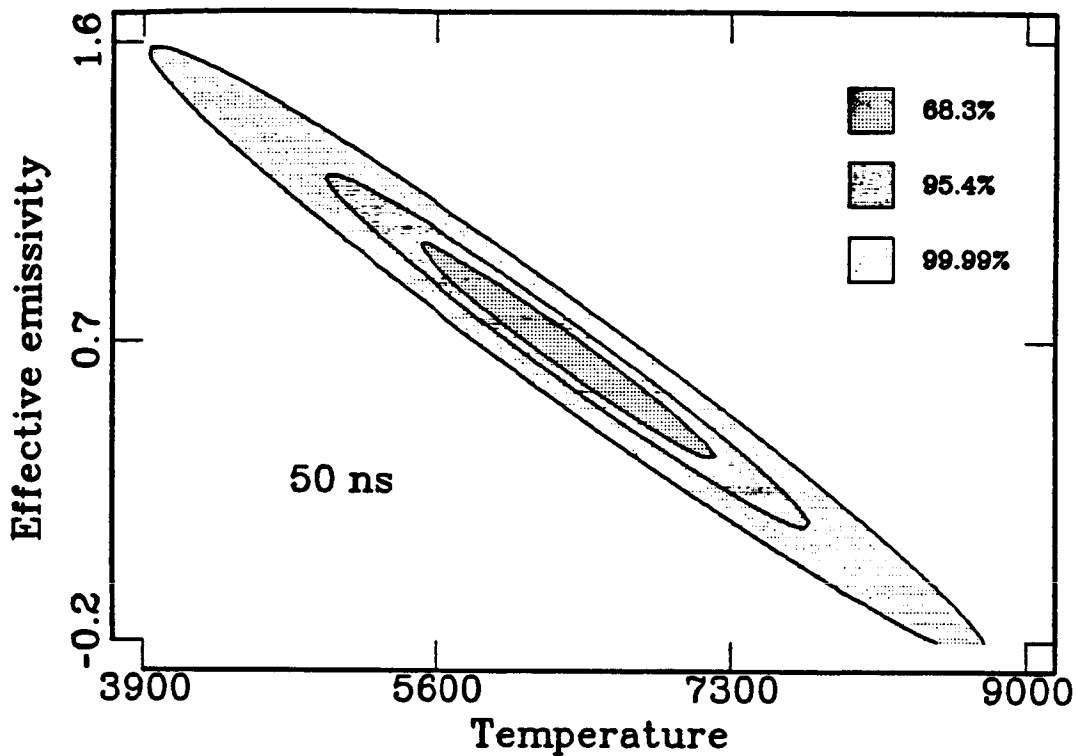
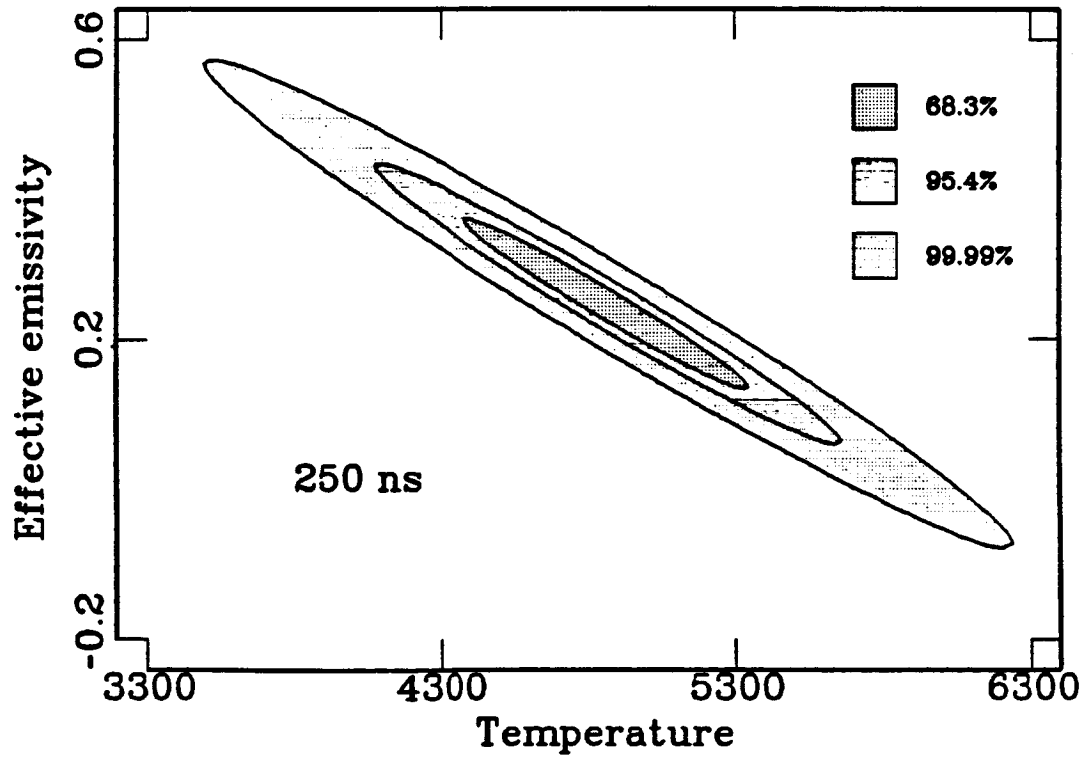
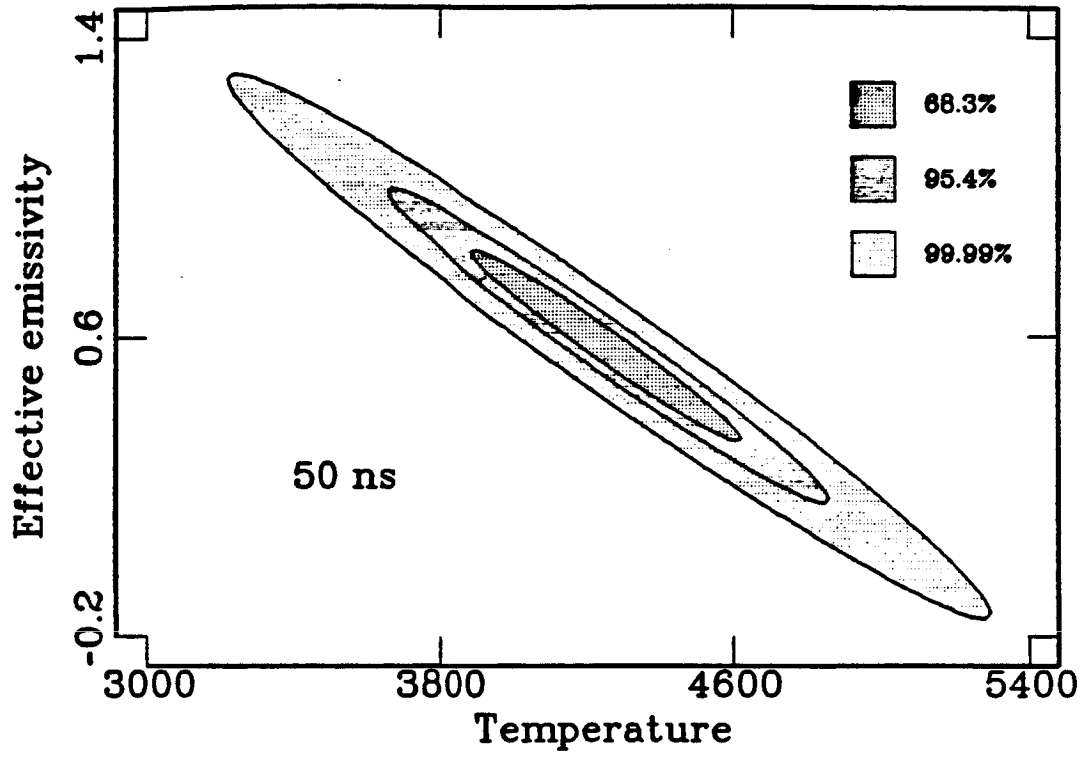


Figure 7.4. Confidence limits for the LM fit displayed in Figures 7.2c-d near the beginning (50 ns) and end (250 ns) of radiation histories fit by greybody model.



the 68.3% level, and about ± 600 K at the 95.4% level.

As stated above, the interface contribution to the observed intensity dominates the SW contribution (Bass *et al.*, 1987). On the basis of this observation, we may reasonably fit a simplified version of the full radiation model to the data via [7.5]. We do this for the Fe-LiF data fit to the greybody model in Figure 7.5. First, we note that, at $t=0$, $I_{\lambda\text{mod}}$ is, from [6.1],

$$\begin{aligned} I_{\lambda\text{mod}}(\lambda,0) &= \hat{\epsilon}_{\lambda\text{INT}}(0)I_{\text{PI}}(\lambda, T_{\text{INT}}(0)) \\ &= [1 - r_{\lambda\text{FS}}]e^{-a_{\lambda\text{USW}}^*}[1 - r_{\lambda\text{SF}}][1 - r_{\lambda\text{INT}}]I_{\text{PI}}[\lambda, T_{\text{INT}}(0)] \end{aligned} \quad [7.9].$$

So the magnitude of $I_{\lambda\text{mod}}(\lambda,0)$ is controlled by the reflectivities, $a_{\lambda\text{USW}}^*$ and the initial value of T_{INT} , which is dependent on the values of T_{F} , ΔT_{FW} , T_{W} and σ_{WF} through [5.12] in the simplest case. The greybody fits in Figure 7.2 suggest that, for this experiment at least, $T_{\text{INT}}(t)$ is approximately constant. Assuming this and $a_{\lambda\text{USW}} = 0$, we approximate [6.1] as

$$\begin{aligned} I_{\lambda\text{mod}}(\lambda,t) &= \hat{\epsilon}_{\lambda\text{INT}}(t)I_{\text{PI}}[\lambda, T_{\text{INT}}(0)] \\ &= (1 - r_{\lambda\text{FS}})(1 - r_{\lambda\text{SF}})(1 - r_{\lambda\text{INT}})e^{-a_{\lambda\text{SW}}^*t/t_{\text{exp}}}I_{\text{PI}}[\lambda, T_{\text{INT}}(0)] \end{aligned} \quad [7.10].$$

In this case, the time dependence of $I_{\lambda\text{mod}}$ is due solely to the SW transmissivity. Using [7.10] in [7.3], along with $T_{\text{INT}}(0) = T_{\text{gb}}(0)$, we may fit the Fe-LiF data for $a_{\lambda\text{SW}}^*$. We present the results of this fit in Figure 7.5. The data are cut off at 160 ns to reduce the influence of possible dynamics or Fe-Fe interface reshock on the fit. The parameter values resulting from this fit are given in Table 7.1. We eliminate $r_{\lambda\text{FS}}$ from the fit since it is equal to 0.08 for LiF, as estimated from $n=1.39$, the index-of-refraction of LiF at STP (CRC Handbook). Since the index-of-refraction of LiF seems to increase with pressure ($\sim 0.002/\text{GPa}$: Burnstein and Smith, 1948), we expect $r_{\lambda\text{SF}} > r_{\lambda\text{FS}}$ for LiF. Clearly, LiF has lost some transparency upon shock compression. The trend in $a_{\lambda\text{SW}}$ toward lower values at longer wavelengths is unresolved but consistent with the Bouguer's law

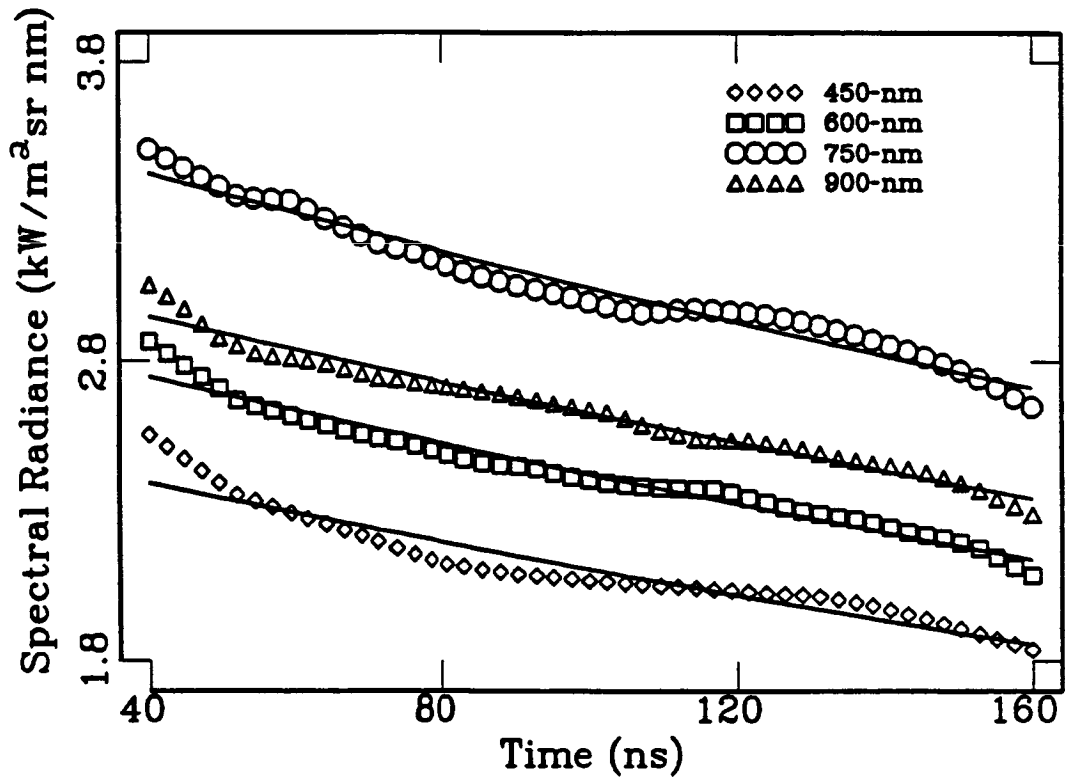


Figure 7.5. Time-dependent spectral radiance fits to the data displayed in Figure 7.3a for the Fe-Fe foil-LiF target. We fit [7.9] to the first half of the Fe-LiF data displayed in Figure 7.3a via [7.2]. The slope of each continuous curve, representing the fit for the corresponding wavelength, constrains the effective normal absorption coefficient of the shocked LiF, while the intercept constrains the Fe-LiF interface and shock-front effective normal reflectivities.

Table 7.1. Simplified Radiation Model Parameters.^a

Wavelength (nm)	$(1-r_{\lambda SF})(1-r_{\lambda INT})$	$a_{\lambda SW}$ (m^{-1})
450	0.76	137
600	0.56	134
750	0.68	125
900	0.67	122

^a For this fit, $x_{FS}=4.15$ mm, $t_{exp}=390$ ns, $T_{INT} = 4200$ K and $r_{\lambda SF} = 0.08$ at all wavelengths in fit.

expectation that $a_\lambda = 4\pi\omega_e/\lambda$, if ω_e , the electromagnetic extinction coefficient (Siegel and Howell, 1981, p. 427), is constant or varies inversely with λ . As suggested above, similar fits for Fe-Al₂O₃ imply that $a_{\lambda_{USW}} > a_{\lambda_{SW}}$, an intriguing possibility which we do not yet understand.

Lastly, we take the results of the greybody fit shown in Figure 7.1d for the Fe-Fe-Al₂O₃ experiment, assume $T_{gb}(t) = T_{INT}(t)$, and use [5.10] to write

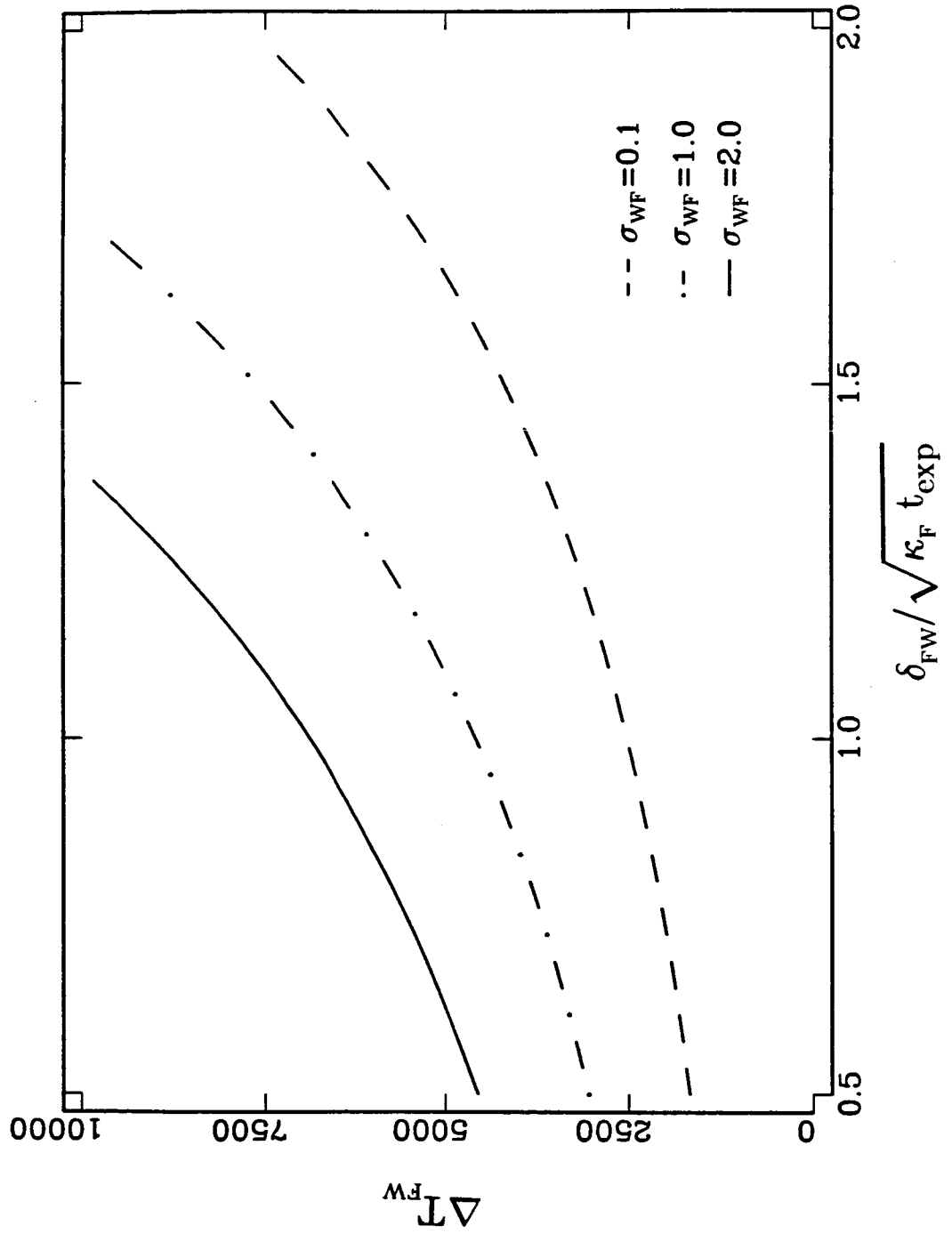
$$\Delta T_{FW} = \frac{(1 + \sigma_{WF})}{\text{erfc}\{\delta_{FW}/2\sqrt{\kappa_F t_{exp}}\}} [T_{gb}(0) - T_{gb}(t_{exp})] \quad [7.11].$$

With $T_{gb}(0) - T_{gb}(t_{exp}) = 1200$ K from the fit displayed in Figure 7.1d, we may calculate the trade-off between the FL-TW interface temperature due to reshock, ΔT_{FW} , and the ratio of the reshocked-layer thickness, δ_{FW} , to the FL conduction length scale, $\sqrt{\kappa_F t_{exp}}$, for different values of the FL-TW interface mismatch, σ_{WF} . These calculations, displayed in Figure 7.6, imply that the larger the reshocked-layer thickness relative to the FL conduction length scale, the higher the reshock temperature at a given thermal mismatch. For this particular experiment, we expect $\sigma_{WF} \lesssim 0.1$ from calculations discussed above; we also expect $\Delta T_{FW} \lesssim 2000$ K from the calculations presented in Figure 4.5a. In this case, Figure 7.6 and model calculations imply that $\delta_{FW} \lesssim 2\sqrt{\kappa_F t_{exp}} \sim 10^{-5}$ m. Since this is a film experiment, with $d \sim 10^{-6}$ m, we tentatively conclude that all of the film layer experienced reshock in this experiment.

§8. Summary

We consider the effects of release/reshock, phase transitions, and conduction on the shock-compressed temperatures of the target components and their interfaces. Comparison of the model with the results of experiments on Fe-Fe-LiF and Fe-Fe-Al₂O₃ targets suggests the following:

Figure 7.6. Magnitude of temperature at FL-TW interface due to reshock, ΔT_{FW} , versus the ratio of the reshocked layer thickness, δ_{FW} , to the conduction length scale, $\sqrt{\kappa_F t_{exp}}$. This trade-off is constrained by the magnitude of $T_{gb}(0) - T_{gb}(t_{exp})$ from the greybody fit for the Fe-Fe-Al₂O₃ data displayed in Figure 7.2a.



1. Release/reshock calculations for Fe-Fe-Al₂O₃ targets, in comparison with the experimental results of Bass *et al.* (1987), suggest that Fe experiences approximately 200-1500 K of reshock heating at both Fe foil-Al₂O₃ and Fe film-Al₂O₃ interfaces when released from ≈ 245 -300 GPa to interface pressures of 190-230 GPa. Below 190 GPa, reshock for Fe-Al₂O₃ interfaces appears to be minimal. Both the data and calculations suggest that the degree of reshock is strongly pressure-dependent, which is consistent with the results of Urtiew and Grover (1974). In contrast, Fe released from the same range of Hugoniot pressures to Fe-LiF interface pressures between ≈ 130 and 160 GPa experiences little or no reshock. This more ideal nature of Fe-LiF interfaces is enhanced by the fact that, besides being a poorer shock-impedance match to Fe than Al₂O₃, it is also a poorer thermal match, resulting in less change in the interface temperature away from the Fe-release state temperature. Comparison of data and calculations for both of these windows suggest that, while attention to the initial conditions of the interface is essential to minimize reshock, a more important factor may be the choice of window.
2. In the absence of energy sources and significant energy flux from other parts of the target, the rate of change of the interface temperature, $T_{\text{INT}}(t)$, is proportional to $-\mu \exp(-\mu^2)$, where $\mu = \delta_{\text{FW}} / 2\sqrt{\kappa_{\text{F}}t}$. For Fe at FL-TW interfaces, $\sqrt{\kappa_{\text{F}}t_{\text{exp}}} \sim 10 \mu\text{m}$; consequently, a 100 μm reshocked-Fe layer would relax very little, remaining near $T_{\text{INT}}(0)$ on the time scale of the experiment. However, if $\delta_{\text{FW}} \sim 1 \mu\text{m}$, $T_{\text{INT}}(t)$ relaxes almost instantaneously to its value $T_{\text{INT}}(\infty)$. $T_{\text{INT}}(t)$ is resolvably time-dependent for $\delta_{\text{FW}} \sim 2\sqrt{\kappa_{\text{F}}t_{\text{exp}}}$.

3. Greybody fits to an Fe film-Al₂O₃ experiment of Bass *et al.* (1987) show the greybody effective emissivity, $\hat{\epsilon}_{\text{gb}}(t)$, to increase slightly with time, while the greybody temperature, $T_{\text{gb}}(t)$, decreases with time. This behavior is characteristic of most Fe-Al₂O₃ experiments. The decrease of $T_{\text{gb}}(t)$ can be explained in terms of the model for $T_{\text{INT}}(t)$, and it implies that $\delta_{\text{FW}} \sim 2\sqrt{\kappa_{\text{F}} t_{\text{exp}}}$ for this experiment. Further, assuming $T_{\text{gb}}(t) = T_{\text{INT}}(t)$, the greybody fit constrains the amount of reshock, ΔT_{FW} , to be $\lesssim 2000$ K with $\sigma_{\text{WF}} \sim 0.1$ and $\delta_{\text{FW}} \lesssim 2\sqrt{\kappa_{\text{F}} t_{\text{exp}}}$. A slight decrease of the Al₂O₃ absorption coefficient upon shock compression can explain the slight increase of $\hat{\epsilon}_{\text{gb}}(t)$ with time. This may be consistent with the observation that the refractive index of Al₂O₃ seems to decrease with pressure. In contrast, greybody fits to data from an Fe-Fe foil-LiF target show a relatively constant greybody temperature and decreasing greybody emissivity. The constant greybody temperature implies a constant interface temperature, as we expect for an interface experiencing minimal reshock, while the decaying $\hat{\epsilon}_{\text{gb}}(t)$ is consistent with a shock-induced increase in the absorption coefficient of LiF. Setting $T_{\text{INT}}(0) = T_{\text{gb}}(0)$, we fit a simplified version of the full radiation model to these data to find $a_{\lambda_{\text{SW}}} \sim 100 \text{ m}^{-1}$ (Table 7.1) for LiF, shocked to 122 GPa in this experiment.

4. Finally, we note that the equilibrium thermodynamic Hugoniot temperature of Fe is strongly influenced by electronic and/or anharmonic contributions to c_{v} at high pressure, as evidenced by both 1) the results of Boness *et al.* (1986) when used in Equation (8), and 2) by requiring the solid Fe Hugoniot and an extrapolation of the experimentally constrained Fe melting curve (Williams and Jeanloz, 1986) referenced to this Hugoniot, to intersect at 245 GPa (Brown and McQueen, 1982). This last constraint provides a value of $\Omega(\rho_i) = 0.046 \text{ J/kg}\cdot\text{K}^2$, as compared to

$\Gamma(\rho_i) = 0.090 \text{ J/kg}\cdot\text{K}^2$ from the work of Boness *et al.* (1986), suggesting some anharmonic contribution to c_v of ϵ -Fe. These results substantiate the arguments of Brown and McQueen (1982, 1986) for the importance of including electronic contributions to c_v when calculating T_H of shock compressed metals.

Acknowledgements. We thank William W. Anderson, Mark B. Boslough, A. James Friedson, Tan Hua, Dion L. Heinz, Douglas R. Schmitt, and James A. Tyburczy for enlightening discussions. We also thank J. Michael Brown and two anonymous reviewers for constructive comments on an earlier version of this work. Support from NSF grants EAR-8608249 and 8608969 is gratefully acknowledged. Contribution 4488, Division of Geological and Planetary Sciences, California Institute of Technology, Pasadena, CA 91125.

§9. Appendix A: Equilibrium Thermodynamics and Shock Compression

The calculations discussed in the text for Fe-Fe- Al_2O_3 and Fe-Fe-LiF targets are based on classical (*i.e.*, equilibrium) thermodynamic models of the Helmholtz free energy, $F(T, \rho)$, for the solid- and liquid-states of Fe. As discussed in the text, this model is based on 1) a Debye model for the harmonic contribution and 2) the low temperature ($T \ll T_F$, the Fermi temperature) electronic contribution and 3) high temperature ($T > \Theta_D$, the Debye temperature) anharmonic contribution, which we combine for simplicity, since they are of the same order in T . The liquid-state model is presented elsewhere (Svendsen *et al.*, 1987, Chapter V). In the last two parts of this appendix, we detail certain relationships between isentropic and Hugoniot states using this model, and a method to recenter experimental U-v relations to the STP density of high pressure phase, both of which are used in the calculations.

A.1. Solid-State Equilibrium Thermodynamic Model

For a cubic or isotropic solid material subject to an isotropic state of stress, the combination of the Debye model for the harmonic contribution along with the high-temperature anharmonic and low-temperature electronic contributions provides an expression for the Helmholtz free energy, $F(T, \rho)$, *i.e.* (*e.g.*, Wallace, 1972, Sects. 5, 19 & 24; [4.25] in the text)

$$F(T, \rho) \equiv \left\{ \Phi(\rho) + \frac{9}{8} \nu R \Theta_D(\rho) \right\} \\ + 3\nu R \left\{ \ln[1 - e^{-\chi_D}] - \frac{1}{3} E_D(\chi_D) \right\} T + A_2(\rho) T^2 - \frac{1}{2} \Gamma(\rho) T^2 \quad [A.1]$$

Note that F has units of J/mol. For simplicity, we neglect possible band-structure and electron-phonon interaction contributions to F in writing [A.1]. Relation [A.1] is correct to $O(T^{-3})$ in the anharmonic contribution to F , and to all orders for the harmonic contribution in the context of the Debye approximation. This slight inconsistency is due to the unavailability of a tractable anharmonic model, analogous to the Debye model, for the materials of interest. Also, for Fe, we are guided by the results of Andrews (1973), who was able to fit various data on the thermostatic properties of the α and ϵ -phases with a Debye model for the harmonic contribution to F , ignoring anharmonicity altogether (although anharmonicity may be reflected in the value of his Γ). As discussed in the text, the anharmonic coefficient $A_2(\rho)$ is dependent on the particular model chosen for the pressure and temperature dependence of the anharmonic phonon-frequency spectrum. Since we do not have such a model for the materials of interest here, we simply combine it with the electronic contribution to form $\Omega(\rho)$, as given in the text.

On this basis, [A.1] provides the means to a rational parameterization of the approximate density- and temperature-dependence of a number of solid-

state properties, such as the pressure, *i.e.*,

$$P(T, \rho) \equiv \rho \left\{ \frac{\partial F}{\partial \ln \rho} \right\}_T \equiv P(0, \rho) + 3\nu R \rho \gamma_D E_D(\chi_D) T + \frac{1}{2} \rho \omega \Omega T^2 \quad [\text{A.2}]$$

with

$$P(0, \rho) \equiv \rho \left\{ \frac{d\Phi}{d \ln \rho} \right\} + \frac{9}{8} \nu R \rho \Theta_D \gamma_D \quad [\text{A.3}],$$

where γ_D is the lattice Grüneisen's parameter in the Debye approximation, as defined in the text. From [A.1], the molar entropy is given by

$$S(T, \rho) \equiv - \left\{ \frac{\partial F}{\partial T} \right\}_\rho = 3\nu R \left\{ \frac{4}{3} E_D(\chi_D) - \ln[1 - e^{-\chi_D}] \right\} + \Omega T \quad [\text{A.4}].$$

The isothermal bulk modulus is given by

$$K_T(T, \rho) \equiv \rho \left\{ \frac{\partial P}{\partial \rho} \right\}_T = K(0, \rho) \quad [\text{A.5}]$$

$$+ 3\nu R \rho \gamma_D (1 - q_D - 3\gamma_D) E_D(\chi_D) T + 9\nu R \rho \gamma_D \left\{ \frac{\gamma_D \chi_D}{[e^{\chi_D} - 1]} \right\} T$$

$$+ \frac{1}{2} \rho \omega (1 - \omega) \Omega T^2$$

with

$$K(0, \rho) \equiv P(0, \rho) + \rho \left\{ \rho \left\{ \frac{d\Phi}{d\rho} \right\} + \rho^2 \left\{ \frac{d^2\Phi}{d\rho^2} \right\} \right\} + \rho \left\{ \frac{9}{8} \nu R \gamma_D \Theta_D (\gamma_D - q_D) \right\}$$

and

$$q_D \equiv - \left\{ \frac{d \ln \gamma_D}{d \ln \rho} \right\} \quad [\text{A.6}],$$

which is assumed constant. The molar heat capacity at constant volume (density) is

$$C_v(T, \rho) \equiv -T \left\{ \frac{\partial^2 F}{\partial T^2} \right\}_\rho = 3\nu R \left\{ 4E_D(\chi_D) - \frac{3\chi_D}{[e^{\chi_D} - 1]} \right\} + \Omega T \quad [\text{A.7}].$$

The change in pressure with temperature at constant density given by, from [A.3]

$$\rho \gamma C_v = \left\{ \frac{\partial P}{\partial T} \right\}_\rho = \alpha K_T = 3\nu R \rho \gamma_D \left\{ 4E_D(\chi_D) - \frac{3\chi_D}{[e^{\chi_D} - 1]} \right\} + \rho \omega \Omega T \quad [\text{A.8}].$$

From [A.7] and [A.8], we have

$$\gamma C_v = \gamma_D C_v + (\omega - \gamma_D) \Omega T \quad [\text{A.9}],$$

and so

$$\gamma = \gamma_D + (\omega - \gamma_D) \frac{\Omega}{C_v} T \quad [\text{A.10}],$$

which is very weakly temperature-dependent above Θ_D since $\omega \approx \gamma_D$ and $\Omega \lesssim 3\nu R$. Other properties given by a ratio of the derivatives of $F(T, \rho)$ include the coefficient of thermal expansion,

$$\alpha(T, \rho) = \frac{\rho(\gamma C_v)}{K_T}, \quad [\text{A.11}]$$

the isentropic bulk modulus

$$K_s(T, \rho) = K_T + \rho(\gamma C_v) \gamma T, \quad [\text{A.12}]$$

and the heat capacity at constant pressure,

$$C_p(T, \rho) = C_v(1 + \alpha \gamma T) \quad [\text{A.13}],$$

These are the solid-state model properties used in the text.

A.2. Connection of Isentrope and Hugoniot

To use the model as detailed above, we need to calculate the change of certain model properties, such as P , with density at zero temperature. So, we relate the zero temperature model properties to the known change in density along an appropriate isentrope or the Hugoniot, as follows. From [A.3], we have

$$P(0, \rho) = P(T_s, \rho) - 3\nu R \rho \gamma_D E_D(\chi_D) T_s - \frac{1}{2} \rho \omega \Omega T_s^2 \quad [\text{A.14}]$$

with $\chi_D \equiv \Theta_D / T_s$. $P(T_s, \rho)$ is given by [4.27] in the text, *i.e.*,

$$P(T_s, \rho_H) = \rho_H \gamma_H \Delta e_s(\rho_H) + \frac{\rho_H}{\rho_i} [1 - (1 + \frac{1}{2} \gamma_H) \eta_H^*] (P_H + P_i) - P_i \quad [\text{A.15}]$$

and Δe_s is calculated numerically, as discussed in the text. In a similar fashion, we have, from [A.5] and [A.12],

$$\begin{aligned} K_T(0, \rho) = K_s(T, \rho) - \rho \gamma c_v T - 3\nu R \rho \gamma_D (1 - q_D - 3\gamma_D) E_D(\chi_D) T \\ - 9\nu R \rho \gamma_D \frac{\gamma_D \chi_D}{[e^{\chi_D} - 1]} T - \frac{1}{2} \rho (1 - \omega) \omega \Omega T^2 \end{aligned} \quad [\text{A.16}]$$

To get an expression for $K_s(T, \rho)$ along the Hugoniot, we follow McQueen *et al.* (1967) in equating an infinitesimal change in specific internal energy (SIE) along the Hugoniot with one along an equilibrium thermodynamic path, as follows. From the first law of equilibrium thermodynamics, we may write, at a given density ρ_r , the relation

$$e(s, \rho_r) = e(s_r, \rho_r) + \int_{s_r}^s T(s^*, \rho_r) ds^* \quad [\text{A.17}],$$

where $e(s, \rho)$ is the SIE and s is the specific entropy. Since we have assumed the shock-compressed state is one of thermodynamic equilibrium, we may set $\rho_r = \rho_H$, $s_r = s_H$, and write

$$de(s, \rho_H) = de(s_H, \rho_H) + d \left\{ \int_{s_H}^s T(s^*, \rho_H) ds^* \right\} \quad [\text{A.18}],$$

giving us an expression relating an infinitesimal change in SIE along the Hugoniot, $de(s_H, \rho_H)$, in terms of one at the same density but at another specific entropy. From [4.1] in the text, we have another expression for $de(s_H, \rho_H)$, *i.e.*,

$$de(s_H, \rho_H) = \frac{1}{2\rho_H^2} [P_H + P_i] d\rho_H + \frac{1}{2\rho_H^\alpha} \eta_H dP_H \quad [\text{A.19}].$$

Substituting this into [A.18], we have

$$Tds + \frac{P}{\rho_H^2} d\rho_H = \frac{1}{2\rho_H^2} [P_H + P_i] d\rho_H + \frac{1}{2\rho_H^\alpha} \eta_H dP_H + d\left\{ \int_{s_H}^s T(s^*, \rho_H) ds^* \right\} \quad [\text{A.20}].$$

Now assuming $s = s(P, \rho)$ (*i.e.*, $e = e(P, \rho)$), we have

$$Tds = \frac{1}{\rho\gamma} dP - \frac{K_s}{\rho^2\gamma} d\rho \quad [\text{A.21}].$$

Putting this into [A.20] and rearranging, we obtain

$$\begin{aligned} K_s = \gamma_H P - \frac{1}{2} \gamma_H [P_H + P_i] + [1 - (1 + \frac{1}{2} \gamma_H) \eta_H] \left\{ \frac{dP_H}{d\eta_H} \right\} \\ - \gamma_H \rho_H^2 \frac{\partial}{\partial \rho_H} \left\{ \int_{s_H}^s T(s^*, \rho_H) ds^* \right\} \end{aligned} \quad [\text{A.22}],$$

where $\gamma_H = \gamma_H(s_H, \rho_H)$. Letting $P \rightarrow P_H$ and $s \rightarrow s_H$, we obtain the desired expression

$$K_s(T_H, \rho_H) = [1 - (1 + \frac{1}{2} \gamma_H) \eta_H] \left(\frac{dP_H}{d\eta_H} \right) + \frac{1}{2} \gamma_H [P_H - P_i] \quad [\text{A.23}].$$

In the text, we further assume $\gamma_H = \gamma_{DH}$ *i.e.*, that γ is a function of density alone.

A.3. Relations Between Isentropic and Hugoniot Properties

The purpose of this part of Appendix A is to detail some relations used in the text to relate Hugoniot information to the isentropic properties of low- and high-pressure phases referenced to the same initial state (*i.e.*, T_i and P_i in the text). Among other things, we derive an isentropic equation of state for high-pressure phase of the material based solely on the U-v relation for this phase, as mentioned in the text. First, we outline a number of established relations based on the balance relations for mass and momentum across the shock front and a relationship between the shock-wave propagation velocity and material velocity (*i.e.*, U-v) relation, and then we show how to use these to find various isentropic properties of high-pressure phases described by the U-v relation.

Assuming the material responds adiabatically as a fluid in hydrostatic equilibrium to shock compression, the balance relations for mass and momentum across a shock front separating a material into two adiabatic, homogeneous fluids in hydrostatic equilibrium are, respectively (see the Introduction to this thesis, [I.30] and [I.50]),

$$\rho_H U_H \equiv \rho_i^\alpha U_i \quad [\text{A.24}]$$

and

$$[[P]] = \rho_i^\alpha U_i [[v]] \quad [\text{A.25}],$$

where $[[P]] \equiv P_H - P_i$ is the jump in pressure, and $[[v]] \equiv v_H - v_i$ the jump in material velocity, across the shock front; P_i and v_i are then the pressure in and the velocity of the material ahead of the shock front. Also, $U_H \equiv u - v_H$ is the speed of propagation of the shock front with respect to the shocked material, $U_i \equiv u - v_i$ is that with respect to the unshocked material, and u is the speed of displacement of the shock front (*i.e.*, the "intrinsic" velocity of the shock front). Equations [A.24] and [A.25] relate 3 unknown, *i.e.* u , v_H , P_H and ρ_H , assuming the initial conditions v_i , P_i and ρ_i^α are known. However, since $U_H = U_i - [[v]]$, we can reduce

this number to 3 (U_i , P_H and ρ_H) by making the constitutive assumption that U_i may be written as a function of $||v||$ in a Taylor's series about v_i . To second order, this is

$$U_i \equiv a_i + b_i ||v|| + c_i ||v||^2 + O(||v||^3) \quad [A.26]$$

with

$$a_i \equiv \lim_{||v|| \rightarrow 0} \left\{ U_i \right\} \quad [A.27]$$

$$b_i \equiv \lim_{||v|| \rightarrow 0} \left\{ \frac{dU_i}{d||v||} \right\} \quad [A.28]$$

and

$$c_i \equiv \frac{1}{2} \lim_{||v|| \rightarrow 0} \left\{ \frac{d^2 U_i}{d||v||^2} \right\} \quad [A.29],$$

giving us 3 equations, [A.24], [A.25] and [A.26], relating 3 unknowns, $||v||$, ρ_H and P_H . Note that a_i and b_i are usually positive, while c_i is usually negative. Using the relative compression, $\eta_H = 1 - \rho_i^\alpha / \rho_H$, as defined in the text, we may write [A.24] as

$$||v|| = \eta_H U_i \quad [A.30].$$

Putting this into [A.25], we have either

$$U_i^2 = \frac{1}{\rho_i^\alpha \eta_H} ||P|| \quad [A.31]$$

or

$$||v||^2 = \frac{\eta_H}{\rho_i^\alpha} ||P|| \quad [A.32],$$

depending on whether or not we eliminate $||v||$ or U_i , respectively. From [A.25] and [A.30], we obtain a relation for U_i in terms of a_i , b_i , c_i and η_H *i.e.*,

$$c_i^2 \eta_H^4 U_i^4 - [(1-b_i \eta_H)^2 - 2a_i c_i \eta_H^2] U_i^2 + a_i^2 = 0 \quad [\text{A.33}].$$

As shown by Prieto and Renero (1970), for $b_i \eta_H \ll 1$, [A.33] has the solution

$$U_i^2 = \frac{a_i^2}{[(1-b_i \eta_H)^2 - 2a_i c_i \eta_H^2]} \quad [\text{A.34}].$$

Putting this into [A.31], we obtain

$$[|P|] = \frac{\rho_i^\alpha a_i^2 \eta_H}{(1-b_i \eta_H)^2 - 2a_i c_i \eta_H^2} \quad [\text{A.35}]$$

which we may rearrange for $\eta_H([|P|])$, *i.e.*,

$$\eta_H = \frac{b_i}{(b_i^2 - 2a_i c_i)} \{ \mu - [(\mu^2 - 1) + 2a_i c_i]^{1/2} \} \quad [\text{A.36}]$$

Note that c_i , when resolvable by experimental data, is usually negative (*e.g.*, Pastine and Piacesi, 1966; Ruoff, 1967; Prieto and Renero, 1970; Brown and McQueen, 1982). In this case, we see that $P_H(c_i=0) \rightarrow \infty$ as $b_i \eta_H \rightarrow 1$, but $P_H(c_i < 0) \rightarrow \rho_i a_i^2 b_i / c_i$ in this same limit (Prieto and Renero, 1970). Clearly, c_i cannot equal zero for physically-reasonable asymptotic behavior. However, if $|c_i| \ll b_i^2 / 4a_i$ (Prieto and Renero, 1970), setting $c_i=0$ for $b_i \eta_H \ll 1$ is at least mathematically valid. If we do this, [A.35] reduces to the so-called shock-wave "equation-of-state" (McQueen *et al.*, 1967). For ϵ and/or other high-pressure phases of Fe, for example, $|c_i|$ should be less than 1.6×10^{-4} s/m (using the appropriate parameters in Table 1) by implication of the apparent accuracy of the linear fit to the U-v data (Brown and McQueen, 1986).

Following Pastine and Piacesi (1966), we may substitute [A.31] into [A.26] and obtain

$$a_i = \lim_{[|v|] \rightarrow 0} \left\{ \frac{1}{\rho_i^\alpha} \frac{[|P|]}{\eta_H} \right\}^{1/2} \quad [\text{A.37}].$$

Since the limits $\rho_H \rightarrow \rho_i^\alpha$, $\eta_H \rightarrow 0$ and $[|P|] \rightarrow 0$ are formally and physically

equivalent to $||v|| \rightarrow 0$, [A.33] becomes

$$a_i = \frac{0}{0} \quad [\text{A.38}],$$

an indeterminate form. However, since both $||P||$ and η_H are analytic functions of η_H or ρ_H via [A.35] and by definition, respectively, we may use L'Hopital's rule to evaluate [A.37], *i.e.*,

$$a_i = \lim_{\rho_H \rightarrow \rho_H^0} \left\{ \left\{ \frac{\rho_H}{\rho_H^0} \right\}^2 \left(\frac{d[||P||]}{d\rho_H} \right) \right\} \quad [\text{A.39}]$$

or

$$a_i = \lim_{\rho_H \rightarrow \rho_H^0} \left\{ \frac{K_H}{\rho_H} \right\}^{1/2} \quad [\text{A.40}]$$

with

$$K_H \equiv \rho_H \left(\frac{d[||P||]}{d\rho_H} \right) = (1 - \eta_H) \left(\frac{dP_H}{d\eta_H} \right) \quad [\text{A.41}],$$

In a similar fashion, we find an expression for b_i , *i.e.*,

$$b_i = \frac{1}{4} \lim_{\rho_H \rightarrow \rho_H^0} [1 + K_H'] \quad [\text{A.42}],$$

with

$$K_H' \equiv \left(\frac{dK_H}{dP_H} \right) = \frac{1}{K_H} (1 - \eta_H)^2 \left(\frac{d^2 P_H}{d\eta_H^2} \right) - 1 \quad [\text{A.43}].$$

Lastly, for c_i , we obtain

$$c_i = \frac{1}{12a_i} \left\{ 2b_i(2 - b_i) + \lim_{\rho_H \rightarrow \rho_H^0} [K_H K_H''] \right\} \quad [\text{A.44}],$$

with

$$K_H'' \equiv \left(\frac{d^2 K_H}{dP_H^2} \right) \quad [A.45]$$

and

$$K_H K_H'' = \frac{1}{K_H} (1-\eta_H)^3 \left(\frac{d^3 P_H}{d\eta_H^3} \right) - (K_H' + 2)(K_H' + 3) \quad [A.46].$$

Since the initial ($||v|| \rightarrow 0$) slope and curvature of the shock-compression locus are equal to those of the isentrope referenced to the same initial state (Bethe, 1942), we have

$$\lim_{\rho_H \rightarrow \rho_i^\alpha} [K_H] = K_{s_1}^\alpha \quad [A.47]$$

and

$$\lim_{\rho_H \rightarrow \rho_i^\alpha} [K_H'] = K_{s_1}^{\alpha'} \quad [A.48].$$

And from [4.10] in the text, we may relate K_H'' to $K_{s_1}^{\alpha''}$, *i.e.*,

$$\lim_{\rho_H \rightarrow \rho_i^\alpha} [K_H K_H''] = K_{s_1}^\alpha K_{s_1}^{\alpha''} + 2b_i \gamma^\alpha(\rho_i^\alpha) \quad [A.49].$$

In these relations, $K_{s_1}^\alpha$, $K_{s_1}^{\alpha'}$ and $K_{s_1}^{\alpha''}$ are the isentropic bulk modulus, and its first and second pressure derivatives at constant entropy, $s_i = s(T_i, P_i)$, of the low-pressure phase, α .

Experimental U-v relations applicable to high-pressure phases of a material are usually centered at the initial density of the low-pressure phase, ρ_i^α . To recenter this U-v relation to the appropriate phase, β , and obtain estimates of certain properties of β referenced to $\rho_i \equiv \rho_i^\beta$, we calculate new values of a_i , b_i and c_i (which represent the experimentally constrained U-v relation for the β -phase, centered at ρ_i^α), *i.e.*, a_i^* , b_i^* and c_i^* . These values of the U-v coefficients, centered at ρ_i , then represent a so-called "metastable" U-v relation equivalent to that obtained by McQueen *et al.* (1967). To calculate a_i^* , b_i^* and c_i^* from

ρ_i^α , a_i , b_i , c_i and ρ_i , we first note that the pressure and density of the β -shock state are related by [A.26] if a_i , b_i and c_i in [A.26], result from a fit to data from that part of the U-v plane representing β . Instead of [A.28] and [A.29], we now have, for the metastable U-v relation

$$[U_i^*]^2 = \frac{1}{\rho_i \eta_H^*} [[P]] \quad [\text{A.50}]$$

and

$$[[v^*]]^2 = \frac{\eta_H^*}{\rho_i} [[P]] \quad [\text{A.51}],$$

where $[[P]]$ is still given by [A.26]. With these, the procedure to find expressions for a_i^* , b_i^* and c_i^* is exactly analogous to that just followed in obtaining [A.30], [A.32] and [A.34] for a_i , b_i and c_i , respectively. All we do is replace U_i with U_i^* , $[[v]]$ with $[[v^*]]$, ρ_i^α with ρ_i , a_i with a_i^* , b_i with b_i^* , and c_i with c_i^* , except in [A.26], because it gives $[[P]]$ and ρ_H for β , referenced to ρ_i^α , as stated above. Consequently,

$$a_i^* = \left\{ \frac{K_H}{\rho_H} \right\}_{\rho_H=\rho_i}^{1/2} = \left\{ \frac{K_{S_1}}{\rho_i} \right\}^{1/2} \quad [\text{A.52}]$$

$$b_i^* = \frac{1}{4} [1 + [K_H']_{\rho_H=\rho_i}] = \frac{1}{4} [1 + K_{S_1}'] \quad [\text{A.53}]$$

and

$$\begin{aligned} c_i^* &= \frac{1}{12a_i^*} \left\{ 2b_i^*(2 - b_i^*) + [K_H K_H'']_{\rho_H=\rho_i} \right\} \\ &= \frac{1}{12a_i^*} \left\{ 2b_i^*[2 - b_i^* + \gamma(\rho_i)] + K_{S_1} K_{S_1}'' \right\} \end{aligned} \quad [\text{A.54}].$$

From this, we see that if $c_i \approx 0$, then

$$K_{S_1} K_{S_1}'' \approx [K_{S_1}' - 7 - 4\gamma(\rho_i)] \quad [\text{A.55}]$$

and this is the case for most materials from the experimental-resolution point-of-view. Assuming that $c_i=0$, [A.35], [A.41], [A.49] and [A.51] provide

$$a_i^* = (1-\eta_i) \left\{ \frac{\rho_i^\alpha(1 + b_i\eta_i)}{(1 - b_i\eta_i)^3} \right\}^{1/2} a_i \quad [\text{A.56}],$$

and from [A.35], [A.43], [A.50], [A.51] and [A.53],

$$b_i^* = \frac{1}{4} \left\{ 1 + \frac{[4(1 - \eta_i)b_i + (2 - \eta_i)b_i^2\eta_i - 1]}{(1 - b_i\eta_i)(1 + b_i\eta_i)} \right\} \quad [\text{A.56}]$$

where $\eta_i \equiv 1 - \rho_i^\alpha / \rho_i$. Note that, from these relations, $a_i^* \rightarrow a_i$ and $b_i^* \rightarrow b_i$ as $\rho_H \rightarrow \rho_i^\alpha$, *i.e.*, as $\eta_i \rightarrow 0$. In principle, [A.40], [A.42] and [A.44] may be used as consistency relations between Hugoniot data and other types of compression data for appropriate materials. Note that we need $\rho_i = \rho_i^\beta$ to obtain a_i^* and b_i^* from this method. If we know this density sufficiently well, we also gain estimates of K_s and K_s' of the high-pressure phase, as well as a_i^* and b_i^* . In this paper, for example, we use [A.45]-[A.46] to estimate the isentropic properties of liquid-Fe referenced to STP given in Table 4.1.

§10. Appendix B: Isentropic Release and Reshock

Considering the shock-compressed material as a thermodynamic "system," and the "lab" as its "surroundings," a balance of energy implies that any infinitesimal change in the specific internal energy of the system, $de(\delta q, \delta w)$, is due to the difference between the net amount of heat transported into the system from the surroundings, δq , and the net amount of work done by the system on its surroundings, δw . If we assume the material to be internally in thermodynamic equilibrium, then $de = Tds - Pd v$ and any infinitesimal change in specific entropy of the system is given by

$$ds = \frac{1}{T} \delta q - \frac{1}{T} [\delta w - Pd v] \quad [\text{B.1}].$$

Adopting the idea that heat transport in or out of the target is insignificant on the time scale of release, we assume that the release path is adiabatic ($\delta q=0$). Further, we assume that the mechanical work done by the system during release is entirely reversible ($\delta w = P dv$). In this case, the release path is both isentropic and adiabatic.

B.1. Phase Transition during Release

If a phase transition occurs during release, the constraint of isentropic release in turn places constraints on the phase transition. Consider a first-order transition from the shock-compressed phase β to a release phase π . In this case, the total specific internal energy, e , total specific entropy, s , and total specific volume, v , of the two-phase system may be written in the form

$$\phi = (1 - \chi)\phi^\beta + \chi\phi^\pi \quad [\text{B.2}],$$

where χ is the mass fraction of π , and $\phi = \{e, s, v\}$. As with a single-component system, an infinitesimal change in specific internal energy of the two-phase system, de , is balanced by the net heat flow into the system from the surroundings, δq , minus the net work done by the system on its surroundings, δw . Assuming that each phase is internally in thermodynamic equilibrium (*i.e.*, temperature, pressure and composition are homogeneous within the phase), an infinitesimal change in total specific entropy of the two-phase, single-component system is, from [B.1] and [B.2],

$$T^\beta ds = \delta q + \chi(T^\beta - T^\pi) ds^\pi + \left\{ (g^\beta - g^\pi) + s^\pi(T^\beta - T^\pi) \right\} d\chi - \delta w_{\text{ir}} \quad [\text{B.3}]$$

where

$$\delta w_{\text{ir}} \equiv \delta w - P^\beta d[(1 - \chi)v^\beta] - P^\pi d[\chi v^\pi]$$

is the nonrecoverable work done by the system on the surroundings, and g is

the specific Gibbs free energy. The second term on the right-hand side of [B.3] is the entropy produced by heat flow between phases, while the third term is that produced by mass exchange between phases. A sufficient, but not necessary, set of conditions for isentropic ($ds=0$) release through the mixed-phase region is then, on the basis of [B.3], (1) adiabatic release ($\delta q=0$), (2) mechanical equilibrium ($P^\beta=P^\pi$) in the system plus reversible (Pdv) work on the surroundings ($P=P^\beta=P^\pi$), (3) internal thermal ($T^\beta=T^\pi$) and (4) chemical ($g^\beta=g^\pi$) equilibrium. Conversely, if these conditions prevail, release through the mixed-phase region will be isentropic. Clearly, even if release is isentropic through the mixed-phase region, it is no guarantee that the phase transition will occur in thermodynamic (*i.e.*, thermal, mechanical and chemical) equilibrium.

We choose to satisfy the constraint of isentropic release by assuming the conditions discussed above consistent with this, *i.e.*, 1) release is adiabatic, 2) all work is recoverable and 3) the phase transition occurs in thermodynamic equilibrium. On this basis, we need an expression for the change in pressure and temperature across an isentropic phase transition. With $s=s(P,T)$ for each phase, an infinitesimal change of s in the mixed-phase region is, from [B.2] with $\phi=s$,

$$ds = [c_p^\beta + \chi \Delta c_p] d \ln T - [\alpha^\beta v^\beta + \chi \Delta(\alpha v)] dP + \Delta s d\chi \quad [B.4],$$

where c_p is the specific heat at constant pressure, v is the specific volume, α is the thermal expansion, and $\Delta\phi \equiv \phi^\pi - \phi^\beta$ is the jump of any quantity ϕ across the mixed-phase region. For an isentrope through the mixed-phase region, $ds = 0$. Putting this condition into [B.4], and noting that pressure and temperature do not vary independently along the equilibrium phase boundary, *i.e.*, $\Delta v dP = \Delta s dT_{PB}$, we have

$$\begin{aligned} & \{(c_p^\beta + \chi \Delta c_p) \Delta v - [\alpha^\beta v^\beta + \chi \Delta(\alpha v)] T_{PB}(P) \Delta s\} dP \\ & + \Delta s T_{PB}(P) \Delta s d\chi = 0 \end{aligned} \quad [B.5],$$

Now we show that this relation for an isentropic path through the mixed-phase region is separable, and so an exact differential. Let

$$\Pi(P, \chi) \equiv (c_p^\beta + \chi \Delta c_p) \Delta v - T_{\text{PB}} [\alpha^\beta v^\beta + \chi \Delta(\alpha v)] \Delta s \quad [\text{B.6}]$$

and

$$X(P) \equiv \Delta s T_{\text{PB}} \Delta s \quad [\text{B.7}].$$

Then [B.5] becomes

$$\Pi(P, \chi) dP + X(P) d\chi = 0$$

From [B.6] and [B.7], we have

$$\Pi_\chi(P, \chi) \equiv \left\{ \frac{\partial \Pi}{\partial \chi} \right\} = \Delta c_p \Delta v - T_{\text{PB}} \Delta(\alpha v) \Delta s \quad [\text{B.8}]$$

and

$$\begin{aligned} X_P(P) &\equiv \left\{ \frac{dX}{dP} \right\} = \Delta s \left\{ \frac{dT_{\text{PB}}}{dP} \right\} \Delta s + 2\Delta s T_{\text{PB}} \left\{ \frac{d\Delta s}{dP} \right\}_{\text{PB}} \\ &= \left\{ \Delta v + 2T_{\text{PB}} \left\{ \frac{d\Delta s}{dP} \right\}_{\text{PB}} \right\} \Delta s \end{aligned} \quad [\text{B.9}].$$

Note that both of these partial derivatives are functions only of pressure along the phase boundary. Since at any point along the phase boundary, $P^\beta = P^\pi$, we have

$$\left\{ \frac{d\Delta s}{dP} \right\}_{\text{PB}} = \frac{\Delta c_p}{T_{\text{PB}}} \frac{\Delta v}{\Delta s} - \Delta(\alpha v) \quad [\text{B.10}].$$

Putting this into [B.9], we have

$$X_P(P) = [\Delta v - 2 T_{\text{PB}} \Delta(\alpha v)] \Delta s + 2\Delta c_p \Delta v \quad [\text{B.11}].$$

The condition for [B.5] to be an exact differential is $X_P = \Pi_\chi$. Since, from [B.8] and [B.11], this is clearly not true, [B.5] is not an exact differential equation, in

its current form. However, we may attempt to put it into such a form by solving

$$\mu \Pi(P, \chi) dP + \mu X(P) d\chi = 0 \quad [\text{B.12}],$$

where μ is the integrating factor. Putting these into the exactness criterion, we require

$$[\mu \Pi]_{\chi} = [\mu X]_P \quad [\text{B.13}].$$

Since we already know $\Pi(P, \chi)$ and $X(P)$, we solve [B.12] for μ , *i.e.*,

$$\Pi \mu_{\chi} - X \mu_P + (\Pi_{\chi} - X_P) \mu = 0 \quad [\text{B.14}].$$

Note that $(\Pi_{\chi} - X_P)$ is a function of P only. In this case, we set $\mu_{\chi} = 0$ and solve

$$\mu_P = \frac{(\Pi_{\chi} - X_P)}{X} \mu \quad [\text{B.15}]$$

to obtain the integrating factor

$$\mu(P) \equiv \exp \left\{ \int^P \frac{1}{\Delta s} \left\{ \Delta(\alpha v) - \frac{\Delta v}{T_{PB}(P^*)} \left\{ 1 + \frac{\Delta c_P}{\Delta s} \right\} \right\} dP^* \right\} \quad [\text{B.16}].$$

With $\mu(P)$, [B.5] in the form [B.12] is now exact. On this basis, we may solve [B.5] as follows. We define

$$\Psi_P(P, \chi) = \mu(P) \Pi(P, \chi) \quad [\text{B.17}]$$

and

$$\Psi_{\chi}(P, \chi) = \mu(P) X(P) \quad [\text{B.18}].$$

Integrating [B.17] with respect to pressure at constant composition, we obtain

$$\Psi(P, \chi) = \int^P \mu(P^*) \Pi(P^*, \chi) dP^* + g(\chi) \quad [\text{B.19}],$$

where $g(\chi)$ is at most an arbitrary function of composition. Putting this into [B.18], we have

$$\Psi_{\chi}(P) = \mu(P)X(P) = \int^P \mu(P^*)\Pi_{\chi}(P^*,\chi)dP^* + g_{\chi}(\chi) \quad [\text{B.20}]$$

Solving this for $g_{\chi}(\chi)$, we find

$$g_{\chi}(\chi) = \mu(P)X(P) - \int^P \mu(P^*)\Pi_{\chi}(P^*,\chi)dP^* \quad [\text{B.21}]$$

Even though it appears that $g(\chi)$ is a function of pressure, it cannot be, by its definition, [B.20]. Further, since

$$\Pi_{\chi}(P,\chi) = \Delta c_p \Delta v - T_{PB} \Delta(\alpha v) \Delta s \quad [\text{B.22}]$$

is actually not a function of χ , we have

$$g(\chi) \equiv \chi g_{\chi}(\chi) \quad [\text{B.23}],$$

and so

$$\Psi(P,\chi) = \chi \mu(P)X(P) + \int^P \mu(P^*)\{\Pi(P^*,\chi) - \chi \Pi_{\chi}(P^*)\}dP^* \quad [\text{B.24}]$$

with

$$\Pi - \Pi_{\chi} = c_p^{\beta} \Delta v - T_{PB} \alpha^{\beta} v^{\beta} \Delta s \quad [\text{B.25}].$$

Putting [B.25] into [B.24], we obtain

$$\Psi(P,\chi) = \chi \mu(P) X(P) + \int^P \mu(P^*)[c_p^{\beta} \Delta v - T_{PB}(P^*) \alpha^{\beta} v^{\beta} \Delta s]dP^* \quad [\text{B.26}].$$

Note that $\Psi(P,\chi)$ is equal to some constant since

$$\Psi_{\chi}d\chi + \Psi_P dP = 0 \quad [\text{B.27}]$$

by definition, [B.12] above. Relation [B.26] is subject to the following boundary condition:

$$\Psi(P_{\text{PB}}^{\beta}, \chi = 0) = \int^{P_{\text{PB}}^{\beta}} \mu(P) [c_p^{\beta} \Delta v - T_{\text{PB}}(P) \alpha^{\beta} v^{\beta} \Delta s] dP^* = \text{constant} \quad [\text{B.28}].$$

Using this condition, we have the solution to [B.5] for χ as a function of pressure along the phase boundary, *i.e.*

$$\chi(P) = \frac{1}{\Delta s \mu(P_{\text{PB}}) \Delta v} \int_{P_{\text{PB}}^{\beta}}^P \mu(P^*) [T_{\text{PB}}(P^*) \alpha^{\beta} v^{\beta} \Delta s - c_p^{\beta} \Delta v] dP^* \quad [\text{B.29}].$$

In [B.29], P_{PB}^{β} is the pressure at which the release path of β intersects the π - β phase boundary, *i.e.*, where $\chi = 0$. In the models, we evaluate [B.29] numerically along the phase boundary, $T_{\text{PB}}(P)$, until 1) $\chi = 1$ (complete transformation) or 2) $T_{\text{PB}} = T_{\text{PB}}(P_{\text{R}})$ (partial transformation). In the former case, the new phase then releases to P_{R} along a path beginning at the pressure and temperature on the phase boundary where $\chi = 1$.

B.2. Complete Release and Reshock

Since the free surface of the completely released material has not been shocked, an impedance match between 1) the unshocked material, which impacts the next target material at the free-surface velocity achieved upon complete release (see text), and 2) the next target material provides us with the pressure of the DP or FL reshocked state, P_{RS} . This reshocked state quickly relaxes via reverberations to a state with the same normal components of stress and material velocity as the shock-compressed state of the next target component. We assume that this occurs isentropically.

The complete release process brings the material to a low-pressure state with a lower density and higher temperature than the density and temperature

of the unshocked starting material. From this point of view, assuming all states achieve thermodynamic equilibrium, we may use an energy balance in the pressure-density plane, such as that used in the obtaining the expressions for T_H in the text (*e.g.*, [4.46]), to connect the reshocked state with a state along the principal Hugoniot of the reshocked-state phase having the same density as the reshocked phase. Referring to Figure B.1, assume the shocked material experiences complete release to a pressure P_i , an absolute temperature T_R , and a phase π in thermodynamic equilibrium possessing a mass density $\rho_R^\pi \equiv \rho^\pi(T_R, P_i)$, specific entropy $s_R^\pi \equiv s^\pi(T_R, P_i)$, and specific internal energy $e_R^\pi \equiv e(s_R^\pi, \rho_R^\pi)$ (point A, Figure B.1). Further, assume this material is immediately “reshocked” to a pressure P_{RS} , temperature T_{RS} , and phase δ in thermodynamic equilibrium having a mass density $\rho_{RS}^\delta \equiv \rho^\delta(T_{RS}, P_{RS})$, specific entropy $s_{RS}^\delta \equiv s^\delta(T_{RS}, P_{RS})$, and specific internal energy $e_{RS}^\delta \equiv e(s_{RS}^\delta, \rho_{RS}^\delta)$ (point E, Figure B.1). Also, assume that the material deforms as a fluid. In this case, we may connect the complete release (point A, Figure B.1) and reshocked (point E, Figure B.1) states by the Rankine Hugoniot relation, *i.e.*,

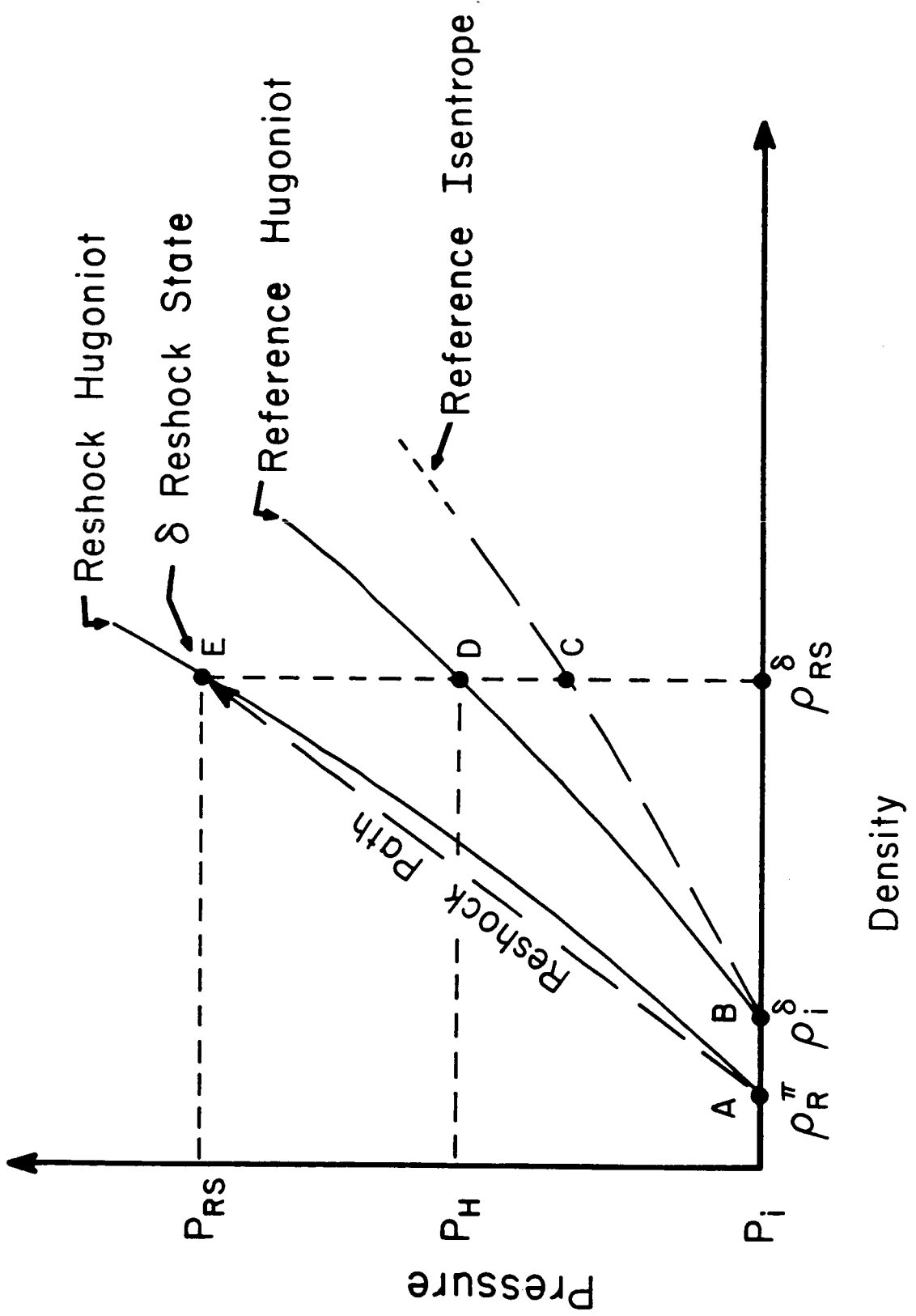
$$e_{RS}^\delta - e_R^\pi = \frac{1}{2\rho_R^\pi} \eta_{RS} [P_{RS} + P_i] \quad [B.30]$$

with

$$\eta_{RS} \equiv 1 - \rho_R^\pi / \rho_{RS}^\delta$$

being the relative compression of the material along the reshock path. In the text, we used the concept of an equivalent thermodynamic path to connect the initial and shock-compressed states of a material, occupying different phases of that material. Applying this to the present case, we may connect states A and E in Figure B.1 via a path A→B→C→D→E using a known reference Hugoniot, which ideally would be the “principal” (*i.e.*, referenced to STP) Hugoniot of δ . Assume that the reference Hugoniot begins at a density $\rho_i^\delta = \rho(T_i, P_i)$,

Figure B.1 Diagram depicting release-reshock calculation.



represented by point B in Figure B.1. The reshock path between A and E is then represented by

$$\begin{aligned}
 e_{RS}^{\delta} - e_R^{\pi} &= e(s_i^{\delta}, \rho_i^{\delta}) - e(s_R^{\pi}, \rho_R^{\pi}) & (A \rightarrow B) \\
 &+ e(s_i^{\delta}, \rho_{RS}^{\delta}) - e(s_i^{\delta}, \rho_i^{\delta}) & (B \rightarrow C) \\
 &+ e(s_{RS}^{\delta}, \rho_{RS}^{\delta}) - e(s_i^{\delta}, \rho_{RS}^{\delta}) & (C \rightarrow E) \\
 &= \frac{1}{2\rho_R^{\pi}} \eta_{RS} [P_{RS} + P_i] & (A \rightarrow E)
 \end{aligned}$$

[B.31]

from [B.30]. Unless otherwise noted, all quantities apply to δ in the rest of this section. Since part of the path represented by [B.31], i.e., B→D, is the equivalent equilibrium thermodynamic path for shock compression of the material from ρ_i^{δ} to ρ_{RS}^{δ} , we have

$$\begin{aligned}
 e(s_H, \rho_{RS}) - e(s_i, \rho_i) &= e(s_i, \rho_{RS}) - e(s_i, \rho_i) & (B \rightarrow C) \\
 &+ e(s_H, \rho_{RS}) - e(s_i, \rho_{RS}) & (C \rightarrow D) \\
 &= \frac{1}{2\rho_i} \eta_H [P_H + P_i] & (B \rightarrow D)
 \end{aligned}$$

[B.32]

with

$$\eta_H = 1 - \rho_i / \rho_{RS}$$

and

$$P_H = P_i + \frac{\rho_i a_i^2 \eta_H}{(1 - a_i \eta_H)^2}$$

from [4.15] in the text. Substituting [B.32] into [B.31], we have

$$\frac{1}{2\rho_R^{\pi}} \eta_{RS} [P_{RS} + P_i] = e(s_i, \rho_i) - e(s_R^{\pi}, \rho_R^{\pi}) \quad (A \rightarrow B)$$

$$+ \frac{1}{2\rho_i} \eta_H [P_H + P_i] \quad (\text{B} \rightarrow \text{D})$$

$$+ e(s_{RS}, \rho_{RS}) - e(s_H, \rho_{RS}) \quad (\text{D} \rightarrow \text{E})$$

[B.33].

Assuming, as before, that γ , the equilibrium thermodynamic Grüneisen's parameter, is a function of density alone, [16] from the text allows us to write, for the path from D \rightarrow E, the relation

$$e(s_{RS}, \rho_{RS}) - e(s_H, \rho_{RS}) = \frac{1}{\rho_{RS} \gamma_{RS}} \left\{ P_{RS} - P_H \right\} \quad [\text{B.34}]$$

with $\gamma_{RS} = \gamma(\rho_{RS})$. Substituting [B.33] into [A1.32] and rearranging, we obtain

$$\Upsilon_{RS} P_{RS} = (1-\phi) \Upsilon_H P_H + \frac{1}{2} \phi \gamma_{RS} P_i + \rho_R^\pi \gamma_{RS} \Delta e_{IR} \quad [\text{B.35}]$$

with

$$\phi \equiv 1 - \rho_R^\pi / \rho_i$$

$$\Upsilon_{RS} \equiv [1 - (1 + \frac{1}{2} \gamma_{RS}) \eta_{RS}]$$

$$\Upsilon_H \equiv [1 - (1 + \frac{1}{2} \gamma_{RS}) \eta_H]$$

and

$$\Delta e_{IR} \equiv [e(s_i, \rho_i) - e(s_R^\pi, \rho_R^\pi)] .$$

Requiring $P_{RS} \rightarrow P_i$ as $\rho_{RS} \rightarrow \rho_R^\pi$, we obtain from [B.35]

$$P_i = (1 - \phi) [\Upsilon_H P_H]_{\rho_{RS} = \rho_R^\pi} + \frac{1}{2} \gamma_R^\pi \phi P_i + \rho_R^\pi \gamma_R^\pi \Delta e_{IR} \quad [\text{B.36}].$$

Rearranging [B.36], we have

$$\Delta e_{IR} = \frac{1}{\rho_R^\pi \gamma_R^\pi} \left\{ (1 - \frac{1}{2} \gamma_R^\pi \phi) P_i - (1 - \phi) [\Upsilon_H P_H]_{\rho_{RS} = \rho_R^\pi} \right\} \quad [\text{B.37}],$$

giving us an expression for the difference in energy between the complete release and reference states. If $P_i \equiv 0$, then

$$\Delta e_{\text{R}} = \frac{-1}{\rho_{\text{R}}^{\pi} \gamma_{\text{R}}^{\pi}} (1-\phi) [\Upsilon_{\text{H}}^{\text{P}}]_{\rho_{\text{RS}} = \rho_1}.$$

With these relations, we obtain a metastable U-v relation (Appendix A), which allows us to calculate the density of the reshocked state from the pressure, and with both of these, we we calculate the temperature via the appropriate expression in the text.

§11. Appendix C: Energy Transport Model

In this appendix, we 1) derive conditions under which radiation and/or conduction may be an important means of energy transport in the shock-compressed or released states of the target components, and 2) establish energy balance relations for the target components to be used in Appendix IV and the text. We attempt 1) via a dimensional analysis of the local energy balance in a radiating, conducting target represented as a rectangular Cartesian continuum with material properties assumed to be isotropic and homogeneous in the reference (deformed) state. In constructing this energy balance, we assume that the radiant energy density and radiation stresses are negligible in comparison with the corresponding thermomechanical quantities. We also assume an equilibrium caloric constitutive relation for the specific internal energy of the relevant deformed state of each target component. With the deformed state as the reference state, then, we may assume, for example, that the components of the heat flux q^i are given by the classic Fourier relation in an isotropic medium

$$q^i \equiv -k \delta^{ij} T_{,j} \quad [\text{C.1}],$$

where k is the thermal conductivity. Under these circumstances, the local balance of energy around the (deformed) reference state R is represented by

$$\rho_R c_{P,R} \partial_t T(x^i, t) = k_R T_{,ii}(x^i, t) - h^i_{,i}(x^i, t) + r(x^i, t) \quad [C.2].$$

In this relation, T is the absolute temperature, h^i are the components of the radiant energy flux, and we have combined terms for the specific internal energy supply and mechanical dissipation rates to form $r(x^i, t)$. Also, ρ_R , $c_{P,R}$ and k_R are the density, specific heat at constant pressure and thermal conductivity of the reference state, R . Note that, in [C.2], time is judged relative to the beginning of the reference state, $\partial_t \equiv \partial/\partial t$, and $\psi_{,i}$ denotes partial differentiation of any field quantity $\psi(x^i, t)$ with respect to x^i , the coordinates of the reference configuration R . Of the terms in [C.2], neither $h^i_{,i}$, the divergence of the radiative flux, nor r , the specific internal energy production rate, is specified. To find an expression for $h^i_{,i}$, we first need to discuss radiative transport in the target.

All radiative transport models discussed in this paper are founded in geometric optics and the classical equation of transport ([C.3] below), both of which assume an optically isotropic propagation medium (*i.e.*, one with a uniform index of refraction). The form of this equation used in this appendix presumes that 1) all processes affecting the observed radiation intensity (scattering, absorption, *etc.*) are independent of the intensity of the sources and 2) any scattering is elastic and isotropic. Under these conditions, the change in the quasi-static spectral intensity, $i_\lambda'(s^j)$, at a point $P(x^j)$ in the direction \vec{s} is given by (*e.g.*, Siegel & Howell, 1981, Eq. 14-4)

$$s^j \partial_{,j} i_\lambda' = -a_\lambda i_\lambda' + a_\lambda i_{\lambda e}' - \sigma_\lambda i_\lambda' + \frac{\sigma_\lambda}{4\pi} \int_{\omega=4\pi} i_\lambda'(\omega^*) d\omega^* \quad [C.3]$$

This is the radiant energy transport at a point $P(x^j)$ per unit time, per unit projected surface area normal to \vec{s} , per unit wavelength interval $d\lambda$ about a single wavelength λ , per unit solid angle in a single direction \vec{s} . Note that the subscript λ denotes a spectral quantity. i_λ' is quasi-static because we assume it is not explicitly dependent on time, but only implicitly so through temperature,

etc.. In [C.3], $\partial_{,j} \equiv \partial/\partial s^j$, $a_\lambda = a_\lambda(\lambda, T, P)$ and $\sigma_\lambda = \sigma_\lambda(\lambda, T, P)$ are the spectral absorption and scattering coefficients, respectively, and $i_{\lambda e}' = i_{\lambda e}'(\lambda, T)$ is the spectral emission intensity, all along \vec{s} . The first term on the right-hand side of [C.3] is the loss of intensity by absorption (including the negative contribution from induced emission), the second is the gain by all emission processes except induced emission, the third is the loss of intensity by scattering, and the last is the intensity gained by scattering into the \vec{s} direction from the solid angle ω . Note that we assume, in writing [C.3], that the wavelength of the radiation is not changed as a result of these processes. If we integrate [C.3] over all solid angles and wavelengths, assuming any scattering to be isotropic, we obtain $h^i_{,i}$ at a point $P(x^j)$, i.e.,

$$h^i_{,i} = 4\pi \int_0^\infty a_\lambda(\lambda^*) [i_{\lambda e}'(\lambda^*) - \bar{\tau}_\lambda(\lambda^*)] d\lambda^* \quad [C.4]$$

(e.g., Siegel & Howell, 1981). In this relation, the first term represents the rate of emission of radiation per unit volume in all directions, while the second, given by

$$\bar{\tau}_\lambda(\lambda) \equiv \int_{\omega=4\pi} i_{\lambda}'(\lambda, \omega^*) d\omega^*,$$

is the radiation intensity scattered from all directions into P at wavelength λ . In principle, we could substitute [C.4] into [C.2] and try to solve the resulting nonlinear integrodifferential equation for the temperature field in the medium of interest. However, here we want only to establish the magnitude of $h^i_{,i}$ relative to other terms in the energy balance, [C.2].

To judge the relative magnitude of the terms constituting [C.2], we render them nondimensional (ND) by the following transformation

$$\{x^i, t, T, h^i, r\} \rightarrow \{x_R \xi^i, t_R \tau, T_R + \Delta T_R \Theta, h_R h^i, r_R r\} \quad [C.5].$$

In this transformation, Θ and T_R are the ND and reference (*e.g.*, Hugoniot or release state) temperatures of the material, while ΔT_R is the difference between T_R and some "maximum" possible temperature such that $\Theta \lesssim O(1)$. For example, if T_R is the release-state temperature, ΔT_R represents the difference between it and the reshocked-state temperature at the same pressure (see text). Substituting [C.5] into [C.2], we obtain

$$\partial_t \Theta - Pe_R^{-1} \Theta_{,ii} + Bo_R^{-1} h^i_{,i} = Da_R e \quad [C.6].$$

In this expression,

$$Pe_R \equiv \frac{x_R^2}{t_R \kappa_R}$$

is the Peclet number, $\kappa_R \equiv k_R / \rho_R c_{P,R}$ is the thermal diffusivity,

$$Bo_R \equiv \frac{\rho_R c_{P,R} \Delta T_R}{h_R t_R}$$

is the Boltzmann number, and

$$Da_R \equiv \frac{r_R t_R}{\rho_R c_{P,R} \Delta T_R}$$

is the Damköhler number, of state R. Pe_R , Bo_R and Da_R are, respectively, the ratios of 1) free enthalpy flux to conductive flux, 2) free enthalpy flux to radiative flux, and 3) generalized internal energy supply rate to free enthalpy flux. We are particularly interested in Pe_R and Bo_R , since their respective magnitudes will control the relative contributions of conduction and radiation to the energy transfer in the interior (away from the boundaries) of any layer of the target model. To obtain the magnitude of Bo_R , we first require an expression for h_R , which may be obtained from [C.4]. First, we assume $i_{\lambda e}'(\lambda)$ is given by

$$i_{\lambda e}'(\lambda) = i_{\lambda pl}(n_\lambda, \lambda, T) \quad [C.7],$$

where $i_{\lambda pl}(\lambda, T)$ is the Planck function and n_λ is the index of refraction of the medium around P. Then, defining 1), the Planck mean absorption coefficient

(e.g., Siegel & Howell, 1981)

$$\langle a \rangle_{pl}(T,P) \equiv \frac{\int_0^{\infty} a_{\lambda}(\lambda, T, P) i_{\lambda pl}(n_{\lambda}, \lambda, T) d\lambda}{\int_0^{\infty} i_{\lambda e}'(\lambda) d\lambda} \quad [C.8]$$

and 2), the incident mean absorption coefficient

$$\langle a \rangle_{in}(T,P) \equiv \frac{\int_0^{\infty} a_{\lambda}(\lambda, T, P) \bar{\tau}_{\lambda}(\lambda) d\lambda}{\int_0^{\infty} \bar{\tau}_{\lambda}(\lambda) d\lambda} \quad [C.9]$$

where

$$\bar{\tau} \equiv \int_0^{\infty} \bar{\tau}_{\lambda}(\lambda) d\lambda ,$$

and noting that, if n_{λ} is independent of λ ,

$$\int_0^{\infty} i_{\lambda e}'(\lambda) d\lambda = n^2 \sigma_{sb} T^4 ,$$

(where $\sigma_{sb} \equiv 5.6696 \times 10^{-8} \text{W/m}^2\text{-K}^4$ is the Stefan-Boltzmann constant), we may put [C.4] in the form

$$h^i_{,i} = 4\pi [\langle a \rangle_{pl} n^2 \sigma_{sb} T^4 - \langle a \rangle_{in} \bar{\tau}] \quad [C.10].$$

Nondimensionalizing [C.10] with the appropriate transformations in [C.5] plus $\bar{\tau} \rightarrow \bar{\tau}_R \bar{\tau}$, we have

$$h^i_{,i} = \frac{h_R}{x_R} [\langle a \rangle_{pl} [1 + \Phi_R \Theta]^4 - \langle a \rangle_{in} \bar{\tau}] \quad [C.11],$$

where $\bar{\tau}_R \equiv n_R^2 \sigma_{SB} T_R^4$,

$$h_R \equiv 4\pi x_R a_R n_R^2 \sigma_{SB} T_R^4$$

and $\Phi_R = \Delta T_R / T_R$. Substituting h_R into the Boltzmann number, we obtain

$$Bo_R = \frac{\rho_R c_{PR} \Delta T_R}{4\pi a_R \bar{\tau}_R n_R^2 \sigma_{SB} T_R^4} \quad [C.12].$$

From [C.6] and [C.12], we see that radiative transfer will be an important means of energy transfer in an optically thick ($Bo_R(a_R \rightarrow \infty) \rightarrow 0$) and/or high-temperature medium, but not in an optically thin ($Bo_R(a_R \rightarrow 0) \rightarrow \infty$) medium, all other parameters being finite.

At a boundary between two target components, we have a slightly different energy balance to consider. If we assume that the boundary is material and does not contribute to the balance of energy across it, the local balance of energy across the boundary between layers I and J takes the form

$$[q_i^i + h_i^i] \nu^i = [q_j^j + h_j^j] \nu^j \quad [C.13],$$

where ν^i is the "outward" normal unit vector to the interface. Using [C.1] and the definition of h_R given above, this takes on the ND form

$$\Theta_{i,i} \nu^i - \frac{k_j \Delta T_j}{k_i \Delta T_i} \Theta_{j,i} \nu^i = Sk_i^{-1} \left\{ h_i^i \nu^i - \frac{a_j n_j^2 T_j^2}{a_i n_i^2 T_i^2} h_j^j \nu^j \right\} \quad [C.14],$$

where Sk_Q is the Stark number of layer Q, given by (see text)

$$Sk_Q \equiv \frac{k_Q \Delta T_Q}{4\pi a_Q x_Q^2 n_Q^2 \sigma_{SB} T_Q^4} \quad [C.15],$$

which is a measure of conductive to radiative flux across a layer x_Q thick with effective temperature gradient $\Delta T_Q / x_Q$. Estimates of the parameters in these relations for the high-pressure states of the metallic DP, FL and dielectric SW are given in the following table:

Table C.1. Order-of-magnitude shock compressed/released-state parameters.

Parameter	metal	dielectric	SI units
ρ_R	10^4	10^3	kg/m ³
$c_{P,R}$	10^3	10^3	J/kg·K
k_R^\dagger	10^2	10^1	W/m·K
T_R	10^4	10^3	K
ΔT_R	10^3	10^3	K
n_R	1	1	
a_R^\dagger	$>10^6$	10	m ⁻¹
x_{exp}	$<10^{-5}$	10^{-3}	m
t_{exp}	10^{-7}	10^{-7}	s
Pe_R	<1	$<10^6$	
Bo_R	10	$<10^9$	
Sk_R	10	10^3	

† - STP values.

The quantities ρ_R , $c_{P,R}$, T_R , ΔT_R , t_{exp} and n_R are relatively well-known (*i.e.*, to within a factor of 2) through the impedance match and equilibrium thermodynamic shock compression/release calculations discussed in the text. Most uncertain of all material parameters constituting Bo_R and Pe_R , and so $Sk_R \equiv Bo_R/Pe_R$, are the thermal conductivity, k_R , and the absorption coefficient, a_R , of the high-pressure state of each layer. For perfect crystalline nonmetals, $k \approx 1/T$, while for metals, $k \approx$ constant at high temperature, respectively

(*e.g.*, Berman, 1976; for minerals, see Roufosse & Klemens, 1974), implying that the values of k_R in Table C.1 are upper bounds if these dependences are relatively insensitive to pressure. If we assume that k for metals is dominated by its electronic component, k_e , we can use the Wiedemann-Franz-Lorenz (WFL) relation ([5.7] in text) to estimate k from electrical resistance data, or some assumption on ρ_e , since the relevant data are relatively scarce. Bridgman (1952) investigated the change in electrical resistance of many statically-compressed materials, including iron, but only at low pressure ($\lesssim 10$ GPa). Keeler (1971) investigated the change in the electrical resistance of shock-compressed copper and iron up to 140 GPa. He found that ρ_e of shock-compressed Cu decreased from ≈ 16.7 to 5.6 $n\Omega\cdot m$ with pressure up to ≈ 100 GPa; a datum at 140 GPa implies that the resistivity of Cu reaches a minimum between 100 and 140 GPa and then increases to ≈ 0.83 $n\Omega\cdot m$ at 140 GPa. As for Fe, the data imply that its electrical resistivity decreases from ≈ 2.5 to 0.47 $n\Omega\cdot m$ between 13 and 140 GPa (above the $\alpha \rightarrow \epsilon$ transition). In light of [5.7], these trends imply that the thermal conductivities of shock-compressed Cu and Fe increase with shock pressure, against the high-temperature expectation expressed above. Consequently, we may assume with some basis that the STP value of k provides a lower bound to the high P,T value of the metallic target components, k_R .

The thermal conductivity of dielectric target components is dominated by the lattice contribution, k_p , at high pressure, we may estimate k from the lattice thermal-conductivity model of Roufosse & Klemens (1974), who argue that the acoustic branches of the phonon-spectrum dominate k_p . Using this assumption, they arrive at an expression for k_p , *i.e.*,

$$k_p = \frac{B'}{T} \left\{ \frac{2}{3} \left\{ \frac{T_1}{T} \right\}^{1/2} + \frac{1}{3} \left\{ \frac{T}{T_1} \right\} \right\} \quad [C.17]$$

with

$$T_1 \equiv \frac{n^{2/3}}{2^{1/6}[3\pi^2]^{5/3}} \frac{M_a v_\phi^2}{k_B \gamma^2}$$

and

$$B' \equiv \frac{1}{2^{1/6} 3^{2/3} \pi^{7/3}} \frac{M_a}{a^2 n^{1/3}} \frac{v_\phi^3}{\gamma_p^2},$$

where n is the number of atoms in the unit cell, M_a is the atomic mass, v_ϕ is the velocity of sound, k_B is Boltzmann's constant, and a^3 is the atomic volume, and γ_p is the acoustic-phonon Grüneisen's parameter. This relation is consistent with the $k \propto 1/T$ expectation at low pressure. However, if the effect of pressure is to increase k , then k may change little from its STP value. Arguments in favor of this are given by, *e.g.*, Roufosse & Jeanloz (1983), who find that various two-body interatomic force models appropriate for halides predict an increase in k_p with density and a decrease across polymorphic phase transitions with an increase in coordination. We use [C.16], [C.17], the solid-state thermostat model presented in Appendix A, and the equilibrium shock-compression relations presented in the text to estimate high P,T values of k_e for metals and k_p for dielectrics in our targets. These calculations, discussed in the text, are consistent with assuming the STP value of k for metals and nonmetals is a lower bound to the high P,T values of k for these materials.

As for the absorption coefficient, we expect the STP values given in Table C.1, like those for k , to be lower bounds, since absorption in the optical band is most likely to increase with pressure and temperature (*e.g.*, Siegel & Howell, 1981). Only a few initially transparent materials, such as Al_2O_3 (Bass *et al.*, 1987), retain their original transparency upon shock compression to high pressure ($\lesssim 250$ GPa).

Note that the following comments for the FL apply to the DP as well. From Table C.1 values, we expect $Bo_F \lesssim 10^7/a_F$ and $Bo_W \sim 10^{10}/a_W$ for the FL and SW, respectively. Since we have no upper bounds on a_F and a_W , we cannot really say that radiation will never be important within the FL and SW, but it seems unlikely. What we can say is that if $a_F \lesssim 10^7 \text{ m}^{-1}$ and $a_W \lesssim 10^{10} \text{ m}^{-1}$, radiative transport should not contribute significantly to the energy balance within the FL and SW (shocked window), respectively, on the time scale of the experiments. Note that this bound for a_F is probably underestimated, since we have assumed a rather large value for T_R in the DP or FL (Table C.1). As for conduction, we have, from Table C.1, $Pe_F \lesssim 10^{12} x_F^2$ and $Pe_W \lesssim 10^{12} x_W^2$, and this implies that conduction will be significant over a length scale of $\lesssim 10^{-6} \text{ m}$ in the DP, FL and/or SW. On this basis, it is likely that conduction will contribute to the energy balance in both the FL and SW on the time scale of the experiment over a length scale equal to the thickness of the FL, since we expect k_W and especially k_F , to increase with pressure and temperature (*i.e.*, during shock compression). From all this, we believe that the values of Bo_R and Pe_R given in Table C.1 are upper bounds to all relevant values of these parameters at higher pressures and temperatures. In order to emphasize the uncertainty of k_R , a_R and the governing length scales, x_F and x_W , of the FL and SW, respectively, we write [C.6] for the DP, FL and SW, and [C.13] for the interface, using the values for the better constrained parameters from Table C.1, in the following forms (with $I \rightarrow \text{FL}$ and $J \rightarrow \text{SW}$):

$$\partial_t \Theta_F - 10^{-14} \frac{k_F}{x_F^2} \Theta_{F,ii} + 10^{-7} a_F h_{F,i}^i = Da_F e_F, \quad [\text{C.18}]$$

$$\partial_t \Theta_W - 10^{-13} \frac{k_W}{x_W^2} \Theta_{W,ii} + 10^{-10} a_W h_{W,i}^i = Da_W e_W, \quad [\text{C.19}]$$

and

$$\Theta_{F,i} \nu^i = \frac{k_W x_F}{k_F x_W} \Theta_{W,i} \nu^i + 10^6 \frac{a_F x_F^2}{k_F} h_{F,i}^i \nu^i$$

$$- 10^5 \frac{x_F x_w a_w}{k_F} h_w^i \nu^i \quad [C.20].$$

For a given layer to be, in effect, spatially infinite with respect to a given process (*i.e.*, the boundaries have no effect on the process), its length scale must be at least an order-of-magnitude less than the layer thickness. The conductive length scale is $x_{\text{Room}} \equiv \sqrt{\kappa_R t_{\text{exp}}}$, while that for radiation is $x_{\text{Rad}} \equiv a_R^{-1}$. The STP values of these length scales, given in Table C.1, when compared to x_R of each layer, imply that both the DP and SW are infinite with respect to conduction, but that the SW is finite, while the DP is infinite, with respect to radiation. This implies that any conduction in the DP and SW, and radiative transfer in the DP, will be quite localized on the time scale of the experiments, but radiation will pass essentially unhindered through the SW for $a_R \lesssim x_R^{-1} \sim 10^3 \text{m}^{-1}$. In this case, only the interface, shock front and USW free surface will significantly affect the radiation intensity. We consider the effect on radiation of propagation across the interface, SW, shock front, USW and its free surface in Appendix V. By the same reasoning, we conclude that any conduction effects on energy transport affecting the observed radiation field will be confined to a region near the FL-SW interface on the order of the FL thickness. On this length scale, heterogeneous heating at the DP-FL interface and/or phase changes between the DP-FL and FL-SW interfaces may also contribute to the temperature field in the neighborhood of the FL-SW interface. In light of all this, we assume that x_F and x_w are given by the corresponding values of x_{Room} for the DP and SW. Putting these into [C.18]-[C.19] and reducing them, we obtain

$$\partial_\tau \Theta_F - 10^{-2} k_F \Theta_{F,ii} + 10^{-7} a_F h_F^i{}_{,i} = Da_F e_F \quad [C.21],$$

$$\partial_\tau \Theta_w - 10^{-1} k_w \Theta_{w,ii} = Da_w e_w \quad [C.22],$$

and

$$\Theta_{F,i} \nu^i = \frac{k_w}{k_F} \Theta_{F,i} \nu^i + 10^{-6} \frac{a_F}{k_F} h_F^i \nu^i \quad [C.23].$$

where we have eliminated the radiative terms for the SW in [C.22] and [C.23], since a_w would have to be on the order of 10^9 m^{-1} before radiative transfer is important in the shocked (or unshocked) TW and across the FL-SW interface, regardless of the value of x_w . If a_f is much larger (*e.g.*, 10^8 m^{-1}) and k_f much smaller (*e.g.*, 10) than their values given in Table C.1, radiative transfer could influence energy transport in the DP, and across the FL-SW interface. However, for lack of better information, we adopt the values in Table C.1, thereby assuming that the thermal conductivity of the DP, FL and SW, and the absorption coefficient of the DP and FL, are effectively unaffected by compression/release. In this case, [C.21]-[C.22] become

$$\partial_\tau \Theta_f - \text{Pe}_f^{-1} \Theta_{f,ii} = \text{Da}_f e_f, \quad [\text{C.24}]$$

$$\partial_\tau \Theta_w - \text{Pe}_w^{-1} \Theta_{w,ii} = \text{Da}_w e_w, \quad [\text{C.25}]$$

and

$$\Theta_{D,i} \nu^i = \frac{k_w \Delta T_w x_f}{k_f \Delta T_f x_w} \Theta_{w,i} \nu^i \quad [\text{C.26}].$$

where $\{\text{Pe}_f, \text{Pe}_w\} \sim 1$ (with $x_f \sim x_w 10^{-6}$) and

$$\frac{k_w \Delta T_w x_f}{k_f \Delta T_f x_w} \sim 0.1.$$

In this case, radiative transfer does not contribute substantially to energy transport in any part of the DP-TW system. So, we are left to investigate the effects of conduction at the interface through relations [C.24]-[C.26] in the next section, and effects of radiative transport through the FL-SW interface, SW, shock front, USW and its free surface by way of a model based on [C.3], in Appendix E.

§12. Appendix D: Conductive Transport in the Target

The scaling arguments presented in Appendix C provide some idea of conditions under which conduction and/or radiation may be an important means of energy transport in the interior of each layer of the target, and across the boundaries between the layers. With some basis for believing that we are in the range of conditions where conduction dominates radiation as a means of energy transport, we decouple these processes and treat them separately. In this section, we establish a simple conduction model for our target geometry. We adopt the framework of Grover and Urtiew (1974), who assumed that 1) significant conduction takes place only along the direction of shock-propagation (*i.e.*, is one-dimensional), and 2) shock-compression transfers energy to the material much faster than it can be conducted away. This last assumption allows us to treat the DP and TW as thermal half-spaces. Choosing the thickness of the FL, d , as the governing length scale, we have, from [AIII.25] and [AIII.26], the ND energy balance for the DP ($-\infty < \xi < -1$), FL ($-1 < x < 0$) or TW ($0 < \xi < \infty$):

$$\Theta_{A,\xi\xi}(\xi,\tau) - Pe_A \partial_\tau \Theta_A(\xi,\tau) = -Pe_A Da_A e_A(\xi,\tau) , \quad \tau > 0 \quad [D.1],$$

where A is the released DP or FL, or the shocked TW. We use the Laplace transform (LT) technique (*e.g.*, Carslaw and Jaeger, 1959) to solve [D.1] for each layer. Applying this transform to [D.1], we obtain

$$\theta_{A,\xi\xi} - [q_A(s)]^2 \theta_A = -\phi_A(\xi,s) \quad [D.2],$$

where $\theta(\xi,s)$ is the LT of $\Theta(\xi,\tau)$, s is the LT variable, $q_A(s) \equiv \sqrt{Pe_A s}$, and

$$\phi_A(\xi,s) \equiv Pe_A [Da_A e_A(\xi,s) + \Theta_A(\xi,0)] \quad [D.3],$$

which contains the ND initial conditions $\Theta_A(\xi,0)$. The general solution of [D] is given by

$$\theta_A(\xi,s) = b_A(s)e^{q_A \xi} + c_A(s)e^{-q_A \xi} + \theta_{A,p}(\xi,s) \quad [D.4]$$

with

$$\theta_{Ap}(\xi, s) = \frac{1}{2q_A} \int_{-\infty}^{\xi} [e^{q_A(s-\xi)} - e^{-q_A(s-\xi)}] \phi_A(\zeta, s) d\zeta$$

being the particular solution of [D.2]. The boundary conditions include the requirements that $\theta_D(\xi, \tau)$ and $\theta_F(\xi, \tau)$ and $\theta_w(\xi, \tau)$ remain bounded as $\xi \rightarrow -\infty$ and $\xi \rightarrow +\infty$, respectively. Consequently, we have

$$c_D = \frac{1}{2q_D} \int_{-\infty}^0 e^{q_D \zeta} \phi_D(\zeta, s) d\zeta$$

and

$$b_w = \frac{1}{2q_w} \int_0^{\infty} e^{-q_w \zeta} \phi_w(\zeta, s) d\zeta.$$

Using these and writing [D.4] for each layer, we have

$$\theta_D(\xi, s) = b_D e^{q_D \xi} + \theta_{Dp}(\xi, s), \quad -\infty < \xi < -1 \quad [D.5]$$

$$\theta_F(\xi, s) = b_F(s) e^{q_F \xi} + c_F(s) e^{-q_F \xi} + \theta_{Fp}(\xi, s), \quad -1 < \xi < 0 \quad [D.6]$$

and

$$\theta_w(\xi, s) = c_w e^{-q_w \xi} + \theta_{wp}(\xi, s), \quad 0 < \xi < \infty \quad [D.7].$$

Now θ_{Dp} and θ_{wp} are given by

$$\theta_{Dp}(\xi, s) = \frac{1}{2q_D} \left\{ \int_{-\infty}^{\xi} e^{q_D(s-\xi)} \phi_D(\zeta, s) d\zeta + \int_{\xi}^0 e^{q_D(\xi-\zeta)} \phi_D(\zeta, s) d\zeta \right\} \quad [D.8]$$

and

$$\theta_{wp}(\xi, s) = \frac{1}{2q_w} \left\{ \int_0^{\xi} e^{-q_w(\xi-\zeta)} \phi_w(\zeta, s) d\zeta + \int_{\xi}^{\infty} e^{-q_w(\zeta-\xi)} \phi_w(\zeta, s) d\zeta \right\} \quad [D.9].$$

Relations [D.5]-[D.7] contain 4 unknowns, b_D , b_F and c_F , and c_W , requiring us to specify 4 more boundary conditions. We obtain these by assuming the usual continuity of energy flux and temperature across each interface in the target. In the transform domain, these are given by

$$-k_D \Phi_D \partial_\xi \theta_D(-1,s) = -k_F \Phi_F \partial_\xi \theta_F(-1,s) \quad [D.10]$$

$$\frac{1}{s} T_D + \Phi_D \theta_D(-1,s) = \frac{1}{s} T_F + \Phi_F \theta_F(-1,s) \quad [D.11]$$

$$-k_F \Phi_F \partial_\xi \theta_F(0,s) = -k_W \Phi_W \partial_\xi \theta_W(0,s) \quad [D.12]$$

and

$$\frac{1}{s} T_F + \Phi_F \theta_F(0,s) = \frac{1}{s} T_W + \Phi_W \theta_W(0,s) \quad [D.13].$$

Putting [D.6]-[D.9] into [D.10]-[D.13], we obtain

$$\begin{pmatrix} \sigma_{DF} e^{-q_D} & -e^{-q_F} & e^{q_F} & 0 \\ e^{-q_D} & -e^{-q_F} & -e^{q_F} & 0 \\ 0 & 1 & -1 & \sigma_{WF} \\ 0 & 1 & 1 & -1 \end{pmatrix} \begin{pmatrix} b'_D \\ b'_F \\ c'_F \\ c'_W \end{pmatrix} = \begin{pmatrix} b_1 \\ b_2 \\ b_3 \\ b_4 \end{pmatrix} \quad [D.14]$$

with

$$b_1 \equiv \frac{\sigma_{DF} \Phi_D}{2q_D} \int_{-\infty}^{-1} e^{q_D(1+s)} \phi_D(\zeta,s) d\zeta$$

$$b_2 \equiv \frac{1}{s} \Delta T_{FD} - \frac{\Phi_D}{2q_D} \int_{-\infty}^{-1} e^{q_D(1+s)} \phi_D(\zeta,s) d\zeta$$

$$b_3 \equiv \frac{\Phi_F}{2q_F} \int_{-1}^0 [e^{q_F \zeta} + e^{-q_F \zeta}] \phi_F(\zeta,s) d\zeta + \frac{\sigma_{WF} \Phi_W}{2q_W} \int_0^\infty e^{-q_W \zeta} \phi_W(\zeta,s) d\zeta$$

$$b_4 \equiv \frac{1}{s} \Delta T_{WF} - \frac{\Phi_F}{2q_F} \int_{-1}^0 [e^{q_F \zeta} - e^{-q_F \zeta}] \phi_F(\zeta,s) d\zeta + \frac{\Phi_W}{2q_W} \int_0^\infty e^{-q_W \zeta} \phi_W(\zeta,s) d\zeta$$

and $b'_D \equiv \Phi_D b_D$, $b'_F \equiv \Phi_F b_F$, etc.. If the coefficient matrix is nonsingular, i.e.,

$$D(s) = -(1 + \sigma_{WF})(1 + \sigma_{DF}) \left\{ e^{q_F - q_D} - \nu_{DF} \nu_{WF} e^{-(q_D + q_F)} \right\} \neq 0$$

where

$$\sigma_{WF} \equiv \left\{ \frac{k_{WF} \rho_W c_{\sigma W}}{k_F \rho_F c_{\sigma F}} \right\}^{1/2}, \quad \sigma_{DF} \equiv \left\{ \frac{k_D \rho_D c_{\sigma D}}{k_F \rho_F c_{\sigma F}} \right\}^{1/2},$$

and

$$\nu_{DF} \equiv \frac{(\sigma_{DF} - 1)}{(\sigma_{DF} + 1)}, \quad \nu_{WF} \equiv \frac{(\sigma_{WF} - 1)}{(\sigma_{WF} + 1)},$$

the system [D.14] has a unique solution. Noting that

$$\begin{aligned} \frac{1}{D(s)} &= \frac{e^{q_D - q_F}}{(1 + \sigma_{DF})(1 + \sigma_{WF})[1 - \nu_{DF} \nu_{WF} e^{-2q_F}]} \\ &= \frac{e^{q_D}}{(1 + \sigma_{DF})(1 + \sigma_{WF})} \sum_{m=0}^{\infty} (\nu_{DF} \nu_{WF})^m e^{-q_F(2m+1)} \end{aligned}$$

for $-1 < \nu_{DF} \nu_{WF} e^{-2q_F} \leq 1$, we invert the coefficient matrix in [D.14] to obtain

$$\begin{pmatrix} b'_D \\ b'_F \\ c'_F \\ c'_W \end{pmatrix} = \frac{1}{(1 + \sigma_{DF})(1 + \sigma_{WF})} \sum_{m=0}^{\infty} (\nu_{DF} \nu_{WF})^m e^{-q_F(2m+1)} \quad [D.15]$$

$$\times \begin{pmatrix} a_{11} & a_{12} & 2e^{q_D} & 2\sigma_{WF} e^{q_D} \\ (1 - \sigma_{WF}) & (\sigma_{WF} - 1)\sigma_{DF} & (1 + \sigma_{DF}) & (1 + \sigma_{DF})\sigma_{WF} e^{q_F} \\ (1 + \sigma_{WF})\sigma_{DF} & -(1 + \sigma_{WF})\sigma_{DF} & (1 - \sigma_{DF})e^{-q_F} & (1 - \sigma_{DF})\sigma_{WF} e^{-q_F} \\ 2 & -2\sigma_{DF} & a_{34} & a_{44} \end{pmatrix} \begin{pmatrix} b_1 \\ b_2 \\ b_3 \\ b_4 \end{pmatrix}$$

with

$$a_{11} \equiv (1 + \sigma_{WF})[e^{q_F} - \nu_{WF} e^{-q_F}]e^{q_D}$$

$$a_{12} \equiv (1 + \sigma_{WF}) [e^{q_F} + \nu_{WF} e^{-q_F}] e^{q_D}$$

$$a_{34} \equiv (1 + \sigma_{DF}) [e^{q_F} - \nu_{DF} e^{-q_F}]$$

and

$$a_{44} \equiv -(1 + \sigma_{DF}) [e^{q_F} + \nu_{DF} e^{-q_F}] .$$

Expanding these out and substituting them into [D.5]-[D.7], we obtain the solutions in the LT domain. We then transform these back to the time domain using the convolution theorem and the following inverse transform (e.g., Carslaw and Jaeger, 1959):

$$\mathbf{L}^{-1} \left\{ \frac{e^{-zs^{1/2}}}{s^{(n+1)/2}} \right\} = (4\tau)^{1/2} i^n \text{erfc} \left\{ \frac{z}{2\tau^{1/2}} \right\} , \quad n = -1, 0, 1, \dots$$

with $\text{Re}\{z\} \geq 0$. In this relation, $i^n \text{erfc}(z)$ is the complementary error function of order n , with

$$i^{-1} \text{erfc}(z) \equiv \frac{2}{\pi^{1/2}} e^{-z^2}$$

$i^0 \text{erfc}(z) \equiv \text{erfc}(z)$, and

$$2n i^n \text{erfc}(z) = i^{n-2} \text{erfc}(z) - 2z i^{n-1} \text{erfc}(z) .$$

Consequently, the temperature field for $-\infty < \xi \leq -1$, $\tau > 0$, i.e., the DP, is given by

$$\begin{aligned} T(\xi, \tau) = & T_D + \Phi_D \int_{-\infty}^{-1} \int_0^\tau G_D(\xi, \zeta, \tau - \mu) \phi_D(\zeta, \mu) d\mu d\zeta \\ & + \frac{\Delta T_{FD}}{(1 + \sigma_{DF})} \sum_{m=0}^{\infty} (\nu_{DF} \nu_{WF})^m \text{erfc} \{ [2m - \kappa_{FD}(1 + \xi)] \omega_F \} \\ & + \frac{\Delta T_{FD}}{(1 + \sigma_{DF})} \sum_{m=0}^{\infty} (\nu_{DF} \nu_{WF})^m \nu_{WF} \text{erfc} \{ [2(m+1) - \kappa_{FD}(1 + \xi)] \omega_F \} \end{aligned}$$

$$\begin{aligned}
 & + \int_{-1}^0 \int_0^\tau F_D(\xi, \zeta, \tau - \mu) \phi_F(\zeta, \tau - \mu) d\mu d\zeta + \int_0^\infty \int_0^\tau W_D(\xi, \zeta, \tau - \mu) \phi_W(\zeta, \mu) d\mu d\zeta \\
 & + \frac{2\sigma_{WF}\Delta T_{WF}}{(1+\sigma_{DF})(1+\sigma_{WF})} \sum_{m=0}^{\infty} (\nu_{DF}\nu_{WF})^m \operatorname{erfc}\{[(2m+1)-\kappa_{FD}(1+\xi)]\omega_F\} \quad [D.16].
 \end{aligned}$$

In this relation, we have defined $\kappa_{FD} \equiv \sqrt{\kappa_F/\kappa_D}$, $\omega_F \equiv \sqrt{Pe_F/4\tau}$,

$$G_D(\xi, \zeta, \tau) \equiv \frac{1}{2} \left\{ \frac{1}{\pi Pe_D \tau} \right\}^{1/2} \sum_{m=0}^{\infty} (\nu_{DF}\nu_{WF})^m ,$$

$$\cdot \left\{ \begin{array}{l} e^{-\{[2m+\kappa_{FD}(\xi-\zeta)]\omega_F\}^2} + \nu_{DF} e^{-\{[2m-\kappa_{FD}(\xi+\zeta+2)]\omega_F\}^2} \\ - \nu_{WF} e^{-\{[2(m+1)-\kappa_{FD}(\xi+\zeta+2)]\omega_F\}^2} - \nu_{DF}\nu_{WF} e^{-\{[2(m+1)+\kappa_{FD}(\xi-\zeta)]\omega_F\}^2} , \quad -\infty < \zeta < \xi , \\ \\ e^{-\{[2m+\kappa_{FD}(\zeta-\xi)]\omega_F\}^2} + \nu_{DF} e^{-\{[2m-\kappa_{FD}(\zeta+\xi+2)]\omega_F\}^2} \\ - \nu_{WF} e^{-\{[2(m+1)-\kappa_{FD}(\zeta+\xi+2)]\omega_F\}^2} - \nu_{DF}\nu_{WF} e^{-\{[2(m+1)+\kappa_{FD}(\zeta-\xi)]\omega_F\}^2} , \quad \xi < \zeta < -1 , \end{array} \right.$$

$$\begin{aligned}
 F_D(\xi, \zeta, s) & \equiv \frac{\Phi_F}{(1+\sigma_{DF})} \left\{ \frac{1}{\pi Pe_F \tau} \right\}^{1/2} \sum_{m=0}^{\infty} (\nu_{DF}\nu_{WF})^m \\
 & \cdot \left\{ e^{-\{[(2m+1)+\zeta-\kappa_{FD}(1+\xi)]\omega_F\}^2} - \nu_{WF} e^{-\{[(2m+1)-\zeta-\kappa_{FD}(1+\xi)]\omega_F\}^2} \right\} ,
 \end{aligned}$$

$$W_D(\xi, \zeta, s) \equiv \frac{\Phi_W}{(1+\sigma_{DF})} \left\{ \frac{1}{\pi Pe_W \tau} \right\}^{1/2} \sum_{m=0}^{\infty} (\nu_{DF}\nu_{WF})^m e^{-\{[(2m+1)+\kappa_{FW}\zeta-\kappa_{FD}(1+\xi)]\omega_F\}^2} ,$$

and $\kappa_{FW} \equiv \sqrt{\kappa_F/\kappa_W}$. The temperature field for $-1 \leq \xi \leq 0$, $\tau > 0$, i.e. the FL, is given by

$$\begin{aligned}
 T(\xi, \tau) & = T_F + \int_{-\infty}^{-1} \int_0^\tau D_F(\xi, \zeta, \tau - \mu) \phi_D(\zeta, \mu) d\mu d\zeta \\
 & + \frac{\sigma_{DF}\Delta T_{DF}}{(1+\sigma_{DF})} \sum_{m=0}^{\infty} (\nu_{DF}\nu_{WF})^m \operatorname{erfc}\{[(2m+1)+\xi]\omega_F\} \\
 & - \frac{\sigma_{DF}\Delta T_{DF}}{(1+\sigma_{DF})} \sum_{m=0}^{\infty} (\nu_{DF}\nu_{WF})^m \nu_{WF} \operatorname{erfc}\{[(2m+1)-\xi]\omega_F\}
 \end{aligned}$$

$$\begin{aligned}
 & + \Phi_F \int_{-1}^0 \int_0^\tau G_F(\xi, \zeta, \tau - \mu) \phi_F(\zeta, \tau - \mu) d\mu d\zeta \\
 & + \int_0^\infty \int_0^\tau W_F(\xi, \zeta, \tau - \mu) \phi_W(\zeta, \mu) d\mu d\zeta \\
 & + \frac{\sigma_{WF} \Delta T_{WF}}{(1 + \sigma_{WF})} \sum_{m=0}^{\infty} (\nu_{DF} \nu_{WF})^m \operatorname{erfc}\{[2m - \xi] \omega_F\} \\
 & - \frac{\sigma_{WF} \Delta T_{WF}}{(1 + \sigma_{WF})} \sum_{m=0}^{\infty} (\nu_{DF} \nu_{WF})^m \nu_{DF} \operatorname{erfc}\{[2(m+1) + \xi] \omega_F\} \quad [D.17],
 \end{aligned}$$

with

$$\begin{aligned}
 D_F(\xi, \zeta, \tau) \equiv & \frac{\sigma_{DF} \Phi_D}{(1 + \sigma_{DF})} \left\{ \frac{1}{\pi P e_D \tau} \right\}^{1/2} \sum_{m=0}^{\infty} (\nu_{DF} \nu_{WF})^m \\
 & \cdot \left\{ e^{-\{[(2m+1) + \xi - \kappa_{FD}(1+\zeta)] \omega_F\}^2} - \nu_{WF} e^{-\{[(2m+1) - \xi - \kappa_{FD}(1+\zeta)] \omega_F\}^2} \right\}
 \end{aligned}$$

$$\begin{aligned}
 G_F(\xi, \zeta, \tau) \equiv & \frac{1}{2} \left\{ \frac{1}{\pi P e_F \tau} \right\}^{1/2} \sum_{m=0}^{\infty} (\nu_{DF} \nu_{WF})^m \\
 & \cdot \begin{cases} \begin{aligned} & e^{-\{[2m + (\xi - \zeta)] \omega_F\}^2} - \nu_{WF} e^{-\{[2m - (\xi + \zeta)] \omega_F\}^2} \\ & - \nu_{DF} e^{-\{[2(m+1) + (\xi + \zeta)] \omega_F\}^2} + \nu_{DF} \nu_{WF} e^{-\{[2(m+1) - (\xi - \zeta)] \omega_F\}^2} \end{aligned} , & -1 < \zeta < \xi , \\ \\ \begin{aligned} & e^{-\{[2m + (\zeta - \xi)] \omega_F\}^2} - \nu_{WF} e^{-\{[2m - (\zeta + \xi)] \omega_F\}^2} \\ & - \nu_{DF} e^{-\{[2(m+1) + (\zeta + \xi)] \omega_F\}^2} + \nu_{DF} \nu_{WF} e^{-\{[2(m+1) - (\zeta - \xi)] \omega_F\}^2} \end{aligned} , & \xi < \zeta < 0 , \end{cases}
 \end{aligned}$$

$$\begin{aligned}
 W_F(\xi, \zeta, \tau) \equiv & \frac{\sigma_{WF} \Phi_W}{(1 + \sigma_{WF})} \left\{ \frac{1}{\pi P e_W \tau} \right\}^{1/2} \sum_{m=0}^{\infty} (\nu_{DF} \nu_{WF})^m \\
 & \cdot \left\{ e^{-\{[2m - \xi + \kappa_{FWS}] \omega_F\}^2} - \nu_{DF} e^{-\{[2(m+1) + \xi + \kappa_{FWS}] \omega_F\}^2} \right\} .
 \end{aligned}$$

Lastly, for $0 \leq \xi < \infty$, $\tau > 0$, i.e., the TW, we obtain

$$\begin{aligned}
 T(\xi, \tau) = & T_w + \int_{-\infty}^{-1} \int_0^{\tau} D_w(\xi, \varsigma, \tau - \mu) \phi_D(\varsigma, \mu) d\mu d\varsigma \\
 & + \frac{2\sigma_{DF} \Delta T_{DF}}{(1 + \sigma_{DF})(1 + \sigma_{WF})} \sum_{m=0}^{\infty} (\nu_{DF} \nu_{WF})^m \operatorname{erfc}\{[(2m+1) + \kappa_{FW}\xi] \omega_F\} \\
 & + \int_{-1}^0 \int_0^{\tau} F_w(\xi, \varsigma, \tau - \mu) \phi_F(\varsigma, \tau - \mu) d\mu d\varsigma \\
 & + \Phi_w \int_0^{\infty} \int_0^{\tau} G_w(\xi, \varsigma, \tau - \mu) \phi_w(\varsigma, \mu) d\mu d\varsigma \\
 & + \frac{\Delta T_{FW}}{(1 + \sigma_{WF})} \sum_{m=0}^{\infty} (\nu_{DF} \nu_{WF})^m \operatorname{erfc}\{[2m + \kappa_{FW}\xi] \omega_F\} \\
 & + \frac{\Delta T_{FW}}{(1 + \sigma_{WF})} \sum_{m=0}^{\infty} (\nu_{DF} \nu_{WF})^m \nu_{DF} \operatorname{erfc}\{[2(m+1) + \kappa_{FW}\xi] \omega_F\} \quad [D.18],
 \end{aligned}$$

with

$$\begin{aligned}
 D_w(\xi, \varsigma, \tau) \equiv & \frac{2\sigma_{DF} \Phi_D}{(1 + \sigma_{DF})(1 + \sigma_{WF})} \left\{ \frac{1}{\pi P e_D \tau} \right\}^{\frac{1}{2}} \\
 & \cdot \sum_{m=0}^{\infty} (\nu_{DF} \nu_{WF})^m e^{-\{[(2m+1) + \kappa_{FW}\xi - \kappa_{FD}(1+\varsigma)] \omega_F\}^2} \\
 F_w(\xi, \varsigma, \tau) \equiv & \frac{\Phi_F}{(1 + \sigma_{WF})} \left\{ \frac{1}{\pi P e_F \tau} \right\}^{\frac{1}{2}} \\
 & \cdot \sum_{m=0}^{\infty} (\nu_{DF} \nu_{WF})^m \left\{ e^{-\{[2m - \varsigma + \kappa_{FW}\xi] \omega_F\}^2} - \nu_{DF} e^{-\{[2(m+1) + \varsigma + \kappa_{FW}\xi] \omega_F\}^2} \right\} \\
 G_w(\xi, \varsigma, \tau) \equiv & \frac{1}{2} \left\{ \frac{1}{\pi P e_w \tau} \right\}^{\frac{1}{2}} \sum_{m=0}^{\infty} (\nu_{DF} \nu_{WF})^m \\
 & \cdot \begin{cases} e^{-\{[2m + \kappa_{FW}(\xi - \varsigma)] \omega_F\}^2} + \nu_{WF} e^{-\{[2m + \kappa_{FW}(\xi + \varsigma)] \omega_F\}^2} \\ - \nu_{DF} e^{-\{[2(m+1) + \kappa_{FW}(\xi + \varsigma)] \omega_F\}^2} - \nu_{DF} \nu_{WF} e^{-\{[2(m+1) + \kappa_{FW}(\xi - \varsigma)] \omega_F\}^2} & , 0 < \varsigma < \xi, \\ \\ e^{-\{[2m + \kappa_{FW}(\varsigma - \xi)] \omega_F\}^2} + \nu_{WF} e^{-\{[2m + \kappa_{FW}(\varsigma + \xi)] \omega_F\}^2} \\ - \nu_{DF} e^{-\{[2(m+1) + \kappa_{FW}(\varsigma + \xi)] \omega_F\}^2} - \nu_{DF} \nu_{WF} e^{-\{[2(m+1) + \kappa_{FW}(\varsigma - \xi)] \omega_F\}^2} & , \xi < \varsigma < \infty, \end{cases}
 \end{aligned}$$

Each of the source terms now has the form

$$\phi_A(\xi, \tau) \equiv Pe_A [Da_A e_A(\xi, \tau) + \Theta(\xi, 0)\delta(\tau)] \quad [D.19],$$

where $\delta(\tau)$ is the Dirac delta-function.

As discussed in the text, we assume that compression/release processes in the target establish an initial ($t=0$) temperature profile in the DP-FL-TW system of the form

$$T(x, 0) \equiv \begin{cases} T_D & -\infty < x < -(\delta_D + d) \\ T_D + \Delta T_D & -(\delta_D + d) < x < -d \\ T_F + \Delta T_{FD} & -d < x < -(d - \delta_{FD}) \\ T_F & -(d - \delta_{FD}) < x < -\delta_{FW} \\ T_F + \Delta T_{FW} & -\delta_{FW} < x < 0 \\ T_W & 0 < x < \infty \end{cases} \quad [D.20].$$

In this relation, d is the FL thickness, T_D and T_F are the temperatures of the DP and FL, respectively, established by direct release from the shock-compressed state to the pressure of the shock-compressed TW, and Φ_D , ΔT_{FD} and ΔT_{FW} are the temperatures reflecting some degree of reshock heating in layers of thickness δ_D , δ_{FD} and δ_{FW} , respectively, in the DP and FL at the DP-FL interface, and in the FL at the FL-TW interface, respectively. Substituting these into the source terms, ϕ_A , we have

$$\phi_D(\xi, \tau) \equiv Pe_D \left\{ Da_D e_D(\xi, \tau) + [h(\xi + 1 + \delta_D^*) - h(\xi + 1)] \frac{\Delta T_D}{\Phi_D} \right\} \quad [D.21]$$

$$\begin{aligned} \phi_F(\xi, \tau) \equiv & Pe_F Da_F e_F(\xi, \tau) + Pe_F [h(\xi + 1) - h(\xi + 1 - \delta_{FD}^*)] \frac{\Delta T_{FD}}{\Phi_F} \\ & + Pe_F [h(\xi + \delta_{FW}^*) - h(\xi)] \frac{\Delta T_{FW}}{\Phi_F} \end{aligned} \quad [D.22]$$

and

$$\phi_W(\xi, \tau) \equiv Pe_W Da_W e_W(\xi, \tau) \quad [D.23],$$

where $h(x)$ is the unit-step function, and $\delta_i^* \equiv di/d$. Using [D.21], the temperature in the DP ($-\infty < \xi \leq -1$, $\tau > 0$) is given by

$$T(\xi, \tau) = T_D + [g_D^-(\xi, \tau, -(1+\delta_D), \xi) + g_D^+(\xi, \tau, \xi, -1)] \Delta T_D + a_D(\xi, \tau) \Delta T_{DF} \\ + f_D(\xi, \tau, -1, -1 + \delta_{FD}) \Delta T_{FD} + f_D(\xi, \tau, -\delta_{FW}, 0) \Delta T_{FW} + b_D(\xi, \tau) \Delta T_{WF} \quad [D.24],$$

with

$$g_D^\pm(\xi, \tau, a, b) \equiv \pm \frac{1}{2} \sum_{m=0}^{\infty} (\nu_{DF} \nu_{WF})^m \operatorname{erfc}\{[2m \pm \kappa_{FD}(a-\xi)]\omega_F\} \\ \mp \frac{1}{2} \sum_{m=0}^{\infty} (\nu_{DF} \nu_{WF})^m \operatorname{erfc}\{[2m \pm \kappa_{FD}(b-\xi)]\omega_F\} \\ - \frac{1}{2} \sum_{m=0}^{\infty} (\nu_{DF} \nu_{WF})^m \nu_{DF} \operatorname{erfc}\{[2m - \kappa_{FD}(2+\xi+a)]\omega_F\} \\ + \frac{1}{2} \sum_{m=0}^{\infty} (\nu_{DF} \nu_{WF})^m \nu_{DF} \operatorname{erfc}\{[2m - \kappa_{FD}(2+\xi+b)]\omega_F\} \\ + \frac{1}{2} \sum_{m=0}^{\infty} (\nu_{DF} \nu_{WF})^m \nu_{WF} \operatorname{erfc}\{[2(m+1) - \kappa_{FD}(2+\xi+a)]\omega_F\} \\ - \frac{1}{2} \sum_{m=0}^{\infty} (\nu_{DF} \nu_{WF})^m \nu_{WF} \operatorname{erfc}\{[2(m+1) - \kappa_{FD}(2+\xi+b)]\omega_F\} \\ \pm \frac{1}{2} \sum_{m=0}^{\infty} (\nu_{DF} \nu_{WF})^{m+1} \operatorname{erfc}\{[2(m+1) \pm \kappa_{FD}(a-\xi)]\omega_F\} \\ \mp \frac{1}{2} \sum_{m=0}^{\infty} (\nu_{DF} \nu_{WF})^{m+1} \operatorname{erfc}\{[2(m+1) \pm \kappa_{FD}(b-\xi)]\omega_F\} \\ a_D(\xi, \tau) \equiv \frac{1}{(1 + \sigma_{DF})} \sum_{m=0}^{\infty} (\nu_{DF} \nu_{WF})^m \operatorname{erfc}\{[2m - \kappa_{FD}(1+\xi)]\omega_F\} \\ + \frac{1}{(1 + \sigma_{DF})} \sum_{m=0}^{\infty} (\nu_{DF} \nu_{WF})^m \nu_{WF} \operatorname{erfc}\{[2(m+1) - \kappa_{FD}(1+\xi)]\omega_F\}, \\ f_D(\xi, \tau, a, b) \equiv \frac{1}{(1 + \sigma_{DF})} \sum_{m=0}^{\infty} (\nu_{DF} \nu_{WF})^m \operatorname{erfc}\{[(2m+1) + a - \kappa_{FD}(1+\xi)]\omega_F\} \\ - \frac{1}{(1 + \sigma_{DF})} \sum_{m=0}^{\infty} (\nu_{DF} \nu_{WF})^m \operatorname{erfc}\{[(2m+1) + b - \kappa_{FD}(1+\xi)]\omega_F\} \\ + \frac{1}{(1 + \sigma_{DF})} \sum_{m=0}^{\infty} (\nu_{DF} \nu_{WF})^m \nu_{WF} \left\{ \operatorname{erfc}\{[(2m+1) - a - \kappa_{FD}(1+\xi)]\omega_F\} \right.$$

$$\begin{aligned}
 & + \frac{1}{(1 + \sigma_{DF})} \sum_{m=0}^{\infty} (\nu_{DF} \nu_{WF})^m \nu_{WF} \left\{ \operatorname{erfc}\{[(2m+1)-a-\kappa_{FD}(1+\xi)]\omega_F\} \right. \\
 b_D(\xi, \tau) \equiv & \frac{2\sigma_{WF}}{(1 + \sigma_{DF})(1 + \sigma_{WF})} \sum_{m=0}^{\infty} (\nu_{DF} \nu_{WF})^m \operatorname{erfc}\{[(2m+1)-\kappa_{FD}(1+\xi)]\omega_F\} .
 \end{aligned}$$

The function $g_D^\pm(\xi, \tau, a, b)$ comes from the integration of the second term on the right-hand side of [D.16] using the source term from [D.21]; a and b are the lower and upper limits of the spatial integration, respectively. We get g_D^+ from g_D^\pm by using the upper signs in each term having both + and - signs, while g_D^- is given by the lower signs in each term.

The temperature in the FL ($-1 \leq \xi \leq 0$, $\tau > 0$), using [D.22], becomes

$$\begin{aligned}
 T(\xi, \tau) = T_F + d_F(\xi, \tau, -1 + \delta_D, -1) \Delta T_D + a_F(\xi, \tau) \Delta T_{DF} \\
 + \psi_F(\xi, \tau) \Delta T_{FD} + \pi_F(\xi, \tau) \Delta T_{FW} + b_F(\xi, \tau) \Delta T_{WF} \quad [D.25],
 \end{aligned}$$

with

$$\begin{aligned}
 d_F(\xi, \tau, a, b) \equiv & \frac{\sigma_{DF}}{(1 + \sigma_{DF})} \sum_{m=0}^{\infty} (\nu_{DF} \nu_{WF})^m \operatorname{erfc}\{[(2m+1)+\xi-\kappa_{FD}(1+b)]\omega_F\} \\
 & - \frac{\sigma_{DF}}{(1 + \sigma_{DF})} \sum_{m=0}^{\infty} (\nu_{DF} \nu_{WF})^m \operatorname{erfc}\{[(2m+1)+\xi-\kappa_{FD}(1+a)]\omega_F\} \\
 & - \frac{\sigma_{DF}}{(1 + \sigma_{DF})} \sum_{m=0}^{\infty} (\nu_{DF} \nu_{WF})^m \nu_{WF} \operatorname{erfc}\{[(2m+1)-\xi-\kappa_{FD}(1+b)]\omega_F\} \\
 & + \frac{\sigma_{DF}}{(1 + \sigma_{DF})} \sum_{m=0}^{\infty} (\nu_{DF} \nu_{WF})^m \nu_{WF} \operatorname{erfc}\{[(2m+1)-\xi-\kappa_{FD}(1+a)]\omega_F\} , \\
 a_F(\xi, \tau) \equiv & \frac{\sigma_{DF}}{(1 + \sigma_{DF})} \sum_{m=0}^{\infty} (\nu_{DF} \nu_{WF})^m \left\{ \operatorname{erfc}\{[(2m+1)+\xi]\omega_F\} - \nu_{WF} \operatorname{erfc}\{[(2m+1)-\xi]\omega_F\} \right\} \\
 \psi_F(\xi, \tau) \equiv & \begin{cases} g_F^-(\xi, \tau, -1, \xi) + g_F^+(\xi, \tau, \xi, -1 + \delta_{FD}) , & \xi \leq -1 + \delta_{FD} , \\ g_F^-(\xi, \tau, -1, -1 + \delta_{FD}) , & \xi \geq -1 + \delta_{FD} , \end{cases} \\
 \pi_F(\xi, \tau) \equiv & \begin{cases} g_F^+(\xi, \tau, -\delta_{FW}, 0) , & \xi \leq -\delta_{FW} , \\ g_F^-(\xi, \tau, -\delta_{FW}, \xi) + g_F^+(\xi, \tau, \xi, 0) , & \xi \geq -\delta_{FW} , \end{cases} \\
 g_F^\pm(\xi, \tau, a, b) \equiv & \pm \frac{1}{2} \sum_{m=0}^{\infty} (\nu_{DF} \nu_{WF})^m \operatorname{erfc}\{[2m \pm (a-\xi)]\omega_F\} \\
 & \mp \frac{1}{2} \sum_{m=0}^{\infty} (\nu_{DF} \nu_{WF})^m \operatorname{erfc}\{[2m \pm (b-\xi)]\omega_F\}
 \end{aligned}$$

$$\begin{aligned}
 & + \frac{1}{2} \sum_{m=0}^{\infty} (\nu_{DF} \nu_{WF})^m \nu_{WF} \operatorname{erfc}\{[2m - (\xi + a)]\omega_F\} \\
 & - \frac{1}{2} \sum_{m=0}^{\infty} (\nu_{DF} \nu_{WF})^m \nu_{WF} \operatorname{erfc}\{[2m - (\xi + b)]\omega_F\} \\
 & - \frac{1}{2} \sum_{m=0}^{\infty} (\nu_{DF} \nu_{WF})^m \nu_{DF} \operatorname{erfc}\{[2(m+1) + (\xi + a)]\omega_F\} \\
 & + \frac{1}{2} \sum_{m=0}^{\infty} (\nu_{DF} \nu_{WF})^m \nu_{DF} \operatorname{erfc}\{[2(m+1) + (\xi + b)]\omega_F\} \\
 & \mp \frac{1}{2} \sum_{m=0}^{\infty} (\nu_{DF} \nu_{WF})^{m+1} \operatorname{erfc}\{[2(m+1) \mp (a - \xi)]\omega_F\} \\
 & \pm \frac{1}{2} \sum_{m=0}^{\infty} (\nu_{DF} \nu_{WF})^{m+1} \operatorname{erfc}\{[2(m+1) \mp (b - \xi)]\omega_F\}
 \end{aligned}$$

$$b_F(\xi, \tau) \equiv \frac{\sigma_{WF}}{(1 + \sigma_{WF})} \sum_{m=0}^{\infty} (\nu_{DF} \nu_{WF})^m \left\{ \operatorname{erfc}\{[2m - \xi]\omega_F\} - \nu_{DF} \operatorname{erfc}\{[2(m+1) + \xi]\omega_F\} \right\}.$$

Lastly, the temperature in the TW ($0 \leq \xi < \infty$, $\tau > 0$), using [D.22], is given by

$$\begin{aligned}
 T(\xi, \tau) = T_w + d_w(\xi, \tau; -(1 + \delta_D), -1) \Delta T_D + a_w(\xi, \tau) \Delta T_{DF} + f_w(\xi, \tau; -1, -1 + \delta_{FD}) \Delta T_{FD} \\
 + f_w(\xi, \tau; -\delta_{FW}, 0) \Delta T_{FW} + b_w(\xi, \tau) \Delta T_{FW} \quad [D.26],
 \end{aligned}$$

with

$$\begin{aligned}
 a_w(\xi, \tau) & \equiv \frac{2\sigma_{DF}}{(1 + \sigma_{DF})(1 + \sigma_{WF})} \sum_{m=0}^{\infty} (\nu_{DF} \nu_{WF})^m \operatorname{erfc}\{[(2m+1) + \kappa_{FW}\xi]\omega_F\} \\
 b_w(\xi, \tau) & \equiv \frac{1}{(1 + \sigma_{WF})} \sum_{m=0}^{\infty} (\nu_{DF} \nu_{WF})^m \operatorname{erfc}\{[2m + \kappa_{FW}\xi]\omega_F\} \\
 & + \frac{1}{(1 + \sigma_{WF})} \sum_{m=0}^{\infty} (\nu_{DF} \nu_{WF})^m \nu_{DF} \operatorname{erfc}\{[2(m+1) + \kappa_{FW}\xi]\omega_F\} \\
 d_w(\xi, \tau, a, b) & \equiv \frac{\sigma_{DF}}{(1 + \sigma_{DF})(1 + \sigma_{WF})} \sum_{m=0}^{\infty} \operatorname{erfc}\{[(2m+1) + \kappa_{FW}\xi - \kappa_{FD}(1+b)]\omega_F\} \\
 & + \frac{\sigma_{DF}}{(1 + \sigma_{DF})(1 + \sigma_{WF})} \sum_{m=0}^{\infty} \operatorname{erfc}\{[(2m+1) + \kappa_{FW}\xi - \kappa_{FD}(1+a)]\omega_F\} \\
 f_w(\xi, \tau, a, b) & \equiv \frac{1}{(1 + \sigma_{WF})} \sum_{m=0}^{\infty} \operatorname{erfc}\{[2m + \kappa_{FW}\xi - b]\omega_F\} \\
 & - \frac{1}{(1 + \sigma_{WF})} \sum_{m=0}^{\infty} \operatorname{erfc}\{[2m + \kappa_{FW}\xi - a]\omega_F\}
 \end{aligned}$$

$$\begin{aligned}
 & + \frac{1}{(1+\sigma_{\text{WF}})} \sum_{m=0}^{\infty} \nu_{\text{DF}} \operatorname{erfc}\{[2(m+1)+\kappa_{\text{FW}}\xi+b]\omega_{\text{F}}\} \\
 & - \frac{1}{(1+\sigma_{\text{WF}})} \sum_{m=0}^{\infty} \nu_{\text{DF}} \operatorname{erfc}\{[2(m+1)+\kappa_{\text{FW}}\xi+a]\omega_{\text{F}}\} ,
 \end{aligned}$$

These last 3 sets of expressions are those used in the text for the temperature of DP, FL, and TW as a function of distance away from the FL-TW interface and time.

§13. Appendix E: Radiative Transport Model

As discussed briefly in the text, radiation from sources at the interface and/or the shocked TW may be affected by radiative transfer through the shocked TW, shock front, unshocked TW and its free surface. In general, radiation sources include 1) the FL at the interface, 2) gas or other trapped material at the interface and/or 3) the shocked TW. The FL is generally a metal (*i.e.*, an opaque material), while the TW is generally an oxide, halide or silicate. Many of these latter materials are of natural origin, possessing color and containing inclusions of various sizes, some of which are potential scatterers (*e.g.*, apparent Rayleigh scattering in CaO: Boslough *et al.*, 1984). These possibilities motivate us to formulate a model from [AIII.3] and the geometry of the target of sufficient generality to deal with emission, absorption and/or isotropic scattering in the shocked and/or unshocked TW. Note that in writing [AIII.3], we have already assumed isotropic scattering. For tractability, we must accept this as a limitation of the model. We have no *a priori* reason, of course, to expect this to be true in shocked or unshocked TW containing scatterers.

Since our experiments are calibrated, we need worry only about the differences between calibration and experimental configurations, which include radiation sources, and the effects of the 1) shocked TW, 2) shock front, 3) unshocked TW and 4) TW free surface on the on the source radiation. In what

follows, the subscripts "INT," "SF," "USW" and "FS" will stand for the interface, shock front, unshocked TW and its free surface, respectively. For simplicity, we assume the target may be approximated optically as a set of parallel plane layers. In this representation, the temperature and material properties of the FL, shock and unshocked TW are assumed to vary at most only along the direction of shock propagation, \vec{x} ; *i.e.*, the layers are of infinite extent in \vec{y} and \vec{z} . Further, we assume that i'_λ is axisymmetric about \vec{s} ; in this case, i'_λ depends only on $s = |\vec{s}|$ and the angle between \vec{s} and \vec{x} , which we designate ϕ , so that $i'_\lambda = i'_\lambda(s, \phi)$. Introducing the extinction coefficient, $K_\lambda \equiv a_\lambda + \sigma_\lambda$, the differential opacity, $d\kappa_\lambda \equiv K_\lambda(s)ds$, and the albedo for scattering, $\Omega_{\lambda o} \equiv \sigma_\lambda / K_\lambda$, into [AIII.3], with $dr = dx / \cos\phi$, the radiation intensity in all directions forward ($' \rightarrow +$) in a plane layer is given by the solution of (*e.g.*, Siegel and Howell, 1981)

$$\begin{aligned} & \mu \partial_{\kappa_\lambda} i_\lambda^+(\kappa_\lambda, \mu) + i_\lambda^+(\kappa_\lambda, \mu) \\ & = (1 - \Omega_{\lambda o}) i'_{\lambda e}(\kappa_\lambda) + \frac{\Omega_{\lambda o}}{2} \int_0^1 [i_\lambda^+(\kappa_\lambda, \mu^*) + i_\lambda^-(\kappa_\lambda, -\mu^*)] d\mu^* \end{aligned} \quad [\text{E.1}],$$

and

$$\begin{aligned} & -\mu \partial_{\kappa_\lambda} i_\lambda^+(\kappa_\lambda, -\mu) + i_\lambda^+(\kappa_\lambda, -\mu) \\ & = (1 - \Omega_{\lambda o}) i'_{\lambda e}(\kappa_\lambda) + \frac{\Omega_{\lambda o}}{2} \int_0^1 [i_\lambda^+(\kappa_\lambda, \mu^*) + i_\lambda^-(\kappa_\lambda, -\mu^*)] d\mu^* \end{aligned} \quad [\text{E.2}].$$

In these relations, $\partial_{\kappa_\lambda} \equiv \partial / \partial \kappa_\lambda$, $\mu \equiv |\cos\phi|$,

$$\kappa_\lambda(x) \equiv \int_0^x K_\lambda(\xi) d\xi \quad [\text{E.3}]$$

is now a function of x , $\kappa_{\lambda d} \equiv \kappa_\lambda(d)$, and d is the layer thickness. Radiative transport in each layer of our target is then governed by [E.1] and [E.2]. Given

a target geometry like that of Figures 1 and 2, we assume that observed radiation will be dominated by radiation from the target of nearly normal incidence (*i.e.*, $\mu \equiv 1$). This is the fundamental simplifying assumption of the radiative transport model used in our work. Mathematically we express it in the form

$$i_{\lambda}^{\pm}(\kappa_{\lambda}, \pm\mu) = i_{\lambda}^{\pm}(\kappa_{\lambda}) \delta(1-\mu) \quad [\text{E.4}],$$

where $\delta(x)$ is Dirac's delta-function. In effect, this assumption imposes a very special averaging on the optical properties of the model, *i.e.*, that model properties are dominated by radiation incident perpendicular to the layering of the target. Putting [E.4] into [E.1] and [E.2], we obtain

$$\partial_{\kappa_{\lambda}} i_{\lambda}^{+}(\kappa_{\lambda}) + i_{\lambda}^{+}(\kappa_{\lambda}) = (1-\Omega_{\lambda o}) i'_{\lambda e}(\kappa_{\lambda}) + \frac{\Omega_{\lambda o}}{2} [i_{\lambda}^{+}(\kappa_{\lambda}) + i_{\lambda}^{-}(\kappa_{\lambda})] \quad [\text{E.5}],$$

$$-\partial_{\kappa_{\lambda}} i_{\lambda}^{-}(\kappa_{\lambda}) + i_{\lambda}^{-}(\kappa_{\lambda}) = (1-\Omega_{\lambda o}) i'_{\lambda e}(\kappa_{\lambda}) + \frac{\Omega_{\lambda o}}{2} [i_{\lambda}^{+}(\kappa_{\lambda}) + i_{\lambda}^{-}(\kappa_{\lambda})] \quad [\text{E.6}].$$

Now we define

$$I_{\lambda}^{\pm} \equiv i_{\lambda}^{+} \pm i_{\lambda}^{-}.$$

Substituting I_{λ}^{+} and I_{λ}^{-} into [E.5] and [E.6], adding and subtracting them, we obtain

$$\partial_{\kappa_{\lambda}} I_{\lambda}^{-} + I_{\lambda}^{+} = 2\beta_{\lambda}^2 i'_{\lambda e}(\kappa_{\lambda}) + \Omega_{\lambda o} I_{\lambda}^{+} \quad [\text{E.7}],$$

and

$$\partial_{\kappa_{\lambda}} I_{\lambda}^{+} + I_{\lambda}^{-} = 0 \quad [\text{E.8}]$$

with $\beta_{\lambda} \equiv \sqrt{(1-\Omega_{\lambda o})}$. Eliminating I_{λ}^{-} from these expressions, we obtain a differential equation for I_{λ}^{+} , *i.e.*,

$$\partial_{\kappa_{\lambda}}^2 I_{\lambda}^{+} - \beta_{\lambda}^2 I_{\lambda}^{+} = -2\beta_{\lambda}^2 i'_{\lambda e}(\kappa_{\lambda}) \quad [\text{E.9}].$$

For $\Omega_{\lambda o} \neq \{1, f(\kappa_{\lambda})\}$, which is the case if we assume that 1) $a_{\lambda} \neq 0$ and 2) a_{λ} and $\sigma_{\lambda} \neq f(\kappa_{\lambda})$ in each layer of our model, the general solution of [E.9] is given by

$$I_{\lambda}^{+}(\kappa_{\lambda}) = Ce^{\beta_{\lambda}\kappa_{\lambda}} + De^{-\beta_{\lambda}\kappa_{\lambda}} + \beta_{\lambda} \int_0^{\kappa_{\lambda}} \sinh[\beta_{\lambda}(\kappa_{\lambda}^{*} - \kappa_{\lambda})] i'_{\lambda e}(\kappa_{\lambda}^{*}) d\kappa_{\lambda}^{*} \quad [\text{E.10}].$$

Then from [E.8], we have

$$\begin{aligned} I_{\lambda}^{-}(\kappa_{\lambda}) &= -\partial_{\kappa_{\lambda}} I_{\lambda}^{+} \\ &= -\beta_{\lambda} Ce^{\beta_{\lambda}\kappa_{\lambda}} + \beta_{\lambda} De^{-\beta_{\lambda}\kappa_{\lambda}} + \beta_{\lambda}^2 \int_0^{\kappa_{\lambda}} \cosh[\beta_{\lambda}(\kappa_{\lambda}^{*} - \kappa_{\lambda})] i'_{\lambda e}(\kappa_{\lambda}^{*}) d\kappa_{\lambda}^{*} \end{aligned} \quad [\text{E.11}].$$

From [E.10], [E.11] and the definitions of I_{λ}^{\pm} , we then obtain

$$\begin{aligned} i_{\lambda}^{\pm}(\kappa_{\lambda}) &= \frac{1}{2} [I_{\lambda}^{+} \pm I_{\lambda}^{-}] \\ &= \frac{1}{2} (1 \mp \beta_{\lambda}) Ce^{\beta_{\lambda}\kappa_{\lambda}} + \frac{1}{2} (1 \pm \beta_{\lambda}) De^{-\beta_{\lambda}\kappa_{\lambda}} + i_{\lambda p}^{\pm}(\kappa_{\lambda}) \end{aligned} \quad [\text{E.12}],$$

with

$$i_{\lambda p}^{\pm}(\kappa_{\lambda}) = \frac{1}{2} \beta_{\lambda} \int_0^{\kappa_{\lambda}} [(1 \pm \beta_{\lambda}) e^{\beta_{\lambda}(\kappa_{\lambda}^{*} - \kappa_{\lambda})} - (1 \mp \beta_{\lambda}) e^{-\beta_{\lambda}(\kappa_{\lambda}^{*} - \kappa_{\lambda})}] i'_{\lambda e}(\kappa_{\lambda}^{*}) d\kappa_{\lambda}^{*}.$$

From [E.12], we have the following conditions at the boundaries of the layer for backward and forward propagating radiation:

$$\begin{aligned} i_{\lambda}^{-}(0) &= \frac{1}{2} (1 + \beta_{\lambda}) C + \frac{1}{2} (1 - \beta_{\lambda}) D, \\ i_{\lambda}^{-}(\kappa_{\lambda d}) &= \frac{1}{2} (1 + \beta_{\lambda}) Ce^{\beta_{\lambda}\kappa_{\lambda d}} + \frac{1}{2} (1 - \beta_{\lambda}) De^{-\beta_{\lambda}\kappa_{\lambda d}} + i_{\lambda p}^{-}(\kappa_{\lambda d}), \\ i_{\lambda}^{+}(0) &= \frac{1}{2} (1 - \beta_{\lambda}) C + \frac{1}{2} (1 + \beta_{\lambda}) D, \end{aligned}$$

and

$$i_{\lambda}^{+}(\kappa_{\lambda d}) = \frac{1}{2} (1 - \beta_{\lambda}) Ce^{\beta_{\lambda}\kappa_{\lambda d}} + \frac{1}{2} (1 + \beta_{\lambda}) De^{-\beta_{\lambda}\kappa_{\lambda d}} + i_{\lambda p}^{+}(\kappa_{\lambda d}).$$

We need only two of these to find C and D; for reasons apparent later, we

choose the second and third relations. Solving these for C and D, and substituting the resulting expressions for C and D into the first and fourth relations, we obtain

$$i_{\lambda}^{-}(0) = \frac{2(1-\beta_{\lambda}^2)\sinh[\beta_{\lambda}\kappa_{\lambda d}]i_{\lambda}^{+}(0) + 4\beta_{\lambda}[i_{\lambda}^{-}(\kappa_{\lambda d}) - i_{\lambda p}^{-}(\kappa_{\lambda d})]}{[(1+\beta_{\lambda})^2e^{\beta_{\lambda}\kappa_{\lambda d}} - (1-\beta_{\lambda})^2e^{-\beta_{\lambda}\kappa_{\lambda d}}]} \quad [\text{E.13}]$$

and

$$i_{\lambda}^{+}(\kappa_{\lambda d}) = \frac{4\beta_{\lambda}i_{\lambda}^{+}(0) + 2(1-\beta_{\lambda}^2)\sinh[\beta_{\lambda}\kappa_{\lambda d}][i_{\lambda}^{-}(\kappa_{\lambda d}) - i_{\lambda p}^{-}(\kappa_{\lambda d})]}{[(1+\beta_{\lambda})^2e^{\beta_{\lambda}\kappa_{\lambda d}} - (1-\beta_{\lambda})^2e^{-\beta_{\lambda}\kappa_{\lambda d}}]} + i_{\lambda p}^{+}(\kappa_{\lambda d}) \quad [\text{E.14}].$$

With $\beta_{\lambda}=\beta_{\lambda_{\text{SW}}}$ and $\kappa_{\lambda d}=\kappa_{\lambda_{\text{SF}}}$, these relations apply to the shocked TW; with $\beta_{\lambda}=\beta_{\lambda_{\text{USW}}}$, $\kappa_{\lambda d}=\kappa_{\lambda_{\text{FS}}}-\kappa_{\lambda_{\text{SF}}}$ and $i_{\lambda p}^{\pm}(\kappa_{\lambda d})=0$ (no sources), they apply to the unshocked TW.

Next, we assume that 1) the opacity of the FL is sufficiently large so that any radiation observed from it originates near the interface (the diffusion limit for radiative transport), and 2) all boundaries are optically smooth, so that radiation incident on these boundaries is refracted and reflected according Fresnel's laws (*e.g.*, Siegel and Howell, 1981). Basically, by doing this, we neglect any scattering properties these boundaries may have. Using [E.13]-[E.14], and assigning each boundary of our target an intrinsic normal spectral reflectivity, r_{λ} , given by (*e.g.*, Siegel and Howell, 1981)

$$r_{\lambda_{\text{AB}}} \equiv \frac{(n_{\lambda_{\text{A}}}-n_{\lambda_{\text{B}}})^2 + (\omega_{\lambda_{\text{A}}}-\omega_{\lambda_{\text{B}}})^2}{(n_{\lambda_{\text{A}}}+n_{\lambda_{\text{B}}})^2 + (\omega_{\lambda_{\text{A}}}+\omega_{\lambda_{\text{B}}})^2}$$

for normal incidence on the boundary between layers A and B possessing complex indices of refraction $n_{\lambda_{\text{A}}}+i\omega_{\lambda_{\text{A}}}$ and $n_{\lambda_{\text{B}}}+i\omega_{\lambda_{\text{B}}}$ (where $\omega_{\lambda}\propto\alpha_{\lambda}$), respectively, we may construct the boundary and layer conditions for the model. At the interface ($x=\kappa_{\lambda}=0$), radiation traveling forward into the shocked TW, $i_{\lambda_{\text{SW}}}^{+}(0)$,

is composed of radiation emerging at the shocked-TW-side of the interface from the FL and/or gas, $S_{\lambda_{INT}}^+(0)$, plus that component of the backward-traveling radiation ($i_{\lambda_{SW}}^-(0)$) reflected off the interface back into the forward direction, *i.e.*,

$$i_{\lambda_{SW}}^+(0) = S_{\lambda_{INT}}^+(0) + r_{\lambda_{INT}} i_{\lambda_{SW}}^-(0) \quad [E.15].$$

This is the boundary condition at the interface. From [E.13] and [E.14], we have conditions for forward and backward-traveling radiation in the shocked TW ($0 < x < x_{SF}$, $0 < \kappa_{\lambda} < \kappa_{\lambda_{SF}} = \kappa_{\lambda}(x_{SF})$):

$$i_{\lambda_{SW}}^-(0) = c_1 i_{\lambda_{SW}}^+(0) + c_2 i_{\lambda_{SW}}^-(\kappa_{\lambda_{SF}}) + S_{\lambda_{SW}}^-(\kappa_{\lambda_{SF}}) \quad [E.16]$$

$$i_{\lambda_{SW}}^+(\kappa_{\lambda_{SF}}) = c_2 i_{\lambda_{SW}}^+(0) + c_1 i_{\lambda_{SW}}^-(\kappa_{\lambda_{SF}}) + S_{\lambda_{SW}}^+(\kappa_{\lambda_{SF}}) \quad [E.17].$$

At the shock front ($x = x_{sf}$, $\kappa_{\lambda_{SF}} = \kappa_{\lambda}(x_{sf})$), we have radiation transmission in both directions and reflection from both of its sides, *i.e.*,

$$i_{\lambda_{SW}}^-(\kappa_{\lambda_{SF}}) = c_3 i_{\lambda_{USW}}^-(\kappa_{\lambda_{SF}}) + r_{\lambda_{SF}} i_{\lambda_{SW}}^+(\kappa_{\lambda_{SF}}) \quad [E.18]$$

$$i_{\lambda_{USW}}^+(\kappa_{\lambda_{SF}}) = c_4 i_{\lambda_{SW}}^+(\kappa_{\lambda_{SF}}) + r_{\lambda_{SF}} i_{\lambda_{USW}}^-(\kappa_{\lambda_{SF}}) \quad [E.19]$$

Again using [E.13] and [E.14], the conditions in the unshocked window ($x_{SF} < x < x_{FS}$, $\kappa_{\lambda_{SF}} < \kappa_{\lambda} < \kappa_{\lambda_{FS}} = \kappa_{\lambda}(x_{FS})$) are given by (with $i_{\lambda_{eSW}}^+(\kappa_{\lambda}) \equiv 0$: *i.e.*, no emission from the unshocked window)

$$i_{\lambda_{USW}}^-(\kappa_{\lambda_{SF}}) = c_5 i_{\lambda_{USW}}^+(\kappa_{\lambda_{SF}}) + c_6 i_{\lambda_{USW}}^-(\kappa_{\lambda_{FS}}) \quad [E.20]$$

$$i_{\lambda_{USW}}^+(\kappa_{\lambda_{FS}}) = c_6 i_{\lambda_{USW}}^+(\kappa_{\lambda_{SF}}) + c_5 i_{\lambda_{USW}}^-(\kappa_{\lambda_{FS}}) \quad [E.21].$$

Lastly, at the unshocked window free surface ($x = x_{fs}$, $\kappa_{\lambda_{FS}} = \kappa_{\lambda}(x_{fs})$), radiation traveling back into the unshocked window, $i_{\lambda_{USW}}^-(\kappa_{\lambda_{FS}})$, is equal to that component of the forward-traveling radiation incident at the free surface, $i_{\lambda_{USW}}^+(\kappa_{\lambda_{FS}})$, ($x = x_{fs}$, $\kappa_{\lambda_{FS}} = \kappa_{\lambda}(x_{fs})$) reflected into the window, *i.e.*,

$$i_{\lambda_{USW}}^-(\kappa_{\lambda_{FS}}) = r_{\lambda_{FS}} i_{\lambda_{USW}}^+(\kappa_{\lambda_{FS}}) \quad [E.22].$$

The coefficients and source terms in these relations are given by

$$c_1 \equiv \frac{2(1-\beta_{\lambda_{SW}}^2)\sinh[\beta_{\lambda_{SW}}\kappa_{\lambda_{SF}}]}{[(1+\beta_{\lambda_{SW}})^2 e^{\beta_{\lambda_{SW}}\kappa_{\lambda_{SF}}} - (1-\beta_{\lambda_{SW}})^2 e^{-\beta_{\lambda_{SW}}\kappa_{\lambda_{SF}}]} ,$$

$$c_2 \equiv \frac{4\beta_{\lambda_{SW}}}{[(1+\beta_{\lambda_{SW}})^2 e^{\beta_{\lambda_{SW}}\kappa_{\lambda_{SF}}} - (1-\beta_{\lambda_{SW}})^2 e^{-\beta_{\lambda_{SW}}\kappa_{\lambda_{SF}}]} ,$$

$$c_3 \equiv (1-r_{\lambda_{SF}}) \equiv c_4 ,$$

$$c_5 \equiv \frac{2(1-\beta_{\lambda_{USW}}^2)\sinh[\beta_{\lambda_{USW}}(\kappa_{\lambda_{FS}}-\kappa_{\lambda_{SF}})]}{[(1+\beta_{\lambda_{USW}})^2 e^{\beta_{\lambda_{USW}}(\kappa_{\lambda_{FS}}-\kappa_{\lambda_{SF}})} - (1-\beta_{\lambda_{USW}})^2 e^{-\beta_{\lambda_{USW}}(\kappa_{\lambda_{FS}}-\kappa_{\lambda_{SF}})}]} ,$$

$$c_6 \equiv \frac{4\beta_{\lambda_{USW}}}{[(1+\beta_{\lambda_{USW}})^2 e^{\beta_{\lambda_{USW}}(\kappa_{\lambda_{FS}}-\kappa_{\lambda_{SF}})} - (1-\beta_{\lambda_{USW}})^2 e^{-\beta_{\lambda_{USW}}(\kappa_{\lambda_{FS}}-\kappa_{\lambda_{SF}})}]} ,$$

$$S_{\lambda_{INT}}^+(0) \equiv (1-r_{\lambda_{INT}}) i_{\lambda_{INT}}^+(0) ,$$

$$S_{\lambda_{SW}}^-(\kappa_{\lambda_{SF}}) \equiv \frac{-4\beta_{\lambda_{SW}}}{[(1+\beta_{\lambda_{SW}})^2 e^{\beta_{\lambda_{SW}}\kappa_{\lambda_{SF}}} - (1-\beta_{\lambda_{SW}})^2 e^{-\beta_{\lambda_{SW}}\kappa_{\lambda_{SF}}]} i_{\lambda_{SWP}}^-(\kappa_{\lambda_{SF}}) ,$$

and

$$S_{\lambda_{SW}}^+(\kappa_{\lambda_{SF}}) \equiv i_{\lambda_{SWP}}^+(\kappa_{\lambda_{SF}}) - \frac{2(1-\beta_{\lambda_{SW}}^2)\sinh[\beta_{\lambda_{SW}}\kappa_{\lambda_{SF}}]}{[(1+\beta_{\lambda_{SW}})^2 e^{\beta_{\lambda_{SW}}\kappa_{\lambda_{SF}}} - (1-\beta_{\lambda_{SW}})^2 e^{-\beta_{\lambda_{SW}}\kappa_{\lambda_{SF}}]} i_{\lambda_{SWP}}^-(\kappa_{\lambda_{SF}}) .$$

Relations [E.15]-[E.22] constitute 8 equations in 8 unknowns. We are particularly interested in calculating $i_{\lambda_{USW}}^+(\kappa_{\lambda_{FS}})$, since the radiation escaping the target destined for detection is then given by

$$i_{\lambda_{obs}}(\kappa_{\lambda_{FS}}) = (1-r_{\lambda_{FS}}) i_{\lambda_{USW}}^+(\kappa_{\lambda_{FS}}) \quad [E.23].$$

The system [E.15]-[E.22] may be cast into the following matrix form

$$\begin{pmatrix} -\Gamma_{\lambda_{INT}} & 1 & 0 & 0 & 0 & 0 & 0 & 0 \\ 1 & -c_1 & -c_2 & 0 & 0 & 0 & 0 & 0 \\ 0 & -c_2 & -c_1 & 1 & 0 & 0 & 0 & 0 \\ 0 & 0 & 1 & -\Gamma_{\lambda_{SF}} & -c_4 & 0 & 0 & 0 \\ 0 & 0 & 0 & -c_3 & -\Gamma_{\lambda_{SF}} & 1 & 0 & 0 \\ 0 & 0 & 0 & 0 & 1 & -c_5 & -c_6 & 0 \\ 0 & 0 & 0 & 0 & 0 & -c_6 & -c_5 & 1 \\ 0 & 0 & 0 & 0 & 0 & 0 & 1 & -\Gamma_{\lambda_{FS}} \end{pmatrix} \begin{pmatrix} i_{\lambda_{SW}}^-(0) \\ i_{\lambda_{SW}}^+(0) \\ i_{\lambda_{SW}}^-(\kappa_{\lambda_{SF}}) \\ i_{\lambda_{SW}}^+(\kappa_{\lambda_{SF}}) \\ i_{\lambda_{USW}}^-(\kappa_{\lambda_{SF}}) \\ i_{\lambda_{USW}}^+(\kappa_{\lambda_{SF}}) \\ i_{\lambda_{USW}}^-(\kappa_{\lambda_{FS}}) \\ i_{\lambda_{USW}}^+(\kappa_{\lambda_{FS}}) \end{pmatrix} = \begin{pmatrix} S_{\lambda_{INT}}^+(0) \\ S_{\lambda_{SW}}^-(\kappa_{\lambda_{SF}}) \\ S_{\lambda_{SW}}^+(\kappa_{\lambda_{SF}}) \\ 0 \\ 0 \\ 0 \\ 0 \\ 0 \end{pmatrix} \quad [E.24].$$

In matrix notation, this is $[A]\{i\}=\{d\}$, where $[A]$ is a reflectivity-transmissivity matrix, $\{i\}$ is a vector of the forward and backward traveling radiation intensities at the boundaries, and $\{d\}$ is a radiation source vector. Decomposing $[A]$ into upper and lower bidiagonal matrices, $[A_L]$ and $[A_U]$, respectively, we find the solution of $[A_L]\{v\}=\{d\}$ and use this to solve $\{i\}=[A_U]^{-1}\{v\}$. Solving this system gives us an expression for $i_{\lambda_{USW}}^+(\kappa_{\lambda_{FS}})$, which we substitute into [E.22] to obtain

$$i_{\lambda_{obs}}(\kappa_{\lambda_{FS}}) = \Gamma_{\lambda} [S_{\lambda_{INT}}(0) + S_{\lambda_{SW}}(\kappa_{\lambda_{SF}})] \quad [E.25],$$

In this relation, we have

$$\begin{aligned} \Gamma_{\lambda} &\equiv \Xi_{\lambda}^{-1}[(1-\Gamma_{\lambda_{SF}})(1-\Gamma_{\lambda_{FS}})c_6], \\ \Xi_{\lambda} &\equiv [(1-\Gamma_{\lambda_{INT}}c_1)(1-c_1\Gamma_{\lambda_{SF}}) - \Gamma_{\lambda_{INT}}c_2^2\Gamma_{\lambda_{SF}}][(1-\Gamma_{\lambda_{SF}}c_5)(1-c_5\Gamma_{\lambda_{FS}}) - \Gamma_{\lambda_{SF}}c_6^2\Gamma_{\lambda_{FS}}] \\ &\quad - [(1-\Gamma_{\lambda_{INT}}c_1)c_1 + \Gamma_{\lambda_{INT}}c_2^2](1-\Gamma_{\lambda_{SF}})^2[(1-c_5\Gamma_{\lambda_{FS}})c_5 + c_6^2\Gamma_{\lambda_{FS}}] \end{aligned}$$

is the effective transmissivity of the shocked TW, shock front, unshocked TW and its free surface,

$$S_{\lambda_{SW}}(\kappa_{\lambda_{SF}}) \equiv \int_0^{\kappa_{\lambda_{SF}}} A_{\lambda}(\kappa_{\lambda_{SF}}, \xi) i'_{\lambda_{e_{SW}}}(\xi) d\xi$$

$$A_\lambda(\kappa_{\lambda_{\text{SF}}}, \xi) \equiv \frac{1}{2} \beta_{\lambda_{\text{SW}}} [(1 - r_{\lambda_{\text{INT}}} c_1)(1 + \beta_{\lambda_{\text{SW}}}) - [c_1 + (c_2^2 - c_1^2) r_{\lambda_{\text{INT}}}] (1 - \beta_{\lambda_{\text{SW}}})] e^{\beta_{\lambda_{\text{SW}}}(\xi - \kappa_{\lambda_{\text{SF}}})} \\ - \frac{1}{2} \beta_{\lambda_{\text{SW}}} [(1 - r_{\lambda_{\text{INT}}} c_1)(1 - \beta_{\lambda_{\text{SW}}}) - [c_1 + (c_2^2 - c_1^2) r_{\lambda_{\text{INT}}}] (1 + \beta_{\lambda_{\text{SW}}})] e^{-\beta_{\lambda_{\text{SW}}}(\xi - \kappa_{\lambda_{\text{SF}}})}$$

is the intensity of sources in the shocked TW along κ_λ , and

$$S_{\lambda_{\text{INT}}}(0) \equiv c_2(1 - r_{\lambda_{\text{INT}}}) i_{\lambda_{\text{INT}}}^+(0)$$

is the combined effective intensity of all interface sources. Relation [E.25] is the principal result of this appendix, and constitutes the simplest model incorporating scattering, absorption and multiple reflections that we can derive for radiative transport in the target. As it stands, [E.25] is sufficiently general for comparison with observations from a number of different radiation experiments. At this point, however, our main interest is in the interface experiments discussed in the text, so we now specialize [E.25] to this purpose.

For cases where there is apparently no scattering in the shocked TW, and none in the unshocked TW, we may set $\beta_{\lambda_{\text{SW}}} \equiv \beta_{\lambda_{\text{USW}}} \equiv 1$ in [E.25]; in this case, $c_1 \equiv c_5 \equiv 0$ and

$$c_2 = \tau_{\lambda_{\text{SW}}} \equiv e^{-\kappa_{\lambda_{\text{SF}}}} \quad , \quad c_6 = \tau_{\lambda_{\text{USW}}} \equiv e^{-(\kappa_{\lambda_{\text{FS}}} - \kappa_{\lambda_{\text{SF}}})} \quad \text{[E.26]}$$

$$\Xi_\lambda = (1 - r_{\lambda_{\text{FS}}} \tau_{\lambda_{\text{USW}}}^2 r_{\lambda_{\text{SF}}}) - \tau_{\lambda_{\text{SW}}}^2 [r_{\lambda_{\text{FS}}} (1 - 2r_{\lambda_{\text{SF}}}) c_6^2 + r_{\lambda_{\text{SF}}}] r_{\lambda_{\text{INT}}} \quad \text{[E.27]}$$

and

$$A_\lambda(\kappa_{\lambda_{\text{SF}}}, \xi) = \tau_{\lambda_{\text{SW}}} [e^\xi + r_{\lambda_{\text{INT}}} e^{-\xi}] \quad \text{[E.28].}$$

From [E.27], we note that, in general, neglect of multiple reflections when $\{r_\lambda, \tau_\lambda\} \rightarrow 1$ is clearly incorrect and can lead to underestimate of the source intensity by the model. However, for the experiments of interest here, we do have $r_\lambda \sim 0$. In this case,

$$\Xi_\lambda(\lambda, t) \gtrsim 1 - (r_{\lambda_{\text{FS}}} + r_{\lambda_{\text{INT}}}) r_{\lambda_{\text{SF}}} - r_{\lambda_{\text{FS}}} (1 - 2r_{\lambda_{\text{SF}}}) r_{\lambda_{\text{INT}}} = 1 - \mathcal{O}(r^2) \quad \text{[E.29]}$$

and multiple reflections are, to first order, negligible. Now if we assume each region of the dynamic target optical geometry possesses a distinct extinction coefficient, and that, in each layer of the target, optical properties are homogeneous, we have

$$K_{\lambda}(x) = \begin{cases} K_{\lambda_{SW}}(\lambda), & 0 < x < x_{SF}^{-}, \\ K_{\lambda_{SF}}(\lambda), & x_{SF}^{-} < x < x_{SF}^{+}, \\ K_{\lambda_{USW}}(\lambda), & x_{SF}^{+} < x < d, \end{cases} \quad [E.30]$$

where x_{SF}^{-} is the position of the shock-front in the SW, x_{SF}^{+} its position in the USW, and $x_{SF}^{+} - x_{SF}^{-}$ is the shock-front thickness. Putting this into [E.10], we have

$$\kappa_{\lambda_{SF}}(\lambda, x) = K_{\lambda_{SW}}(\lambda) x_{SF}^{-} \quad [E.31]$$

and

$$\kappa_{\lambda_{FS}}(\lambda, x) = K_{\lambda_{SW}}(\lambda) x_{SF}^{-} + K_{\lambda_{SF}}(\lambda) (x_{SF}^{+} - x_{SF}^{-}) + K_{\lambda_{USW}}(\lambda) (d - x_{SF}^{-}) \quad [E.32].$$

For steady shock-wave propagation (*i.e.*, constant U), x and t are not independent, and we may write

$$x_{SF}^{-}(t) = (u - v^{-})t \quad [E.33]$$

and

$$x_{SF}^{+}(t) = (u - v^{+})t \quad [E.34],$$

where u is the speed of displacement of the shock front, and v^{-} and v^{+} are the material velocities behind and in front of the shock front (see General Introduction). Putting these in, we have

$$\kappa_{\lambda_{FS}}(\lambda, t) = K_{\lambda_{SW}}(\lambda) (u - v^{-})t + K_{\lambda_{SF}}(\lambda) (v^{-} - v^{+})t + K_{\lambda_{USW}}(\lambda) [d - (u - v^{+})t] \quad [E.35].$$

Defining

$$K_{\lambda_{SW}}^{*}(\lambda) = K_{\lambda_{SW}}(\lambda) (u - v^{-}) t_{\text{exp}} \quad [E.36]$$

$$K_{\lambda_{SF}}^{*}(\lambda) = K_{\lambda_{SF}}(\lambda) (v^{-} - v^{+}) t_{\text{exp}} \quad [E.37]$$

and

$$K_{\lambda_{\text{USW}}}^*(\lambda) = K_{\lambda_{\text{USW}}}(\lambda) d \quad [\text{E.38}]$$

as nondimensional extinction coefficients, and setting $v^+ = 0$, we have

$$\kappa_{\lambda_{\text{FS}}}(\lambda, t) = K_{\lambda_{\text{SW}}}^*(\lambda) t/t_{\text{exp}} + K_{\lambda_{\text{SF}}}^*(\lambda) t/t_{\text{exp}} + K_{\lambda_{\text{USW}}}^*(\lambda) (1-t/t_{\text{exp}}) \quad [\text{E.39}].$$

If we treat the shock front as a 2-D boundary, rather than a thin layer, $K_{\lambda_{\text{SF}}} \rightarrow 0$.

In this case, we have

$$\kappa_{\lambda_{\text{SF}}}(\lambda, t) = K_{\lambda_{\text{SW}}}^*(\lambda) t/t_{\text{exp}} \quad [\text{E.40}]$$

and

$$\kappa_{\lambda_{\text{FS}}}(\lambda, t) = \kappa_{\lambda_{\text{SF}}}(\lambda, t) + K_{\lambda_{\text{SW}}}^*(\lambda) t/t_{\text{exp}} + K_{\lambda_{\text{USW}}}^*(\lambda) (1-t_{\text{exp}}) \quad [\text{E.41}].$$

[E.40] and [E.41] are the expression we use in [E.26] and the text. Lastly, if we assume that sources in the SW are distributed uniformly, $i'_{\lambda_{\text{eSW}}}(\xi)$ is independent of x , *i.e.*, spatially uniform, and from [E.22], this implies

$$\begin{aligned} S_{\lambda_{\text{SW}}}(\kappa_{\lambda_{\text{SF}}}) &= \int_0^{\kappa_{\lambda_{\text{SF}}}} A_{\lambda}(\kappa_{\lambda_{\text{SF}}}, \xi) i'_{\lambda_{\text{eSW}}}(\xi) d\xi \\ &= (1-\tau_{\lambda_{\text{SW}}})(1+r_{\lambda_{\text{INT}}}\tau_{\lambda_{\text{SW}}}) I_{\text{PI}}(\lambda, T_{\text{SW}}) \end{aligned} \quad [\text{E.42}],$$

assuming that $i'_{\lambda_{\text{eSW}}}$ is given by the Planck function. Putting these results into [E.25], we obtain, with $\Xi_{\lambda} \sim 1$

$$i_{\lambda_{\text{obs}}}(\lambda, t) = \Gamma_{\lambda} [S_{\lambda_{\text{INT}}}(0) + S_{\lambda_{\text{SW}}}(\kappa_{\lambda_{\text{SF}}})] \quad [\text{E.43}]$$

with

$$\Gamma_{\lambda} \equiv (1-r_{\lambda_{\text{FS}}})\tau_{\lambda_{\text{USW}}}(1-r_{\lambda_{\text{SF}}})$$

and

$$S_{\lambda_{\text{INT}}}(0) \equiv \tau_{\lambda_{\text{SW}}}(1-r_{\lambda_{\text{INT}}}) I_{\text{PI}}[\lambda, T_{\text{INT}}(t)],$$

which is the expression we use in the text. The Hugoniot temperature SW, T_{SW} , is homogeneous, uniform, and constant since we assume a uniform distribution of SW sources. The interface temperature, $T_{INT}(t)$, however, is a function of time, or constant, in the context of the conduction model discussed in Appendix D.

§14. References

- Ahrens, T. J., D. L. Anderson, and A. E. Ringwood, Equation of state and crystal structure of high-pressure phases of shocked silicates and oxides, *Rev. Geophys.*, **7**, 667-707, 1969.
- Al'tshuler, V. L., M. N. Pavlovskii, L. V. Kuleshova, and G. V. Simakov, Investigation of alkali-metal halides at high pressures and temperatures produced by shock compression, *Soviet Physics - Solid State*, **5**, 203-220, 1962.
- Anderson, O.L., E. Schreiber, R. C. Liebermann, and N. Soga, Some elastic constant data on minerals relevant to geophysics, *Rev. Geophys.*, **6**, 491-524, 1968.
- Anderson, O. L., Properties of iron at the earth's core conditions, *Geophys. J. R. Astr. Soc.*, **84**, 561-579, 1986.
- Andrews, D. J., Equation of state of the alpha and epsilon phases of iron, *J. Phys. Chem. Solids*, **34**, 825-840, 1973.
- Barker, L. M., and R. E. Hollenbach, Shock wave study of the $\alpha \rightleftharpoons \epsilon$ transition in iron, *J. Appl. Phys.*, **45**, 4872-4887, 1974.
- Bass, J. D., B. Svendsen, and T. J. Ahrens, The temperatures of shock-compressed iron, in *High Pressure Research in Geophysics and Geochemistry*, edited by M. Manghnani and Y. Syono, Terra Publishing Co., Tokyo, in press, 1987 (Chapter IV).
- Berman, R., *Thermal Conduction in Solids*, 193 pp., Oxford University Press,

- Oxford, 1976.
- Bethe, H., Theory of shock waves for an arbitrary equation of state, *Office of Scientific Research and Development Report No. 545*, Serial No. 237, 1942.
- Bevington, P. R., *Data Reduction and Error Analysis for the Physical Sciences*, 336 pp., McGraw-Hill, New York, 1969.
- Boehler, R., The phase diagram of iron to 430 kbar, *Geophys. Res. Lett.*, **13**, 1153-1156, 1986.
- Boehler, R., and J. Ramakrishnan, Experimental results on the pressure dependence of the Grüneisen parameter: A review, *J. Geophys. Res.*, **85**, 6996-7002, 1980.
- Boness, D. A., J. M. Brown, and A. K. McMahan, The electronic thermodynamics of iron under earth core conditions, *Phys. Earth Planet. Int.*, **42**, 227-240, 1986.
- Boslough, M. B., Shock-wave properties and high-pressure equations of state of geophysically important materials, *Ph.D. Dissertation*, 171 pp., California Institute of Technology, Pasadena, California, 1984.
- Boslough, M. B., A model for time dependence of shock-induced thermal radiation of light, *J. Appl. Phys.*, **56**, 3394-3399, 1985.
- Boslough, M. B., T. J. Ahrens, and A. C. Mitchell, Shock temperatures in CaO, *J. Geophys. Res.*, **89**, 7845-7851, 1984.
- Brannon, P. J., C. H. Conrad, R. W. Morris, E. D. Jones, and J. R. Asay, Studies of the spectral and spatial characteristics of shock-induced luminescence from x-cut quartz, *J. Appl. Phys.*, **54**, 6374-6381, 1984.
- Bridgman, P. W., The resistance of 72 elements, alloys and compounds to 100,000 kg/cm², *Proc. Am. Acad. Arts Sci.*, **81**, 167-251, 1952.
- Brown, J. M., and R. G. McQueen, The equation of state for iron and the earth's core, in *High Pressure Research in Geophysics*, 611-622, edited

- by S. Akimoto and M. H. Manghnani, Academic Press, New York, 1982.
- Brown, J. M., and R. G. McQueen, Phase transitions, Gruneisen parameter, and elasticity for shocked iron between 77 GPa and 400 GPa, *J. Geophys. Res.*, **91**, 7485-7494, 1986.
- Bukowinski, M. S. T., A theoretical equation of state for the inner core, *Phys. Earth Planet. Inter.*, **14**, 333-344, 1977.
- Burnstein, E., and P. L. Smith, Photoelastic properties of cubic crystals, *Phys. Rev.*, **74**, 229-230, 1948.
- Carslaw, H. S., and J. C. Jaeger, *Conduction of Heat in Solids*, 510 pp., Clarendon Press, Oxford, 1959.
- Davis, T. A., and K. Vedam, Photoelastic properties of sapphire, *J. Op. Soc. Am.*, **57**, 4555-4556, 1967.
- Desai, P. D., Thermodynamic properties of iron and silicon, *J. Phys. Chem. Ref. Data*, **15**, 967-983, 1986.
- Drotning, W. D., Thermal expansion of iron, cobalt, nickel and copper at temperatures up to 600 K above melting, *High Temp.-High Pressures*, **13**, 441-458, 1981.
- Fowles, R., and R. F. Williams, Plane stress propagation in solids, *J. Appl. Phys.*, **41**, 360-363, 1970.
- Gopal, E. S. R., *Specific heat at low temperatures*, 240 pp., Plenum Press, New York, 1966.
- Grady, D. E., Shock deformation of brittle solids, *J. Geophys. Res.*, **85**, 913-924, 1980.
- Grover, R., and P. A. Urtiew, Thermal relaxation at interfaces following shock compression, *J. Appl. Phys.*, **45**, 146-152, 1974.
- Jamieson, J. C., H. H. Demarest Jr., and D. Schiferl, A re-evaluation of the Gruneisen parameter for the earth's core, *J. Geophys. Res.*, **83**, 5929-5935, 1978.

- Jeanloz, R., and T. J. Ahrens, Anorthite: Thermal equation of state at high pressure, *Geophys. J. R. Astr. Soc.*, **62**, 529-549, 1980.
- Jephcoat, A. P., H. K. Mao, and P. M. Bell, Static compression of iron to 78 GPa with rare gas solids as pressure-transmitting media, *J. Geophys. Res.*, **91**, 4677-4684, 1986.
- Keeler, R. N., Electrical conductivity of condensed media at high pressures, in *Physics of High Energy Density, Proc. Intern. School of Physics "Enrico Fermi," Course XLVII*, 106-125, edited by P. Cadirola and H. Knoepfel, Academic Press, New York, 1971.
- Kondo, K. E., and T. J. Ahrens, Heterogeneous shock-induced thermal radiation in minerals, *Phys. Chem. Minerals*, **9**, 173-181, 1983.
- Kormer, S. B., Optical study of the characteristics of shock-compressed condensed dielectrics, *Sov. Phys. Uspekhi*, **11**, 229-254, 1968.
- Lyzenga, G. A., Shock temperatures of materials: experiments and applications to the high-pressure equation of state, *Ph.D. Dissertation*, 208 pp., California Institute of Technology, Pasadena, California, 1980.
- Lyzenga G. A., and T. J. Ahrens, Shock temperature measurements in Mg_2SiO_4 and SiO_2 at high pressures, *Geophys. Res. Lett.*, **7**, 141-145, 1980.
- Lyzenga, G. A., T. J. Ahrens and A. C. Mitchell, Shock temperatures of SiO_2 and their geophysical implications, *J. Geophys. Res.*, **88**, 2431-2444, 1983.
- Marsh, S. P., ed., Al_2O_3 , in *Shock Hugoniot Data*, 89, University of California at Los Angeles Press, Los Angeles, 1980.
- McQueen, R. G., S. P. Marsh, and J. N. Fritz, Hugoniot equation of state of twelve rocks, *J. Geophys. Res.*, **72**, 4999-5036, 1967.
- Pastine, D. J., and D. Piacesi, The existence and implications of curvature in the relation between shock and particle velocities for metals, *J. Phys. Chem. Solids*, **27**, 1783-1792, 1966.

- Press, W. H., B. P. Flannery, S. A. Teukolsky, and W. T. Vetterling, *Numerical Recipes: The Art of Scientific Computing*, 818 pp., Cambridge University Press, New York, 1986.
- Prieto, F. E., and C. Renero, Equation for the shock adiabat, *J. Appl. Phys.*, **41**, 3876-3883, 1970.
- Rice, M. H., R. G. McQueen, and J. M. Walsh, Compressibility of solids by strong shock waves, *Solid State Phys.*, **6**, 1-63, 1958.
- Robie, R. A., B. S. Hemingway, and J. R. Fisher, Thermodynamic properties of minerals and related substances at 298.15 K and 1 bar (10^5 Pascals) pressure and at higher temperatures, *USGS Bulletin No. 1452*, 456 pp., 1978.
- Roufousse, M. C., and P. G. Klemens, Lattice thermal conductivity of minerals at high temperature, *J. Geophys. Res.*, **79**, 703-705, 1974.
- Roufousse, M. C., and R. Jeanloz, Thermal conductivity of minerals at high pressures: the effect of phase transitions, *J. Geophys. Res.*, **88**, 7399-7408, 1983.
- Ruoff, A. L., Linear shock-velocity-particle-velocity relationship, *J. Appl. Phys.*, **38**, 4976-4980, 1967.
- Schmitt, D. R., B. Svendsen, and T. J. Ahrens, Shock-induced radiation from minerals, in *Shock Waves in Condensed Matter*, 261-265, edited by Y. M. Gupta, Plenum Press, New York, 1986.
- Siegel, R., and J. R. Howell, *Thermal Radiation Heat Transfer*, 862 pp., McGraw-Hill, New York, 1981.
- Somerville, M., and T. J. Ahrens, Shock compression of KFeS_2 and the question of Potassium in the Core, *J. Geophys. Res.*, **85**, 7016-7024, 1980.
- Stacey, F. D., B. J. Brennan, and R. D. Irvine, Finite strain theories and comparisons with seismological data, *Geophys. Surv.*, **4**, 189-232, 1981.
- Stevenson, D. J., Applications of liquid-state physics to the earth's core, *Phys.*

- Earth. Planet. Inter.*, **22**, 42-52, 1980.
- Svendsen, B., and T. J. Ahrens, Thermal history of shock-compressed solids, in *Shock Waves in Condensed Matter*, 607-611, edited by Y. M. Gupta, Plenum Press, New York, 1986.
- Svendsen, B., and T. J. Ahrens, Shock-induced temperatures of MgO, *Geophys. J. R. Astr. Soc.*, in press, 1987 (Chapter II).
- Svendsen, B., W. W. Anderson, T. J. Ahrens, and J. D. Bass, Ideal Fe-FeS, Fe-FeO phase relations and the earth's core, submitted to *Phys. Earth. Planet. Int.*, 1987 (Chapter V).
- Touloukian, Y. S., R. W. Powell, C. Y. Ho, and P. G. Klemens, *Thermophysical Properties of Matter, Volume 1: Thermal Conductivity*, Thermophysical Properties Research Center of Purdue University, Data Series, Plenum Publishing Corporation, New York, 1970.
- Touloukian, Y. S., R. H. Powell, C. Y. Ho, and P. G. Klemens, *Thermophysical Properties of Matter, Volume 12: Thermal expansion*, Thermophysical Properties Research Center of Purdue University, Data Series, Plenum Publishing Corporation, New York, 1975.
- Ullman, W., and V. L. Pan'kov, A new structure of the equation of state on its application in high-pressure physics and geophysics, *Verö Zentralist. Phys. Erde* No. 41, 1-201, 1976.
- Urtiew, P. A., Effect of shock loading on transparency of sapphire crystals, *J. Appl. Phys.*, **45**, 3490-3493, 1974.
- Urtiew, P. A., and R. Grover, Temperature deposition caused by shock interactions with material interfaces, *J. Appl. Phys.*, **45**, 140-145, 1974.
- Urtiew, P. A., and R. Grover, The melting temperature of magnesium under shock loading, *J. Appl. Phys.*, **48**, 1122-1126, 1977.
- Van Thiel, M., ed., *Compendium of Shock Wave Data*, Section A2: Inorganic Compounds, Report UCRL-50108, 50 pp., Lawrence Livermore

- Laboratory, Livermore, 1977.
- Wallace, D. C., *Thermodynamics of Crystals*, 484 pp., John Wiley and Sons, New York, 1972.
- Watt, J. P., and T. J. Ahrens, Shock wave equations of state using mixed-phase regime data, *J. Geophys. Res.*, 89, 7836-7844, 1984.
- Weast, R. C., ed., *CRC Handbook of Chemistry and Physics*, 60th edition, 2449 pp., CRC Press, Boca Raton, Florida, 1979.
- Williams, Q., and R. Jeanloz, Melting of Fe and FeS to 100 GPa, *EOS*, 67, 1240, 1986.
- Wise, J. L., and L. C. Chhabildas, Laser interferometer measurements of refractive index in shock-compressed materials, *Shock Waves in Condensed Matter*, 441-454, edited by Y. M. Gupta, Plenum Press, New York, 1986.
- Young, D. A., and R. Grover, Theory of the iron equation of state and melting curve to very high pressures, *Shock Waves in Condensed Matter-1983*, 65-67, edited by J. A. Asay, R. A. Graham and G. K. Straub, North-Holland, New York, 1984.

Chapter II

Shock-Induced Temperatures of MgO†

Bob Svendsen and Thomas J. Ahrens

Seismological Laboratory,
California Institute of Technology, Pasadena, California, 91125, USA.

† *Geophysical Journal, Royal Astronomical Society*, in press.

Abstract

Shock-compressed MgO radiates thermally at temperatures between 2900 and 3700 K in the 170-200 GPa pressure range. A simple energy-transport model of the shocked-MgO targets allows us to distinguish between different shock-induced radiation sources in these targets and estimate spectral absorption-coefficients, a_{MgO} , for shocked MgO (*e.g.*, at 203 GPa, $a_{\text{MgO}} \sim 6300, 7500, 4200$ and 3800 m^{-1} , at 450, 600, 750 and 900 nm, respectively). The experimentally inferred temperatures of the shock-compressed states of MgO are consistent with temperatures calculated for MgO assuming that 1) it deforms as an elastic fluid, 2) it has a Dulong-Petit value for specific heat at constant volume in its shocked state, 3) it undergoes no phase transformation below 200 GPa, and 4) the product of the equilibrium thermodynamic Gruneisen's parameter, γ , and the mass density, ρ , is constant and equal to 4729.6 kg/m^3 .

§1. Introduction

The mechanical response of materials to high pressure has traditionally been investigated by shock-wave or static-compression experiments that constrain, among other things, the pressure-density "equation-of-state" behavior of these materials. As first demonstrated by Soviet workers (summarized by Kormer, 1968), optical radiation from the shock-compressed state of certain transparent materials has the potential to constrain the temperature of their compressed state. The emission of radiation from shock-compressed transparent materials is rather remarkable from the point of view that these materials are, at least initially, dielectrics. Shock compression apparently transforms ionic materials (*e.g.*, NaCl) into semiconductors (Kormer *et al.*, 1966) with electrical conductivity up to 10^{10} -times that of the uncompressed material. Among initially-covalent materials, Ahrens (1966) inferred a $\sim 10^2$ increase in the electrical conductivity of MgO shock-compressed above 92 GPa, and Knittle and

Jeanloz (1986) inferred a similar increase in the electrical conductivity of FeO statically compressed above 70 GPa. For MgO, at least, this change in electrical conductivity at high pressure is thought likely due to extrinsic (*e.g.*, defect) processes, rather than to band-gap closure (*e.g.*, Liberman, 1978; Chang and Cohen, 1984), as discussed below.

Oxides accepted as predominant chemical end-members of the material constituting the earth's mantle include MgO, FeO, Al₂O₃, CaO and SiO₂. Of these, (Mg,Fe)O may be an actual constituent of the earth's mantle below 670 km (*e.g.*, Jeanloz & Thompson, 1983). Hence the complete (P, T, ρ) equation-of-state of MgO is relevant to studies of the earth's mantle. Among the mantle oxides, radiation emitted from SiO₂ (Lyzenga *et al.*, 1983) and CaO (Boslough *et al.*, 1984) shock-compressed above 60 and 140 GPa, respectively, has been studied using optical pyrometry (Kormer, 1968; Lyzenga, 1980). Optical radiation from MgO, Al₂O₃ and SiO₂, all shock-compressed to pressures below 75 GPa, has also been studied spectroscopically (Schmitt & Ahrens, 1984; Schmitt *et al.*, 1986). If the wavelength-dependence of this radiation is consistent with a grey-body source, it may be interpreted in terms of the temperature and effective emissivity of the shock-compressed material. In the pressure range investigated, shock-induced radiation from both initially amorphous SiO₂ (10 to 110 GPa) and initially crystalline (B1) CaO (140 to 180 GPa) is consistent with this type of source. Radiation from α -SiO₂, however, is clearly consistent with a grey-body source only above 60 GPa (Lyzenga *et al.*, 1983; Schmitt *et al.*, 1986). Note that shock-compressed SiO₂ transforms to stishovite above 16 GPa and melts above 70 GPa (Lyzenga *et al.*, 1983), while shock-compressed CaO transforms from a B1 to a B2 structure (Jeanloz *et al.*, 1980), and FeO to an unidentified phase (*e.g.*, Jeanloz & Ahrens, 1980a; Jackson & Ringwood, 1981), both above 70 GPa. Both MgO and Al₂O₃ apparently do not change phase during shock compression. Considering the sensitivity of optical radiation to

energy processes, as well as the complexity of interpretation introduced by dynamic phase transformations (*e.g.*, SiO₂: Lyzenga *et al.*, 1983), we studied the thermomechanical response of shock-compressed MgO as a material apparently uncomplicated by phase transitions, at least below 200 GPa. Since the experimental results we present below are consistent with a simple thermodynamic model of MgO, which includes the assumption of no phase transition, we conducted only 4 experiments.

§2. Experimental

We conducted the experiments on a two-stage, light-gas gun (*e.g.*, Jeanloz & Ahrens, 1980a; Figure 2.1). In these, a lexan-encased tantalum (Ta) flyer-plate, moving at 5.7 to 6.5 km/sec (Table 4.1), impacted a 1.5 mm-thick Ta driver-plate in contact with the (100) face of a 3 mm-thick synthetic single-crystal of magnesium oxide (MgO: similar to those used by Vassiliou & Ahrens, 1981). We covered the free surface of the MgO crystal with an aluminum mask to avoid observing radiation from the target's edge. Radiation from the target reflects off a mirror, propagates through an objective lens, and is directed by a (dichroic) pellicle beam splitter and two half-silvered beam splitters into 4 detectors filtered at nominal wavelengths of 450, 600, 750 and 900 nm. We recorded the signal from each detector on a Tektronix 485 single-sweep oscilloscope and a LeCroy (model 8081) 100-MHz transient recorder.

Wanting to observe radiation from MgO, we attempted to minimize the radiation intensity of the Ta-MgO interface by vapor-depositing 500-1000 nm of silver (Ag) on MgO, and then placing the Ag "film" in mechanical contact with the Ta driver-plate to form the target. Requiring a material that would not maintain a high temperature during the experiment, we chose Ag for its high thermal conductivity at standard temperature and pressure (STP: 298 K and

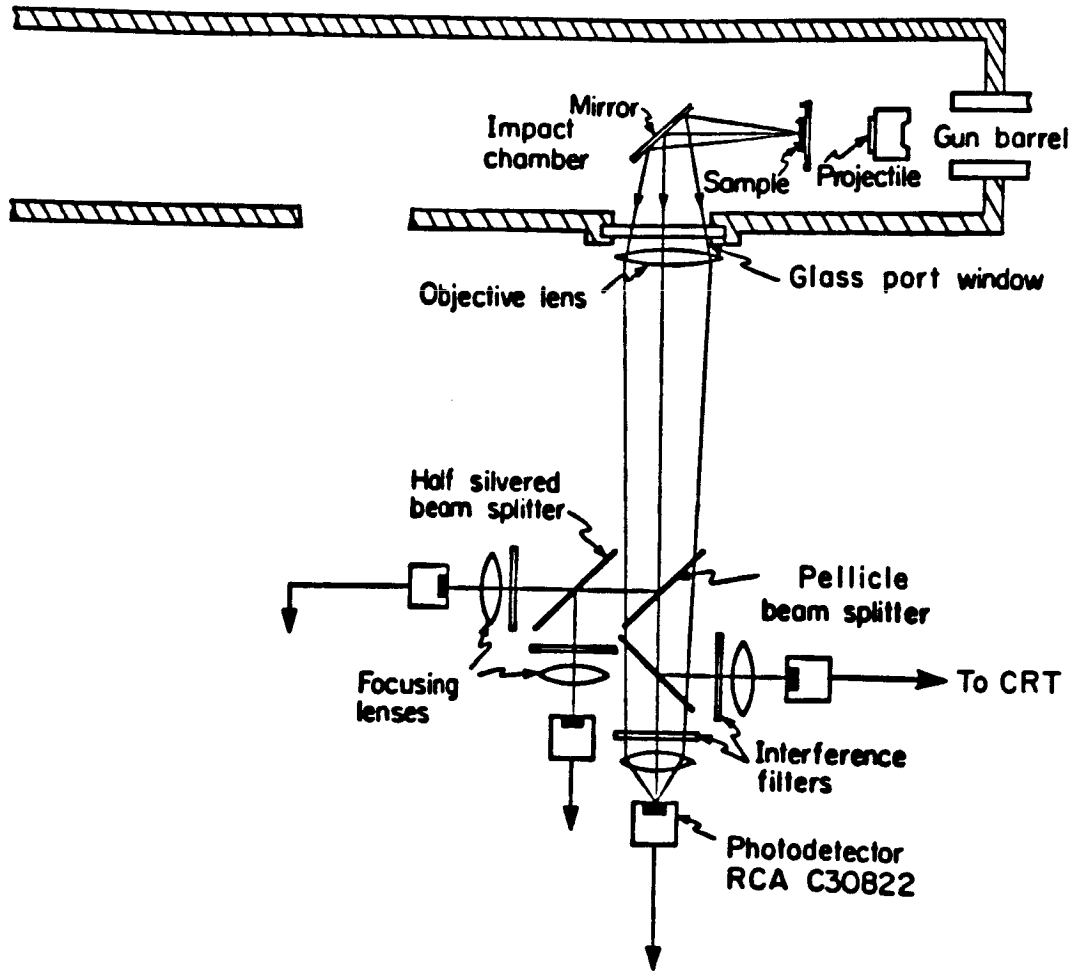


Figure 2.1. Geometry of the light-gas gun radiation experiment after Boslough (1984). The projectile, shot through the barrel, impacts the sample at velocities between 5.7 and 6.4 km/sec. Radiation from the sample is bent 90° by the mirror, travels through the objective lens, and is divided up by the three-beam-splitter arrangement among the 4 channels of the pyrometer. The resulting signals from the photodiode in each channel are monitored by oscilloscopes and LeCroy transient digital recorders.

0.1 MPa) and ease of deposition. We expected this Ag film to absorb any radiation from the Ta-Ag interface, heat up much less than a mechanical Ta-MgO interface (Urtiew & Grover, 1974), and contain no trapped gas that could also contribute to interface radiation (Boslough, 1985).

§3. Model Calculations and Data Analysis

Our experiment begins when the projectile, containing the Ta flyer plate, impacts the Ta driver plate. This process generates two shock waves at the flyer driver interface, one traveling forward into the driver plate and the other back into the projectile. When the shock wave propagating through the driver plate reaches the driver plate-film (Ta-Ag) interface, a lower-amplitude shock continues into the lower shock-impedance Ag-film, and a release wave is reflected into the driver plate. Once the interface is compressed, the balance of mass and momentum require that the component of the material velocity and stress fields, respectively, in the driver plate and film normal to the interface be continuous across it. Consequently, the compressed state of the driver plate releases to a state having nearly the magnitude of the normal stress and material velocity of the shocked-Ag film. An analogous process occurs at the Ag-MgO interface, releasing the shock-compressed Ag to a state with essentially the same normal material velocity and stress as the shock-compressed MgO. Since the film is so thin, the driver plate releases (a second time) shortly after this to a similar state. Wave reverberations quickly bring the driver plate and film to states with the normal stress and material velocity of the shocked-MgO. All of this occurs on a time scale less than 1 nanosecond (ns), and is not detectable by the pyrometer.

The basic data are in the form of radiation intensities at the four wavelengths mentioned above, and these are measured as a function of time. Clearly, the time-resolution of the data is much better than the wavelength-

resolution. We present an example of these data in Figure 3.1, an oscilloscope record at 750 nm for shot 146 (Table 4.1). Using the known radiation intensity of a standard lamp (Boslough, 1984) at the observed wavelengths, we transform these raw data into experimental spectral radiation intensities (in the form of spectral radiance) as a function of time. The result of this procedure for shot 146 data is displayed in Figure 3.2.

We interpret the temporal and wavelength variations of data in the context of the following model, a slight modification of Boslough's (1985) model (see also Boslough *et al.*, 1986; Chapter I, §6. and Appendix E). We assume that the shock-compressed/released Ag-film at the Ag-MgO interface, and shock-compressed MgO, are the only sources contributing to the observed radiation. Further, assume that the shocked-MgO layer radiates uniformly along the direction of shock propagation over the time scale of the observations. Then the total radiation intensity, $I_{\lambda\text{mod}}(\lambda, t)$, a function of wavelength (λ), and time after the onset of radiation from the target, t , is the sum of that fraction of each source intensity that emerges from the front of the target, *i.e.*,

$$I_{\lambda\text{mod}}(\lambda, t) \equiv \hat{\epsilon}_{\lambda\text{MgO}}(t) I_{\lambda\text{pl}}(\lambda, T_{\text{MgO}}) + \hat{\epsilon}_{\lambda\text{INT}}(t) I_{\lambda\text{pl}}[\lambda, T_{\text{INT}}(t)] \quad [3.1],$$

where the " λ " subscript indicates a spectral quantity. In [3.1], T_{MgO} is the shock-compressed (Hugoniot) temperature of MgO (assumed homogeneous, uniform and constant), and $T_{\text{INT}}(t)$ is the temperature of Ag at the Ag-MgO interface. Further,

$$\hat{\epsilon}_{\lambda\text{MgO}}(t) \equiv [1-r_{\lambda\text{FS}}] \tau_{\lambda\text{MgO},\text{O}}(t) [1-r_{\lambda\text{SF}}] [1+r_{\lambda\text{INT}} \tau_{\lambda\text{MgO}}(t)] [1-\tau_{\lambda\text{MgO}}(t)] \quad [3.2]$$

and

$$\hat{\epsilon}_{\lambda\text{INT}}(t) \equiv [1-r_{\lambda\text{FS}}] \tau_{\lambda\text{MgO},\text{O}}(t) [1-r_{\lambda\text{SF}}] \tau_{\lambda\text{MgO}}(t) [1-r_{\lambda\text{INT}}] \quad [3.3]$$

are the effective normal spectral emissivities of the shocked-MgO and Ag at the Ag-MgO interface, respectively, while $r_{\lambda\text{FS}}$, $r_{\lambda\text{SF}}$ and $r_{\lambda\text{INT}}$ are the effective normal

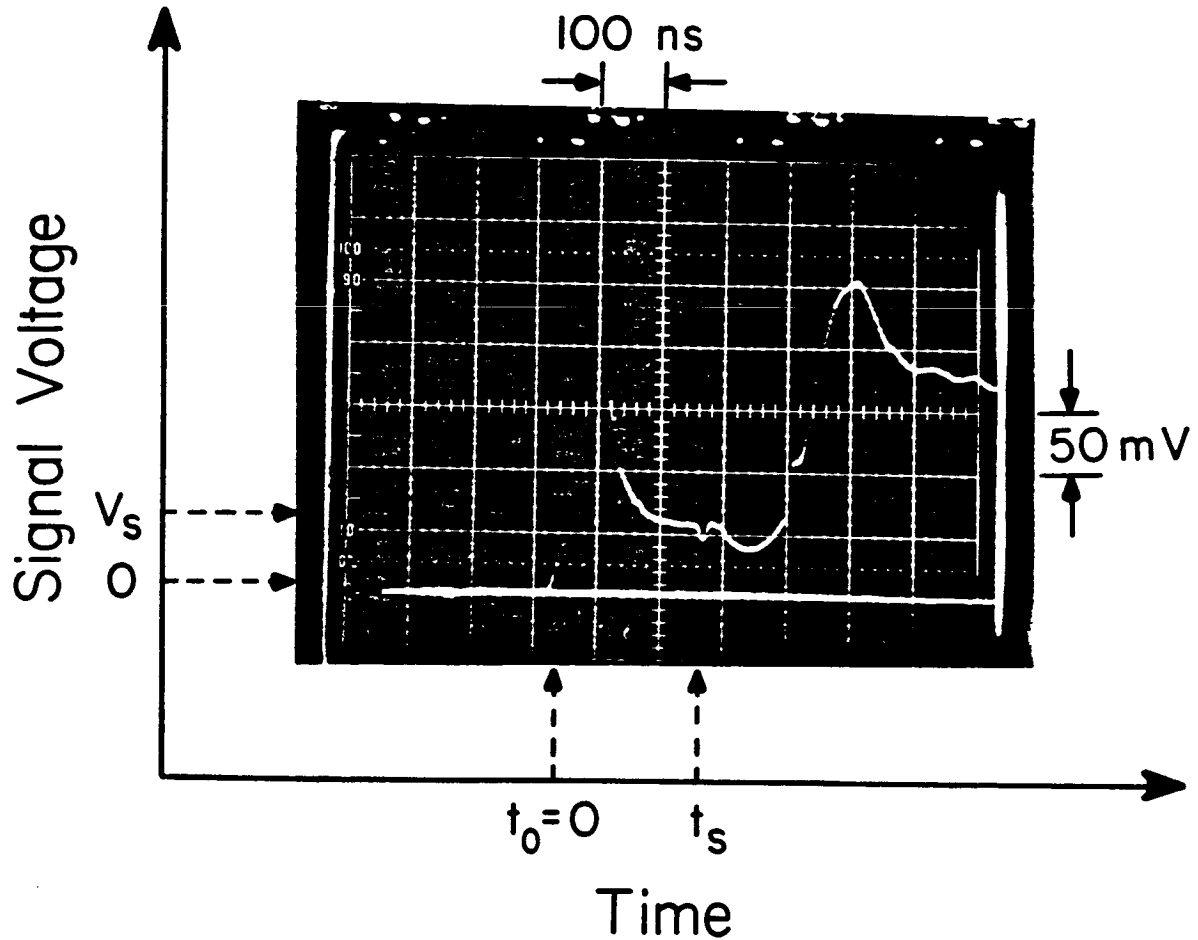
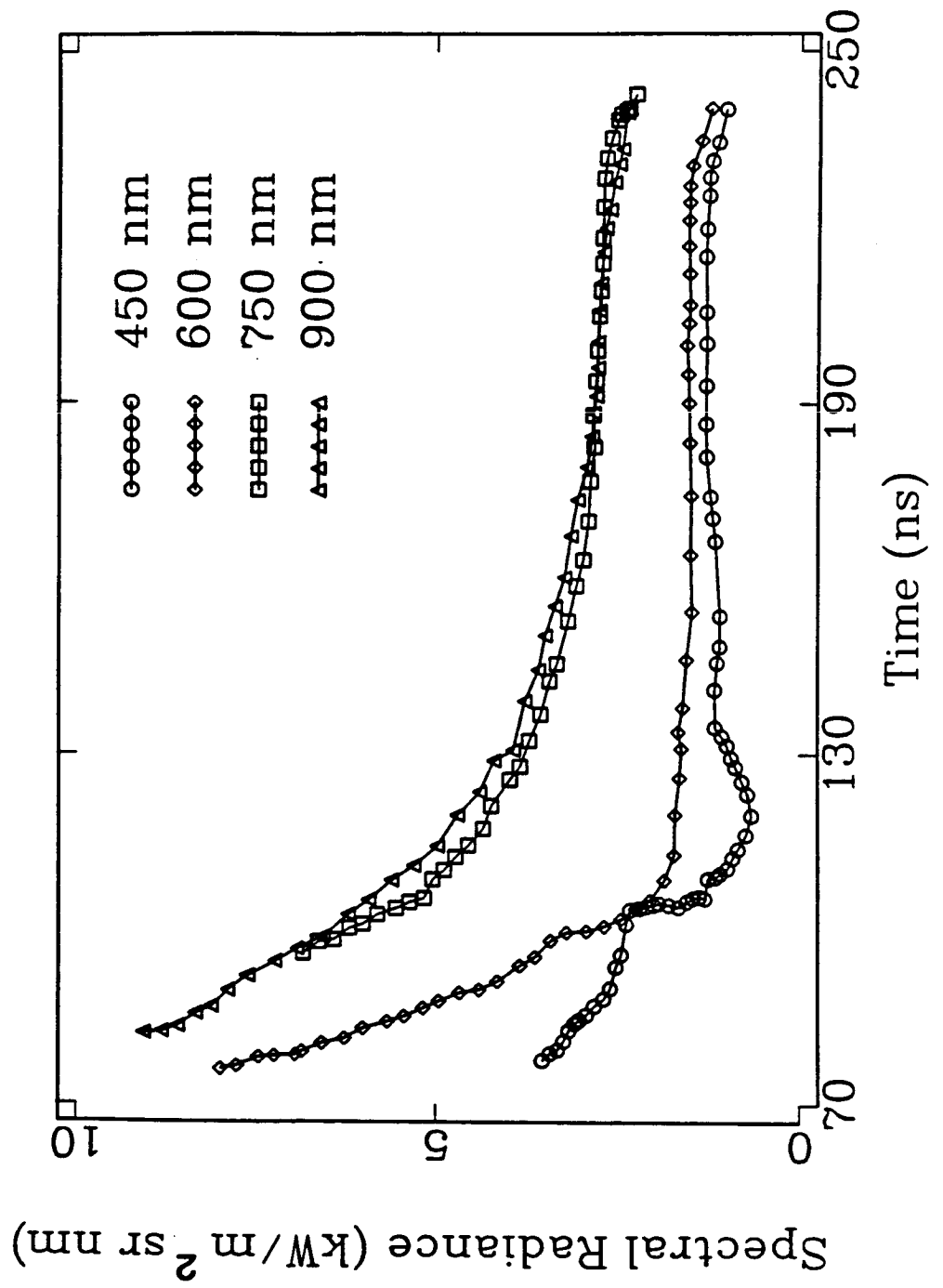


Figure 3.1. Oscilloscope record of radiation intensity history at 750 nm for shot 146. The radiation intensity rises sharply off-scale at $t=0$ as the shock wave compresses the Ag-MgO interface to high temperature (see Table 2). Decay of the interface temperature and/or absorption of interface radiation in the growing shocked-MgO layer (see text) causes the observed intensity to decrease sharply with time to about 170 ns into the experiment, at which point the radiation intensity becomes approximately time-independent. After about 240 ns (t_s), the shock wave reaches the free surface of the MgO, and the experiment is over.

Figure 3.2. Spectral radiance data for shot 146 at 450, 600, 750 and 900 nm.
Note that $t=0$ in this figure has the same meaning as in Figure 3.1.



spectral reflectivities of the MgO free-surface, shock front and Ag-MgO interface, respectively. Also,

$$\tau_{\lambda\text{MgO},0}(t) \equiv \exp[-a_{\lambda\text{MgO},0}^*(1-t/t_{\text{exp}})] \quad [3.4]$$

and

$$\tau_{\lambda\text{MgO}}(t) \equiv \exp[-a_{\lambda\text{MgO}}^* t/t_{\text{exp}}] \quad [3.5]$$

are the effective normal spectral transmissivities of unshocked and shocked-MgO layers, respectively. In [3.4] and [3.5], $a_{\lambda\text{MgO},0}^*$ and $a_{\lambda\text{MgO}}^*$ are nondimensional forms of the effective normal spectral coefficients of absorption in unshocked and shocked-MgO, respectively, given by

$$a_{\lambda\text{MgO}}^* \equiv a_{\lambda\text{MgO}} (U - v_{\text{MgO}}) t_{\text{exp}} \quad [3.6]$$

and

$$a_{\lambda\text{MgO},0}^* \equiv a_{\lambda\text{MgO},0} U t_{\text{exp}} \quad [3.7]$$

Note that $t_{\text{exp}} \equiv d/U$ is the experimental time scale, U is the shock wave velocity in MgO, d is the initial thickness of the MgO layer in the target, and v_{MgO} is the material velocity of the shock-compressed state of MgO. Lastly, we have

$$I_{\lambda\text{pl}}(\lambda, T) \equiv \frac{C_1}{\lambda^5 [e^{C_2/\lambda T} - 1]}$$

(with $C_1 \equiv 1.19088 \times 10^{-16} \text{W}\cdot\text{m}^2$ and $C_2 \equiv 1.4388 \times 10^{-2} \text{m}\cdot\text{K}$) as the Planck function.

Assuming the optical boundaries (*e.g.*, Ag-MgO interface) are smooth (*i.e.*, surface roughness much less than radiation wavelength), the effective normal spectral reflectivity of the boundary between any two of these layers is a function of the change in the (complex) index of refraction across the boundary (*e.g.*, Siegel & Howell, 1981; see below). The effective emissivities [3.2] and [3.3] are correct to first order in $r_{\lambda\text{FS}}$, $r_{\lambda\text{SF}}$ and $r_{\lambda\text{INT}}$; we assume second- and higher-order

reflections are negligible (Boslough, 1985; Chapter I, Appendix E). Because of this approximation, [3.2] and [3.3] are, strictly speaking, lower bounds to $\hat{\epsilon}_{\lambda\text{MgO}}(t)$ and $\hat{\epsilon}_{\lambda\text{NT}}(t)$, respectively. Boslough (1985) also implicitly assumes $r_{\lambda\text{NT}} = 0$ in [3.2]. Although the absorption coefficients and reflectivities are written without an explicit dependence on λ , they may be wavelength-dependent, as discussed below.

Of all parameters influencing $I_{\lambda\text{mod}}(\lambda, t)$, only $T_{\text{NT}}(t)$ is assumed to be potentially time-dependent. This clearly complicates the time-dependence of the observed radiation. In addition, through the Planck function, $T_{\text{NT}}(t)$ can influence the wavelength-dependence of $I_{\lambda\text{mod}}(\lambda, t)$ with time. A number of models for $T_{\text{NT}}(t)$ are considered by Grover & Urtiew (1974; see also Chapter I, §5. and Appendix D). For completeness, and as a basis for assumption, we outline one of these models, presumed appropriate to the MgO experiments discussed in this work. Assume that 1) energy transport is predominantly parallel to the direction of shock propagation (*i.e.*, one-dimensional), 2) conduction is the only energy transport process that substantially affects the temperature in any part of the target on the time scale of the experiment, and 3) shock compression/release processes in the target establish an initial ($t=0$) temperature profile in the Ta-Ag-MgO system of the form

$$T(x,0) \equiv \begin{cases} T_{\text{Ta}}, & -\infty < x < -\delta, \\ T_{\text{Ag}}, & -\delta < x < 0, \\ T_{\text{MgO}}, & 0 < x < \infty, \end{cases} \quad [3.8],$$

where δ is the film thickness. Note that we assume the driver plate (Ta) and MgO are thermal half-spaces. This last assumption presumes that shock compression/release is much faster than conduction in any part of the target. T_{Ta} and T_{Ag} are the temperatures of the partially released Ta and Ag, both at the pressure of the Ag-MgO interface (*i.e.*, pressure of the shock-compressed

MgO). In the context of this model, all material properties of each target component are constants, and referenced to their respective states at the pressure of the Ag-MgO interface.

The temperature of a singly shock-compressed material, T_H , may be estimated from a classical thermodynamic energy balance (*e.g.*, Ahrens *et al.*, 1969; Jeanloz & Ahrens, 1980b; see Chapter I, §4. and Appendix A) in which we assume the material compresses as an elastic fluid. It is possible that Ta (above ~ 295 GPa: Brown & Shaner, 1984) and/or Ag ($\lesssim 185$ GPa: Lyzenga, 1980) melts in the range of pressures and temperatures achieved in our experiments. The data of Carter *et al.* (1971), Vassiliou & Ahrens (1981; and our results below) show no clearly resolvable phase transition in MgO below 200 GPa. For simplicity, we assume that Ta and Ag do not change phase in our experiments. If this is wrong, the values of T_H we estimate for Ta and Ag are upper bounds to the true shock-compressed temperature (everything else being equal), since shock-induced phase transformations use energy otherwise available for heating the material. In the absence of phase changes, then, our estimate of T_H is given by

$$T_H = \left[T_s - \frac{1}{c_v} \Delta e_s \right] + \frac{1}{2c_v} \left\{ \frac{1}{\rho_i} - \frac{1}{\rho_H} \right\} P_H \quad [3.9]$$

assuming that c_v , the specific heat at constant volume of the shock-compressed state, is independent of temperature. The subscripts "i," "H," "S," and "V" designate initial (STP), shock-compressed, constant entropy and constant volume states of the material, respectively. In [3.9], Δe_s is the change in specific internal energy of the material compressed isentropically (at specific entropy s_i) from its density at STP, ρ_i , to a density ρ_H (that of the shock-compressed state), while T_s is the temperature of the material along the isentrope referenced to s_i and ρ_i . Also, P_H is the pressure of the shock-compressed state.

We estimate ρ_H from the balance of mass and momentum across 1) the shock front in each target material, and 2) the material boundaries between the target materials (impedance match: Rice *et al.*, 1958), by making the constitutive assumption that the component of the shock-wave velocity normal to the shock front, U , is a function of the change in the normal component of the material velocity, v , across the shock front. On the basis of the U - v data for Ta, Ag and MgO, we assume that U is a linear function of v (Table 3.1). The change in temperature along the compression isentrope, T_s , may be estimated from the classical thermodynamic Grüneisen's parameter, γ , via the relation

$$\gamma \equiv \left\{ \frac{\partial \ln T}{\partial \ln \rho} \right\}_s. \quad [3.10]$$

Since we assume $\gamma\rho$ is constant in all model calculations, this relation integrates to

$$T_s = T(s_i, \rho_H) \equiv T(s_i, \rho_i) \exp \left\{ \gamma(\rho_i) \left[1 - \frac{\rho_i}{\rho_H} \right] \right\}.$$

Relations [3.9] and [3.10] imply that T_H is dependent on γ only indirectly, through T_s . We estimate Δe_s from a third-order spatial finite-strain parameterization (*e.g.*, Davies, 1973). Consequently, $\Delta e_s = \Delta e_s(\rho_i/\rho_H, K_{s_i}, K'_{s_i})$, where K_{s_i} and K'_{s_i} are the (STP) isentropic bulk modulus and its first pressure derivative, respectively, of the material (Table 3.2).

As stated above, T_{Ta} and T_{Ag} are the temperatures of Ta and Ag at the pressure of shock-compressed MgO. We estimate the change in temperature due to release of Ta and Ag from their respective shock-compressed states, to their respective released states, by assuming that release occurs isentropically. This allows us to use [3.10], assuming no phase transitions occur during release. Also, we assume that each interface is smooth (Urtiew & Grover, 1974; see Chapter I) in the sense that the shock front is thicker than the interface "gap"

Table 3.1. Standard Temperature and Pressure (STP) Parameters.

Property	Symbol	Ta	Ag	MgO	Units
Density	ρ	16.676 ^a	10.501 ^a	3.583 ^a	Mg/m ³
Intercept of U-v relation‡	a	3.293 ^b (±0.049)†	3.27 ^c	6.61 ^d (±0.060)	km/sec
Slope of U-v relation	b	1.307 ^b (±0.025)	1.55 ^c	1.36 ^d (±0.020)	
Bulk modulus	K_s	180.8 ^e	109.6 ^e	162.7 ^f (±0.2)	GPa
$(\partial K_s/\partial P)_s$	K'_s	4.23 ^g	5.20 ^g	4.27 ^d (±0.24)	
Specific heat	c_p	140.2 ^a	235.5 ^a	937.4 ^a	J/kg·K
Thermal expansion	α	1.8 ^h	5.7 ^h	2.7 ^h	×10 ⁻⁵ K ⁻¹
Melting temperature	T_M	3287 ^a	1234 ^a	3125 ^a	K
Grüneisen's parameter	γ	1.4 ⁱ	2.5 ⁱ	1.3 ⁱ	
Thermal conductivity	k	57.5 ^j	427. ^j	60 ^j	W/m·K
Elastic Debye temperature	θ_D	263.8 ^k	226.4 ^k	942 ^l	K

† Uncertainties as quoted in source.

‡ *i.e.*, $U=a+bv$.

^a Robie *et al.* (1978).

^b Mitchell and Nellis (1981).

^c Marsh (1980).

^d Vassiliou and Ahrens (1981).

^e Calculated assuming $K_s \equiv \rho a^2$.

^f Jackson and Neisler (1982).

^g Calculated assuming $K'_s \equiv 4b-1$.

^h Touloukian *et al.* (1975).

ⁱ Calculated from $\gamma \equiv \alpha K_s / \rho c_p$.

^j Touloukian *et al.* (1970a).

^k Alers (1965).

^l Kieffer (1979).

(Urtiew and Grover, 1974) due to roughness of the surfaces forming the interface. This is consistent with the expectation that the Ag-MgO interface should be smooth, as discussed above. At this idealized interface, Ta releases directly to the pressure of shock-compressed Ag, and then both Ta and Ag release to the pressure of shock-compressed MgO.

To calculate the release temperature, we need the density of Ag and Ta in their respective release states. We estimate this using the variational method of Lyzenga & Ahrens (1978) to obtain a lower bound on the density of the chosen release state. This gives us, in turn, a lower bound on the temperature of that state through [3.10]. As with the calculations of T_H , we neglect the effects of phase transitions driven by release and/or recompression on the resulting interface temperature.

As boundary conditions, we assume that the temperature and energy flux are continuous across the Ta-Ag and Ag-MgO interfaces, and use [3.8] to solve for the Ag-MgO interface temperature, $T_{NT}(t)$, *i.e.*,

$$T_{NT}(t) = T_{Ag} + \frac{2\sigma_{Ta|Ag}(T_{Ta} - T_{Ag})}{(1+\sigma_{MgO|Ag})(1+\sigma_{Ta|Ag})} \phi(t) - \frac{\sigma_{MgO|Ag}(T_{Ag} - T_{MgO})}{(1+\sigma_{MgO|Ag})} \psi(t) \quad [3.11].$$

In [3.11], we have

$$\phi(t) \equiv \sum_{m=0}^{\infty} (\nu_{MgO|Ag} \nu_{Ta|Ag})^m \operatorname{erfc}[(m + \frac{1}{2})\xi\sqrt{t_{exp}/t}]$$

and

$$\psi(t) \equiv 1 - \nu_{Ta|Ag} \operatorname{erfc}[\xi\sqrt{t_{exp}/t}] + \sum_{m=1}^{\infty} (\nu_{MgO|Ag} \nu_{Ta|Ag})^m \theta_m(t)$$

with

$$\theta_m(t) \equiv \operatorname{erfc}[m\xi\sqrt{t_{exp}/t}] - \nu_{Ta|Ag} \operatorname{erfc}[(m+1)\xi\sqrt{t_{exp}/t}] .$$

Also in [3.11], $\xi \equiv \delta/\sqrt{\kappa_{Ag}t_{exp}}$, while

$$\sigma_{\text{Ta|Ag}} \equiv \left\{ \frac{k_{\text{Ta}} \rho_{\text{Ta}} c_{p,\text{Ta}}}{k_{\text{Ag}} \rho_{\text{Ag}} c_{p,\text{Ag}}} \right\}^{1/2} \quad [3.12]$$

and

$$\sigma_{\text{MgO|Ag}} \equiv \left\{ \frac{k_{\text{MgO}} \rho_{\text{MgO}} c_{p,\text{MgO}}}{k_{\text{Ag}} \rho_{\text{Ag}} c_{p,\text{Ag}}} \right\}^{1/2} \quad [3.13]$$

are the thermal-inertia "mismatches" (Carslaw & Jaeger, 1959, p. 321) between Ta and Ag, and between MgO and Ag, respectively, at the pressure of the Ag-MgO interface. The parameters $\nu_{\text{MgO|Ag}}$ and $\nu_{\text{Ta|Ag}}$ represent combinations of $\sigma_{\text{MgO|Ag}}$ and $\sigma_{\text{Ta|Ag}}$, respectively, *i.e.*,

$$\nu_{\text{MgO|Ag}} \equiv \frac{(\sigma_{\text{MgO|Ag}} - 1)}{(\sigma_{\text{MgO|Ag}} + 1)}$$

and

$$\nu_{\text{Ta|Ag}} \equiv \frac{(\sigma_{\text{Ta|Ag}} - 1)}{(\sigma_{\text{Ta|Ag}} + 1)}.$$

In [3.12] and [3.13], k , ρ and c_p are the thermal conductivity, density and specific heat at constant pressure, respectively, of the designated material and appropriate state of each material at the pressure of shock-compressed MgO. To estimate the values of $\sigma_{\text{Ta|Ag}}$ and $\sigma_{\text{MgO|Ag}}$ at high pressure, we need the appropriate values of k , ρ and c_p . The densities result from the impedance match and/or isentropic release calculations, while the high-pressure specific heats at constant pressure come from the relation

$$c_p = 3nR(1 + \alpha\gamma T)/M, \quad [3.14]$$

where n is the number of components in the formula unit, M is the molecular weight, R is the gas constant, and α is the thermal expansion (assumed independent of pressure and temperature). Note that we assume the high-temperature limit for c_v ($3nR/M$). In the context of the Debye model, this presumes that all target components are well above their Debye temperatures

(STP values are given in Table 3.3). In addition, this assumes that the electronic contributions to c_v are small relative to $3nR/M$. Since the lowest-order electronic contribution to c_v scales with temperature, c_v would be larger than assumed here if these contributions are significant. If this is true, our estimates of both c_v and c_p will be too low, while the temperatures will be too high, at a given pressure.

Assuming that k_{Ta} and k_{Ag} are dominated by their electronic contributions, we assume the relevance of the Wiedemann-Franz-Lorenz (WFL) relation

$$\frac{\rho_e k}{T} = 2.45 \times 10^{-8} \text{ W}\cdot\Omega/\text{K}^2 \quad [3.15]$$

(*e.g.*, Berman, 1976), where ρ_e is the electrical resistivity, to estimate k_{Ta} and k_{Ag} from electrical resistance data on shocked-Ta and Ag, respectively. To our knowledge, shock data exist for Ag (Dick & Styris, 1975) up to 12 GPa, but not for Ta. Bridgman (1952) investigated the change in electrical resistance of many statically compressed materials, including Ta and Ag, but again only at low pressure ($\lesssim 10$ GPa). Keeler (1971) investigated the change in the electrical resistance of shock-compressed copper and iron up to 140 GPa. He found that the resistivity of shock-compressed Cu decreased from ≈ 1.67 to $0.56 \mu\Omega\cdot\text{cm}$ with pressure up to ≈ 100 GPa; a datum at 140 GPa implies that the resistivity of Cu reaches a minimum between 100 and 140 GPa and then increases to $\approx 0.83 \mu\Omega\cdot\text{cm}$ at 140 GPa. As for Fe, the data imply that its electrical resistivity decreases from ≈ 2.5 to $0.47 \mu\Omega\cdot\text{cm}$ between 13 and 140 GPa (above the $\alpha \rightarrow \epsilon$ transition). In light of [15], these trends imply that the thermal conductivities of shock-compressed Cu and Fe increase with shock pressure. On the basis of the behavior of Cu, we naively assume that the electrical conductivity of Ta and Ag generally increases with shock pressure. Then, from [15], we see that a calculation of k_{Ta} and k_{Ag} using the STP electrical resistivities ($\rho_{e,Ta} = 12.45 \mu\Omega\cdot\text{cm}$ and $\rho_{e,Ag} = 1.59 \mu\Omega\cdot\text{cm}$: Weast, 1979), along with the

appropriate release-state temperatures of Ta and Ag, respectively, will give us a lower bound on these thermal conductivities. As for k_{MgO} , we assume it is dominated by its lattice component at high pressure, and use the lattice thermal-conductivity model of Roufosse & Klemens (1974) to estimate it. This assumption is supported by band-gap calculations for MgO (*e.g.*, Liberman, 1978), and, in view of [3.15], by the results of Ahrens (1966), which suggest that the electrical resistivity of MgO is $\sim 10^9 \mu\Omega\cdot\text{cm}$ above 92 ± 7 GPa.

Having established the means, we calculate selected model parameters at high pressure from the STP parameters given in Table 3.1 and list the results for each experiment in Table 3.2. From the impedance match and partial-release calculations, we obtain the density of Ta, Ag and MgO at the pressure of shock-compressed MgO, and from these, through [3.8] and [3.9], we obtain T_{Ta} , T_{Ag} and T_{MgO} for each experiment. Using these with [3.14], [3.15] and the model of Roufosse & Klemens (1974), we estimate $\sigma_{\text{MgO|Ag}}$ and $\sigma_{\text{Ta|Ag}}$ for each experiment and compare them with their STP values in Table 3.3. Also, we have calculated $\sigma_{\text{MgO|Ag}}$ and $\sigma_{\text{Ta|Ag}}$ as a function of Ag-MgO interface conditions (pressure) and displayed them in Figure 3.3. Again, the values of k for each materials, especially the metals, are probably the most uncertain aspect of these estimates. On this basis, we see that $\sigma_{\text{Ta|Ag}}$ is approximately independent of pressure and temperature. However, $\sigma_{\text{MgO|Ag}}$ decreases steadily from approximately 0.44 at STP to 0.03 at 200 GPa, mainly because of the large increase in k_{Ag} (Tables 3.1 and 3.2).

From [3.11], the initial value of $T_{\text{INT}}(t)$ is given by

$$T_{\text{INT}}(0) = T_{\text{Ag}} - \frac{\sigma_{\text{MgO|Ag}}(T_{\text{Ag}} - T_{\text{MgO}})}{(1 + \sigma_{\text{MgO|Ag}})} \quad [3.16]$$

This is also the value of $T_{\text{INT}}(t)$ with $\xi = \infty$. For $t = \infty$ or $\xi = 0$, $T_{\text{INT}}(t)$ is given by

Table 3.2. Model Parameter Estimates for MgO Experiments.

Shot	Material	Shock-compressed state			Ag-MgO interface state			
		P (GPa)	T (K)	ρ (Mg/m ³)	T (K)	ρ (Mg/m ³)	k (W/m·K)	c_p (J/kg·K)
166	Ta	336.6	14430	28.130	11860	22.750	2336.	165
	Ag	277.7	13560	17.190	11400	15.440	17600.	487
	MgO	174.0	2913	5.345	2913	5.345	32.6	1324
147	Ta	349.1	15320	28.350	12600	22.90	2477.	167
	Ag	288.2	14330	17.290	12060	15.53	18570.	500
	MgO	181.1	3032	5.426	3028	5.43	32.1	1326
145	Ta	364.3	16420	28.600	13470	23.010	2651.	169
	Ag	300.9	15270	17.410	12810	15.590	19760.	516
	MgO	187.9	3257	5.442	3257	5.442	31.5	1332
146	Ta	395.0	18730	29.130	15320	23.280	3014.	173
	Ag	326.7	17240	17.640	14420	15.750	22230.	548
	MgO	203.1	3667	5.536	3667	5.536	30.5	1342

Figure 3.3. Estimates of $\sigma_{\text{Ta|Ag}}$ and $\sigma_{\text{MgO|Ag}}$ as a function of the Ag-MgO interface pressure. The decrease of $\sigma_{\text{MgO|Ag}}$ with pressure is due to the temperature-dependence of the the Wiedemann-Franz-Lorenz thermal-conductivity parameterization for Ta and Ag given in the text, causing k_{Ta} and k_{Ag} to increase with pressure. These curves are lower bounds to $\sigma_{\text{Ta|Ag}}$ and $\sigma_{\text{MgO|Ag}}$ if k_{Ta} and k_{Ag} become independent of temperature at high pressure (see text).

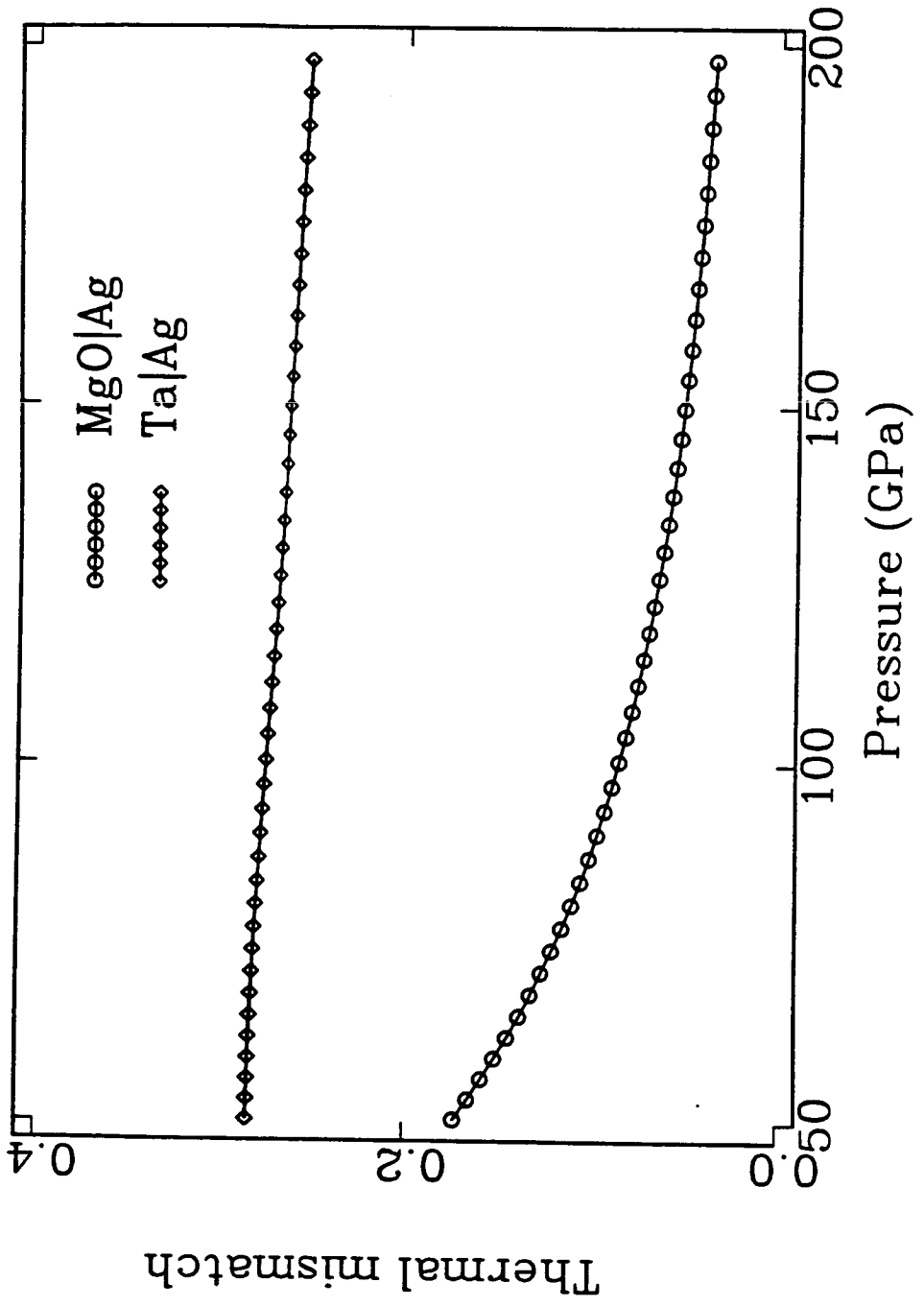


Table 3.3. Thermal-Inertia Mismatch Estimates at STP and High Pressure.

Conditions	$\sigma_{\text{Ta Ag}}$	$\sigma_{\text{MgO Ag}}$
STP	0.36	0.44
Shot 166	0.26	0.04
Shot 147	0.26	0.04
Shot 145	0.25	0.04
Shot 146	0.25	0.03

$$T_{\text{INT}}(\infty) = T_{\text{Ag}} + \frac{2 [\sigma_{\text{Ta|Ag}}(T_{\text{Ta}} - T_{\text{Ag}}) - \sigma_{\text{MgO|Ag}}(T_{\text{Ag}} - T_{\text{MgO}})]}{(1 + \sigma_{\text{Ta|Ag}})(1 + \sigma_{\text{MgO|Ag}})} \sum_{m=0}^{\infty} (\nu_{\text{Ta|Ag}} \nu_{\text{MgO|Ag}})^m \quad [3.17]$$

For shot 146 conditions, $T_{\text{INT}}(0)=14070$ K and $T_{\text{INT}}(\infty)=13910$ K. Note that $T_{\text{INT}}(t)$ is bounded below by $T_{\text{INT}}(\infty)$ in this case. The time-dependence of $T_{\text{INT}}(t)$, embodied in $\phi(t)$ and $\psi(t)$, can more easily be seen in the following approximations to $T_{\text{INT}}(t)$. For $\xi \rightarrow 0$, $\phi(t)$ and $\theta_m(t)$ are given by

$$\phi(t) \sim \sum_{m=0}^{\infty} (\nu_{\text{Ta|Ag}} \nu_{\text{MgO|Ag}})^m \left\{ 1 - (2m+1)\xi \left(\frac{t_{\text{exp}}}{\pi t} \right)^{1/2} e^{-(m+1/2)^2 \xi^2 t_{\text{exp}}/t} \right\}$$

and [3.18]

$$\psi(t) \sim (1 - \nu_{\text{Ta|Ag}}) + 2\nu_{\text{Ta|Ag}} \xi \left(\frac{t_{\text{exp}}}{\pi t} \right)^{1/2} + \sum_{m=1}^{\infty} (\nu_{\text{MgO|Ag}} \nu_{\text{Ta|Ag}})^m \theta_m(t)$$

with

$$\theta_m(t) \sim (1 - \nu_{\text{Ta|Ag}}) - 2\nu_{\text{Ta|Ag}} \xi \left(\frac{t_{\text{exp}}}{\pi t} \right)^{1/2} \left\{ m e^{-m^2 \xi^2 t_{\text{exp}}/t} - \nu_{\text{Ta|Ag}} (m+1) e^{-(m+1)^2 \xi^2 t_{\text{exp}}/t} \right\}$$

And for $\xi \rightarrow \infty$, we have

$$\phi(t) \sim \frac{1}{\xi} \left(\frac{t}{\pi t_{\text{exp}}} \right)^{1/2} \sum_{m=0}^{\infty} (\nu_{\text{Ta|Ag}} \nu_{\text{MgO|Ag}})^m \frac{1}{(m + 1/2)} e^{-(m+1/2)^2 \xi^2 t_{\text{exp}}/t}$$

and [3.19]

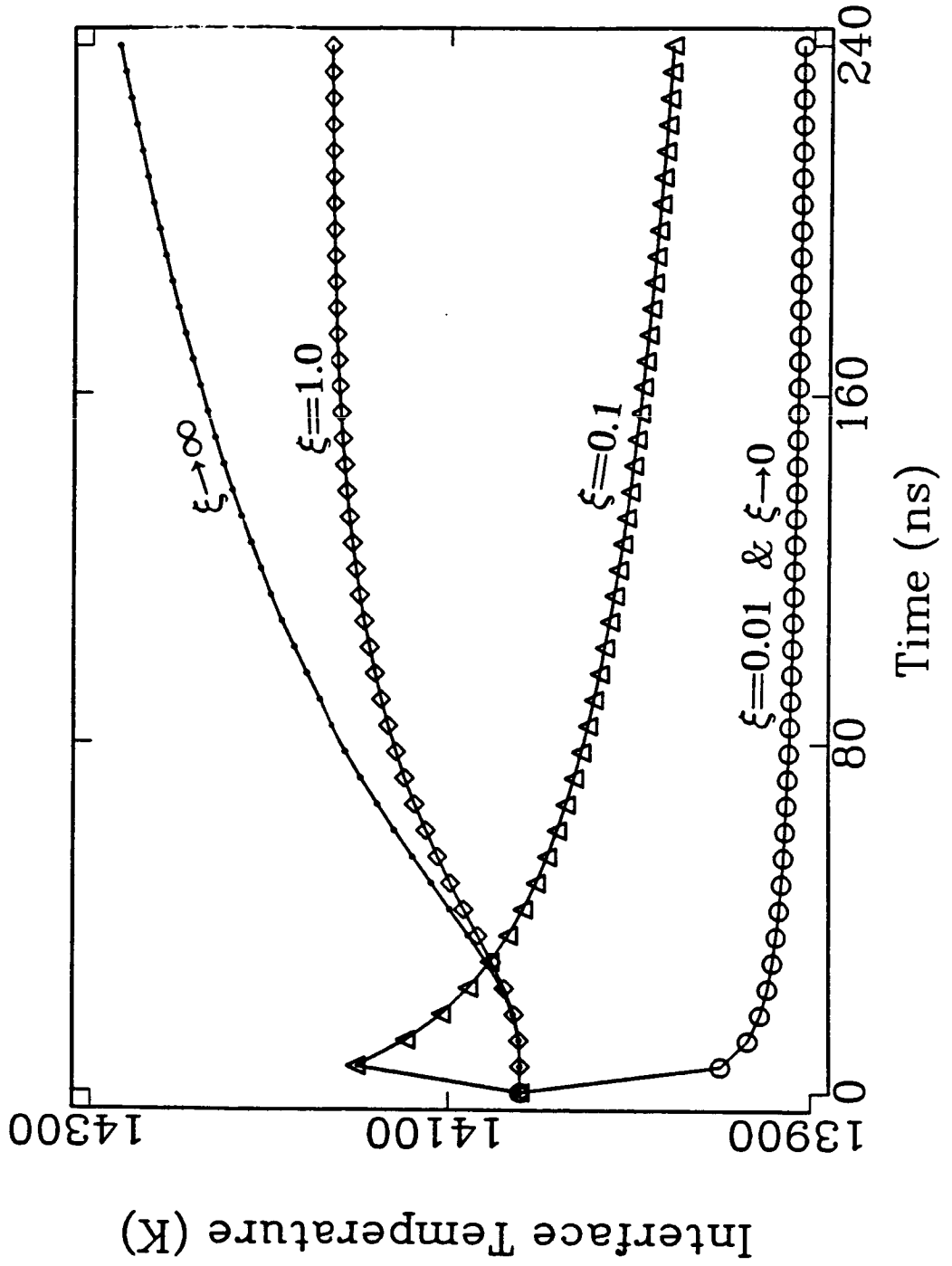
$$\psi(t) \sim 1 - \frac{\nu_{\text{Ta|Ag}}}{\xi} \left(\frac{t}{\pi t_{\text{exp}}} \right)^{1/2} e^{-\xi^2 t_{\text{exp}}/t} + \sum_{m=1}^{\infty} (\nu_{\text{MgO|Ag}} \nu_{\text{Ta|Ag}})^m \theta_m(t)$$

with

$$\theta_m(t) \sim \frac{1}{\xi} \left(\frac{t}{\pi t_{\text{exp}}} \right)^{1/2} \left\{ \frac{1}{m} e^{-m^2 \xi^2 t_{\text{exp}}/t} - \frac{\nu_{\text{Ta|Ag}}}{(m+1)} e^{-(m+1)^2 \xi^2 t_{\text{exp}}/t} \right\}.$$

From the parameters in Table 3.2, we have $\sqrt{\kappa_{\text{Ag}} t_{\text{exp}}} \sim 10^{-5}$ m for shot 146

Figure 3.4. Model Ag-MgO interface temperature, $T_{\text{INT}}(t)$, as a function of time for different nondimensional Ag-film thicknesses, $\xi = \delta / \sqrt{\kappa_{\text{Ag}} t_{\text{exp}}}$, where δ is the Ag-film thickness and κ_{Ag} its thermal conductivity at the Ag-MgO interface pressure. This calculation is for shot 146 conditions, with $\sigma_{\text{Ta|Ag}}=0.25$, $\sigma_{\text{MgO|Ag}}=0.03$, $T_{\text{Ta}}=15320$ K, $T_{\text{Ag}}=14420$ K, and $T_{\text{MgO}}=3667$ K (Table 3.2). From these, we have $T_{\text{INT}}(t=0)=14070$ K and $T_{\text{INT}}(t=\infty)=13910$ K, as defined in the text. The circles represent $\xi = 0.01$ and $\xi \rightarrow 0$ (the latter from [3.18] in text, respectively, while the diamonds and dots are for $\xi = 1.0$ and $\xi \rightarrow \infty$ ([3.19] in text), respectively.



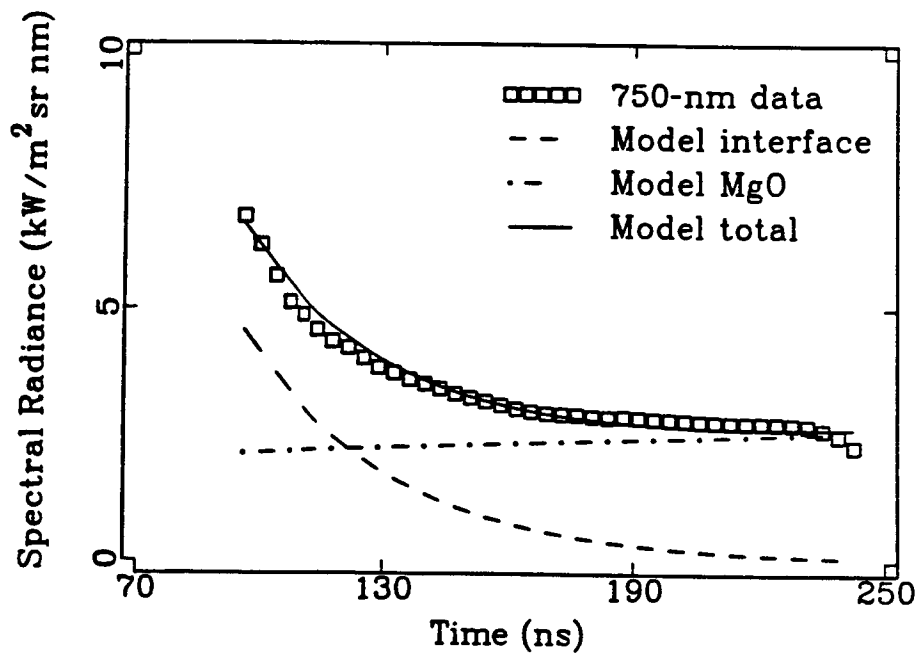
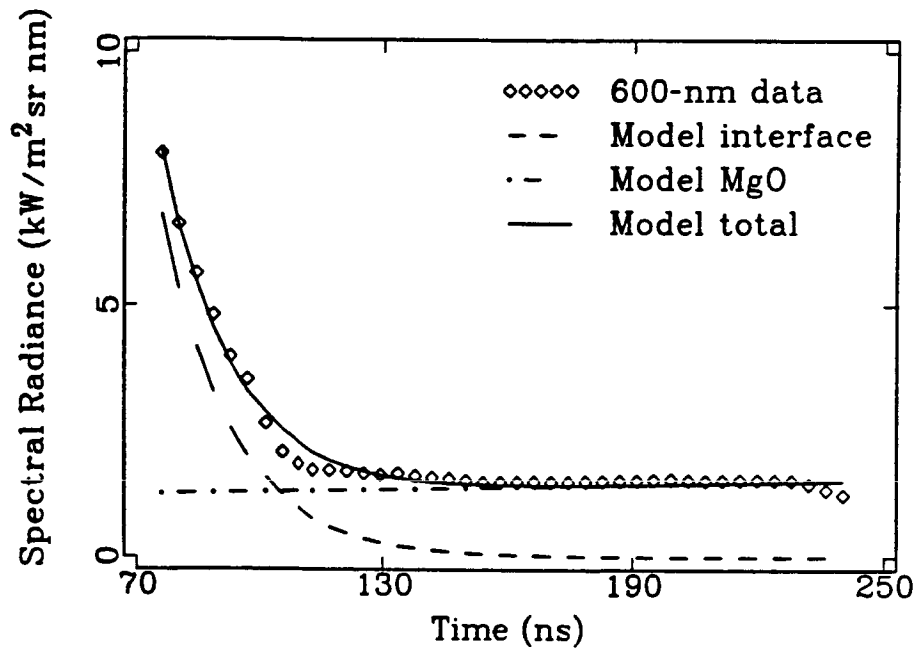
conditions; consequently, with $\delta \lesssim 10^{-6} \text{m}$, we have a (conductively) thin film ($\xi \lesssim 0.1$). Using these estimates for shot 146 conditions, we display $T_{\text{INT}}(t)$, calculated for 3 different values of ξ (1.0, 0.1 and 0.01), and $\sigma_{\text{Ta|Ag}}$ and $\sigma_{\text{MgO|Ag}}$ for the conditions of this shot (Table 3.3), in Figure 3.4. We also plot the 2 approximations ($\xi \rightarrow 0$, [3.18], and $\xi \rightarrow \infty$, [3.19]) in this figure. Clearly, over the entire range of ξ , $T_{\text{INT}}(t)$ lies within about 200 K of $T_{\text{INT}}(0)$. In particular, with $\xi \lesssim 0.1$, $T_{\text{INT}}(t)$ is essentially independent of time and approximately equal to $T_{\text{INT}}(\infty)$. We note that $T_{\text{INT}}(t)$ will approach T_{MgO} only if $\sigma_{\text{MgO|Ag}} \gg 1$ ($k_{\text{Ag}} \rightarrow 0$ or $k_{\text{MgO}} \rightarrow \infty$) and $\xi \ll 1$. So, assuming our estimate of $\sigma_{\text{MgO|Ag}}$ is reasonable, we have some justification for assuming that $T_{\text{INT}}(t)$ is essentially constant, and approximately equal to $T_{\text{INT}}(\infty)$, during the experiment.

With these considerations in mind, we display an example fit to the data for shot 146 in Figure 3.5, assuming that $T_{\text{INT}}(t)$ is time-independent. Assuming that our measurement errors are independently random, and normally-distributed around the model that actually fits the data, the "best fit" to the data is achieved through minimization of the functional $\chi^2(\lambda)$, given by

$$\begin{aligned} \chi^2(\lambda) &= \chi^2[\lambda; r_{\lambda\text{SF}}, a_{\lambda\text{MgO}}, r_{\lambda\text{INT}}, T_{\text{INT}}] \\ &\equiv \frac{1}{[\sigma(\lambda)]^2} \sum_t [I_{\lambda\text{exp}}(\lambda, t) - I_{\lambda\text{mod}}(\lambda, t)]^2 \end{aligned} \quad [3.20],$$

(*e.g.*, Press *et al.*, 1986), where $\sigma(\lambda)$ is the uncertainty of the data at wavelength λ . Using a golden section (GS) search technique (*e.g.*, Press *et al.*, 1986), we fit $I_{\lambda\text{mod}}(\lambda, t)$ to $I_{\lambda\text{exp}}(\lambda, t)$ by fixing $r_{\lambda\text{SF}}$, $a_{\lambda\text{MgO}}$ to known values (Table 3.4), and T_{MgO} to its value as given by [9] and the parameters in Table 3.4. Fixing T_{MgO} to this value is justified by agreement with the results of greybody fits discussed below. In addition, the fit results are not sensitive to T_{MgO} in this case (Chapter I, §6. and §7.). In this case, we vary $r_{\lambda\text{SF}}$, $a_{\lambda\text{MgO}}$, $r_{\lambda\text{INT}}$ and T_{INT} to minimize $\chi^2(\lambda)$. Even though the fit using [3.20] will produce λ -dependent optical parameters as the

Figure 3.5. Spectral radiance data and model fit at 600 nm (part a) and 750 nm (part b) for shot 146. Parameters for the fits are given in Table 3.4. The fit implies that the data are largely consistent with a high, time-independent interface temperature ($T_{\text{INT}}=20000$ K for 146), strongly absorbing shocked MgO (Table 3.4), and the estimated values for T_{MgO} (Table 3.2) used in the fits. It also implies that the contribution from the shocked MgO dominates that from Ag at the interface after ~ 100 ns.



data allows, we really cannot quantitatively assess 1) the ability of the data to resolve the wavelength-dependence of these parameters, 2) whether we have too many or few free parameters (even though they are all physically well-established), and 3) whether we have over- or under-estimated measurement uncertainties, all because the data lack sufficient wavelength-resolution (*i.e.*, we have 4 wavelength-dependent parameters and data at 4 wavelengths). In fact, all we can really resolve is the wavelength-averaged magnitude of the model parameters that are potentially wavelength-dependent. If we had sufficient wavelength-resolution, we could let all free parameters vary as allowed physically in λ, t space, and invert for their best values. However, the resolution of the data with respect to the wavelength-dependence of $r_{\lambda\text{STP}}$, $a_{\lambda\text{MgO}}$, $r_{\lambda\text{INT}}$ is, at best, poor. Keeping all this in mind, we display the results of this fit for shot 146 data in Table 3.4. Beyond the data resolution problem, we note that the potential wavelength-dependence of the parameters allowed to vary in the fit, (especially $a_{\lambda\text{MgO}}$) is also dependent on our assumption of constant $T_{\text{INT}}(t)$. From [2] and [3], we see that $T_{\text{INT}}(t)$, $a_{\lambda\text{MgO},0}$ and $a_{\lambda\text{MgO}}$ control the slope and magnitude, while the effective reflectivities and T_{MgO} influence only the magnitude, of $I_{\lambda\text{mod}}(\lambda, t)$. With a fixed $a_{\lambda\text{MgO},0}$, and $T_{\text{INT}} \gg T_{\text{MgO}}$, then, the fit is most sensitive to T_{INT} and $a_{\lambda\text{MgO}}$; these should be best resolved. The results of this fit (Table 3.4) suggest that shocked MgO at 200 GPa is ~ 50 -100 times more absorptive than at STP. Further, along with $r_{\lambda\text{INT}}$ (Table 3.4), $a_{\lambda\text{MgO},0}$ may be wavelength-dependent. Also, we note that the fits favor a much larger T_{INT} (~ 20000 K: Table 3.4) than $T_{\text{INT}}(0)$ calculated above for shot 146. This large value of T_{INT} implies that the Ag film is 1) is slightly porous (~ 8 -10%) and/or 2) reshocked at the Ag-MgO interface (Urtiew and Grover, 1974). Trapped gas at Ag-MgO interface as radiation source (Boslough, 1985) seems unlikely since it was formed under vacuum. However, we cannot rule out the influence of processes (*e.g.*, reshocking) at the Ta-Ag interface on T_{INT} . The decay of radiation intensity for

Table 3.4. Radiation Model Parameters† for Shot 146.

Wavelength (nm)	$a_{\lambda_{MgO},O}^{\dagger}$ (m^{-1})	$r_{\lambda_{SF}}$	$a_{\lambda_{MgO}}$ (m^{-1})	$r_{\lambda_{INT}}$
450	68	0.1	6300	0.9
600	82	0.3	7500	0.2
750	97	0.1	4200	0.6
900	128	0.1	3800	0.5

† $T_{INT} = 20000$ K, $T_{MgO} = 3667$ K, and $r_{\lambda_{SF}} = 0.08$ at all wavelengths in fit. $r_{\lambda_{SF}}$ was calculated from $n_{\lambda_{MgO},O} = 1.736$ (Weast, 1979) and formula for effective normal spectral reflectivity given in text.

‡ calculated from data of Touloukian *et al.* (1970c) and $d = 2.562$ mm for shot 146 (Table 6).

shot 146 is progressively faster going toward shorter wavelengths (*i.e.*, from 900 to 450 nm: Figure 3.2). This can happen if $T_{\text{INT}}(t)$ decays very strongly over time, and/or the effective spectral absorption-coefficient increases toward shorter wavelengths. We do not see a cross over of the radiation intensities at shorter wavelengths, however, implying that a strong decay of $T_{\text{INT}}(t)$ to near T_{MgO} does not dominate the time-dependence of $T_{\text{INT}}(t)$. If $T_{\text{INT}}(t)$ does decay strongly, the magnitude of $a_{\lambda\text{MgO}}$ would be less and its wavelength-dependence different. In this sense, our assumption of constant T_{INT} has given us an upper bound on the magnitude of $a_{\lambda\text{MgO}}$.

In context of our model, the effective normal spectral reflectivity of the boundary between any two (dynamic) target components i and j is given by (*e.g.*, Siegel & Howell, 1981)

$$r_{\lambda} \equiv \frac{(n_{\lambda i} - n_{\lambda j})^2 + (\omega_{\lambda i} - \omega_{\lambda j})^2}{(n_{\lambda i} + n_{\lambda j})^2 + (\omega_{\lambda i} + \omega_{\lambda j})^2} .$$

In this relation, n_{λ} and ω_{λ} are the real and imaginary parts of the complex index of refraction of the material, and, as with all the other optical parameters, they are both potentially λ -dependent. ω_{λ} is also known as the electromagnetic extinction coefficient. The values of $r_{\lambda\text{SF}}$ from the fit imply that the refractive index of MgO changes very little upon shock compression up to 200 GPa. This is consistent with the low-pressure data of Vedam & Schmidt (1966), which imply that the refractive index of MgO actually decreases very slightly ($\sim 1.5 \times 10^{-3}/\text{GPa}$) because of the decrease in electronic polarizability, which dominates the intrinsic increase in refractive index with pressure. The slightly higher value of $r_{\lambda\text{SF}}$ at 600 nm is clearly warranted by the data (see below), and may represent a dependence of $n_{\lambda\text{MgO}}$ on wavelength. Noting that $a_{\lambda\text{MgO}} = 4\pi\omega_{\lambda\text{MgO}}/\lambda$ (*e.g.*, Siegel & Howell, 1981), where $\omega_{\lambda\text{MgO}}$ is the extinction coefficient of shocked MgO, our results imply that $\omega_{\lambda\text{MgO}} \sim 10^{-3}$, also consistent

with a small value for $r_{\lambda_{SP}}$. The values of $r_{\lambda_{INT}}$ in Table 3.4 may be compared with $r_{\lambda_{INT}}(600 \text{ nm}) = 0.9$ at STP, calculated with $n_{\lambda_{Mg}} = 0.18$, $\omega_{\lambda_{Mg}} = 3.64$ at 600 nm (Svet, 1965) and $n_{\lambda_{MgO}} = 1.736$ (Table 3.4). Since $\omega_{\lambda_{MgO}}$ appears to be too small to affect $r_{\lambda_{INT}}$ significantly, the decrease of $r_{\lambda_{INT}}$ at high pressure implied by the fit may represent a change mainly in $n_{\lambda_{Mg}}$ and/or $\omega_{\lambda_{Mg}}$ with pressure.

The strongest result of this fit is that MgO is significantly more opaque at high pressure. This is consistent with the results of Gaffney & Ahrens (1973), who observed a wavelength-independent increase in opacity at 46.5 GPa in MgO. This change in opacity may be due to shock-induced defect structures, since MgO did not recover its transparency during release. With the possible exception of Al_2O_3 (Bass *et al.*, 1987; but see Urtiew, 1974), all initially transparent materials studied so far (*e.g.*, LiF: Kormer, 1968; $\text{CaAl}_2\text{Si}_2\text{O}_8$: Boslough *et al.*, 1986) lose some transparency during shock compression. We note that a similar fit to shot 145 data is qualitatively consistent with that for shot 146 data.

To get more precise estimates of the optical parameters, we need further constraints on $\hat{\epsilon}_{\lambda_{INT}}(t)$ and $T_{INT}(t)$. One possible means to this is the use of two recording systems during the experiment, one set to record the initial intensity of the interface radiation, and the other set to record the expected intensity of the sample radiation. In this way the early history of the radiation intensity should constrain the early time-dependence of $\hat{\epsilon}_{\lambda_{INT}}(t)$ and $T_{INT}(t)$, before the optical properties of shocked MgO can significantly affect the observed radiation intensity.

Having some understanding of the time- and wavelength-dependence of the observed radiation intensity, we can, with some justification, fit the greybody relation

$$I_{\lambda_{gb}}(\lambda, t) \equiv \hat{\epsilon}_{fit}(t) I_{\lambda_{pl}}[\lambda, T_{fit}(t)] \quad [3.21]$$

at a given time, which we designate t_r , to the end of the observed radiation histories and find the effective emissivity and temperature of shocked MgO. The choice of t_r is motivated by the calculated shock-wave transit time through the MgO, but is not critically dependent on this choice, as we show below.

To fit $I_{\lambda gb}(\lambda, t)$ to the data, we again use the χ^2 measure. In this case, it is given by

$$\begin{aligned} \chi^2(t_r) &= \chi^2[t_r; \hat{\epsilon}_{\text{fit}}, T_{\text{fit}}] \\ &\equiv \sum_{\lambda} \left\{ \frac{1}{[\sigma(\lambda)]^2} \{ I_{\lambda \text{exp}}(\lambda, t_r) - \hat{\epsilon}_{\text{fit}}(t_r) I_{\lambda \text{pl}}[\lambda, T_{\text{fit}}(t_r)] \}^2 \right\} \end{aligned} \quad [3.22].$$

Unlike [3.20], the sum is now over all wavelengths observed in the experiment. On this basis, $\hat{\epsilon}_{\text{exp}}(t_r)$ and $T_{\text{exp}}(t_r)$ represent the values of $\hat{\epsilon}_{\text{fit}}(t_r)$ and $T_{\text{fit}}(t_r)$ that minimize $\chi^2(t_r)$. Since the fit is with respect to wavelength, the value of $\hat{\epsilon}_{\text{exp}}(t_r)$ represents a wavelength-average of $\hat{\epsilon}_{\lambda \text{MgO}}(\lambda, t_r)$. Since $\chi^2(t_r)$ is a nonlinear functional of temperature, we find its minimum numerically using 1) GS search, as above, and 2) the method of Levenberg as formulated by Marquardt (LM). See, for example, Press *et al.* (1986), for details on both of these methods. To obtain starting values of $\hat{\epsilon}_{\text{fit}}(t)$ and $T_{\text{fit}}(t)$ for the nonlinear fit, we use Wien's approximation to $I_{\lambda \text{pl}}(\lambda, T)$ in $\chi^2(t_r)$, which follows from $I_{\lambda \text{pl}}(\lambda, T)$ in the limit $\exp(C_2/\lambda T) \gg 1$, *i.e.*,

$$I_{\lambda \text{wgb}}(\lambda, t) \equiv \hat{\epsilon}_{\text{fit}}(t) I_{\lambda \text{wi}}(\lambda, t) = \hat{\epsilon}_{\text{fit}}(t) \frac{2C_1}{\lambda^5} e^{-C_2/\lambda T_{\text{fit}}(t)}. \quad [3.23]$$

The relative error incurred in approximating $I_{\lambda \text{pl}}$ by $I_{\lambda \text{wi}}$ is equal to $\exp(-C_2/\lambda T)$; this approximation is accurate to within 1% for $\lambda T < 3 \times 10^{-3} \text{m} \cdot \text{K}$ (Siegel & Howell, 1981). Since we can fit Wien's relation to the data via linear least squares, we can solve for $\hat{\epsilon}_{\text{fit}}(t_r)$ and $T_{\text{fit}}(t_r)$ directly (*i.e.*, without iteration).

We argue above that the radiation intensity at the end of the record likely represents only that of shocked MgO. In this case, from relations [3.1] and [3.2], we also see that, with $\hat{\epsilon}_{\lambda\text{NIT}}(\lambda, t=t_r \approx t_{\text{exp}}) \approx 0 \ll \hat{\epsilon}_{\lambda\text{MgO}}(\lambda, t_r)$,

$$I_{\lambda\text{mod}}(\lambda, t_r) \approx \hat{\epsilon}_{\lambda\text{MgO}}(t_r) I_{\lambda\text{pl}}(\lambda, T_{\text{MgO}}) \quad [3.24]$$

with

$$\hat{\epsilon}_{\lambda\text{MgO}}(t_r) \approx (1 - r_{\lambda\text{FS}}) (1 - r_{\lambda\text{SF}}) (1 + r_{\lambda\text{NIT}} e^{-2a_{\lambda\text{MgO}}^*}) (1 - e^{-2a_{\lambda\text{MgO}}^*}) . \quad [3.25]$$

Recalling that $r_{\lambda\text{FS}}$ is independently established (Table 3.4), and taking the values of $r_{\lambda\text{SF}}$, $a_{\lambda\text{MgO}}^*$ and $r_{\lambda\text{NIT}}$ established by the model fit, we may "correct" the radiation data and fit for $\hat{\epsilon}_{\text{exp}}(t_r)$ $T_{\text{exp}}(t_r)$ as above. This is a somewhat crude way of correcting for apparent λ -dependence of $\hat{\epsilon}_{\lambda\text{MgO}}$ from the fit using [3.20] discussed above. In principle, this should allow us to fit for $T_{\text{exp}}(t_r)$ alone, but we allow $\hat{\epsilon}_{\text{exp}}(t_r)$ to vary because we already set $\hat{\epsilon}_{\text{exp}}(t_r) = 1$ in one of the GS fits (*i.e.*, out of curiosity).

Unlike the previous fit, we have 4 data and 2 parameters (at least for shots 145 and 146) in the greybody fit. However, we are still confined to wavelength-average values for $\hat{\epsilon}_{\text{exp}}(t_r)$. We present the results of both the corrected (using [3.24]-[3.25]) and uncorrected fits in Table 3.5, and plot the uncorrected fit for shots 145 and 146 in Figures 3.6a and 3.6b, respectively. The results for shot 166 (Table 3.5) do not include a LM fit because the method requires at least 3 data points for a fit to 2 parameters. The uncertainties associated with the GS fits represent measurement uncertainties mapped into uncertainties for $\hat{\epsilon}_{\text{exp}}(t_r)$ and $T_{\text{exp}}(t_r)$ through use of [3.26]-[3.29] given below. However, the uncertainty associated with each LM fit is the standard deviation of that fit. Roughly speaking, the values of $\chi^2(t_r)$ given in Table 3.5 can be compared to the number of data minus the number of parameters in the fit to judge its "goodness." On this basis, the fit for shot 145 is not as "good" as that for 166, and especially 146. The experimental uncertainties for shots 166 and 147 are much lower, of

Table 3.5. Greybody Fits to Radiation Data at t_r .

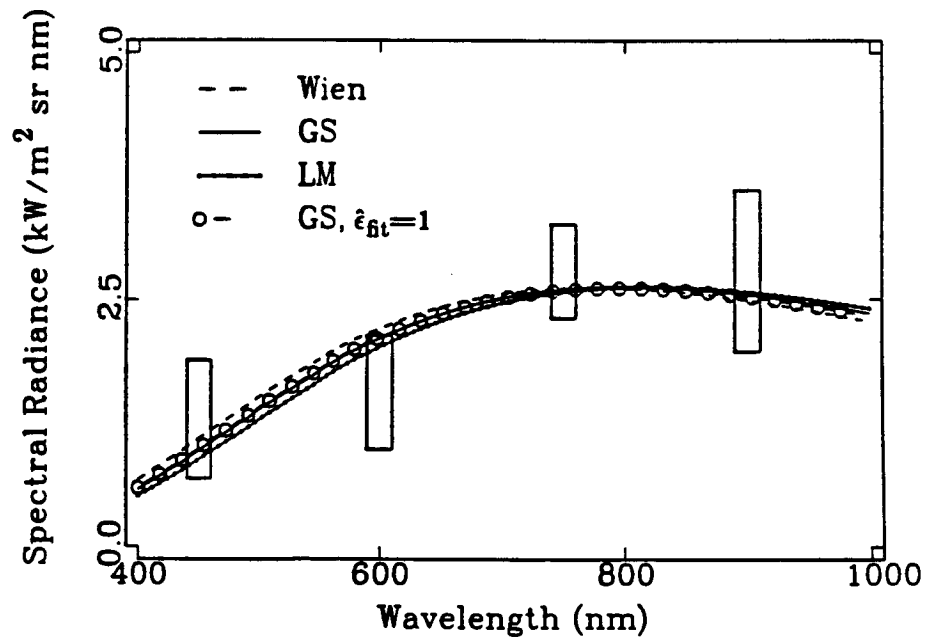
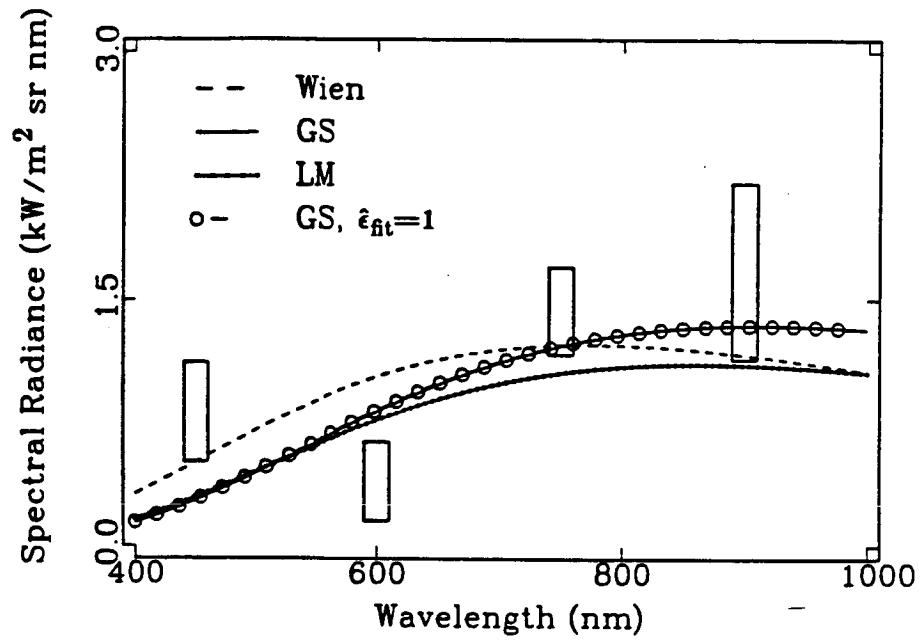
Shot	Parameter (t_r)	Uncorrected				Corrected			
		Wien	GS	LM	GS ($\hat{\epsilon}_{fit}=1$)	Wien	GS	LM	GS ($\hat{\epsilon}_{fit}=1$)
166 (750,900)§	$\hat{\epsilon}_{exp}$ (285 ns)	1.02 (0.22)	1.00 (0.22)†			1.23 (0.22)	1.18 (0.22)		
	T_{exp} (285 ns)		3046 (120)	3056 (120)		3054 (115)		3062 (120)	3081 (120)
	χ^2		0.001	0.0005		0.02		0.001	0.0005
147 (600)	T_{exp} (210 ns)				2981 (120)				3071 (130)
145 (all)	$\hat{\epsilon}_{exp}$ (210 ns)	0.41 (0.80)	1.02 (0.80)	0.64 (0.18)‡		0.50 (0.80)	1.02 (0.80)	0.75 (0.21)	
	T_{exp} (210 ns)	3739	3174 (480)	3352 (355)	3186 (200)	3756 (355)	3281 (485)	3372 (375)	3292 (220)
	χ^2	9.68	7.29	8.70	7.33	9.69	7.58	8.77	7.62
146 (all)	$\hat{\epsilon}_{exp}$ (200 ns)	0.88 (0.69)	1.04 (0.69)	1.17 (0.17)		1.07 (0.69)	1.21 (0.69)	1.42 (0.20)	
	T_{exp} (200 ns)	3735	3615 (385)	3530 (80)	3639 (390)	3757 (415)	3663 (395)	3549 (100)	3784 (420)
	χ^2	1.64	1.41	1.35	1.45	1.64	1.46	1.36	1.70

† - Golden section search fit. Uncertainties represent experimentally-based uncertainties.

‡ - Levenberg-Marquardt fit. Uncertainties represent standard deviations of corresponding fit.

§ - Wavelengths used in fit.

Figure 3.6. Greybody fits to uncorrected shot-145 data (part a) and shot-146 data (part b) as a function of wavelength for $\hat{\epsilon}_{\text{exp}}(t_r)$ and $T_{\text{exp}}(t_r)$. The size of the data rectangles represent experimental uncertainty. Note the deviation (*i.e.*, outside experimental uncertainty) at 600 nm of the spectral radiance below the various fits. This observation is substantiated as a larger value of $r_{\lambda_{\text{FS}}}(600 \text{ nm})$ (Table 3.4) in the fit of Figure 6b at 600 nm.



course, mainly because they are based on only two wavelengths and a single wavelength, respectively. For shots 145 and 146, within the fit uncertainty, the LM and GS results agree (Table 3.5). Also, there is, within uncertainty, no difference between the corrected and uncorrected results (the corrected-data results are slightly closer to the calculated values of T_{MGO} as listed in Table 3.2). Except for the shot-145 LM results, the effective emissivities of the LM and GS fits are ≥ 1 , an unphysical result. However, the associated data and fit uncertainties easily allow the effective emissivities to be less than unity. Also, as noted by Boslough & Ahrens (1986), $\hat{\epsilon}_{\text{fit}}$ is much more sensitive to data scatter (in λ and/or t), whether due to uncorrected wavelength-dependences in the data, or experimental measurement errors. This results from the functional form of $I_{\lambda\text{gb}}$, as can be seen from the following relations:

$$\frac{\delta T_{\text{fit}}}{T_{\text{fit}}} \approx \left(\frac{\partial \ln T_{\text{fit}}}{\partial \ln I_{\lambda\text{gb}}} \right)_{\hat{\epsilon}_{\text{fit}}, \lambda} \frac{\delta I_{\lambda\text{gb}}}{I_{\lambda\text{gb}}} \quad [3.26]$$

and

$$\frac{\delta \hat{\epsilon}_{\text{fit}}}{\hat{\epsilon}_{\text{fit}}} \approx \left(\frac{\partial \ln \hat{\epsilon}_{\text{fit}}}{\partial \ln I_{\lambda\text{gb}}} \right)_{T_{\text{fit}}, \lambda} \frac{\delta I_{\lambda\text{gb}}}{I_{\lambda\text{gb}}} \quad [3.27],$$

where

$$\left(\frac{\partial \ln T_{\text{fit}}}{\partial \ln I_{\lambda\text{gb}}} \right)_{\hat{\epsilon}_{\text{fit}}, \lambda} = \frac{\mu}{(1 + \mu) \ln(1 + \mu)} < 1 \quad , \quad \mu > 0 \quad [3.28],$$

$$\left(\frac{\partial \ln \hat{\epsilon}_{\text{fit}}}{\partial \ln I_{\lambda\text{gb}}} \right)_{T_{\text{fit}}, \lambda} = 1 \quad [3.29],$$

and

$$\mu = \frac{2C_1 \hat{\epsilon}_{\text{fit}}}{\lambda^5 I_{\lambda\text{gb}}}$$

(note that λ and $\hat{\epsilon}_{\text{fit}}$ are fixed in this last relation). From these relations we see

that a given variation of $I_{\lambda\text{exp}}$, and hence $I_{\lambda\text{gb}}$ in the fit, will have a larger impact on $\hat{\epsilon}_{\text{fit}}$ than T , *i.e.*, $\delta T_{\text{fit}}/T_{\text{fit}} < \delta \hat{\epsilon}_{\text{fit}}/\hat{\epsilon}_{\text{fit}}$ for all $\delta I_{\lambda\text{gb}}/I_{\lambda\text{gb}}$. Consequently, it is not surprising that $\hat{\epsilon}_{\text{exp}}(t_r)$ could be greater than unity with any significant scatter, if not constrained to be less than or equal to unity in the fit.

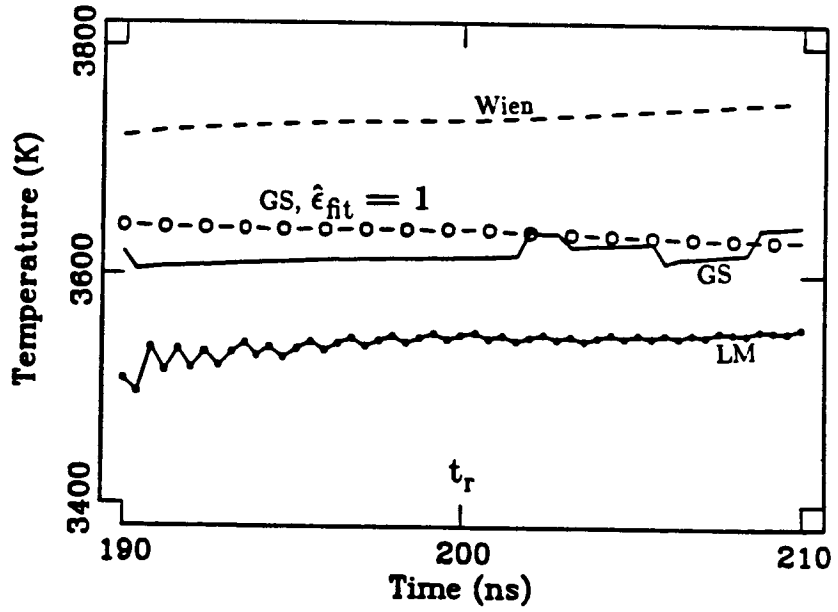
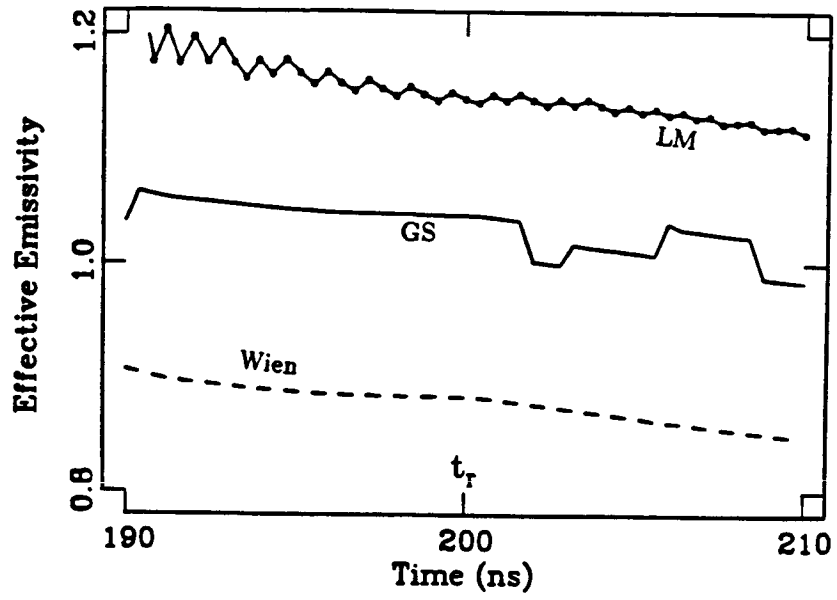
The fits displayed in Figures 3.6a-b for shots 145 and 146, respectively, both show that the 600-nm data lie significantly below the fits. This is also suggested by the model results displayed in Figure 3.5 for shot 146, where $r_{\lambda\text{exp}}(600\text{ nm})=0.3$. This deviation probably does not represent systematic error, since we have never seen anything like it in the data from other experiments of this nature. That it reflects a property of shock-compressed MgO is supported by the radiation spectrum of shock-compressed MgO at 60 GPa (Schmitt & Ahrens, 1984), which is nonthermal and displays a sharp drop in intensity below ~ 650 nm, possibly due to λ -dependent absorption and/or reflectivity. This possibility is consistent with the results of the fit displayed in Table 3.4. This apparent nonblackbody trend in the MgO data is one possible cause of "data scatter" leading to nonphysical values of $\hat{\epsilon}_{\text{fit}}$, as discussed above.

That our choice of t_r , within a given window of time, is not essential to our results can be shown by fitting a window of time around t_r and displaying the consequences. We do this for shot 146 uncorrected data and display the results in Figure 3.7. As evident, the fit is essentially time-independent 10 ns on either side of t_r . This is true for the fits to shots 166 and 145 as well.

§4. Discussion

In Table 4.1, we list the greybody fit and uncertainties, along with the calculated shock-wave velocities, shock-transit times, pressure and temperature, for each experiment. The uncertainties of calculated quantities are based on a propagation of the parameter uncertainties listed in Table 3.1 through the

Figure 3.7. Greybody effective emissivity, $\hat{\epsilon}_{\text{exp}}(t)$ (part a), and temperature, $T_{\text{exp}}(t)$ (part b), as a function of time near the end of the radiation history for shot 146. The fits are essentially time-independent in this time window centered on t_r .



calculation of each quantity. The values of $\hat{\epsilon}_{\text{exp}}(t_r)$ and $T_{\text{exp}}(t_r)$ in Table 4.1 are those for the GS fit with $\hat{\epsilon}_{\text{fit}}$ and T_{fit} variable, which we choose as representative of the other estimates, within experimental uncertainties. The average uncertainty of T_{MgO} is somewhat higher than, but relatively close to, the average experimental uncertainty of $T_{\text{exp}}(t_r)$. Note that the calculated shock-wave transit times through MgO are, on average, about 40 ns less than the duration of each experiment, as defined by a break in the radiation history about 240 ns after the rise in radiation intensity (see Figures 3.2 and 3.3, and compare with t_{st} for shot 146 in Table 4.1) due to release of MgO. This seems to be a real discrepancy; experimental times should be resolvable to within ± 5 ns. We have no explanation at this point.

The good agreement between the temperatures inferred from the radiation data and calculation using [3.9] implies *a posteriori* that the assumptions that 1) MgO compresses as an elastic fluid, 2) MgO does not change phase during shock compression, and 3) $c_v = 3nR$ for MgO, are valid for the range of pressures covered by our experiments. The first assumption implies that the temperatures achieved by MgO during shock compression in the pressure range covered are governed by its bulk elastic properties and lattice specific heat. At much lower pressures (≤ 60 GPa), MgO radiates nonthermally (Schmitt & Ahrens, 1984), which is also consistent with these calculations; T_{MgO} in this pressure range is ≤ 500 K.

No variation of c_v and/or γ is reflected in the uncertainties for T_{MgO} listed in Table 4.1. Any variation of these parameters would, of course, only increase the uncertainty of T_{MgO} , which already encompasses that of $T_{\text{exp}}(t_r)$. In other words, unless we "assume" that we can actually calculate T_{MgO} much better than indicated by its uncertainties listed in Table 4.1, $T_{\text{exp}}(t_r)$ cannot place bounds on a possible variation of c_v or γ , because the uncertainty of T_{MgO} is larger than that of $T_{\text{exp}}(t_r)$. With this in mind, we can alter the values of c_v

Table 4.1. Experimental Results and Model Estimates.

Shot	Experimental Results						Model estimates			
	ρ (Mg/m ³)	d (mm)	v_{imp} (km/s)	$\hat{\epsilon}_{exp}$	T_{exp} (K)	t_r (ns)	U (km/s)	t_{st} (ns)	P_{MgO} (GPa)	T_{MgO} (K)
166	3.562 (0.002)†	3.468 (0.005)	5.73 (0.04)	1.18 (0.22)	3081 (120)	285 (10)	12.10 (0.14)	286.6 (3.4)	174.0 (2.6)	2913 (415)
147	3.595 (0.002)	2.513 (0.002)	5.87 (0.03)	1.00 (0.33)	3071 (130)	205 (10)	12.22 (0.14)	205.7 (2.4)	181.1 (2.3)	3028 (430)
145	3.577 (0.002)	2.621 (0.003)	6.04 (0.03)	1.03 (0.79)	3281 (375)	210 (10)	12.38 (0.15)	211.7 (2.5)	187.9 (2.6)	3257 (445)
146	3.587 (0.002)	2.562 (0.004)	6.36 (0.03)	1.19 (0.69)	3663 (395)	200 (10)	12.68 (0.15)	202.0 (2.5)	203.1 (2.8)	3667 (495)

† - measurement uncertainty.

ρ - STP bulk density.

d - Sample thickness.

v_{imp} - Impact velocity.

U - Calculated shock wave velocity.

t_{st} - Calculated transit time of shock wave through MgO.

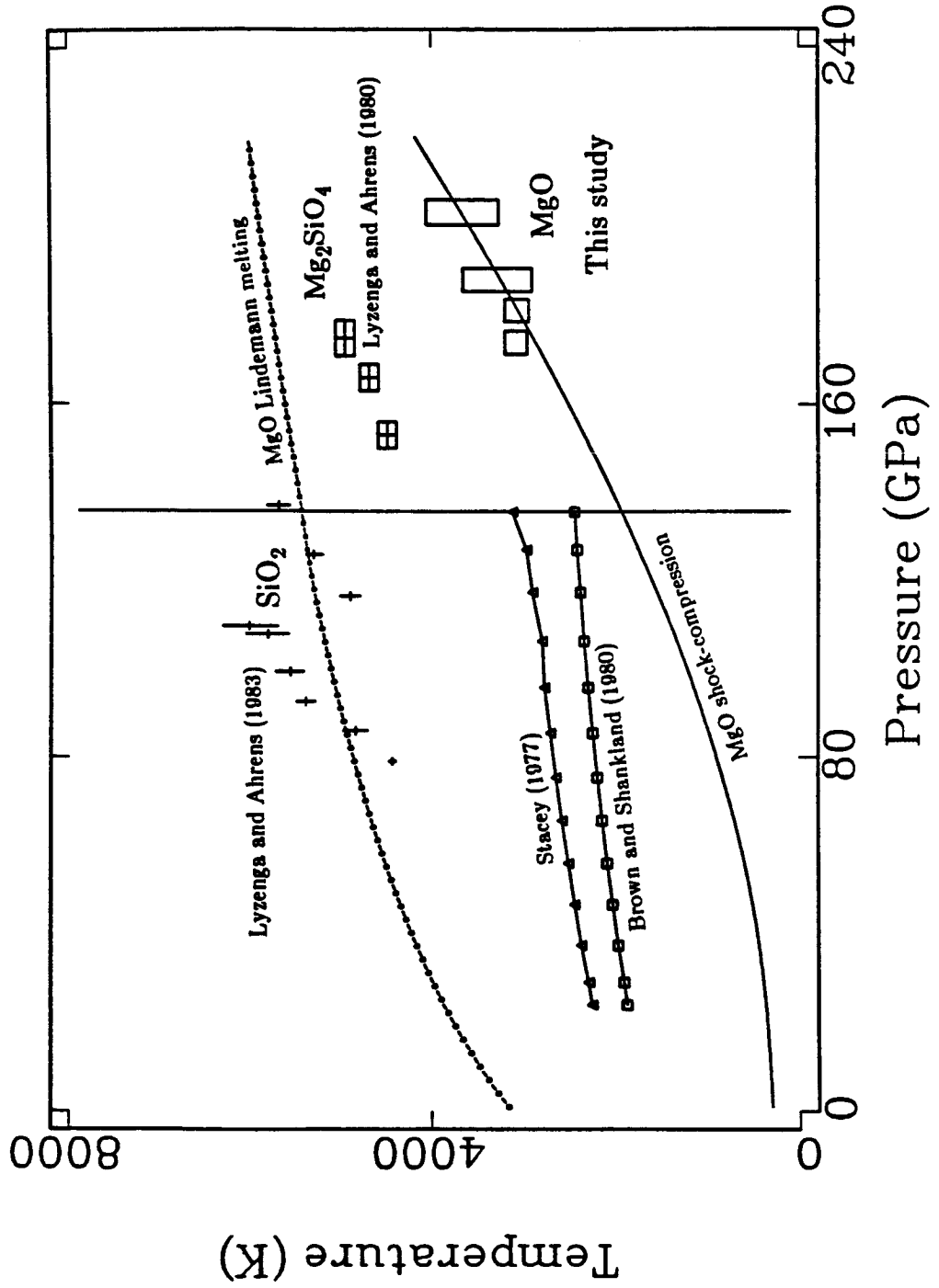
P_{MgO} - Calculated pressure of shock-compressed state of MgO.

T_{MgO} - Calculated temperature of shock-compressed state of MgO.

and γ given in Table 3.1 and obtain other values for T_{MgO} than those given in Tables 3.2 and 4.1. As discussed above, T_{MgO} is much more sensitive to variations in c_v than γ . For example, using the conditions of shot 146, if we first vary γ_0 , and then $c_v = 3nR/M$, of MgO (Table 3.1) by $\pm 10\%$, we get a ± 20 and ± 350 K variation in T_{MgO} , respectively.

We display the experimental results in Figure 4.1 along with temperatures inferred from radiation data for SiO_2 (Lyzena *et al.*, 1983) and Mg_2SiO_4 (Lyzena & Ahrens, 1980). The continuous curve is the calculated locus of shock-compressed states for MgO, and the dot-dashed curve is a Lindemann estimate of the melting curve of MgO, calculated from the parameters listed in Table 3.1 by assuming the compression of solid-MgO along the melting curve is equal to that along the MgO shock-compression curve at the same pressure (Chapter I, §4.). Also displayed are the mantle temperature profiles of Brown & Shankland (1980) and Stacey (1977), which are together representative of the range of models currently considered plausible. From the agreement of data and calculations, and in light of the Lindemann estimate, we conclude that MgO does not change phase below 200 GPa. Not shown in Figure 4.1 is the intersection of the model shock-compression and Lindemann curves for MgO at 265 GPa. On the basis of the "ideal" behavior exhibited by MgO up to this point, we speculate that it won't melt below ≈ 265 GPa. Also, if MgO has an effective emissivity near unity between 170 and 200 GPa, as our results suggest, then the observations of Kondo & Ahrens (1983) and Schmitt & Ahrens (1984), as well as the models of Svendsen & Ahrens (1986), imply that MgO probably does not localize thermal energy below this pressure. Any localization should catalyze melting or other energetically favored transitions at higher pressures. Shock-induced deformation in MgO is localized (Chen *et al.*, 1975) in the form of microfracturing up to 60 GPa, but apparently this has no impact on the temperature field, in contrast to other oxides such as SiO_2 (Schmitt & Ahrens,

Figure 4.1. Experimental and model pressure-temperature shock compression results for MgO. The Lindemann melting and shock compression curves for MgO are calculated from the parameters for MgO in Table 3.1. The MgO experimental results are represented by rectangles. Also shown are the mantle temperature profiles of Stacey (1977) and Brown and Shankland (1980), as well as the experimental results of Lyzenga *et al.* (1983) for SiO₂ and Lyzenga and Ahrens (1980) for Mg₂SiO₄. Note that the MgO experimental results are quite consistent with the model curve and well-below the Lindemann estimate.



1984). Apparently the energy dissipated in localized deformation in shocked-MgO is efficiently transported away before an energy density sufficient to effect melting or solid-solid transformation is attained (Svendsen & Ahrens, 1986).

What are the processes responsible for the transition of MgO from predominantly a nonthermal to a thermal radiator (with $\epsilon \rightarrow 1$) between 60 and 170 GPa? The apparent change in electrical resistivity of shocked-MgO from $\gtrsim 10^3$ to $\sim 10 \Omega \cdot \text{m}$ above 92 GPa (Ahrens, 1966) is consistent with either 1) closure of the valence-conduction electron band-gap, or 2) proliferation of initially present or shock-induced (Gager *et al.*, 1964) defects possessing free electrons. However, since the MgO band-gap appears to increase in the pressure range of our experiments (Lieberman, 1978; Bukowinski, 1980; Chang and Cohen, 1984), we speculate that, at high pressures above ~ 100 GPa, defects in thermal equilibrium with MgO are responsible for the observed radiation from MgO.

§5. Summary

We use a model of conductive and radiative transport among the target components of our experiments to interpret the radiation history of the target in terms of its optical and thermal properties, and infer the shock-compressed temperature of MgO. On this basis, we have the following results:

1. The model for conduction between the Ta driver, Ag film and MgO implies that the Ag-MgO interface temperature, $T_{\text{INT}}(t)$, will be approximately constant on the time scale of the radiation observations (~ 200 ns) for values of the nondimensional interface thickness ξ less than 0.1 (Ag-film thickness $\delta \lesssim 1000$ nm) or greater than 1.0 ($\delta > 10 \mu\text{m}$). Estimates of this thickness for the Ag film of each experiment imply that $\xi < 0.1$ for all experiments. The model implies that $T_{\text{INT}}(t)$ cannot decrease by more than about 200 K in any of the experiments (regardless of the value of ξ) because of the large

thermal-inertia mismatch between Ag and MgO.

2. Assuming $T_{\text{INT}}(t)$ is independent of time, a fit of the radiative-transport model to MgO radiation-history data implies that shocked MgO is ~ 100 times more absorbing ($a_{\text{MgO}} \sim 6300, 7500, 4200$ and 3800 m^{-1} at 450, 600, 750 and 900 nm, respectively, at 203 GPa) than unshocked MgO in the pressure range covered by the experiments. The coefficient of absorption for shocked MgO and the effective normal spectral reflectivity of the shock-front and Ag-MgO interface are wavelength-dependent in this fit (Table 3.4). Also, T_{INT} from this fit is much higher ($\sim 20000 \text{ K}$) than estimated from ideal-release calculations for solid Ag-film, implying that the Ag film may be slightly porous ($\lesssim 10 \%$) and/or reshocked. Independent constraints on $T_{\text{INT}}(t)$ and $\hat{\epsilon}_{\text{INT}}(t)$ through modification of the experiment to record both interface and sample radiation intensities are needed to pin down these possibilities.

3. The radiative transport model fits imply that greybody fits to the end of the radiation histories for each experiment constrain the effective normal (wavelength-averaged) emissivity and absolute temperature of MgO. Using two different fitting techniques, we establish, within experimental uncertainty, the robustness of our fits. The greybody fits agree well with model temperature calculations, implying that, between 170 and 200 GPa, MgO compresses as an elastic fluid with a Dulong-Petit specific-heat value. The agreement between $T_{\text{exp}}(t_r)$ and T_{MgO} , the latter calculated assuming no phase transformations, as well as the values of $\hat{\epsilon}_{\text{exp}}(t_r)$ ($\sim 0.1-1$, Table 3.5), together imply that MgO does not change phase below 200 GPa. In addition, since the calculated shock-compression curve and Lindemann melting curve of MgO intersect at 265 GPa, we speculate that it will not melt

below this pressure.

4. Comparison of the experimental results for MgO with those of SiO₂ and Mg₂SiO₄ shows that the shock-compressed temperatures of Mg₂SiO₄ lie between those of SiO₂ (below) and MgO (above), analogous to the density-pressure relations between these materials, and emphasizing the role of the bulk elastic properties of these materials in controlling the first-order magnitude of their respective shock-compressed temperatures. Comparison of the extrapolated MgO shock-compression curve with a range of possible mantle temperature profiles implies that shocked MgO is colder than the lower mantle by ~ 1000 - 1500 K at the same pressure.

Acknowledgements. We thank Papo Gelle, Mike Long, Chuck Manning and Leon Young for experimental assistance. Gregory Miller, Jay D. Bass, Douglas R. Schmitt and James A. Tyburczy provided enlightening discussions. We also thank Mark B. Boslough and an anonymous reviewer for constructive comments on the first draft of this paper. Support from NSF grant EAR-8608249 is gratefully acknowledged. Contribution 4413, Division of Geological and Planetary Sciences, California Institute of Technology, Pasadena, California.

§6. References

- Ahrens, T. J., High-pressure electrical behavior and equation of state of magnesium oxide from shock wave measurements, *J. Appl. Phys.*, **37**, 2532-2541, 1966.
- Ahrens, T. J., D. L. Anderson & A. E. Ringwood, Equation of state and crystal

- structure of high-pressure phases of shocked silicates and oxides, *Rev. Geophys.*, **7**, 667-707, 1969.
- Alers, G. A., Use of sound velocity measurements in determining the Debye temperature of solids, in *Physical Acoustics*, **3B**, 1-42, edited by W. P. Mason, Academic Press, New York, 1965.
- Bass, J. D., B. Svendsen & T. J. Ahrens, The temperatures of shock-compressed iron, in *High Pressure Research in Geophysics and Geochemistry*, edited by M. Manghnani & Y. Syono, Terra Publishers, Tokyo, in press, 1987.
- Berman, R., *Thermal conduction in Solids*, 193 pp., Oxford University Press, Oxford, 1976.
- Boslough, M. B., Shock-wave properties and high-pressure equations of state of geophysically important materials, *Ph.D. Dissertation*, 171 pp., California Institute of Technology, Pasadena, California, 1984.
- Boslough, M. B., A model for time dependence of shock-induced thermal radiation of light, *J. Appl. Phys.*, **56**, 3394-3399, 1985.
- Boslough, M. B., T. J. Ahrens & A. C. Mitchell, Shock temperatures in CaO, *J. Geophys. Res.*, **89**, 7845-7851, 1984.
- Boslough, M. B., T. J. Ahrens & A. C. Mitchell, Shock temperatures in anorthite glass, *Geophys. J. R. astr. Soc.*, **84**, 475-489, 1986.
- Bridgman, P. W., The resistance of 72 elements, alloys and compounds to 100,000 kg/cm², *Proc. Am. Acad. Arts Sci.*, **81**, 167-251, 1952.
- Brown, J. M. & T. Shankland, Thermodynamic parameters of the earth as determined from seismic profiles, *Geophys. J. R. astr. Soc.*, **66**, 579-596, 1980.
- Brown, J. M. & J. W. Shaner, Rarefaction velocities in shocked tantalum and the high pressure melting point, in *Shock waves in Condensed Matter - 1983*, pp. 91-94, edited by J. R. Asay, R. A. Graham & G. K. Straub, Elsevier Science Publishers B.V., 1984.

- Bukowinski, M., Pressure bonding in MgO, *J. geophys. Res.*, **85**, 285-292, 1980.
- Burnstein, E. & P. L. Smith, Photoelastic properties of cubic crystals, *Phys. Rev.*, **74**, 229-230, 1948.
- Carslaw, H. S. & J. C. Jaeger, *Conduction of heat in solids*, 510 pp., Clarendon Press, Oxford, 1959.
- Carter, W. J., S. P. Marsh, J. N. Fritz & R. G. McQueen, The equation of state of selected materials for high-pressure references, in *Accurate Characterization of the High-Pressure Environment*, pp. 147-158, NBS Special Publication 326, 1971.
- Chang, K. J. & M. L. Cohen, 1975. High-pressure behavior of MgO: Structural and electronic processes, *Phys. Rev. B*, **30**, 4774-4780.
- Chen, Y., M. M. Abraham, T. J. Turner & C. M. Nelson, Luminescence in deformed MgO, CaO and SrO, *Phil. Mag.*, **20**, 99-112, 1975.
- Davies, G. F., Quasi-harmonic finite strain equations-of-state of solids, *J. Phys. Chem. Solids*, **34**, 1417-1429, 1973.
- Dick, J. J. & D. L. Styris, Electrical resistivity of silver foils under uniaxial shock-wave compression, *J. Appl. Phys.*, **46**, 1602-1617, 1975.
- Gaffney, E. S. & T. J. Ahrens, Optical absorption spectra of ruby and periclase at high shock pressure, *J. Geophys. Res.*, **78**, 5942-5953, 1973.
- Gager, W. B., M. J. Klein & W. H. Jones, The generation of vacancies in MgO single crystals by explosive shock, *Appl. Phys. Lett.*, **5**, 130-131, 1964.
- Grover, R. & P. A. Urtiew, Thermal relaxation at interfaces following shock compression, *J. Appl. Phys.*, **45**, 146-152, 1974.
- Jackson, I. & A. E. Ringwood, High-pressure polymorphism of the iron oxides, *Geophys. J. R. astr. Soc.*, **64**, 767-783, 1981.
- Jackson, I. & H. Niesler, The elasticity of periclase to 3 GPa and some geophysical implications, in *High-Pressure Research in Geophysics* (Adv. Earth Planet. Sci., 12), 93-113, edited by S. Akimoto & M. H. Manghnani,

- 1982.
- Jeanloz, R. & T. J. Ahrens, Equations of state of FeO and CaO, *Geophys. J. R. astr. Soc.*, **62**, 505-528, 1980a.
- Jeanloz, R. & T. J. Ahrens, Anorthite: thermal equation of state to high pressures, *Geophys. J. R. astr. Soc.*, **62**, 529-549, 1980b.
- Jeanloz, R., T. J. Ahrens, H. K. Mao & P. M. Bell, B1-B2 transition in calcium oxide from shock-wave and diamond cell experiments, *Science*, **206**, 829-830, 1980.
- Jeanloz, R. & A. B. Thompson, Phase transitions and mantle discontinuities, *Rev. Geophys. Space Phys.*, **21**, 51-74, 1983.
- Keeler, R. N., Electrical conductivity of condensed media at high pressures, in *Physics of High Energy Density, Proc. Intern. School of Physics "Enrico Fermi," Course XLVII*, pp. 106-125, Academic Press, New York, 1971.
- Kieffer, S. W., Thermodynamics and lattice vibrations of minerals: 3. Lattice dynamics and an approximation for minerals with application to simple substances and framework silicates, *Rev. Geophys. Space Phys.*, **17**, 35-59, 1979.
- Knittle, E. & R. Jeanloz, High-pressure metallization of FeO and implications for the Earth's core, *Geophys. Res. Lett.* **13**, 1541-1544, 1986.
- Kondo, K. E. & T. J. Ahrens, Heterogeneous shock-induced thermal radiation in minerals, *Phys. Chem. Minerals*, **9**, 173-181, 1983.
- Kormer, S. B., Optical study of the characteristics of shock-compressed condensed dielectrics, *Sov. Phys. Uspekhi*, **11**, 229-254, 1968.
- Kormer, S. B., M. V. Sinitsyn, G. A. Kirillov & L. T. Popova, An experimental determination of the light absorption coefficient in shock-compressed NaCl. The absorption and conductivity mechanism, *Sov. Phys.-JETP*, **22**, 97-105, 1966.
- Lieberman, D. A., Self-consistent field electronic structure calculations for

- compressed magnesium oxide, *J. Phys. Chem. Solids*, **39**, 255-257, 1978.
- Lyzenga, G. A., Shock Temperatures of Materials: Experiments and Applications to the High Pressure Equation of State, *Ph.D. Dissertation*, 201 pp., California Institute of Technology, Pasadena, California, 1980.
- Lyzenga, G. A. & T. J. Ahrens, The relation between the shock-induced free-surface velocity and the postshock specific volume of solids, *J. Appl. Phys.*, **49**, 201-204, 1978.
- Lyzenga, G. A. & T. J. Ahrens, Shock temperature measurements in Mg_2SiO_4 and SiO_2 at high pressures, *Geophys. Res. Lett.*, **7**, 141-144, 1980.
- Lyzenga, G. A., T. J. Ahrens & A. C. Mitchell, Shock temperatures of SiO_2 and their geophysical implications, *J. Geophys. Res.*, **88**, 2431-2444, 1983.
- Marsh, S. P., ed., *LASL shock Hugoniot data*, 658 pp., University of California Press, Los Angeles, 1980.
- Mitchell, A. C. & W. J. Nellis, Shock compression of aluminum, copper and tantalum, *J. Appl. Phys.*, **52**, 3363-3374, 1981.
- Press, W. H., B. P. Flannery, S. A. Teukolsky & W. T. Vetterling, *Numerical Recipes: The Art of Scientific Computing*, 818 pp., Cambridge University Press, New York, 1986.
- Rice, W. H., R. G. McQueen & J. M. Walsh, Compressibility of solids by strong shock waves, *Solid State Phys.*, **6**, 1-63, 1958.
- Robie, R. A., B. S. Hemingway & R. J. Fisher, *Thermodynamic properties of minerals and related substances at 298.15 K and 1 bar (10^5 Pascals) pressure and at higher temperatures*, 456 pp., USGS Bulletin 1452, Government Printing Office, Washington, D.C., 1978.
- Roufousse, M. C. & P. G. Klemens, Lattice thermal conductivity of minerals at high temperature, *J. Geophys. Res.*, **79**, 703-705, 1974.
- Schmitt, D. R. & T. J. Ahrens, Emission of shock compressed solids, in *Shock waves in Condensed Matter - 1983*, pp. 313-316, edited by J. R. Asay, R.

- A. Graham & E. K. Straub, Elsevier Science Publishers B.V., 1984.
- Schmitt, D. R., B. Svendsen & T. J. Ahrens, Shock-induced radiation from minerals, in *Shock waves in condensed matter - 1985*, pp. 261-266, edited by Y. M. Gupta, Plenum Press, New York, NY, 1986.
- Schneider, H. & I. Jung, Structural deformation of experimentally shock-loaded periclase (MgO) *Phil. Mag.*, **27**, 140-144, 1982.
- Siegel, R. & J. R. Howell, *Thermal radiation heat transfer*, 862 pp., McGraw-Hill Book Company, New York, 1981.
- Stacey, F., A thermal model of the earth, *Phys. Earth Planet. Int.*, **15**, 341-348, 1977.
- Svendsen, B. & T. J. Ahrens, Thermal history of shock-compressed solids, in *Shock waves in Condensed Matter - 1985*, pp. 607-613, edited by Y. M. Gupta, Plenum Press, New York, NY, 1986.
- Svendsen, B., J. D. Bass & T. J. Ahrens, Optical radiation from shock-compressed interfaces and materials, *High Pressure Research in Geophysics and Geochemistry*, edited by M. H. Manghnani, & Y. Syono, Terra Publishers, Tokyo, in press, 1987 (Chapter I).
- Svet, D. I., *Thermal Radiation: Metals, Semiconductors, Ceramics, Partly Transparent Bodies, and Films*, Consultants Bureau, Plenum Publishing Corporation, New York, 1965.
- Touloukian, Y. S., R. W. Powell, C. Y. Ho & P. G. Klemens, *Thermophysical Properties of Matter, Volume 1: Thermal Conductivity*, Thermophysical Properties Research Center of Purdue University, Data Series, Plenum Publishing Corporation, New York, 1970a.
- Touloukian, Y. S., R. W. Powell, C. Y. Ho & P. G. Klemens, *Thermophysical Properties of Matter, Volume 7: Thermal Radiative Properties, metallic elements and alloys*, Thermophysical Properties Research Center of Purdue University, Data Series, Plenum Publishing Corporation, New York,

1970b.

Touloukian, Y. S., R. W. Powell, C. Y. Ho & P. G. Klemens, *Thermophysical Properties of Matter, Volume 8: Thermal Radiative Properties, nonmetallic solids*, Thermophysical Properties Research Center of Purdue University, Data Series, Plenum Publishing Corporation, New York, 1970c.

Touloukian, Y. S., R. W. Powell, C. Y. Ho & P. G. Klemens, *Thermophysical Properties of Matter, Volume 12: Thermal expansion*, Thermophysical Properties Research Center of Purdue University, Data Series, Plenum Publishing Corporation, New York, 1975.

Urtiew, P. A., Effect of shock loading on transparency of sapphire crystals, *J. Appl. Phys.*, **45**, 3490-3493, 1974.

Urtiew, P. A. & R. Grover, Temperature deposition caused by shock interactions with material interfaces, *J. Appl. Phys.*, **45**, 140-145, 1974.

Vedam, K. & E. D. D. Schmidt, Variation of refractive index of MgO with pressure to 7 kbar, *Phys. Rev.*, **146**, 548-554, 1966.

Weast, R. C., ed., *CRC Handbook of Chemistry and Physics*, 60th edition, CRC Press, 1979.

Chapter III

Shock-Induced Temperatures of $\text{CaMgSi}_2\text{O}_6$ †

Bob Svendsen and Thomas J. Ahrens

Seismological Laboratory,
California Institute of Technology, Pasadena, California, 91125, USA.

† submitted to *Journal of Geophysical Research*

Abstract

Optical radiation from shock-compressed crystal $\text{CaMgSi}_2\text{O}_6$ (diopside) constrains crystal $\text{CaMgSi}_2\text{O}_6$ Hugoniot temperatures of 3500-4800 K in the 150-170 GPa pressure range, while glass $\text{CaMgSi}_2\text{O}_6$, with a density 87% that of crystal $\text{CaMgSi}_2\text{O}_6$, achieves Hugoniot temperatures of 3600-3800 K in the 105-107 GPa pressure range. The radiation history of each of these materials implies that the shock-compressed states of each are highly absorptive, with effective absorption coefficients of $\gtrsim 500\text{--}1000\text{ m}^{-1}$. Calculated Hugoniot states for these materials, when compared to the experimental results, imply that crystal $\text{CaMgSi}_2\text{O}_6$ Hugoniot states in the 150-170 GPa range represent a high-pressure phase (HPP) solid (or possibly liquid) phase with an STP density of $\approx 4100 \pm 200\text{ kg/m}^3$, STP Grüneisen's parameter of $\approx 1.5 \pm 0.5$ and STP HPP-LPP specific internal energy difference, $\Delta e_i^{\beta-\alpha}$, of $0.9 \pm 0.5\text{ MJ/kg}$. These results are consistent with a $\text{CaSiO}_3\text{-MgSiO}_3$ perovskite high-pressure phase assemblage. For glass $\text{CaMgSi}_2\text{O}_6$, we have the same range of HPP properties, except that $\Delta e_i^{\beta-\alpha}$ is $2.3 \pm 0.5\text{ MJ/kg}$, a strong indication that the glass $\text{CaMgSi}_2\text{O}_6$ Hugoniot states occupy the liquid-phase in the system $\text{CaMgSi}_2\text{O}_3$. Comparison of the pressure-temperature Hugoniot of crystal $\text{CaMgSi}_2\text{O}_6$ with the Hugoniots of its constituent oxides (*i.e.*, SiO_2 , CaO and MgO) demonstrates the primary influence of the HPP STP density of these materials on the magnitude of the temperature in their shock-compressed states. The crystal Di pressure-temperature Hugoniot constrained by the experimental results lies at 2500-3000 K between 110 and 135 GPa, within the plausible range of lowermost-mantle temperature profiles.

§1. Introduction

Mg-Fe oxides and/or silicates are currently believed to dominate the composition of the earth's mantle. $\text{CaMgSi}_2\text{O}_6$, which in mineral form is known as diopside, represents one of several pyroxene compositions relevant to investigations of composition of the earth's mantle, and is the only natural pyroxene to form large, transparent single crystals suitable for shock-temperature investigation. The possibility that the earth accreted inhomogeneously (*e.g.*, Turekian and Clark, 1969), or strongly differentiated during core formation implies that certain regions of the mantle, such as D'', may be composed of oxides and/or silicates of much more refractory elements, such as Ca and/or Al. A number of previous static and dynamic experimental efforts (*e.g.*, Liu, 1978, 1979a; Svendsen and Ahrens, 1983; Boslough *et al.*, 1984; Boslough *et al.*, 1986) and modeling efforts (*e.g.*, Ruff and Anderson, 1980) have directly or indirectly addressed this issue. In particular, calculations indicate that $\text{CaMgSi}_2\text{O}_6$ (Di) could be one of the earliest phases to condense out of the solar nebula (Grossman and Larimer, 1974), and so may be a major participant in inhomogeneous accretion. In this paper, we use the shock-induced radiation from Di to constrain its Hugoniot temperature. Combining these constraints with previous work on the mechanical response of Di to shock compression, we place constraints on the pressure-density-temperature equation of state of the high-pressure phase(s) (HPP's) of Di. The high-pressure ($\gtrsim 50\text{-}80$ GPa: Svendsen and Ahrens, 1983) shock-compressed states of crystal Di are likely to represent an assemblage of $\text{CaSiO}_3\text{-MgSiO}_3$ perovskites (Liu, 1979b).

§2. Experimental

We conducted the experiments on a two-stage, light-gas gun (*e.g.*, Jeanloz and Ahrens, 1980a; Figure 2.1). In these, a lexan-encased tantalum (Ta) flyer plate, accelerated to velocities between 4.7 and 6.1 km/sec (Table 5.1),

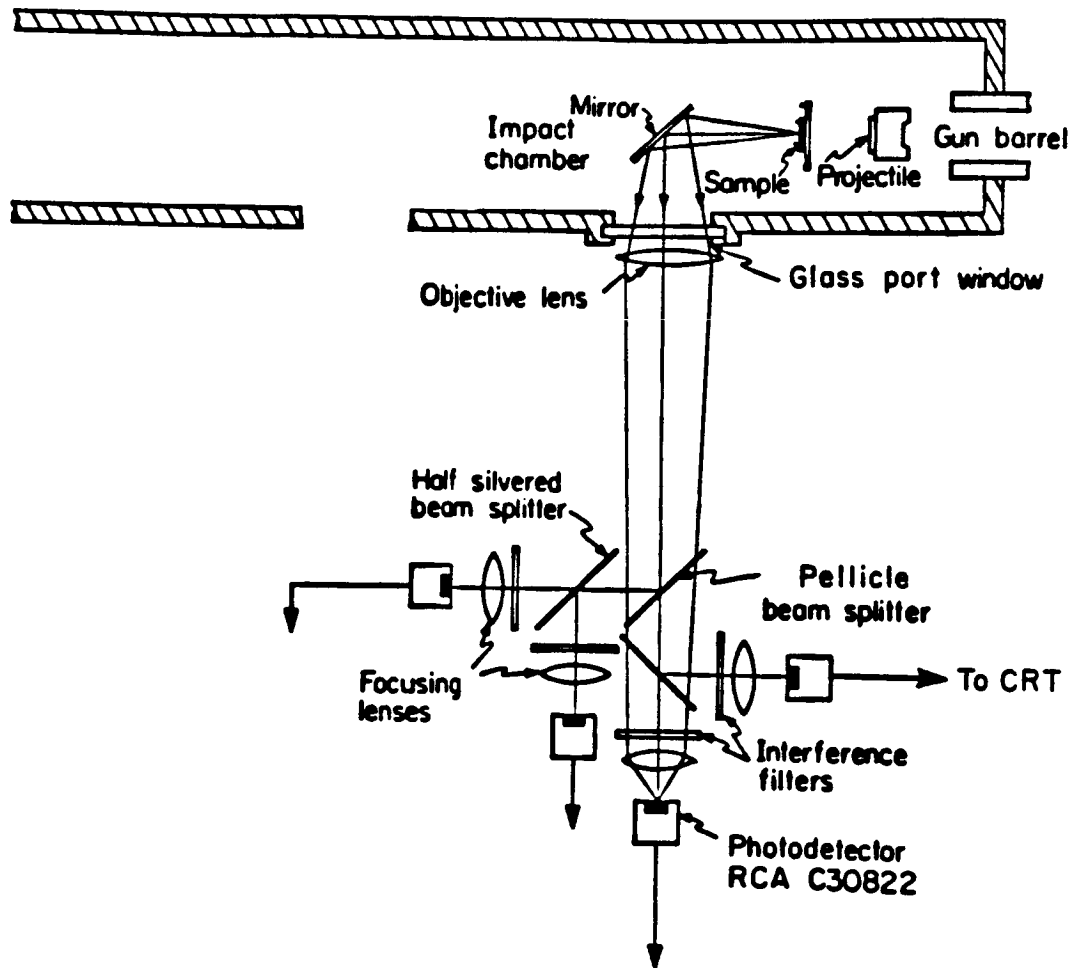


Figure 2.1. Geometry of the light-gas gun radiation experiment after Boslough (1984). The projectile, shot through the barrel, impacts the sample at velocities between 5.7 and 6.4 km/sec. Radiation from the sample is bent 90° by the mirror, travels through the objective lens, and is divided up by the three beam splitter arrangement among the 4 channels of the pyrometer. The resulting signals from the photodiode in each channel are monitored by oscilloscopes and LeCroy transient digital recorders.

impacted a 1.5 mm-thick Ta driver plate in contact with an approximately 2 mm-thick (100)-oriented, transparent crystal Di samples or 4 mm-thick, transparent glass Di samples (Table 5.1). We covered the free surface of the samples with an aluminum mask to avoid observing radiation from the target's edge. Radiation from the target reflects from a mirror, propagates through an objective lens, and is directed by a (dichroic) pellicle beam splitter and two half-silvered beam splitters into 4 detectors filtered at nominal wavelengths of 450, 600, 750 and 900 nm. We recorded the signal from each detector with a Tektronix 485 single-sweep oscilloscope and a LeCroy (model 8081) 100-MHz transient recorder.

The densities of crystal Di samples (Table 5.1) agree well with the ideal value of 3277 kg/m^3 (Robie *et al.*, 1978). This is consistent with the microprobe analyses of our sample materials, given in Table 2.1. The glass Di samples are about 13.6% less dense than the crystal samples; this is consistent with the density of glass Di used, for example, in spectroscopic studies (Binsted *et al.*, 1985).

As in previous studies (*e.g.*, Lyzenga, 1980; Boslough *et al.* 1984), we vapor-deposited 500-1000 nm of silver (Ag) on the sample and then placed the Ag "film" in contact with the Ta driver plate to minimize radiation from an otherwise rough driver plate-sample interface. We expected this Ag film to absorb any radiation from the Ta-Ag interface, heat up much less than a mechanical Ta- $\text{CaMgSi}_2\text{O}_6$ interface (Urtiew and Grover, 1974), and contain no trapped gas that could also contribute to interface radiation (Boslough, 1984).

§3. Data Analysis

Our data set consists of six experiments: four on diopside ($\text{CaMgSi}_2\text{O}_6$, Di) single-crystals (140, 141, 169 and 170, Table 5.1), and two on $\text{CaMgSi}_2\text{O}_6$ (Di) glass (196 and 197, Table 5.1). We record the radiation intensity from the

Table 2.1. Microprobe Analyses of Starting Materials.

Shot	140,141†	169,170‡	196,197§
Na ₂ O	0.38*	0.48	0.01
MgO	17.40	17.63	15.75
Al ₂ O ₃	0.36	0.22	0.03
SiO ₂	55.74	55.32	58.48
CaO	25.15	24.78	26.07
TiO ₂	0.02	0.11	0.00
Cr ₂ O ₃	0.07	0.48	0.00
MnO	0.08	0.04	0.01
FeO	0.82	0.96	0.00
Total	99.97	99.68	100.37
En	48.4	49.0	49.0
Wo	50.3	49.5	51.0
Fs	1.4	1.5	0.0

† Diopside from DeKalb, NY, supplied by S. Huebner, USGS, Reston, VA.

‡ Russian diopside, supplied by Gem Obsessions, San Diego, CA.

§ Diopside glass, supplied by G. Miller, Caltech, and G. Fine, Corning Glass Co.

* weight. %

target as a function of time at the wavelengths stated above. In Figures 3.1 and 3.2, we display examples of these data at 750 nm. The data shown in Figure 3.1 are from crystal Di (shot 141, Table 5.1), while those shown in Figure 3.2 are from glass diopside (shot 197, Table 5.1). These radiation histories are representative of those at all other observed wavelengths and in all other experiments. With the known radiation intensity of a standard lamp (Boslough, 1984) at the observed wavelengths, we transform these raw data into experimental spectral radiation intensities (in the form of spectral radiance) as a function of time. The radiance data for all experiments are listed in Table 3.1.

As stated above, the target consists of a Ta driver-plate, Ag film layer and sample layer. Radiation from the target is first observed when the shock wave compresses the Ag film at the Ag-sample interface (t_0 , Figure 3.1 or 3.2). As shown most clearly in Figure 3.2, the radiation intensity in all experiments rises sharply to a peak value, and then as the shock wave propagates into the sample, the intensity decays almost as quickly to a time-independent magnitude reflecting that of the shocked sample. Since the Ag film is almost certainly much hotter than the sample over the time scale of the experiment (Boslough, 1984; Svendsen and Ahrens, 1987), the strong decay of the initial radiation intensity is most likely due to shock-induced opacity of the shocked sample (Boslough, 1985). With the possible exception of Al_2O_3 (Bass *et al.*, 1987), all initially transparent materials studied so far (*e.g.*, LiF: Kormer, 1968; $\text{CaAl}_2\text{Si}_2\text{O}_8$: Boslough *et al.*, 1986) lose some transparency during shock compression. In the present case, the thermal radiation from Ag at the Ag-sample interface is apparently strongly absorbed by the shocked sample such that observed radiation intensity is quickly dominated by the sample intensity (Boslough, 1985). Hence, we observe a fast decay of the initial high intensity and a subsequent time-independent radiation intensity displayed in Figures 3.1 and 3.2. To demonstrate these considerations from a model viewpoint, we

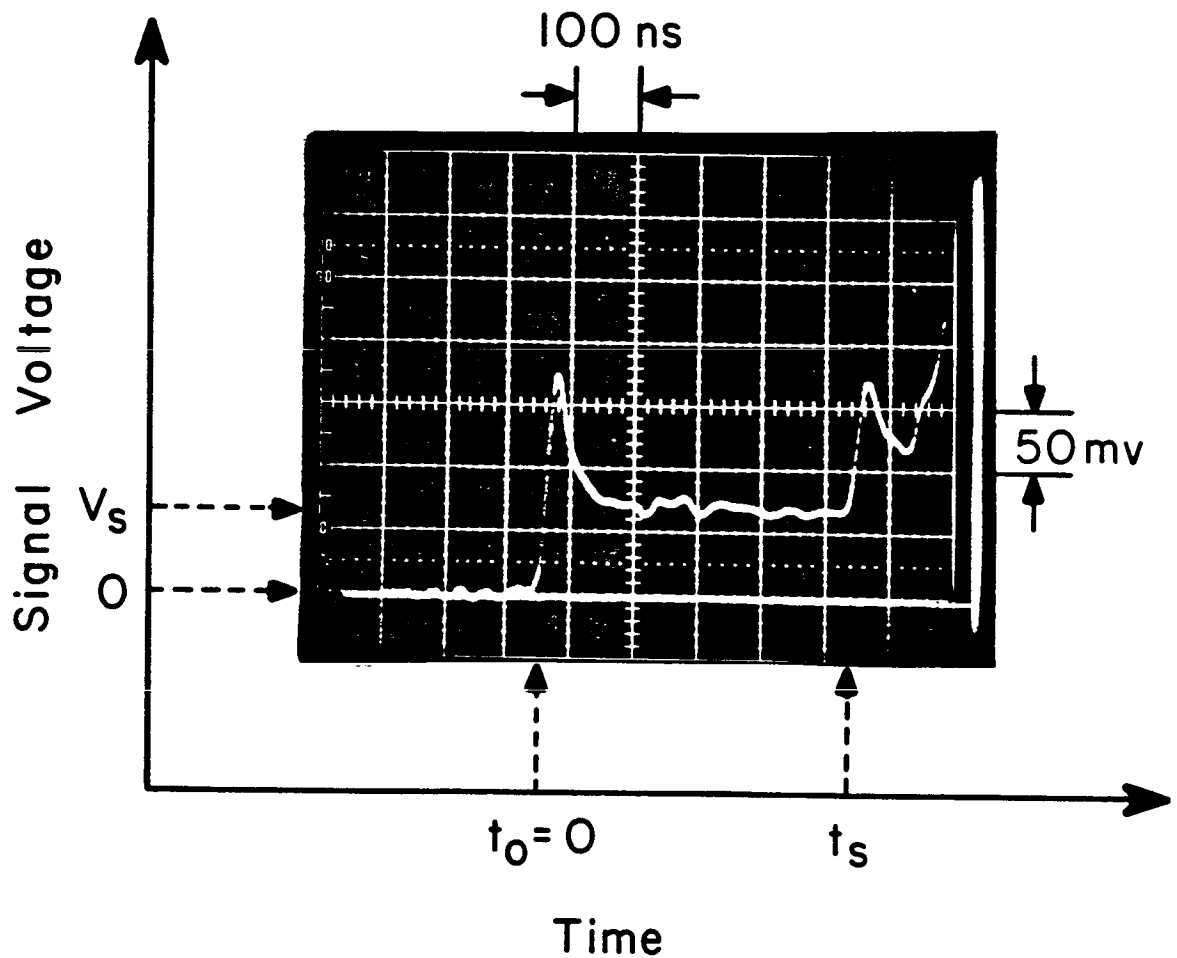


Figure 3.1 Radiation intensity versus time record for shot 197 on diopside glass at 750 nm. The time $t=0$ marks the arrival of the shock-front at the Ag-Di interface, while t_s marks the point in the radiation history (with intensity V_s) used to determine spectral radiance of glass Di at this wavelength.

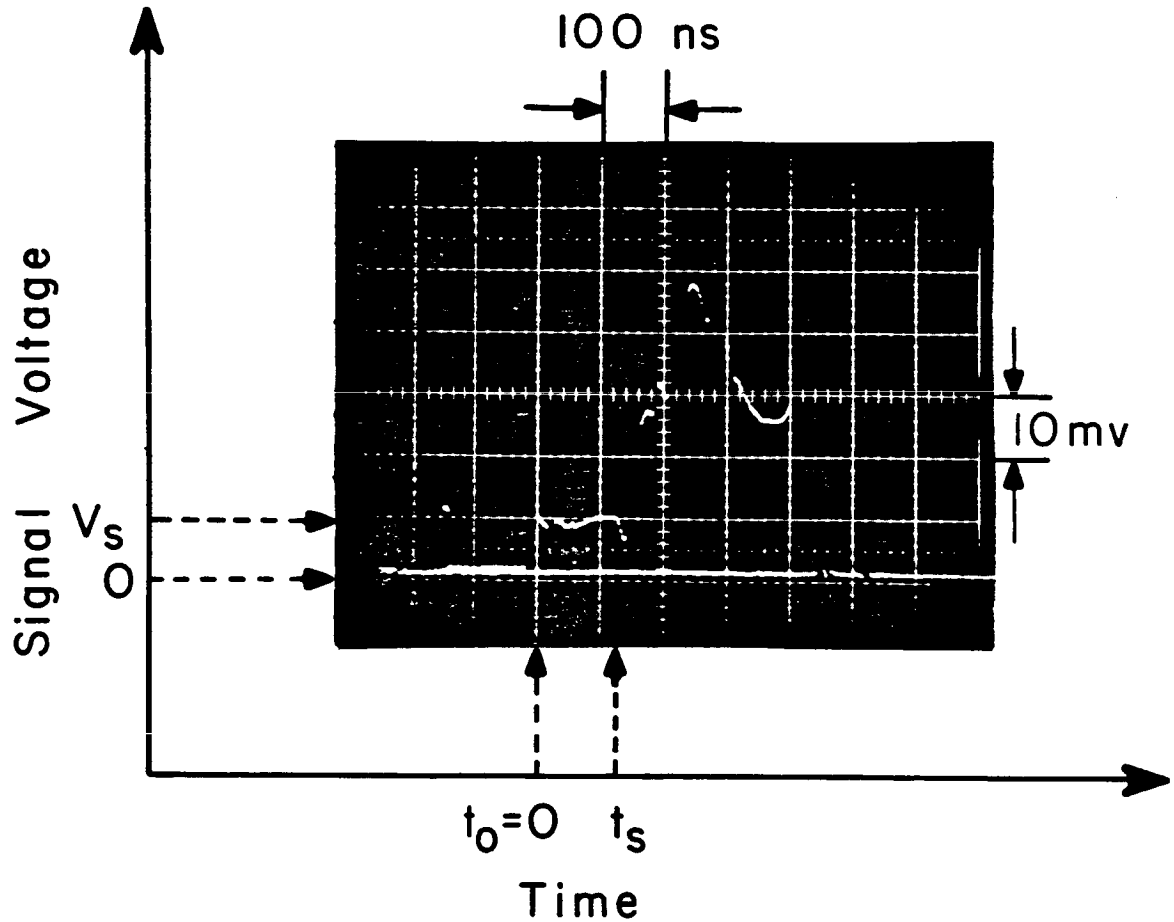


Figure 3.2. Radiation intensity at 750 nm versus time record for shot 141 on diopside single-crystal. Duration of sample radiation intensity is much shorter than that of glass experiment shown in Figure 3.1 because crystal sample is thinner (Table 5.1).

Table 3.1. Radiation Data and Fits.

Shot	Spectral Radiance (kW/m ² ·sr·nm)				Fits				
	450 (nm)	600 (nm)	750 (nm)	900 (nm)	Parameter(t _r)	Wien	GS†	LM‡	GS (ε _{fit} =1)
140		3.15 (0.59)	3.09 (0.45)	2.87 (0.81)	$\hat{\epsilon}_{\text{exp}}$ (140 ns)	0.65 (0.37)	0.59 (0.37)	0.56 (0.23)	
					T _{exp} (140 ns)	4152 (351)	4215 (364)	4270 (356)	3803 (293)
					χ^2	0.14	0.06	0.06	0.05
141	6.14 (1.21)	5.38 (1.00)	6.06 (0.77)	5.71 (0.93)	$\hat{\epsilon}_{\text{exp}}$ (145 ns)	0.71 (0.34)	0.65 (0.34)	0.75 (0.11)	
					T _{exp} (145 ns)	4737 (346)	4782 (356)	4643 (153)	4372 (297)
					χ^2	3.44	3.13	3.05	3.55
169	5.11 (0.18)	6.58 (0.31)	6.53 (0.33)	5.49 (0.31)	$\hat{\epsilon}_{\text{exp}}$ (198 ns)	0.91 (0.27)	0.86 (0.27)	0.86 (0.18)	
					T _{exp} (198 ns)	4522 (263)	4552 (268)	4555 (178)	4428 (251)
					χ^2	0.30	0.21	0.21	0.48
170	0.82 (0.13)	1.56 (0.17)	2.34 (0.26)	2.29 (0.26)	$\hat{\epsilon}_{\text{exp}}$ (170 ns)	1.01 (0.25)	1.04 (0.25)	1.06 (0.17)	
					T _{exp} (170 ns)	3539 (143)	3508 (141)	3498 (90)	3539 (143)
					χ^2	1.61	1.43	1.42	1.52
196	1.35 (0.48)	2.14 (0.33)	2.96 (0.42)	3.24 (0.51)	$\hat{\epsilon}_{\text{exp}}$ (485 ns)	1.09 (0.44)	1.23 (0.44)	1.63 (0.26)	
					T _{exp} (485 ns)	3695 (243)	3585 (231)	3422 (100)	3711 (247)
					χ^2	1.99	1.20	1.03	1.72
197	1.37 (0.41)	3.18 (0.39)	3.46 (0.50)	3.74 (0.56)	$\hat{\epsilon}_{\text{exp}}$ (475 ns)	1.51 (0.39)	1.51 (0.39)	1.38 (0.22)	
					T _{exp} (475 ns)	3610 (208)	3610 (208)	3663 (96)	3866 (239)
					χ^2	0.50	0.50	0.46	1.23

† - Golden section search fit. Uncertainties represent experimentally-based uncertainties, and this fit is unweighted.

‡ - Levenberg-Marquardt fit. Uncertainties represent standard deviations of corresponding fit, and this is a weighted fit.

represent the observed radiation intensity, $I_{\lambda\text{exp}}(\lambda, t)$, in terms of a model intensity, $I_{\lambda\text{mod}}(\lambda, t)$, as a function of wavelength (λ), and time after the onset of radiation from the target, t , *i.e.*,

$$I_{\lambda\text{mod}}(\lambda, t) = \hat{\epsilon}_{\lambda\text{I}}(t) I_{\lambda\text{pl}}[\lambda, T_{\text{I}}(t)] + \hat{\epsilon}_{\lambda\text{S}}(t) I_{\lambda\text{pl}}(\lambda, T_{\text{S}}) \quad [3.1].$$

In [3.1], T_{S} is the shock-compressed (Hugoniot) sample (S) temperature assumed homogeneous, uniform and constant, and $T_{\text{I}}(t)$ is the temperature of Ag at the Ag-sample interface (I), which may be time-dependent (Grover and Urtiew, 1974). Further,

$$\hat{\epsilon}_{\lambda\text{I}}(t) \equiv [1-r_{\lambda\text{FS}}] \tau_{\lambda\text{US}}(t) [1-r_{\lambda\text{SF}}] \tau_{\lambda\text{S}}(t) [1-r_{\lambda\text{INT}}] \quad [3.2]$$

$$\hat{\epsilon}_{\lambda\text{S}}(t) \equiv [1-r_{\lambda\text{FS}}] \tau_{\lambda\text{US}}(t) [1-r_{\lambda\text{SF}}] [1+r_{\lambda\text{INT}} \tau_{\lambda\text{S}}(t)] [1-\tau_{\lambda\text{S}}(t)] \quad [3.3]$$

are the effective normal spectral emissivities of the Ag at the Ag-sample interface and shocked sample, respectively, while $r_{\lambda\text{FS}}$, $r_{\lambda\text{SF}}$ and $r_{\lambda\text{INT}}$ are the effective normal spectral reflectivities of the unshocked sample (US) free-surface, shock front and Ag-sample interface, respectively. Also,

$$\tau_{\lambda\text{US}}(t) \equiv \exp[-a_{\lambda\text{US}}^* (1-t/t_{\text{exp}})] \quad [3.4]$$

and

$$\tau_{\lambda\text{S}}(t) \equiv \exp[-a_{\lambda\text{S}}^* t/t_{\text{exp}}] \quad [3.5]$$

are the effective normal spectral transmissivities of unshocked sample and shocked sample layers, respectively. In [3.4] and [3.5], $a_{\lambda\text{US}}^*$ and $a_{\lambda\text{S}}^*$ are nondimensional forms of the effective normal spectral coefficients of absorption in the unshocked and shocked samples, respectively, given by

$$a_{\lambda\text{S}}^* \equiv a_{\lambda\text{S}} (U-v_{\text{S}}) t_{\text{exp}} \quad [3.6]$$

and

$$a_{\lambda\text{US}}^* \equiv a_{\lambda\text{US}} U t_{\text{exp}} \quad [3.7].$$

Note that $t_{\text{exp}} \equiv d/U$ is the experimental time scale, U is the shock wave velocity in the sample, d is the initial thickness of the sample layer in the target, and v_s is the shock-induced material velocity of the shocked sample. Lastly, we have

$$I_{\lambda\text{pl}}(\lambda, T) \equiv \frac{C_1}{\lambda^5 [e^{C_2/\lambda T} - 1]}$$

(with $C_1 \equiv 1.19088 \times 10^{-16} \text{W} \cdot \text{m}^2$ and $C_2 \equiv 1.4388 \times 10^{-2} \text{m} \cdot \text{K}$) as the Planck function.

If we assume the shocked sample is strongly absorptive, we have $a_{\lambda s}^* \gtrsim 1$ or $a_{\lambda s} \gtrsim 1/(d - v_s t_{\text{exp}})$ from [3.6], and so $\tau_{\lambda s}(t) \sim 0$ from [3.5]. In this case, $\hat{\epsilon}_{\lambda s}(t) \sim 0$ from [3.2], and

$$\hat{\epsilon}_{\lambda s}(t) \rightarrow \hat{\epsilon}_{\lambda s} \equiv (1 - r_{\lambda\text{FS}})(1 - r_{\lambda\text{SF}}) \quad [3.8]$$

from [3.3]. Note that $\hat{\epsilon}_{\lambda s}$ is then time-independent. Putting these results into [3.1], we have

$$I_{\lambda\text{mod}}(\lambda, t) \rightarrow I_{\lambda\text{mod}}(\lambda) \approx (1 - r_{\lambda\text{FS}})(1 - r_{\lambda\text{SF}}) I_{\lambda\text{pl}}(\lambda, T_s) = \hat{\epsilon}_{\lambda s} I_{\lambda\text{pl}}(\lambda, T_s) \quad [3.9],$$

which represents a constant radiation intensity at a given wavelength, as observed in the data (Figures 3.1 and 3.2). The minimum values of $a_{\lambda s}$ required by the condition $a_{\lambda s} \gtrsim 1/(d - v_s t_{\text{exp}})$ may be calculated from the experimental parameters listed in Table 3.1. We list the results of this calculation in Table 3.1, where we see that, for crystal Di, $a_{\lambda s} \gtrsim 700\text{--}1100 \text{ m}^{-1}$, while for glass Di, we have $a_{\lambda s} \gtrsim 420 \text{ m}^{-1}$.

As the shock wave reaches the free surface of the unshocked sample (t_s in Figure 3.1 or 3.2), the radiation intensity again becomes transient, and the experiment is over. Since we want to infer the shock-compressed temperature of the sample from the shock-induced sample radiation, and since [3.9] is most likely valid for $t \approx t_{\text{exp}}$, we use the magnitude of the radiation intensity at t_{exp} (Table 3.1, just prior to t_s , Figure 3.1 or 3.2) and each wavelength to

constrain the temperature of the shocked sample. Assuming the spectral reflectivities $r_{\lambda_{FS}}$ and $r_{\lambda_{SF}}$ are independent of wavelength, [3.9] is analogous to the greybody relation, *i.e.*,

$$I_{\lambda_{gb}}(\lambda, t_{\text{exp}}) \equiv \hat{\epsilon}_{\text{fit}}(t_{\text{exp}}) I_{\lambda_{pl}}(\lambda, T_{\text{fit}}) \quad [3.10].$$

Comparing [3.9] and [3.10], we see that $\hat{\epsilon}_{\text{fit}}(t_{\text{exp}})$ should constrain the value of $(1-r_{\lambda_{FS}})(1-r_{\lambda_{SF}})$. The value of t_{exp} reflects the calculated shock-wave transit time through the sample, but is not critically dependent on this choice (Svendsen and Ahrens, 1987) as long as the optical parameters of the unshocked material (*e.g.*, $a_{\lambda_{US}}$) are not strongly wavelength-dependent. At t_{exp} , then we measure the spectral radiance at 4 wavelengths (450, 600, 750 and 900 nm), and we may fit $I_{\lambda_{gb}}(\lambda, t_{\text{exp}})$ to these data via the χ^2 statistic (*e.g.*, Press *et al.*, 1986). In this case, it is given by

$$\begin{aligned} \chi^2(t_{\text{exp}}) &= \chi^2[t_{\text{exp}}; \hat{\epsilon}_{\text{fit}}, T_{\text{fit}}] \\ &\equiv \sum_{\lambda} \left\{ \frac{1}{[\sigma(\lambda)]^2} \{ I_{\lambda_{\text{exp}}}(\lambda, t_{\text{exp}}) - \hat{\epsilon}_{\text{fit}}(t_{\text{exp}}) I_{\lambda_{pl}}[\lambda, T_{\text{fit}}(t_{\text{exp}})] \}^2 \right\} [3.11], \end{aligned}$$

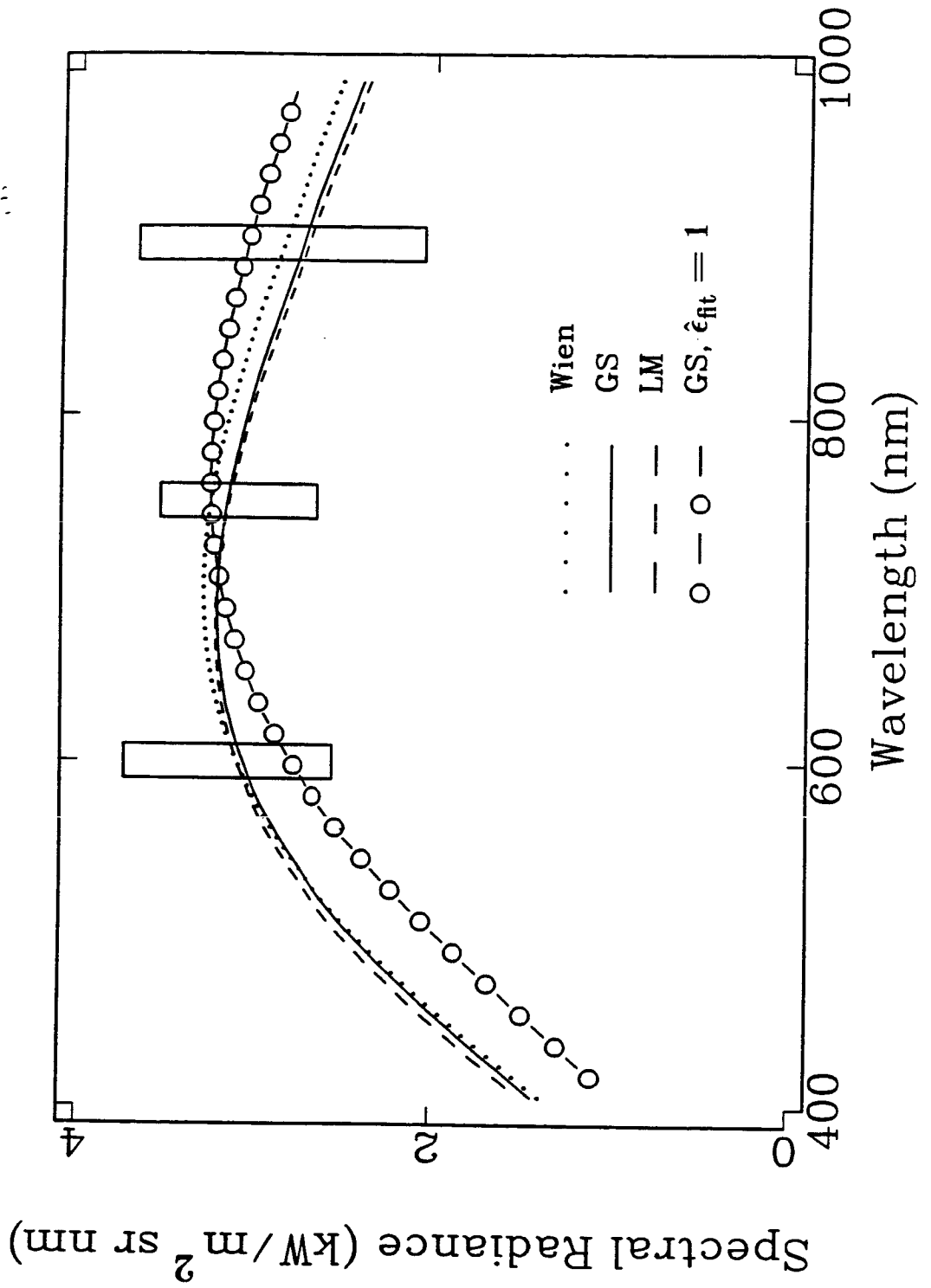
where $\sigma(\lambda)$ are the experimental uncertainties at each wavelength. On this basis, $\hat{\epsilon}_{\text{exp}}(t_{\text{exp}})$ and $T_{\text{exp}}(t_{\text{exp}})$ represent the values of $\hat{\epsilon}_{\text{fit}}(t_{\text{exp}})$ and $T_{\text{fit}}(t_{\text{exp}})$ that minimize $\chi^2(t_{\text{exp}})$; in light of [3.8] and [3.9], this implies that $\hat{\epsilon}_{\text{exp}} = \hat{\epsilon}_{\lambda_S}$ and $T_{\text{exp}} = T_S$. Since the fit is an average over λ , the value of $\hat{\epsilon}_{\text{exp}}$ represents a λ -average of $\hat{\epsilon}_{\lambda_S}$. Since χ^2 is a nonlinear functional of temperature, we find its minimum numerically using 1) Golden section (GS) search, and 2) the method of Levenberg as formulated by Marquardt (LM). See, for example, Press *et al.* (1986), for details on both of these methods. To obtain starting values of $\hat{\epsilon}_{\text{fit}}(t)$ and $T_{\text{fit}}(t)$ for the nonlinear fit, we use Wien's approximation to $I_{\lambda_{pl}}(\lambda, T)$ in $\chi^2(t_{\text{exp}})$ which follows from $I_{\lambda_{pl}}(\lambda, T)$ in the limit $\exp(C_2/\lambda T) \gg 1$, *i.e.*,

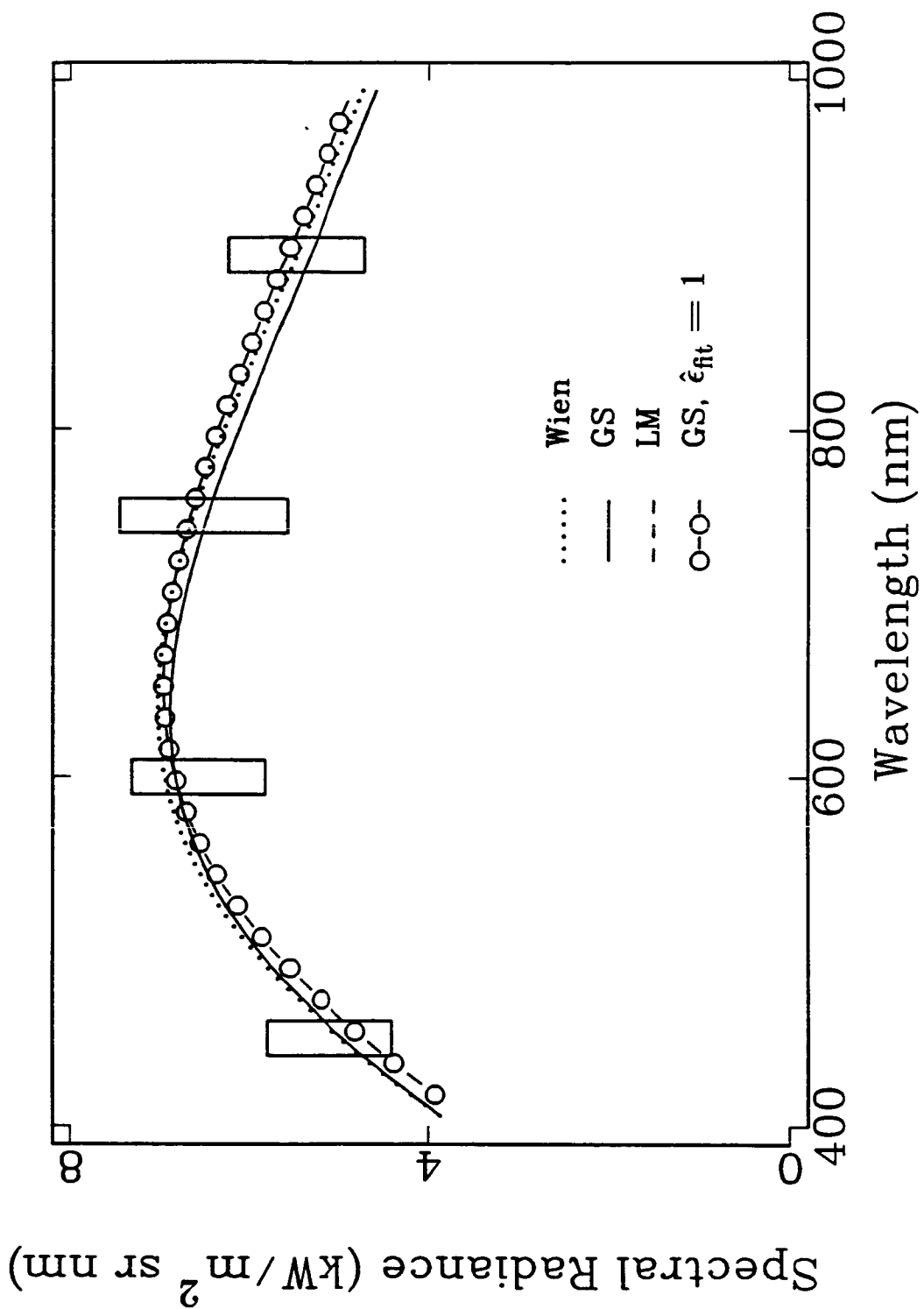
$$I_{\lambda_{wgb}}(\lambda, t) \equiv \hat{\epsilon}_{\text{fit}}(t) I_{\lambda_{wi}}(\lambda, t) = \hat{\epsilon}_{\text{fit}}(t) \frac{2C_1}{\lambda^5} e^{-C_2/\lambda T_{\text{fit}}(t)} \quad [3.12].$$

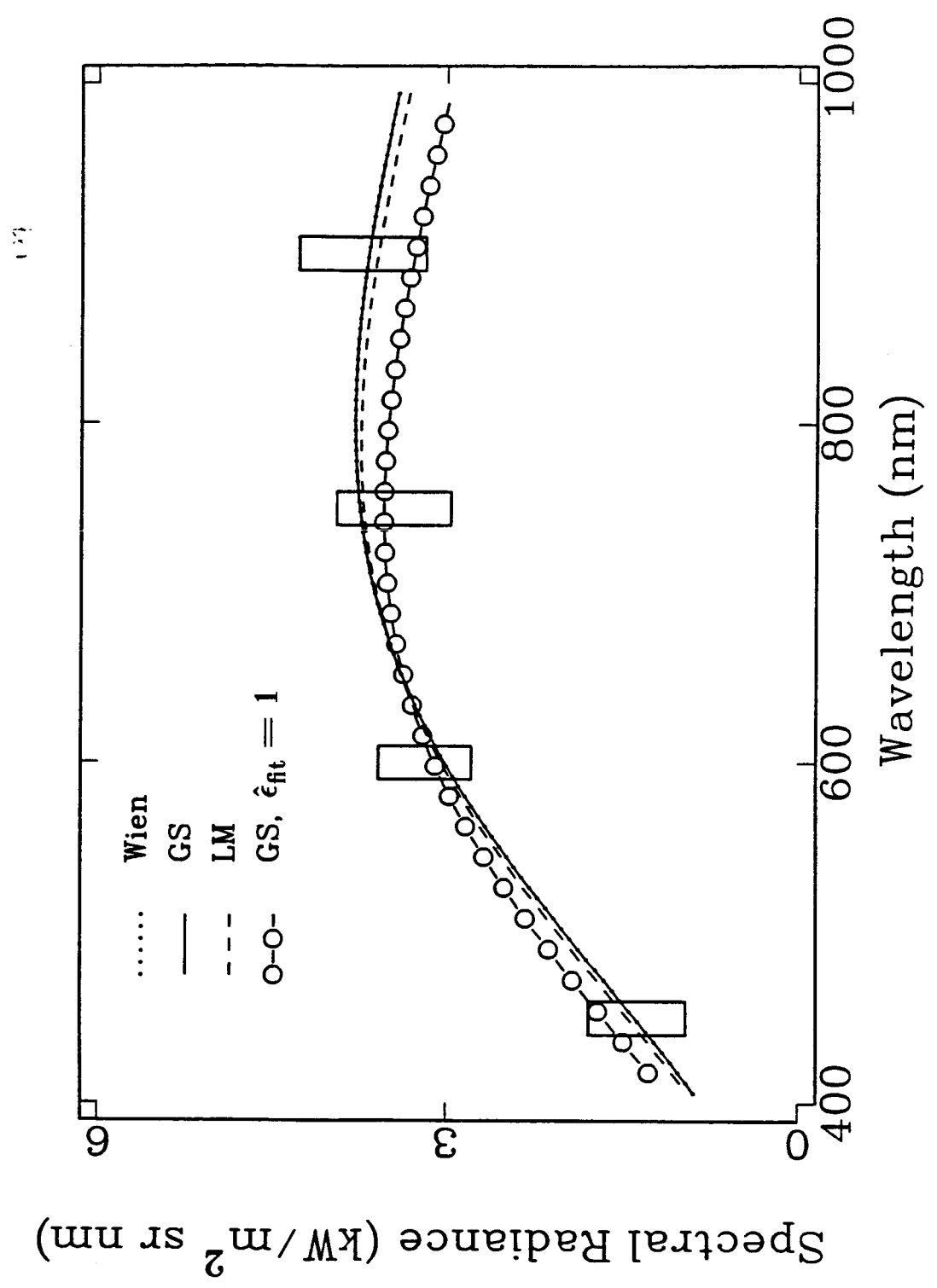
We fit Wien's relation to the data via linear least-squares, and solve for $\hat{\epsilon}_{\text{fit}}(t_{\text{exp}})$ and $T_{\text{fit}}(t_{\text{exp}})$.

We present the results of the greybody fit for the six experiments in Table 3.1, and we plot these results in Figures 3.3a-c. We note that, with 3 or 4 data points and 2 parameters in each of these fits, a χ^2 value of ~ 2 is representative of a "good" fit; this value is very sensitive to measurement uncertainties, as can be seen from [3.10]. In this case, the values of χ^2 in Table 3.1 imply that we may have overestimated measurement uncertainties. Also, note that T_{exp} is much less sensitive to uncertainties than $\hat{\epsilon}_{\text{exp}}$, given the form of $I_{\lambda\text{gb}}$ (Svendsen and Ahrens, 1987). In Table 3.1, the uncertainties quoted with the GS fits represent measurement uncertainties mapped into uncertainties for $\hat{\epsilon}_{\text{exp}}(t_{\text{exp}})$ and $T_{\text{exp}}(t_{\text{exp}})$ (Boslough *et al.*, 1986). However, the uncertainty quoted with each LM fit is the standard deviation of that fit. Note that the GS and LM fits for shot 196, and the Wien, GS and LM fits for shot 197, give $\hat{\epsilon}_{\text{exp}}$ well above unity, which is an unphysical result. As noted by Boslough *et al.* (1986), however, $\hat{\epsilon}_{\text{fit}}$ is much more sensitive to data scatter, whether due to uncorrected λ -dependences in the data, or experimental measurement errors. As can be seen from the corresponding GS fits where $\hat{\epsilon}_{\text{fit}}$ is set equal to one, the variable $\hat{\epsilon}_{\text{fit}}$ fits for shots 196 and 197 may then underestimate the value of T_{exp} by ~ 200 K. Also note that the value of $\hat{\epsilon}_{\text{exp}}$ for all experiments and all fits is $\gtrsim 0.1$, which implies that we are observing relatively homogeneous radiation from the sample, as opposed to localized, "shear-band" radiation seen in many shock-compressed oxides and silicates at lower ($\lesssim 70$ GPa) pressure (*e.g.*, Kondo and Ahrens, 1983; Schmitt *et al.*, 1986). Although the constraint is very poor, we note that, from the identification $(1-r_{\lambda\text{FS}})(1-r_{\lambda\text{SF}}) \approx \hat{\epsilon}_{\text{exp}}$, as discussed above, $r_{\lambda\text{SF}} \sim 0.1$ with $r_{\lambda\text{FS}} \sim 0.1$, for shots 140 and 141, at least.

Figure 3.3. Spectral radiance versus wavelength and greybody fits constraining $\hat{\epsilon}_{\text{exp}}(t_{\text{exp}})$ and $T_{\text{exp}}(t_{\text{exp}})$ for shot 140 data. The size of the data rectangles represents the experimental uncertainty. The data and fits in parts (a), (b), and (c) are from shots 140, 169 and 197, respectively.







§4. Hugoniot Calculations and Comparison with Data

We calculate the density, ρ_H and pressure, P_H of the shock-compressed Di states, from an impedance match (Rice *et al.*, 1958) between the target components assuming a linear shock velocity, U , material velocity, v , relation, *i.e.*, $U = a_i + b_i v$. For Ta, we use $\rho_i^\alpha = 16675 \text{ kg/m}^3$, $a_i = 3290 \text{ m/s}$ and $b_i = 1.31$ (Mitchell and Nellis, 1981), while for Ag, we use $\rho_i^\alpha = 10501 \text{ kg/m}^3$, $a_i = 3270 \text{ m/s}$ and $b_i = 1.55$ (Marsh, 1980). We assume that the U - v relation for crystal Di, which is experimentally constrained to 100 GPa (Svendsen and Ahrens, 1983) is valid to 170 GPa (Table 4.1). Since there are no U - v data for glass Di, we must estimate the U - v coefficients for glass Di, a_{ig} and b_{ig} , from those of the corresponding crystal material, a_{ic} and b_{ic} . With a_{ig} and b_{ig} , we may calculate the impedance match for glass Di targets, and so estimate the experimental glass Di Hugoniot states. Since the U - v relation represents a Taylor's series expansion of $U(v)$ about the initial state $v=0$, a_i and b_i are defined by

$$a_i \equiv \lim_{v \rightarrow 0} \left\{ U^2 \right\}^{1/2} \quad [4.1]$$

$$b_i \equiv \lim_{v \rightarrow 0} \left\{ \frac{dU}{dv} \right\} \quad [4.2].$$

Now, we may connect U and v to P_H via the relations

$$U^2 = \frac{1}{\rho_i^\alpha \eta_H} [P_H - P_i] \quad [4.3]$$

and

$$v^2 = \frac{\eta_H}{\rho_i^\alpha} [P_H - P_i] \quad [4.4].$$

Using [4.1] and [4.2] in [4.3] and [4.4], and noting that the limit $\rho_H \rightarrow \rho_i^\alpha$ is equivalent to $v \rightarrow 0$, we obtain

Table 4.1. Standard Temperature and Pressure (STP) Parameters.

Property	Symbol	Ta	Ag	CaMgSi ₂ O ₆	Units
Density	ρ	16676 ^a	10501 ^a	3277 ^a	kg/m ³
Intercept, U-v relation†	a	3290 ^b	3270 ^c	5620 ^d	m/s
Slope, U-v relation	b	1.307 ^b	1.55 ^c	1.27 ^d	
Bulk modulus	K_S	180.8 ^e	109.6 ^e	103.5 ^e	GPa
$(\partial K_S / \partial P)_S$	K'_S	4.23 ^f	5.20 ^f	4.08 ^f	
Coefficient of thermal expansion	α	1.8 ^g	5.7 ^g	3.2 ^h	$\times 10^{-5} \text{ K}^{-1}$
Specific heat at constant pressure	c_P	140.2 ^a	235.5 ^a	769.0 ^a	J/kg·K
Grüneisen's parameter	γ	1.4 ⁱ	2.5 ⁱ	1.3 ⁱ	
Melting temperature	T_M	3287 ^a	1234 ^a	1664 ^a	K
Elastic Debye temperature	θ_D	263.8 ^j	226.4 ^j	654 ^k	K

^a Robie *et al.* (1978).

^b Mitchell and Nellis (1981).

^c Marsh (1980).

^d Svendsen and Ahrens (1983).

^e Calculated assuming $K_S = \rho a^2$.

^f Calculated with $K'_S = 4b - 1$.

^g Touloukian *et al.* (1975).

^h Stebbins *et al.* (1983).

ⁱ Calculated from $\gamma = \alpha K_S / \rho c_P$.

^j Alers (1965).

^k Kieffer (1979).

† i.e., $U = a + bv$

$$a_i = \left\{ \lim_{\rho_H \rightarrow \rho_i^\alpha} \left(\frac{dP_H}{d\rho_H} \right) \right\}^{1/2} \quad [4.5]$$

and

$$b_i = \frac{1}{4} \left\{ 1 + \lim_{\rho_H \rightarrow \rho_i^\alpha} \left\{ \frac{d \ln B_H}{d \ln \rho_H} \right\} \right\} \quad [4.6]$$

with

$$B_H \equiv \rho_H \left\{ \frac{dP_H}{d\rho_H} \right\} \quad [4.7].$$

We relate glass and crystal Di Hugoniot states at the same density, occupying the same phase, via the relation (Appendix A)

$$P_{gH}(\rho_H) = \frac{(1-\phi)[1-(1+\frac{1}{2}\gamma_H)\eta_{cH}]}{[1-(1+\frac{1}{2}\gamma_H)\eta_{gH}]} P_{cH} + \gamma_H \frac{\frac{1}{2}\phi P_i + \rho_{ig}^\alpha \Delta e_i^{c-g}}{[1-(1+\frac{1}{2}\gamma_H)\eta_{cH}]} \quad [4.8].$$

Relation [4.8] depends on the assumption that γ , the equilibrium thermodynamic Grüneisen's parameter, is a function of density alone. In [4.8], $\gamma_H \equiv \gamma(\rho_H)$, $\eta_{gH} \equiv 1 - \rho_{ig}^\alpha / \rho_H$ is the relative compression of the glass, $\eta_{cH} \equiv 1 - \rho_{ic}^\alpha / \rho_H$ is the relative compression of the crystal, $\phi \equiv 1 - \rho_{ig}^\alpha / \rho_{ic}^\alpha$ is the "porosity," and $\Delta e_i^{c-g} \equiv e(\rho_{ic}^\alpha, s_{ic}^\alpha) - e(\rho_{ig}^\alpha, s_{ig}^\alpha)$ is the difference in specific internal energy between the glass and crystal in the low pressure phase at T_i and P_i . Further, P_{gH} is the pressure of the glass Hugoniot state, P_{cH} is the pressure of the crystal Hugoniot state, ρ_{ig}^α and s_{ig}^α are the initial glass density and specific entropy, and ρ_{ic}^α and s_{ic}^α are the initial crystal density and specific entropy. Since relations [4.1]-[4.7] are valid for any "hydrodynamic" starting material, we have

$$a_{ig} = \lim_{\rho_H \rightarrow \rho_{ig}^\alpha} \left(\frac{dP_{gH}}{d\rho_H} \right)^{1/2} \quad [4.9]$$

$$b_{ig} = \frac{1}{4} \left\{ 1 + \lim_{\rho_H \rightarrow \rho_{ig}^\alpha} \left\{ \left(\frac{d \ln B_{gH}}{d \ln \rho_H} \right) \right\} \right\} \quad [4.10]$$

for glass Di, with P_{gH} given by [4.8]. Note that [4.7] relates the density derivatives of P_{gH} to those of P_{cH} , which we obtain from (McQueen *et al.*, 1967)

$$P_{cH} = P_i + \frac{\rho_{ic}^\alpha a_{ic}^2 \eta_{cH}}{(1 - b_{ic} \eta_{cH})^2} \quad [4.11].$$

the so-called shock wave equation-of-state. So, via [4.8]-[4.10], we may calculate a_{ig} and b_{ig} as functions of ρ_{ig}^α , ρ_{ic}^α , a_{ic} and b_{ic} . These then allow us to calculate an impedance match for targets containing glass Di as the sample material, and obtain an estimate of the glass Di P_H , ρ_H state. We also use [4.8] to estimate the $\rho_H(P_{gH})$ and so $T_H(P_{gH})$ via [4.12] below.

The temperature of a singly shock-compressed material, T_H , may be estimated from an equilibrium thermodynamic energy balance (*e.g.*, McQueen *et al.*, 1967; Ahrens *et al.*, 1969; Jeanloz and Ahrens, 1980b; Chapter I, §4) in which we assume the material compresses adiabatically, and as an elastic fluid. On this basis, if we compress a material from an initial state (P_i, T_i) to a shock-compressed state (P_H, T_H), assuming the material undergoes a phase transition from a low-pressure phase, α , to a high pressure phase, β , the Hugoniot temperature of the β -phase, T_H , may be written

$$T_H = T_{s_i} + \frac{1}{c_v} \left\{ \frac{1}{2} \left\{ \frac{1}{\rho_i^\alpha} - \frac{1}{\rho_H} \right\} P_H - [\Delta e_{s_i} + \Delta e_i^{\beta-\alpha}] \right\} \quad [4.12],$$

with $\eta_H \equiv 1 - \rho_i^\alpha / \rho_H$ being the relative compression. To write [4.12], we assume that c_v , the specific heat at constant volume of the shock-compressed state, is independent of temperature, which is justified *a posteriori* by our results below. The subscripts "i", "H", "S" and "V" designate initial, shock-compressed, constant entropy and constant volume states of the material, respectively. Note that all quantities in [4.12], and the expressions to follow, apply to the high-

pressure phase, β , unless otherwise designated. In [4.12], $\Delta e_i^{\beta-\alpha}$ is the difference in specific internal energy between the two phases at T_i and P_i , Δe_{s_i} is the change in specific internal of β compressed isentropically (at specific entropy s_i) from its density at STP, ρ_i , to a density ρ_H (that of the shock-compressed state), while T_s is the temperature of the material along the isentrope referenced to s_i and ρ_i . Also, P_H is the pressure of the shock-compressed state.

The temperature, T_s , along the compression isentrope may be estimated from γ via the relation

$$T_s = T(s_i, \rho_H) \equiv T_i \exp \left\{ \gamma(\rho_i) \left[1 - \frac{\rho_i}{\rho_H} \right] \right\} \quad [4.13],$$

since we assume $\gamma\rho$ is constant in all model calculations. Lastly, we estimate Δe_{s_i} from the same energy balance used to obtain [4.12], the expression for T_H (Chapter I, §4).

Since we usually have values for ρ_{ig}^α , ρ_{ic}^α , a_{ic} and b_{ic} *a priori*, and we can estimate a_{ig} and b_{ig} as discussed above, we use these to calculate impedance matches for targets containing crystal and glass Di. The impedance match gives us $\rho_{ch}P_{ch}$ and $\rho_{gh}P_{gh}$. With these, we have $T_{ch}(P_{ch})$ and $T_{gh}(P_{gh})$ from [4.12], given estimates of r_i , γ and c_v for β , as well as $\Delta e_i^{\beta-\alpha}$ ($\Delta e_i^{\beta-\alpha} + \Delta e_i^{c-g}$ for the glass). Requiring $P_{gh} \rightarrow P_i$ as $\rho_H \rightarrow \rho_{ig}^\alpha$, we have Δe_i^{c-g} from [4.12], *i.e.*,

$$\Delta e_i^{c-g} = \frac{1}{\rho_{ig}^\alpha \gamma_{ig}} \left\{ \left(1 - \frac{1}{2} \gamma_{ig} \phi \right) P_i - (1-\phi) \left[1 - \left(1 + \frac{1}{2} \gamma_{ig} \right) \eta_{cg} \right] P_{ch}(\rho_{ig}^\alpha) \right\},$$

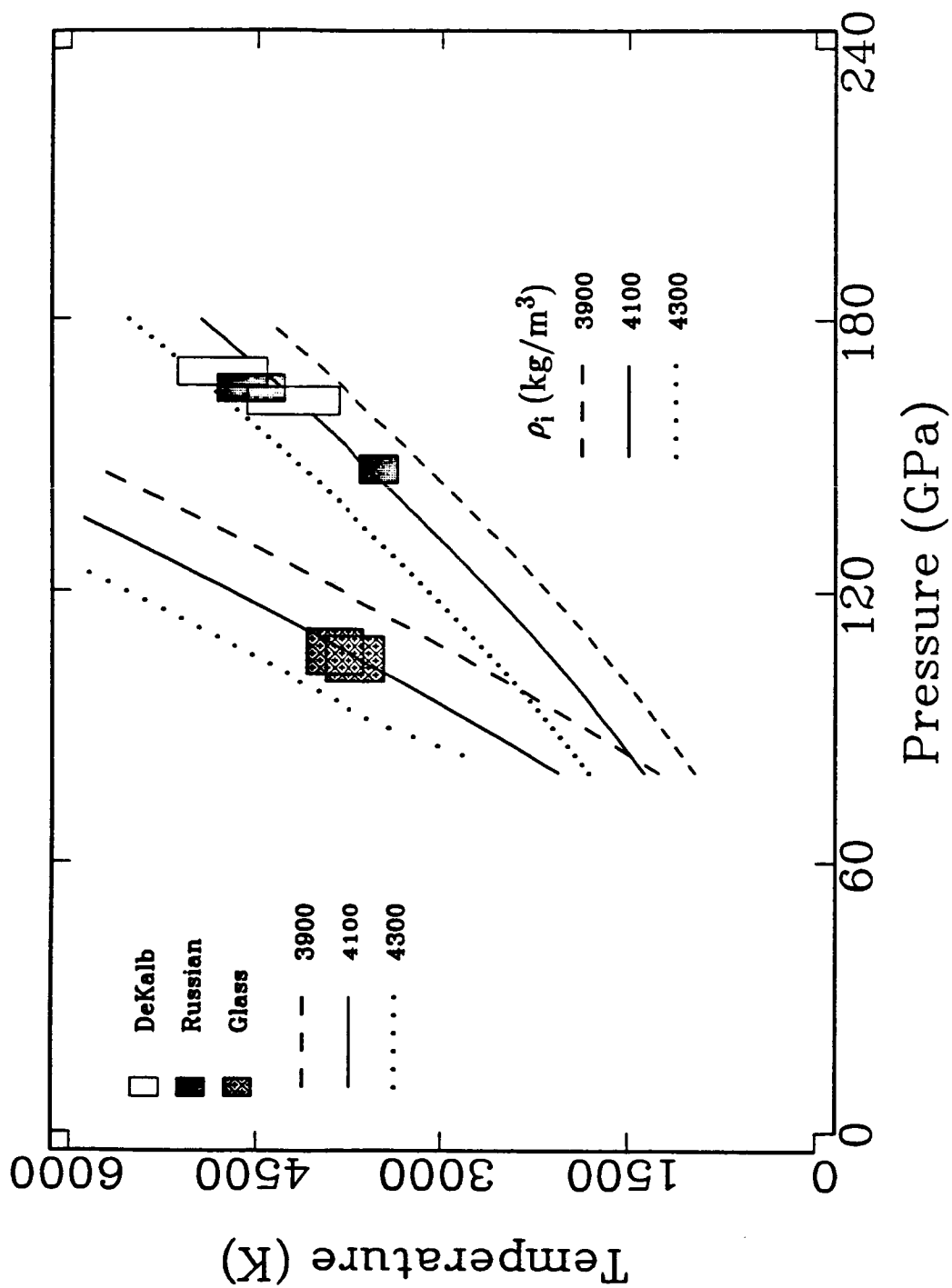
with $\eta_{cg} \equiv 1 - \rho_{ic}^\alpha / \rho_{ig}^\alpha$ and $\gamma_{ig} \equiv \gamma(\rho_{ig}^\alpha)$. In this case, T_H for glass and crystal Di starting materials depends on the basic unknowns ρ_i , γ and c_v for the high-pressure phase, β , as well as $\Delta e_i^{\beta-\alpha}$. From [4.12], we see that the slope of $T_H(P_H)$ is controlled by the magnitude of c_v , while the initial value of T_H is governed by $\Delta e_i^{\beta-\alpha}$. Further, from [4.12] and [4.13], we see that γ influences T_H via the isentropic properties T_s and Δe_{s_i} . In addition, γ influences the Hugoniot

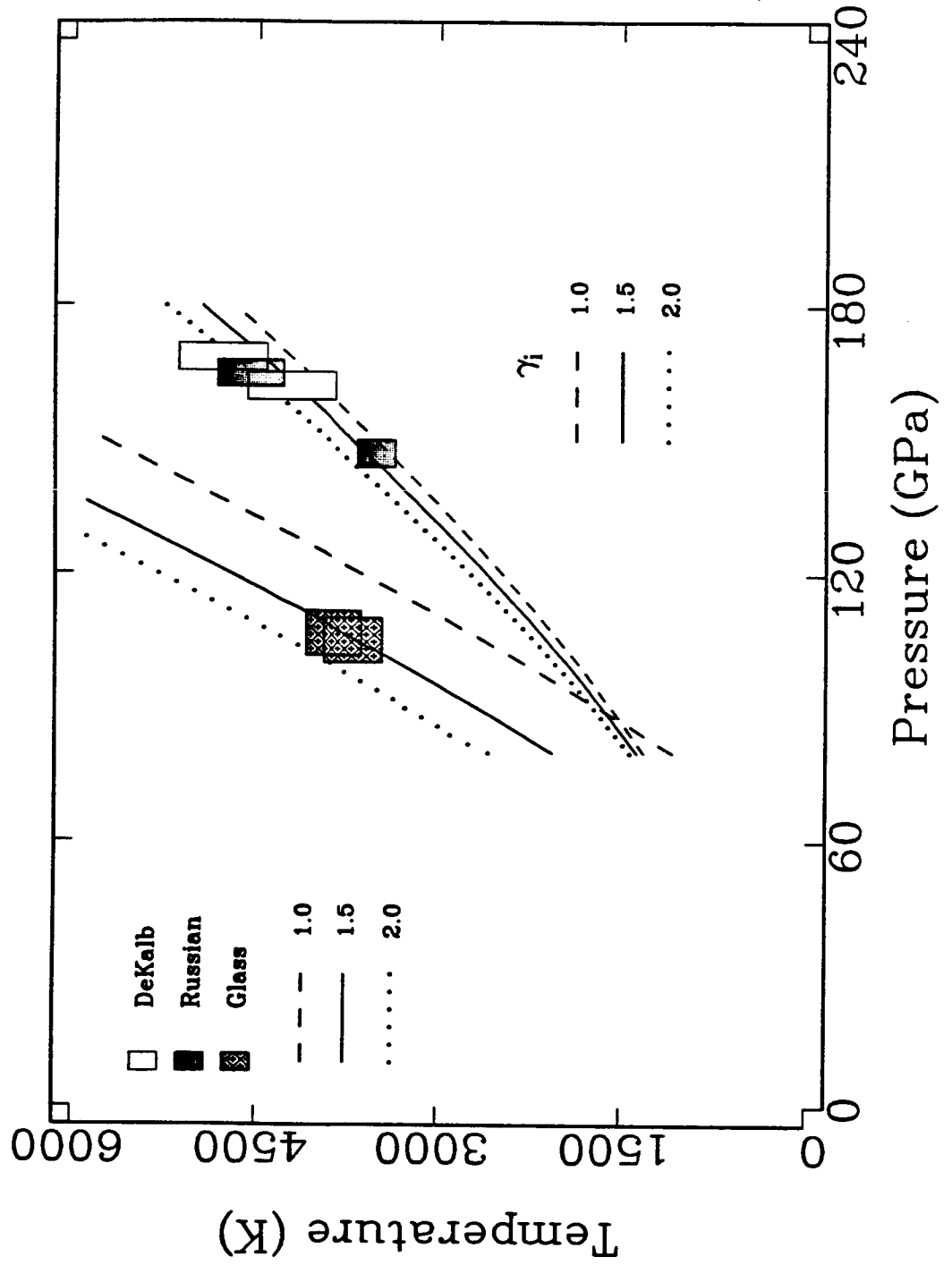
temperature of glass Di through [4.8]. The density of β at T_i and P_i , ρ_i , influences T_H indirectly, but significantly, through [4.12], [4.13], and $\gamma(\rho)$.

In Figures 4.1a-c, we display calculated Hugoniot for crystal and glass Di that "fit" the shock temperatures constrained by the data discussed above. We give a range of these Hugoniot based on a range of values for ρ_i (3900-4300 kg/m³, Figure 4.1a), $\gamma_i = \gamma(\rho_i)$ (1-2, Figure 4.1b), and $\Delta e_i^{\beta-\alpha}$ (0.4-1.4 MJ/kg for crystal Di, and 1.8-2.8 MJ/kg for glass Di, Figure 4.1c) to demonstrate the sensitivity of T_H to these unknowns. In all these calculations, we assume that c_v is given by its classic lattice value, $3\nu R/M$ (Table 4.1). The experimental results for the slope of $T_H(P_H)$ for the crystal and glass Di Hugoniot suggest that this is not an unreasonable assumption, although there are not enough data to rule out a pressure-temperature dependent c_v (e.g., Lyzenga *et al.*, 1983; Boslough *et al.*, 1986). From previous work on the pressure-density Hugoniot of Di (Ahrens *et al.*, 1966; Svendsen and Ahrens, 1983), the range of possible ρ_i values shown in Figure 4.1a for HPP Di are based on mixed-oxide and perovskite models for HPP Di. Comparing the results in these figures, we see that T_H for crystal Di is most sensitive to ρ_i , followed by $\Delta e_i^{\beta-\alpha}$ and then γ_i . For glass Di, T_H may be slightly more sensitive to γ_i than $\Delta e_i^{\beta-\alpha}$, but not really knowing a plausible range of values for these parameters, we find it hard to say.

From the curves in Figures 4.1a and 4.1c, we note that the glass data would also be satisfied by the combination of a lower initial density (3900 kg/m³) and lower value of $\Delta e_i^{\beta-\alpha}$ (1.8 MJ/kg); this is also consistent with the glass Di states representing liquid. Even if $\rho_i \approx 4100$ kg/m³ for glass Di, melting is favored, considering the magnitude of $\Delta e_i^{\beta-\alpha}$ (2.3 MJ/kg) needed to "fit" these data. The magnitude of $\Delta e_i^{\beta-\alpha}$ for the "best-fit" crystal Di Hugoniot (0.8 MJ/kg, Table 4.2) is of the same order as those estimated for some silicate and oxide dynamic solid-solid phase transformations (e.g., 0.82 MJ/kg, α -SiO₂→stishovite, Lyzenga *et al.*, 1983). If the glass data represent a solid-

Figure 4.1. Shock temperature versus pressure for crystal and glass Di, and model Hugoniot for a range of values of (a) the STP density of the high-pressure phase (HPP), ρ_i , (b) the equilibrium thermodynamic Gruneisen's parameter, γ_i , and (c) the difference in specific internal energy between phases at STP, $\Delta e_i^{\beta-\alpha}$.





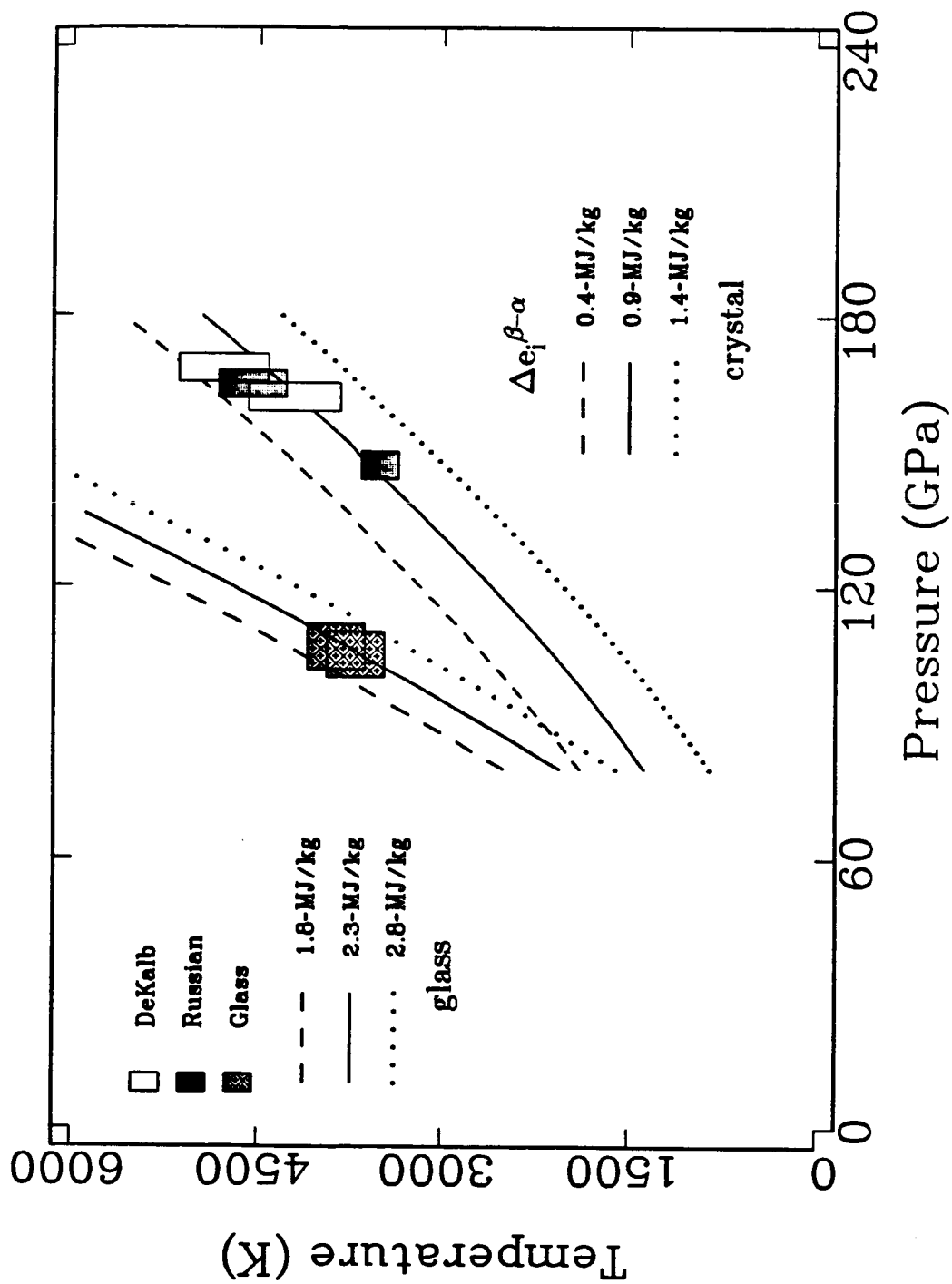


Table 4.2. CaMgSi₂O₆ STP parameters.

Property	Symbol	crystal	glass	Units
U-v relation†				
Density	ρ	3277 ^a	2828 ^b	kg/m ³
Intercept	a	5620 ^c	4775 ^d	m/s
Slope	b	1.27 ^c	1.28 ^d	
High-pressure phase				
Density	ρ	4100 ^e	4100 ^e	kg/m ³
Intercept	a	7826 ^e	7826 ^e	m/s
Slope	b	1.22 ^e	1.22 ^e	
Bulk modulus	K_s	251 ^f	251 ^f	GPa
$(\partial K_s/\partial P)_s$	K'_s	3.90 ^g	3.90 ^g	
Grüneisen's parameter‡	γ	1.5 ^h	1.5 ^h	
Specific heat§	c_v	1151.8	1151.8	J/kg·K
HPP-LPP energy difference	$\Delta e_1^{\beta-\alpha}$	0.9 ^h	2.3 ^h	MJ/kg

† i.e., $U=a+bv$. These relations are valid for $v > 2000$ m/s.

‡ $\rho\gamma$ =constant assumed in all calculations.

§ Dulong-Petit value, used for c_v in all calculations.

^a Robie *et al.* (1978).

^b Table IV.

^c Svendsen & Ahrens (1983).

^d from method in text.

^e HPP U-v relation (Chapter I, §4).

^f assuming $K_s = \rho a^2$.

^g $(\partial K_s/\partial P)_s = 4b-1$ (Ruoff, 1967).

^h from model calculations in text.

solid plus melting transition, this implies a value for $\Delta e_i^{\beta-\alpha}$ of ≈ 1.5 MJ/kg for melting of HPP Di. This compares, for example, with 1.6 MJ/kg estimated by Lyzenga *et al.* (1983) for the stishovite \rightarrow liquid SiO₂ transition. This line of thought also leads us to believe that the glass Di data represent liquid Di, while the crystal Di data represent a mixture of high-pressure oxide (B2-CaO, MgO plus stishovite) and/or perovskite (CaSiO₃ plus MgSiO₃, or CaSiO₃ - MgSiO₃ solid solution) phases.

§5. Discussion

In Table 5.1, we list the greybody fit and uncertainties, along with the calculated shock-wave velocities, shock-transit times, pressure and temperature, for each experiment. The values of $\hat{\epsilon}_{\text{exp}}(t_{\text{exp}})$ and $T_{\text{exp}}(t_{\text{exp}})$ in Table 5.1 for shots 140, 141, 169 and 170 are those for the GS fit with $\hat{\epsilon}_{\text{fit}}$ and T_{fit} variable, which we choose as representative of the other estimates, within experimental uncertainties. As discussed above, since $\hat{\epsilon}_{\text{exp}}(t_{\text{exp}})$ for shots 196 and 197 are significantly greater than unity, we choose the GS fit with $\hat{\epsilon}_{\text{fit}}$ set to one as the "experimental results" for these shots as listed in Table 5.1.

We display the "best fit" Hugoniot to the present experimental results (continuous curve) in Figure 5.1 along with other experimental results inferred from radiation data for SiO₂ (Lyzenga *et al.*, 1983), CaO (Boslough *et al.*, 1986), and MgO (Svendsen & Ahrens, 1987). Also shown are the mantle temperature profiles of Brown & Shankland (1980) and Stacey (1977). These two models represent the range of models currently considered plausible. The HPP Di results fall between the CaO and MgO results, and well below those for stishovite and liquid-SiO₂. To first order, this is due to the differences in the STP densities of the HPP's of each material. MgO, which apparently does not undergo any phase transformation below 200 GPa (Vassiliou and Ahrens, 1981;

Table 5.1. Experimental Results and Model Estimates.

Shot	Experimental Results					Calculated Results					
	ρ (kg/m ³)	d (mm)	v_{im} (m/s)	$\hat{\epsilon}_{exp}$	T_{exp} (K)	U (m/s)	v (m/s)	$a_{\lambda SS}$ (m ⁻¹)	t_{st} (ns)	P_H (GPa)	T_H (K)
140	3282 (6)†	1.868 (0.010)	5983 (60)	0.57 (0.23)	4215 (364)	11210	4403	880	167	162	4190
141	3283 (6)	1.566 (0.010)	6143 (50)	0.90 (0.20)	4782 (356)	11360	4518	1061	140	169	4524
169	3290 (5)	2.424 (0.004)	6048 (40)	0.97 (0.24)	4555 (268)	11300	4448	681	192	165	4313
170	3289 (7)	1.970 (0.010)	5593 (50)	0.85 (0.14)	3508 (141)	10850	4121	818	182	147	3590
196	2829 (1)	4.008 (0.004)	4673 (30)	1.00 (0.44)	3711 (231)	9678	3884	417	414	105	3660
197	2827 (1)	3.966 (0.001)	4729 (30)	1.00 (0.39)	3866 (208)	9733	3885	420	408	107	3795

† - measurement uncertainty.

ρ - STP bulk density.

d - Sample thickness.

v_{im} - Impact velocity.

$\hat{\epsilon}_{exp}$ - Experimentally-constrained greybody effective emissivity.

T_{exp} - Experimentally-constrained greybody absolute temperature.

t_r - Time during radiation history when I_{exp} used to constrain T_{exp} and $\hat{\epsilon}_{exp}$ was read.

U - Calculated shock wave velocity through sample.

v - Calculated material velocity of shocked sample.

$a_{\lambda SS}$ - lower bound to absorption coefficient of shocked sample.

t_{st} - Calculated shock wave transit time through sample.

P_H - Calculated shock-compressed pressure of sample.

T_H - Calculated shock-compressed temperature of sample.

Figure 5.1. Experimental and model pressure-temperature Hugoniot results for HPP Di, along with results for B2-CaO (Boslough *et al.*, 1984), MgO (Svendsen and Ahrens, 1987), and SiO₂ stishovite and liquid (Lyzenga *et al.*, 1983). Also shown are the mantle temperature profiles of Stacey (1977) and Brown and Shankland (1980). The vertical line marks the pressure of the mantle-core boundary (135.7 GPa).

Svendsen and Ahrens, 1987) has an STP density of 3583 kg/m^3 , B2-CaO has an initial density of $\approx 3800\text{-}4000 \text{ kg/m}^3$ (Jeanloz and Ahrens, 1980a; Boslough *et al.*, 1984), HPP solid Di is likely to have a slightly larger ρ_i ($\approx 4100 \text{ kg/m}^3$, Table 4.3) than B2-CaO, as discussed above, and stishovite has an STP density of $\approx 4300 \text{ kg/m}^3$. This is also true because the values of $\Delta e_1^{\beta-\alpha}$ for each material are approximately the same. Since B2-CaO and HPP Di apparently have very similar ρ_i , other factors, such as compressibility (B2-CaO has a lower bulk modulus than HPP Di: Jeanloz and Ahrens, 1980a; Boslough *et al.*, 1984; Svendsen and Ahrens, 1983), become important. B2-CaO is more compressible than HPP Di, and so its Hugoniot temperature rises more quickly than HPP Di.

Low-pressure static studies of Di (*e.g.*, Liu, 1979b) imply that $\text{CaMgSi}_2\text{O}_6$ may disproportionate into CaSiO_3 perovskite and MgSiO_3 perovskite above $\approx 20 \text{ GPa}$ and 1000 C . Our results are not inconsistent with this, and yet we really cannot distinguish between perovskite and mixed-oxide (or some combination) assemblage. The model we favor (Table 4.3) is more likely representative of the perovskite mixture for $\text{CaMgSi}_2\text{O}_6$ (Svendsen and Ahrens, 1983).

In comparison with the mantle temperature profiles displayed in Figure 5.1, we note that both B2-CaO and HPP Di Hugoniot may be at about the same temperature at the pressures of the lowermost mantle. We note that some of the compositional models for the lowermost mantle (*e.g.*, Ruff and Anderson, 1980), known as the D" region, contain significant amounts of more refractory oxides and/or silicates (*i.e.*, CaO , Al_2O_3 , CaSiO_3 , *etc.*).

§6. Summary

Observed radiation from shock-compressed crystal $\text{CaMgSi}_2\text{O}_6$ (Di) constrains Hugoniot temperatures of $3500\text{-}4800 \text{ K}$ for this material in the $150\text{-}170 \text{ GPa}$ pressure range, while glass $\text{CaMgSi}_2\text{O}_6$, with a starting density 87% that of

crystal Di, achieves Hugoniot temperatures of 3600-3800 K in the 105-107 GPa pressure range. The shock-induced radiation history for these materials implies that both shock-compressed crystal and glass Di are strong absorbers ($a_{\lambda s} \geq 500-1000 \text{ m}^{-1}$). Calculated Hugoniot states for these materials, in comparison with the experimental results, suggest that crystal Di Hugoniot states in the 150-170 GPa range represent an HPP solid (or possibly liquid) phase with an STP density of $4100 \pm 200 \text{ kg/m}^3$, STP Grüneisen's parameter of 1.5 ± 0.5 and STP HPP-LPP specific internal energy difference of $0.9 \pm 0.5 \text{ MJ/kg}$. These parameters are consistent with either a Ca-Mg mixed-oxide or perovskite assemblage. For glass Di, we have the same range of HPP properties, except that $\Delta e_i^{\beta-\alpha}$ is $2.3 \pm 0.5 \text{ MJ/kg}$, a strong indication that the glass Di Hugoniot states occupy the liquid-phase of $\text{CaMgSi}_2\text{O}_6$, and that $\Delta e_i^{\beta-\alpha} \approx 1.5 \text{ MJ/kg}$ for HPP-Di melting. This value for $\Delta e_i^{\beta-\alpha}$ is similar to the shock-temperature results for SiO_2 (Lyzenga *et al.*, 1983). Comparison of the experimentally constrained pressure-temperature Hugoniot of crystal Di with the experimentally constrained Hugoniots of its constituent oxides (*i.e.*, SiO_2 , CaO and MgO) demonstrates the strong influence of the HPP, STP density of these materials on the magnitude of the temperature in their shock-compressed states. The experimentally constrained crystal Di Hugoniot falls within the plausible range (2500-3000 K) of mantle temperature profiles in the range of pressures (110-135 GPa) corresponding to the lowermost mantle.

Acknowledgements. We thank Papo Gelle, Mike Long, Chuck Manning and Leon Young for experimental assistance, and Gregory Miller, Jay D. Bass, Douglas R. Schmitt and James A. Tyburczy for enlightening discussions. Support under NASA and NSF grants NGL-05-002-105 and EAR-86-08249, respectively, is gratefully acknowledged. Contribution 4480, Division of Geological and

Planetary Sciences, California Institute of Technology, Pasadena, California.

§7. References

- Ahrens, T. J., J. T. Rosenburg, and M. H. Ruderman, Dynamic properties of rocks, *Stanford Research Institute, Final Report No. DA-45-146-XZ-277*, SRI Project FGU-4816, Sept. 1966.
- Ahrens, T. J., D. L. Anderson, and A. E. Ringwood, Equation of state and crystal structure of high-pressure phases of shocked silicates and oxides, *Rev. Geophys.*, **7**, 667-707, 1969.
- Alers, G. A., Use of sound velocity measurements in determining the Debye temperature of solids, in *Physical Acoustics*, **3B**, 1-42, edited by W. P. Mason, Academic Press, New York, 1965.
- Bass, J. D., B. Svendsen, and T. J. Ahrens, The temperatures of shock-compressed iron, *High Pressure Research in Geophysics and Geochemistry*, edited by M. Manghni and Y. Syono, Terra Publishing Co., Tokyo, in press, 1987.
- Binsted, N., G. N. Greaves, and C. M. B. Henderson, An EXAFS study of glassy and crystalline phases of compositions $\text{CaAl}_2\text{Al}_2\text{Si}_2\text{O}_8$ and $\text{CaMgSi}_2\text{O}_6$, *Contrib. Mineral. Petrol.*, **89**, 103-109, 1985.
- Boslough, M. B., Shock-wave properties and high-pressure equations of state of geophysically important materials, *Ph.D. Dissertation*, 171 pp., California Institute of Technology, Pasadena, California, 1984.
- Boslough, M. B., A model for time dependence of shock-induced thermal radiation of light, *J. Appl. Phys.*, **56**, 3394-3399, 1985.
- Boslough, M. B., T. J. Ahrens, and A. C. Mitchell, Shock temperatures in CaO, *J. Geophys. Res.*, **89**, 7845-7851, 1984.
- Boslough, M. B., T. J. Ahrens, and A. C. Mitchell, Shock temperatures in anorthite glass, *Geophys. J. R. Astr. Soc.*, **84**, 475-489, 1986.

- Brown, J. M., and T. Shankland, Thermodynamic parameters of the earth as determined from seismic profiles, *Geophys. J. R. Astr. Soc.*, **66**, 579-596, 1980.
- Grossman, L., and J. W. Larimer, Early chemical history of the solar system, *Rev. Geophys. Space Phys.*, **12**, 71-101, 1974.
- Grover, R., and P. A. Urtiew, Thermal relaxation at interfaces following shock compression, *J. Appl. Phys.*, **45**, 146-152, 1974.
- Jeanloz, R., and T. J. Ahrens, Equations of state of FeO and CaO, *Geophys. J. R. Astr. Soc.*, **62**, 505-528, 1980a.
- Jeanloz, R., and T. J. Ahrens, Anorthite: thermal equation of state to high pressures, *Geophys. J. R. astr. Soc.*, **62**, 529-549, 1980b.
- Kieffer, S. W., Thermodynamics and lattice vibrations of minerals: 4. Application to chain and sheet silicates and orthosilicates, *Rev. Geophys. Space Phys.*, **18**, 862-886, 1980.
- Kondo, K. E., and T. J. Ahrens, Heterogeneous shock-induced thermal radiation in minerals, *Phys. Chem. Minerals*, **9**, 173-181, 1983.
- Kormer, S. B., Optical study of the characteristics of shock-compressed condensed dielectrics, *Sov. Phys. Uspekhi*, **11**, 229-254, 1968.
- Liu, L. G., A new high-pressure phase of $\text{Ca}_2\text{Al}_2\text{SiO}_7$ and implications for the earth's interior, *Earth Planet. Sci. Lett.*, **40**, 401-406, 1978.
- Liu, L. G., High-pressure phase transformations in the system $\text{CaSiO}_3\text{-Al}_2\text{O}_3$, *Earth Planet. Sci. Lett.*, **43**, 331-335, 1979a.
- Liu, L. G., The system enstatite-wollastonite at high pressures and temperatures, with emphasis on diopside, *Phys. Earth Planet. Int.*, **19**, P15-P18, 1979b.
- Lyzenga, G. A., Shock temperatures of materials: experiments and applications to the high-pressure equation of state, *Ph.D. Dissertation*, 208 pp., California Institute of Technology, Pasadena, California, 1980.

- Lyzenga, G. A., T. J. Ahrens, and A. C. Mitchell, Shock temperatures of SiO_2 and their geophysical implications, *J. Geophys. Res.*, **88**, 2431-2444, 1983.
- Marsh, S. P., ed., *LASL Shock Hugoniot Data*, 658 pp., University of California Press, Los Angeles, 1980.
- McQueen, R. G., S. P. Marsh, and J. N. Fritz, Hugoniot equation of state of twelve rocks, *J. Geophys. Res.*, **72**, 4999-5036, 1967.
- Mitchell, A. C., and W. J. Nellis, Shock compression of aluminum, copper and tantalum, *J. Appl. Phys.*, **52**, 3363-3374, 1981.
- Press, W. H., B. P. Flannery, S. A. Teukolsky, and W. T. Vetterling, *Numerical Recipes: The Art of Scientific Computing*, 818 pp., Cambridge University Press, New York, 1986.
- Rice, W. H., R. G. McQueen, and J. M. Walsh, Compressibility of solids by strong shock waves, *Solid State Phys.*, **6**, 1-63, 1958.
- Robie, R. A., B. S. Hemingway, and R. J. Fisher, Thermodynamic properties of minerals and related substances at 298.15 K and 1 bar (10^5 Pascals) pressure and at higher temperatures, 456 pp., *USGS Bulletin No. 1452*, Government Printing Office, Washington, D.C., 1978.
- Ruff, L. J., and D. L. Anderson, Core formation, evolution and convection: a geophysical model, *Phys. Earth Planet. Int.*, **21**, 181-201, 1980.
- Ruoff, A. L., Linear shock velocity-particle velocity relation, *J. Appl. Phys.*, **38**, 4976-4980, 1967.
- Schmitt, D. R., B. Svendsen, and T. J. Ahrens, Shock-induced radiation from minerals, in *Shock Waves in Condensed Matter*, 261-266, edited by Y. M. Gupta, Plenum Press, New York, 1986.
- Stacey, F., A thermal model of the earth, *Phys. Earth Planet. Int.*, **15**, 341-348, 1977.
- Stebbins, J. F., I. S. E. Carmichael and D. J. Weill, The high-temperature liquid

- and glass heat contents and heats of fusion of diopside, albite, sanidine and nepheline, *Am. Mineral.*, **68**, 717-730, 1983.
- Svendsen, B., and T. J. Ahrens, Dynamic compression of diopside and salite to 200 GPa, *Geophys. Res. Lett.*, **7**, 501-504, 1983.
- Svendsen, B., and T. J. Ahrens, Shock-induced temperatures of MgO, *Geophys. J. R. Astr. Soc.*, in press, 1987.
- Touloukian, Y. S., R. W. Powell, C. Y. Ho, and P. G. Klemens, *Thermophysical Properties of Matter, Volume 12: Thermal expansion*, Thermophysical Properties Research Center of Purdue University, Data Series, Plenum Publishing Corporation, New York, 1975.
- Turekian, K. K., and S. P. Clark, Jr., Inhomogeneous accretion model of the earth from the primitive solar nebula, *Earth Planet. Sci. Lett.*, **6**, 346-348, 1969.
- Urtiew, P. A., and Grover, R., Temperature deposition caused by shock interactions with material interfaces, *J. Appl. Phys.*, **45**, 140-145, 1974.
- Vassiliou, M. S. and T. J. Ahrens, Hugoniot equation of state of periclase to 200 GPa, *Geophys. Res. Lett.*, **8**, 729-732, 1981.

Chapter IV

The Temperatures of Shock-compressed Iron†

Jay D. Bass§, Bob Svendsen‡ and Thomas J. Ahrens‡

§Department of Geology,
University of Illinois, Urbana, Illinois 61801, USA.

‡Seismological Laboratory,
California Institute of Technology, Pasadena, California 91125, USA.

†*High Pressure Research in Geophysics*, in press

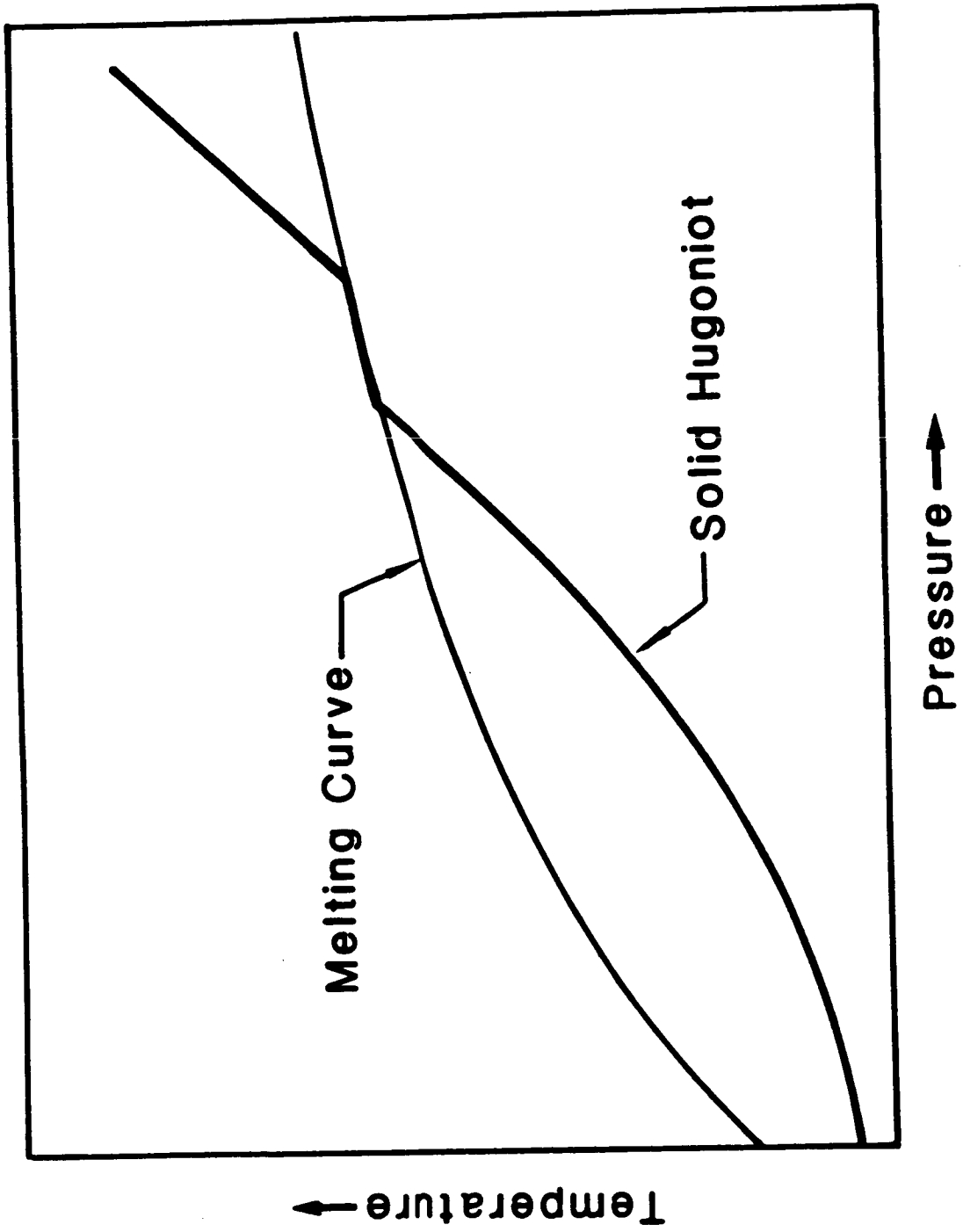
Abstract

Measurements of the temperature of Fe under shock compression have been performed to Hugoniot pressures of 300 GPa. The samples consist of thin Fe films, 0.5 to 9.5 μm in thickness, or Fe foils in contact with a transparent anvil of either single-crystal Al_2O_3 or LiF. Temperatures at the sample/anvil interface are obtained by measuring the spectral radiance of the interface, for the duration of the shock transit through the anvil, using a 4-color optical radiometer. On the basis of our experimental data we conclude that a measure of the sample Hugoniot temperature, as opposed to the temperature of the Al_2O_3 anvil, can thus be obtained. Our results further indicate that the Al_2O_3 remains at least partially transparent to pressures of at least 230 GPa and temperatures of over 9,000 K. We obtain a melting temperature of Fe along the Hugoniot of 6700 ± 400 K at 243 GPa. Taken together with recent determinations of melting temperatures to 100 GPa (Williams *et al.*, 1987), our results place an upper bound on the temperature at the inner core-outer boundary of 7800 ± 500 K.

§1. Introduction

The properties of matter at exceedingly high degrees of compression may be investigated using shock wave techniques. In a typical equation-of-state experiment it is usual to determine the shock velocity (U), material or particle velocity (v), and the differences in pressure (P), specific volume (v), and internal energy (E) between the initial state and the shock-compressed state. The techniques used to perform such experiments are relatively well developed and have been described in many articles published over the past two decades. However, the above mentioned parameters do not by themselves give a unique thermodynamic description of a material in the shock-compressed, or Hugoniot state. In particular, the temperature along the Hugoniot, or locus of shock-compressed states, is generally undefined. Using modern shock wave techniques, pressures on

Figure 1.1. Schematic diagram illustrating the effect of a phase boundary with positive Clayperon slope, dP/dT , upon the equilibrium Hugoniot temperatures.



the order of several hundred GPa, corresponding to those of the Earth's lower mantle and core, are easily attained in solid samples. The concomitant temperatures reached in these experiments are generally many thousands of Kelvins. In order to apply the results of shock wave experiments to states off the Hugoniot, for example adiabats or isotherms, it is necessary to either measure or calculate Hugoniot temperatures achieved during shock loading. Although Hugoniot temperatures may be calculated, this procedure is subject to large uncertainties because of imperfect knowledge of thermal properties such as Grüneisen's parameter and the specific heat.

An additional motivation for performing shock-temperature measurements is to identify the existence of phase transitions along the shock compression curve. It has been found that many phase transitions, especially those involving only a small density change, are not obvious in terms of Hugoniot parameters, and are manifest only as subtle changes of slope in the $U-v$ or $P-v$ Hugoniot relationship of a given material. However, such phase transitions may have a more pronounced signature in the $T-P$ plane. When the Hugoniot intersects a phase boundary there will be, in principle, a substantial offset, or discontinuity in the Hugoniot $T-P$ curve (Kormer, 1968). As shown in Figure 1.1, the Hugoniot will coincide with a phase boundary over some pressure interval, which is determined by the amount of energy needed to drive the transition to completion. Such behavior has been inferred from shock-induced radiation data on NaCl (Kormer *et al.*, 1965; Ahrens *et al.*, 1982).

In this paper we present the results of our initial attempts to measure the temperature of Fe under shock loading, using a 4-channel optical radiometric technique. Although similar measurements have been made on a variety of transparent materials in recent years, the extension of this methods to opaque materials has a number of serious experimental difficulties, which will be discussed below. To the best of our knowledge, the results summarized in this

paper represent the most extensive data set obtained to date on the temperature of a shock-compressed opaque material. We have chosen Fe for our initial experiments because of its geophysical importance as a probable major constituent of the earth's core.

§2. Experimental Method

All of our experiments were performed using a two-stage light-gas gun (Jones *et al.*, 1966; Jeanloz and Ahrens, 1977), in which lexan projectiles bearing Ta flyer plates were accelerated to velocities of up to 6.5 km/s. Impact velocities were measured by taking two flash X-radiographs of the projectile in flight, and are known to better than 0.5% accuracy. Pressures in each part of the sample assembly, which will be described in detail below, were calculated using the impedance matching method (Rice *et al.*, 1958). Necessary equation-of-state parameters are given by Mitchell and Nellis (1981, Ta), Brown and McQueen (1986, Fe), Carter (1973, LiF), and the 19 highest pressure data points listed by Marsh (1980) for Al₂O₃.

The basis of the experimental method used in our study is to record the spectral radiance emitted by the sample when it is shock-compressed to high pressure and temperature. Assuming that the sample emits light as a greybody, data obtained at several discreet wavelength bands may be fit to the function

$$L(\lambda) = \epsilon C_1 \lambda^{-5} (\exp(C_2/\lambda T) - 1)^{-1} \quad [2.1],$$

where L , the spectral radiance, is the observed quantity in the experiment. In each experiment, data are obtained at the four wavelengths 450, 600, 750 and 900 nm, and using [2.1], values for the temperature and emissivity are obtained by a least-squares regression. This technique was initially developed by Kormer *et al.* (1965), who used a two-color pyrometer to determine the Hugoniot temperature of transparent samples. Later versions of this instrument employing six

or four channels in the visible portion of the spectrum were designed by Lyzenga and Ahrens (1979) and Boslough (1984), respectively.

In our experiments we have used the optical recording apparatus designed by Boslough (1984), a schematic diagram of which is shown in Figure 2.1. Light emitted by the sample is directed to a collimating lens by an expendable front surface mirror. The lens is positioned at one focal distance (50 cm) from the sample. The collected light is then separated into four parts by way of three beamsplitters, is demagnified and focused onto four photodiodes. The image of the sample is far smaller than the active area of the photodiodes, so that the photodiodes do not have to be positioned with a high degree of precision. An interference filter is situated in front of each photodiode to pass only a limited band (≈ 40 nm FWHM) about each desired central wavelength. The output voltage of each photodiode is amplified and recorded on an oscilloscope and a high-speed digital recorder, thus providing redundancy in each measurement and a backup of each channel. Further details of the system are given by Boslough (1984).

For shock temperature experiments on opaque materials, the construction of the target assembly is of critical importance. As shown in Figure 2.2, the main components of the assembly are a 0.5 mm thick Fe driver plate, either a film ($< 10 \mu\text{m}$ thick) or foil ($30 \mu\text{m}$ thick) of Fe, which is the actual sample, and a 16×3 mm thick disc of single-crystal sapphire or LiF. The sapphire serves both as an anvil, to maintain the Fe sample at high pressure after the shock front traverses the Fe- Al_2O_3 interface, and as a window through which thermal radiation must be transmitted during an experiment. Therefore, the criteria that are important in choosing an anvil/window material are that it have a shock impedance as close as possible to that of the metallic sample, thereby minimizing release or reshocking of the sample upon arrival of the shock at the interface, and that the anvil remain transparent when shocked to high pressures.

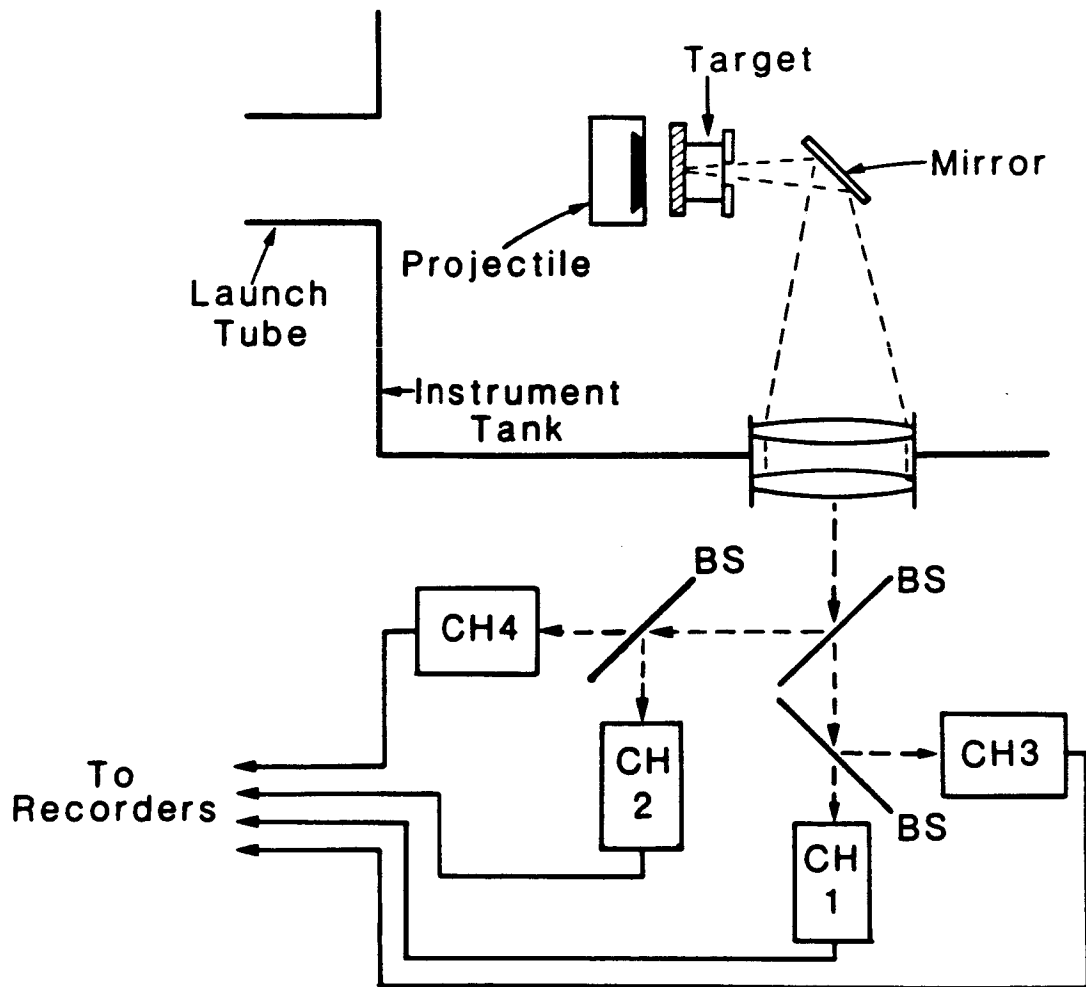


Figure 2.1. Diagram of the main components of the shock temperature measurement system. The path of light radiated by the sample is indicated by the dashed lines. Each of the four channels (CH#) in the radiometer consists of an interference filter, a lens for demagnifying the image, a photodiode, and an amplifier.

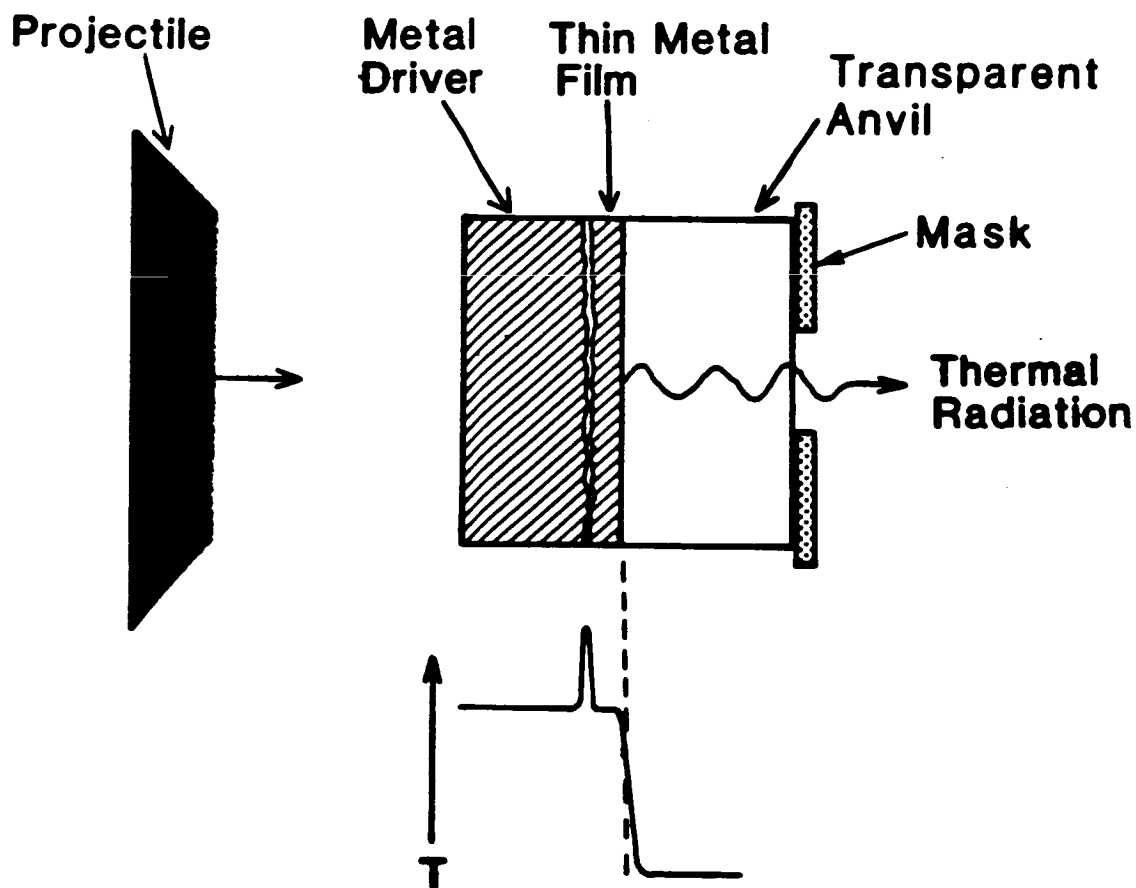


Figure 2.2. The target used in shock temperature experiments on opaque samples. A foil may be used as a sample in place of the film. A schematic diagram of the temperature profile in various parts of the assembly is shown at the bottom of the figure.

One general conclusion from optical studies on shocked materials in this and several other laboratories is that initially transparent materials seem to radiate as blackbodies, or greybodies with emissivities close to 1, when shocked above phase transition pressures. This implies that the occurrence of phase transitions along the Hugoniot tends to yield an opaque material. Therefore, we have followed the strategy of Lyzenga and Ahrens (1979), and Urtiew and Grover (1977) and chosen Al_2O_3 as our primary anvil material because it does not undergo any known phase transitions along the Hugoniot. We note, moreover, that Al_2O_3 has been observed to remain transparent to static pressures in excess of 500 GPa (Xu *et al.*, 1986) and under dynamic loading to at least 100 GPa (Urtiew, 1974). Al_2O_3 also provides the optimal impedance match to Fe out of all potential window materials.

Urtiew and Grover (1974) have performed a theoretical analysis of the heat generated at the interface between a sample and a window upon passage of a shock wave through the interface. These authors considered the effects of two types of interface imperfections: a small uniform space or gap between the two materials, and roughness, or topography on the surface of the opaque sample. In the first case the metal sample has a free surface at which, upon arrival of the shock front, the material is released to atmospheric pressure and some elevated temperature in a near adiabatic fashion. The hot, released material at the surface subsequently impacts the anvil surface, thus reshocking the sample to high pressure and a temperature that is greater than would be attained along the principal Hugoniot of the sample. The case of surface roughness was treated as a layer of porous sample material adjacent to the anvil, again leading to temperatures at the interface that are higher than the Hugoniot temperatures of either the anvil or a perfectly dense sample.

From the above studies it is clear that in order to measure an interface temperature that is directly related to the Hugoniot temperature, the sample

must be in near perfect contact with the window. This was experimentally verified by Lyzenga and Ahrens (1979), who performed shock temperature measurements on Ag using three different target configurations. They found that the direct impact of an Ag projectile onto a Al_2O_3 window, and the use of a Ag foil wrung onto the anvil, led to transients in the spectral radiance versus time data. A sample of vapor-deposited Ag on an Al_2O_3 substrate gave a much more stable signal. Base upon the experience of Lyzenga and Ahrens with Ag, we decided to prepare samples with vapor deposition using a Varian electron beam evaporative coating system. This technique maximizes the chances of obtaining a flawless contact between the sample and window on an atomic scale, thus obviating any thermal signal due to an interfacial gap. However, as discussed later, our data indicated that ideal interface conditions were attained in only a fraction of the samples. Fe was deposited under a total vapor pressure of 3×10^{-7} torr at a rate of approximately 25 angstroms per second. Films with thicknesses of $0.5 \mu\text{m}$ (in the first successful run) to $9.5 \mu\text{m}$ were produced. A calibrated crystal oscillator with a characteristic frequency that changes as a film is deposited upon it, was positioned near the substrate to monitor the deposition rate and final film thickness. Our experience has been that Fe adheres poorly to Al_2O_3 , and a majority of the films would peel off of the substrate either during, or a short time after, coating. This problem became more severe as we tried to increase the film thickness, but was somewhat alleviated by extremely thorough cleaning of the substrate prior to coating.

The thickness of the sample film is an important consideration in this experiment. Because the interface between the driver and film sample cannot be perfect, there is a possibility of significant heat production for the reasons discussed above. If a film is too thin, this heat could diffuse to the sample/anvil interface on the time scale of the experiment, thus yielding an erroneously high temperature that increases with time. It was not possible to determine *a priori*

what a safe minimum film thickness would be, since we have little or no information on the appropriate thermal properties at elevated temperatures and pressures. Therefore, we simply tried to obtain as thick a film as possible and found $9\mu\text{m}$ to be the approximate upper limit of our techniques. Our experimental data indicate that this thickness is satisfactory, because the shot records show no consistent evidence for heat diffusion to the sample-anvil interface. In fact, most of our records showed a light decrease in the intensity of light as the shock front progressed through the window. This is most easily interpreted as a change in the optical properties of the window material under shock loading.

As a source of Fe for the films and driver plates we used a low carbon steel ("Cor 99", Corey Steel Co., Chicago, IL), with a total impurity content of less than 0.12% (analysis supplied by the manufacturer). The density was measured by the Archimedian method to be $7.84\pm 0.02\text{ gm/cm}^3$, just slightly lower than the x-ray value of 7.874 gm/cm^3 (Berry, 1967). In the last film experiment, a commercial Fe powder of nominal 99.9% purity was used. The Fe film from one sample was peeled off the substrate and examined by X-ray powder diffractometry. A well-defined peak corresponding to the most intense (110) diffraction maximum of $\alpha\text{-Fe}$ was found, indicating that the films are highly crystalline rather than in an amorphous state.

The vapor deposition method is an extremely time-consuming method of preparing samples. As an alternative, we investigated the possibility of using thin Fe foils as samples in five experiments. Fe foils of 0.03 mm thickness and nominal 99.99% purity were obtained by Alfa Products and used as samples in this series of shots.

§3. Results

Figure 3.1 shows the raw oscillographic data from one of the shock temperature experiments. A noteworthy feature of these record is that there is no

evidence of a "spike," or strong transient in light intensity when the shock reaches the interface, or the thermal relaxation of a thin Fe layer, which is extremely hot due to porosity. It is also important to note that the voltage, or intensity of light, is nearly constant in time, indicating that thermal diffusion from the driver/film interface to the film/anvil interface is probably not significant. All of the voltage records from the experiments at higher pressures showed a modest to a rapid decrease in light intensity with time, although no spikes were observed. One interpretation of the decrease in light intensity is that the sapphire anvil is appreciably absorbing in the optical range above pressures of about 225 GPa. Only experiment #167 (Table 4.1) at 196 GPa exhibited a modest increase of light intensity with time, and the reason for this behavior is as yet unresolved.

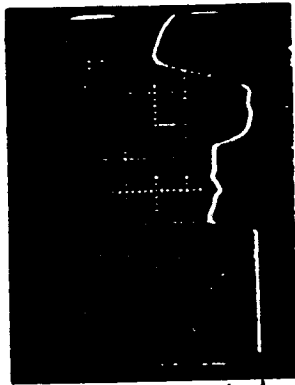
The spectral radiance values obtained from the voltage data of Figure 3.1 are plotted in Figure 3.2. Because the spectral radiance is never precisely constant as a function of time, it is important to consider that part of the voltage-time record is appropriate to use for obtaining a Hugoniot temperature. We have chosen to read the initial part of each record, just after the sharp increase in voltage which corresponds to arrival of the shock at the interface. In this way we obtain a measure of the thermal radiance of the sample viewed through unshocked, transparent anvil material. This choice should minimize potential problems due to light absorption by the anvil, diffusion of heat from the driver/sample interface to the sample/anvil interface, and contributions to the signal by the shocked anvil.

For the purpose of transforming the observed voltages to a temperature, it is necessary to calibrate the pyrometer with a standard light source. As described by Boslough (1984), we use the chopped signal from a tungsten lamp of known spectral irradiance (Optronics Laboratories, Orlando, Florida). The resulting experimental values of spectral radiance may then be fitted to a

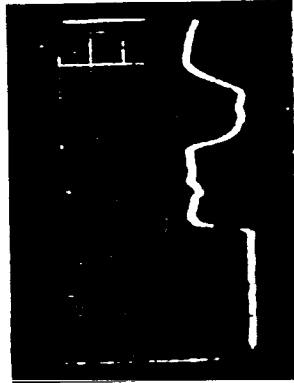
Figure 3.1. Oscillographic record of voltage as a function of time for one of the shock temperature experiments. The amplitude of the voltage above the baseline seen in the initial ≈ 400 ns of the record, is proportional to the spectral radiance at the sample/anvil interface.

Fe on Al₂O₃ Radiance Measurements
P_H = 225 GPa P_I = 178 GPa

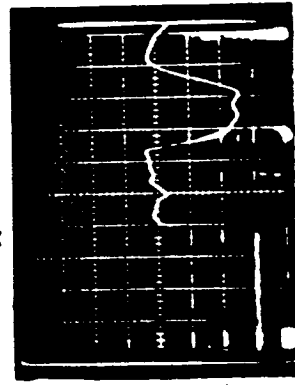
$\lambda = 450 \text{ nm}$



$\lambda = 600 \text{ nm}$



$\lambda = 750 \text{ nm}$



$\lambda = 900 \text{ nm}$



Shock Arrival At Anvil Free Surface
Shock Arrival At Interface

Voltage

Time

radiation function, such as Planck's Law, to obtain the temperature and emissivity of the sample-anvil interface. In Figure 3.2 we show least squares fits to the data using the emissivity obtained by regression, and also a value of unity as appropriate for a black body. It is clear that the data are described far better by using a greybody (emissivity $\neq 1$) rather than a blackbody function; this is quantitatively expressed by emissivity values that are statistically different from one (Table 4.1). The errors shown in Figure 3.2, and listed in Table 4.1 for the interface temperature, take into account the estimated uncertainties in reading the baseline and signal voltages on the oscillograms (or transient recorder plots), the calibration voltages, the spectral irradiance of the calibration lamp, and diameter of the mask aperture.

The data from our experiments yield temperature values for the sample material at the interface with the anvil. In order to obtain the Hugoniot temperature of the sample, it is necessary to correct the interface temperatures for two effects: the influence of the relatively cold anvil, and partial release of the Fe due to the impedance mismatch of the sample and anvil materials. In the ideal situation where the sample has no porosity and is in perfect contact with the anvil, it has been shown (Grover and Urtiew, 1974) that the interface temperature T_i , is independent of time and is related to the temperature of the released sample, T_r , by

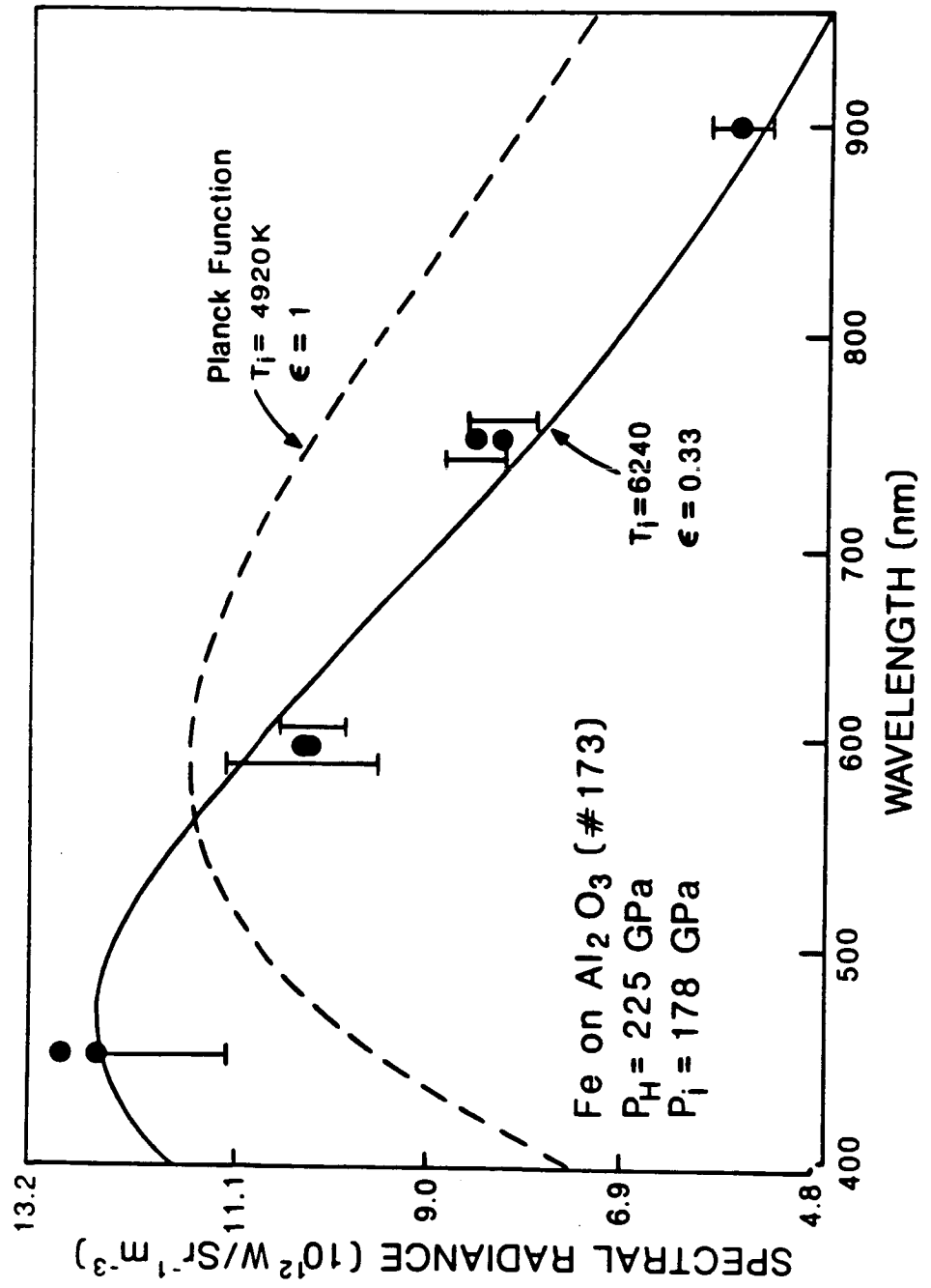
$$T_i = T_r + \frac{(T_a - T_r)}{(1 + \alpha)} \quad [3.1].$$

Here, T_a is the Hugoniot temperature of the anvil, and α is given by

$$\alpha = \left\{ \frac{\kappa_r}{\kappa_a} \right\} \left\{ \frac{D_a}{D_r} \right\}^{1/2} = \left\{ \frac{\kappa_r \rho_r C_r}{\kappa_a \rho_a C_a} \right\}^{1/2} \quad [3.2],$$

where κ and D are thermal conductivity and diffusivity, respectively, ρ is density, C is the specific heat, and the subscripts r and a refer to released Fe, and

Figure 3.2. The data from Figure 3.1, and additional data from digital recorders, plotted in terms of spectral radiance versus wavelength. The solid curve is obtained from least-square regression for both temperature and emissivity using Planck's Law; the dashed curve is the least-squares solution for temperature alone with the emissivity fixed at unity.



Hugoniot state of the anvil, respectively.

The thermal properties needed to evaluate α in [3.2] have not been measured under the extreme P and T conditions of our experiments, and α must therefore be estimated from available data and theory. For the anvil materials, we first evaluate the effect of temperature on the lattice contribution to the thermal conductivity, $\kappa_a(P,T)$. Low-pressure conductivity data were fit to expressions of the form $\kappa(0,T)=A_1+B_1/T$ yielding coefficients of $A_1=2.599$ W/m·K, $B_1=1.176 \times 10^4$ W/m for Al_2O_3 (Kingery *et al.*, 1954), and $A_1=-0.2023$, $B_1=3.671 \times 10^3$ for LiF (Men' *et al.*, 1974). These equations allowed for calculation of $\kappa_a(0,T)$ at the anvil Hugoniot temperature. The effect of pressure on the anvil conductivity was then calculated using the Debye-Grüneisen approximation $\delta\kappa/\kappa \approx 7\delta\rho/\rho$, presented by Roufousse and Jeanloz (1983). In order to evaluate this last expression, the anvil density at 0.1 MPa and the appropriate Hugoniot temperature is obtained from the thermal expansivity in the form $d\ln\rho/dT=A_2+B_2T$. Values of $A_2(298\text{K})=9.8 \times 10^{-5}\text{K}^{-1}$ and $B_2=1.2 \times 10^{-7}\text{K}^{-2}$ were used for LiF (Pathak and Vasavada, 1972; Rapp and Merchant, 1973), and $A_2=1.62 \times 10^{-5}\text{K}^{-1}$, $B_2=1.1 \times 10^{-8}\text{K}^{-2}$ for Al_2O_3 (Touloukian *et al.*, 1975). Finally, the heat capacity of the anvils was approximated by the high-temperature Dulong-Petit limit, whereas the Hugoniot density was determined from the Rankine-Hugoniot relations.

The thermal properties of Fe needed in [3.2] refer to a partially released state if the shock impedance of the anvil is lower than that of Fe, as is true for Al_2O_3 and LiF. The released density was calculated using the method of Lyzenga and Ahrens (1978), while the heat capacity was assumed to be the Dulong-Petit value plus an electronic contribution as given by Brown and McQueen (1986). The incorporation of an electronic contribution to C_v does not affect the corrected Hugoniot temperatures (Figure 4.1) by more than

approximately 50 K. In order to obtain the thermal conductivity of Fe we chose a different approach than that used for the anvil material. Experimental data have been obtained for the electrical conductivity, σ , of Fe under shock conditions by Keeler (1971). Electrical conductivity can, in turn, be related to the thermal conductivity of metals via the Wiedemann-Franz relation

$$\kappa=L\sigma T \quad [3.3],$$

where L, the Lorentz number, has a relatively constant value of about $2.45 \times 10^{-8} \text{W} \cdot \Omega / \text{K}^2$ for most metals. A linear least-squares regression of σ versus compression, ρ_0/ρ , yielded an excellent fit with a correlation coefficient of -0.992. The data used for this curve-fitting were taken from Matassov (1977, fig. 7.4). Knowing the compression of Fe in the release state, we obtain κ_r for Fe by assuming that the temperature of the released Fe, needed in the Wiedemann-Franz relation, is given by the observed interface temperature T_i . A value of α is calculated using [3.2], thereby allowing an initial value for the released temperature, T_r , to be determined by [3.1]. The entire procedure was repeated iteratively, using T_r in [3.3] to obtain an improved value of κ_r , and then recalculating T_r , until T_r converged to a stable value.

At this point in the data reduction we have the temperature of Fe in a partially released state of lower pressure than the Hugoniot. To obtain the Hugoniot temperature, it is necessary to correct for the effects of partial release, which we do by using the relation

$$T_r = T_h \exp \left\{ - \int_{v_h}^{v_r} (\gamma/v) dv \right\}$$

where γ is the Grüneisen parameter of Fe. We assume a constant value of $\gamma\rho=16.7 \text{ gm/cm}^3$ (Brown and McQueen, 1986) and obtain the released volume, v_r , using the method of Lyzenga and Ahrens (1978). Further details of these

calculations, as well as theoretical Hugoniot temperature calculations, are given by Svendsen *et al.* (1987; Chapter I, § 4).

§4. Discussion

A complete summary of our results is given in Table 4.1. Perhaps the most important point to be made is that we have obtained a wide range of inferred Hugoniot temperatures of between $\approx 6,000$ to over 11,000 K. Because the calculated Hugoniot temperatures of Al_2O_3 are lower by several thousand degrees (Table 4.1 and Svendsen *et al.*, 1987), these data represent compelling evidence that the temperature of the opaque sample, as opposed to that of the anvil material, is measured using the technique employed in this study. Although anomalously high temperatures have previously been measured for insulators under shock compression (*e.g.*, Schmitt and Ahrens, 1984), this appears to be a relatively low-pressure phenomenon related to localized "shear band" deformation of the sample, which is not operative at high (≈ 100 GPa) pressures. Moreover, the high "shear band" temperatures are usually typified by emissivities at least one order of magnitude smaller than those measured in the present study. We conclude, therefore, that we are in fact able to record the temperature of Fe in a shock-induced, high-pressure state. This also implies that the Al_2O_3 anvil remains at least partially transparent under P and T conditions defined by the Hugoniot pressure in the anvil and the interface temperature (≈ 230 GPa and 7000-9000 K).

It is apparent from Table 4.1 that the range of inferred Hugoniot temperatures are larger than would be expected from the precision of the data. Moreover, it is equally clear that most of the obvious possible sample defects, such as an imperfect sample-anvil interface or sample porosity, would yield anomalously high temperatures. Thus, the lowest observed temperatures should most closely approximate the true Hugoniot temperatures. In Figure 4.1 we have plotted our

Table 4.1. Results of Shock Temperature Measurements on Fe

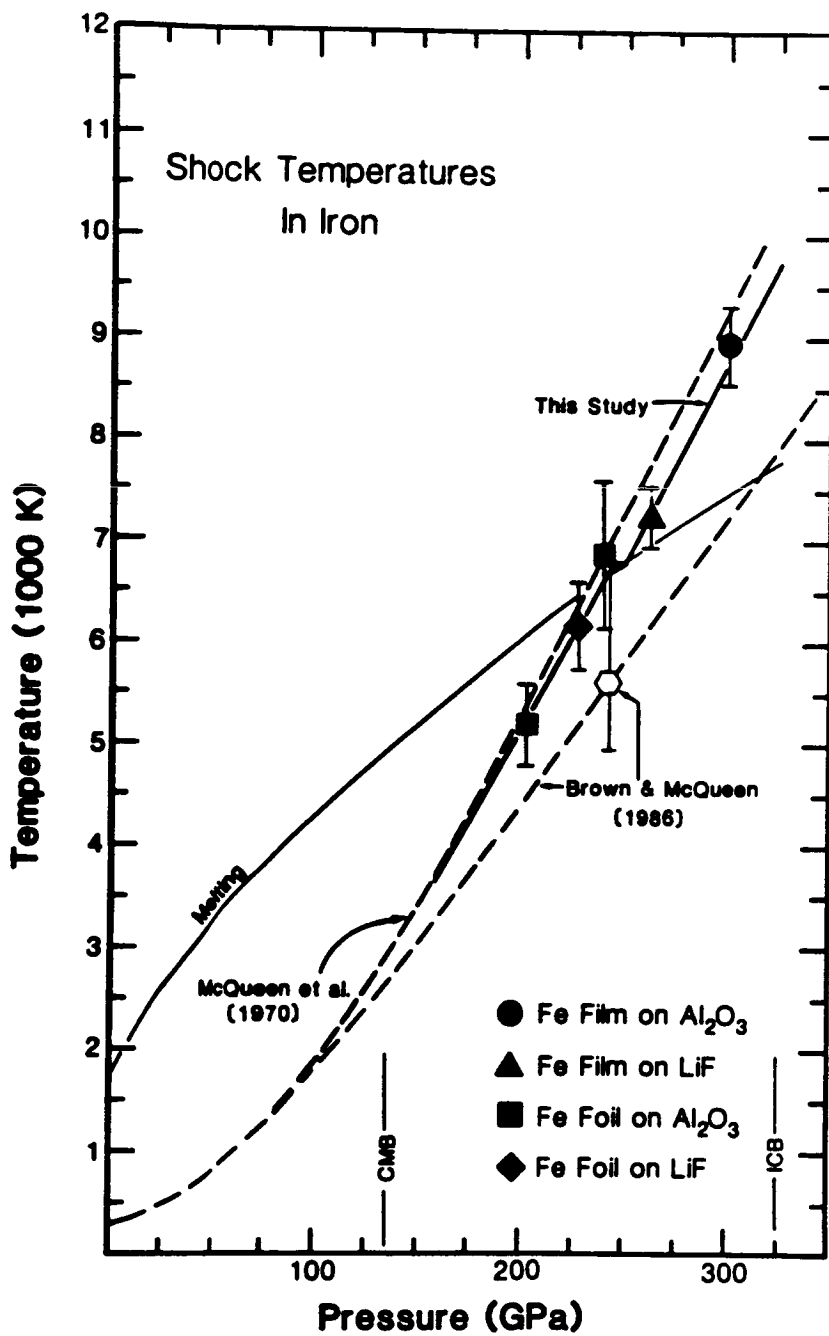
Shot No.	Sample	Anvil Type	P_h (GPa) Fe	P_a (GPa) Anvil	T_i (K) [†] Interface	T_a (K) Anvil	T_h (K) Fe	ϵ^\ddagger
167	Film	Al ₂ O ₃	196	157	4750 ±420	1340	6110	0.29 ±.14
189	Foil	Al ₂ O ₃	202	161	4010 ±420	1380	5200	0.29 ±.14
173	Film	Al ₂ O ₃	226	178	6240 ±170	1550	7910	0.33 ±.05
190	Foil	LiF	227	122	4660 ±420	2790	6180	0.39 ±.19
188	Foil	Al ₂ O ₃	241	188	5390 ±740	1660	6870	0.10 ±.6
191	Film	Al ₂ O ₃	244	190	6990 ±350	1680	8950	0.47 ±.15
183	Foil	Al ₂ O ₃	245	191	6970 ±280	1690	8920	0.34 ±.07
157	Film	Al ₂ O ₃	251	195	6380 ±300	1730	8200	0.70 ±.12
159	Film	LiF	263	140	5270 ±280	3410	7240	0.96 ±.22
192	Film	Al ₂ O ₃	263	203	9220 ±800	1820	11610	0.29 ±.30
174	Film	Al ₂ O ₃	268	207	7580 ±420	1860	9670	0.46 ±.13
181	Foil	Al ₂ O ₃	276	212	9300 ±550	1920	11730	0.32 ±.14
168	Film	Al ₂ O ₃	300	228	6990 ±330	2090	8930	0.86 ±.16

[†]unweighted fit.

[‡] ϵ = effective emissivity

All Hugoniot pressures (P_h) are measured with a precision of better than ± 1 GPa. Note that P_h for the anvil is also the pressure in the partially released Fe after the shock wave enters the anvil.

Figure 4.1. Hugoniot temperatures, deduced from our experimental data, as a function of pressure. The heavy solid line and filled symbols are from the present study. The dashed curves are calculated Hugoniot temperatures that differ mainly in the assumptions made about the specific heat of Fe: McQueen *et al.* (1970) assume $C_{\text{v}} = 3R$, whereas Brown and McQueen (1986) incorporate an additional electronic term. The melting curve is consistent with our shock temperature measurements as well as the melting. Data of Williams *et al.* (1987) obtained in the diamond anvil cell at pressure up to 100 GPa. Pressures at the core-mantle (CMB) and inner core-outer core (ICB) boundaries are indicated.



interpretation of the Fe Hugoniot temperatures based upon the data obtained thus far. Also shown in Figure 4.1 are the calculated Hugoniot temperatures of Brown and McQueen (1986), which take into account possible electronic contributions to the specific heat of Fe, and the Hugoniot temperature calculations of McQueen *et al.* (1970), which do not include these effects. Electronic contributions increase C_v and thus lower the Hugoniot temperature at any given pressure (see Brown and McQueen, 1986). The fact that our lowest temperature datum define a P-T trend intermediate between these two theoretical bounds strongly suggests that these data represent the true Hugoniot temperatures of Fe.

Brown and McQueen (1986) have, on the basis of sound velocity measurements, identified two phase transitions along the Hugoniot of Fe at pressures of 200 and 243 GPa; these are inferred to represent ϵ - γ and γ -melt transitions, respectively. The lowest pressure data in Figure 4.1 exceed 200 GPa and we therefore cannot tell whether or not the ϵ to γ transition has any resolvable effect on the P-T trajectory. However, there is a suggestion of an offset in the Hugoniot temperatures above 241 GPa (Figure 4.1) that is analogous to the effect shown schematically in Figure 4.1. Thus, our data are consistent with the interpretation of the Hugoniot intersecting a melting curve of positive slope at 242 GPa, as suggested by Brown and McQueen (1986) and shown in Figure 4.1. This interpretation of our data indicates a thermal offset of the Hugoniot of approximately 450 K, in very good agreement with the estimate of 350 K by Brown and McQueen (1986).

We are currently unsure as to why some of the experimental data yield anomalously high temperatures (Table 4.1). Although great care was taken to produce suitable sample assemblies in a consistent manner, we can only conclude that many of the samples were defective in some way. As discussed in a previous section, the obvious possibilities are an interfacial gap between the foil

sample and the anvil, and porosity of the films. We have calculated the temperatures that would be expected in Fe for the case of an uniform interfacial gap and obtain values that far exceed our observed range of inferred Hugoniot temperatures. For example, at 250 GPa, the temperature of Fe which has been released to atmospheric pressure from the Hugoniot state and reshocked upon impact with a Al_2O_3 anvil is calculated to be 16,700 K. This value is much larger than the values of 8,200-11,700 that were experimentally observed at similar pressures. Therefore, we conclude that none of our foils were separated from the anvils by a uniform gap, although imperfect contact over a fraction of the sample area could have produced the high temperatures observed in some of our foil shots.

It is also possible that heat generated at the driver plate-sample interface was able to diffuse through the sample on the time scale of the experiment. We tested this hypothesis by performing two experiments (#191 and #192) with thin film samples. These samples were sufficiently thin to transmit visible light and assured us of detecting a portion of the light generated at the driver-sample interface, which should be at a much higher temperature than the Hugoniot state of Fe (see Figure 2.2). These experiments yielded much higher temperatures (Table 4.1) than those shown in Figure 4.1. Coupled with the observation that the shot records (Figure 3.1) did not show an increase of voltage with time, indicating no heat diffusion toward the sample-anvil interface, we rejected this as an explanation of the high temperatures observed in many of the shots.

Because of the small mass and delicate nature of the film samples, we have not yet been able to measure the porosity of the films. Therefore, we cannot rule out the possibility of a variable amount of porosity from one sample to another to explain the discrepancies between the results in Figure 4.1, and the higher temperature data listed in Table 4.1. Nonetheless, we maintain that the

interpretation shown in Figure 4.1, the set of lowest shock temperatures representing the Hugoniot temperatures of Fe, is reasonable and the most logical conclusion to be drawn based on available data. It is noteworthy that the data shown in Figure 4.1 consist of several types of sample assemblies: both foils and films on both Al_2O_3 and LiF substrates. As discussed above, each of these sample configurations has a different experimental problem associated with the construction of a suitable target: the foils are most likely to be plagued by interface gaps, while the films are observed to be in perfect contact but may be slightly porous. However, it is significant that the data in Figure 4.1 tightly define a Hugoniot P-T trajectory that is within the range of previously calculated theoretical bounds, and is also wholly consistent with the presence of a melting transition that has been identified by an independent experimental technique. It is highly unlikely that experiments using different types sample assemblies would be in error by the same amount. Such a situation would require that the excess temperature produced by interfacial gaps in the foil shots be equal to the excess temperature produced by porosity in the film shots. We prefer the simpler explanation that the data shown in Figure 4.1 are the Hugoniot temperatures of Fe. This is further supported by the agreement of the shock-temperature data with independent measurements of the melting temperature of Fe under static conditions in a diamond anvil cell (Williams *et al.*, 1987).

Our shock-temperature data constrain the melting point of Fe along the Hugoniot to be 6700 ± 400 K at a pressure of 243 GPa. This value is significantly higher than the recent estimate of 5000-5700 K by Brown and Mc Queen (1986), and suggests that electronic contributions to the specific heat of Fe may not be as significant as assumed in their calculations (see also Boness *et al.*, 1986). When combined with the melting experiments under static pressures to 100 GPa by Williams *et al.* (1987), we obtain a melting curve for Fe as shown in Figure

4.1. This curve indicates that Fe melts at temperatures of 4800 ± 200 K at 136 GPa, the pressure at the core-mantle boundary, and 7800 ± 500 K at 330 GPa, the inner-outer core boundary pressure.

§5. References

- Ahrens, T. J., G. A. Lyzenga, and A. C. Mitchell, Temperatures induced by shock waves in minerals: applications to geophysics, in *High Pressure Research in Geophysics*, 570-594, edited by S. Akimoto and M.H. Manghni, Academic Press, New York, 1982.
- Anderson, O. L., Properties of iron at the earth's core conditions, *Geophys. J. R. astr. Soc.*, **84**, 561-579, 1986.
- Berry, L. G., ed., *Powder Diffraction File*, **6**, Joint Committee on Powder Diffraction Standards, Philadelphia, Pennsylvania, 1967.
- Boness, D. A., J. M. Brown, and A. K. McMahan, The electronic thermodynamics of iron under earth core conditions, *Phys. Earth Planet. Int.*, **42**, 227-240, 1986.
- Boslough, M. B., Shock-wave properties and high-pressure equations of state of geophysically important materials, *Ph.D. Dissertation*, 171 pp., California Institute of Technology, Pasadena, California, 1984.
- Brown, J. M., and R. G. McQueen, Phase transitions, Grüneisen parameter and elasticity for shocked iron between 77 GPa and 400 GPa, *Jour. Geophys. Res.*, **91**, 7485-7494, 1986.
- Carter, W.J., Hugoniot equation of state of some alkali halides, *High Temperatures-High Pressures*, **5**, 313-318, 1973.
- Grover, R., and P. A. Urtiew, Thermal relaxation at interfaces following shock compression, *J. Appl. Phys.*, **45**, 146-152, 1974.
- Jeanloz, R., and T. J. Ahrens, Pyroxenes and olivines: structural implications of shock-wave data for high pressure phases, in *High-Pressure Research:*

- Applications to Geophysics*, 439-461, edited by M. H. Manghnani and S. Akimoto, Academic Press, New York, 1977.
- Jones, A. H., W. M. Isbell, and C. J. Maiden, Measurements of the very-high-pressure properties of materials using a light-gas gun, *J. Appl. Phys.*, **37**, 3493-3499, 1966.
- Keeler, R. N., Electrical conductivity of condensed media at high pressures, in *Physics of High Energy Density, Proc. International School of Phy. "Enrico Fermi" XLVIII*, edited by P. Cadirola and H. Knoepfel, 106-125, Academic Press, New York, 1971.
- Kingery, W. D., J. Francl, R. L. Coble, and T. Vasilos, Thermal conductivity: x, data for several pure oxide materials corrected to zero porosity, *J. Amer. Cer. Soc.*, **37**, 107-110, 1954.
- Kormer, S. B., Optical study of the characteristics of shock-compressed condensed dielectrics, *Soviet Physics USP.*, **11**, 229-254, 1968.
- Kormer, S. B., M. V. Sinitsyn, G. A. Kirilov, and V. D. Urlin, Experimental determination of temperature in shock-compressed NaCl and KCl and of their melting curves at pressures up to 700 kbar, *Soviet Phys. JETP*, **21**, 689-700, 1965.
- Lyzenga, G. A., Shock temperatures of materials: experiments and applications to high-pressure equation of state, *Ph.D. Dissertation*, 208 pp., California Institute of Technology, Pasadena, California, 1980.
- Lyzenga, G. A. and T. J. Ahrens, The relation between the shock-induced free-surface velocity and the postshock specific volume of solids, *J. Appl. Phys.*, **49**, 201-204, 1978.
- Lyzenga, G. A. and T. J. Ahrens, Multiwavelength optical pyrometer for shock compression experiments, *Rev. Sci. Instrum.*, **50**, 1421-1424, 1979.
- Marsh, S. P., ed., *LASL Shock Hugoniot Data*, 260-263, University of California Press, Los Angeles, 1980.

- Matassov, G., The electrical conductivity of iron-silicate alloys at high-pressure and the earth's core, *Ph.D. Dissertation*, 180 pp., University of California, Livermore, California. Lawrence Livermore Document UCRL-52322, 1977.
- McQueen, R. G., S. P. Marsh, J. W. Taylor, J. N. Fritz, and W. J. Carter, The equation of state of solids from shock wave studies, in *High-Velocity Impact Phenomena*, 293-417, edited by R. Kinslow, Academic Press, New York, 1970.
- Men', A. A., A. Z. Chechel'nitskii, V. A. Sokolov, and E. N. Simun, Thermal conductivity of lithium fluoride in the 300-1100 K temperature range, *Sov. Phys. Solid State*, **15**, 1844-1845, 1974.
- Mitchell, A. C., and W. J. Nellis, Shock compression of aluminum, copper, and tantalum, *J. Appl. Phys.*, **52**, 3363-3375, 1981.
- Pathak, P. D., and N. G. Vasavada, Thermal expansion of LiF by x-ray diffraction and the temperature variation of its frequency spectrum, *Acta Cryst.*, **A28**, 30-33, 1972.
- Rapp, J. E., and H. D. Merchant, Thermal expansion of alkali halides from 70 to 570 K, *J. Appl. Phys.*, **44**, 3919-3923, 1973.
- Rice, M. H., R. G. McQueen, and J.M. Walsh, Compression of solids by strong shock waves, *Solid State Phy.*, **6**, 1-63, edited by F. Seitz and D. Turnbull, Academic Press, New York, 1958.
- Roufousse, M. C., and R. Jeanloz, Thermal conductivity of minerals at high pressure: the effect of phase transitions, *J. Geophys. Res.*, **88**, 7933-7409, 1983.
- Schmitt, D. R. and T. J. Ahrens, Emission spectra of shock-compressed solids, in *Shock Waves in Condensed Matter - 1983*, 313-316, edited by J.R. Asay, R. A. Graham and G. K. Straub, North-Holland, Amsterdam, 1984.
- Strong, H. M., R. E. Tuft, and R. E. Hanneman, The iron fusion curve and the

- γ - δ -1 triple point, *Metal. Trans.*, **4**, 2657-2661, 1973.
- Svendsen, B., J. D. Bass, and T. J. Ahrens, Optical radiation from shock-compressed materials and interfaces, in *High Pressure Research in Geophysics*, edited by M. Manghnani and S. Akimoto, Terra Publishing Co., in press, 1987.
- Touloukian, Y. S., R. W. Powell, C. Y. Ho, and P. G. Klemens, *Thermophysical Properties of Matter, Volume 12: Thermal Expansion*, Thermophysical Properties Research Center of Purdue University, Data Series, Plenum Publishing Corporation, New York, 1975.
- Urtiew, P. A., Effect of shock loading on transparency of sapphire crystals, *J. Appl. Phys.*, **45**, 3490-3493, 1974.
- Urtiew, P. A. and R. Grover, Temperature deposition caused by shock interaction with material interfaces, *J. Appl. Phys.*, **45**, 140-145, 1974.
- Urtiew, P. A., and R. Grover, The melting temperature of magnesium under shock loading, *J. Appl. Phys.*, **48**, 1122-1126, 1977.
- Williams, Q., R. Jeanloz, J. D. Bass, B. Svendsen, and T. J. Ahrens, The melting curve of iron to 250 Gigapascals: A constraint on the temperature at the earth's center, *Science*, **236**, 181-182, 1987.
- Xu, J. A., H. K. Mao, and P. M. Bell, High-pressure ruby and diamond fluorescence: observations at 0.21 to 0.55 terapascal, *Science*, **232**, 1404-1406, 1986.

Chapter V

Ideal Fe-FeS, Fe-FeO Phase Relations and the Earth's Core†

Bob Svendsen, William W. Anderson, Thomas J. Ahrens

Division of Geological and Planetary Sciences,
California Institute of Technology, Pasadena, California, 91125, USA.

Jay D. Bass

Department of Geology,
University of Illinois, Urbana, Illinois, 61801, USA.

†submitted to *Physics of the Earth and Planetary Interiors*.

Abstract

Liquid-state and solid-state model fits to melting data for Fe, FeS and FeO provide constraints for calculating ideal phase relations in Fe-FeS and Fe-FeO systems in the pressure range corresponding to the earth's outer core. The liquid-state model fit to the Fe melting data of Williams and Jeanloz (1986) places constraints on the temperature and other properties along the liquidus above the range of their data. The temperature along the best-fit Fe liquidus is 5000 K at 136 GPa and 7250 K at 330 GPa, which is somewhat lower than that implied by the Hugoniot results (~ 7800 K). This discrepancy may be due to the reshock effect discussed above, or some inaccuracy in the extrapolation, presuming the Hugoniot results represent the equilibrium melting behavior of Fe. Constraints on the solidi of FeS and FeO from the comparison of data and solid-state model calculations imply that FeS and FeO melt at approximately 4610 K and 5900 K, respectively, at 136 GPa, and approximately 6150 K and 8950 K, respectively, at 330 GPa. Calculations for the equilibrium thermodynamic properties of solid and liquid Fe along the coincident solidus and liquidus imply that the entropy of melting for Fe is approximately independent of pressure at a value of approximately R (where R is Ryberg's constant), while the change in the molar heat capacity across the transition increases with pressure from approximately $0.5 R$ to $4R$ between standard pressure and 330 GPa. We use these constraints to construct ideal-mixing phase diagrams for Fe-FeS and Fe-FeO systems at outer core pressures, assuming that Fe and FeS, or Fe and FeO, respectively, are the solid phases in equilibrium with the liquid Fe-FeS or Fe-FeO mixtures, respectively. Calculated Fe-FeO eutectic compositions at 330 GPa (15-20 mole % O) are less than 25 mole % O, while calculated Fe-FeS eutectic compositions at 330 GPa (23-30 mole % S) are generally greater than 25 mole % S. Combined with density considerations, these calculations imply that an O-rich outer core is more likely to lie on the FeO-rich side of the Fe-

FeX eutectic, while an S-rich outer core is more likely to lie on the Fe-rich side of the Fe-FeX eutectic. In addition, eutectic temperatures in both systems are ≥ 5000 K at 330 GPa. Widely accepted temperature profiles for the outer core, ranging from ≤ 3000 K at the 136 GPa, the core-mantle boundary, to ≤ 4200 K at 330 GPa, the outer-inner core boundary, are about 1000-1500 K below this value. In the context of the outer-inner core boundary-phase boundary hypothesis, this discrepancy implies that at least one boundary layer of 1000-1500 K exists in the mantle, possibly at its base in the D'' region.

§1. Introduction

Temperature is perhaps the most influential and elusive of all thermodynamic fields defining the physical state of terrestrial planetary interiors. Being fundamental to the thermomechanical behavior and evolution of these interiors (*e.g.*, O'Connell and Hager, 1980; Janle and Meissner, 1986), it has been a central part of innumerable modeling efforts (*e.g.*, Stacey and Loper, 1984). Unsupported by independent means, however, the value of this modeling is somewhat ambiguous. High-pressure and temperature experimental work on cosmochemically or physically plausible constituent materials, such as Fe and its alloys (*e.g.*, FeS and FeO), has the potential to constrain the complete equilibrium thermodynamic "equation-of-state" of these materials and provide such independent constraints. In this paper, we discuss some implications of recent static (Fe and Fe_{0.9}S, Williams and Jeanloz, 1986; FeO, Knittle and Jeanloz, 1987) and dynamic (Fe, Bass *et al.*, 1987; Fe_{0.9}S, Anderson *et al.*, 1987) experiments, and their potential impact on the question of the temperature profile in the earth's outer core (OC), and the temperature of the inner-core boundary (ICB).

Birch (1952) first noted that his uncompressed density profile of the core was ~ 10 -15% less than that of pure Fe (or Fe-Ni: McQueen and Marsh, 1966)

along its Hugoniot at corresponding pressures. Knopoff and MacDonald (1959) suggested that Birch's observation implied that Fe must be combined with one or more elements, X_i (*e.g.*, H, He, C, N, Si, O and/or S), of significantly smaller atomic number, in the core. This possibility has since accreted a vast literature (see Jacobs, 1975; Ringwood, 1979; Stevenson, 1981) concerned with candidate X_i and their potential role in core formation, dynamics and evolution through phase relations in the Fe- X_i system. The relevance of high-pressure, high-temperature experiments toward constraint of the temperature profile in the OC rests on the hypothesis (Verhoogen, 1961) that the inner core (IC) is growing at the expense of the OC, the ICB then being a phase boundary in the Fe- X_i system. From this perspective, if the OC mixture Fe- X_i is a eutectic system, and if its composition lies on the Fe-rich side of the eutectic, pure Fe or Fe containing "small" amounts of some or all of the of the X_i may crystallize out at the ICB to form the IC, leaving the coexisting liquid more highly concentrated in the X_i . In this case, the ICB will be a compositional and a phase boundary, and the temperature of the ICB should then be bounded above by the melting temperature of pure Fe and below by the eutectic temperature of the system at the ICB.

To explore possible high-pressure phase relations of Fe-X systems, we use the recent experimental results on the solid-liquid phase boundaries of Fe (Brown and McQueen, 1986; Williams *et al.*, 1987), FeS (Fe_xS : Brown *et al.*, 1984; Williams and Jeanloz, 1986; Anderson *et al.*, 1987a) and FeO (Fe_xO : Anderson *et al.*, 1987a; Knittle and Jeanloz, 1987) to constrain models for Fe, FeO and FeS solidi via a parameterization using Lindemann's law and the Hugoniot states of these materials. In addition, we use the Fe melting data of Williams and Jeanloz (1986), as given in Williams *et al.* (1987), to constrain an Fe liquidus and the equilibrium thermodynamic properties of liquid Fe in the context of a liquid-state perturbation model (*e.g.*, Stevenson, 1980) for Fe.

With these models, we may rationally extrapolate the experimental results for these materials to OC pressures, and use these extrapolations to explore possible equilibrium phase relations of Fe-S and Fe-O systems, in a similar fashion to the work of Stevenson (1981) and Anderson *et al.* (1987b) on Fe-S systems.

§2. High-Pressure Liquid-State Model for Fe

At high pressure and/or temperature, the influence of repulsive interatomic or intermolecular forces on the structure and properties of most liquids suggests a high-pressure, temperature model for these liquids in which the constituents interact only repulsively. A logical extreme of this idea is represented by the "hard-sphere" model of a liquid (*e.g.*, Hansen and MacDonald, 1975; Barker and Henderson, 1976), which assumes the liquid is composed of perfectly spherical "particles," each having a diameter d , which interact in a pairwise fashion via a potential, $\psi_{\text{HS}}(r)$, of the form

$$\psi_{\text{HS}}(r) = \begin{cases} \infty & r < d \\ 0 & r \geq d \end{cases} \quad [2.1],$$

where r is the (radial) distance from the center of either sphere involved in the interaction. The collective interactions between the liquid constituents are, to some degree, correlated (*i.e.*, nonrandom) and give the liquid an effective (short range) structure. For a liquid of N constituents, occupying a volume V , which interact in a spherically symmetric fashion, this structure is described by the radial pair-distribution function, $g(r)$, defined such that $4\pi\rho_N r^2 g(r)$ is the number of spheres r to $r+dr$ away from the center of a given sphere in the liquid, where $\rho_N \equiv N/V$ is the number density of spheres. In particular, note that $g_{\text{HS}}(r)$, the hard-sphere radial distribution function, is zero for $r < d$, since $g(r)$ is proportional to $\exp[-\beta\psi(r)]$, where $\beta \equiv 1/k_B T$, T is the absolute temperature, and k_B is Boltzmann's constant. X-ray diffraction and other techniques have found that

the effective radial distribution function of many liquids, including liquid Fe at standard pressure (*e.g.*, Waseda and Ohtani, 1974; Gopal Rao and Sen, 1976; Vorob'ev *et al.*, 1977), is quite similar to $g_{\text{HS}}(r)$, suggesting that the constituents of these liquids interact in a "hard-sphere-like," radially symmetric fashion. This observation, combined with the fact that, via statistical mechanics and numerical simulations, the equilibrium thermodynamic properties of hard-sphere liquids are well established (*e.g.*, Barker and Henderson, 1976), suggests that the corresponding properties of these liquids can be related, or referenced, to those of a hard-sphere liquid (Zwanzig, 1954). Via the relation between the interaction potential, canonical partition function, and Helmholtz free energy, this idea leads to a relationship between the Helmholtz free energy of the liquid, $F_{\text{liq}}(T, \rho_N)$, and that of the equivalent hard-sphere system, $F_{\text{HS}}(T, \rho_N)$, of the form

$$F_{\text{liq}} \leq F_{\text{mod}} \equiv F_{\text{HS}} + F_{\text{INT}} \quad [2.2]$$

(*e.g.*, Mansoori and Canfield, 1969). In [2.2], F_{INT} is the total pair-interaction contribution to F_{mod} , *i.e.*,

$$F_{\text{INT}} \equiv 2\pi\rho_N \int_d^{\infty} \psi(r)g_{\text{HS}}(r)r^2 dr \quad [2.3],$$

where $\psi(r)$ is the effective pair-interaction potential of the liquid constituents. To use [2.2], we need expressions for $g_{\text{HS}}(r)$, F_{HS} , and $\psi(r)$. There exists no exact solution for $g_{\text{HS}}(r)$, $r \geq d$; among the approximate solutions, that formulated by Percus and Yevick (1959; PY), which assumes that any two liquid constituents are essentially uncorrelated at distances greater than $r=d$, agrees best with computer simulations (*e.g.*, Alder and Wainwright, 1957). This agreement has motivated a wealth of analytic results for the thermodynamic properties of a PY hard-sphere fluid, including F_{HS} , making it the logical choice as a reference system.

Because we cover a wide range of pressures and temperatures, including low pressures, we choose a pair potential representing both repulsive (high P,T) and attractive (low P,T) interactions. In particular, we assume the so-called "Double-Yukawa" potential (*e.g.*, Foiles and Ashcroft, 1981)

$$\psi(r) \equiv \frac{\epsilon\sigma}{r} \left\{ e^{-\lambda(r-\sigma)} - e^{-\omega(r-\sigma)} \right\} \quad [2.4].$$

In [2.4], σ represents the distance away from the center of each sphere where the potential is equal to zero, *i.e.*, $\psi(\sigma) = 0$, while λ^{-1} is the characteristic length scale of repulsive interaction, and ω^{-1} that for attraction interactions. Also, ϵ is related to the potential energy of interaction at equilibrium separation. Physically, we expect $\lambda > \omega$, since repulsion and attraction are dominantly short and long-range interactions, respectively. In this case, note that $\psi(r) > 0$ for $r < \sigma$, and $\psi(r) < 0$ for $r \geq \sigma$. We use the Yukawa potential because 1) it is fairly general, and 2) a number of analytic results exist for thermodynamic systems based on this potential via statistical mechanics, as we relate below and in Appendix A.

For a liquid metal such as Fe, electronic processes may contribute to F ; consequently, we need to add a term F_{el} to F_{mod} such that $F_{mod} \equiv F_{HS} + F_{INT} + F_{el}$. As discussed by Stevenson (1980), for example, electronic contributions to F_{liq} may significantly influence the cohesive energy, incompressibility and heat capacity of the liquid. We represent F_{el} by its low temperature (T much less than the Fermi temperature) Sommerfeld expansion (*e.g.*, Wallace, 1972)

$$F_{el} = -\frac{1}{2}\Gamma T^2 \quad [2.5].$$

In [2.5], Γ is the density of electron states at zero temperature, related to the electronic Grüneisen's parameter, γ_e , via the relation (*e.g.*, Wallace, 1972)

$$\gamma_e \equiv \left(\frac{d \ln \Gamma}{d \ln \rho_N} \right) \quad [2.6]$$

Hence, Γ is a function of density alone. Assuming γ_e is constant, [2.6] implies

$$\Gamma(\rho_N) = \Gamma(\rho_{Nr}) \left\{ \frac{\rho_N}{\rho_{Nr}} \right\}^{\gamma_e} \quad [2.7],$$

where ρ_{Nr} is some reference density at which Γ is known. The values of Γ and γ_e of the ϵ and γ phases of Fe have recently been calculated by Boness *et al.* (1986). They argue that the values of Γ and γ_e so constrained should work for liquid-Fe at high pressures as well. We adopt their assertion in the calculations presented below.

From these ingredients, we can develop relations for the equilibrium thermodynamic properties of a homogeneous liquid, which we do in Appendix A. Here, we are particularly interested in relating pressure and temperature to model parameters, since we want to constrain a liquid-state model for Fe from the melting data of Williams and Jeanloz (1986; see also Williams *et al.*, 1987), which are in the form of temperatures in the solid and liquid approximately adjacent to the phase boundary at a series of pressures. From Appendix A, we have the following relations for temperature and pressure in the liquid as a function of the mass density of the liquid, ρ , and model parameters, *i.e.* ([A.65] and [A.66]),

$$T = E T^*(\rho, \hat{\eta}; \lambda^*, \omega^*, \zeta) \quad [2.8]$$

and

$$P = \frac{R}{M} E P^*(\rho, \hat{\eta}; \lambda^*, \omega^*, \zeta, E, \rho_{Nr}, \Gamma, \gamma_e) \quad [2.9]$$

respectively. In [2.8] and [2.9], we have $\lambda^* \equiv \lambda \sigma$, the nondimensional repulsive length scale, $\omega^* \equiv \omega \sigma$, the nondimensional attractive length scale, $\hat{\eta} \equiv \frac{\pi}{6} \rho_N d^3$, the

equilibrium packing fraction of liquid constituents,

$$\zeta \equiv \sigma \left\{ \frac{\rho_N}{\rho} \right\}^{\frac{1}{3}} = \left\{ \frac{N_A}{M} \right\}^{\frac{1}{3}},$$

where N_A is Avogadro's number, and $E \equiv \epsilon/k_B$. Also, R is Ryberg's constant, M is the atomic weight, and ρ_r , Γ_r and γ_e are a reference mass density, density of electronic states at zero temperature, and electronic Grüneisen's parameter, respectively. These last 3 quantities are constrained independently, and so held constant during the fit. In particular, for Fe, we use $\rho_r = 8352 \text{ kg/m}^3$, $\Gamma_r = 5 \text{ mJ/mol}\cdot\text{K}^2$ and $\gamma_e = 1.34$. These are, respectively, the measured STP density (Jephcoat *et al.*, 1986), the calculated electronic density of states at zero temperature and the temperature and electronic Grüneisen's parameter (Boness *et al.*, 1986), of ϵ -Fe. Since Γ is a function of density only, we may recenter it to the standard pressure, melting temperature density of liquid Fe, 7015 kg/m^3 (Drotning, 1981). In this case, we have $\Gamma(7015) = 6.31 \text{ mJ/mol}\cdot\text{K}^2$, which is reasonably consistent with $\Gamma(7015) = 6.42 \text{ mJ/mol}\cdot\text{K}^2$ for liquid Fe from the work of Yokoyama *et al.* (1983). With these 3 parameters fixed, [2.8] and [2.9] relate 4 variables (T, P, ρ and $\hat{\eta}$) and 4 constant unknowns, or parameters (E, λ^*, ω^* and ζ). We may eliminate either ρ or $\hat{\eta}$ between [2.8] and [2.9] to obtain

$$T = \hat{T}(P, \hat{\eta}; E, \lambda^*, \omega^*, \zeta) \quad \text{or} \quad T = \bar{T}(P, \rho; E, \lambda^*, \omega^*, \zeta) \quad [2.10],$$

respectively. Since we have no other relation(s) among the variables, [2.10] implies that we must choose either ρ or $\hat{\eta}$ as a parameter of the fit. This choice is not difficult, since ρ must change with pressure and temperature along the liquidus. Assuming that $\hat{\eta}$ is constant along the liquidus is not unfounded; computer simulations imply that $\hat{\eta} \approx 0.45$ along the liquidus (Alder and Wainwright, 1957), regardless of the density. Assuming this would tie the variation of the hard-sphere diameter, d , directly to that of the density along the liquidus, since

by definition of the packing fraction, d then varies inversely with the cube root of the density. So, with $\hat{\eta}$ as parameter of the fit, we have

$$T_M = \hat{T}(P; \lambda^*, \omega^*, \hat{\eta}, \zeta, E) \quad [2.11]$$

giving us five parameters to constrain from the fit: E , $\hat{\eta}$, λ^* , ω^* and ζ .

We compare models and data in the context of the standard Poisson statistic (*e.g.*, Bevington, 1969; Press *et al.*, 1986), χ^2 . In our case, it is given by

$$\chi^2(\mathbf{a}) \equiv \sum_{k=1}^N \frac{1}{[\sigma_T(P_k)]^2} \left\{ T_{M_{\text{data}}}(P_k) - T_{M_{\text{mod}}}(P_k; \mathbf{a}) \right\}^2. \quad [2.12]$$

In this relation, $T_{M_{\text{data}}}(P_k)$, $T_{M_{\text{mod}}}(P_k; \mathbf{a})$ and $\sigma_T(P_k)$ are the experimental and model melting temperatures, and the experimental uncertainties, respectively, all at a particular pressure, P_k . Also, N is the number of data points. $T_{M_{\text{mod}}}$ is given by [2.11]. The "vector" \mathbf{a} is the model parameter vector, with components a_p , in our case given by

$$a_p \equiv \{ \lambda^*, \omega^*, \hat{\eta}, \zeta, E \} \quad [2.13].$$

We minimize $\chi^2(\mathbf{a})$ using a combination of 1) multidimensional Golden Section (GS) search to explore the $\chi^2(\mathbf{a})$ hypersurface for the distribution of local minima, and 2) the Levenburg-Marquardt (LM) algorithm (*e.g.*, Press *et al.*, 1986) to solve [2.12] locally and iteratively to find the "best fit" values of the a_p , $a_{p(\text{min})}$, defined by

$$\frac{\partial \chi^2(\mathbf{a})}{\partial \mathbf{a}} = 0.$$

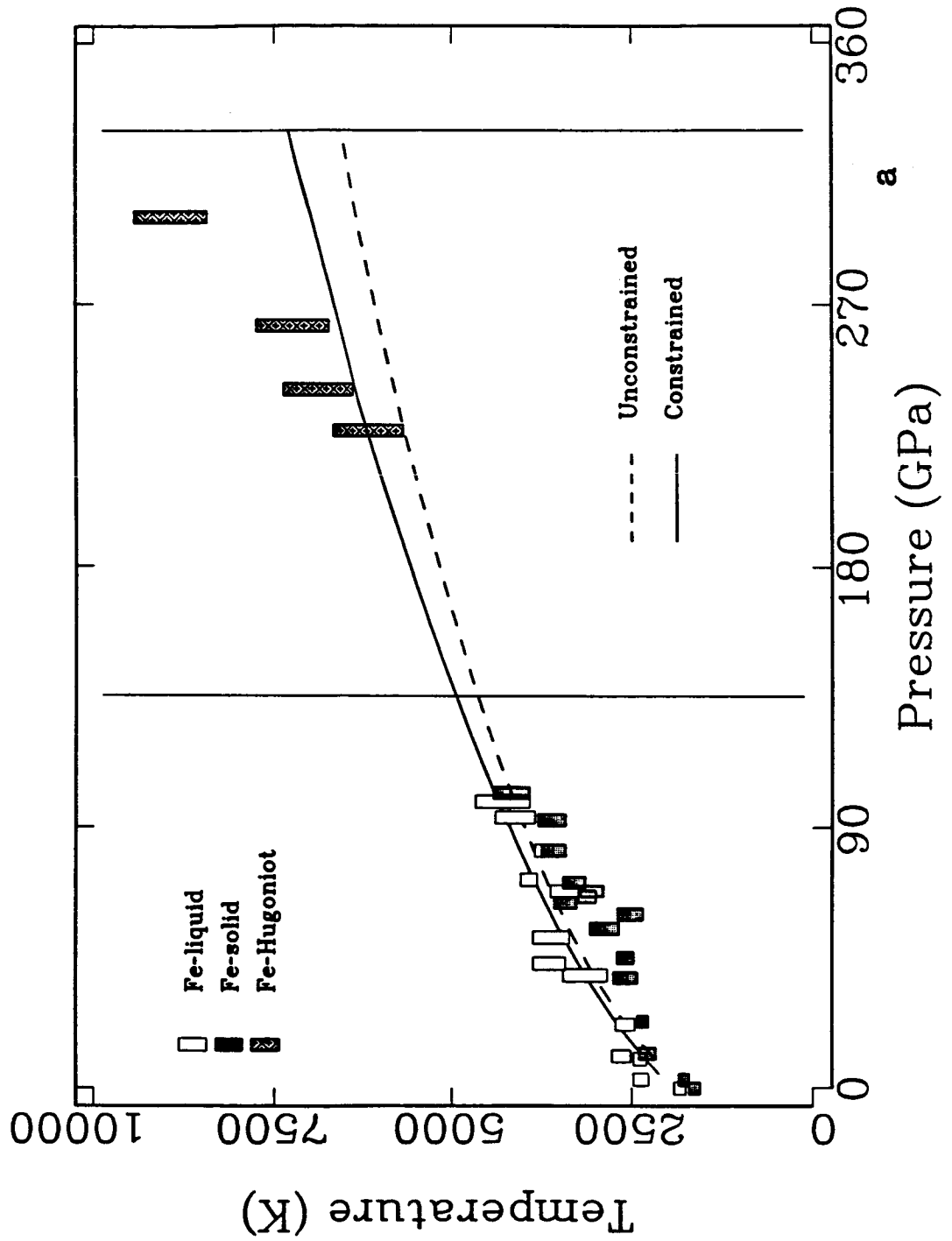
This algorithm searches down successive independent (*i.e.*, conjugate) gradients, and terminates the iterative process when either a preset value of χ^2 (56, which is twice the "best" theoretically-expectable value; see below) and/or χ^2 does not decrease by some chosen amount (1%) between successive iterations. We present examples of "best fits" in Figure 2.1a, along with the Fe melting data of

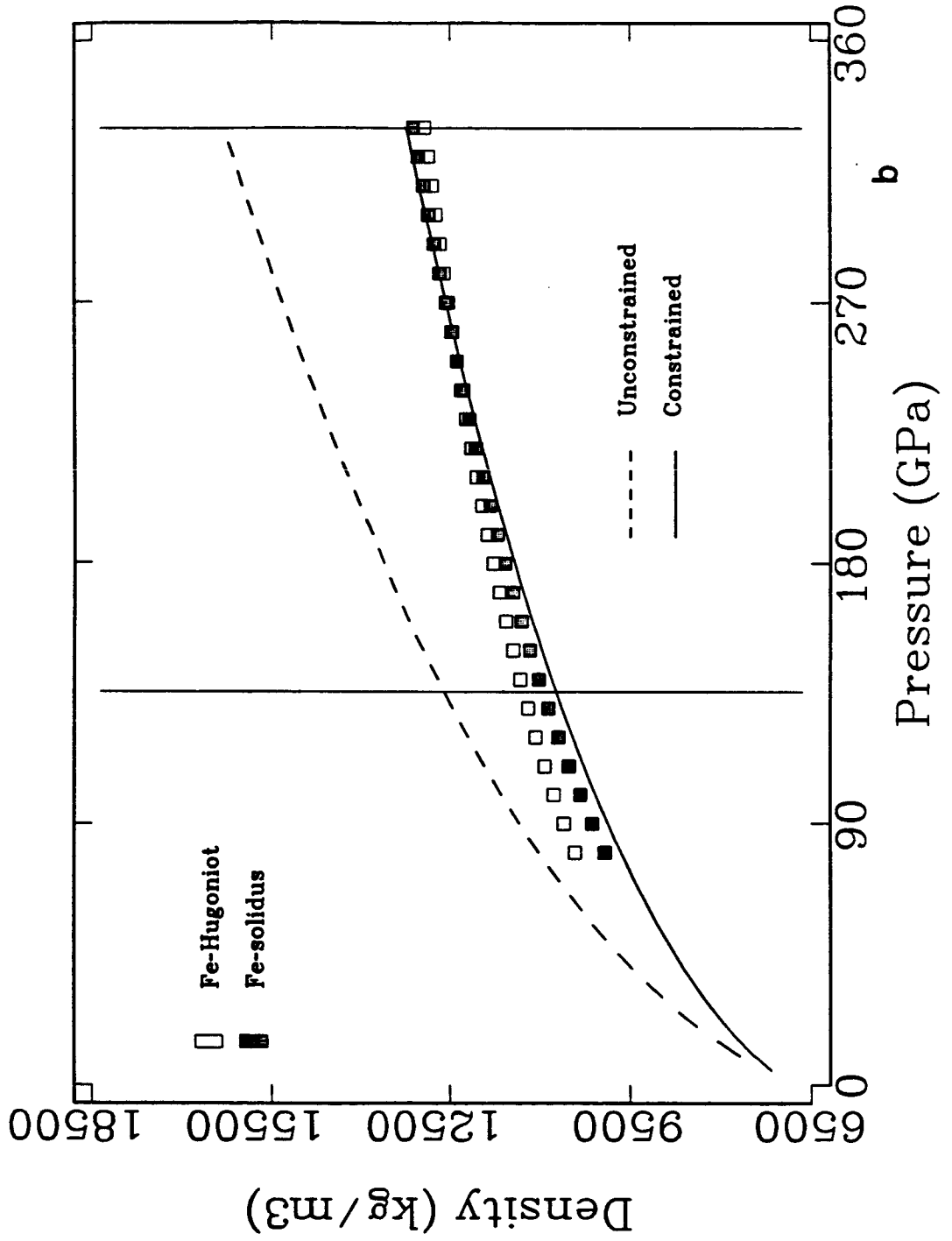
Williams and Jeanloz (1986), as given in Williams *et al.* (1987), and compare these fits with the Fe shock temperature results of Bass *et al.* (1987). In their diamond cell experiments, Williams and Jeanloz were able to directly observe Fe melting; the "Fe-solid" points correspond to the highest temperature at which Fe was entirely solid, while those labeled "Fe-liquid" correspond to the lowest temperatures at which Fe was entirely liquid. We use all these points (28) as given, along with their associated uncertainties, in the fit. This allows the LM algorithm to find the "best" compromise among them, each datum influencing the fit according to how "well" or "poorly" they are determined, as indicated by their associated uncertainties and implemented in the χ^2 statistic. The first fit, shown by the dashed line, represents an entirely unconstrained fit, *i.e.*, all parameters are allowed to vary during the fit. This fit has a χ^2 of 150, with parameter values $\lambda^*=8.50$, $\omega^*=0.361$, $\hat{\eta}=0.451$, $\zeta=0.0808$ m/kg^{1/3}, and $E=203$ K. The value of χ^2 for a "good" fit is roughly given by the difference between the number of data and fit parameters; in our case, then, we might expect $\chi^2 \sim 23$ at best. That our best fit is six times this value is not completely unexpected, considering the amount of "scatter" in the data. With this model fit, we calculate a number of liquid-Fe properties using the relations detailed in Appendix A and discussed below. Of particular importance is the density of Fe along the liquidus, ρ_M^l , given by, from [2.9]

$$\rho_M^l = \rho_M^l(P; \lambda^*, \omega^*, \hat{\eta}, \zeta, E, \rho_N, \Gamma_r, \gamma_e) \quad [2.14],$$

which we plotted in Figure 2.1b versus pressure, along with perhaps the best constraint we have on Fe at high-pressure, *i.e.*, density along the Fe Hugoniot. We have also plotted the density of solid Fe at the liquidus temperature, using the Hugoniot density as reference via the method discussed below; these points are labeled "Fe-solidus" in Figure 2.1b. With the expectations that the density of liquid Fe should 1) be less than that of solid Fe at the same pressure and

Figure 2.1. Liquid state model fits to the Fe melting data of Williams and Jeanloz (1986). Part (a) depicts the temperature fits versus pressure. The dashed curve represents the best unconstrained fit to the data, while the continuous curve represents the best fit with the liquidus density constrained to be less than or equal to that of the solidus, as referenced to the Hugoniot, as shown in part (b). Each solidus or hugoniot point (rectangle) represents $\pm 20 \text{ kg/m}^3$ and $\pm 2 \text{ GPa}$. Vertical lines represent pressure at core-mantle boundary (136 GPa) and outer-inner core boundary (330 GPa).





temperature (for a positive Claperyon slope), and 2) approach the density of solid-Fe along the phase boundary at high pressure, this fit that looks reasonable in T-P space appears highly unlikely in P- ρ space. This fit is characteristic of all local minima on the χ^2 hypersurface investigated in a completely unconstrained fashion.

Given the unacceptable liquidus density prediction from the completely unconstrained fits, we are compelled to constrain the density of liquid-Fe along the liquidus to be less than or equal to that estimated for solid-Fe at (approximately) the same temperature during the fit. Among the model fits satisfying this constraint, the one represented by the continuous curve in Figures 2.1a and 2.1b is "most" consistent with other information on liquid Fe, as we discuss below. This fit has a χ^2 of 250 and fit parameters $\lambda^*=8.02$, $\omega^*=0.872$, $\hat{\eta}=0.49$, $\zeta=0.0605$ m/kg^{1/3} and $E=2190$ K. Note that this is a significantly worse fit than the first, on the basis of χ^2 alone. Note that this fit predicts significantly higher temperatures along the Fe liquidus than the first, a reasonable result in order to have a smaller liquidus density at the same pressure. This fit also predicts a much higher (200-1000 K) melting temperature for Fe between 136 and 330 GPa than most previous predictions (*e.g.*, Brown and McQueen, 1986; Anderson, 1982; but see Abelson, 1981; Bass *et al.*, 1987; Williams *et al.*, 1987). Both of the fits imply that liquid Fe "ion-ion" interactions are strongly repulsive; this is consistent with the observation that liquid-Fe is a "good" hard-sphere fluid. These results imply that the variation of density along the phase boundary may provide a more sensitive measure of model parameters than the coincident variation of temperature.

If we extrapolate the properties of liquid Fe predicted by this last model fit to standard pressure (SP, 0.1 MPa), we may compare them with data constraining these properties or other calculations, as appropriate. The results of this are presented in Table 2.1. Recall that we have used only the high-pressure data of

Table 2.1. Standard Pressure (0.1 MPa) Liquid Fe Properties.

Property	Symbol	Experimental		Models	SI Units
Melting temperature	T_M	1809 ^a		1910†	K
Mass Density	ρ	7015 ^b		6857	kg/m ³
Molar Entropy	S	99.7 ^c		91.6	J/mol·K
Packing Fraction†	η	0.45 ^d		0.49	
Heat capacity, constant V	C_V	33.3 ^e		37.1 ^d 39.0	J/mol·K
Isothermal Bulk Modulus	K_T			89 ^d 87	GPa
Grüneisen's parameter	γ	2.44 ^e	1.67 ^f	1.62	
Isentropic Bulk Modulus	K_S	110 ^g	136 ^h	111	GPa
Thermal expansion	α	88 ^b	122 ^e	83 ^d 89	μK^{-1}
Heat capacity, constant P	C_P	46.6 ⁱ		49.8	J/mol·K
Bulk Velocity	v_ϕ	3930 ^j	4400 ^k	4017	m/s
Electrical Resistivity	ρ_e	1.4 ^l			$\mu\Omega\cdot\text{m}$
Shear Viscosity	μ	2.1 ^e	4.8-7.0 ^m	2.5	mPa·s
Thermal Conductivity	k	32 ^e		34	W/m·K
Self-Diffusion	D			4996	nm ² /s

†Unless otherwise indicated, all model values are from present work.

‡Fit parameter.

^a Robie *et al.* (1978).

^b Drotning (1981).

^c Hultgren *et al.* (1973).

^d Yokoyama *et al.* (1983).

^e given in Stevenson (1981).

^f calculated from $\gamma = \alpha K_S / \rho C_P$.

^g calculated from $K_S = \rho v_\phi^2$ using v_ϕ from ^j.

^h calculated from $K_S = \rho v_\phi^2$ using v_ϕ from ^k.

ⁱ Desai (1986).

^j Kurz and Lux (1969).

^k Filipov *et al.* (1966).

^l Busch and Güntherodt (1974).

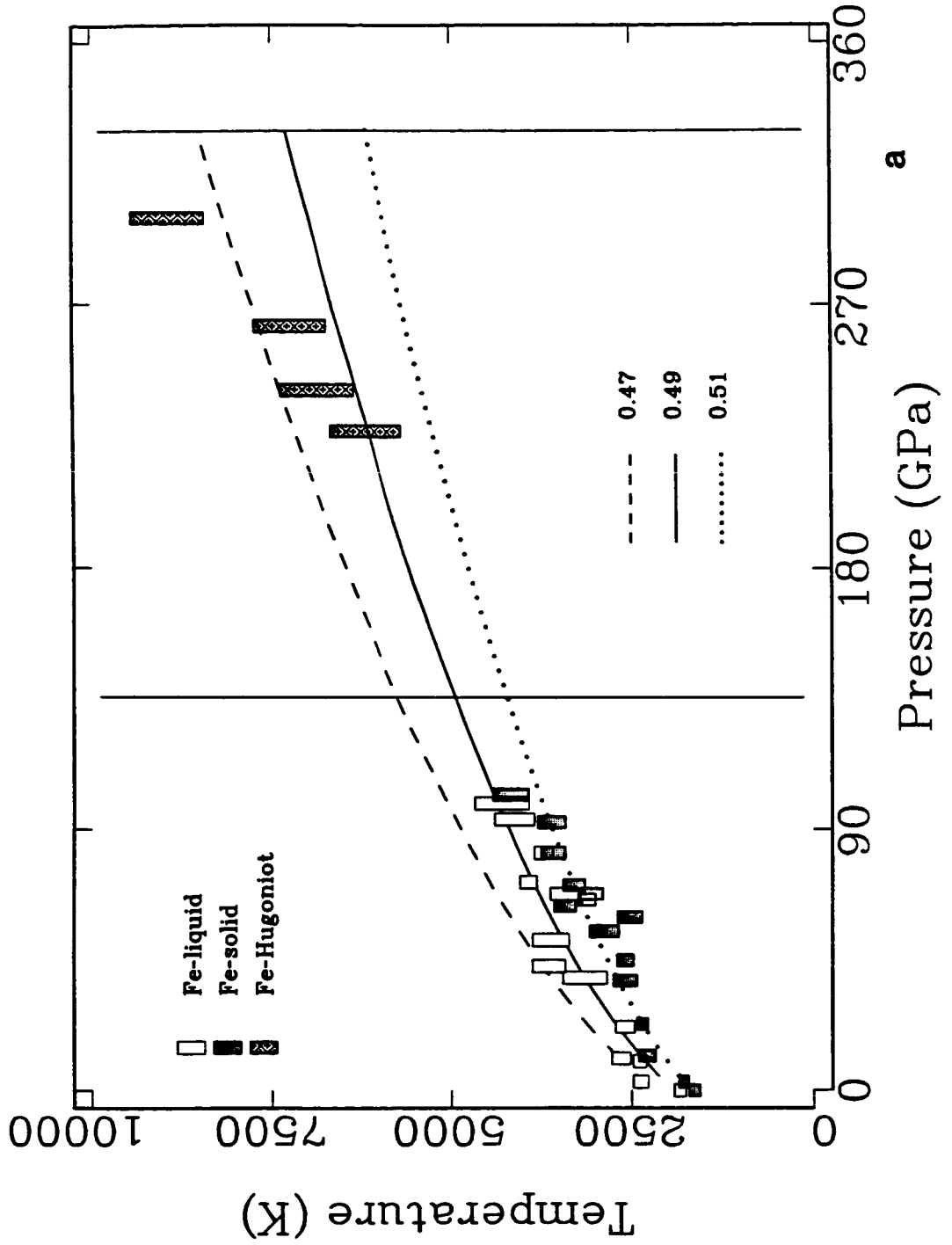
^m given in Gans (1972).

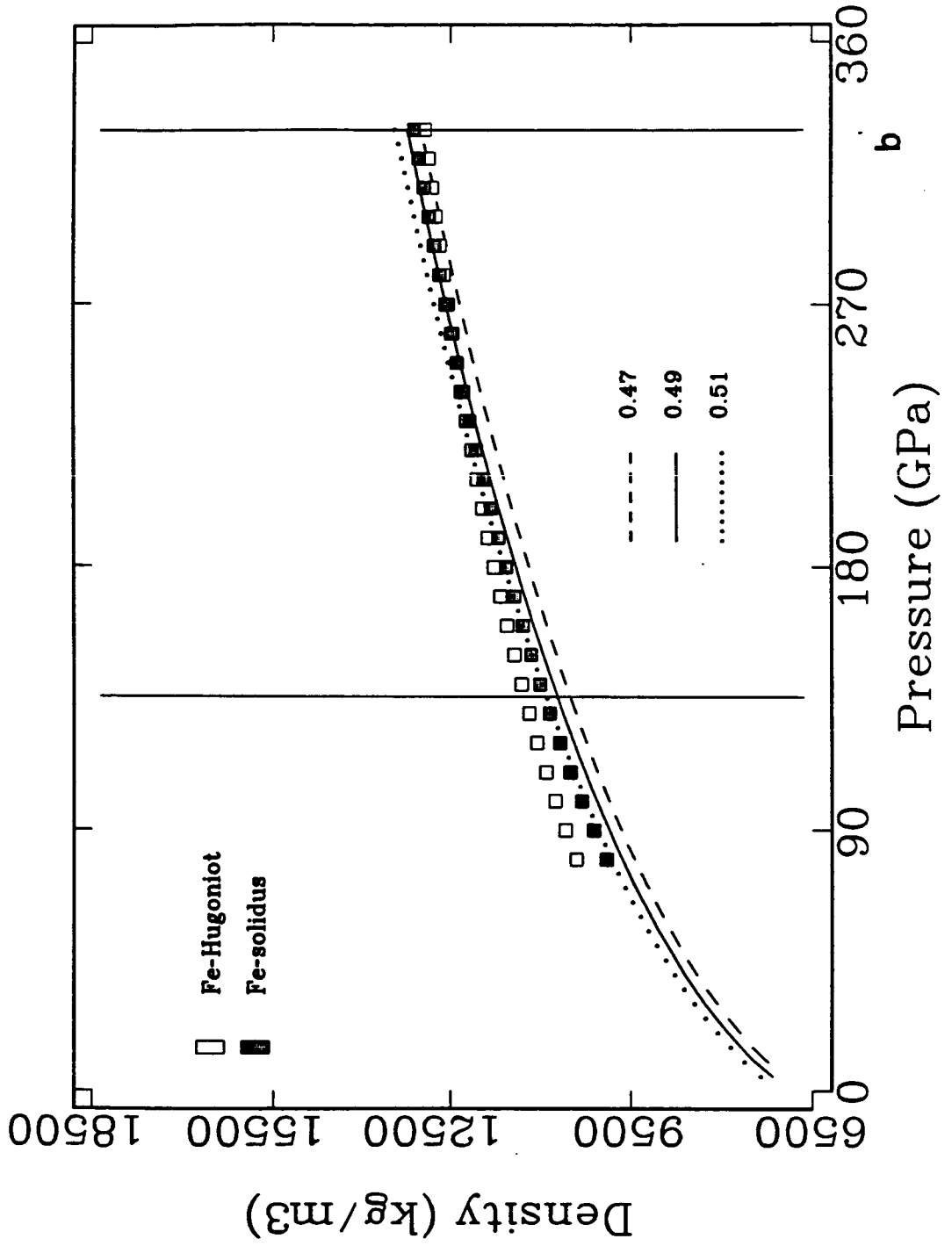
Williams and Jeanloz (1986) to constrain the best fit, *i.e.*, no other SP liquid Fe properties besides γ_e and $\Gamma(\rho_{Nr})$ constrain it. Notable discrepancies between experimental and model fit values include the first five quantities listed in Table 2.1, *i.e.*, the melting temperature, liquid density, the molar entropy, the equilibrium packing fraction, and the molar heat capacity at constant volume. The fact that the molar entropy falls below the experimental value is partially due to the relatively high value of $\hat{\eta}$ favored by the fit, since the entropy of the hard-sphere reference system decreases with increasing $\hat{\eta}$ (via [A.43], Appendix A). Attempted fits with $\hat{\eta}$ fixed at 0.45, the value favored by liquid-state numerical simulations (Alder and Wainwright, 1957), predicted higher liquidus temperatures (>8200 K at 330 GPa: see liquidus variation with $\hat{\eta}$ in Figure 2.2a) at high pressure. Note that temperature along the liquidus is much more sensitive to $\hat{\eta}$ than density, as shown in Figures 2.2a and 2.2b. Since we have held $\Gamma(\rho_{Nr})$ and γ_e constant in the fits, it is possible to "improve" the agreement between some of the fitted and experimental properties by adjusting these parameters away from their independently established values. Another reason we should have some discrepancies between the model fit and liquid Fe properties is that we have not included an explicit contribution to the Helmholtz free energy at zero temperature from the Fe valence electrons (D. J. Stevenson, personal communication). This would introduce further parameters for the fit to constrain, and given the data scatter and relative insensitivity of the model parameters to the temperature along the phase boundary, we refrain from doing this.

§3. Hugoniot and Solid-State Calculations

We estimate the high pressure and temperature states of solid Fe, FeS and FeO from an equilibrium thermodynamic model referenced to the experimentally constrained shock-compressed (Hugoniot) states of these materials. Since

Figure 2.2. Temperature fits (part a) versus pressure for different values of the equilibrium packing fraction, $\hat{\eta}$, around the best fit value. The corresponding liquid density along these curves is shown in part (b).





we are interested in the high pressure, temperature states of initially semiconducting or metallic solids that are all likely to be metallic at high pressure, we construct a model Helmholtz free-energy (HFE), $F(T, \rho)$, from contributions reflecting the influence of both lattice and electronic processes. We assume the Debye model to represent the harmonic lattice free energy, the low temperature (T much less than the Fermi temperature) approximation to the electronic free energy, $-\frac{1}{2}\Gamma(\rho)T^2$ (as above for liquid Fe), and the high-temperature (T greater than the Debye temperature, Θ_D) approximation to the anharmonic free energy, $A_2(\rho)T^2$, where $A_2(\rho)$ is related to the temperature dependence of the phonon-frequency spectrum at constant pressure and high temperature (Wallace, 1972). Neglecting potential lattice-electron and band-structure contributions to the molar Helmholtz free energy, $F(T, \rho)$, we have

$$F(T, \rho) \equiv \Phi(\rho) + 3\nu R \left\{ \frac{3}{8}\chi_D + \ln[1 - e^{-\chi_D}] - \frac{1}{3}E_D(\chi_D) \right\} T \\ + A_2(\rho)T^2 - \frac{1}{2}\Gamma(\rho)T^2 \quad [3.1].$$

In [3.1], $\Phi(\rho)$ is the zero-temperature lattice potential energy function, $\Theta_D(\rho)$ is the Debye temperature, $\chi_D = \chi_D(T, \rho)$ is the ratio of the Debye temperature to the absolute temperature, ν is the number of atoms in the chemical formula, and $E_D(\xi)$ is the Debye internal-energy function (*e.g.*, Gopal, 1966), given by

$$E_D(\xi) \equiv \frac{3}{\xi^3} \int_0^\xi \frac{x^3}{[e^x - 1]} dx \quad [3.2]$$

Θ_D is related to a lattice Grüneisen's parameter, γ_b , by (Wallace, 1972)

$$\gamma_b = \left\{ \frac{d \ln \Theta_D}{d \ln \rho} \right\} \quad [3.3].$$

If we assume

$$\gamma_D(\rho) = \gamma_D(\rho_i) \left\{ \frac{\rho_i}{\rho} \right\}^{q_D} \quad [3.4],$$

then we may write

$$\Theta_D(\rho) = \Theta_D(\rho_i) \exp \left\{ \frac{\gamma_D(\rho_i)}{q_D} \left\{ 1 - \left\{ \frac{\rho_i}{\rho} \right\}^{q_D} \right\} \right\} \quad [3.5].$$

The high-temperature ($T > \Theta_D$) anharmonic contribution to the free energy, $A_2(\rho)T^2$ (Wallace, 1972), has the same temperature-dependence as the electronic contribution to F , as given by [2.5] in the last section. In this sense, at least, the high-temperature anharmonic and low-temperature electronic contributions are indistinguishable. By analogy with [2.5], we assume, for simplicity, that

$$\Omega(\rho) \equiv \Gamma(\rho) - 2A_2(\rho) \equiv \Omega(\rho_i) \left\{ \frac{\rho_i}{\rho} \right\}^\omega \quad [3.6].$$

In the calculations presented below, we constrain the values of $\Omega(\rho_i)$ and ω empirically by requiring the high-pressure-phase (β) Hugoniot and melting curve of Fe, FeS and FeO to intersect at an "appropriate" pressure. As discussed in the previous section, we have a further constraint on $\Gamma(\rho)$ for Fe from the work of Boness *et al.* (1986).

Since we are working at high temperatures, *i.e.* $T > \Theta_D$, we may use the high-temperature approximation ($\chi_D \equiv \Theta_D(\rho_H)/T \rightarrow 0$) of the harmonic contribution to $F(T, \rho)$. Detailing this approximation in Appendix B, we obtain from it expressions for 1) the high-temperature molar entropy:

$$S \equiv 3\nu R \left\{ \frac{4}{3} - \ln[\chi_D] + \frac{1}{40} \chi_D^2 \right\} + \Omega T \quad [3.7]$$

2) the high-temperature molar heat capacity at constant volume:

$$C_V \equiv T \left(\frac{\partial S}{\partial T} \right)_{v,N} = 3\nu R \left[1 - \frac{1}{20} \chi_D^2 \right] + \Omega T \quad [3.8]$$

and 3), the high-temperature isothermal bulk modulus:

$$K_T = K(0, \rho) + \frac{3\nu R}{M} \rho \gamma_b \left\{ (1 - \omega_b) \left[1 + \frac{1}{20} \chi_b^2 \right] + \frac{1}{10} \chi_b^2 \right\} T + \frac{1}{2} \rho \omega (1 - \omega) \frac{\Omega}{M} T^2 \quad [3.9]$$

with

$$K_T(0, \rho) = \rho \left\{ 2\rho \left[\frac{d\Phi}{d\rho} \right] + \rho^2 \left[\frac{d^2\Phi}{d\rho^2} \right] \right\}.$$

From these expressions, we have

$$\rho \gamma c_v \equiv \left[\frac{\partial P}{\partial T} \right]_{v,N} = \rho \left\{ \gamma_b c_v + (\omega - \gamma_b) \frac{\Omega}{M} T \right\} \quad [3.10],$$

where $c_v = C_v/M$ is the specific heat at constant volume. From [3.8] and [3.10], we have the high-temperature equilibrium thermodynamic Grüneisen parameter

$$\gamma = \frac{\gamma c_v}{c_v} = \gamma_b + (\omega - \gamma_b) \frac{\Omega}{C_v} T \quad [3.11].$$

Note that γ , as given by [3.11], is very weakly temperature-dependent, since $\omega \approx \gamma_b$ (at least for Fe) in the range of pressures and temperatures of interest. On this basis, we assume in what follows that γ a function of density alone, and equal to γ_b in the solids of interest. From [3.9] and [3.10], we have the coefficient of thermal expansion

$$\alpha = \frac{\rho(\gamma c_v)}{K_T} \quad [3.12].$$

Lastly, [3.8], [3.11], and [3.12], combined with

$$\frac{K_s}{K_T} = \frac{C_p}{C_v} = (1 + \alpha \gamma T) \quad [3.13]$$

provide the isentropic bulk modulus, K_s , and molar heat capacity at constant pressure, C_p . We use these expressions, particularly S , α and C_p , in what follows.

Assuming that Fe, FeS, and FeO shock compress as fluids, we calculate the pressure, P_H , and density, ρ_H , of a given Hugoniot state on the basis of the experimentally constrained shock velocity, U , material velocity, v , relation, *i.e.*, $U = a_1 + b_1 v$, via the shock-wave "equation of state"

$$\eta_H = \frac{1}{b_1} [\mu - (\mu^2 - 1)^{1/2}] \quad [3.14]$$

(for $b_1 \eta_H < 1$) with

$$\mu = \mu(P_H) \equiv 1 + \frac{\rho_1^\alpha a_1^2}{2b_1(P_H - P_i)}$$

(*e.g.*, McQueen *et al.*, 1967). In this relation, ρ_1^α is the uncompressed density of the material occupying the low-pressure-phase, α , and $\eta_H \equiv 1 - \rho_1^\alpha / \rho_H$ is the relative compression, P_H is the Hugoniot pressure, P_i is the initial pressure, and the subscripts "i" and "H" stand for the initial (T_i, P_i) and Hugoniot states, respectively. With the assumption that the Hugoniot state is one of thermodynamic equilibrium, we construct an internal energy balance in the pressure-density plane to calculate the temperature of the Hugoniot state, T_H (*e.g.*, McQueen *et al.*, 1967; Ahrens *et al.*, 1969), of a high-pressure phase, β , of the material. This is represented by the relation

$$\int_{T(s_1, \rho_H)}^{T_H} c_v(T, \rho_H) dT = \Delta e_v \quad [3.15]$$

where

$$\Delta e_v \equiv \frac{1}{2\rho_1^\alpha} \eta_H [P_H + P_i] - [\Delta e_i^{\beta-\alpha} + \Delta e_s] \quad [3.16]$$

is the difference in specific internal energy between the Hugoniot and principal isentrope of β at constant volume (density, ρ_H). Note that all quantities discussed in this section refer to the β -phase, unless otherwise designated. In [30], $\Delta e_i^{\beta-\alpha} \equiv e(s_1^\beta, \rho_1^\beta) - e(s_1^\alpha, \rho_1^\alpha)$ is the difference in specific internal energy between α

and β at T_i and P_i , and $\Delta e_{s_1} \equiv e(s_1, \rho_H) - e(s_1, \rho_1)$ is the change in specific internal energy along an isentrope of β with specific entropy s_1 , referenced to a density ρ_1 . Also, $T(s_1, \rho_H)$ represents the temperature along this isentrope at a density ρ_H , the Hugoniot-state density of β , and $\chi_D = \Theta_D/T_{s_1}$. Assuming $T_H > \Theta_D$, we may substitute [3.9] into [3.15] to obtain a cubic equation for T_H with solution

$$T_H = 2\sqrt{p} \cos \left\{ \frac{1}{3} \cos^{-1} \left\{ \frac{q}{p\sqrt{p}} \right\} \right\} - \frac{2\nu R}{\Omega(\rho_H)} \quad [3.17]$$

(Svendsen *et al.*, 1987; Chapter I, §4), with

$$p \equiv 4 \left\{ \frac{\nu R}{\Omega(\rho_H)} \right\}^2 + \frac{2M}{3\Omega(\rho_H)} \Lambda(\rho_H)$$

$$q \equiv - \frac{\nu R}{\Omega(\rho_H)} \left\{ \frac{2M}{\Omega(\rho_H)} \Lambda(\rho_H) + \frac{3}{20} [\Theta_D(\rho_H)]^2 + 8 \left\{ \frac{\nu R}{\Omega(\rho_H)} \right\}^2 \right\}$$

and

$$\Lambda(\rho_H) \equiv \Delta e_{\nu}(\rho_H) + \frac{3\nu R}{M} E_D(\xi_D) T_{s_1} + \frac{9\nu R}{8M} \Theta_D(\rho_H) + \frac{1}{2M} \Omega(\rho_H) T_{s_1}^2 .$$

We calculate $\Delta e_{s_1}(\rho_H) = \Delta e_{s_1}(\rho_1, K_{s_1}, K'_{s_1}, \rho_H)$ using third-order spatial finite-strain theory. We estimate K_{s_1} and K'_{s_1} , the STP isentropic bulk modulus and its first pressure derivative, respectively, of the high-pressure phase, from the metastable U-v relation of the high-pressure phase (McQueen *et al.*, 1967; Svendsen *et al.*, 1987), which in turn is constrained from ρ_1^α , a_1 and b_1 . Also, we calculate $T(s_1, \rho_H)$ from the relation

$$\left(\frac{\partial \ln T}{\partial \ln \rho} \right)_s = \gamma \quad [3.18]$$

assuming $\gamma = \gamma_D(\rho)$. In this case, the relation for $T(s_1, \rho_H)$ is of the same form as that for $\Theta_D(\rho)$ given by [3.10] above. With $T_i = 298$ K, $P_i = 0.1$ MPa (*i.e.*, STP), and ρ_1^α , a_1 and b_1 constrained from pressure-density shock-experiments, we see

from [3.17] that T_H depends on $\Delta e_i^{\beta-\alpha}$ and 6 STP properties of the high-pressure phase, β , *i.e.*

$$\{\rho_i, \Delta e_i^{\beta-\alpha}, \gamma_D(\rho_i), q_D, \Theta_D(\rho_i), \Omega(\rho_i), \omega\} \quad [3.19]$$

Of these, T_H is most sensitive to ρ_i , $\Delta e_i^{\beta-\alpha}$ and $\Omega(\rho_i)$ (Svendsen *et al.*, 1987). To reduce the number of free parameters, we assume $q_D=1$ for Fe, FeS and FeO, $\omega=1$ for FeS and FeO, and $\omega=1.34$ for Fe. The parameter ω for Fe is chosen in order to facilitate comparison of the $\Omega(\rho_i)$ values for Fe obtained below with the values of $\Gamma(\rho_i)$ and γ_e calculated by Boness *et al.* (1986) for ϵ -Fe and γ -Fe. Since ρ_i for Fe, FeS and FeO FeS, FeO and Fe are constrained by previous work, we fix it as well. We constrain $\Delta e_i^{\beta-\alpha}$ from the energy balance used to obtain T_H in the limit $\rho_H \rightarrow \rho_i$ assuming γ is a function of volume only (Svendsen *et al.*, 1987). We have Θ_D for ϵ -Fe from Andrews (1973), and we estimate it for the the high-pressure phases of FeS and FeO from the relation

$$\Theta_D = \frac{h}{k_B} \left\{ \frac{9\nu\rho_i N}{4\pi M} \right\}^{1/3} v_m$$

by assuming the mean sound velocity of the high-pressure phase, v_m , is equal to the bulk velocity of the high pressure phase, v_ϕ , where $v_\phi \equiv \sqrt{K_{sp}/\rho_i}$. This estimate is an upper bound to the actual value of Θ_D , since it ignores the contribution of transverse vibrations to v_m . All of these parameter values are given in Table 3.1, leaving us with 2 "degrees of freedom", *i.e.*, $\gamma_D(\rho_i)$ and $\Omega(\rho_i)$, when calculating T_H .

Solidus Calculations and Fits

Following many workers (*e.g.*, Stacey, 1977), we use Lindemann's law, *i.e.*,

$$\left\{ \frac{dT_M}{d\rho_M^s} \right\}_{\text{Lindemann}} \equiv 2 \frac{T_M}{\rho_M^s} (\gamma_{DM}^s - \frac{1}{3}) \quad [3.20]$$

Table 3.1. High-Pressure Solid State STP Parameters for Fe, FeS and FeO.

Property	Symbol	Fe	FeS	FeO	SI Units
Molecular weight	M	0.055847 ^a	0.087907 ^a	0.071846 ^a	kg/mol
Impedance match					
Mass density	ρ_i^α	7850 ^b	4613 ^c	5554 ^d	kg/m ³
Intercept, U-v relation	a_i	3955 ^b	3865 ^c	4070 ^e	m/s
Slope, U-v relation	b_i	1.580 ^b	1.351 ^c	1.503 ^e	
High-Pressure solid phase					
Mass density	ρ_i	8352 ^f	5600 ^g	6050 ^d	kg/m ³
HPP-LPP SIE [†] difference	$\Delta e_i^{\beta-\alpha}$	70 ^h	800 ^h	145 ^h	kJ/kg
Intercept, U-v relation	a_i^*	4517 ^h	5327 ^h	4823 ^h	m/s
Slope, U-v relation	b_i^*	1.57 ^h	1.32 ^h	1.49 ^h	
Isentropic Bulk Modulus	K_s	170 ⁱ	159 ⁱ	141 ⁱ	GPa
$(\partial K_s / \partial P)_s$	K_s	5.28 ^j	4.28 ^j	4.95 ^j	
Debye temperature	Θ_D	385 ^k	674 ^l	670 ^l	K
AE [§] exponent	ω	1.34 ^m	1.0 ⁿ	1.0 ⁿ	
Hugoniot-Solidus					
Melting Temperature	T_M	1809	1468	1652	K
AE coefficient	Ω	3.35	11.43	7.54	mJ/mol·K ²
Thermal Expansion	α	45	155	100	μK^{-1}
Debye γ	γ_D	1.93	1.50	1.90	

[†]Specific internal energy.

^aRobie *et al.* (1978).

^bBrown and McQueen (1986).

^cBrown *et al.* (1984).

^dJeanloz and Ahrens (1980).

^eFit to U-v data in ^d.

^fJephcoat *et al.* (1986).

^gPichulo *et al.* (1976).

[§]Anharmonic-electronic.

^hfrom ρ_i and U-v relation (see text).

ⁱassuming $K_s = \rho a_i^2$.

^jfrom $K_s = 4b_i^* - 1$ (Ruoff, 1967).

^kAndrews (1973).

^lfrom ρ_i and a_i^* (see text).

^m γ_e of ϵ -Fe (Boness *et al.*, 1986) assumed.

ⁿassumed.

to parameterize the solid-two phase boundary (*i.e.*, solidus). In [3.20], γ_{DM}^s is the lattice Grüneisen's parameter at the melting point, given by $\gamma_{\text{D}}(\rho_{\text{M}}^s)$ in the context of the Debye approximation used in this work, ρ_{M}^s is the density of the solid along the phase boundary, and T_{M} is the melting temperature. Since we assume above that $\gamma_{\text{D}}(\rho)$ is given by usual power-law relation ([3.5] above), [3.20] may be integrated to give

$$T_{\text{M}}(\rho_{\text{M}}^s) = T_{\text{M}}(\rho_{\text{M}_1}^s) \left\{ \frac{\rho_{\text{M}_1}^s}{\rho_{\text{M}}^s} \right\}^{\frac{2}{3}} \exp \left\{ \frac{2\gamma_{\text{D}}(\rho_{\text{M}_1}^s)}{c_{\text{D}}} \left\{ 1 - \left\{ \frac{\rho_{\text{M}_1}^s}{\rho_{\text{M}}^s} \right\}^{c_{\text{D}}} \right\} \right\} \quad [3.21],$$

where $\rho_{\text{M}_1}^s \equiv \rho^s(T_{\text{M}_1}, P_i)$ is the density of the solid at the melting temperature $T_{\text{M}}(\rho_{\text{M}_1}^s) \equiv T_{\text{M}}(P_i)$. Since the equilibrium thermodynamic properties as developed from [3.1] and its high-temperature approximation (Appendix B) are functions of temperature and density, we may calculate the variation of any of these properties, $\psi(T, \rho)$, with temperature at constant pressure from the relation

$$\psi(T, P_{\text{ref}}) = \psi(T_{\text{ref}}, P_{\text{ref}}) + \int_{T_{\text{ref}}}^T \left\{ \frac{\partial \psi}{\partial T} \right\}_P dT, \quad [3.22],$$

where

$$\left\{ \frac{\partial \psi}{\partial T} \right\}_P = \left\{ \frac{\partial \psi}{\partial T} \right\}_\rho - \alpha \rho \left\{ \frac{\partial \psi}{\partial \rho} \right\}_T \quad [3.23],$$

and P_{ref} and T_{ref} are a pressure and temperature at which we know ψ . In particular, with $\psi = \rho^s$, the density of the solid along the solidus, ρ_{M}^s , may be estimated from the density determined experimentally along the Hugoniot, ρ_{H} , via a simultaneous solution of [3.21] and

$$\rho_{\text{M}}^s(P) = \rho_{\text{H}}(P) \exp \left\{ - \int_{T_{\text{H}}}^{T_{\text{M}}} \alpha [T, \rho(T, P)] dT \right\} \quad [3.24]$$

for $T_{\text{M}}(\rho_{\text{M}}^s) = T_{\text{M}}(P)$ and $\rho_{\text{M}}^s(T_{\text{M}}) = \rho_{\text{M}}^s(P)$. We evaluate [3.24] numerically during

the simultaneous solution, using [3.12] for $\alpha(T, \rho)$ and [3.17] for T_H . This solution is subject to the initial conditions

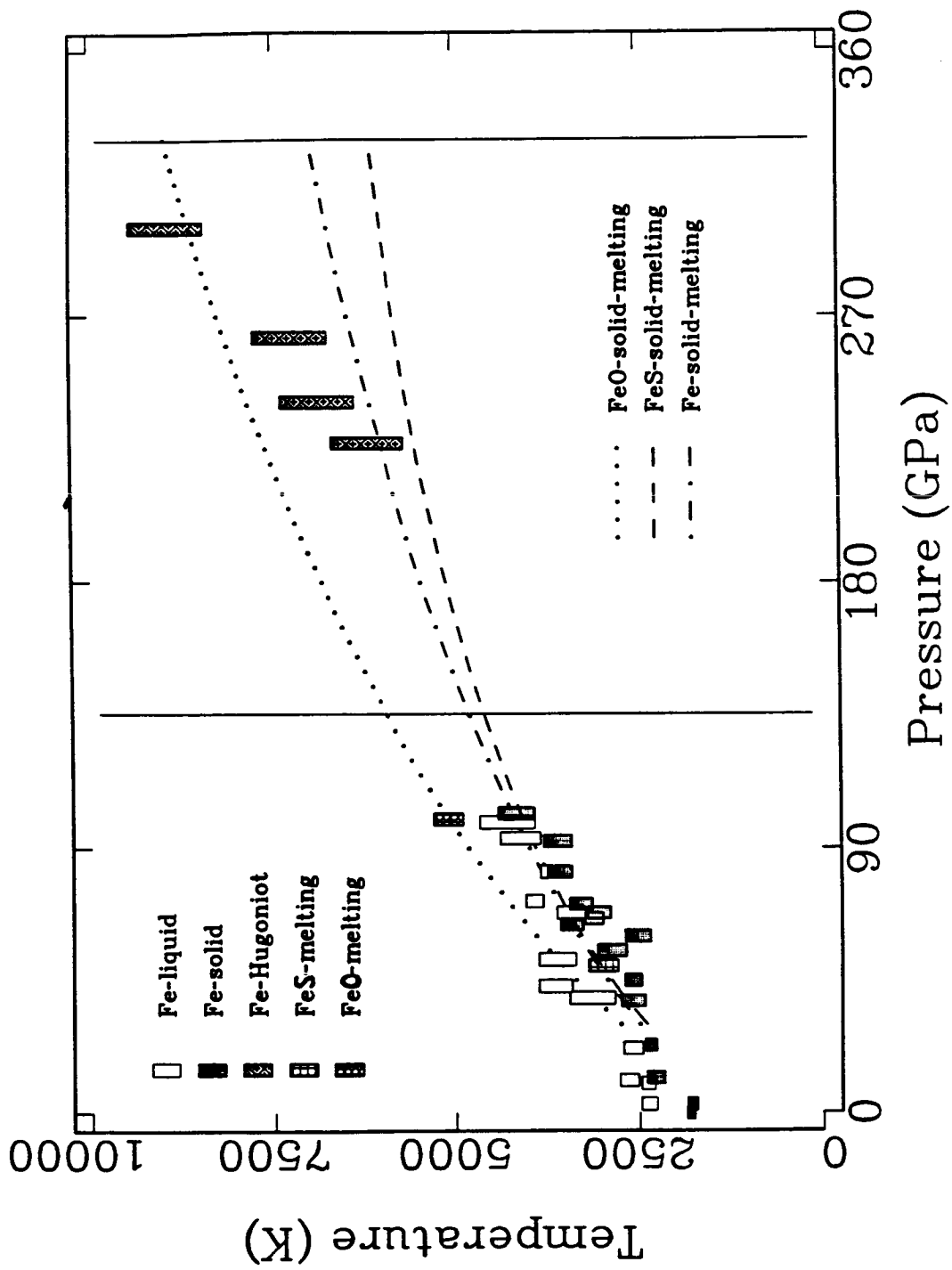
$$\rho_{M_1}^s = \rho_i [1 - \alpha_i (T_{M_1} - T_i)] \quad [3.25]$$

and

$$\gamma_D(\rho_{M_1}^s) = \gamma_D(\rho_i) \left\{ \frac{\rho_i}{\rho_{M_1}^s} \right\}^{\Omega_D} = \frac{\gamma_D(\rho_i)}{[1 - \alpha_i (T_{M_1} - T_i)]^{\Omega_D}} \quad [3.26],$$

where $T_{M_1} = T_M(P_i)$ is the standard pressure melting temperature of the material, and $\alpha_i = \alpha(T_i, P_i)$ the STP coefficient of thermal expansion. By combining the solidus and Hugoniot temperatures and densities via [3.17], [3.21] and [3.24]-[3.26], we have a simultaneous calculation for $T_M(P)$, $\rho_M^s(P)$ and $T_H(P)$ dependent on 4 "free" parameters: $\gamma_D(\rho_i)$, $\Omega(\rho_i)$, α_i and T_{M_1} . To fit the solidus calculated in this fashion to the melting data, we again employ the χ^2 statistic, as given in [3.1], with $T_{M_{mod}} = T_{M_{mod}}(P; a)$ now given by [3.19], to fit a Lindemann solidus to the Fe melting data of Williams and Jeanloz (1986), and compare this fit to the Fe shock temperature results of Bass *et al.* (1987). For the FeS and FeO solidi, however, we use [3.19] to calculate, rather than fit, these solidi because there is only one high-pressure datum for each of these materials currently available to the public. We display the results of the Fe fit, and the FeS and FeO calculations in Figure 3.1. The FeS melting point at 50 GPa is from the work of Williams and Jeanloz (1986; 3000 K), and this is consistent with the results of Anderson *et al.* (1987a), while that for FeO is from the work of Knittle and Jeanloz (1987), who state that "... at approximately 100 GPa the melting temperature of FeO exceeds 5000 K..." On this "factual" basis, we assume 5100 K. The best fit Fe-solidus shown in Figure 3.1 has a χ^2 of 70; parameters for these curves are given in Table 3.1. This χ^2 is substantially lower than that of the best fit Fe-liquidus partly because the fit via [3.17], [3.19] and [3.22] is numerically stable only above 20 GPa, and so we fit the 19 data

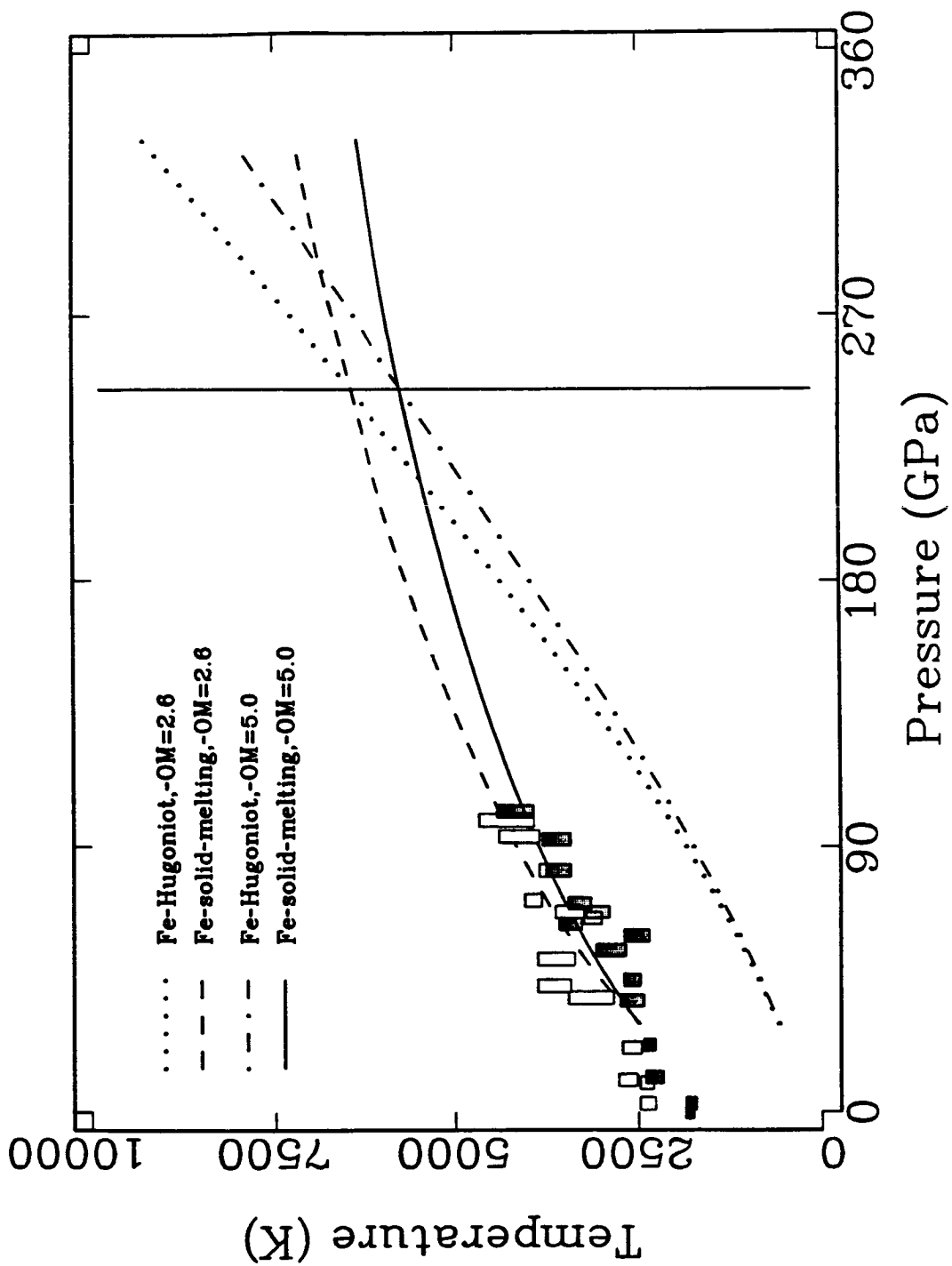
Figure 3.1. Solidus fit to Fe melting data, and calculated FeO and FeS solidi constrained by corresponding data. The FeO datum at 100 GPa is from the work of Knittel and Jeanloz (1987), while that for FeS at 50 GPa is from Williams and Jeanloz (1987). The FeS curve is also consistent with the lower pressure constraints on FeS melting from the shock-wave experiments of Anderson *et al.* (1987).



above this pressure. In addition, the largest differences between the solidus and Hugoniot densities (temperatures) occur at low pressure; consequently, the corrections are largest at low pressure, and hence most suspect. Notice the the solidi (Figure 3.1) curve down too much to asymptote out at the SP melting temperature without a seemingly unphysical change in curvature and slope. The use of a linear relation between density and temperature at SP, [3.20], also contributes to this. A quadratic or other higher-order relation would give more reasonable asymptotic behavior, but of course at the expense of yet more parameters to constrain.

Comparing the density-constrained Fe liquidus in Figure 2.1 and the best-fit solidus, we see that the best-fit liquidus lies at a higher temperature than the corresponding solidus. If we fit the "best" Fe-liquidus model with a Lindemann solidus, we obtain $\gamma_D(\rho_i)=1.90$, $\Omega(\rho_i)=2.6$ mJ/mol·K², $\alpha_i = 58.4$ μ K⁻¹, $T_M = 1810$ K and $\chi^2 = 125$. However, if we require $\Omega(\rho_i)=5$ mJ/mol·K², the value of $\Gamma(\rho_i)$ calculated theoretically by Boness *et al.* (1986) for ϵ -Fe (here adjusted to the density of ϵ -Fe from Jephcoat *et al.*, 1986), in a fit to the data of Williams and Jeanloz (1986), we obtain $\gamma_D(\rho_i)=1.79$, $\alpha_i = 54.5$ μ K⁻¹, and $T_M=1809$ K, with $\chi^2=75$. These last two fits are displayed in Figure 3.2, along with the associated Hugoniots. Since ρ_H and ρ_M^* are connected via α , which is initially small, and decreases with pressure (see below), it turns out that the solidi are not very sensitive to $\Omega(\rho_i)$. Experimental constraints on the pressure at which liquid-solid phase boundary and high-pressure phase Hugoniot of Fe (245 GPa: Brown and McQueen, 1982) and FeS (125-150 GPa: Brown *et al.*, 1984) intersect provide a stronger constraint on the value of $\Omega(\rho_i)$, which controls the slope of $T_H(P)$, as implied by [3.17]. This intersection is shown for the two Fe-solidi displayed in Figure 3.2. We apply this as an additional constraint in the Fe solidus fits, and the FeS solidus calculation. To our knowledge, there exists no experimentally motivated range of

Figure 3.2. Intersection of two Fe Hugoniot and melting curve at 245 GPa.
"OM" represents value of Ω in units of $\text{J/mol}\cdot\text{K}^2$.



pressures over which the FeO Hugoniot and melting curve are likely to intersect, but it is almost certainly above 70 GPa (Jeanloz and Ahrens, 1980; Knittle and Jeanloz, 1987), and probably above 245 GPa, where the Fe Hugoniot and solidus apparently intersect, since the solidus extrapolated from the datum of Knittle and Jeanloz (1987) is $\gtrsim 1000$ K above the solidus at a given pressure above 100 GPa.

With parameters values established by the fit, the solid-state model provides us with specific values for the equilibrium thermodynamic properties as functions of temperature and density. However, since we can calculate $\rho = \rho(T, P)$ via

$$\rho(T, P) = \rho(T_H, P) \exp \left\{ - \int_{T_H}^T \alpha[T, \rho(T, P)] dT \right\}, \quad [3.27]$$

at high pressure and temperature, referenced to the Hugoniot state $\{T_H, P_H, \rho_H\}$, the model functions then depend on pressure and temperature. On this basis, we use the Fe solidus fit (Figure 3.2, dash curve) to the constrained-density Fe liquidus obtained in the last section to calculate the equilibrium thermodynamic properties of solid Fe at the melting temperature as a function of pressure and compare them to the corresponding liquid-Fe properties in Table 3.2. We note that ϵ -Fe is probably not the solid phase in equilibrium with liquid-Fe; above 5 GPa, γ -Fe is most likely the solid phase of Fe coexisting with liquid Fe (*e.g.*, Anderson, 1982). We have tacitly assumed that this is of no consequence at high pressure; even if it were, γ -Fe is not sufficiently well characterized at high pressure for us to distinguish it from ϵ -Fe at high pressure.

For the phase relations discussed below, we are particularly interested in S , the molar entropy, and C_p , the molar heat capacity, of the liquid and solid. From Table 3.2, we have $\Delta S_{Fe}^{l-\epsilon} \equiv S_{Fe}^l - S_{Fe}^s = 8.3 \text{ J/mol}\cdot\text{K} (0.99\cdot R)$ and

Table 3.2. High-Pressure Solid & Liquid Fe Model Properties.

	P=136 GPa (CMB)			P=330 GPa (ICB)			SI Units
	Hugoniot	Solidus	Liquidus	Hugoniot†	Solidus	Liquidus	
T	3063	5007	4937	9275	7219	7296	K
ρ	11250	10880	10720	12900	13060	13220	kg/m ³
S	78.1	96.1	104.7	109.2	101.1	108.9	J/mol·K
c_V	30.2	34.8	41.3	38.2	36.8	42.1	J/mol·K
K_T	677	584	630	1386	1495	1324	GPa
γ	1.40	1.43	2.41	1.27	1.26	2.54	
K_S	713	654	857	1518	1593	1792	GPa
α	12.6	16.8	30.3	8.1	7.2	19.1	μK^{-1}
c_P	31.8	39.1	56.2	41.9	39.2	56.9	J/mol·K
v_ϕ	7958	7702	8943	10850	11040	11640	m/s
μ			9			14	mPa·s
k			89			133	W/m·K
D			6645			8488	nm ² /s

† - Metastable ϵ Hugoniot.

$\Delta C_{\text{P,Fe}}^{l-s} \equiv C_{\text{P,Fe}}^l - C_{\text{P,Fe}}^s = 17.1 \text{ J/mol}\cdot\text{K} (2.06\cdot\text{R})$ at 136 GPa, while $\Delta S_{\text{Fe}}^{l-s} = 7.8 \text{ J/mol}\cdot\text{K} (0.94\cdot\text{R})$ and $\Delta C_{\text{P,Fe}}^{l-s} = 17.7 \text{ J/mol}\cdot\text{K} (2.13\cdot\text{R})$ at 330 GPa. These compare with $\Delta S_{\text{Fe}}^{l-s} = 7.7 \text{ J/mol}\cdot\text{K} (0.93\cdot\text{R})$ (Desai, 1986) and $\Delta C_{\text{P,Fe}}^{l-s} = 4.2 \text{ J/mol}\cdot\text{K} (0.51\cdot\text{R})$ (Hultgren *et al.*, 1973) at SP. A number of theoretical and experimental studies (see, for example, Stishov, 1975) on elemental compounds suggest that 1) the value of the entropy of melting, ΔS^{l-s} , varies little among these substances, and approaches R at high temperature, 2) ΔS^{l-s} varies with the volume change upon melting, Δv^{l-s} , such that $\Delta S^{l-s} \rightarrow 0.693$ (*i.e.*, $\ln 2$) R as $\Delta v^{l-s} \rightarrow 0$. In the context of a simple cell order-disorder model (Stishov, 1975), we note that $\Delta S^{l-s} \sim R$ for complete disorder (*i.e.*, one "atom" per cell, no short-range order) among the liquid constituents, while $\Delta S^{l-s} \sim 0.693R$ for pair ordering (*i.e.*, up to two atoms per cell, randomly occupied cells, short-range order). In addition, Gschneider (1964) has found, for a number of close-packed monatomic solids, that $\Delta S^{l-s} \sim 1.1523\cdot R$. Our results are somewhat contrary to this, since we calculate high-pressure values for $\Delta S_{\text{Fe}}^{l-s}$ of the same magnitude as the SP value. As for the large increase in $\Delta C_{\text{P,Fe}}^{l-s}$ with pressure calculated here, we have no theoretical explanation at this point, but it is at least partly because γ increases with pressure in the liquid (Tables 2.1 and 3.2) but decreases with pressure in the solid. This behavior for γ is not unexpected (Knopoff and Shapiro, 1970). Also, the thermal expansion of the liquid is about twice that of the solid along the phase boundary. With these results, we may now address phase relations in Fe-S and Fe-O systems.

§4. Fe-FeX Phase Diagrams and Implications for the Core

The results of the solidus and liquidus models given in the previous section for Fe, FeS and FeO may be used to calculate ideal phase relations between liquid and solid Fe-X mixtures, in the context of the following model. We assume that these mixtures coexist in thermodynamic equilibrium, *i.e.*,

$$\begin{aligned} T^l &= T = T^s \\ P^l &= P = P^s \\ \mu_i^l &= \mu_i^s \end{aligned} \quad [4.1],$$

where the superscript l denotes a property of the liquid, and superscript s a property of the solid. The equilibrium chemical potential for component i in phase α (*i.e.*, solid or liquid) is defined by

$$\mu_i^\alpha(T, P, x_i^\alpha) \equiv \mu_i^\alpha(T, P, 1) + RT \ln a_i^\alpha(T, P, x_i^\alpha) \quad [4.2]$$

(*e.g.*, Prigogine and Defay, 1954). In this relation, $\mu_i^\alpha(T, P, 1)$ is the chemical potential of pure i in phase α , $a_i^\alpha(T, P, x_i^\alpha)$ is the activity of i in the phase- α mixture, defined by

$$a_i^\alpha(T, P, x_i^\alpha) \equiv \lambda_i^\alpha(T, P, x_i^\alpha) x_i^\alpha, \quad [4.3]$$

where λ_i^α is the activity coefficient, and x_i^α the mole fraction, of component i in phase α .

Following Stevenson (1981), we assume that both the liquid and solid Fe-X mixtures are fully associated, *i.e.*, $\text{FeX} \rightleftharpoons \text{Fe} + \text{X}$ in both phases. This implies that FeX is a distinct, energetically favored species, along with Fe and X, in both phases. In this context, Prigogine and Defay (1954) have shown that the chemical potentials of the species Fe and X are equal to those of components Fe and X, implying that,

$$\mu_{\text{FeX}}^\alpha(T, P, x^\alpha) \equiv \mu_{\text{Fe}}^\alpha(T, P, x^\alpha) + \mu_{\text{X}}^\alpha(T, P, x^\alpha) \quad [4.4]$$

$$\equiv \mu_{\text{FeX}}^\alpha(T, P, \frac{1}{2}) + RT \ln a_{\text{FeX}}^\alpha(T, P, x^\alpha) \quad [4.5],$$

where μ_{FeX}^α is the chemical potential of FeX in phase α , and we have defined x^α as the mole fraction of X in phase α ; then $1-x^\alpha$ is the mole fraction of Fe in α . Substituting [4.2] into [4.4] for Fe and X, we obtain, from [4.4] and [4.5]

$$a_{\text{FeX}}^\alpha = a_{\text{Fe}}^\alpha a_{\text{X}}^\alpha e^{-B\Delta\mu_{\text{FeX}}^\alpha} = \lambda_{\text{Fe}}^\alpha \lambda_{\text{X}}^\alpha x^\alpha (1-x^\alpha) e^{-B\Delta\mu_{\text{FeX}}^\alpha} \quad [4.6]$$

where $B \equiv 1/RT$, and we have defined

$$\Delta\mu_{\text{Fe-X}}^{\alpha}(T,P) \equiv \mu_{\text{FeX}}^{\alpha}(T,P,x^{\alpha} \equiv \frac{1}{2}) - \mu_{\text{Fe}}^{\alpha}(T,P,x^{\alpha}=0) - \mu_{\text{X}}^{\alpha}(T,P,x^{\alpha}=1) \quad [4.7].$$

Now, by definition, a_{FeX}^{α} must be unity when $x^{\alpha} = \frac{1}{2}$. Putting this "boundary condition" into [4.6], we have

$$\lambda_{\text{Fe}}^{\alpha}(\frac{1}{2}) \lambda_{\text{X}}^{\alpha}(\frac{1}{2}) \equiv 4e^{B\Delta\mu_{\text{Fe-X}}^{\alpha}} \quad [4.8].$$

With this, a_{FeX}^{α} becomes

$$a_{\text{FeX}}^{\alpha} \equiv 4 \left\{ \frac{\lambda_{\text{Fe}}^{\alpha} \lambda_{\text{X}}^{\alpha}}{\lambda_{\text{Fe}}^{\alpha}(\frac{1}{2}) \lambda_{\text{X}}^{\alpha}(\frac{1}{2})} \right\} x^{\alpha}(1-x^{\alpha}) \quad [4.9],$$

and this is the expression we require to use [4.5] for $\mu_{\text{FeX}}^{\alpha}$. Now we turn to phase equilibria in the Fe-FeX subsystem.

The equilibrium liquid-solid phase boundaries in the Fe-FeX subsystem are defined by (from [4.1]₃)

$$\mu_{\text{Fe}}^l(T,P,x^l) = \mu_{\text{Fe}}^s(T,P,x^s) \quad [4.10]$$

and

$$\mu_{\text{FeX}}^l(T,P,x^l) = \mu_{\text{FeX}}^s(T,P,x^s) \quad [4.11].$$

Substituting [4.2], with $i = \text{Fe}$, and [4.5] into these, we obtain

$$\lambda_{\text{Fe}}^l(1-x^l) = \lambda_{\text{Fe}}^s(1-x^s) e^{-B\Delta\mu_{\text{Fe}}^{l-s}} \quad [4.12]$$

and

$$\lambda_{\text{Fe}}^l \lambda_{\text{X}}^l x^l (1-x^l) = \lambda_{\text{Fe}}^s \lambda_{\text{X}}^s x^s (1-x^s) \frac{\lambda_{\text{Fe}}^l(\frac{1}{2}) \lambda_{\text{X}}^l(\frac{1}{2})}{\lambda_{\text{Fe}}^s(\frac{1}{2}) \lambda_{\text{X}}^s(\frac{1}{2})} e^{-B\Delta\mu_{\text{FeX}}^{l-s}} \quad [4.13],$$

where

$$\Delta\mu_{\text{Fe}}^{l-s}(T,P) \equiv \mu_{\text{Fe}}^l(T,P,0) - \mu_{\text{Fe}}^s(T,P,0) \quad [4.14]$$

and

$$\Delta\mu_{\text{FeX}}^{l-s}(T,P) \equiv \mu_{\text{FeX}}^l(T,P,\frac{1}{2}) - \mu_{\text{FeX}}^s(T,P,\frac{1}{2}) \quad [4.15].$$

Note that $\Delta\mu_{\text{Fe}}^{l-s}(T_{\text{M,Fe}},P) \equiv \Delta\mu_{\text{FeX}}^{l-s}(T_{\text{M,FeX}},P) \equiv 0$ by [4.1]₃. Following Stevenson (1981), we expand $\Delta\mu_{\text{Fe}}^{l-s}(T,P)$ and $\Delta\mu_{\text{FeX}}^{l-s}(T,P)$ at constant pressure about the states $\{T \equiv T_{\text{M,Fe}}, P, x^l \equiv x^s \equiv 0\}$ and $\{T \equiv T_{\text{M,FeX}}, P, x^l \equiv x^s \equiv \frac{1}{2}\}$, respectively, to second order in $(T-T_{\text{M}})$, i.e.,

$$\Delta\mu_{\text{Fe}}^{l-s}(T,P) \sim T(\xi_{\text{Fe}}-1) \left\{ \Delta S_{\text{Fe}}^{l-s}(T_{\text{M,Fe}},P,0) - \frac{1}{2} \Delta C_{\text{P,Fe}}^{l-s}(T_{\text{M,Fe}},P,0) (\xi_{\text{Fe}}-1) \right\} \quad [4.16]$$

and

$$\Delta\mu_{\text{FeX}}^{l-s}(T,P) \sim T(\xi_{\text{FeX}}-1) \left\{ \Delta S_{\text{FeX}}^{l-s}(T_{\text{M,FeX}},P,\frac{1}{2}) - \frac{1}{2} \Delta C_{\text{P,FeX}}^{l-s}(T_{\text{M,FeX}},P,\frac{1}{2}) (\xi_{\text{FeX}}-1) \right\} \quad [4.17],$$

where $\Delta S_i^{l-s} \equiv \Delta S_i^{l-s}(P, T_{\text{M},i}, x^l \equiv x^s)$ and $\Delta C_{\text{P},i}^{l-s} \equiv \Delta C_{\text{P},i}^{l-s}(P, T_{\text{M},i}, x^l \equiv x^s)$ are the contrasts in entropy and specific heat at constant pressure of component i between liquid and solid phases at the indicated reference conditions. Also, we have defined $\xi_{\text{Fe}} \equiv T_{\text{M,Fe}}/T$ and $\xi_{\text{FeX}} \equiv T_{\text{M,FeX}}/T$.

Following Stevenson (1981), we now apply [4.14] and [4.15] to the case where Fe and FeX mix ideally in the liquid state. In this case, we have $\lambda_{\text{Fe}}^l = \lambda_{\text{X}}^l = 1$ for all x^l . Putting these into [4.12] and [4.13], we have

$$(1-x^l) = \lambda_{\text{Fe}}^s (1-x^s) e^{-B\Delta\mu_{\text{Fe}}^{l-s}} \quad [4.18]$$

and

$$x^l (1-x^l) = \frac{\lambda_{\text{Fe}}^s \lambda_{\text{X}}^s}{\lambda_{\text{Fe}}^s (\frac{1}{2}) \lambda_{\text{X}}^s (\frac{1}{2})} x^s (1-x^s) e^{-B\Delta\mu_{\text{FeX}}^{l-s}} \quad [4.19].$$

Further, we assume that Fe and FeX are completely immiscible in the solid state. In this case, $x^s = 0$ on the Fe-rich side of the phase diagram, as given by [4.18], while $x^s = \frac{1}{2}$ on the FeX-rich side, as given by [4.19]; consequently,

[4.18] and [4.19] reduce to

$$x^l = 1 - e^{-B\Delta\mu_{Fe}^{l-s}} \quad [4.20]$$

for the Fe-rich side of the phase diagram ($\lambda_{Fe}^s (x^s=0) = 1$), and

$$x^l = \frac{1}{2} \left\{ 1 - \left(1 - e^{-B\Delta\mu_{FeX}^{l-s}} \right)^{1/2} \right\} \quad [4.21]$$

for the FeX-rich side, respectively. Elimination of either x^l or T from [4.20] and [4.21] provides us with implicit expressions for the eutectic temperature, T_{eu} , or composition, x_{eu} , respectively, of the system, *i.e.*,

$$x_{eu} = x_{eu}(\xi_M \Delta S_{Fe}^{l-s}, \Delta C_{P,Fe}^{l-s}, \Delta S_{FeX}^{l-s}, \Delta C_{P,FeX}^{l-s})$$

and

$$T_{eu} = T_{eu}(T_{M,Fe}, \Delta S_{Fe}^{l-s}, \Delta C_{P,Fe}^{l-s}, T_{M,FeX}, \Delta S_{FeX}^{l-s}, \Delta C_{P,FeX}^{l-s})$$

where $\xi_M \equiv T_{M,FeX}/T_{M,Fe}$ is the ratio of end-member melting temperatures. In Figure 4.1, we display x_{eu} as a function of ξ_M for different values of ΔS^{l-s} , assuming $\Delta S^{l-s} = \Delta S_{Fe}^{l-s} = \Delta S_{FeX}^{l-s}$ and $\Delta C_{P,Fe}^{l-s} = 0 = \Delta C_{P,FeX}^{l-s}$. As evident, the eutectic composition will be more X-rich as the melting temperature of FeX decreases below that of Fe, the more drastically as ΔS^{l-s} increases. Assuming $T_{M,Fe} = 7250$ K from above, the variation of T_{eu} with ξ_M displayed in Figure 4.2 shows that the eutectic temperature increases with ξ_M for a given value of ΔS^{l-s} and decreases with ΔS^{l-s} at a given value of ξ_M . Consequently, T_{eu} will take on a minimum value for minimum values ξ_M and ΔS^{l-s} , and $\Delta C_P^{l-s} = 0$.

Having established values for $T_{M,Fe}$, $T_{M,FeX}$, ΔS_{Fe}^{l-s} and $\Delta C_{P,Fe}^{l-s}$ above, we now assume that ΔS_{FeX}^{l-s} for X=O,S are given by their SP values, *i.e.*, $\Delta S_{FeO}^{l-s} = 22.0$ J/mol·K (Robie *et al.*, 1978) and $\Delta S_{FeS}^{l-s} = 13.4$ J/mol·K (Robie *et al.*, 1978), respectively, and that either $\Delta C_{P,FeX}^{l-s} = \Delta C_{P,Fe}^{l-s}$ or $\Delta C_{P,FeX}^{l-s} = 0 = \Delta C_{P,Fe}^{l-s}$, in order to calculate ideal-mixing liquids for Fe-FeX via [4.20] and [4.21]. We display the results of this in Figures 4.3a-b for P=136

Figure 4.1. Eutectic composition versus the ratio of end member melting temperatures, showing the dominant influence of this property on the eutectic composition. "Ds" represents ΔS^{l-s} in units of R, and $\Delta C_p^{l-s}=0$ for this calculation.

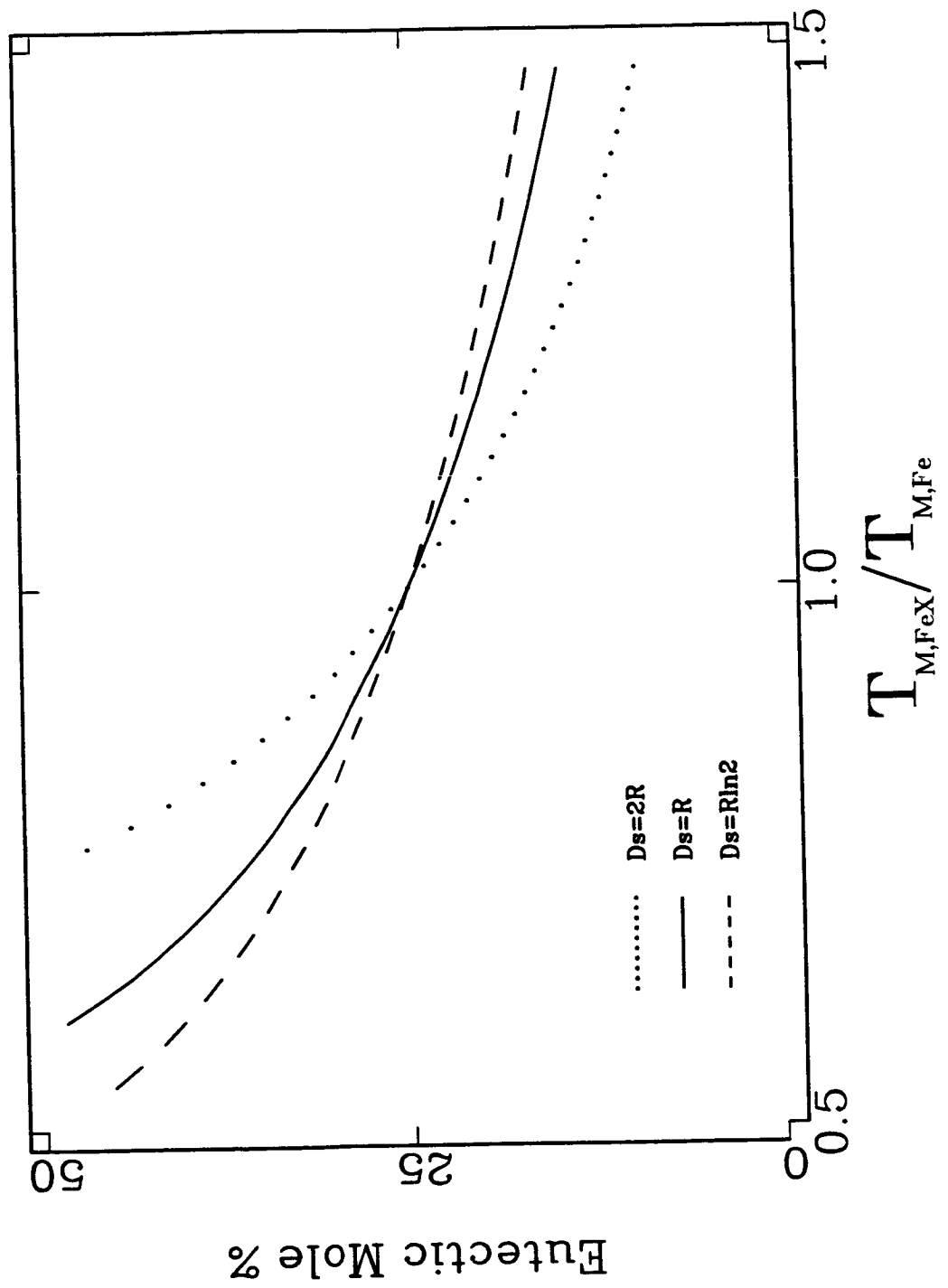
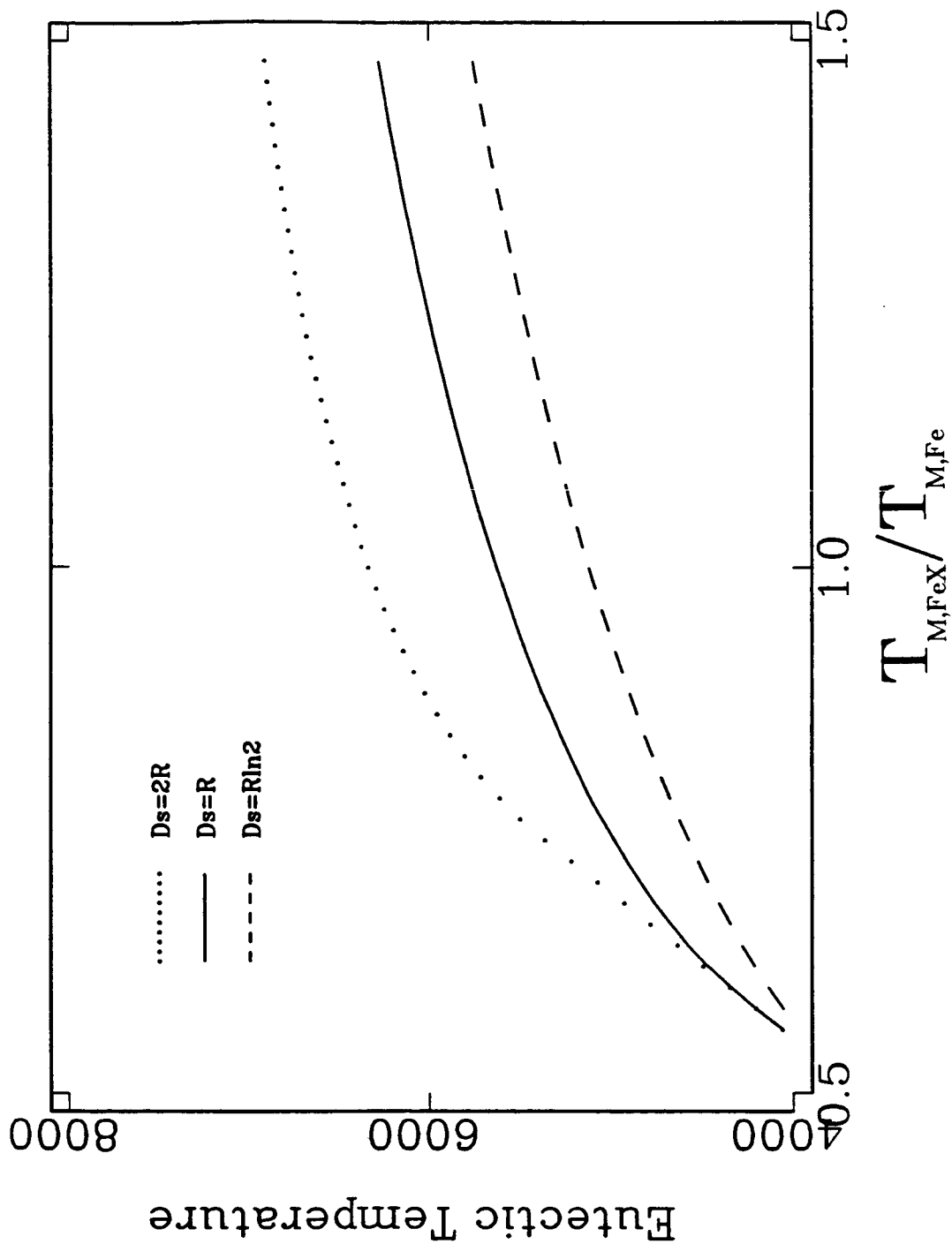


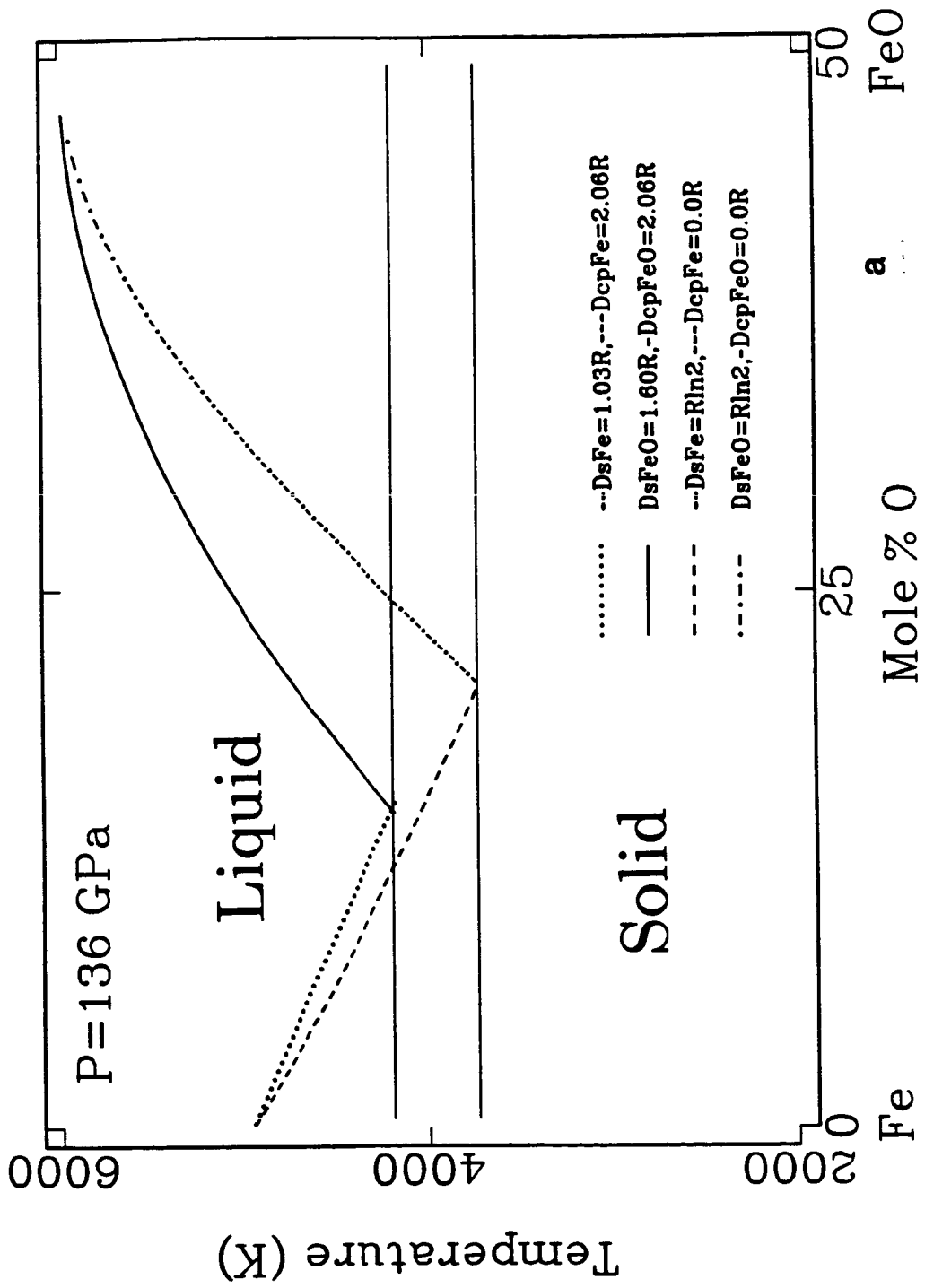
Figure 4.2. Eutectic temperature versus ratio of end member melting temperatures referenced to $T_{MFe}=7250$ at $P=330$ GPa. "Ds" has same meaning as in Figure 5.

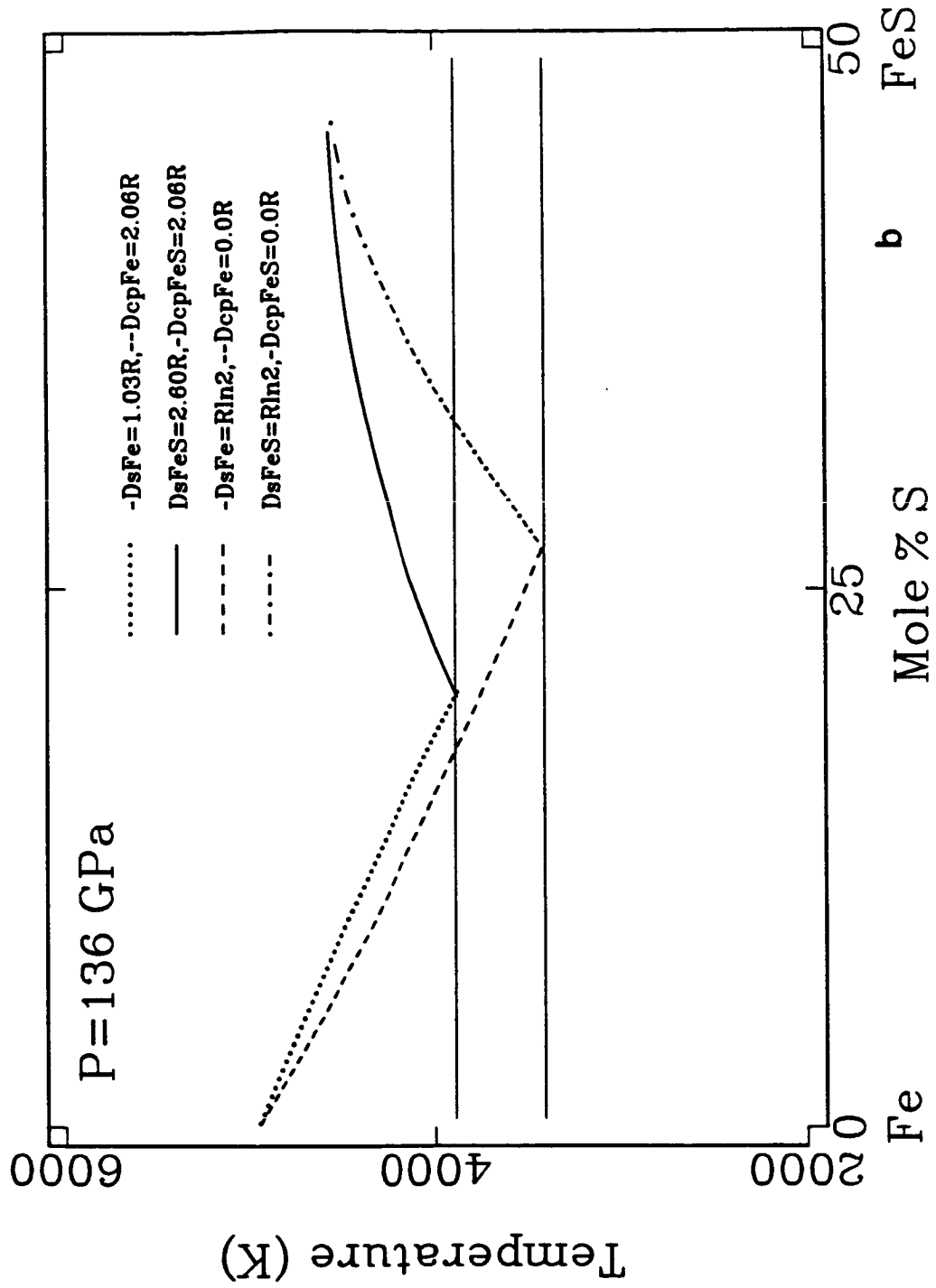


GPa, the pressure at the core-mantle boundary (CMB), and in Figures 4.4a-b for $P=330$ GPa, the pressure of the outer-inner core boundary (ICB). As evident, the value of ΔC_p^{l-s} affects mainly the curvature of the liquidus, while ΔS^{l-s} affects its slope. As implied from Figure 4.2, we obtain the minimum value of T_{eu} for the minimum value of ΔS^{l-s} and $\Delta C_p^{l-s}=0$ in Figures 4.3a-b and 4.4a-b. Via the results of Figure 4.1, we also see that, because $T_{MFeS}/T_{MFe} < 1$ while $T_{MFeO}/T_{MFe} > 1$, the Fe-FeS eutectic composition shifts toward the FeS rich side of the system, whereas the Fe-FeO eutectic composition falls toward the Fe-rich side, both at 136 GPa and 330 GPa. The significantly higher melting temperature of FeO as compared to Fe or FeS (Figure 3.1) at a given pressure suggests that this compound is relatively stable at high pressures and temperatures, and probably remains largely associated during melting. In this case, it is reasonable to assume that the liquidus and solidus coincide in the Fe-O system at the composition FeO, as done above. For these very same reasons, of course, this assumption is suspect for the Fe-S system, *i.e.*, FeS is less stable as a solid than either Fe or FeO, hence more likely to melt incongruently than FeO; further, since the effective radii of Fe and (metallized) S atoms at high pressure are apparently almost identical (Boness *et al.*, 1986).

As pointed out by numerous workers (*e.g.*, Stevenson, 1981), the OC is most likely a mixture of Fe, Ni and a number of other elements X_i whose presence is required to lower the melting point of the OC below its temperature. Besides the usual cosmochemical considerations, the idea that these elements must have a mean atomic weight significantly less than Fe or Ni rests principally on the observation that the seismically constrained density profile of the OC is $\sim 10\%$ lower than that of shock-compressed Fe at the same pressure. More recently, Brown and McQueen (1982) compared their experimental results for elastic-wave velocities in shock-compressed Fe with the outer core seismic

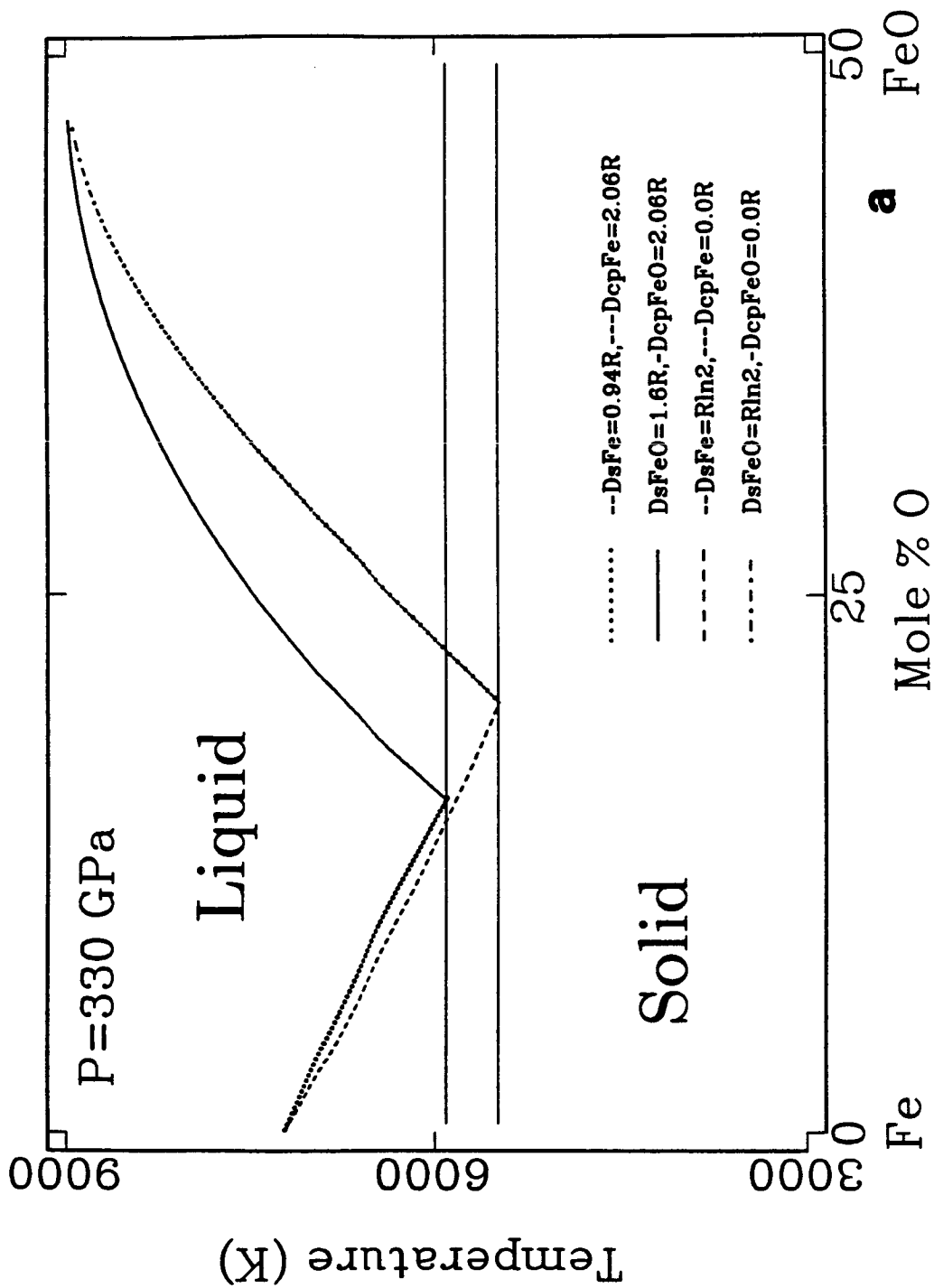
Figure 4.3. Model temperature versus mole %X in the Fe-FeO (part a) and Fe-FeS (part b) systems at the pressure of the core-mantle boundary (CMB), 135 GPa. "Ds" and "Dcp" stand for ΔS^{l-s} and ΔC_p^{l-s} for the indicated end-member

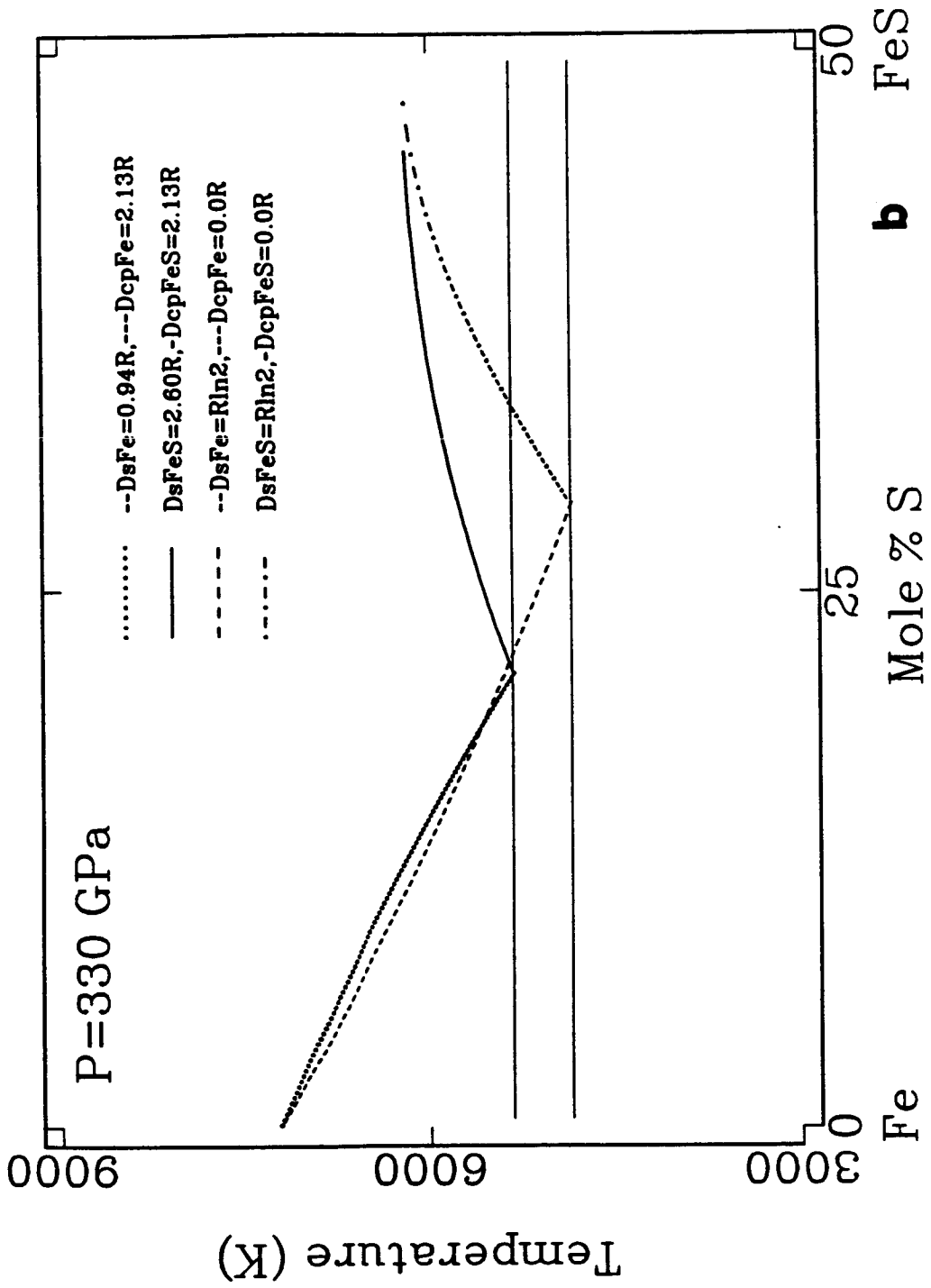




velocity profiles. The value of either of these comparisons (again, at the same pressure) rests strongly on a knowledge of 1) the temperature difference between shock-compressed Fe and the OC and 2) the effect of mixing other elements with Fe under core conditions (*e.g.*, Birch, 1952; Jeanloz, 1979). Considering that seismic density profiles depend on velocity profiles and models, the velocity comparison should be more decisive than that for density, at least from the seismic viewpoint. As noted by Stacey *et al.* (1981), uncertainties in the temperature profile of the OC, combined with uncertainties in the seismically constrained density profile, may admit, from the density viewpoint alone, the possibility of no light component. Since the OC density profile is inherently less well constrained than the velocity profile, the observation that the OC does not support shear in the seismic frequency band in concert with the idea that $T_{MFe} > T_{OC}$ together constitute perhaps the most compelling evidence for the OC to be a liquid Fe,Ni-X_i mixture. With this in mind, we note that, as calculated above, the melting temperature of FeO is about 1500 K greater than that of Fe at 330 GPa, which is in turn about 1000 K greater than that of FeS at this pressure, we note that calculated Fe-FeO eutectic compositions at 330 GPa (15-20 mole % O) are less than 25 mole % O, while calculated Fe-FeS eutectic compositions at 330 GPa (23-30 mole % S) are generally greater than 25 mole % S. The mass density of the Earth's outer core just above the inner core boundary is approximately 12160 kg/m³, and we note that this is also the density of an ideal mixture of 93 mole % Fe and 7 mole % S (*i.e.*, 14 mole % FeS), and a similar mixture of approximately 72 mole % Fe and 28 mole % O (56 mole % FeO). Consequently, these calculations and considerations imply that an O-rich outer core is more likely to lie on the FeO-rich side of the Fe-FeX eutectic, while an S-rich outer core is more likely to lie on the Fe-rich side of the Fe-FeX eutectic.

Figure 4.4. Model temperature versus mole %X in the Fe-FeO (part a) and Fe-FeS (part b) systems at the pressure of the outer-inner core boundary (ICB), 330 GPa.



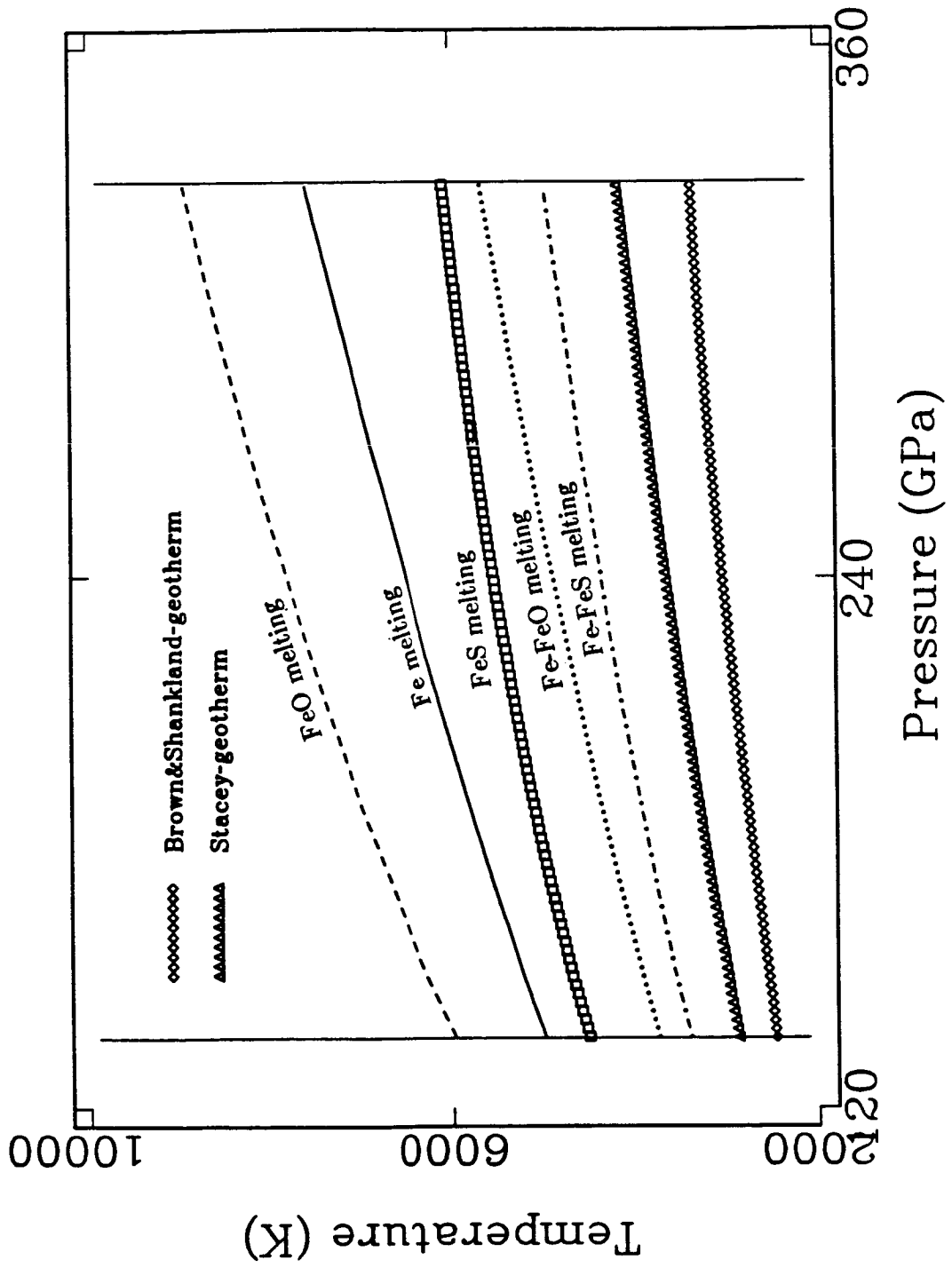


Comparing the Fe-FeO eutectic compositions in Figure 4.3a and 4.4a, and the Fe-FeS eutectic compositions in Figures 4.3b and 4.4b, we see that the eutectic compositions in both of these systems are relatively insensitive to pressure. This is largely due to the fact that ξ_m , which controls x_{eu} as shown in Figure 4.1, is insensitive to pressure for both Fe-FeS and Fe-FeO. The eutectic temperatures, however, vary between about 4000 and 6000 K between 136 and 330 GPa. Assuming $\Delta S^{l-s} \sim \ln 2R$ is a reasonable lower-bound to ΔS^{l-s} , then, the temperature of the outer core must be above this value to remain a liquid Fe-X mixture. As can be seen in Figure 4.5, this idea implies that current estimates of the temperature profile of the outer core, bounded below by that of Brown and Shankland (1980), and above by that of Stacey (1977), are 1000-1500 K too low, and should be above approximately 4000 K at 136 GPa and 5000 K at 330 GPa. Also, with a temperature of $\lesssim 3000$ K at the top of the D'' region, for example, this implies a thermal boundary layer $\gtrsim 1000$ -1500 K somewhere in the mantle, possibly also supporting the need of multiple boundary layers in the mantle (*e.g.*, Jeanloz and Richter, 1979; Spiliopoulos and Stacey, 1984), a larger contribution from primordial heat to the current heat flux out of the Earth, and a larger initial energy budget for the Earth.

§5. Summary

Liquid-state and solid-state model fits to melting data for Fe, FeS and FeO provide constraints for calculating ideal phase relations in Fe-FeS and Fe-FeO systems in the pressure range corresponding to the earth's outer core. The liquid-state model fit to the Fe melting data of Williams and Jeanloz (1986) places constraints on the temperature and other properties along the liquidus above the range of their data. The temperature along the best-fit Fe liquidus is 5000 K at 136 GPa and 7250 K at 330 GPa, which is somewhat lower than that implied by the Hugoniot results (~ 7800 K). This discrepancy may be due to

Figure 4.5. Temperature versus pressure along the model Fe, FeS and FeO melting curves, as well as those along the minimum temperature ($\Delta S^{l-s} = R \log 2$, $\Delta C_p^{l-s} = 0$) Fe-FeS and Fe-FeO eutectics compared to outer-core temperature profiles of Stacey (1977; triangles) and Brown and Shankland (1980; diamonds). Along the Fe-FeS eutectic, the mole % X ranges from 25% at the CMB to 27% at the ICB, while along the Fe-FeO eutectic it ranges from 13% at the CMB to 12% at the ICB.



the reshock effect discussed above, or some inaccuracy in the extrapolation, presuming the Hugoniot results represent the equilibrium melting behavior of Fe. Constraints on the solidi of FeS and FeO from the comparison of data and solid-state model calculations imply that FeS and FeO melt at 4610 K and 5100 K, respectively, at 136 GPa, and 6150 K and 8950 K, respectively, at 330 GPa. Calculations for the equilibrium thermodynamic properties of solid and liquid Fe along the coincident solidus and liquidus imply that the entropy of melting for Fe is approximately independent of pressure at a value of approximately R (where R is Ryberg's constant), while the change in the molar heat capacity across the transition increases with pressure from approximately $0.5 R$ to $4R$ between standard pressure and 330 GPa. We use these constraints to construct ideal-mixing phase diagrams for Fe-FeS and Fe-FeO systems at outer core pressures, assuming that Fe and FeS, or Fe and FeO, respectively, are the solid phases in equilibrium with the liquid Fe-FeS or Fe-FeO mixtures, respectively. The composition of the Fe-X ($X=O$ or S) liquid mixture relative to the eutectic composition of the Fe-FeX system determines whether Fe or FeX will solidify at the liquidus. For these ideal mixing calculations, the eutectic composition is controlled by the ratio of the end-member (*i.e.*, Fe and FeX) melting temperatures at a given pressure. If Fe and FeX have the same melting temperature, for example, the eutectic composition is 25 mole % X; if the melting temperature of FeX is greater or less than Fe, the eutectic composition will be displaced to more Fe or FeX rich compositions, respectively. Since, as quoted above, the melting temperature of FeO is about 1500 K greater than that of Fe at 330 GPa, which is in turn about 1000 K greater than that of FeS at this pressure, we note that calculated Fe-FeO eutectic compositions at 330 GPa (15-20 mole % O) are less than 25 mole % O, while calculated Fe-FeS eutectic compositions at 330 GPa (23-30 mole % S) are generally greater than 25 mole % S. The mass density of the Earth's outer core just above the inner core boundary is

approximately 12160 kg/m^3 , and we note that this is also the density of an ideal mixture of 93 mole % Fe and 7 mole % S (*i.e.*, 14 mole % FeS), and a similar mixture of approximately 72 mole % Fe and 28 mole % O (56 mole % FeO). Consequently, these calculations and considerations imply that an O-rich outer core is more likely to lie on the FeO-rich side of the Fe-FeX eutectic, while an S-rich outer core is more likely to lie on the Fe-rich side of the Fe-FeX eutectic.

The temperature of the Fe-FeS eutectic are lower than the Fe-FeO eutectic, being approximately 5000 K at 330 GPa. Note that the eutectic temperature represents a lower bound to temperatures at the outer-inner core boundary under the hypothesis that this boundary represents the liquidus in an Fe-X mixture. Eutectic and end-member melting temperatures in both the Fe-FeS and Fe-FeO systems imply, in the context of the outer-inner core boundary-phase boundary hypothesis, that previous widely-accepted temperature profiles for the outer core, ranging from $\lesssim 3000 \text{ K}$ at the 136 GPa, the core-mantle boundary, to $\lesssim 4200 \text{ K}$ at 330 GPa, the outer-inner core boundary, are about 1000-1500 K too low. This possibility implies that at least one boundary layer of 1000-1500 K exists in the mantle, possibly at its base in the D'' region.

Acknowledgements. We thank Dave Stevenson for giving us his ideas, from which we have fashioned this work. Support provided by NSF Grants EAR-86-08244 and EAR-85-08969, and NASA grant NGL 105-002-105. Contribution 4299, Division of Geological and Planetary Sciences, California Institute of Technology, Pasadena, CA, 91125.

§6. Appendix A: Equilibrium Thermodynamic Model for a Liquid

The equilibrium thermodynamic properties of liquid-Fe discussed in the text are referenced to those of a hard-sphere liquid via the Gibbs-Bogolyubov (GB) inequality (*e.g.*, Isihara, 1968; Hansen and McDonald, 1975). This

inequality states that the equilibrium thermodynamic Helmholtz free energy (HFE) of the liquid, $F_{\text{liq}}(T, \rho)$, is bounded above by the HFE of an "equivalent" system of hard spheres which interact with each other (to first order) as do the actual "ions" or "particles" of the liquid. For a liquid metal, the GB inequality takes the form

$$F_{\text{liq}} \leq F_{\text{mod}} = F_{\text{HS}} + F_{\text{INT}} + F_{\text{el}} \quad [\text{A.1}]$$

Note that this HFE has units of Joules. In this expression, F_{HS} is the HFE of the hard-sphere reference system, F_{INT} is the "ion-ion" interaction contribution to F , and F_{el} is the electronic contribution to F . F_{HS} may be obtained from the compressibility equation-of-state (Carnaghan and Starling, 1969) or the virial expansion (*e.g.*, Hansen and McDonald, 1975). As discussed by Foiles and Ashcroft (1981), the virial form of F_{HS} may provide a better approximation to F_{HS} and the liquid pressure than the compressibility form, since the virial form directly represents the pressure, and is one derivative less removed from F_{HS} than the compressibility form. Since we are interested in the pressure and temperature, as discussed below, we use the virial form of F_{HS} . For a single-component liquid of N particles, occupying a volume V , this is

$$F_{\text{HS}}^{\text{vir}} = F_{\text{ig}} + Nk_{\text{B}}T \left\{ \frac{6\eta}{(1-\eta)} + 2\ln(1-\eta) \right\} \quad [\text{A.2}],$$

respectively, where $\eta \equiv \pi\rho_{\text{N}}d^3/6$ is the hard-sphere packing fraction, equal to the product of the volume of a single sphere $\pi d^3/6$, and the number density of spheres, $\rho_{\text{N}} \equiv N/V$. Note that d is the diameter of a given sphere. In [A.2], F_{ig} is the HFE of a single-component ideal gas, *i.e.*,

$$F_{\text{ig}} = Nk_{\text{B}}T[\ln(\rho_{\text{N}}\Lambda^3) - 1] \quad [\text{A.3}].$$

In [A.3], $\Lambda \equiv h/[2\pi mk_{\text{B}}T]^{1/2}$, h is Planck's constant, m is the mass of a single particle (sphere), and k_{B} is Boltzmann's constant.

The total pair-interaction contribution to F , F_{INT} , is given to first order by the relation

$$F_{\text{INT}} = 2\pi(N-1)\rho_N \int_0^{\infty} [\psi(r) - \psi_{\text{HS}}(r)]g_{\text{HS}}(r)r^2dr \quad [\text{A.4}]$$

(*e.g.*, Mansoori and Canfield, 1969). In [A.4], $\psi(r)$ describes the interaction of two liquid particles at a distance r away from the center of a given particle, $g_{\text{HS}}(r)$ is the hard-sphere radial distribution function, defined such that $4\pi\rho_N r^2 g_{\text{HS}}(r)dr$ represents the average number of hard-sphere at a distance r to $r+dr$ away from a given sphere. Also, $\psi_{\text{HS}}(r)$ describes the interaction of two hard-spheres, *i.e.*,

$$\psi_{\text{HS}}(r) = \begin{cases} \infty & r < d \\ 0 & r \geq d \end{cases} \quad [\text{A.5}]$$

Since $g_{\text{HS}}(r)$ is proportional to $\exp[-\beta\psi_{\text{HS}}(r)]$, with $\beta \equiv 1/k_B T$, we see that, from [A.5], $g_{\text{HS}}(r) = 0$ for $r < d$. In this case, the product $\psi_{\text{HS}}(r)g_{\text{HS}}(r)$ is always zero. Consequently, [A.4] may be written

$$F_{\text{INT}} = 2\pi(N-1)\rho_N \int_d^{\infty} \psi(r)g_{\text{HS}}(r)r^2dr \quad [\text{A.6}]$$

since the integral from 0 to d is zero via the definition of $\psi_{\text{HS}}(r)$ in [A.5]. This expresses the physical idea that ions are unlikely to interact at distances closer than their "hard-sphere" diameters. As such, interaction closer than $r=d$ contribute little to F , and this is idealized to nothing in the model. To evaluate [A.6] further, we must assume forms for $\psi(r)$ and $g_{\text{HS}}(r)$. We assume $\psi(r)$ has the Yukawa form

$$\psi(r) = \frac{\sigma}{r} e^{-\lambda r} \quad [\text{A.7}]$$

Then we may put [A.6] into the form

$$\begin{aligned} F_{\text{INT}} &= 2\pi(N-1)\rho_N\epsilon \int_0^\infty e^{-\lambda r} [r g_{\text{HS}}(r)] dr \\ &= 2\pi(N-1)\rho_N\epsilon \mathbf{L}\{r g_{\text{HS}}(r)\}(\lambda) \end{aligned} \quad [\text{A.8}].$$

In [A.8], \mathbf{L} is the Laplace transform operator. This form is advantageous because $\mathbf{L}\{r g_{\text{HS}}(r)\}$ is known analytically for the Percus-Yevick approximation to $g_{\text{HS}}(r)$ (Wertheim, 1963). Note that [A.7] represents only repulsive pair interactions. To assess the possibility of attractive interactions in liquid-Fe, which may be important at lower pressures, we add an attractive term to [A.5] and obtain the so-called "double Yukawa" potential, *i.e.*,

$$\psi(r) \equiv \frac{\epsilon\sigma}{r} \left\{ e^{-\lambda(r-\sigma)} - e^{-\omega(r-\sigma)} \right\} \quad [\text{A.9}].$$

In [A.9], σ represents the distance away from the center of each sphere where attractive and repulsive interactions balance, *i.e.* $\psi(\sigma) = 0$ (equilibrium), while λ^{-1} is the characteristic length scale of repulsive interaction, and ω^{-1} that for attraction interactions. Physically, we expect $\lambda > \omega$, since repulsion and attraction are dominantly short- and long-range interactions, respectively. In this case, note that $\psi(r) > 0$ for $r < \sigma$, and $\psi(r) < 0$ for $r \geq \sigma$.

If we substitute [A.9] into [A.6], we obtain

$$F_{\text{INT}} = 2\pi\rho_N(N-1)\sigma\epsilon \left\{ e^{\lambda\sigma} \mathbf{L}\{r g_{\text{HS}}(r)\}(\lambda) - e^{\omega\sigma} \mathbf{L}\{r g_{\text{HS}}(r)\}(\omega) \right\} \quad [\text{A.10}].$$

Nondimensionalizing r by d , the hard sphere diameter, in [A.10], we have

$$F_{\text{INT}} = 12(N-1)\frac{\epsilon}{c}\eta \left\{ e^{\lambda^*} \mathbf{L}\{\xi g_{\text{HS}}(\xi)\}(\lambda^*c) - e^{\omega^*} \mathbf{L}\{\xi g_{\text{HS}}(\xi)\}(\omega^*c) \right\} \quad [\text{A.11}]$$

with $\xi \equiv r/d$, $\lambda^* \equiv \lambda\sigma$, $\omega^* \equiv \omega\sigma$ and $c \equiv d/\sigma$. From Wertheim (1963), we have

$$\mathbf{L}\{xg_{\text{HS}}(x)\}(\chi) = \frac{\chi L(\chi)}{12\eta[L(\chi) + S(\chi)e^{\chi}]} \quad [\text{A.12}]$$

with

$$L(\chi) \equiv 12\eta[(1+2\eta) + (1+\frac{1}{2}\eta)\chi]$$

and

[A.13]

$$S(\chi) \equiv (1-\eta)^3\chi^3 + 6\eta(1-\eta)\chi^2 + 18\eta^2\chi - 12\eta(1+2\eta),$$

when $g_{\text{HS}}(r)$ is approximated by the Percus-Yevick relation (Percus and Yevick, 1959). Putting [A.12] into [A.11], we obtain

$$F_{\text{INT}} = (N-1)\epsilon[H(c,\eta;\lambda^*) - H(c,\eta;\omega^*)] \quad [\text{A.14}],$$

where

$$H(c,\eta;\mu) \equiv \mu e^{\mu} \frac{L(\mu c, \eta)}{[L(\mu c, \eta) + S(\mu c, \eta)e^{\mu c}]} \quad [\text{A.15}].$$

In the text, we represent F_{e1} by its low temperature (T much less than the Fermi temperature) Sommerfeld expansion

$$F_{e1} = -\frac{1}{2}\Gamma(\rho)T^2 \quad [\text{A.16}].$$

In [A.16], $\Gamma(\rho)$ is the density of electron energy states at the Fermi energy (surface); it is commonly given the form (*e.g.*, Wallace, 1972)

$$\Gamma(\rho) = \Gamma(\rho_i)(\rho_i/\rho)^{\gamma_e},$$

where γ_e is the electronic thermostatic Grüneisen's parameter of the liquid in this case.

We now nondimensionalize F by the product of the number of particles in the system, N, and $k_B T$, such that $f \equiv \beta F/N = F/Nk_B T$. Also, we define a non-dimensional temperature, $T^* \equiv k_B T/\epsilon$, and a non-dimensional number density, $\rho_N^* = \rho_N \sigma^3$. With these, we rewrite [A.1] as

$$f_{\text{liq}}(T^*, \rho_N^*) \leq f_{\text{mod}} = f_{\text{HS}}(T^*, \rho_N^*, \eta) + f_{\text{NRT}}(T^*, \eta, c; \lambda^*, \omega^*) + f_{\text{el}}(T^*, \rho_N^*) \quad [\text{A.17}]$$

with

$$f_{\text{HS}}^{\text{vir}}(T^*, \rho_N^*, \eta) \equiv f_{\text{ig}}(T^*, \rho_N^*) + \frac{6\eta}{(1-\eta)} + 2\ln(1-\eta) \quad [\text{A.18}],$$

$$f_{\text{ig}}(T^*, \rho_N^*) \equiv \ln(\rho_N^*) - \frac{3}{2}\ln(T^*) + 3\ln(\Lambda^*) - 1 \quad [\text{A.19}],$$

$$f_{\text{NRT}} \equiv \frac{1}{T^*} [H(c, \eta; \lambda^*) - H(c, \eta; \omega^*)] = \frac{1}{T^*} \Delta H(c, \eta; \lambda^*, \omega^*) \quad [\text{A.20}],$$

and

$$f_{\text{el}} \equiv -\frac{1}{2}\Gamma^*(\rho_N^*)T^* = -\frac{1}{2} \frac{\epsilon}{Nk_B^2} \Gamma(\rho_N^*)T^* \quad [\text{A.21}],$$

where $\Lambda^* \equiv h/\sigma\sqrt{2\pi m\epsilon}$, and $(N-1) \approx N$ for a "macroscopic" liquid. In [A.17] and [A.18]-[A.21], λ^* and ω^* are constants, as is σ from the Yukawa potential. So now we have $f_{\text{mod}} = f_{\text{mod}}(T^*, \rho_N^*, \eta, c)$ explicitly. In this case, the total differential of f_{mod} is

$$\begin{aligned} df_{\text{mod}} = & \left\{ \frac{\partial f_{\text{mod}}}{\partial T^*} \right\}_{\rho_N^*, \eta, c} dT^* + \left\{ \frac{\partial f_{\text{mod}}}{\partial \rho_N^*} \right\}_{T^*, \eta, c} d\rho_N^* \\ & + \left\{ \frac{\partial f_{\text{mod}}}{\partial \eta} \right\}_{T^*, \rho_N^*, c} d\eta + \left\{ \frac{\partial f_{\text{mod}}}{\partial c} \right\}_{T^*, \rho_N^*, \eta} dc \end{aligned} \quad [\text{A.22}].$$

Since $\eta \equiv \frac{\pi}{6}\rho_N^*c^3$, however, [A.22] may be written

$$df_{\text{mod}} = \left\{ \frac{\partial f_{\text{mod}}}{\partial T^*} \right\}_{\rho_N^*, c} dT^* + \left\{ \frac{\partial f_{\text{mod}}}{\partial \rho_N^*} \right\}_{T^*, c} d\rho_N^* + \left\{ \frac{\partial f_{\text{mod}}}{\partial c} \right\}_{T^*, \rho_N^*} dc \quad [\text{A.23}]$$

with

$$\left\{ \frac{\partial f_{\text{mod}}}{\partial \rho_N^*} \right\}_{T^*, c} = \left\{ \frac{\partial f_{\text{mod}}}{\partial \rho_N^*} \right\}_{T^*, c, \eta} + \left\{ \frac{\partial f_{\text{mod}}}{\partial \eta} \right\}_{T^*, c, \rho_N^*} \left\{ \frac{\partial \eta}{\partial \rho_N^*} \right\}_c \quad [\text{A.24}],$$

$$\left\{ \frac{\partial f_{\text{mod}}}{\partial c} \right\}_{T^*, \rho_N^*} = \left\{ \frac{\partial f_{\text{mod}}}{\partial c} \right\}_{T^*, \rho_N^*, \eta} + \left\{ \frac{\partial f_{\text{mod}}}{\partial \eta} \right\}_{T^*, \rho_N^*, c} \left\{ \frac{\partial \eta}{\partial c} \right\}_{\rho_N^*} \quad [\text{A.25}],$$

and

$$\left\{ \frac{\partial \eta}{\partial \rho_N^*} \right\}_c = \frac{\eta}{\rho_N^*} \neq f(\rho_N^*), \quad \left\{ \frac{\partial \eta}{\partial c} \right\}_{\rho_N^*} = \frac{3\eta}{c} \quad [\text{A.26}].$$

Now, in equilibrium, $f_{\text{liq}} = f_{\text{liq}}(T^*, \rho_N^*)$ for the single-component system we have here. Consequently,

$$df_{\text{liq}} = \left\{ \frac{\partial f_{\text{liq}}}{\partial T^*} \right\}_{\rho_N^*} dT^* + \left\{ \frac{\partial f_{\text{liq}}}{\partial \rho_N^*} \right\}_{T^*} d\rho_N^* \quad [\text{A.27}].$$

From [A.27], at constant T^* and ρ_N^* , we have $df_{\text{liq}} = 0$, while from [A.23], we have, at constant T^* and ρ_N^*

$$df_{\text{mod}})_{T^*, \rho_N^*} = \left\{ \frac{\partial f_{\text{mod}}}{\partial c} \right\}_{T^*, \rho_N^*} dc$$

therefore, to have $df_{\text{mod}})_{T^*, \rho_N^*} = 0$ for arbitrary dc , we require

$$\left\{ \frac{\partial f_{\text{mod}}}{\partial c} \right\}_{T^*, \rho_N^*} \equiv 0 \quad [\text{A.28}]$$

for f_{mod} to be an equilibrium thermodynamic state function. More explicitly, [A.28] states, using [A.18]-[A.21], that

$$\begin{aligned} \left\{ \frac{\partial f_{\text{mod}}}{\partial c} \right\}_{T^*, \rho_N^*} &= \left\{ \frac{\partial f_{\text{mod}}}{\partial c} \right\}_{T^*, \rho_N^*, \eta} + \left\{ \frac{\partial f_{\text{mod}}}{\partial \eta} \right\}_{T^*, \rho_N^*, c} \left\{ \frac{\partial \eta}{\partial c} \right\}_{T^*, \rho_N^*} \\ &= \frac{1}{T^*} \left\{ \frac{\partial \Delta H}{\partial c} \right\}_{T^*, \rho_N^*, \eta} + \left\{ \frac{1}{T^*} \left\{ \frac{\partial \Delta H}{\partial \eta} \right\}_{T^*, \rho_N^*, c} + f_{\text{HS}}^{(1)} \right\} \frac{3\eta}{c} \equiv 0 \end{aligned}$$

where [A.29]

$$f_{\text{HS}}^{(n)} \equiv \left\{ \frac{d^{(n)} f_{\text{HS}}}{d\eta^{(n)}} \right\}.$$

We may rewrite [A.29] as an implicit function for the equilibrium value of c , i.e.

$$I_1(T^*, c, \eta) = \frac{3\eta}{c} f_{\text{HS}}^{(1)} + \frac{1}{T^*} \left\{ \left\{ \frac{\partial \Delta H}{\partial c} \right\}_{T^*, \rho_N^*, \eta} + \left\{ \frac{\partial \Delta H}{\partial \eta} \right\}_{T^*, \rho_N^*, c} \frac{3\eta}{c} \right\} = 0 \quad [\text{A.30}]$$

and we may solve this simultaneously with

$$I_2(\rho_N^* c, \eta) = \eta - \pi/6 \rho_N^* c^3 = 0 \quad [\text{A.31}].$$

for c or η as a function of T^* and ρ_N^* . Relation [A.31] comes from the definition of the packing fraction; together with [A.30], it gives us two equations among 4 unknowns (c, η, T^* and ρ_N^*). Mathematically, any two of these may be considered, via [A.30] and [A.31], as independent; T^* and ρ_N^* are the logical choice from the equilibrium thermodynamic perspective. On this basis, we designate the values of c and η given implicitly by [A.30]-[A.31] as $\hat{c} = \hat{c}(T^*, \rho_N^*)$ and $\hat{\eta} = \hat{\eta}(T^*, \rho_N^*)$, the equilibrium values of c and η , respectively, for a given equilibrium state (T^*, ρ_N^*) . In practice, any two of the 4 variables may be considered independent. For [A.28] to constrain a minimum value of f_{mod} , and so a least-upper-bound to $f_{\text{liq}}(T^*, \rho_N^*)$ via the GB inequality, we also require

$$\left\{ \frac{\partial^2 f_{\text{mod}}}{\partial c^2} \right\}_{T^*, \rho_N^*} > 0 \quad [\text{A.32}].$$

Consequently, with $f_{\text{mod}}(T^*, \rho_N^*, c, \eta)$ satisfying [A.28] and [A.32], and \hat{c} and $\hat{\eta}$ constrained from [A.30]-[A.31], we may write

$$\begin{aligned} f_{\text{liq}}(T^*, \rho_N^*) &\approx f_{\text{mod}}(T^*, \rho_N^*) \\ &= f_{\text{ig}}(T^*, \rho_N^*) + f_{\text{HS}}[\hat{\eta}(T^*, \rho_N^*)] + \frac{1}{T^*} \Delta H[\hat{c}(T^*, \rho_N^*), \hat{\eta}(T^*, \rho_N^*)] + f_{\text{el}}(T^*, \rho_N^*) \end{aligned} \quad [\text{A.33}]$$

as the basic model relation for the equilibrium HFE of the liquid. In this case, we may derive all equilibrium thermodynamic properties from [A.33]. For example, the pressure is then

$$P \equiv - \left\{ \frac{\partial F}{\partial V} \right\}_{T, N} = - \left\{ \frac{\partial (F/N)}{\partial (V/N)} \right\}_{T, N} = \beta^{-1} \rho_N \rho_N^* \left\{ \frac{\partial f_{\text{mod}}}{\partial \rho_N^*} \right\}_{T^*} \quad [\text{A.34}]$$

Defining a nondimensional pressure, $p \equiv \beta P / \rho_N$, and substituting [A.18]-[A.21]

into [A.33], we have

$$\begin{aligned}
 p = \rho_N^* \left(\frac{\partial f_{\text{mod}}}{\partial \rho_N^*} \right)_{T^*} &= 1 + f_{\text{HS}}^{(1)} \rho_N^* \left(\frac{\partial \hat{\eta}}{\partial \rho_N^*} \right)_{T^*} \\
 &+ \frac{1}{T^*} \left\{ \left(\frac{\partial \Delta H}{\partial \hat{c}} \right)_{\hat{\eta}} \rho_N^* \left(\frac{\partial \hat{c}}{\partial \rho_N^*} \right)_{T^*} + \left(\frac{\partial \Delta H}{\partial \hat{\eta}} \right)_{\hat{c}} \rho_N^* \left(\frac{\partial \hat{\eta}}{\partial \rho_N^*} \right)_{T^*} \right\} \\
 &+ \frac{1}{2} \gamma_e \Gamma^* T^* \tag{A.35}
 \end{aligned}$$

Now, from the definition of the packing fraction, we may write

$$\rho_N^* \left(\frac{\partial \hat{\eta}}{\partial \rho_N^*} \right)_{T^*} = \hat{\eta} + \frac{3\hat{\eta}}{\hat{c}} \rho_N^* \left(\frac{\partial \hat{c}}{\partial \rho_N^*} \right)_{T^*} \tag{A.36}$$

Substituting this into [A.35], we obtain

$$\begin{aligned}
 p = 1 + \hat{\eta} \left\{ f_{\text{HS}}^{(1)} + \frac{1}{T^*} \left(\frac{\partial \Delta H}{\partial \hat{\eta}} \right)_{\hat{c}} \right\} \\
 + \left\{ \frac{1}{T^*} \left(\frac{\partial \Delta H}{\partial \hat{c}} \right)_{\hat{\eta}} + \left\{ \frac{1}{T^*} \left(\frac{\partial \Delta H}{\partial \hat{\eta}} \right)_{\hat{c}} + f_{\text{HS}}^{(1)} \right\} \frac{3\hat{\eta}}{\hat{c}} \right\} \rho_N^* \left(\frac{\partial \hat{c}}{\partial \rho_N^*} \right)_{T^*} \\
 + \frac{1}{2} \gamma_e \Gamma^* T^* \tag{A.37}
 \end{aligned}$$

By [A.29] the third term on the right-hand side of [A.37] is zero. Therefore,

$$p = 1 + \hat{\eta} \left\{ f_{\text{HS}}^{(1)} + \frac{1}{T^*} \left(\frac{\partial \Delta H}{\partial \hat{\eta}} \right)_{\hat{c}} \right\} + \frac{1}{2} \gamma_e \Gamma^* T^* \tag{A.38}$$

Now, the entropy is defined by

$$S \equiv - \left(\frac{\partial F}{\partial T} \right)_{V,N} = -Nk_B \left\{ f_{\text{mod}} + T^* \left(\frac{\partial f_{\text{mod}}}{\partial T^*} \right)_{\rho_N^*} \right\} \tag{A.39}$$

and S has units of J/K. A natural nondimensional entropy is then

$$\begin{aligned}
 s &\equiv \frac{S}{Nk_B} = - \left[f_{\text{mod}} + T^* \left(\frac{\partial f_{\text{mod}}}{\partial T^*} \right)_{\rho_N^*} \right] \\
 &= \frac{3}{2} - f_{\text{ig}} - f_{\text{HS}} - \left\{ f_{\text{HS}}^{(1)} + \frac{1}{T^*} \left(\frac{\partial \Delta H}{\partial \hat{\eta}} \right)_{\hat{c}} \right\} T^* \left(\frac{\partial \hat{\eta}}{\partial T^*} \right)_{\rho_N^*} \\
 &\quad - \frac{1}{T^*} \left(\frac{\partial \Delta H}{\partial \hat{c}} \right)_{\hat{\eta}} T^* \left(\frac{\partial \hat{c}}{\partial T^*} \right)_{\rho_N^*} + \Gamma^* T^* \tag{A.40}
 \end{aligned}$$

Now, from the definition of the packing fraction, we have

$$T^* \left(\frac{\partial \hat{\eta}}{\partial T^*} \right)_{\rho_N^*} = \frac{3\hat{\eta}}{\hat{c}} T^* \left(\frac{\partial \hat{c}}{\partial T^*} \right)_{\rho_N^*} . \tag{A.41}$$

Putting this into [A.40], we obtain

$$\begin{aligned}
 s &= \frac{3}{2} - f_{\text{ig}} - f_{\text{HS}} \\
 &\quad - \left\{ \frac{1}{T^*} \left(\frac{\partial \Delta H}{\partial \hat{c}} \right)_{\hat{\eta}} + \left\{ \frac{1}{T^*} \left(\frac{\partial \Delta H}{\partial \hat{\eta}} \right)_{\hat{c}} + f_{\text{HS}}^{(1)} \right\} \frac{3\hat{\eta}}{\hat{c}} \right\} T^* \left(\frac{\partial \hat{c}}{\partial T^*} \right)_{\rho_N^*} + \Gamma^* T^* \tag{A.42}
 \end{aligned}$$

From [A.29], the fourth term on the right hand side is zero. Therefore,

$$s = \frac{3}{2} - f_{\text{ig}} - f_{\text{HS}} + \Gamma^* T^* = s_{\text{ig}} - f_{\text{HS}} + \Gamma^* T^* \tag{A.43}$$

From [A.39], we have the nondimensional specific heat at constant volume, *i.e.*,

$$c_v \equiv \frac{C_v}{Nk_B} = T^* \left(\frac{\partial s}{\partial T^*} \right)_{\rho_N^*} = \frac{3}{2} - f_{\text{HS}}^{(1)} T^* \left(\frac{\partial \hat{\eta}}{\partial T^*} \right)_{\rho_N^*} + \Gamma^* T^* \tag{A.44}$$

where C_v has units of J/particle·K. Other properties include the change in pressure with temperature at constant volume and number of particles, *i.e.*,

$$\begin{aligned}
 \rho_N \gamma C_v &\equiv \alpha K_T \equiv \left(\frac{\partial P}{\partial T} \right)_{V,N} = \frac{\partial}{\partial T} \Bigg|_{V,N} [\beta^{-1} p \rho_N] \\
 &= \rho_N k_B \left\{ p + T^* \left(\frac{\partial p}{\partial T^*} \right)_{\rho_N^*} \right\} \tag{A.45}
 \end{aligned}$$

Therefore,

$$\gamma_{c_v} = p + T^* \left(\frac{\partial p}{\partial T^*} \right)_{\rho_N^*} \quad [A.46]$$

From [A.38], we have

$$\begin{aligned} T^* \left(\frac{\partial p}{\partial T^*} \right)_{\rho_N^*} &= \left\{ \left(\frac{\partial \hat{\eta}}{\partial T^*} \right)_{\rho_N^*} - \frac{\hat{\eta}}{T^*} \right\} \Delta H_{,\hat{\eta}} \\ &+ \left\{ [f_{HS}^{(1)} + \hat{\eta} f_{HS}^{(2)}] + \frac{\hat{c}}{3} \Delta H_{,\hat{\eta}\hat{c}} + \hat{\eta} \Delta H_{,\hat{\eta}\hat{\eta}} \right\} \left(\frac{\partial \hat{\eta}}{\partial T^*} \right)_{\rho_N^*} \\ &+ \frac{1}{2} \gamma_e \Gamma^* T^* \end{aligned} \quad [A.47].$$

The isothermal bulk modulus is given by

$$\begin{aligned} K_T &\equiv \rho \left(\frac{\partial P}{\partial \rho} \right)_{T,N} = \rho_N^* \left(\frac{\partial}{\partial \rho_N^*} \right)_{T^*} [\beta^{-1} \rho_N P] \\ &= \beta^{-1} \rho_N [p + \rho_N^* \left(\frac{\partial p}{\partial \rho_N^*} \right)_{T^*}] \end{aligned} \quad [A.48].$$

The nondimensional form of this is then

$$k_T \equiv \beta K_T / \rho_N = p + \rho_N^* \left(\frac{\partial p}{\partial \rho_N^*} \right)_{T^*} \quad [A.49].$$

We note that the macroscopic structure factor of the liquid, $a(0)$, is equal to $1/k_T$. From [A.38], we have

$$\begin{aligned} \rho_N^* \left(\frac{\partial p}{\partial \rho_N^*} \right)_{T^*} &= \hat{\eta} \left\{ f_{HS}^{(1)} + \frac{1}{T^*} \Delta H_{,\hat{\eta}} + \hat{\eta} [f_{HS}^{(2)} + \frac{1}{T^*} \Delta H_{,\hat{\eta}\hat{\eta}}] \right\} \\ &+ \left\{ \frac{3\hat{\eta}}{\hat{c}} [f_{HS}^{(1)} + \frac{1}{T^*} \Delta H_{,\hat{\eta}} + \hat{\eta} f_{HS}^{(2)} + \frac{1}{T^*} \Delta H_{,\hat{\eta}\hat{\eta}}] + \frac{\hat{\eta}}{T^*} \Delta H_{,\hat{\eta}\hat{c}} \right\} \rho_N^* \left(\frac{\partial \hat{c}}{\partial \rho_N^*} \right)_{T^*} \\ &- \frac{1}{2} \gamma_e^2 \Gamma^* T^* \end{aligned} \quad [A.50].$$

The second term on the right-hand side of this last expression may be written

$$\hat{\eta} \left. \frac{\partial}{\partial \hat{\eta}} \right\}_{T^*, c} \left\{ \frac{3\hat{\eta}}{\hat{c}} [f_{\text{HS}}^{(1)} + \frac{1}{T^*} \Delta H_{,\hat{\eta}}] + \frac{1}{T^*} \Delta H_{,\hat{c}} \right\}.$$

By [A.29] and the fact that

$$\Delta H_{,\hat{c}\hat{\eta}} = \Delta H_{,\hat{\eta}\hat{c}},$$

we see that this second term is actually zero. Consequently,

$$\rho_N^* \left(\frac{\partial p}{\partial \rho_N^*} \right)_{T^*} = \hat{\eta} \left\{ [f_{\text{HS}}^{(1)} + \hat{\eta} f_{\text{HS}}^{(2)}] + \frac{1}{T^*} [\Delta H_{,\hat{\eta}} + \hat{\eta} \Delta H_{,\hat{\eta}\hat{\eta}}] \right\} - \frac{1}{2} \gamma_c^2 \Gamma^* T^* \quad [\text{A.51}].$$

With [A.33]-[A.51], we may calculate equilibrium thermodynamic properties that are defined by ratios of the derivatives of f_{mod} . For example, the equilibrium thermodynamic Grüneisen's parameter is given by

$$\gamma = \frac{\gamma c_v}{c_v} \quad [\text{A.52}],$$

while the coefficient of thermal expansion is

$$\alpha = \frac{\rho \gamma c_v}{K_T} = \gamma c_v \frac{1}{T^* k_T} \frac{k_B}{\epsilon} \quad [\text{A.53}].$$

From this, a natural nondimensional form of α is

$$\alpha^* = \frac{\epsilon}{k_B} \alpha = \frac{\gamma c_v}{k_T T^*} \quad [\text{A.54}]$$

The nondimensional specific heat at constant pressure is then

$$c_p = c_v (1 + \alpha^* \gamma T^*) \quad [\text{A.55}].$$

And the nondimensional isentropic bulk modulus is given by

$$\begin{aligned} k_s \equiv \frac{\beta K_s}{\rho_N} &= k_T + k_T \alpha \gamma T = k_T + \rho_N \gamma \frac{c_v}{N} \frac{\beta}{\rho_N} \gamma T \\ &= k_T + (\gamma c_v) \gamma \end{aligned} \quad [\text{A.56}].$$

Lastly, the velocity of sound in the liquid is given by

$$v_\phi \equiv \left\{ \frac{K_s}{\rho} \right\}^{1/2} = \left\{ \frac{N_A \epsilon}{M} \right\}^{1/2} [k_s T^*]^{1/2} \quad [\text{A.57}],$$

where N_A is Avogadro's number and M is the molar mass of the liquid. The nondimensional form of v_ϕ is then

$$v_\phi^* = [k_s T^*]^{1/2} \quad [\text{A.58}].$$

To calculate the above expressions for the equilibrium properties of the liquid, we require an expression for $(\partial \hat{\eta} / \partial T^*)_{\rho_N^*}$. From [A.30], [A.31] and the implicit function theorem, we have $\hat{c} = \hat{c}(T^*, \rho_N^*)$ and $\hat{\eta} = \hat{\eta}(T^*, \rho_N^*)$ in equilibrium. In many of the above expressions, we have used the relation, from [A.31]

$$\left(\frac{\partial I_2}{\partial T^*} \right)_{\rho_N^*} = 0 \quad \rightarrow \quad \left(\frac{\partial \hat{\eta}}{\partial T^*} \right)_{\rho_N^*} = \frac{3\hat{\eta}}{\hat{c}} \left(\frac{\partial \hat{c}}{\partial T^*} \right)_{\rho_N^*} \quad [\text{A.59}].$$

From [A.30], we have

$$\begin{aligned} \left\{ \frac{\partial I_1}{\partial T^*} \right\} &= \left\{ \frac{3}{\hat{c}} \left(\frac{\partial \hat{\eta}}{\partial T^*} \right)_{\rho_N^*} - \frac{3\hat{\eta}}{\hat{c}} \left(\frac{\partial \hat{c}}{\partial T^*} \right)_{\rho_N^*} \right\} [f_{\text{HS}}^{(1)} + \frac{1}{T^*} \Delta H_{,\hat{\eta}}] \\ &+ \frac{3\hat{\eta}}{\hat{c}} \left\{ [f_{\text{HS}}^{(2)} + \frac{1}{T^*} \Delta H_{,\hat{\eta}\hat{\eta}}] \left(\frac{\partial \hat{\eta}}{\partial T^*} \right)_{\rho_N^*} + \frac{1}{T^*} \Delta H_{,\hat{\eta}\hat{c}} \left(\frac{\partial \hat{c}}{\partial T^*} \right)_{\rho_N^*} - \frac{1}{T^{*2}} \Delta H_{,\hat{\eta}} \right\} \\ &+ \frac{1}{T^*} \left[\Delta H_{,\hat{c}\hat{\eta}} \left(\frac{\partial \hat{\eta}}{\partial T^*} \right)_{\rho_N^*} + \Delta H_{,\hat{c}\hat{c}} \left(\frac{\partial \hat{c}}{\partial T^*} \right)_{\rho_N^*} \right] - \frac{1}{T^{*2}} \Delta H_{,\hat{c}} = 0 \quad [\text{A.59}]. \end{aligned}$$

Therefore, from [A.58] and [A.59], we have

$$\begin{aligned} &\left\{ \frac{\partial \ln \hat{\eta}}{\partial \ln T^*} \right\}_{\rho_N^*} \\ &= \frac{3[\hat{c} \Delta H_{,\hat{c}} + 3\hat{\eta} \Delta H_{,\hat{\eta}}]}{6\hat{\eta}[T^* f_{\text{HS}}^{(1)} + \Delta H_{,\hat{\eta}}] + 9\hat{\eta}^2[T^* f_{\text{HS}}^{(2)} + \Delta H_{,\hat{\eta}\hat{\eta}}] + 6\hat{c}\hat{\eta} \Delta H_{,\hat{\eta}\hat{c}} + \hat{c} \Delta H_{,\hat{c}\hat{c}}} \end{aligned} \quad [\text{A.60}],$$

the desired expression for the change in the equilibrium packing fraction with nondimensional temperature at constant nondimensional number density.

To fit this model to the experimental Fe melting data of Williams and Jeanloz (1986), given as $T_M(P) \pm \Delta T_M(\Delta P)$, we require an expression for the temperature as a function of pressure in the liquid at the conditions along the phase boundary. Rearranging [A.30], we obtain

$$T = \epsilon T^*(\hat{c}, \hat{\eta}; \lambda^*, \omega^*) = \frac{-E}{3\hat{\eta}f_{HS}^{(1)}} \left\{ \hat{c} \Delta H_{,\hat{c}} + 3\hat{\eta} \Delta H_{,\hat{\eta}} \right\} \quad [A.61]$$

for temperature in the liquid, with $\epsilon \equiv \epsilon/k_B$. From [A.38], we have a relation for pressure in the liquid, *i.e.*,

$$\begin{aligned} P &= \frac{R}{M} \epsilon \rho p^*(\hat{c}, \hat{\eta}; \lambda^*, \omega^*, \epsilon) \\ &= \frac{R}{M} \epsilon \rho \left\{ \hat{\eta} \Delta H_{,\hat{\eta}} + (1 + \hat{\eta}f_{HS}^{(1)})T^* + \frac{1}{2} \gamma_e \frac{E}{R} \Gamma(\rho) T^{*2} \right\} \end{aligned} \quad [A.62],$$

where $\Gamma(\rho)$ is assumed to be a known function of mass density, ρ , and so not a "free" parameter. Now, using the definition of the packing fraction, we may write \hat{c} as a function of mass density, ρ , and packing fraction, $\hat{\eta}$, *i.e.*,

$$\hat{c} = \frac{1}{\zeta} \left\{ \frac{6\hat{\eta}}{\pi\rho} \right\}^{1/3} \quad [A.63],$$

where we have introduced $\zeta \equiv \rho_N^*/\rho$, which is related to σ , *i.e.*,

$$\sigma = \zeta \left\{ \frac{M}{N_A} \right\}^{1/3} \quad [A.64].$$

With these, we have

$$T = \epsilon T^*(\rho, \hat{\eta}; \lambda^*, \omega^*, \zeta) \quad [A.65]$$

and

$$P = \frac{R}{M} \epsilon \rho p^*(\rho, \hat{\eta}; \lambda^*, \omega^*, \epsilon, \zeta) \quad [A.66],$$

giving us 2 equations relating 4 variables, *i.e.*, P , T , ρ and $\hat{\eta}$, and 4 parameters, *i.e.*, ϵ , λ^* , ω^* , ζ . These are the expressions we use in the text.

Liquid-state transport properties

With the hard-sphere model for $F_{\text{liq}}(T, \rho)$, we may also estimate near-equilibrium transport properties for Fe from the theory of Longuet-Higgins and Pople (1956) for a dense fluid of hard spheres. They derive the following relationships for the shear viscosity, μ , bulk viscosity, κ , and coefficient of self-diffusion, D , assuming $g_{\text{HS}}(r)$ is independent of the rate of strain, and for the thermal conductivity, k , assuming $g_{\text{HS}}(r)$ is independent of the temperature gradient:

$$\mu = \frac{24}{5\pi d^2} \left\{ \frac{m\epsilon}{\pi} \right\}^{1/2} T^{*1/2} \hat{\eta}(p-1) \quad [\text{A.67}],$$

$$\kappa = \frac{5}{3} \mu \quad [\text{A.68}],$$

$$k = \frac{5}{2} \frac{k_B}{m} \mu \quad [\text{A.69}],$$

and

$$D = \frac{d}{2} \left\{ \frac{\pi\epsilon}{m} \right\}^{1/2} \frac{T^{*1/2}}{(p-1)} \quad [\text{A.70}],$$

respectively. As discussed by Longuet-Higgins and Pople, the absolute values of these expressions do not reflect the influence of attractive interparticle forces. They suggest that this may be remedied by replacing the pressure, P , with the "kinetic pressure," $T(\partial P/\partial T)_v$, to account for the idea that attractive forces reduce the effective pressure in a real fluid below P , the external pressure, because they result in a decrease of internal ("cohesive") energy with density. The pressure and kinetic pressure are related by the identity

$$\left(\frac{\partial E}{\partial V} \right)_T = T \left(\frac{\partial P}{\partial T} \right)_V - P \quad [\text{A.71}]$$

where $E=F+TS$ is the internal energy. From this, we see that their suggestion implies that $(\partial E/\partial V)_T \approx 0$; this is strictly true for a fluid of hard spheres, since $F+TS=3k_B T=E$ for such a fluid. Since the liquid-state model used in this work is based on a potential that includes attractive interparticle interactions, we incorporate this suggestion into our calculations by replacing p with γ_{c_v} in [A.67]-[A.70], where γ_{c_v} is given by [A.46] above.

§7. Appendix B: High-Temperature Solid-State Model Expressions

In this appendix we document the relation between the exact solid-state model relations based on [3.1] and the high-temperature approximation (equations [3.7]-[3.10]) used in the text. From the expression for $F(T,\rho)$, [3.1], we have 1) the pressure:

$$P(T,\rho) \equiv \rho \left\{ \frac{\partial F}{\partial \ln \rho} \right\}_T \equiv P(0,\rho) + \frac{3\nu R}{M} \rho \gamma_D E_D(\chi_D) T + \frac{1}{2M} \rho \omega \Omega T^2 \quad [\text{B.1}]$$

with

$$P(0,\rho) \equiv \rho \left\{ \frac{d\Phi}{d \ln \rho} \right\} + \frac{9}{8} \nu R \rho \Theta_D \gamma_D,$$

2) The molar entropy:

$$S(T,\rho) \equiv - \left\{ \frac{\partial F}{\partial T} \right\}_V = 3\nu R \left\{ \frac{4}{3} E_D(\chi_D) - \ln[1 - e^{-\chi_D}] \right\} + \Omega T \quad [\text{B.2}],$$

3) The isothermal bulk modulus:

$$K_T(T,\rho) \equiv \rho \left\{ \frac{\partial P}{\partial \rho} \right\}_T = K(0,\rho) + \frac{3\nu R}{M} \rho \gamma_D (1 - q_D - 3\gamma_D) E_D(\chi_D) T + 9\nu R \rho \gamma_D \left\{ \frac{\gamma_D \chi_D}{[e^{\chi_D} - 1]} \right\} T$$

$$+ \frac{1}{2M} \rho \omega (1 - \omega) \Omega T^2 \quad [\text{B.3}],$$

with

$$K(0, \rho) \equiv P(0, \rho) + \rho \left\{ \rho \left\{ \frac{d\Phi}{d\rho} \right\} + \rho^2 \left\{ \frac{d^2\Phi}{d\rho^2} \right\} \right\} + \rho \left\{ \frac{9\nu R}{8M} \gamma_D \Theta_D(\gamma_D - \alpha_D) \right\},$$

4) The molar heat capacity at constant volume:

$$C_v(T, \rho) \equiv -T \left\{ \frac{\partial^2 F}{\partial T^2} \right\}_\rho = 3\nu R \left\{ 4E_D(\xi_D) - \frac{3\xi_D}{[e^{\xi_D} - 1]} \right\} + \Omega T \quad [\text{B.4}],$$

and 5) the change in pressure with temperature at constant volume (density),
i.e.,

$$\begin{aligned} \rho \gamma C_v(T, \rho) &\equiv \alpha K_T \equiv \left\{ \frac{\partial P}{\partial T} \right\}_\rho \\ &= \frac{3\nu R}{M} \rho \gamma_D \left\{ 4E_D(\xi_D) - \frac{3\xi_D}{[e^{\xi_D} - 1]} \right\} + \rho \omega \frac{\Omega}{M} T \end{aligned} \quad [\text{B.5}].$$

The high-temperature approximations ($\xi_D \equiv \Theta_D(\rho)/T \ll 1$) to P , S , C_v and K_T may be obtained from [B.2]-[B.5] by expanding $E_D(\xi_D)$ and the other ξ_D functions into their high-temperature forms, i.e., as $\xi_D \rightarrow 0$,

$$\begin{aligned} E_D &= \frac{3}{(\xi_D)^3} \int_0^{\xi_D} x^2 \left\{ 1 - \frac{1}{2}x + \frac{1}{12}x^2 + \dots \right\} dx \\ &= 1 - \frac{3}{8}\xi_D + \frac{1}{20}\xi_D^2 + O(\xi_D^3) \end{aligned} \quad [\text{B.6}],$$

$$\begin{aligned} \ln[1 - e^{-\xi_D}] &= \ln \xi_D + \ln\left(1 - \frac{1}{2}\xi_D + \dots\right) \\ &= \ln \xi_D - \frac{1}{2}\xi_D + \frac{1}{24}\xi_D^2 + O(\xi_D^3) \end{aligned} \quad [\text{B.7}],$$

and

$$\frac{\xi_D}{[e^{\xi_D} - 1]} = 1 - \frac{1}{2}\xi_D + \frac{1}{12}\xi_D^2 + O(\xi_D^3) \quad [B.8].$$

Putting these into [3.1] in the text, we obtain, to $O(\xi_D^3)$:

$$F(T, \rho) = \Phi(\rho) + 3\nu R \left\{ \ln \xi_D - 1 + \frac{1}{40}\xi_D^2 \right\} T - \frac{1}{2}\Omega T^2 \quad [B.9],$$

$$P(T, \rho) = P(0, \rho) + 3\nu R \rho \gamma_D \left\{ 1 + \frac{1}{20}\xi_D^2 \right\} T + \frac{1}{2}\rho \omega \Omega T^2 \quad [B.10],$$

with

$$P(0, \rho) \equiv \rho \left\{ \frac{d\Phi}{d \ln \rho} \right\},$$

$$S = 3\nu R \left\{ \frac{4}{3} - \ln[\xi_D] + \frac{1}{40}\xi_D^2 \right\} + \Omega T \quad [B.11],$$

$$K_T = K(0, \rho)$$

$$+ \frac{3\nu R}{M} \rho \gamma_D \left\{ (1 - \omega) \left[1 + \frac{1}{20}\xi_D^2 \right] + \frac{1}{10}\xi_D^2 \right\} T + \frac{1}{2}\rho \omega (1 - \omega) \frac{\Omega}{M} T^2 \quad [B.12],$$

with $K_T(0, \rho)$ now given by

$$K_T(0, \rho) = \rho \left\{ 2\rho \left[\frac{d\Phi}{d\rho} \right] + \rho^2 \left[\frac{d^2\Phi}{d\rho^2} \right] \right\}$$

$$\rho \gamma_V = \alpha K_T = \frac{3\nu R}{M} \rho \gamma_D \left[1 - \frac{1}{20}\xi_D^2 \right] + \rho \omega \frac{\Omega}{M} T \quad [B.13],$$

and

$$C_V = 3\nu R \left[1 - \frac{1}{20}\xi_D^2 \right] + \Omega T \quad [B.14].$$

These are the basic solid-state model relations used in the text.

§8. References

- Abelson, R. S., Monte Carlo calculations of Fe melting, *Ph.D. Dissertation*, University of California at Los Angeles, Los Angeles, 1981.
- Ahrens, T. J., D. L. Anderson, and A. E. Ringwood, Equation of state and crystal structure of high-pressure phases of shocked silicates and oxides, *Rev. Geophys.*, **7**, 667-707, 1969.
- Alder, B. J., and T. E. Wainwright, Phase transitions for a hard-sphere system, *J. Chem. Phys.*, **27**, 1208-1209, 1957.
- Anderson, O. L., The earth's core and the phase diagram of iron, *Phil. Trans. R. Soc. Lond.*, **A306**, 21-35, 1982.
- Anderson, W. W., A. J. Campbell, and T. J. Ahrens, Melting of iron sulfide and iron oxide at high pressure, *Proc. Lunar Planet. Sci. Conf. XVII*, 23-24, 1987a.
- Anderson, W. W., T. J. Ahrens, and B. Svendsen, Melting in the Fe-FeS system and its relation to the composition of the cores of earth and mars, *Proc. Lunar Planet. Sci. Conf. XVII*, 21-22, 1987b.
- Andrews, D. J., Equation of state of the alpha and epsilon phases of iron, *J. Phys. Chem. Solids*, **34**, 825-840, 1973.
- Ashcroft, N. W., and J. Lekner, Structure and resistivity of liquid metals, *Phys. Rev.*, **145**, 83-90, 1966.
- Barker, L. A., and D. Henderson, What is "liquid"? Understanding the states of matter, *Rev. Mod. Phys.*, **48**, 587-671, 1976.
- Barker, L. M., and R. E. Hollenbach, Shock wave study of the $\alpha \rightleftharpoons \epsilon$ transition in iron, *J. Appl. Phys.*, **45**, 4872-4887, 1974.
- Bass, J. D., B. Svendsen, and T. J. Ahrens, The temperatures of shock-compressed iron, *High-Pressure Research in Geophysics and Geochemistry*, edited by M. Manghnani and Y. Syono, Terra Publishing Co., Tokyo, in press, 1987.

- R. Berman, *Thermal Conduction in Solids*, 193 pp., Oxford University Press, Oxford, 1976.
- Bevington, P. R., *Data Reduction and Error Analysis for the Physical Sciences*, 336 pp., McGraw-Hill, New York, 1969.
- F. Birch, Elasticity and constitution of the earth's interior, *J. Geophys. Res.*, **57**, 227-286, 1952.
- Boness, D. A., J. M. Brown, and A. K. McMahan, The electronic thermodynamics of iron under earth's core conditions, *Phys. Earth Planet. Int.*, **42**, 227-240, 1986.
- Brown, J. M., and T. J. Shankland, Thermodynamic parameters in the earth as determined from seismic profiles, *Geophys. J. R. Astr. Soc.*, **66**, 579-596, 1980.
- Brown, J. M., and R. G. McQueen, The equation of state for iron and the earth's core, in *High Pressure Research in Geophysics*, 611-622, edited by S. Akimoto and M. H. Manghnani, Academic Press, New York, 1982.
- Brown, J. M., T. J. Ahrens, and D. L. Shampine, Hugoniot data for pyrrhotite and the earth's core, *J. Geophys. Res.*, **89**, 6041-6048, 1984.
- Brown, J. M., and R. G. McQueen, Phase transitions, Grüneisen parameter and elasticity for shocked iron between 77 GPa and 400 GPa, *J. Geophys. Res.*, **91**, 7485-7494, 1986.
- Busch G., and H.-J. Güntherodt, Electronic properties of liquid metals and alloys, *Solid State Phys.*, **29**, 235-313, 1974.
- Carnaghan, N. F., and K. E. Starling, Compressibility equation of state for hard spheres, *J. Chem. Phys.*, **51**, 635-645, 1969.
- Desai, P. D., Thermodynamic properties of iron and silicon, *J. Phys. Chem. Ref. Data*, **15**, 967-983, 1986.
- Drotning, W. D., Thermal expansion of iron, cobalt, nickel and copper at temperatures up to 600 K above melting, *High Temp.-High Pressures*, **13**,

- 441-458, 1981.
- Filipov, S. I., N. B. Kazov, and L. A. Pronin, Velocities of ultrasonic waves, compressibility of liquid metals, and their relation to various physical properties (in Russian), *Izv. v̄yssh. ucheb. Zaved. chern. Metall.*, No. 9, 8-14, 1966.
- Foiles, S. M., and N. W. Ashcroft, Variational theory of phase separation in binary liquid mixture, *J. Chem. Phys.*, **75**, 3954-3958, 1981.
- Gans, R. F., Viscosity of the earth's core, *J. Geophys. Res.*, **77**, 360-366, 1972.
- Gopal Rao, R. V., and D. Sen, Structure factor and isothermal compressibility of liquid transition metals, *Ind. J. Pure Appl. Phys.*, **14**, 853-855, 1976.
- Gopal, E. S. R. *Specific Heat at Low Temperatures*, 240 pp., Plenum Press, New York, 1966.
- Grover, R., Liquid-metal equation-of-state based on scaling, *J. Appl. Phys.*, **55**, 3435-3441, 1971.
- Gschneider, K. A., Physical properties and inter-relationships of metallic and semi-metallic elements, *Sol. State Phys.*, **16**, 275-426, 1964.
- Hansen, J. P., and I. R. McDonald, *Theory of Simple Liquids*, 350 pp., Academic Press, New York, 1976.
- Hultgren, R., P. D. Desai, D. T. Hawkins, M. Gleiser, K. K. Kelly, and D. D. Wagman, *Selected Values of the Thermodynamic Properties of the Elements*, American Society of Metals, Metal Park, Ohio, 1973.
- Isihara, A., The Gibbs-Bogolyubov inequality, *J. Phys. A (Proc. Phys. Soc.)*, ser. 2, **1**, 539-548, 1968.
- Jacobs, J. A., *The Earth's Core*, 253 pp., Academic Press, New York, 1975.
- Jamieson, J. C., H. H. Demarest, Jr. and D. Schieferl, A reevaluation of the Grüneisen's parameter for the earth's core, *J. Geophys. Res.*, **83**, 5929-5935, 1978.
- Janle, P. and R. Meissner, Structure and evolution of the terrestrial planets,

- Surv. Geophys.*, **8**, 107-186, 1986.
- Jeanloz, R., Properties of iron at high pressures and the state of the core, *J. Geophys. Res.*, **84**, 6059-6069, 1980.
- Jeanloz, R., and T. J. Ahrens, Equations of state of FeO and CaO, *Geophys. J. R. Astr. Soc.*, **62**, 505-528, 1980.
- Jeanloz, R., and F. M. Richter, Convection, composition and the thermal state of the lower mantle, *J. Geophys. Res.*, **84**, 5497-5504, 1979.
- Jephcoat, A. P., H. K. Mao and P. M. Bell, Static compression of iron to 78 GPa with rare gas solids as pressure-transmitting media, *J. Geophys. Res.*, **91**, 4677-4686, 1986.
- King, H. E., Jr., and C. T. Prewitt, High-pressure and high-temperature polymorphism of iron sulfide (FeS), *Acta. Cryst.*, **B38**, 1877-1887, 1982.
- E. Knittle and R. Jeanloz, The melting of metallic FeO to over 100 GPa: Implications for core temperature and composition, *Proc. Lunar Planet. Sci. Conf. XVIII*, 495-496, 1987.
- Knopoff, L., and G. F. MacDonald, Earth core reported not to be pure iron, *Sci. News Lett.*, **75**, 307, 1959.
- Knopoff, L., and J. N. Shapiro, Pseudo Grüneisen parameter for liquids, *Phys. Rev. B*, **1**, 3893-3985, 1970.
- Kurz, W., and B. Lux, Velocity of sound in iron and iron alloys in the solid and molten state, *High Temp.-high Press.*, **1**, 387-399, 1969.
- Liu, L.-G., and W. A. Bassett, The melting of iron up to 200 kbar, *J. Geophys. Res.*, **80**, 3277-3282, 1975.
- Longuet-Higgins, H. C., and J. A. Pople, Transport properties of a dense fluid of hard spheres, *J. Chem. Phys.*, **25**, 884-889, 1956.
- Mansoori, G. A., and F. B. Canfield, Variational approach to the equilibrium thermodynamic properties of simple liquids. I, *J. Chem. Phys.*, **51**, 4958-4967, 1969.

- McQueen, R. G., and S. P. Marsh, Shock-wave compression of iron-nickel alloys and the earth's core, *J. Geophys. Res.*, **71**, 1751-1756, 1966.
- McQueen, R. G., S. P. Marsh and J. N. Fritz, Hugoniot equation of state of twelve rocks, *J. Geophys. Res.*, **72**, 4999-5036, 1967.
- O'Connell, R. J., and B. H. Hager, On the thermal state of the earth, in *Physics of the Earth's Interior*, Enrico Fermi International School of Physics, Course 78, 270-317, edited by A. Dziewonski and E. Boschi, North-Holland, Amsterdam, 1980.
- Percus, J. E., and G. J. Yevick, Analysis of Classical Statistical Mechanics by Means of Collective Coordinates, *Phys. Rev.*, **110**, 1-13, 1959.
- Pichulo, R. O., T. Takahashi, and J. S. Weaver, High pressure polymorphs of FeS (abstract), *EOS*, **57**, 340, 1976.
- Press, W. H., B. P. Flannery, S. A. Teukolsky, and W. T. Vetterling, *Numerical Recipes: The Art of Scientific Computing*, 818 pp., Cambridge University Press, New York, 1986.
- Prigogine, I., and R. Defay, *Chemical Thermodynamics*, 500 pp., Longmans Green and Co., London, 1954.
- Rice, M. H., R. G. McQueen and J. M. Walsh, Compression of solids by strong shock waves, *Sol. State Phys.*, **6**, 1-63, 1958.
- Robie, R. A., B. S. Hemingway, and J. R. Fisher, Thermodynamic properties of minerals and related substances at 298.15 K and 1 bar (10^5 Pascals) pressure and at higher temperatures, 456 pp., *USGS Bulletin 1452*, 1978.
- Ruoff, A. I., Linear shock-velocity-particle-velocity relationship, *J. Appl. Phys.*, **38**, 4976-4980, 1967.
- Ringwood, A. E., *Origin of the Earth and Moon*, 259 pp., Springer-Verlag, New York, 1979.
- Spiliopoulos, S. A., and F. D. Stacey, The earth's thermal profile: Is there a mid-mantle thermal boundary layer?, *J. of Geodynamics*, **1**, 67-77, 1984.

- Stacey, F. D., A thermal model of the earth, *Phys. Earth Planet. Inter.*, **15**, 341-348, 1977.
- Stacey, F. D., and R. D. Irvine, Theory of melting: Thermodynamic basis of Lindemann's law, *Aust. J. Phys.*, **30**, 631-640, 1978.
- Stacey, F. D., B. J. Brennan and R. D. Irvine, Finite strain theories and comparisons with seismological data, *Geophys. Surv.*, **4**, 189, 1981.
- Stacey, F. D., and D. E. Loper, Thermal histories of the core and mantle, *Phys. Earth Planet. Inter.*, **36**, 99-115, 1984.
- Stevenson, D. J., Application of liquid-state physics to the earth's core, *Phys. Earth Planet. Int.*, **22**, 42-52, 1980.
- Stevenson, D. J., Models of the earth's core, *Science*, **214**, 611-618, 1981.
- Stishov, S. M., The thermodynamics of melting of simple substances, *Sov. Phys. Usp.*, **17**, 625-643, 1975.
- Svendsen, B., J. D. Bass and T. J. Ahrens, Optical radiation from shock-compressed interfaces and materials, submitted to *Phys. Reports*, 1987 (Chapter I).
- Wallace, D. C., *Thermodynamics of Crystals*, 484 pp., John Wiley and Sons, Inc., New York, 1972.
- Wertheim, M. S., Exact solution of the Percus-Yevick integral equation for hard spheres, *Phys. Rev. Lett.*, **10**, 321-323, 1963.
- Verhoogen, J., Heat balance of the earth's core, *Geophys. J.* **4**, 276, 1961.
- Vorob'ev, Yu. N., G. S. Yur'ev, E. A. Klimenkov, B. A. Baum, and Yu. A. Bazin, Interior interaction in melts of iron, cobalt and nickel (in Russian), *Izv. Vyssh. Uchebn. Zaved., Fiz., No. 1*, 146-149, 1977.
- Waseda, Y., and M. Ohtani, Static structure of liquid noble and transition metals by X-ray diffraction, *Phys. stat. sol. (b)*, **62**, 535-546, 1974.
- Williams, Q., and R. Jeanloz, Melting of Fe and FeS to 100 GPa, *EOS*, **68**, 1043, 1986.

- Williams, Q., R. Jeanloz, J. D. Bass, B. Svendsen and T. J. Ahrens, The melting curve of iron to 2.5 Mbar: First experimental constraint on the temperature at the earth's center, *Science*, **214**, 1020-1022, 1987.
- Yokoyama, I., I. Ohkoshi and T. Satoh, Thermodynamic properties of liquid Fe, Co and Ni based on the Perkus-Yevick phonon description, *J. Phys. F: Met. Phys.*, **13**, 729-737, 1983.
- Young, D. A., and R. Grover, Theory of the iron equation of state and melting curve to very high pressures, *Shock Waves in Condensed Matter - 1983*, 65-67, edited by J. R. Asay, R. A. Graham and G. K. Straub (eds.), Elsevier Science Publishers B. V., 1984.
- Zwanzig, R. W., High-temperature equation of state by a perturbation method. I. Nonpolar gases, *J. Chem. Phys.*, **22**, 1420-1428, 1954.